Exploration of Aromaticity, Through-Space Effect, and Nature of CC Bonds in Chemistry using Molecular Electrostatic Potential Analysis

By

ANJALI KRISHNA P. K.
10CC18A39002

A thesis submitted to the
Academy of Scientific & Innovative Research
for the award of the degree of

DOCTOR OF PHILOSOPHY
in
SCIENCE

Under the supervision of
Dr. C. H. SURESH

**CSIR-National Institute for Interdisciplinary
Science and Technology (CSIR-NIIST)
Thiruvananthapuram – 695019, India**

Academy of Scientific and Innovative Research
AcSIR Headquarters, CSIR-HRDC campus
Sector 19, Kamla Nehru Nagar,
Ghaziabad, U.P. – 201 002, India

December 2023

Council of Scientific & Industrial Research
National Institute for Interdisciplinary Science and Technology
Thiruvananthapuram-695019, Kerala, India

Dr. C. H. Suresh
Chief Scientist
Chemical Sciences & Technology Division
Tel: +91- 4712515472
E-mail: sureshch@gmail.com
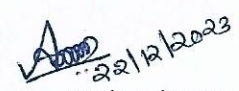   sureshch@niist.res.in

CERTIFICATE

This is to certify that the work incorporated in this Ph.D. thesis entitled, "**Exploration of Aromaticity, Through-Space Effect, and Nature of CC Bonds in Chemistry using Molecular Electrostatic Potential Analysis**", submitted by Anjali Krishna P. K. to the Academy of Scientific and Innovative Research (AcSIR) in fulfillment of the requirements for the award of the Degree of Doctor of Philosophy in Science, embodies original research work carried-out by the student. We, further certify that this work has not been submitted to any other University or Institution in part or full for the award of any degree or diploma. Research materials obtained from other sources and used in this research work have been duly acknowledged in the thesis. Images, illustrations, figures, tables *etc.*, used in the thesis from other sources, have also been duly cited and acknowledged.

22/12/2023

Anjali Krishna P. K.

22/12/2023

22/12/2023

Dr. C. H. Suresh

22/12/2023

STATEMENTS OF ACADEMIC INTEGRITY

I Anjali Krishna P. K., a Ph.D. student of the Academy of Scientific and Innovative Research (AcSIR) with Registration No. 10CC18A39002 hereby undertake that, the thesis entitled **"Exploration of Aromaticity, Through-Space Effect, and Nature of CC Bonds in Chemistry using Molecular Electrostatic Potential Analysis"** has been prepared by me and that the document reports original work carried out by me and is free of any plagiarism in compliance with the UGC Regulations on *"Promotion of Academic Integrity and Prevention of Plagiarism in Higher Educational Institutions (2018)"* and the CSIR Guidelines for *"Ethics in Research and in Governance (2020)"*.

Date : 22/12/2023
Place : Thiruvananthapuram

It is hereby certified that the work done by the student, under my supervision, is plagiarism-free in accordance with the UGC Regulations on *"Promotion of Academic Integrity and Prevention of Plagiarism in Higher Educational Institutions (2018)"* and the CSIR Guidelines for *"Ethics in Research and in Governance (2020)"*.

Name : Dr. C. H. Suresh
Date : 22/12/2023
Place : Thiruvananthapuram

DECLARATION

I, Anjali Krishna P. K. bearing AcSIR Registration No. 10CC18A39002 declare:

(a) that my thesis entitled, "**Exploration of Aromaticity, Through-Space Effect, and Nature of CC Bonds in Chemistry using Molecular Electrostatic Potential Analysis**" is plagiarism free in accordance with the UGC Regulations on *"Promotion of Academic Integrity and Prevention of Plagiarism in Higher Educational Institutions (2018)"* and the CSIR Guidelines for *"Ethics in Research and in Governance (2020)".*

(b) that I would be solely held responsible if any plagiarised content in my thesis is detected, which is violative of the UGC regulations 2018.

22/12/2023

Date : 22/12/2023

Place: Thiruvananthapuram

iv

Acknowledgements

CONTENTS

Chapter 1

Part A: Molecular Electrostatic Potential Analysis: An Overview

Chapter 2

Part A: Electrostatic Topological Viewpoint of π-Conjugation and Aromaticity of Hydrocarbons

Part B: Antiaromaticity-Aromaticity Interplay in Fused Benzenoid Systems using Molecular Electrostatic Potential Topology

Chapter 3
Part A: Electrostatic Potential for Exploring Electron Delocalization in Infinitenes, Circulenes, and Nanobelts

Part B: Utilization of Through-Space Effect to Design Donor-Acceptor Systems without Donors and Acceptors

Chapter 4

Topology of Electrostatic Potential and Electron Density Reveals Covalent to Non-Covalent Carbon-Carbon Bond Continuum

List of Figures

List of Tables

ABBREVIATIONS

A	- Acceptor
A-aA	- Aromatic-antiaromatic
ACID	- Anisotropy of the Induced Current Density
AIM	- Atoms in Molecules
AIMD	- *Ab initio* Molecular Dynamics
AM	- Austin Model
An	- Aniline
APT	- Atomic Polar Tensor
Az	- Azulene
BC	- Benzene-Cyclobutadiene
BCP	- Bond Critical Point
BLA	- Bond Length Alternation
bnp	- Bare Nuclear Potential
BO	- Born–Oppenheimer
BP	- Benzene-Pentalene
CC	- Coupled Cluster
CCP	- Cage Critical Point
CCSD	- Coupled Cluster Single and Double
CI	- Configuration Interaction
CNB	- Carbon Nanobelts
CNT	- Carbon Nanotubes
CP	- Critical Point
D	- Donor
DAMQT	- Deformed Atoms in Molecules in Quantum Theory
DFT	- Density Functional Theory
DPC	- Decapyrrolylcorannulene
DZ	- Double Zeta
$\vec{E}$	- Electric Field
ECP	- Effective Core Potentials
EPIC	- Electrostatic Potential for Intermolecular Complexation
$\vec{F}$	- Force
FET	- Field Effect Transistor
FMO	- Frontier Molecular Orbitals
FORS	- Full-Optimized Reaction Space
G09	- Gaussian 09
G16	- Gaussian 16
GGA	- Generalized Gradient Approximation
GTO	- Gaussian-Type Orbitals
HLG	- HOMO-LUMO gap
HF	- Hartree-Fock
HK	- Hohenberg-Kohn
HOMO	- Highest Occuppied Molecular orbital
HPB	- Hexapyrrolylbenzene

I	- Indole
iI	- Isoindole
KE	- Kinetic Energy
KS	- Kohn Sham
LDA	- Local Density Approximation
LED	- Light-Emitting Diodes
LSDA	- Local Spin Density Approximation
LUMO	- Lowest Unoccupied Molecular Orbital
m-GGA	- *meta*-Generalized Gradient Approximation
MED	- Molecular Electron Density
MESP	- Molecular Electrostatic Potential
MD	- Molecular Dynamics
MM	- Molecular Mechanics
MNDO	- Modified Neglect of Diatomic Overlap
MO	- Molecular Orbital
MP	- Møller-Plesset Perturbation Theory
NC	- Naphthalene-Cyclobutadiene
NDDO	- Neglect of Diatomic Differential Overlap
NICS	- Nuclear Independent Chemical Shift
NMR	- Nuclear Magnetic Resonance
NP	- Naphthalene-Pentalene
OM	- Orthogonalization Models
OPN	- Octapyrrolylnaphthalene
OPV	- Organic Photovoltaics
P	- Pyrrole
PBH	- Polycyclic Benzenoid Hydrocarbon
PES	- Potential Energy Surface
PhC	- Phenanthrene-Cyclobutadiene
PhDP	- Phenyldiyrrole
PhP	- Phenyl Pyrrole
PM	- Parametric Method
PoED	- Polarization of Electron Density
PyC	- Pyrene-Cyclobutadiene
Q	- Quadruple
QM	- Quantum Mechanics
RCP	- Ring Critical Point
RG	- Runge-Gross
SCF	- Self Consistent Field
STO	- Slater-Type Orbitals
T	- Triple
TDDFT	- Time-Dependent Density Functional Theory
TBE	- Through-Bond Effect
TS	- Transition State
TSE	- Through-Space Effect
XC	- Exchange Correlation

PREFACE

Molecular Electrostatic Potential (MESP) analysis is a powerful computational technique employed in theoretical chemistry to investigate the electrostatic properties of molecules. By examining the distribution of electrostatic potential throughout a molecule, MESP analysis provides essential insights into its reactivity, intermolecular interactions, and other chemical behavior of the molecules. This tool plays a crucial role in understanding the charge distribution and identifying regions of positive and negative potential, enabling researchers to predict reaction sites and study various chemical reactions, making it an indispensable tool in modern chemical research.

The MESP analysis demands the computation of electrostatic potential at discrete points in the three-dimensional space surrounding a molecule. This calculation is accomplished through quantum mechanics-based techniques, such as density functional theory (DFT) or *ab initio* calculations. By solving the Schrödinger wave equation for the molecule, these methods offer valuable insights into the distribution of electron density, allowing to map the electrostatic potential and understand how charges are distributed throughout the molecular system. Several fundamental theorems and principles govern the behavior of electric charges and electric fields in electrostatics. The theorems, principles, and equations from quantum chemistry and theoretical physics are essential for providing the theoretical underpinning, computational methodologies, and interpretive tools necessary for understanding and discussing MESP and its implications in molecular modelling and chemical analysis. The profound insights gained from analyzing electrostatic properties make MESP a fundamental and indispensable tool in the realm of theoretical chemistry. The research seeks to address the following key challenges;

Aromaticity and MESP: Aromaticity, a foundational element in the fabric of organic chemistry, embodies a captivating and enduring concept that has significantly influenced our comprehension of molecular structure and reactivity. Can MESP be employed effectively to characterize, quantify, and correlate the electrostatic properties associated

with aromatic/antiaromatic/nonaromatic compounds, offering new insights into the nature of aromaticity and introduce a novel approach for its quantification?

Through-Space Effect: Electronic effects operating through the interconnected network of both σ- and π-bonds are collectively referred to as the through-bond effect, encompassing resonance and inductive effects. In contrast, the through-space effect (TSE) involves electronic interactions between atoms or groups not directly bonded but influencing each other through three-dimensional space. Can we exclusively explore TSE using MESP to deepen our understanding of how molecular geometry and conformation impact electronic properties?

CC Bonds and MESP: The dominance of the carbon-carbon (CC) bond stands out prominently among various linkages in organic molecules. Can the electronic characteristics of diverse CC interactions, encompassing both covalent and noncovalent interactions, be effectively examined using MESP? This study aims to pioneer the integration of all forms of CC interactions, including transition states, to unify and categorize them within a comprehensive framework. By addressing these objectives, the thesis endeavors to illuminate the multifaceted applications of MESP analysis. It aims to showcase the potential of MESP in offering a unified perspective on the electrostatic properties of molecules and CC bonds within the realm of chemistry.

The thesis is structured into four chapters. Part A of Chapter 1 conveys an overview of the MESP including discrete charge electrostatic field and potential, electrostatic theorems, history and development, topology concepts, applications and a general comparison with the concept of molecular electron density (MED). The part B gives an overview of computational chemistry and methodologies employed in the thesis.

Chapter 2 is divided in two parts, where Part A deals with MESP topological study conducted for a variety of conjugated hydrocarbons to understand their π-conjugation features and aromaticity. The value of MESP minimum (V_m) is related to the localized/delocalized distribution of π-electron density. The V_m are located interior to the rings in polycyclic benzenoid hydrocarbons (PBHs) whereas they lie outside the boundary of the rings in antiaromatic and in fused systems consisting of aromatic and

antiaromatic moieties. The V_m points lie on top and bottom of the π-regions in linear polyenes and annulenes, while a degenerate distribution of CPs around the midpoint region of triple bonds is observed in alkynes. The eigenvalues λ_1, λ_2 and λ_3 of the Hessian matrix at V_m are used to define the aromatic character of the cyclic structures. The eigenvalues follow the trend $\lambda_1 \gg \lambda_2 > \lambda_3 \cong 0$ in PBHs, $\lambda_1 > \lambda_2 > \lambda_3 \cong 0$ in linear polyenes and $\lambda_1 > \lambda_2 > \lambda_3 \neq 0$ in antiaromatic systems. The difference in the aromatic character of PBHs from that of benzene is related with the deviations $\Delta\lambda_1$, $\Delta\lambda_2$ and $\Delta\lambda_3$. The total deviation $\sum_{i=1}^{3} \Delta\lambda_i$ is found to be ≤ 0.011 au for all aromatic systems and lies between 0.011 to 0.035 au for all non-aromatic systems. For antiaromatic systems its value is found to be above 0.035 au. Further, $\sum_{i=1}^{3} \Delta\lambda_i$ gives a direct interpretation of Clar's aromatic sextet structures for PBHs. Part B deals with the phenomenon of antiaromaticity-aromaticity interplay in aromatic-antiaromatic (A-aA) fused systems is studied using MESP analysis, which clearly brings out the electron rich π-regions of molecular systems. Benzene, naphthalene, phenanthrene and pyrene are the aromatic units and cyclobutadiene and pentalene are the antiaromatic units considered to construct the A-aA fused systems. The fused system is seen to reduce the antiaromaticity by adopting a configuration containing least number of localized bonds over antiaromatic moieties. This is clearly observed in twenty-five isomers of fused system composed of three naphthalene and two cyclobutadiene units. Denoting the number of π-bonds in the cyclobutadiene rings by the notation (n, n'), the systems belonging to the class (0, 0) and (2, 2) turn out to be the most and least stable configurations respectively. The stability of the fused system depends on the empty π-character of antiaromatic ring, hence naphthalene and benzene prefer to fuse with cyclobutadiene in linear and angular fashion respectively. Generally, a configuration with maximum number of 'empty' rings (0, 0, 0, ...) is considered to be the most stable for the given A-aA system. The stability and aromatic/antiaromatic character of A-aA fused systems with pentalene is also interpreted in a similar way. MESP topology clearly bringing out the distribution of double bonds in the fused systems, leads to a simple interpretation of the aromatic/antiaromatic character of them. Also it leads to powerful predictions on stable macrocyclic A-aA systems.

Chapter 3 is divided in two sections, wherein Part A discusses the π-conjugation, aromaticity, and stability of the newly synthesized 12-infinitene, and of other infinitenes comprising 8-, 10-, 14- and 16-arene rings are investigated using DFT. The π-electron delocalization and aromatic character rooted in infinitenes are quantified in terms of MESP topology. Structurally, the infinitene bears a close resemblance of its helically twisted structure to the infinity symbol. The MESP topology shows that, infinitene possesses an infinity-shaped delocalization of the electron density that streams over the fused benzenoid rings. The parameter $\sum_{i=1}^{3}\Delta\lambda_i$, derived from the eigenvalues (λ_i) corresponding to the MESP minima, is used for quantifying the aromatic character of arene rings of infinitene. The structure, stability and MESP topology features of 8-, 10-, 12-, 14-, and 16-infinitenes are also compared with the corresponding isomeric circulenes and carbon nanobelts. Further, the strain in all such systems is evaluated by considering isomeric planar benzenoid hydrocarbons as reference systems. The 12-infinitene turns out to be the most aromatic and the least strained among all the systems examined. Part B discusses the underlying phenomenon of through-space effect (TSE), which imparts electron donor-acceptor properties to a wide range of chemical systems, including derivatives of pyrrole, indole, isoindole, azulene, and aniline. The TSE is inherent in pyrrole owing to strong polarization of electron density (PoED) from the formally positively charged N-center to the C_3C_4 bonding region. The N→C_3C_4 directional nature of TSE has been effectively employed to design molecules with high charge separation, such as bipyrroles, polypyrroles, phenyl pyrroles, multi-pyrrolyl systems and N-doped nanographenes. In core-expanded structures, the direction of TSE from pyrrole units towards the core leads to highly electron-rich systems, while the opposite arrangement results in highly electron-deficient systems. Similarly, the MESP analysis reveals the presence of TSE in azulene, indole, isoindole, and aniline. Oligomeric chains of these systems are designed in such a way that the direction of TSE is consistent across each monomer, leading to substantial charge separation between the first and last monomer units. Notably, these designed systems exhibit strong donor-acceptor characteristics despite the absence of explicit donor and acceptor moieties, which is supported by FMO analysis, APT charge, NMR data and λ_{max}. Among the systems studied,

the TSE of many experimentally known systems (bipyrroles, phenyl pyrroles, hexapyrrolylbenzene, octapyrrolylnaphthalene, decapyrrolylcorannulene, polyindole, polyazulene *etc.*) is unraveled for the first time, while numerous new systems (polypyrroles, polyisoindole, amino-substituted benzene polymer) are predicted as promising materials for the creation of donor-acceptor systems for optoelectronic applications. These findings demonstrate the potential of TSE in molecular design and provide new avenues for creating functional materials.

The Chapter 4 discusses the covalent and non-covalent nature of carbon-carbon (CC) interactions in a wide range of molecular systems can be characterized using various methods, including the analysis of MESP and MED. These techniques provide valuable insights into the bonding between carbon atoms in different molecular environments. By uncovering a fundamental exponential relationship between the distance of the CC bond and the highest eigenvalue (λ_{v1}) of $V(\mathbf{r})$ at the bond critical point (BCP), this study establishes the continuum model for all types of CC interactions, including transition states. The continuum model is further delineated into three distinct regions, namely covalent, borderline cases, and non-covalent, based on the gradient, λ'_{v1} with the bond distance of the CC interaction. For covalent interactions, this parameter exhibits a more negative value than -5.0 au/Å, while for non-covalent interactions, it is less negative than -1.0 au/Å. Borderline cases, which encompass transition state structures, fall within the range of -1.0 to -5.0 au/Å. Furthermore, this study expands upon Popelier's analysis of the Laplacian of the MED, denoted as $\nabla^2\rho$, to encompass the entire spectrum of covalent, non-covalent, and borderline cases of CC interactions. Therefore, the study presents compelling evidence supporting the concept of a continuum model for CC bonds in chemistry. Additionally, this continuum model is further explored within the context of C-N, C-O, C-S, N-N, O-O, and S-S interactions, albeit with a limited dataset.

MESP's unique ability to offer a comprehensive perspective on electrostatic properties while concurrently probing aromaticity, through-space effects, and CC bonds firmly establishes it as a valuable asset in the toolkit of contemporary chemists. This exploration opens up new horizons for research and innovation, setting the platform for exciting discoveries and applications in the constantly evolving background of chemistry.

Part A:

Molecular Electrostatic Potential Analysis: An Overview
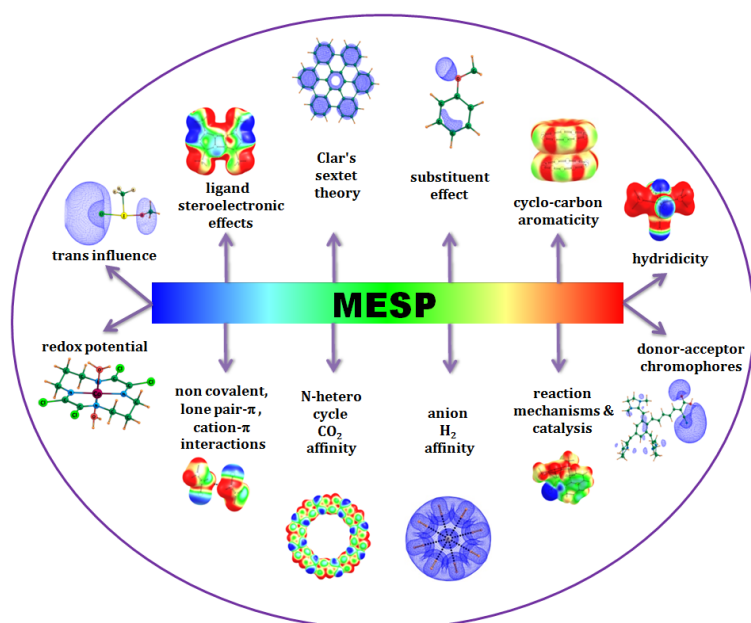
Part B:

Computational Methodology

Part A

Molecular Electrostatic Potential Analysis: An Overview

1.1 Molecular Electrostatic Potential analysis: Fundamental Concepts, Theorems and Progression

Molecular Electrostatic Potential (MESP) analysis is a powerful computational technique employed in theoretical chemistry to investigate the electrostatic properties of molecules.[1, 2] By examining the distribution of electrostatic potential throughout a molecule, MESP analysis provides essential insights into its reactivity, intermolecular interactions, and other chemical behaviour of the molecules.[3] This tool plays a crucial role in understanding the charge distribution and identifying regions of positive and negative potential, enabling researchers to predict reaction sites and study various chemical processes, making it an indispensable tool in modern chemical research.[4]

MESP analysis demands the computation of electrostatic potential at discrete points in the three-dimensional space surrounding a molecule. This calculation is accomplished through quantum mechanics-based techniques, such as Density Functional Theory (DFT)[5, 6] or *ab initio* calculations.[7] By solving the Schrödinger wave equation for the molecule, these methods offer valuable insights into the distribution of electron density, allowing to map the electrostatic potential and understand how charges are distributed throughout the molecular system.[4] The profound insights gained from analyzing electrostatic properties make MESP a fundamental and vital tool in the realm of theoretical chemistry.[8]

1.1.1 Discrete Charge Electrostatic Field and Potential

The core of MESP analysis lies on the concept of partial charges.[9] Within a molecule, atoms consist of positively charged protons in the nucleus and negatively charged electrons outside. Due to the variations in electronegativity, electrons are not equally shared between the atoms, resulting in partial charges on individual atoms. These partial charges collectively give rise to an electrostatic field that surrounds the molecule. The molecular properties, reactivity and other interactive behaviour of the molecular systems are purely influenced by the distribution of these charges, making MESP analysis a valuable tool for understanding molecular properties and behaviour.

The force acting on a positive test charge or a proton placed at a position p(x,y,z) through the electric charge cloud created by molecules, electrons, and nuclei is referred to as the MESP at that particular position in the vicinity of a molecule. This is a real physical quantity that may be measured both theoretically and experimentally using x-ray diffraction studies.[10] The foundation of this concept can be traced back to Coulomb's law, an experimental law that quantifies the force between two stationaries, electrically charged particles.[11] As per Coulomb's law, the force of attraction or repulsion between two point charges $(\vec{F})$ is directly proportional to the product of the charges and inversely proportional to the square of the distance between them:

$$\vec{F} = \frac{q_1 q_2 \hat{\mathbf{r}}}{4\pi\varepsilon_0 r^2}$$

Eq. 1.1

where 'r' is the distance of separation between the two point charges q_1 and q_2. $4\pi\varepsilon_0$ is the proportionality constant wherein ε_0 is the permittivity of a vacuum. The $\hat{\mathbf{r}}$ is the unit vector joining the position vectors q_1 and q_2.
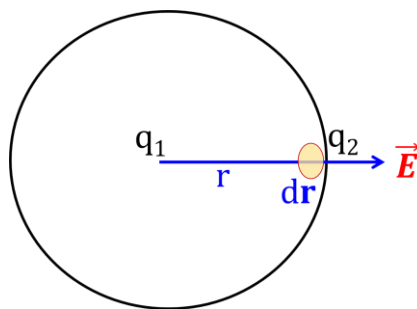
Figure 1.1 Representation of electric filed $(\vec{E})$ due to the point charge q, formed at the position **r**

The electric filed ($\vec{E}$) due to the point charge q, formed at the position **r** (Figure 1.1) can be written as,

$$\vec{E} = \frac{q\mathbf{r}}{4\pi\varepsilon_0|\mathbf{r}^3|} \qquad \text{Eq. 1.2}$$

Consider a system that has several point charges (q_i). For such systems, the overall electric field is represented as the vector sum of the electric fields ($\vec{E}_i$) produced by the individual charges,

$$\vec{E}(\mathbf{r}) = \sum_\alpha \vec{E}_i(\mathbf{r}) \qquad \text{Eq. 1.3}$$

$$\vec{E}(\mathbf{r}) = \frac{1}{4\pi\varepsilon_0} \sum_i \frac{q_i(\mathbf{r}-\mathbf{r}_i)}{|\mathbf{r}-\mathbf{r}_i|^3} \qquad \text{Eq. 1.4}$$

The work done (W) in bringing the test positive charge 'q' from a position A to B in an electric field $\vec{E}$ is given by

$$W = -q \int_{\mathbf{r}_A}^{\mathbf{r}_B} \vec{E}.\,d\mathbf{r} \qquad \text{Eq. 1.5}$$

where $d\mathbf{r}$ is the infinitesimally small displacement in position.

The work done might be referred to as the potential difference given as,

$$W = \Delta V = V_B - V_A \qquad \text{Eq. 1.6}$$

The electrostatic potential, V produced by the single point charge, q_1 at a reference point, $\mathbf{r}_a$ can be defined as the work done in bringing the test positive charge from infinity to a reference point,

$$V = \int_\infty^{\mathbf{r}_a} \frac{q_1}{4\pi\varepsilon_0\mathbf{r}^2} d\mathbf{r} \qquad \text{Eq. 1.7}$$

$$V = \frac{q_1}{4\pi\varepsilon_0\mathbf{r}_a} \qquad \text{Eq. 1.8}$$

Likewise, the potential at a point '**r**' due to a number of point charges 'q_i' located at '$\mathbf{r}_i$' can be represented as,

$$V(\mathbf{r}) = \frac{1}{4\pi\varepsilon_0} \sum_i \frac{q_i}{|\mathbf{r}-\mathbf{r}_i|} \qquad \text{Eq. 1.9}$$

Born-Oppenheimer (BO) approximation treats nuclei as stationary point charges while electrons contain a continuous charge distribution, $\rho(\mathbf{r}')$. Therefore, the charge

distribution in an infinitesimally small volume element $d^3\mathbf{r}'$ around the point $\mathbf{r}'$ is $\rho(\mathbf{r}')d^3\mathbf{r}'$. Hence, the overall potential generated at the point '$\mathbf{r}$' can be given as,

$$V(\mathbf{r}) = \frac{1}{4\pi\varepsilon_0} \int \frac{\rho(\mathbf{r}')}{|\mathbf{r} - \mathbf{r}'|} d^3\mathbf{r}' \qquad \text{Eq. 1.10}$$
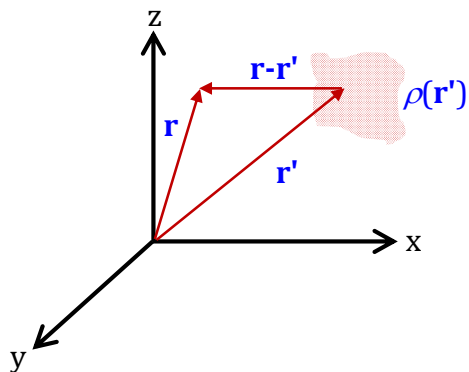
Figure 1.2 Electrostatic potential generated by a continuous charge distribution $\rho(\mathbf{r}')$

If the distinct charge 'q_i' placed at '$\mathbf{r}_i$' and continuous charge distribution, $\rho(\mathbf{r}')$ as shown in Figure 1.2, the electrostatic potential can be written as,

$$V(\mathbf{r}) = \frac{1}{4\pi\varepsilon_0} \left\{ \sum_i \frac{q_i}{|\mathbf{r} - \mathbf{r}_i|} + \int \frac{\rho(\mathbf{r}')}{|\mathbf{r} - \mathbf{r}'|} d^3\mathbf{r}' \right\} \qquad \text{Eq. 1.11}$$

The electric field, $\vec{E}(\mathbf{r})$ due this combination of charges is the $-\nabla V(\mathbf{r})$. *i.e.*,

$$\vec{E}(\mathbf{r}) = \frac{-1}{4\pi\varepsilon_0} \left\{ \sum_i \frac{q_i(\mathbf{r} - \mathbf{r}_i)}{|\mathbf{r} - \mathbf{r}_i|^3} + \int \frac{\rho(\mathbf{r}')(\mathbf{r} - \mathbf{r}')}{|\mathbf{r} - \mathbf{r}'|^3} d^3\mathbf{r}' \right\} \qquad \text{Eq. 1.12}$$

In the case of molecular systems or molecular charge distribution consisting of several positive discrete nuclear charges 'Z_i' and a continuous negative charge density distribution $\rho(\mathbf{r}')$, the $V(\mathbf{r})$ can be represented as,

$$V(\mathbf{r}) = \sum_i \frac{Z_i}{|\mathbf{r} - \mathbf{r}_i|} - \int \frac{\rho(\mathbf{r}')}{|\mathbf{r} - \mathbf{r}'|} d^3\mathbf{r}' \qquad \text{Eq. 1.13}$$

where N is the total number of nuclei, Z_i is the charge of nucleus *i*, located at $\mathbf{r}_i$. The first component in Eq. 1.13 is known as bare nuclear potential (V_{bnp}), which is always non-negative and has no non-nuclear maxima or minima, but it tends to attain an infinite value at the nuclei, which can be regarded a pseudo maximum. The negative potential caused

by the continuous electron density is represented by the second term. As a result, the resulting $V(\mathbf{r})$ might be negative or positive depending on the nature of molecular system.

In a molecular system, the MESP at a specific nucleus 'A' is determined by subtracting the nuclear contribution represented by Z_A. In general, the MESP at the nucleus, V_N is expressed as;

$$V_N = \sum_{B \neq A} \frac{Z_B}{|\mathbf{R}_B - \mathbf{R}_A|} - \int \frac{\rho(\mathbf{r}')}{|\mathbf{r} - \mathbf{r}'|} d^3\mathbf{r}'$$

Eq. 1.14

The MESP is a scalar quantity commonly computed on a cubic grid in most computational systems, and the resulting data can be visualized. Negative MESP values indicate minima and saddle points in regions of high electron density, while positive MESP values signify the influence of the nuclear contribution.

The MESP at a given point in a molecular system indicates the electrostatic energy that a unit test charge would encounter at that point. A negative MESP value implies an attractive interaction with the test charge, whereas a positive MESP value suggests repulsion. The most negative MESP value (MESP minimum) designated as V_m, represents electron localization in molecules. MESP serves as a visual representation of electron density variations, highlighting regions of electron-richness (negative potential) and electron-deficiency (positive potential).

1.1.2 Topological Concepts

The term "topology," derived from the Greek words "topos" (place) and "logos" (study), refers to the detailed examination of a specific area. This concept is often employed in mapping to represent the physical characteristics of a region through contours and elevation lines. Such maps offer a convenient means of illustrating functions with multiple variables. In the realm of molecular science, molecular topology serves as a valuable tool for delving into potential energy surfaces, a crucial aspect of studying reaction dynamics. A topological approach utilizing electronic energy values and their partial derivatives proves advantageous in identifying minima during the optimization of molecular geometry. Specifically, specialized methods are employed to locate

transition states. By integrating these techniques, a more profound understanding of molecular behaviour is achieved, facilitating a comprehensive comprehension of intricate chemical reactions. Molecular topology thus contributes significantly to gaining insights into and advancing our knowledge of complex chemical processes.

The intricate topological characteristics of a scalar function $f(x_1, x_2, x_3 \ldots\ldots\ldots x_n)$ involving multiple variables, which are quantitatively defined through its first and second-order partial derivatives and these derivatives provide crucial information about the function's behaviour.[12] Specifically, the number and nature of critical points play a significant role in defining these features. A critical point (CP) is a point where either all the first-order partial derivatives of the function or the gradient of the field becomes zero, *viz.*,

$$\nabla_i f(x_1, x_2, x_3, \ldots\ldots\ldots\ldots x_n)|_{CP} = 0 \qquad \text{Eq. 1.15}$$

$$\text{or}$$

$$\frac{\partial f}{\partial x_i}\bigg|_{CP} = 0; \; where \; i = 1, 2, 3 \ldots, n \qquad \text{Eq. 1.16}$$

i.e., the CP for the scalar field, $V(\mathbf{r})$ can be determined by finding the points where the magnitude of the first partial derivatives of the function with respect to the variables is minimum. Analyzing these CPs allows us to gain a deeper understanding of the function's extrema and saddle points, providing valuable insights into the function's behaviour aiding in various fields. The collection of nine possible second derivatives of the function can be expressed in the form of a matrix known as the Hessian matrix (H_{ij}). The nature of the CP can be determined by analyzing the signs of the eigenvalues of the H_{ij} at that point. The H_{ij} can be represented as,

$$H_{ij} = \frac{\partial^2 f}{\partial x_i \, \partial x_j}\bigg|_{CP} \qquad \text{Eq. 1.17}$$

The CPs are classified as non-degenerate when none of the eigenvalues of the H_{ij} is zero and as degenerate if at least one of the eigenvalues of the H_{ij} is zero. A non-degenerate CP is characterized by two elements: rank (R) and signature (σ). The 'R' refers to the number of non-zero eigenvalues at the CP, while the 'σ' denotes the difference

between the number of positive eigenvalues and negative eigenvalues. Therefore, a CP is represented as an ordered pair of these two elements as (R, σ). Each CP consist of three eigenvalues and corresponding eigenvectors. Eigenvalues are characterized as the measures of curvature of a function, while the corresponding eigenvectors denote the axes of this curvature. In the Eq. 1.19, the symbols λ_1, λ_2, and λ_3 represent the eigenvalues associated with the function.

$$H = \begin{pmatrix} \dfrac{\partial^2 f}{\partial x^2} & \dfrac{\partial^2 f}{\partial x \, \partial y} & \dfrac{\partial^2 f}{\partial x \, \partial z} \\[2mm] \dfrac{\partial^2 f}{\partial y \, \partial x} & \dfrac{\partial^2 f}{\partial y^2} & \dfrac{\partial^2 f}{\partial y \, \partial z} \\[2mm] \dfrac{\partial^2 f}{\partial z \, \partial x} & \dfrac{\partial^2 f}{\partial z \, \partial y} & \dfrac{\partial^2 f}{\partial z^2} \end{pmatrix}_{\mathbf{r}=\mathbf{r_c}}$$

Eq. 1.18

$$H = \begin{pmatrix} \dfrac{\partial^2 f}{\partial x'^2} & 0 & 0 \\[2mm] 0 & \dfrac{\partial^2 f}{\partial y'^2} & 0 \\[2mm] 0 & 0 & \dfrac{\partial^2 f}{\partial z'^2} \end{pmatrix}_{\mathbf{r}'=\mathbf{r_c}} = \begin{pmatrix} \lambda_1 & 0 & 0 \\ 0 & \lambda_2 & 0 \\ 0 & 0 & \lambda_3 \end{pmatrix}$$

Eq. 1.19
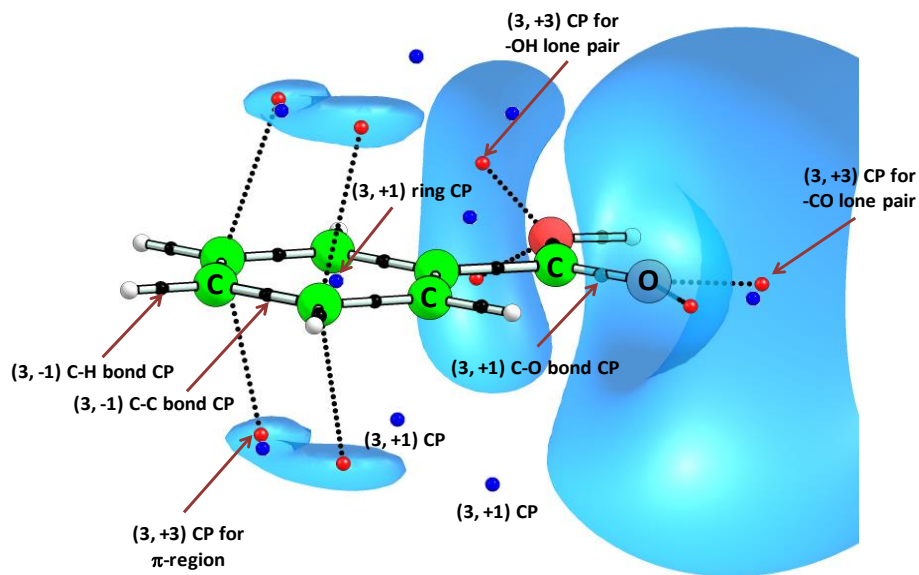
Figure 1.3 MESP topology of benzoic acid. DAMQT 3.2 software is used to locate the CPs. The visualization of the MESP data is done with Chemcraft 1.8 software. MESP topology clearly distinguishes π-region of arene ring, sp³-hybridized -OH lone pair region and sp²-hybridized CO lone pair region.

Consider a function of three variables, $f(x, y, z)$. For non-degenerate CPs of this function, the R is 3, indicating that all three eigenvalues of the H_{ij} are non-zero. In such cases, the σ can have four distinct values: -3, -1, +1, and +3, leading to four types of non-degenerate CPs, *viz*. (3, -3), (3, -1), (3, +1), and (3, +3). The (3, -3) CP is characterized by three negative eigenvalues, representing a local maximum of the function. On the other hand, the CPs of type (3, -1) and (3, +1) signify saddle points, where the eigenvalues have a mix of both positive and negative values. Further, (3, +3) CP corresponds to three positive eigenvalues, indicating a local minimum in the function. A minimum, V_m represents (3, +3) CPs of the MESP. The electrophile tends to position itself near the most negatively valued V_m and the strength of attraction is greatly influenced by the distribution of the MESP around such a CP. Figure 1.3 illustrates a representative example of the MESP topology of benzoic acid.

1.1.3 The Evolution and Historical Development

The applicability of MESP was initially recognized and introduced in chemical systems by Scrocco, Tomasi[13-18] and Pullman.[19-25] It was employed as a guiding scalar field for the initial exploration of the reactive behaviour of molecules.[2, 13, 26-29] Subsequently, significant progress occurred over the years as in-depth investigations and studies on MESP were conducted. The MESP-based electron distribution was pioneered by Politzer.[3, 30-35] Successively, it has been qualitatively applied to predict regions susceptible to electrophilic and nucleophilic attacks in molecules. Identifying positive and negative MESP regions on the molecular surface assists in determining areas preferred for electrophilic and nucleophilic attacks, respectively.[4, 35-37] Gadre played a pioneering role in MESP topological studies by developing algorithms and software for the computation and mapping of MESP topology[1, 8, 38-46] and Suresh *et al*. undertook the topological applications of MESP in various fields.[47] Later, Wheeler, Houk,[48-52] and Galabov[53-61] have also made noteworthy contributions to this field.

Groundbreaking studies led to widespread use of MESP to explain chemical features such as bonding, inductive and resonance effects, and prediction of protonation sites of organic compounds including nucleic acid bases as well as hydration sites of big

molecules, *etc.*[15, 62] MESP has also proved beneficial in studying molecular recognition in biological systems.[33, 63-66] It aids in the qualitative understanding of molecular recognition by representing the enzyme active site and ligand as an electrostatic lock and key model, respectively.[63] The negative value MESP in electron-rich regions that directly correlates with chemical notions such as bonds, lone pairs reveal the role of MESP in elucidating reaction mechanisms and molecular recognition.[45, 47, 67, 68] The MESP analysis can be effectively employed to explain chemical reactivity phenomena such as π-conjugation, aromaticity, substituent effect, ligand electronic effects, trans-influence, redox potential, activation energy, cooperativity, non-covalent interactions, *etc.* As localized/delocalized electron distribution is so closely related to aromaticity, MESP-based analysis is used as a good descriptor of aromaticity.[69-71] MESP at the lone pair region of ligands is also used as a trustworthy electronic parameter to assess their σ-donating ability to electron deficient regions.[72] MESP parameters developed for arene systems are employed as potent probe to measure the substituent effects.[73] MESP may be used to quantify the electronic and steric effects of ligands in complexes, allowing for powerful predictions on their reactive behaviour prior to the experimental study. The MESP topology parameters can be used to evaluate the sites and directionality of bonding in a wide range of non-covalent systems, to explain the strength and features of non-covalent interactions in a variety of systems[74-76] and to differentiate the noncovalent interactions, such as dipolar interactions, C–C interactions and interactions governed by substituents, hetero atoms, *etc.*[77] Also, the change in MESP at the atoms is used to measure electron density reorganization in monomers caused by non-covalent bond formation. This technique introduces novel rational design techniques for tuning stereoelectronic effects in chemical systems for catalytic and optoelectronic applications. It is a highly useful tool for determining the strength of chemical bonding and understanding the chemical reactivity in molecular systems.

1.1.4 Fundamental Electrostatic Relationships

Several fundamental theorems and principles govern the behaviour of electric charges and fields in electrostatics. These basic theorems provide the foundation for

understanding the behaviour of electric charges and fields in electrostatics. They are essential tools for solving problems related to electric charges, electric fields, and electric potential in various physical systems. Coulomb's law, expressed in Eq. 1.1, stands as a cornerstone in this framework, establishing essential principles for the understanding of electrostatic phenomena.

1.1.4.1 Gauss's Theorem

Gauss's law/theorem, also known as Gauss's flux theorem, is a law that establishes a connection between the distribution of electric charge to the resulting electric field. The theorem states that the electric flux across (Φ) any closed surface 'S' is proportional to the net electric charge enclosed by the closed surface. If 'q_i' are the charges enclosed by the surface and '$\vec{E}$' is the corresponding electric field, the Gauss law can be expressed as,

$$\oint \vec{E}.dS = \frac{1}{\varepsilon_0} \sum_i q_i$$

Eq. 1.20

where ε_0 is the electric permittivity and dS is an infinitesimally small area as given in Figure 1.4.
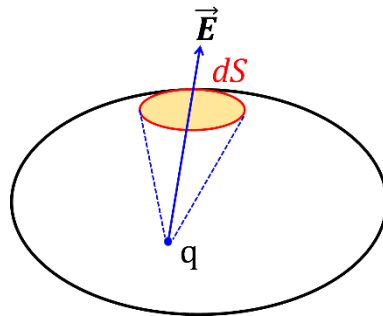
Figure 1.4 Illustration of Gauss's law

If no electric charge is enclosed in the surface, the Eq. 1.20 becomes,

$$\oint \vec{E}.dS = 0$$

Eq. 1.21

12

1.1.4.2 Divergence Theorem

A three dimensional vector '**A**' may be defined in terms of components along three mutually perpendicular axes, given as

$$\mathbf{A} = A_x \mathbf{i} + A_y \mathbf{j} + A_z \mathbf{k}$$
Eq. 1.22

Where **i**, **j** and **k** are unit vectors in three mutually perpendicular cartesian coordinates and A_x, A_y, and A_z are the components of **A**.

The rate of change of a vector or scalar field with respect to a space coordinates is called vector operator ∇, defined as;

$$\nabla = \mathbf{i}\frac{\partial}{\partial x} + \mathbf{j}\frac{\partial}{\partial y} + \mathbf{k}\frac{\partial}{\partial z}$$
Eq. 1.23

The dot product of ∇ operator is called divergence, given as;

$$\nabla \cdot \mathbf{A} = \frac{\partial A_x}{\partial x} + \frac{\partial A_y}{\partial y} + \frac{\partial A_z}{\partial z}$$
Eq. 1.24

Divergence can be defined as the measure of fluid flow per unit volume per unit time. If **A** represents the velocity vector field of the fluid, then ∇·**A** can be defined as the outward flow per unit volume.

The electric flux, Φ of as vector **A** through a closed surface is given by,

$$\Phi = \oint_S \mathbf{A}.\,dS$$
Eq. 1.25

Also, if **A** is the rate of flow per unit area then the total outward flow from as volume Ω is given by, $\int_\Omega \nabla \cdot \mathbf{A}\,dV$.

The divergence theorem states that "for a closed surface S that encloses a volume Ω, the surface and volume integrals are connected in accordance with Gauss's law", given as;

$$\int_\Omega \nabla \cdot \mathbf{A}\,dV = \oint_S \mathbf{A}.\,dS$$
Eq. 1.26

1.1.4.3 Poisson's and Laplace's Equation

According to the divergence theorem, the relationship between $\vec{E}$ and the charge density, ρ can be written as,

$$\nabla \cdot \vec{E} = \frac{\rho}{\varepsilon_0} \qquad\qquad \text{Eq. 1.27}$$

Based on gradient relationship, **E** can be defined as,

$$\vec{E} = -\nabla V \qquad\qquad \text{Eq. 1.28}$$

By comparing Eq. 1.27 and Eq. 1.28 the Gauss's law can be reformulated as,

$$\nabla \cdot \vec{E} = -\nabla \cdot (\nabla V) = \frac{\rho}{\varepsilon_0} \qquad\qquad \text{Eq. 1.29}$$

$$\nabla^2 V = -\frac{\rho}{\varepsilon_0} \qquad\qquad \text{Eq. 1.30}$$

The Eq. 1.30 is called the Poisson's equation and is used in regions where the charge density ρ is non-zero.

In a charge-free region of space, the Eq. 1.30 becomes,

$$\nabla^2 V = 0 \qquad\qquad \text{Eq. 1.31}$$

The Eq. 1.31 is called Laplace's equation.

It was demonstrated that, the electronic charge density of a ground-state atom declines monotonically as a function of radial distance from the nucleus and it is stated that an atom's electrostatic potential must decrease monotonically.[78] This has been proved on the basis of Poisson's equation;

$$\frac{d^2 V(\mathbf{r})}{d\mathbf{r}^2} + \frac{2}{\mathbf{r}} \frac{dV(\mathbf{r})}{d\mathbf{r}} = 4\pi\rho(\mathbf{r}) \qquad\qquad \text{Eq. 1.32}$$

The conditions $\frac{dV}{d\mathbf{r}} = 0$ as well as $\frac{d^2 V}{d\mathbf{r}^2} < 0$ and $\frac{dV}{d\mathbf{r}} = 0$ as well as $\frac{d^2 V}{d\mathbf{r}^2} > 0$ must be satisfied for a relative maximum and a relative minimum, respectively. Later Gadre and Pathak brought out a generalization for the non-existence of maximum[8] for all quantal systems which were limited to the cases of atoms only.

1.1.4.4 Earnshaw's Theorem

In an electric field created by a collection of charges, no charge can be in stable equilibrium. To be in equilibrium, a test positive charge 'q' must have a zero field at that point, and moving the charge away from a point 'p' in any direction should result in a restoring force opposing the displacement.

1.1.4.5 Poincaré–Hopf Relationship

For each CPs, an index I_{CP} with values ± 1 exit depending on the number of negative eigenvalues (i).

$$I_{CP} = (-1)^i \hspace{5cm} \text{Eq. 1.33}$$

The Poincaré-Hopf theorem[79-82] connects the sum of these indices to the Euler characteristic χ, which is an integer number and a topological invariant. If n_{+3}, n_{+1}, n_{-1} and n_{-3} represent the number of (3, +3), (3, +1), (3, -1) and (3, -3) CPs, then

$$n_{+3} + n_{+1} + n_{-1} - n_{-3} = \chi \hspace{4cm} \text{Eq. 1.34}$$

Considering the influence of the asymptotic behaviour on MESP, I_{CP} = +1 for asymptotic minima (n_+) and I_{CP} = -1 for asymptotic maxima (n_-) then,

$$(n_{+3} + n_+) - n_{+1} + n_{-1} - (n_{-3} + n_-) = 0 \hspace{2cm} \text{Eq. 1.35}$$

As a result, Poincaré-Hopf relation adopts a new form that separates the asymptotic CPs given by,

$$n_{+3} - n_{+1} + n_{-1} - n_{-3} = n_+ - n_- \hspace{3cm} \text{Eq. 1.36}$$

In the case of charged systems, determining the asymptotic CPs is equivalent to determining the electronic density.

For positively charged systems, the Poincaré-Hopf relationship becomes

$$n_{+3} - n_{+1} + n_{-1} - n_{-3} = -1 \hspace{3.5cm} \text{Eq. 1.37}$$

and for negatively charged systems the relation becomes,

$$n_{+3} - n_{+1} + n_{-1} - n_{-3} = 1 \hspace{4cm} \text{Eq. 1.38}$$

The Poincare'-Hopf relation Eq. 1.34 for the MESP connects the electronic structure of a molecule, as specified by the CPs, to the angular dependence of electrostatic interactions. This acts as a topological relationship between Lewis' valence and acid-base theory.

1.2 Applications of Molecular Electrostatic Potential

1.2.1 MESP in Understanding the Chemical Reactivity

MESP plays a pivotal role in enhancing our understanding of chemical reactivity. It provides valuable insights into the interactions and transformations that occur within molecules during chemical reactions. MESP offers a unique perspective on the distribution of electric charges within a molecular system, shedding light on regions of attraction and repulsion. Politzer *et al.* showed that by analyzing the MESP distribution, one can predict and rationalize the preferred sites of chemical reactivity, such as nucleophilic and electrophilic centers.[55, 83-85] Negative MESP values highlight regions where electrophilic species are likely to undergo attack, while positive MESP values indicate potential nucleophilic attack sites.[86-89] Furthermore, MESP aids in elucidating reaction mechanisms by visualizing how charges are redistributed during the course of a reaction (Figure 1.5).[68] It assists in identifying transition states, intermediates, and stable products, guiding the interpretation of reaction pathways.[90] MESP serves as a powerful tool that allows chemists to probe the electronic structure of molecules, predict reactive sites, and gain valuable insights into the driving forces behind chemical transformations.[85, 91]
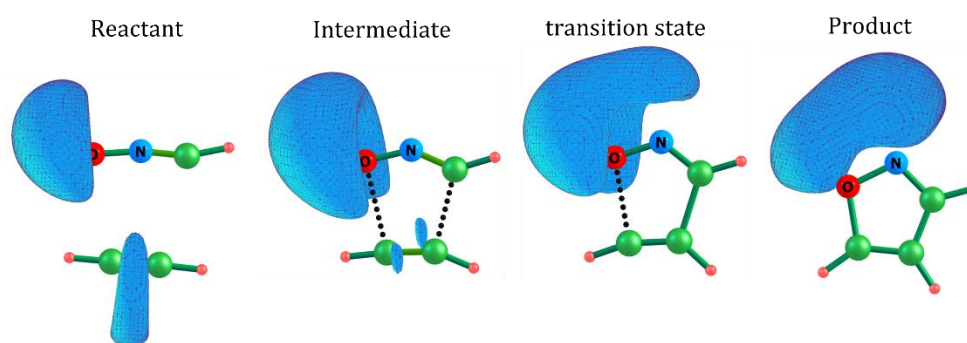
Figure 1.5 MESP isosurfaces along the reaction path for the 1, 3-dipolar cycloaddition of HCNO and HCCH.[90] The isosurface values for reactant, intermediate, transition state and product are -0.03, -0.025, -0.03 and -0.03 au, respectively

1.2.2 MESP as an Electronic Parameter
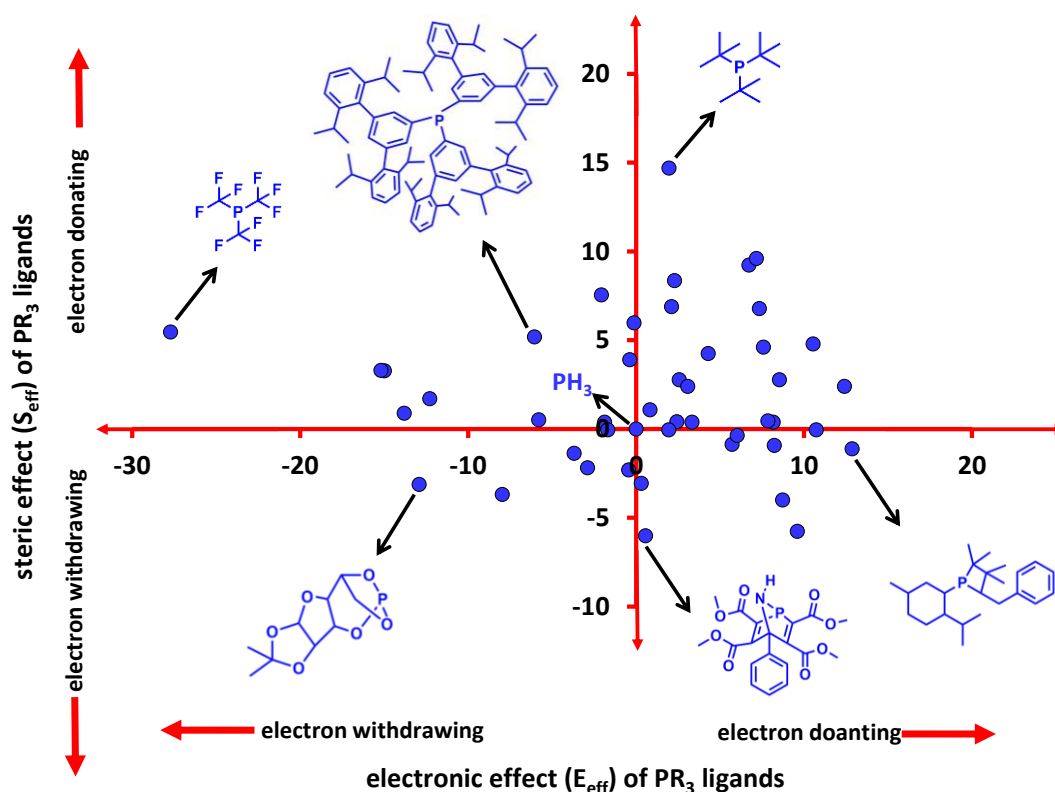
Figure 1.6 Stereoelectronic profile of phosphine ligands[92]

The stereoelectronic characteristics of the ligand environment surrounding the metal center are frequently tuned to gain fine control over the reactivity of organo-transition metal complexes.[93-100] Quantifying the electronic and steric effects of ligands in complexes allows to make significant predictions about their reactive behaviour before conducting more experimental investigation.[101-105] MESP data analysis has been described as a valuable tool for interpreting stereoelectronic properties of diverse ligands in order to fine tune the reactivity and catalytic activity of transition metal complexes. As an electronic descriptor, MESP plays a crucial role in elucidating the electrostatic interactions and behaviour that define molecular properties. MESP quantifies the energy experienced by a unit positive test charge at different locations within a molecule. This energy directly reflects the spatial arrangement of charged and polarized regions, influencing chemical reactivity, molecular stability, and non-covalent interactions. MESP serves as a valuable electronic parameter that unveils the intricate interplay

of charges within molecules, offering a comprehensive framework for analyzing and predicting a wide range of molecular phenomena and interactions.

To tailor the catalytic activity of transition metal complexes, the MESP topology analysis has been effectively employed to assess the stereoelectronic characteristics of a wide range of ligands.[106, 107] The donating power of ligands could be measured directly using MESP V_m at their lone-pair region or at the atom center. Furthermore, the QM/MM (Quantum Mechanics/Molecular Mechanics) technique in combination with MESP analysis has been successful in elucidating the stereoelectronic effect of certain ligands (Figure 1.6). MESP provides effective classification of ligand steric and electronic effects, as well as the development of a stereoelectronic profile for tailoring the ligand environment of a metal complex for increased catalytic activity. Using the MESP parameters, σ-donating ability and steric influence of ligands[108] can be evaluated. The MESP properties demonstrates that by enhancing the negative character of a ligand, increased hydridicity may be achieved for launching an easy water-splitting reaction.[107]

1.2.3 Electrostatic Potential for Intermolecular Complexation Model

The Electrostatic Potential for Intermolecular Complexation (EPIC) Model is a conceptual framework and computational approach used in the study of molecular interactions, particularly focusing on intermolecular complexes formed between different molecules.[109, 110] The EPIC Model employs the principles of electrostatic potential to analyze and predict the binding affinities, stability, and characteristics of these complexes. It provides valuable information for rationalizing and designing molecular recognition processes. In the context of intermolecular interactions, the EPIC Model examines how these electric charge distributions influence the formation and stability of complexes between molecules. The EPIC Model assesses the strength of interactions between molecules by analyzing the electrostatic complementarity between their charge distributions.[111] A MESP based complimentary "lock and key" model were introduced to predict and investigate strength of weak intermolecular interactions.[63, 64, 112-114] The model estimates the contributions of electrostatic energy to attraction or repulsion between distinct chemical entities. MESP topology analysis is a quick and easy approach to characterize the electron-rich lone pair area in molecules. The MESP V_m

point can be used to forecast the orientation of the lone pair carrying molecule when it complexes with an electron deficient π-system.[72, 115, 116] The EPIC Model provides insights into non-covalent interactions by analyzing the electrostatic potential surfaces of interacting molecules and helps to understand the nature and strength of these interactions.[65, 75, 117-120] The MESP topology parameters V_m and V_N are useful to critically assess the sites and directionality of bonding in a variety of non-covalent systems and to describe the strength and characteristics of non-covalent interactions in several hydrogen-, halogen-, aerogen-, pnicogen-, tetrel-, chalcogen- and lithium-bonded systems (Figure 1.7).[74, 76, 121-123] The EPIC Model is also integrated into molecular docking studies as it helps in identifying favourable binding orientations and interaction sites within complex structures.[124] It finds applications in drug design,[125-127] where it aids in the understanding of ligand-receptor interactions,[128-130] and in material science, where it helps to analyze interactions between molecules in materials.[85, 131] Overall, EPIC Model offers a powerful tool for investigating and understanding the intricate electrostatic forces that govern molecular interactions, enabling to explore and predict the behaviour of intermolecular complexes in various fields of study.
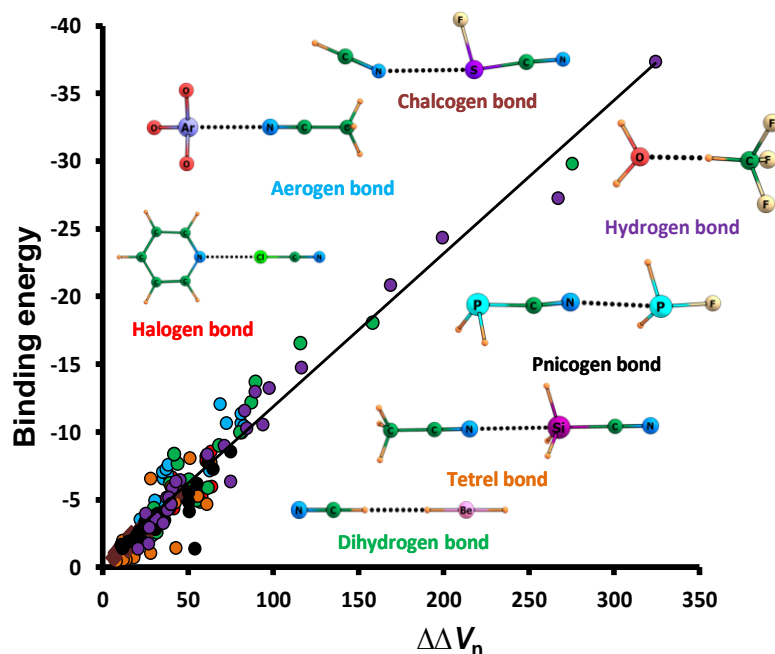
Figure 1.7 Applying MESP reorganization theory to explain positive cooperativity in noncovalent trimer complexes[74]

1.2.4 MESP as an Aromaticity Index

MESP can also serve as an aromaticity index, providing insights into the aromatic character of molecules. By mapping MESP on to the molecular structure, one can evaluate the electron distribution within the conjugated system.[132] The electron rich π-regions of a molecule are often characterized by CPs or V_m in MESP topology analysis, and the approach is primarily used to discern the localization or delocalization of electron density in a system. Aromatic compounds typically exhibit a distinctive pattern of MESP distribution, which reflects the delocalization of π-electrons in the conjugated system. The MESP-derived aromaticity index can be quantified by calculating the MESP distribution over the π-electron cloud of the ring.[113] Application of MESP as an aromaticity index extends to analyzing various aromatic systems, including polycyclic benzenoid hydrocarbons (PBHs), heterocycles, and even transition metal complexes with aromatic ligands. Suresh and Gadre used MESP to examine Clar's sextet theory and demonstrated that the number, type, and distribution of CPs in the MESP topology allows for an exhaustive characterization of the π-regions of PBHs as shown in Figure 1.8.[71, 133] It allows chemists to rapidly assess the aromatic character of molecules and gain insights into their stability, reactivity, and electronic structure. Incorporating MESP into the study of aromaticity adds another dimension in understanding the complex electronic interactions that underlie the special properties of aromatic compounds.[134, 135]

(a)   (b)
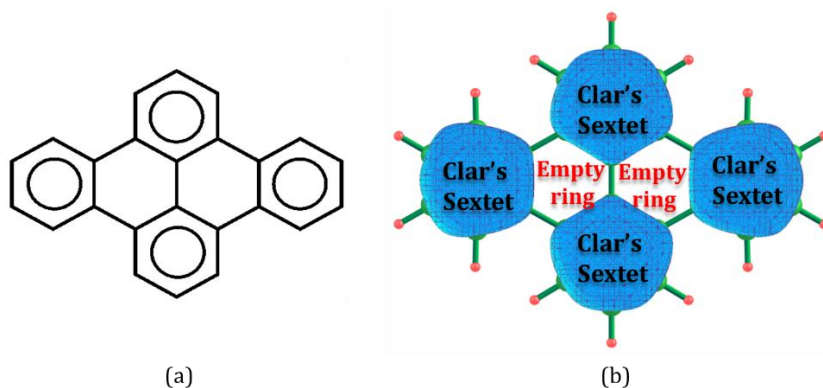
Figure 1.8 (a) Illustration of the aromaticity concept based on Clar's theory employing the (b) MESP maps of a PAH system at isosurfaces of -0.016 au

1.2.5 MESP in Substituent Effect Study

The substituent effect describes how the introduction of different functional groups or atoms can modify the properties of a parent molecule. Politzer and Murray described[136] MESP as simple computational approach for estimating a substitute's total electron-attracting propensity. Further, the study has been extended to evaluate substituent effect on the characteristics of the bridgehead carbon bond.[137] MESP tool is very efficient for understanding and predicting the impact of substituents on the electronic structure and reactivity of molecules. Substituents can have either electron-donating or electron-withdrawing effects on a molecule's electron density. MESP helps to quantify these effects by illustrating how substituents alter the charge distribution along the molecular framework.[54, 138, 139] Electron-donating groups tend to generate negative MESP regions, enhancing nucleophilic reactivity, while electron-withdrawing groups often lead to positive MESP regions, favouring electrophilic reactions.[140, 141] Beyond electronic effects, substituents can introduce steric hindrance, affecting the spatial arrangement of atoms in a molecule.[106, 142] MESP analysis aids in identifying regions of higher steric congestion, which can impact molecular geometry, conformational flexibility, and reaction pathways.[143] MESP values allow the quantitative comparison of substituent effects among different molecules or positions within the same molecule. This enables to rank substituents based on their electronic and steric influences.[73] MESP-based quantification of the substituent effect assists in the rational design of molecules with specific properties. Chemists can use this information to tailor molecular reactivity, stability, and other characteristics by strategically selecting substituents. By employing MESP as a tool for investigating the substituent effect, one can gain a deeper understanding of how different chemical groups modify a molecule's electronic structure and overall behaviour. The change in MESP derived by a functional group on a substituted system serves as a robust indicator of how substituents influence electronic behaviour in chemical reactions. Hence, MESP is regarded as an alternative to other empirical parameters such as the Hammett or Swain-Lupton parameters, or the charge shift.[144] The substituent effect-related variables, including as inductive, resonance, through-space, additive, and proximity effects, can be characterized using MESP topology calculations (Figure 1.9).[74-80] MESP topology computations also resulted in the

characterization of various substituent effect-related concepts such as inductive, resonance, through-space, additive, and proximity effects.[145-149]
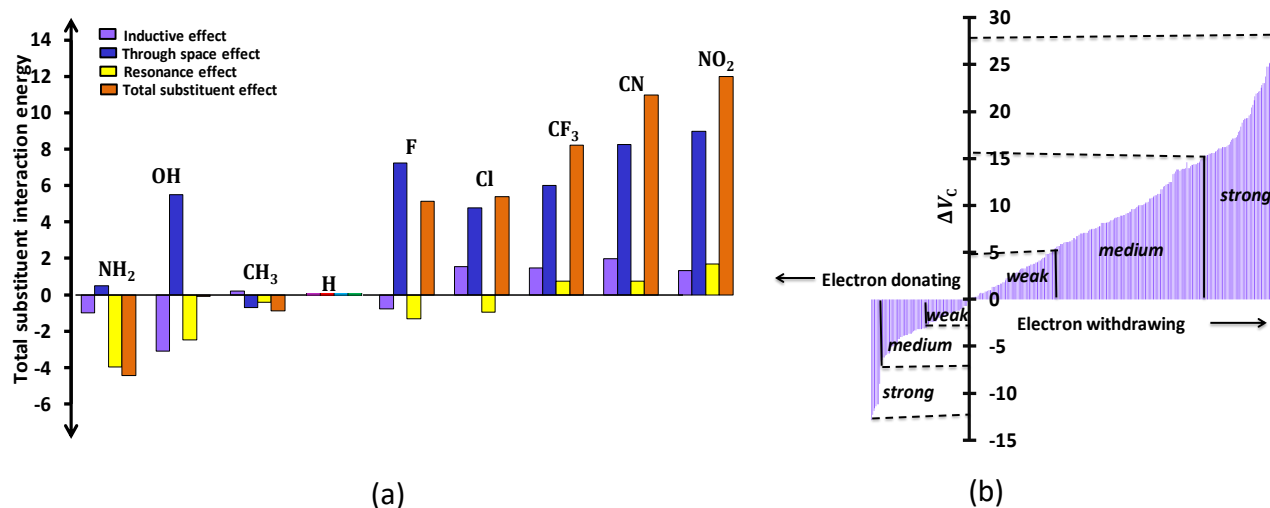
Figure 1.9 (a) Relative contributions of inductive, through-space, and resonance effects of $C_6H_5X\cdots\cdots Na^+$ systems[145] (b) Classification of substituents[73]

1.3 Comparison with Molecular Electron Density

1.3.1 Molecular Electron Density: An Overview

Quantum Theory of Atoms in Molecules (QTAIM) introduced by R. W. F. Bader describes molecular features such as bonds, atoms, and structure using the topology of electron density, $\rho(\mathbf{r})$. The most essential topological features of $\rho(\mathbf{r})$ of a multi-electronic system are governed by the attractive force of nuclei. The spatial distribution of electronic charge in the field of the nuclei and its flow in the presence of external field are derived from the $\rho(\mathbf{r})$. The distribution of $\rho(\mathbf{r})$ in a molecular system is widely accepted as the physical manifestation of the forces acting inside the molecular system. The $\rho(\mathbf{r})$ reaches a maximum at the nuclear positions, and each atom is portrayed by its boundaries dependent on the balance of forces of the system under consideration.[150-152]

The distribution of Molecular Electron Density (MED) is one of the many molecular features of scientific interest that has significant conceptual importance. The

corresponding many-particle wave function $\Psi(x_1, x_2,... x_n)$ may be used to determine the MED in the following way:

$$\rho(\mathbf{r}) = N \sum_\sigma |\Psi(\mathbf{x}_1, \mathbf{x}_2, ... \mathbf{x}_N)|^2 \, d^3\mathbf{r}_2 ... d^3\mathbf{r}_N$$

<div align="right">Eq. 1.39</div>

where $\mathbf{x}_i$ denotes the combined spatial ($\mathbf{r}$) and spin (σ) coordinates of the electron i, and N is the total number of electrons.[45, 150-153] The $\rho(\mathbf{r})$, describes the probability distribution of electrons in the system. In the Eq. 1.39, the summation is applied to all spin coordinates, whereas the integration is applied to all but one spatial coordinate. The probability of finding an electron in an infinitesimally small volume element $d^3\mathbf{r}$ around position $\mathbf{r}$ is proportional to the $\rho(\mathbf{r})d^3\mathbf{r}$. MED is often represented as a three-dimensional isosurface or as a set of contours in certain planes. In the vicinity of the nuclei, the MED profiles have an almost spherical form. Nevertheless, in the bonding region, there is a distinct indication of charge density accumulation.

1.3.2 Topology Features of Molecular Electron Density

The value $\rho(\mathbf{r})$ can take on different characteristics in space, such as being a maximum, a minimum, or a saddle point. These specific points are commonly referred to as CPs. A CP can also be defined as the point on the electron density surface at which the first derivative of the function $\rho(\mathbf{r}_c)$ vanishes, *i.e.*, $\nabla\rho(\mathbf{r}_c) = 0$.

$$\nabla\rho(\mathbf{r}) = \mathbf{i}\,\frac{d\rho}{dx} + \mathbf{j}\,\frac{d\rho}{dy} + \mathbf{k}\,\frac{d\rho}{dz} \rightarrow \begin{cases} = 0 \text{ (at CPs, } \mathbf{r}_c \text{ and at } \infty) \\ \neq 0 \text{(at all CPs)} \end{cases}$$

<div align="right">Eq. 1.40</div>

The gradient of electron density, $\nabla\rho(\mathbf{r})$, at a specific point in space indicates the direction in which $\rho(\mathbf{r})$ experiences the maximum rate of increase, and its magnitude corresponds to the rate of increase in that particular direction. Thus, $\nabla\rho(\mathbf{r})$ is a vector quantity. A CP may correspond to maximum, minimum or a saddle point. Based on its sign, the second derivative of $\rho(\mathbf{r})$, $\nabla\nabla\rho(\mathbf{r})$ is considered for distinguishing a local minimum, a local maximum or a saddle point. Hessian matrix represents the matrix form of nine possible second derivative electron densities at $\mathbf{r}_c$, given as;

$$H = \begin{pmatrix} \dfrac{\partial^2 \rho}{\partial x^2} & \dfrac{\partial^2 \rho}{\partial x\,\partial y} & \dfrac{\partial^2 \rho}{\partial x\,\partial z} \\[2ex] \dfrac{\partial^2 \rho}{\partial y\,\partial x} & \dfrac{\partial^2 \rho}{\partial y^2} & \dfrac{\partial^2 \rho}{\partial y\,\partial z} \\[2ex] \dfrac{\partial^2 \rho}{\partial z\,\partial x} & \dfrac{\partial^2 \rho}{\partial z\,\partial y} & \dfrac{\partial^2 \rho}{\partial z^2} \end{pmatrix}_{\mathbf{r}=\mathbf{r_c}} \qquad \text{Eq. 1.41}$$

This matrix's diagonalization yields a collection of eigenvalues and related eigenvectors. The diagonalization of H is equivalent to a rotation of the coordinate system $\mathbf{r}$(x, y, z) to $\mathbf{r}$(x′, y′, z′) superimposing the new axes x′, y′, z′ with the principal curvature axes of the CP. In Eq. 1.42, λ_1, λ_2, and λ_3 are the curvatures of the density with respect to the three principal axes x′, y′, and z′.

$$H = \begin{pmatrix} \dfrac{\partial^2 \rho}{\partial x'^2} & 0 & 0 \\[2ex] 0 & \dfrac{\partial^2 \rho}{\partial y'^2} & 0 \\[2ex] 0 & 0 & \dfrac{\partial^2 \rho}{\partial z'^2} \end{pmatrix}_{\mathbf{r'}=\mathbf{r_c}} = \begin{pmatrix} \lambda_1 & 0 & 0 \\ 0 & \lambda_2 & 0 \\ 0 & 0 & \lambda_3 \end{pmatrix} \qquad \text{Eq. 1.42}$$

A CP is labeled as an ordered pair (R, σ), where R is the rank and σ the signature. The 'R' is the number of non-zero eigenvalues of $\rho(\mathbf{r})$ at the CPs, and the 'σ' is the algebraic sum of the signs of eigenvalues. A CP with an R < 3 is mathematically unstable and is susceptible to disappear when subjected to slight perturbations in density due to nuclear motion. The existence of a CP with a R < 3 signifies a shift in the topology of density and consequently, a modification in the molecular structure. Due to this, CPs with R < 3 are typically absent in equilibrium charge distributions. For energetically stable nuclear configurations R is equal to 3, and there are four types of CPs with rank 3. The 'σ' of a CP is determined by the algebraic sum of the signs of the curvatures, with each of the three curvatures contributing ±1 based on whether it is positively or negatively curved. The (3, -3) CP known as nuclear critical point (NCP) with three negative eigenvalues where $\rho(\mathbf{r})$ is a local maximum at $\mathbf{r_c}$. The (3, -1) CP is the bond critical point (BCP) with two negative curvatures where $\rho(\mathbf{r})$ is a maximum in the plane defined by these two eigenvectors and minimum along the third axis, which is perpendicular to this plane. The ring critical point

(RCP), (3, +1) CP contain two positive eigenvalues where $\rho(\mathbf{r})$ is a minimum along the plane defined by the corresponding eigenvectors and maximum along the third axis, which is perpendicular to this plane. The (3, +3) CP known as cage critical point (CCP) has three positive curvatures where $\rho(\mathbf{r})$ is a local minimum at $\mathbf{r}_c$.[154] Figure 1.10 illustrates a representative example of the MED topology of C_{60}.
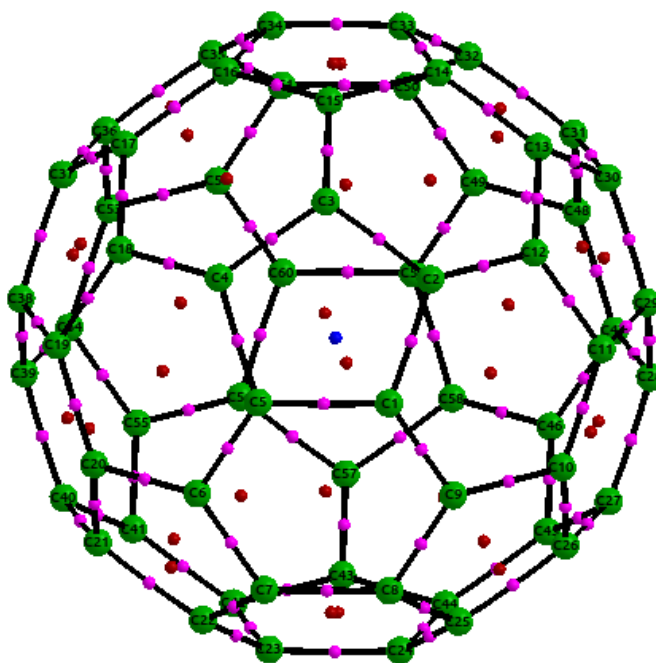
Figure 1.10 Molecular graph of fullerene (C_{60}) showing different CPs of MED. The blue, maroon and pink spheres indicate (3, +3), (3, +1) and (3, -1) CPs respectively.

At a CP, the 'Hessian matrix' is created from the nine possible second derivatives of $\rho(\mathbf{r})$, and the Laplacian $\nabla^2\rho(\mathbf{r})$ is represented as the sum of the eigenvalues (λ_1, λ_2, and λ_3) of the H of $\rho(\mathbf{r})$. The eigenvalues λ_1, λ_2, and λ_3 represent the principal axes of curvature because the magnitudes of the three second derivatives of $\rho(\mathbf{r})$ calculated with respect to these axes are maximized or minimized.

$$\nabla^2\rho(\mathbf{r}) = \nabla(\nabla\rho(\mathbf{r})) = \frac{\partial^2\rho(\mathbf{r})}{\partial x^2} + \frac{\partial^2\rho(\mathbf{r})}{\partial y^2} + \frac{\partial^2\rho(\mathbf{r})}{\partial z^2} = \lambda_1 + \lambda_2 + \lambda_3 \qquad \text{Eq. 1.43}$$

The $\nabla^2\rho(\mathbf{r})$ serves as the foundation for famous electron pair model of Lewis.[155-158] It has the potential to be effectively combined with other major ideas in molecular electronic structure theory. Further, when paired with the electrostatic Hellmann-Feynman

theorem, $\nabla^2\rho(\mathbf{r})$ provides the characterization of binding or non-binding interactions within the molecules.

Bader had established correlations between the parameters of MED topology and fundamental chemical concepts like bond order and bond ellipticity, *etc.*[159, 160] For instance, the bond order (denoted as "b") can be estimated using the relationship $b = e^{[A(\rho_b - B)]}$, where ρ_b represents the MED at the (3, -1) CP, which typically resides between the two bonded atoms A and B. Parameters A and B are appropriately defined constants in this context. Similarly, bond ellipticity can be determined as $\varepsilon = [\lambda_1/\lambda_2 - 1]$ where λ_1 and λ_2 represent the eigenvalues corresponding to the soft curvatures. The MED topology is a widely employed tool for gaining insights into the characteristics and properties of chemical bonds within molecules. It has primarily been employed to analyze electronic rearrangements that occur during the formation of molecules through atom interactions.

1.3.3 MESP and MED: How Are They Related?

1.3.3.1 Similarities and Differences in the Topology

The topological features of MESP are complementary to that of MED, while MESP and MED topological properties have numerous similarities as well as differences.

Similarities:

- The MED exhibits a maximum at the nuclear sites, coinciding with the maxima observed in the MESP

- MESP do not show a non-nuclear maximum just like some cases in MED

- The saddle point, (3, -1) CP present in both the cases signifies the atom-atom interactions

Differences:

- MED is a positive semi-definite function, while MESP can attain both positive and negative values

- MED topology does not directly provide information about the precise location of lone pairs, features of π-bonds, molecular reactivity, *etc.*, which is possible through MESP

However, the idea of electrostatic potential is closely tied to electron density and can play a crucial role in density functional theories. It was given by Poisson's equation as;

$$\nabla^2 V(\mathbf{r}) = (\lambda_1 + \lambda_2 + \lambda_3) = 4\pi\rho(\mathbf{r}) \qquad \text{Eq. 1.44}$$

Part B

Computational Methodology

1.4 An Overview

Computational chemistry constitutes a specialized domain within the realm of chemistry, leveraging computer simulations and mathematical models to delve into the intricacies of molecular behaviour, atomic interactions, and chemical reactions.[161] Its overarching objective is to furnish a deeper understanding of a diverse array of chemical phenomena, encompassing the intrinsic characteristics of solitary molecules as well as intricate and multifaceted chemical processes. Computational chemistry harnesses the techniques and potential of theoretical chemistry and computer simulations to address a wide array of intricate chemical inquiries.[162] Originating from the endeavors of theoretical physicists in 1928 to solve the Schrödinger equation, computational chemistry forms the cornerstone of numerous computational methodologies. Notably, the solutions derived from the Schrödinger equation have demonstrated their ability to replicate experimentally observed attributes in simple systems, such as the helium atom and hydrogen molecule. This initial success spurred the pursuit of approximate solutions for larger systems and precise solutions for basic models, kindling the enthusiasm of chemists and physicists for a qualitative exploration of diverse chemical phenomena.[163]

The evolution of computational chemistry, rooted in the Schrödinger equation, has reached a level of advancement where it offers highly accurate and suitable tools for investigating molecular properties within the realm of quantum mechanics. This discipline provides valuable insights into a multitude of areas, including geometry prediction, molecular properties, spectroscopic characteristics, reaction mechanisms, *etc*. Moreover, computational chemistry exhibits another advantageous facet by enabling the investigation of materials that are either elusive or financially prohibitive to acquire.

Prominent computational techniques encompass *ab initio* quantum chemical methods, DFT methods, semiempirical methods, molecular mechanics (MM), molecular dynamics (MD), and hybrid QM/MM methods. *Ab initio* quantum chemical methods form a category of approaches wherein molecular structures are computed through the utilization of the Schrödinger equation. Semiempirical methods leverage experimentally derived parameters to furnish input for mathematical models. Within DFT, the pivotal parameter of electron density facilitates the computation of the fundamental electronic configuration of atoms, molecules, and solid-state materials. Molecular mechanics relies on force fields encompassing empirical parameters, facilitating the exploration and interpretation of atomic and molecular behaviour. Meanwhile, molecular dynamics calculations unveil the time-dependent dynamics of molecular systems, yielding comprehensive insights into the fluctuations and conformational changes exhibited by biological molecules.

1.4.1 *Ab initio* Quantum Chemical Methods

The foundational premise underlying nearly all quantum mechanical methodologies is the resolution of the Schrödinger equation for a complex assembly comprising numerous electrons and nuclei. The term "*ab initio*" denotes computations grounded in first principles, encompassing the computational solution of the electronic, time-independent Schrödinger equation.[164, 165] This non relativistic time-independent Schrödinger equation is typically expressed as:

$$H\Psi = E\Psi \hspace{4cm} \text{Eq. 1.45}$$

where, H represents the Hamiltonian operator for a system composed of nuclei and electrons, characterized by position vectors R_A and r_i, respectively. Ψ symbolizes the many-electron wave function, and E denotes the energy eigenvalue of the system. The Hamiltonian of multi-electron system (in au) containing N electrons and M nuclei can be represented as,

$$H = -\sum_{i=1}^{N} \frac{1}{2}\nabla_i^2 - \sum_{A=1}^{M} \frac{1}{2M_A}\nabla_A^2 - \sum_{i=1}^{N}\sum_{A=1}^{M} \frac{Z_A}{r_{iA}} + \sum_{i=1}^{N}\sum_{j>i}^{N} \frac{1}{r_{ij}} + \sum_{A=1}^{M}\sum_{B>A}^{M} \frac{Z_A Z_B}{R_{AB}} \qquad \text{Eq. 1.46}$$

where M_A is the ratio of the mass of the nucleus A to the mass of an electron, Z_A is the atomic number of nucleus A, r_{iA} is the distance between i^{th} electron and A^{th} nucleus, r_{ij} is the distance between the ith and j^{th} electrons and R_{AB} is the distance between A^{th} nucleus and B^{th} nucleus. The first term in the Eq. 1.46 is the operator for kinetic energy of electrons, the second term is the operator for kinetic energy of the nuclei, the third term is the Coulombic attraction between electrons and nuclei, fourth term is the repulsion between the electrons and fifth term is the repulsion between the nuclei.

The rigorous resolution of the Schrödinger equation remains essentially confined to the hydrogen atom, with its exact treatment being theoretically attainable in this isolated case. However, to achieve precise calculations for all other systems, certain simplifications become necessary. Among the most prevalent simplifications are the Born–Oppenheimer (BO) approximation and the one-electron approximation.[166, 167] Due to the significantly faster velocity of the electrons, the BO approximation treats the nuclei to be stationary compared to electrons. Consequently, the nuclear kinetic energy term in the Eq. 1.47 vanishes, and the repulsion between nuclei assumes a constant value. This approximation gives rise to the residual electronic Hamiltonian, which characterizes the motion of N electrons and is expressed as,

$$H_{elec} = -\sum_{i=1}^{N} \frac{1}{2}\nabla_i^2 - \sum_{i=1}^{N}\sum_{A=1}^{M} \frac{Z_A}{r_{iA}} + \sum_{i=1}^{N}\sum_{j>i}^{N} \frac{1}{r_{ij}} \qquad \text{Eq. 1.47}$$

The Schrödinger equation involving the electronic Hamiltonian is,

$$H_{elec}\Phi_{elec} = E_{elec}\Phi_{elec} \qquad \text{Eq. 1.48}$$

and the electronic wave function becomes,

$$\Phi_{elec} = \Phi_{elec}(\{r_i\}\,;\{R_A\}) \qquad \text{Eq. 1.49}$$

The Eq. 1.49 describes that motion of electrons which depends explicitly on the electronic coordinates and parametrically on the nuclear coordinates. The electronic energy can be represented as,

$$E_{elec} = E_{elec}(\{\mathbf{R}_A\}) \qquad\qquad \text{Eq. 1.50}$$

The total energy for fixed nuclei must include constant nuclear repulsion term,

$$E_{total} = E_{elec} + \sum_{A=1}^{M}\sum_{B>A}^{M} \frac{Z_A Z_B}{\mathbf{R}_{AB}} \qquad\qquad \text{Eq. 1.51}$$

The equations (Eq. 1.47 to Eq. 1.51) correspond to the electronic problem. Afterwards, the same assumptions are used to solve for the Hamiltonian for the motion of nuclei. Thus, the nuclear Hamiltonian is given as,

$$H_{nucl} = -\sum_{A=1}^{M}\frac{1}{2M_A}\nabla_A^2 + E_{elec}(\{\mathbf{R}_A\}) + \sum_{A=1}^{M}\sum_{B>A}^{M}\frac{Z_A Z_B}{\mathbf{R}_{AB}} \qquad\qquad \text{Eq. 1.52}$$

$$H_{nucl} = -\sum_{A=1}^{M}\frac{1}{2M_A}\nabla_A^2 + E_{total}(\{\mathbf{R}_A\}) \qquad\qquad \text{Eq. 1.53}$$

The total energy term, $E_{total}(\mathbf{R}_A)$ gives information about the potential for nuclear motion. The solution to the nuclear Schrödinger equation describes the vibration, rotation and translation of a molecule and E.

$$H_{nucl}\Phi_{nucl} = E\Phi_{nucl} \qquad\qquad \text{Eq. 1.54}$$

$$\Phi_{nucl} = \Phi_{nucl}(\{\mathbf{R}_A\}) \qquad\qquad \text{Eq. 1.55}$$

where, E is the BO approximation to the total energy, comprised of the electronic, rotational, vibrational, and translational energy terms. The consequent approximation for the total wave function is given as,

$$\Phi(\{\mathbf{r}_i\}\,;\{\mathbf{R}_A\}) = \Phi_{elec}(\{\mathbf{r}_i\}\,;\{\mathbf{R}_A\})\,\Phi_{nucl}(\{\mathbf{R}_A\}) \qquad\qquad \text{Eq. 1.56}$$

Therefore, the BO approximation allows separation of electronic and nuclear Hamiltonians, as well as electronic wave functions where electronic wave functions exhibit explicit dependence on electronic coordinates and parametrical dependence on nuclear coordinates.

1.4.1.1 Hartree-Fock Theory

The Hartree-Fock (HF) calculation stands as the most comprehensive form of *ab initio* computation, wherein the many-electron Schrödinger equation is disentangled into

a series of more manageable one-electron equations. Each of these individual equations is meticulously solved to yield a distinct single-electron wave function, denoted as an orbital. These orbitals adeptly encapsulate the behaviour of an electron within the collective influence of its neighbouring electrons. These wave functions are formed as linear combinations of atomic orbitals or basis functions. However, as a consequence of this construction, HF calculations typically yield computed energies surpassing the Hartree-Fock limit. This calculated energy value serves as an upper bound.[168] To illustrate the exact wave function for a fully interacting system, a simple system comprising non-interacting electrons with the characteristic Hamiltonian can be chosen first.

$$H = \sum_{i=1}^{N} h(i)$$

Eq. 1.57

Here, $h(i)$ is the operator describing the kinetic and potential energies of ith electron. $h(i)$ is an effective one electron Hamiltonian that incorporates average effects of electron-electron repulsion. $h(i)$ constitutes a set of eigenfunctions, represented as spin orbitals, χ_j,

$$h(i)\chi_j(\mathbf{x}_i) = \varepsilon_j\,\chi_j(\mathbf{x}_i)$$

Eq. 1.58

The corresponding many-electron wave function can be written as the product of individual spin orbital wave functions and is called the *Hartree Product* (HP), given by:

$$\Psi^{HP}(\mathbf{x}_1,\mathbf{x}_2,\ldots.,\mathbf{x}_N) = \chi_i(\mathbf{x}_1)\chi_j(\mathbf{x}_2)\ldots..\chi_N(\mathbf{x}_N)$$

Eq. 1.59

The HP exhibits certain limitations that fail to adequately account for electron indistinguishability, it does succeed in discerning the distinct identities of electrons within the context of spin orbitals. Specifically, it designates electron-one to inhabit the spin orbital χ_i, while electron-two is assigned to the spin orbital χ_j. However, in addition to satisfying the Schrödinger equation, an exact wave function must obey antisymmetry principle (Pauli's principle) which states that "*many-electron wave function must exhibit antisymmetry when subjected to the interchange of both the spin and spatial attributes of any two electrons.*"

Consider two electrons, electron one in spin orbital χ_i and electron two in χ_j. Then,

$$\Psi_{1,2}^{HP}(\mathbf{x}_1, \mathbf{x}_2) = \chi_i(\mathbf{x}_1)\chi_j(\mathbf{x}_2)$$
Eq. 1.60

If the electron one is in spin orbital χ_j and electron two in χ_i,

$$\Psi_{2,1}^{HP}(\mathbf{x}_1, \mathbf{x}_2) = \chi_j(\mathbf{x}_1)\chi_i(\mathbf{x}_2)$$
Eq. 1.61

The $\Psi(\mathbf{x}_1, \mathbf{x}_2)$ is antisymmetric with respect to the interchange of two electrons. Then,

$$\Psi_{1,2}^{HP}(\mathbf{x}_1, \mathbf{x}_2) = -\Psi_{2,1}^{HP}(\mathbf{x}_1, \mathbf{x}_2)$$
Eq. 1.62

and the wave function vanishes if both electrons occupy same orbital i.e., $i = j$. In general, an antisymmetric wave function must satisfy the condition:

$$\Phi(\mathbf{x}_1, \dots, \mathbf{x}_i, \dots, \mathbf{x}_j, \dots, \mathbf{x}_N) = -\Phi((\mathbf{x}_1, \dots, \mathbf{x}_i, \dots, \mathbf{x}_j, \dots, \mathbf{x}_N)$$
Eq. 1.63

However, the HP does not satisfy the antisymmetry principle. The antisymmetrized wave function is achieved by organizing the one-electron spin-orbital in the Slater determinant form. The Slater determinant of an N-electron wave function is given as:

$$\Psi(\mathbf{x}_1, \mathbf{x}_2, \dots, \mathbf{x}_N) = \frac{1}{\sqrt{N!}} \begin{vmatrix} \chi_i(\mathbf{x}_1) & \chi_j(\mathbf{x}_1) & \cdots & \chi_N(\mathbf{x}_1) \\ \chi_i(\mathbf{x}_2) & \chi_j(\mathbf{x}_2) & \cdots & \chi_N(\mathbf{x}_2) \\ \cdot & \cdot & & \cdot \\ \cdot & \cdot & & \cdot \\ \cdot & \cdot & & \cdot \\ \chi_i(\mathbf{x}_N) & \chi_j(\mathbf{x}_N) & \cdots & \chi_N(\mathbf{x}_N) \end{vmatrix}$$
Eq. 1.64

where $\frac{1}{\sqrt{N!}}$ is called normalization factor. For N electrons, N spin orbitals are there. The rows of the determinant are designated by electrons ($\mathbf{x}_1$, $\mathbf{x}_2$, *etc.*) and columns by spin orbitals (χ_i, χ_j, *etc.*). The interchange of the coordinates of two electrons will correspond to the interchange of the two rows of the determinant resulting in the sign change. If the two electrons occupy the same spin orbitals, it will result in two equal columns in the determinant, and consequenlty, determinant will be zero. Thus, the Pauli's exclusion principle and antisymmetry condition are satisfied. The normalized form of Slater determinant having only the diagonal elements can be further simplified and expressed as,

$$\Psi(\mathbf{x}_1, \mathbf{x}_2, \dots, \mathbf{x}_N) = |\chi_i \chi_j \dots \chi_N\rangle$$
Eq. 1.65

According to the variation principle, an appropriate wave function of the functional form of Ψ will be the one with the lowest possible energy, which is given as

$$E_0 = \langle \Psi_0 | H | \Psi_0 \rangle \qquad \text{Eq. 1.66}$$

The vibrational flexibility in the wave function Eq. 1.65 is in the choice of spin orbitals, χ. By minimizing E_0 with respect to the choice of χ, it is possible to derive an equation called HF equation, which determines the optimal spin of the orbitals. HF equation is an eigenvalue equation of the form,

$$f(i)\chi(\mathbf{x}_i) = \varepsilon\chi(\mathbf{x}_i) \qquad \text{Eq. 1.67}$$

where, $f(i)$ is the effective one-electron operator, called Fock operator, of the form,

$$f(i) = -\frac{1}{2}\nabla_i^2 - \sum_{A=1}^{M}\frac{Z_A}{r_{iA}} + v^{HF}(i) \qquad \text{Eq. 1.68}$$

where $v^{HF}(i)$ is the average potential experienced by i^{th} electron due to the presence of other electrons. The essence of HF approximation is to replace the complicated many electron problems by one electron problem in which electron-electron repulsion is treated in an average way. The $v^{HF}(i)$ is depends on the spin orbitals of other electrons. Therefore, the HF equation is a non-linear one and the iterative procedure is required to solve it called self-consistent-field (SCF) method. For that, an initial guess at the spin orbitals is made to get the average field by each electron and eigenvalue equation is solved for a new set of spin orbitals. The new spin orbitals will give new fields and the procedure is repeated until self-consistency is attained. The solution to Eq. 1.67 gives a set of orthonormal HF spin orbitals χ_k having orbital energies ε_k. The N spin orbitals with the lowest energies are called occupied orbitals. The Slater determinant formed from occupied spin orbitals is HF ground state wave function, which is the best variational approximation to the ground state of the system. The orbitals other than the occupied spin orbitals are termed as virtual or unoccupied orbitals. For the HF equation Eq. 1.67, there will be infinite number of solutions and infinite number of virtual spin orbitals. A finite set of spatial basis functions $\{\phi_\mu(\mathbf{r})| \mu=1, 2, 3,.....K\}$ are used for solving it. 2K Spin orbitals will be generated in which K with α spin and K with β spin. This give rise to a set of N occupied orbitals $\{\chi_a\}$ and a complementary set of 2K-N unoccupied orbitals $\{\chi_r\}$. A

single Slater determinant formed form the set $\{\chi_a\}$ is the variational HF ground state, which is represented as Ψ_0 or $|\Psi_0\rangle$. With the increase in the size of the basis set the HF energy $E_0 = \langle\Psi_0|H|\Psi_0\rangle$ attains a limit called *Hartree-Fock limit.*

Koopman's theorem and Brillouin's theorem are two significant theorems associated with the HF equations.[169] The Koopman's theorem gives a way to calculate the approximate ionization potentials and electron affinities. The theorem states that "*for an N-electron HF single determinant $|^N\Psi_0\rangle$ with occupied and virtual spin orbital energies $\mathcal{E}_a$ and $\mathcal{E}_r$, the ionization potential to produce (N-1)–electron single determinant $|^{N-1}\Psi_a\rangle$ with identical spin orbitals can be obtained by removing an electron from spin orbital, χ_a is $-\mathcal{E}_a$. Similarly, the electron affinity to produce (N+1)–electron single determinant $|^{N+1}\Psi_r\rangle$ can be obtained by adding an electron to spin orbital, χ_r is $-\mathcal{E}_r$.*" Brillouin's theorem states that "*singly excited determinants, $|\Psi_a^r\rangle$ will not interact directly with a reference HF determinant, $|\Psi_0\rangle$ i.e., $\langle\Psi_0/H/\Psi_a^r\rangle = 0$.*"

Clemens C. J. Roothaan and George G. Hall[170, 171] derived the derivation of HF equations for the closed shell systems, by considering the spin orbitals as linear combinations of basis functions (Φ_μ).

$$\Psi_i = \sum_{\mu=1}^{K} C_{\mu i}\phi_\mu \qquad i = 1, 2, \ldots\ldots, K \qquad \text{Eq. 1.69}$$

Where $C_{\mu i}$ are the coefficients of Φ_μ, and K is the total number of basis functions. The Roothaan-Hall equation for closed shell systems is also known as restricted Hartree-Fock theory (RHF). In a single matrix form of the Eq.1.69 is given as,

$$\mathbf{FC} = \mathbf{SC\varepsilon} \qquad \text{Eq. 1.70}$$

where $\mathbf{F}$ is the Fock matrix, $\mathbf{C}$ is a matrix of coefficients, $\mathbf{S}$ is the overlap matrix of the basis functions and $\mathbf{\varepsilon}$ is the matrix of orbital energies. The HF theory constructed using the Roothaan approach results in certain limitations since all the electron correlation is ignored other than exchange. Though the correlation energy can be a small fraction of the total energy, it can be significant in many systems of physical and chemical interest. Also, basis set requires numerical solution of the four index integrals appearing in the

Fock matrix elements which is a tedious process. Since each index exceeds the total number of basis functions, there will be N^4 total integrals to be evaluated.

1.4.1.2 Post Hartree-Fock Methods

The HF approach accounts for the average impact of electron repulsion but fails to account for electron correlation, limiting its accuracy. Post-Hartree-Fock methods emerge as a suite of techniques devised to enhance the SCF or HF approach by incorporating electron correlation with greater precision.[172, 173] The difference between the exact energy and the energy calculated by the HF approach yields the correlation energy, given as

$$E_{corr} = \varepsilon_0 - E_{HF}$$

Eq. 1.71

where E_{HF} is the energy in the Hartree-Fock limit and ε_0 is the exact non-relativistic energy of a system. Configuration Interaction (CI), Møller-Plesset perturbation theory (MPn), and Coupled Cluster (CC) theory *etc.*, are examples of post-HF approaches.

1.4.2 Semiempirical Methods

Semiempirical quantum chemistry seeks to overcome the two limitations of Hartree-Fock calculations, *viz.*, low speed and low precision, by ignoring or parameterizing some integrals depending on experimental data, such as ionization energies of atoms or dipole moments of molecules. As a result, semiempirical approaches are highly rapid, can be applied to huge molecules, and can produce accurate results when applied to molecules identical to the molecules used for parameterization. On the downside, the accuracy of semiempirical approaches varies between systems.[174, 175]

The Neglect of Diatomic Differential Overlap (NDDO) approach is used in modern semiempirical models, wherein the overlap matrix **S** is replaced with the unit matrix. This permits the HF secular equation |H-ES| = 0 to be replaced with the simpler equation |H-E| = 0.[176, 177] Existing semiempirical models differ in terms of the additional approximations applied while assessing one- and two-electron integrals as well as during the parameterization. Modified Neglect of Diatomic Overlap (MNDO), introduced by

Dewar and Thiel (1977), is a pioneering NDDO model.[178] It parametrizes one-center two-electron integrals using isolated atom spectroscopic data, while other integrals are evaluated through classical electrostatic multipole interactions. Traditional MNDO employs s and p orbital basis sets, while the more recent MNDO/d incorporates d-orbitals, crucial for hypervalent sulfur and transition metals. MNDO's limitations include challenges in characterizing hydrogen bonds due to strong intermolecular repulsion. It also demonstrates limited reliability in predicting formation temperatures. Austin Model 1 (AM1) by Dewar and co-workers,[179] is akin to MNDO in approximating two-electron integrals but modifies nuclear-nuclear core repulsion. This yields simulated van der Waals interactions through non-physical attractive forces. Parameterization, centered on dipole moments, ionization potentials, and geometries, accommodates these changes. AM1 captures hydrogen bonding yet exhibits weaknesses such as overestimating basicity and inaccuracies in predicting the water dimer's lowest energy geometry. Nonetheless, AM1 enhances properties like heats of formation over MNDO. Parametric Method 3 (PM3), developed by James Stewart, shares a Hamiltonian akin to AM1, but diverges in parameterization strategy.[180] While AM1 parameterized on limited atomic data, PM3 prioritizes a broader spectrum of molecular properties, shifting toward a statistical approach. The thermochemical predictions using PM3 slightly outperform those of AM1 method. Widely utilized for quick molecular property estimation, PM3 has been extended to encompass numerous elements, including select transition metals. The PM6[181] and PM7[182] methods essentially cover the whole periodic table and are used for the calculation of molecular and solid state properties, while the Orthogonalization Models (OM1, OM2, and OM3)[183] add orthogonalization corrections in the one-electron terms of the NDDO Fock matrix to account for the Pauli's repulsion.

1.4.3 Density Functional Theory

The discovery of DFT has played an important role in the growth of quantum chemistry.[5, 184, 185] The fundamental disadvantage of the HF approach is the 3N level dependency of the wave function on the number of electrons (N). As the number of electrons rises, the wave function becomes too difficult to operate with. The main notion

behind DFT is that the energy of electronic systems may be determined using its electron density, $\rho(\mathbf{r})$ rather than the wave function utilized in HF theory. *i.e.*, The wave function of an N-electron system is determined by 3N variables, whereas density is determined by only three variables, making it easier to deal with. The foundation of the theory was derived from the Thomas Fermi model proposed in 1927. Hohenberg and Kohn published the first reports on DFT in 1964,[43] followed by Kohn and Sham in 1965.[186] The importance of DFT in comprehending molecular science is acknowledged in the 1998 Nobel Prize in Chemistry, which was shared equally by Walter Kohn "for his development of density-functional theory" and John A. Pople "for his development of computational methods in quantum chemistry."

The wave function Ψ for an N-electron molecule is a function of 3N-spatial coordinates and N-spin coordinates. From Ψ, we can produce the molecule's spin free electron density function, by integrating $\Psi^*\Psi$ over all of the spin coordinates and all the space coordinates, written as,

$$\rho(\mathbf{r}) = \int |\Psi(1, 2, \ldots\ldots N)|^2 \, d\tau \qquad \text{Eq. 1.72}$$

According to the DFT formalism, the electronic energy is a functional of electron density, or there is a one-to-one relationship between the electron density and its energy. In DFT, the system is described by its density $\rho(\mathbf{r})$, which is a function of its many body wave-function, and the dependency is reduced to three spatial coordinates (or four if spin is added) independent of N. This permits the use of DFT on systems containing hundreds or even thousands of atoms. Also, when electron density is integrated across all space, the total number of electrons, N, is obtained.

$$N = \int \rho(\mathbf{r})d\mathbf{r} \qquad \text{Eq. 1.73}$$

1.4.3.1 Thomas-Fermi Model

Thomas and Fermi model for describing energy of a system as a function of total electron density is widely regarded as a predecessor to modern DFT.[187] Thomas and Fermi developed a kinetic energy formulation based on uniform electron gas that treats

electron-nucleus and electron-electron interactions classically[188] wherein the kinetic energy of electron gas (T_{TF}) is solely determined by the electron density $\rho(\mathbf{r})$, represented as,

$$T_{TF}[\rho(\mathbf{r})] = \frac{3}{10}(3\pi^2)^{2/3} \int \rho(\mathbf{r})^{5/3}d\mathbf{r}$$

Eq. 1.74

It is based on the approximation that the kinetic energy of the electrons depends exclusively on $\rho(\mathbf{r})$. As a result, the total energy in terms of $\rho(\mathbf{r})$ may be calculated by combining the electron-nucleus and electron-electron interactions given by,

$$E[\rho(\mathbf{r})] = \frac{3}{10}(3\pi^2)^{2/3} \int \rho(\mathbf{r})^{5/3}d\mathbf{r} - Z\int \frac{\rho(\mathbf{r})}{\mathbf{r}}d\mathbf{r} + \frac{1}{2}\iint \frac{\rho(\mathbf{r}_1)\rho(\mathbf{r}_2)}{|\mathbf{r}_1 - \mathbf{r}_2|}d\mathbf{r}_1 d\mathbf{r}_2$$

Eq. 1.75

where second and third terms symbolize the electron-nucleus attraction and electron-electron repulsions, respectively.

However, its accuracy is restricted by errors caused by erroneous depiction of kinetic energy, exchange energy, and full disregard for electron correlation. The addition of the exchange correlation in Eq. 1.75 resulted in a modified form known as the Thomas-Fermi-Dirac model.[189] Although both models are crucial, the assumptions applied inside make them inferior in the current formalism since they represent the fundamental pieces of DFT. The assumption of homogeneous electron gas is adequate for valence electrons in some systems, but not for atoms and molecules. Two Hohenberg-Kohn theorems underpin current DFT.

1.4.3.2 Hohenberg-Kohn Theorems

The Hohenberg-Kohn (HK) theorems[190] are the theoretical foundations upon which all modern DFTs are built.[186, 191] Electrons interact with one another and with an external potential, according to the DFT formulation. The first theorem states that "*ground-state properties of a many-electron system are uniquely determined by an ground state density,$\rho(\boldsymbol{r})$ that depends only on three spatial coordinates*" or "*the external potential $V_{ext}(\boldsymbol{r})$ is a unique functional of $\rho(\boldsymbol{r})$*". Otherwise, two different external potentials cannot lead to one ground state density. This is demonstrated through the use of the reductio ad

absurdum method. This theorem was then extended to the time-dependent domain, leading to the development of time-dependent density functional theory (TDDFT), which are used to characterize excited states.

The second HK theorem develops an energy functional for the system and demonstrates that the ground-state $\rho(\mathbf{r})$ minimizes this functional. This is a variational theorem, the $\rho(\mathbf{r})$ obeys a variational principle in such a way that the $\rho(\mathbf{r})$ that minimizes the total energy is the exact ground state density. This theorem states that "t*he ground state energy can be obtained variationally: the density that minimizes the total energy is the exact ground state density".* This ground state energy density and energy functional can be further utilized to calculate different properties of the system. The electron density that minimizes the energy of the overall functional is the true electron density corresponding to the full solutions of the Schrödinger Equation.

The total energy of the system is a functional of $\rho(\mathbf{r})$ and can be represented as,

$$E[\rho(\mathbf{r})] = F[\rho(\mathbf{r})] + V_n + \int V_{\text{ext}}(\mathbf{r})\rho(\mathbf{r})\mathrm{d}\mathbf{r}$$

Eq. 1.76

where $F[\rho(\mathbf{r})]$ is the sum of kinetic energy of the electrons, $T_e[\rho(\mathbf{r})]$ and the contribution from inter-electronic interactions, $V_e[\rho(\mathbf{r})]$. V_n represents the inter-nuclear interactions and last term shows the interaction of electrons with nuclei. According to this, the value of any trial energy functional, $E_a[\rho_a(\mathbf{r})]$ is greater than the ground state energy functional, $E_0[\rho_0(\mathbf{r})]$. Although the HK theorems are extremely powerful, they do not offer a way of computing the ground-state density of a system in practice.

1.4.3.3 The Kohn-Sham Equations

Kohn and Sham developed a realistic method for solving the Hohenberg-Kohn theorem. Kohn–Sham equation[190] is the non-interacting Schrödinger equation of a fictitious system of non-interacting electrons that generate the same density as any given system of interacting electrons. The difficulty in calculating $F[\rho(\mathbf{r})]$ using Eq. 1.76 is compensated by separation of the functional given as,

$$F[\rho(\mathbf{r})] = E_{KE}[\rho(\mathbf{r})] + E_{H}[\rho(\mathbf{r})] + E_{XC}[\rho(\mathbf{r})]$$

Eq. 1.77

where, $E_{KE}[\rho(\mathbf{r})]$ is the kinetic energy of non-interacting electrons, given by,

$$E_{KE}[\rho(\mathbf{r})] = \sum_{i=1}^{N} \int \Psi_i(\mathbf{r}) \left(-\frac{\nabla^2}{2}\right) \Psi_i(\mathbf{r}) d\mathbf{r}$$

Eq. 1.78

$E_{H}[\rho(\mathbf{r})]$ is the electron-electron Coulombic energy or Hartree electrostatic energy,

$$E_{H}[\rho(\mathbf{r})] = \frac{1}{2} \iint \frac{\rho(\mathbf{r}_1)\rho(\mathbf{r}_2)}{|\mathbf{r}_1 - \mathbf{r}_2|} d\mathbf{r}_1 d\mathbf{r}_2$$

Eq. 1.79

and $E_{XC}[\rho(\mathbf{r})]$ is the energy contributions from exchange and correlation. The full expression of enery of an *N*-electron system within the structure of Kohn-Sham scheme is obtained by combining the $E_{KE}[\rho(\mathbf{r})]$ and $E_{H}[\rho(\mathbf{r})]$ terms with the electron–nuclear interaction.

$$E[\rho(\mathbf{r})] = \sum_{i=1}^{N} \int \Psi_i(\mathbf{r}) \left(-\frac{\nabla^2}{2}\right) \Psi_i(\mathbf{r}) d\mathbf{r} + \frac{1}{2} \iint \frac{\rho(\mathbf{r}_1)\rho(\mathbf{r}_2)}{|\mathbf{r}_1 - \mathbf{r}_2|} d\mathbf{r}_1 d\mathbf{r}_2 + E_{XC}[\rho(\mathbf{r})] - \sum_{A=1}^{M} \int \frac{Z_A}{\mathbf{r} - \mathbf{R}_A} \rho(\mathbf{r}) d\mathbf{r}$$

Eq.1.80

The exchange correlation functional, $E_{XC}[\rho(\mathbf{r})]$ of a system, not only consists exchange and correlation terms, but depends on the difference between precise kinetic energy and the kinetic energy of non-interacting electrons, $E_{KE}[\rho(\mathbf{r})]$ also. As a result, Kohn and Sham depicted the density of the system as a sum of the square moduli of the N one-electron orthonormal orbitals as,

$$\rho(\mathbf{r}) = \sum_{i=1}^{N} |\psi_i(\mathbf{r})|^2$$

Eq. 1.81

By using the variational condition given in Eq. 1.81, the one-electron Kohn-Sham equation can be formulated as,

$$\left\{-\frac{\nabla_1^2}{2} - \left(\sum_{A=1}^{M} \frac{Z_A}{\mathbf{r}_{1A}}\right) + \int \frac{\rho(\mathbf{r}_2)}{\mathbf{r}_{12}} d\mathbf{r}_2 + V_{XC}[\mathbf{r}_1]\right\} \psi_i(\mathbf{r}_1) = \varepsilon_i \psi_i(\mathbf{r}_1)$$

Eq. 1.82

where ε_i are the orbital energies, and V_{XC} is the exchange-correlation potential which is related to the exchange-correlation energy (E_{XC}) by,

$$V_{XC}[\mathbf{r}] = \frac{\delta E_{XC}[\rho(\mathbf{r})]}{\delta\rho(\mathbf{r})}$$

Eq. 1.83

Now it is made convenient to calculate total electronic energy *viz.* Eq. 1.80. The self-consistent approach is adopted to solve the Kohn–Sham equations, where the convergence is attained initially by a guess of density in Eq. 1.82 to develop a set of orbitals and better value for density, followed by the second iteration and so on.

1.4.3.4 Exchange-Correlation Functionals

The exchange-correlation energy, E_{XC} is generally divided into two terms, an exchange term E_X (associated with the interaction of electrons of the same spin) and a correlation term E_C (associated with the interaction of electrons of opposite spin). The corresponding functionals are exchange functional and correlation functional, respectively.

$$E_{xc}[\rho(\mathbf{r})] = E_x[\rho(\mathbf{r})] + E_c[\rho(\mathbf{r})]$$

Eq. 1.84

The functional dependence of E_{XC} on $\rho(\mathbf{r})$ is expressed as an interaction between the $\rho(\mathbf{r})$ and an energy density, $\mathcal{E}_{xc}$ which is taken as a sum of individual exchange and correlation contributions.

$$E_{xc}[\rho(\mathbf{r})] = \int \rho(\mathbf{r})\, \mathcal{E}_{xc}[\rho(\mathbf{r})]d\mathbf{r}$$

Eq. 1.85

where, $\rho(\mathbf{r})$ is a density per unit volume, whereas $\mathcal{E}_{xc}$ is a density per particle, and the Slater exchange energy density is given by,

$$\mathcal{E}_{xc}[\rho(\mathbf{r})] = -\frac{9\alpha}{8}\left(\frac{3}{\pi}\right)^{\frac{1}{3}} \rho^{\frac{1}{3}}(\mathbf{r})$$

Eq. 1.86

The total density is the sum of α and β spin density contributions ($\rho = \rho_\alpha + \rho_\beta$) where α and β represent spin up and down, respectively. Several approximations for practical applications of DFT, such as local density approximation, generalized gradient approximation, and *meta-* generalized gradient approximation, have been devised by changing the exchange-correlation potential.

1.4.3.4.1 Local Density Approximation

The Local Density Approximation (LDA), which assumes the density behaves locally as a uniform electron gas, is one of the simplest DFT methods.[192, 193] In LDA, the value of $\mathcal{E}_{xc}$ at a position $\mathbf{r}$ might be derived solely from the local value of $\rho(\mathbf{r})$ at that position, with the only requirement that $\rho(\mathbf{r})$ must be single-valued at all positions. Practically, the only functionals that fit this description are those produced through uniform electron gas analysis, hence LDA is rarely employed. The number of electrons N as well as the volume V of the gas are considered to approach infinity but the electron density attains a constant value everywhere.[194] LDA assumes $\mathcal{E}_{xc}$ at any point is a function of $\rho(\mathbf{r})$ at that point and the exchange function can be represented as,

$$E_X^{LDA}[\rho(\mathbf{r})] = -\frac{3}{4}\left(\frac{3}{\pi}\right)^{\frac{1}{3}} \int \rho(\mathbf{r})^{\frac{4}{3}}\, d\mathbf{r}$$

<div align="right">Eq. 1.87</div>

In the case of unequal α and β densities, LDA has largely been substituted by Local Spin Density Approximation (LSDA). LSDA sums individual densities raised to the power of 4/3. It is an exact DFT approach for the uniform electron gas case. For closed shell systems, LDA and LSDA are frequently used interchangeably. The exchange functional in LSDA approach is given by:

$$E_X^{LSDA}[\rho(\mathbf{r})] = -2^{1/3}\left(-\frac{3}{4}\left(\frac{3}{\pi}\right)^{\frac{1}{3}}\right)\int\left(\rho_\alpha(\mathbf{r})^{\frac{4}{3}} + \int \rho_\beta(\mathbf{r})^{\frac{4}{3}}\right) d\mathbf{r}$$

<div align="right">Eq. 1.88</div>

In LDA, it is difficult to obtain the correlation energy per particle E_C separately for the E_{XC}. To satisfy this DFT, Vosko, Wilk and Nusair designed local functionals (VWN)[195] developed several formulations which incorporates Monte Carlo methods.[196]

1.4.3.4.2 Generalized Gradient Approximation

According to Generalized Gradient Approximation (GGA), the exchange-correlation energies depend not only on the density but also on the gradient of the density ($\nabla\rho(\mathbf{r})$),[197, 198] its mathematical expression:

$$E_{XC}[\rho_\alpha(\mathbf{r}), \rho_\beta(\mathbf{r})] \equiv \int \varepsilon_{xc}(\rho_\alpha(\mathbf{r}), \rho_\beta(\mathbf{r}), \nabla\rho_\alpha(\mathbf{r})\rho_\beta(\mathbf{r}))d^3\mathbf{r}$$

<div align="right">Eq. 1.89</div>

Most of the GGA functionals are constructed by adding a correction term to the LDA functional. A. D. Becke (B88) introduced one of the earliest and most widely used GGA exchange functionals in 1988 as a correction to the LSDA exchange energy. The global exchange-correlation energy may be formed by combining the exchange functional B88 with any of its correlation equivalents from this family, such as the LYP[199] and P86[200] functionals. The GGA formalism includes the widely used PW91[201] and PBE[202] correlation and exchange functionals.

1.4.3.4.3 *meta*-Generalized Gradient Approximation

The *meta*-Generalized Gradient Approximation (*m*-GGA) functionals represent further improvement over GGA functionals by adding the Laplacian of the density $\nabla^2\rho$.[203] This category is also covered by functionals that employ orbital information, and calculating the orbital kinetic energy density is numerically more stable than calculating the $\nabla^2\rho$. The cost of the *m*-GGA calculation is comparable to that of a GGA calculation, and given a pure density functional by the former is generally more precise than the latter. B95, B98, *etc.*, are examples of *m*-GGA functionals. The TPSS functional, which incorporates the kinetic energy density and has been demonstrated exceedingly fine for systems including transition metals, is one of the most successful of this type.

1.4.3.4.4 Hybrid Functionals

The introduction of hybrid density functional techniques,[204] in which the exchange-correlation of a GGA or *m*-GGA approach is paired with a fraction of the non-local exchange energy from HF theory, marked a significant leap in the application of DFT to current chemistry. B3LYP, B3P86, B3PW91, B97-1, MPWB1K, and X3LYP are hybrid-GGA methods, whereas B1B95, BB1K, and MPW1B95 are hybrid *m*-GGA methods. The Becke three parameter Lee-Yang-Parr (B3LYP) functional is the most often used expression for the exchange-correlation energy which can be considered as the standard option for a typical quantum chemistry problem. The mathematical form of B3LYP method can be written as,

$$E_{XC}^{B3LYP} = aE_X^{HF} + (1-a)E_X^{LSD} + bE_X^{B88} + E_C^{LSD} + c(E_C^{LYP} - E_C^{LSD})$$

Eq. 1.90

where the empirical constants a, b, c have the values 0.20, 0.72 and 0.81, respectively.

Minnesota functional developed by Truhlar *et al.*, at Minnesota university are based on the *m*-GGA approximation with different fractions of HF exchange. The Minnesota functionals include one *m*-GGA (M06-L), two *m*-GGAs (M11-L and MN12-L), seven global *hybrid m*-GGAs (M05, M05-2X, M06-2X, M08-2X and M08-SO), one range separated *hybrid m*-GGA (M11) and one screened exchange *hybrid m*-GGA (MN12-SX). Among them, the M06 family is one of the most widely utilized and popular one.[205] The most accurate functional available with the current scenario are the double hybrids, which improve on the *hybrid*-GGAs by including some correlation energy computed using the MP2 technique based on the Kohn-Sham orbitals. One of the commonly used double hybrid functionals is the B2-PLYP scheme by Grimme and coworkers.[206]
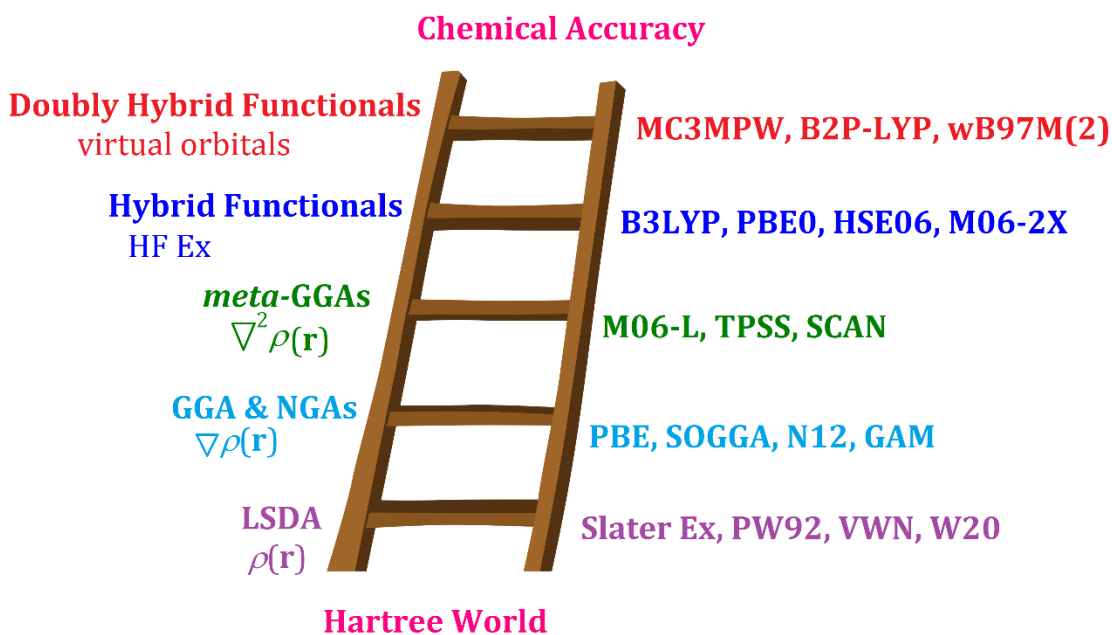
Figure 1.11 Jacob's Ladder of DFT towards chemical accuracy

In 2001, Perdew and Schmidt introduced Jacob's ladder describing various levels of sophistication and hence accuracy in DFT, starts from the Hartree world and ends in the heaven of chemical accuracy (Figure 1.11).[207] It is divided into five rungs that represent

five generations of density functionals, *via*. LDA, GGA, *m*-GGA, *hybrid*-GGA, *hybrid m*-GGA and finally fully non-local description. The accuracy and the complexity of the exchange correlation functional increases upwards the ladder. The lowest rung is the local spin-density approximation of Kohn and Sham, the second rung is the generalized gradient approximation and the higher rungs are increasingly more complex.[208] The sixth rung is the generalized random phase approximation, where both occupied and unoccupied orbitals are utilized in the calculation. Recently, Janesko added a new rung to the ladder, rung 3.5, which is the intermediate between the local and hybrid functional.[209]

1.4.3.5 Dispersion Corrections

To define long-range van der Waals type interaction in molecules, dispersion corrections are added to the KS-DFT functionals.[210-213] The total energy of the system using dispersion correction (E_{MF-D}) is represented as,

$$E_{DFT-D} = E_{KS-DFT} + E_{disp}$$

Eq. 1.91

where E_{KS-DFT} describes the self-consistent Kohn Sham energy functional and the dispersion energy, E_{disp} can be expressed as:

$$E_{disp} = -S_6 \sum_{i=1}^{N_{at}-1} \sum_{j=i+1}^{N_{at}} \frac{C_6^{ij}}{R_{ij}^6} f_{dmp}(R_{ij})$$

Eq. 1.92

where N_{at} is the number of atoms in the system, S_6 is a global scaling factor depending on the dispersion function, C_6^{ij} is the dispersion coefficient for atom pair ij, R_{ij} is the interatomic distance,[214] and f_{dmp} is the damping function used to avoid the near-singularities for small interatomic distance, R which is given by,

$$f_{dmp}(R) = \frac{1}{1 + e^{-\alpha(R/R_0 - 1)}}$$

Eq. 1.93

where R_0 is the sum of atomic van der Waals radii.

1.4.4 Basis sets

A basis set is a collection of functions that are linearly combined to describe molecular orbitals. These basis functions are often conceptualized as representations of atomic orbitals associated with the constituent atoms. In quantum chemical calculations, the introduction of basis sets is crucial as it simplifies the solution of the equations governing molecular orbitals, which would otherwise be challenging to solve. Each molecular orbital (one electron function) Ψ_i is expressed as a linear combination of n basis functions Φ_μ.

$$\Psi_i = \sum_{\mu=1}^{n} c_{\mu i}\Phi_\mu \qquad \text{Eq. 1.94}$$

The coefficients $c_{\mu i}$ are known as molecular orbital expansion coefficients (MO coefficients). Because of these basis functions are usually found near the center of atoms, they are also known as atomic basis functions. The basis functions used in molecular orbital computations are often abbreviated and the theoretical model utilized in MO computations is fully described in the format "theoretical method/basis set." Various types of atomic orbitals are available including Gaussian-type orbitals, Slater-type orbitals, and numerical atomic orbitals. Among them, Gaussian-type orbitals are the most frequently employed one.

Slater Type Orbitals (STOs) are made up of a radial part that describes the radial extend of an orbital and an angular part that describes the shape of the orbital.

$$\Phi_\mu = N \cdot r^{n-1}e^{-\zeta r} \cdot Y_{lm} \qquad \text{Eq. 1.95}$$

The radial part $r^{n-1}e^{-\zeta r}$ depends on the distance r from the origin of the basis function (usually the location of the nucleus), the orbital exponent, ζ and the principal quantum number, n. The spherical part Y_{lm} depends on the angular quantum number l and the magnetic quantum number, m. The normalization constant, N is chosen such that the integral over the square of the basis function yields unity. Taking a 1s orbital as an example, the spherical part as well as the r^{n-1} factor equate to unity and after evaluating the normalization constant, we get:

$$\Phi_{1s} = \frac{\zeta_{1s}^3}{\pi} e^{-\zeta_{1s}\mathbf{r}} . Y_{lm}$$

Eq. 1.96

Since two electron integrals over STOs are difficult to compute, STOs are not very useful for electronic structure computations.

Gaussian Type Orbitals (GTOs) are made up of a radial and a spherical component, but the radial component has a distinct dependence on **r**, given by;

$$g = N e^{-\alpha r^2} x^a y^b z^c$$

Eq. 1.97

The radial extend is proportional to $e^{-\alpha r^2}$, where α being the exponent. The sum of exponents $L = a+b+c$ is used to define the angular momentum of the three basis functions: s-type (L=0), p-type (L=1), d-type (L=2), f-type (L=3), g-type (L=4) *etc.* A simple Gaussian function representing an 1s-type orbital is given by,

$$g_{1s} = \left(\frac{2\alpha_s}{\pi}\right)^{3/4} e^{-\alpha r^2}$$

Eq. 1.98

Because of two electron integrals over GTOs are not difficult to compute, GTOs are particularly useful for electronic structure computations. GTOs have the benefit of being able to do all of the intergrals required for Linear combination of atomic orbital (LCAO) calculations using simple equations. The STO shows a cusp at **r** = 0 while the GTO has an incorrect behaviour at the nucleus and GTOs fall off too quickly as the electron gets further from the nucleus.[215, 216] A comparison between STO and GTO type orbitals are given in Figire 1.12.
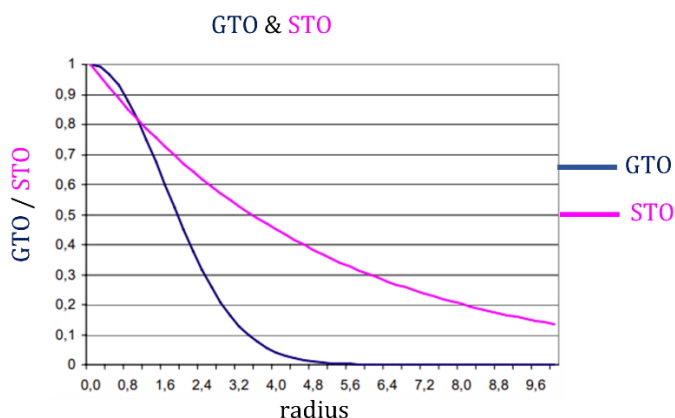
Figure 1.12 Slater type orbitals and Gaussian type orbitals

Single Gaussian functions are not well suited to describe the spatial extend and nodal characteristics of atomic orbitals. To solve this problem, basis functions are described as a sum (a "contraction") of several Gaussian functions (primitives) called contracted Gaussian type orbitals (CGTOs). If more than one basis function is utilized per valence electron, the description of the valence electrons can be greatly enhanced over that in the minimal STO-3G basis set.[217] This type of basis set is known as a "split valence" basis set because the description of valence orbitals is separated into two or more basis functions.[218] The 3-21G basis set is a low-cost, small split valence basis set, where non-valence electrons are characterized by a single basis function that is a contraction of three Gaussian functions and two basis functions characterize each valence electron where first basis function is made up of two Gaussian primitives, whereas the second is made up of a single uncontracted Gaussian primitive.[219] The 3-21G basis set has an unusual development history. The simple modification of the orbital exponents and expansion coefficients used in the construction of other basis sets resulted in a "falling inward" of the inner valence shells. This is because there are only three Gaussian functions available for describing the core region, and adding more primitives to the core region decreases the total energy more than an acceptable description of the valence shell. Most basis set parameters were thus optimized using a significantly larger core space of six Gaussians (6-21G) initially.[220, 221] The key difference between 3-21G and 6-31G is that the latter uses a substantially higher number of primitives in the core as well as the innermost valence shell. The employment of a contraction of six Gaussian primitives for each core orbital considerably enhances the description of the core area. The valence area is characterized once more by two basis functions per atomic orbital. The inner shell is made up of three Gaussian contractions, whereas the outside shell is made up of a single Gaussian primitive. The s and p functions, like other basis sets constructed by the Pople's group, have similar exponents.

Double zeta basis sets, Dunnings D95[222, 223] is generated from an existing large atomic basis set of nine uncontracted Gaussian primitives of s-type and five uncontracted Gaussian primitives of p-type. Six of the nine s-type functions were then combined into a single contraction, while the remaining three s-type functions were left alone. Similarly,

four of the five p-type functions were contracted into a single function, leaving one uncontracted. This results in a basis set of four s-type and two p-type basis functions. To extend the flexibility of the orbital description, double zeta basis sets are usually augmented with higher angular momentum basis functions.[224] A common first step is to add a set of d-type functions to the basis sets of atoms that have occupied s- and p-shells in their electronic ground states. This relates to the addition of a set of p-type functions for hydrogen. There are two distinct notations for specifying the addition of polarization functions. The first notation adds one asterisk to the basis set to represent the addition of polarization functions to non-hydrogen atoms, whereas the second notation adds two asterisks to represent the addition of polarization functions to all atoms including hydrogen. For instance, the 6-31G** basis set is created by adding one set of d-functions to all non-hydrogen atoms and one set of p-functions to all hydrogen atoms to the split valence 6-31G basis set. The polarization functions are clearly defined by their angular quantum number in the second notation. The 6-31G** basis set is thus referred to as "6-31G(d,p)" which is far more versatile since it allows for the specification of numerous sets of polarization functions. The polarization functions for the 6-31G basis are listed as a single set of uncontracted d-type Gaussians. There are six cartesian d-type Gaussian functions (x^2, y^2, z^2, xy, yz, zx) $\exp(-\alpha_d r^2)$, which are comparable to five pure d-type functions (xy, yz, zx, x^2-y^2, $3z^2-r^2$) $\exp(-\alpha_d r^2)$ plus one s-type function.[225]

For *ab initio* MO theory, the theoretical description of negatively charged species is extremely difficult. This is because the extra negative charge spreads outward to a much greater extent than it does in uncharged or positively charged molecules. The standard split valence basis sets are inadequate for describing such a diffuse charge distribution. The use of highly diffused basis functions with correspondingly reduced orbital exponents partially solves this difficulty by allowing the description of electron density very distant from the nucleus. Diffuse basis functions are often added as a separate set of uncontracted Gaussian functions with the same angular momentum as valence electrons. A (+)-sign is added to the usual basis set notation to denote the addition of diffuse basis functions on all non-hydrogen atoms. A second (+)-sign is inserted if diffuse s-type functions are also added to the basic set of hydrogen atoms. For

instance, the 6-31G basis set combined with one set of diffuse sp-functions produces the better "6-31+G" basis set.[226]

All of these basis sets were designed for usage at the Hartree-Fock level of theory, with certain adjustments inserted to better represent experimental results. Recently, there has been a development of basis sets specifically designed for application in correlated approaches. These basis sets are usually at least of double zeta quality and also include polarization functions. The 6-311G(d,p) basis set is a common example. This basis set consists of a core area of six contracted Gaussian primitives and a triply divided valence basis set of three, one, and one Gaussian primitives, respectively. On first-row elements, polarization functions are composed of one set of five pure d-functions, whereas on hydrogen, a set of three p-type orbitals is added. This results in a total of 18 basis functions for each non-hydrogen atom in the first row and 6 basis functions for hydrogen.

Dunning and coworkers introduced[227] a collection of basis sets for correlated calculations. These basis sets are known as correlation consistent (cc) and are meant to integrate a base set of sp-functions with correlation functions. These later functions are chosen in such a way that all functions in a particular set reduce the atomic correlation energy (as computed by CISD). The correlation consistent polarized double zeta basis set labelled "cc-pVDZ" is the smallest member of this series and is frequently used as the starting point for correlated computations. For charged systems, the cc-basis sets must be extended by more diffuse functions. The aug-cc-pVxZ series is a systematic extension that comes from the cc-pVxZ series by adding one set of diffuse functions for each angular momentum type already existing in the associated cc-basis. As a result, the cc-pVDZ adds a diffuse (1s1p1d) set to the final [4s3p2d] aug-cc-pVDZ set. These basis sets are typically used with positively and negatively charged systems.[228, 229]

The generated MOs represent solutions to the Kohn-Sham equation confined within the "function space" defined by the employed basis set. Increasing the number of contracted Gaussians is required to improve the quality of the basis set. A complete basis set may accurately describe any molecular orbital. Unfortunately, since full basis sets

include an endless number of functions, they are impractical for computations. By progressively increasing the number of basis functions and projecting to an infinite-size basis set, we may estimate the complete basis set outcome. The basis sets cc-pVDZ, cc-pVTZ, cc-pVQZ, *etc.*, are examples of a systematic succession of basis sets that may be extrapolated to the whole basis set limit.

When dealing with heavy elements that possess a substantial number of electrons, it becomes imperative to employ a significant quantity of basis functions. Yet, many of these extra electrons primarily constitute core electrons, rendering a minimal representation is satisfactory. In light of this, back in 1935, Hellmann introduced a proposition to replace these electrons with analytical functions, which embody the combined nuclear and electronic core interactions for the remaining electrons. This replacement involves utilizing an approximate pseudopotential, leading to the coining of the term "Effective Core Potentials" (ECPs).[163, 230, 231] ECP treatment on the core electrons gives good results at a fraction of the cost needed for a calculation involving all electrons. For a large core ECP, all orbitals except (n+1)s, (n+1)p and nd are treated as core electrons. Such a treatment usually gives a good geometry for the molecule but the energetics are often found to be approximate. This can be rectified by using a small core ECP where the ns, np, nd and (n+1)s forms the valence orbitals. Such a treatment often increases the computational cost. The popular pseudopotentials commonly used include those of Hay and Wadt developed by Los Alamos National Laboratory (LANL),[232] those of Stevens *et al.*[233] and the Stuttgart–Dresden pseudopotentials developed by Dolg and co-workers.[234] Later, Check *et al.* incorporated polarization and diffuse functions in conjunction with the LANL double zeta basis set.[235]

In this thesis, the primary basis sets utilized for calculations are the Pople basis sets 6-311G(d,p) and 6-311+G(d,p). Additionally, for transition metals, the Hay and Wadt double zeta basis set, in conjunction with the overall combination of ECP and valence basis set LANL2DZ, is employed.

1.4.5 Anisotropy of the Induced Current Density

The Anisotropy of the Induced Current Density (ACID) is a concept that quantifies the directional variation of current density in a molecule under the influence of an external magnetic field. ACID provides insights into the electron circulation patterns within a molecule, revealing areas where the induced current density is more pronounced along specific directions.[236] This information can be valuable for understanding molecular aromaticity, electronic delocalization, and the effects of conjugation. ACID analysis aids in interpreting molecular properties in terms of their response to magnetic fields, shedding light on complex electronic behaviour that contribute to the overall reactivity and stability of molecules. It has applications in various fields, including organic chemistry, material science, and catalysis, offering a deeper understanding of molecular properties and reactivity. The electrostatic surface and electron density are analogous to ACID isosurfaces. Current density vectors can be displayed on the ACID isosurface to provide information on current magnitude and direction (e.g., diatropic or paratropic). The aromatic nature of the molecule is represented by the diatropic vectors on the ACID isosurface, while the antiaromatic character is represented by the paratropic arrangement of the vectors on the surface.

1.4.6 Potential Energy Surface

A potential energy surface (PES) is a mathematical function that calculates energy of a molecule as a function of positions of the atoms in it.[237] The BO approximation is a foundational idea in computational chemistry since it describes molecular geometry and hence permits the concept of potential energy surface. PES of a system provides a full description of all conformers, isomers, and energetically feasible movements. Minima on the PES denotes a low-energy structure or optimized geometry.[238] A PES can have both global and local minima as shown in Figure 1.13. The global minimum denotes a structure with the lowest energy, whereas the local minima reflect conformers or isomers with higher energy. On the PES, the transition state of a reaction is represented as a first-order saddle point, while the reactants and products are marked as minima. A saddle begins with two points—one on the reactant side of the transition state and the other on the

product side. The lowest energy point is incrementally moved towards the other, optimized with the constraint of a fixed distance between them. As these two points converge, they provide improved bounds on the transition state. Ridge following expands on the concept of bracketing the transition state. Two structures, situated on either side of the ridge that separates the reactant and product valleys, are gradually moved towards each other to more precisely enclose the ridge. They are then displaced parallel to the ridge to locate its lowest point, which is the transition state.

A basic PES is similar to a hilly terrain and may be depicted as a topological surface with valleys and hills, with minima represented as valleys. PES analyses can give information on the molecular system. The height and contour of the channel linking the reactant and product valleys may be used to calculate reaction rates. The vibrational spectrum of a molecule can be determined by analyzing the geometry of a valley. Furthermore, the response of energy to electric and magnetic fields impacts molecule characteristics such as dipole moment, polarizability, and NMR shielding.[239]
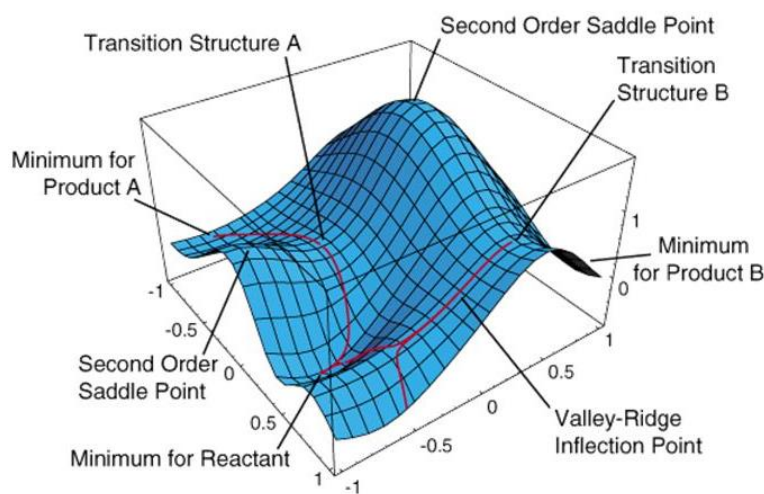
Figure 1.13 The representation of potential energy surface[240]

1.5 Conclusions

Computational chemistry has become an indispensable tool in modern chemistry research, enabling scientists to explore chemical phenomena that are often challenging or impossible to study solely through experimental means. It stands as a potent and

versatile discipline, empowered by the Schrödinger equation and guided by the principles of theoretical chemistry and computer simulations. Its proficiency in unraveling complex chemical quandaries and its potential to explore otherwise challenging materials underscore its significance in modern scientific exploration.

Part A of Chapter 1 offers a succinct glimpse into the evolution and historical development of valuable tool, MESP. This section offers an in-depth discussion of electrostatics of atoms and molecules, delves into topological concepts, explores electrostatic theorems, and demonstrates its extensive applications across various facets of chemistry. It is truly remarkable that a singular scalar field can be effectively employed to unravel a multitude of physicochemical phenomena within the intricate molecular realm. This section also includes a brief description on the notion of MED, its topological features and a general comparison with MESP.

In Part B, the theories and principles underpinning a range of computational chemistry techniques are concisely elucidated. These encompass *ab initio* methods, semiempirical methods, DFT *etc.*, with clear sub-divisions for convenient comprehension. Furthermore, this section provides an overview of essential concepts such as basis sets, potential energy surfaces, *etc*. It is imperative to foster a profound understanding of these computational principles, as it plays a pivotal role in interpreting the results of molecular modeling operations. Ultimately, this understanding facilitates advancements in the implementation of predictive models for chemical properties, offering a reliable and high-quality approach.

1.6 References

1.   S. R. Gadre and R. N. Shirsat, *Electrostatics of atoms and molecules*. 2000: Universities Press.
2.   P. Politzer and D. G. Truhlar, *Chemical Applications of Atomic and Molecular Electrostatic Potentials: Reactivity, Structure, Scattering, and Energetics of Organic, Inorganic, and Biological Systems*, **1981**, 1-6.
3.   P. Politzer and J. S. Murray, *Chemical Reactivity in Confined Systems: Theory, Modelling and Applications*, **2021**, 113-134.
4.   P. Politzer, R. A. Donnelly and K. C. Daiker, *J. Chem. Soc., Chem. Commun.*, **1973**, 617-618.

5. R. G. Parr, *Annu. Rev. Phys. Chem.*, **1983**, 34, 631-656.
6. L. J. Bartolotti and K. Flurchick, *Rev. Comput. Chem.*, **1996**, 187-216.
7. R. G. Parr, *Int. J. Quantum Chem.*, **1990**, 37, 327-347.
8. S. R. Gadre and R. K. Pathak., *Nonexistence of local maxima in molecular electrostatic potential maps*. in *Proc. Indian Ac. Sci. Chem. Sci.* 1990: Springer.
9. R. Sanderson, *Science*, **1955**, 121, 207-208.
10. M. A. Spackman and R. F. Stewart, *Ectrostatic Potentials in Crystals*, in *Chemical Applications of Atomic and Molecular Electrostatic Potentials: Reactivity, Structure, Scattering, and Energetics of Organic, Inorganic, and Biological Systems*, P. Politzer and D.G. Truhlar, Editors. 1981, Springer US: Boston, MA. p. 407-425.
11. I. Falconer, *Metrologia*, **2004**, 41, S107.
12. T. Poston and I. Stewart, *Catastrophe theory and its applications*. 2014: Courier Corporation.
13. E. Scrocco and J. Tomasi, *The electrostatic molecular potential as a tool for the interpretation of molecular properties*, in *New concepts II*. 1973, Springer. p. 95-170.
14. R. Bonaccorsi, E. Scrocco and J. Tomasi, *J. Am. Chem. Soc.*, **1976**, 98, 4049-4054.
15. R. Bonnaccorsi, E. Scrocco, J. Tomasi and A. Pullman, *Theor. Chim. Acta*, **1975**, 36, 339-344.
16. R. Bonaccorsi, A. Pullman, E. Scrocco and J. Tomasi, *Chem. Phys. Lett.*, **1972**, 12, 622-624.
17. R. Bonaccorsi, A. Pullman, E. Scrocco and J. Tomasi, *Theor. Chim. Acta*, **1972**, 24, 51-60.
18. E. Scrocco and J. Tomasi, *Electronic molecular structure, reactivity and intermolecular forces: an euristic interpretation by means of electrostatic molecular potentials*, in *Adv. Quantum Chem.* 1978, Elsevier. p. 115-193.
19. A. Pullman and B. Pullman, *Q. Rev. Biophys.*, **1981**, 14, 289-380.
20. C. Giessner-Prettre and A. Pullman, *Theor. Chim. Acta*, **1972**, 25, 83-88.
21. R. Lavery and B. Pullman, *J. Biomol. Struct. Dyn.*, **1985**, 2, 1021-1032.
22. R. Lavery and B. Pullman, *Nucleic Acids Res.*, **1981**, 9, 3765-3777.
23. R. Lavery and B. Pullman, *Int. J. Quantum Chem.*, **1981**, 20, 259-272.
24. B. Pullman, R. Lavery and A. Pullman, *Eur. J. Biochem.*, **1982**, 124, 229-238.
25. R. Lavery and B. Pullman, *Nucleic Acids Res.*, **1981**, 9, 4677-4688.
26. J. S. Murray and P. Politzer, *Wiley Interdiscip. Rev. Comput. Mol. Sci.*, **2011**, 1, 153-163.
27. P. Politzer, *In Chemical applications ofnlomic and molecular electrostatic potentials; Politzer, P.; Truhlar, DG. Eds*. 1981, Plenum Press: New York and London.
28. P. Politzer and J. S. Murray, *Theor. Chem. Acc.*, **2002**, 108, 134-142.
29. J. S. Murray and K. Sen, **1996**.
30. P. Politzer, *Toxicol. Lett.*, **1988**, 43, 257-276.
31. P. Politzer, L. Abrahmsen and P. Sjoberg, *J. Am. Chem. Soc.*, **1984**, 106, 855-860.
32. P. Politzer and P. R. Laurence, *Carcinogenesis*, **1984**, 5, 845-848.
33. P. Politzer, P. R. Laurence and K. Jayasuriya, *Environ. Health Perspect.*, **1985**, 61, 191-202.
34. P. Politzer and J. S. Murray, *Theor. Chem. Acc.*, **2021**, 140, 1-8.

35. P. Politzer, N. Sukumar, K. Jayasuriya and S. Ranganathan, *J. Am. Chem. Soc.*, **1988**, 110, 3425-3430.
36. P. Politzer, K. C. Daiker and R. A. Donnelly, *Cancer Lett.*, **1976**, 2, 17-23.
37. T. Brinck, J. S. Murray and P. Politzer, *Mol. Phys.*, **1992**, 76, 609-617.
38. S. R. Gadre, S. V. Bapat, K. Sundararajan and I. H. Shrivastava, *Chem. Phys. Lett.*, **1990**, 175, 307-312.
39. S. R. Gadre and R. D. Bendale, *Chem. Phys. Lett.*, **1986**, 130, 515-521.
40. S. R. Gadre, S. A. Kulkarni and I. H. Shrivastava, *J. Chem. Phys.*, **1992**, 96, 5253-5260.
41. S. R. Gadre, S. A. Kulkarni, C. Suresh and I. H. Shrivastava, *Chem. Phys. Lett.*, **1995**, 239, 273-281.
42. S. R. Gadre and A. Kumar, *J. Chem. Sci.*, **2016**, 128, 1519-1526.
43. S. R. Gadre and S. S. Pundlik, *J. Am. Chem. Soc.*, **1995**, 117, 9559-9563.
44. S. R. Gadre and I. H. Shrivastava, *J. Chem. Phys.*, **1991**, 94, 4384-4390.
45. S. R. Gadre, C. H. Suresh and N. Mohan, *Molecules*, **2021**, 26, 3289.
46. A. Kumar and S. R. Gadre, *J. Chem. Theory Comput.* , **2016**, 12, 1705-1713.
47. C. H. Suresh, G. S. Remya and P. K. Anjalikrishna, *Wiley Interdiscip. Rev. Comput. Mol. Sci.*, **2022**, 12, e1601.
48. S. E. Wheeler and K. N. Houk, *J. Chem. Theory Comput.*, **2009**, 5, 2301-2312.
49. S. E. Wheeler and K. N. Houk, *J. Am. Chem. Soc.*, **2009**, 131, 3126-3127.
50. S. E. Wheeler and J. W. Bloom, *Chem. Commun.*, **2014**, 50, 11118-11121.
51. S. E. Wheeler and K. Houk, *J. Am. Chem. Soc.*, **2008**, 130, 10854-10855.
52. S. E. Wheeler, *Acc. Chem. Res.*, **2013**, 46, 1029-1038.
53. B. Galabov and P. Bobadova-Parvanova, *J. Mol. Struct.*, **2000**, 550, 93-98.
54. B. Galabov, V. Nikolova and S. Ilieva, *Chem. Eur. J.*, **2013**, 19, 5149-5155.
55. V. Dimitrova, S. Ilieva and B. Galabov, *J. Phys. Chem. A*, **2002**, 106, 11801-11805.
56. B. Galabov and P. Bobadova-Parvanova, *J. Phys. Chem. A*, **1999**, 103, 6793-6799.
57. B. Galabov, P. Bobadova-Parvanova, S. Ilieva and V. Dimitrova, *J. Mol. Struct.: THEOCHEM*, **2003**, 630, 101-112.
58. B. Galabov, S. Ilieva, G. Koleva, W. D. Allen, H. F. Schaefer Iii and P. Von R. Schleyer, *Wiley Interdiscip. Rev. Comput. Mol. Sci.*, **2013**, 3, 37-55.
59. M. Dimitrova and B. Galabov, *Croat. Chem. Acta*, **2009**, 82, 21-25.
60. B. Galabov, S. Ilieva, B. Hadjieva, Y. Atanasov and H. F. Schaefer Iii, *J. Phys. Chem. A*, **2008**, 112, 6700-6707.
61. S. Ilieva and B. Galabov, *Electrostatic potential at nuclei: an accurate reactivity descriptor for organic compounds*, in *Advanced Methods and Applications in Chemoinformatics: Research Progress and New Applications*. 2012, IGI Global. p. 280-317.
62. F. A. Bulat, A. Toro-Labbé, T. Brinck, J. S. Murray and P. Politzer, *J. Mol. Model.*, **2010**, 16, 1679-1691.
63. P. Nagy and G. Náray-Szabó, *Can. J. Chem.*, **1985**, 63, 1694-1698.
64. G. Náray-Szabó, *J. Mol. Recognit.*, **1993**, 6, 205-210.
65. P. Politzer, J. S. Murray and Z. Peralta-Inga, *Int. J. Quantum Chem.*, **2001**, 85, 676-684.
66. S. Mecozzi, A. P. West Jr and D. A. Dougherty, *Proc. Natl. Acad. Sci.*, **1996**, 93, 10566-10571.
67. D. K. Roy, P. Balanarayan and S. R. Gadre, *J. Chem. Sci.*, **2009**, 121, 815-821.

68. C. Suresh, N. Koga and S. R. Gadre, *J. Org. Chem.*, **2001**, 66, 6883-6890.
69. C. H. Suresh and N. Koga, *J. Org. Chem.*, **2002**, 67, 1965-1968.
70. C. H. Suresh and N. Koga, *Chem. Phys. Lett.*, **2006**, 419, 550-556.
71. K. P. Vijayalakshmi and C. H. Suresh, *New J. Chem.*, **2010**, 34, 2132-2138.
72. N. Mohan, C. H. Suresh, A. Kumar and S. R. Gadre, *Phys. Chem. Chem. Phys.*, **2013**, 15, 18401-18409.
73. G. S. Remya and C. H. Suresh, *Phys. Chem. Chem. Phys.*, **2016**, 18, 20615-20626.
74. P. V. Bijina and C. H. Suresh, *J. Phys. Chem. A*, **2020**, 124, 2231-2241.
75. J. S. Murray and P. Politzer, *Wiley Interdiscip. Rev. Comput. Mol. Sci.*, **2017**, 7, e1326.
76. N. Mohan and C. H. Suresh, *J. Phys. Chem. A*, **2014**, 118, 1697-1705.
77. K. Remya and C. H. Suresh, *Phys. Chem. Chem. Phys.*, **2015**, 17, 18380-18392.
78. H. Weinstein, P. Politzer and S. Srebrenik, *Theor. Chim. Acta*, **1975**, 38, 159-163.
79. P. Balanarayan and S. R. Gadre, *J. Chem. Phys.*, **2003**, 119, 5037-5043.
80. D. Roy, P. Balanarayan and S. R. Gadre, *J. Chem. Phys.*, **2008**, 129.
81. S. Jenkins, Z. Liu and S. R. Kirk, *Mol. Phys.*, **2013**, 111, 3104-3116.
82. M. Leboeuf, A. M. Köster, K. Jug and D. R. Salahub, *J. Chem. Phys.*, **1999**, 111, 4893-4905.
83. P. Sjoberg and P. Politzer, *J. Phys. Chem. C*, **1990**, 94, 3959-3961.
84. C. Suresh, N. Koga and S. R. Gadre, *Organometallics*, **2000**, 19, 3008-3015.
85. L. Liu, L. Miao, L. Li, F. Li, Y. Lu, Z. Shang and J. Chen, *J. Phys. Chem. Lett.*, **2018**, 9, 3573-3579.
86. A. M. Bayoumy, M. Ibrahim and A. Omar, *Opt. Quantum Electron.*, **2020**, 52, 1-13.
87. J. Cao, Q. Ren, F. Chen and T. Lu, *Sci. China Chem.*, **2015**, 58, 1845-1852.
88. C. Cárdenas, N. Rabi, P. W. Ayers, C. Morell, P. Jaramillo and P. Fuentealba, *J. Phys. Chem. A*, **2009**, 113, 8660-8667.
89. J. V. Correa, P. Jaque, J. Oláh, A. Toro-Labbé and P. Geerlings, *Chem. Phys. Lett.*, **2009**, 470, 180-186.
90. P. Balanarayan, R. Kavathekar and S. R. Gadre, *J. Phys. Chem. A*, **2007**, 111, 2733-2738.
91. D. M. Hayes and P. A. Kollman, *J. Am. Chem. Soc.*, **1976**, 98, 7811-7816.
92. J. Mathew, T. Thomas and C. H. Suresh, *Inorg. Chem.*, **2007**, 46, 10800-10809.
93. P. C. J. Kamer, P. W. N. M. Van Leeuwen and J. N. H. Reek, *Acc. Chem.Res.*, **2001**, 34, 895-904.
94. J. G. De Vries and L. Lefort, *Chem. Eur. J.*, **2006**, 12, 4722-4734.
95. J. Jover and N. Fey, *Chem. Asian J.*, **2014**, 9, 1714-1723.
96. D. R. Palo and C. Erkey, *Organometallics*, **2000**, 19, 81-86.
97. D. J. Durand and N. Fey, *Chem.Rev.*, **2019**, 119, 6561-6594.
98. U. Christmann and R. Vilar, *Angew. Chem. Int. Ed.*, **2005**, 44, 366-374.
99. J.-P. Corbet and G. Mignani, *Chem. Rev.*, **2006**, 106, 2651-2710.
100. B. C. Hamann and J. F. Hartwig, *J. Am. Chem.Soc.*, **1998**, 120, 3694-3703.
101. N. Fey, A. G. Orpen and J. N. Harvey, *Coord. Chem. Rev.*, **2009**, 253, 704-722.
102. N. Fey, J. N. Harvey, G. C. Lloyd-Jones, P. Murray, A. G. Orpen, R. Osborne and M. Purdie, *Organometallics*, **2008**, 27, 1372-1383.
103. L. Cavallo, A. Correa, C. Costabile and H. Jacobsen, *J. Organomet. Chem.*, **2005**, 690, 5407-5413.
104. R. H. Crabtree, *J. Organomet. Chem.*, **2005**, 690, 5451-5457.

105. D.-P. Song, X.-C. Shi, Y.-X. Wang, J.-X. Yang and Y.-S. Li, *Organometallics*, **2012**, 31, 966-975.
106. J. Mathew and C. H. Suresh, *Organometallics*, **2011**, 30, 3106-3112.
107. J. Mathew and C. H. Suresh, *Organometallics*, **2011**, 30, 1438-1444.
108. B. A. Anjali and C. H. Suresh, *ACS Omega*, **2017**, 2, 4196-4206.
109. T. Brinck, *The use of the electrostatic potential for analysis and prediction of intermolecular interactions*, in *Theor. Comput. Chem.*, C. Párkányi, Editor. 1998, Elsevier. p. 51-93.
110. A. Daolio, A. Pizzi, M. Calabrese, G. Terraneo, S. Bordignon, A. Frontera and G. Resnati, *Angew. Chem. Int. Ed.* , **2021**, 60, 20723-20727.
111. S. S. Pundlik and S. R. Gadre, *J. Phys. Chem. B* **1997**, 101, 9657-9662.
112. S. R. Gadre and S. S. Pundlik, *J. Phys. Chem. B*, **1997**, 101, 3298-3303.
113. S. S. Pingale, S. R. Gadre and L. J. Bartolotti, *J. Phys. Chem. A*, **1998**, 102, 9987-9992.
114. S. R. Gadre and A. D. Kulkarni, **2000**.
115. S. R. Gadre and A. Kumar, *Noncovalent forces*, **2015**, 391-418.
116. A. Kumar, S. R. Gadre, N. Mohan and C. H. Suresh, *J. Phys. Chem. A*, **2014**, 118, 526-532.
117. C. H. Suresh and S. Anila, *Acc. Chem. Res.*, **2023**.
118. A. Daolio, A. Pizzi, M. Calabrese, G. Terraneo, S. Bordignon, A. Frontera and G. Resnati, *Angew. Chem.*, **2021**, 133, 20891-20895.
119. J. S. Murray, K. Paulsen and P. Politzer. *Molecular surface electrostatic potentials in the analysis of non-hydrogen-bonding noncovalent interactions*. in *Proc. Indian Acad. Sci.* . 1994: Springer.
120. S. E. Wheeler and J. W. Bloom, *J. Phys. Chem. A*, **2014**, 118, 6133-6147.
121. P. V. Bijina and C. H. Suresh, *J. Chem. Sci.*, **2016**, 128, 1677-1686.
122. P. V. Bijina and C. H. Suresh, *J. Chem. Sci.*, **2016**, 128, 1677-1686.
123. S. Scheiner, *J. Comput. Chem.*, **2018**, 39, 500-510.
124. G. Pèpe, D. Siri and J.-P. Reboul, *J. Mol. Struct. THEOCHEM*, **1992**, 256, 175-185.
125. P.-A. Carrupt, N. El Tayar, A. Karlén and B. Testa, *Meth. Enzymol.*, **1991**, 203, 638-677.
126. P. C. Rathi, R. F. Ludlow and M. L. Verdonk, *J. Med. Chem.*, **2019**, 63, 8778-8790.
127. P. K. Weiner, R. Langridge, J. M. Blaney, R. Schaefer and P. A. Kollman, *Proc. Natl. Acad. Sci.*, **1982**, 79, 3754-3758.
128. D. Hadži, M. Hodošček, D. Kocjan, T. Šolmajer and F. Avbelj, *Croat. Chem. Acta*, **1984**, 57, 1065-1074.
129. C. A. Helm, W. Knoll and J. N. Israelachvili, *Proc. Natl. Acad. Sci.*, **1991**, 88, 8169-8173.
130. J. S. O. De Castro, J. C. Pinheiro, S. S. D. S. De Morais, H. R. Bitencourt, A. F. De Figueiredo, M. a. B. Dos Santos, F. Dos Santos Gil and A. C. B. Pinheiro, *J. Biophys. Chem.*, **2023**, 14, 1-29.
131. H. Yao, D. Qian, H. Zhang, Y. Qin, B. Xu, Y. Cui, R. Yu, F. Gao and J. Hou, *Chin. J. Chem.*, **2018**, 36, 491-494.
132. A. K. Phukan, R. P. Kalagi, S. R. Gadre and E. D. Jemmis, *Inorg. Chem.*, **2004**, 43, 5824-5832.
133. C. Suresh and S. R. Gadre, *J. Org. Chem.*, **1999**, 64, 2505-2512.
134. A.-R. Nekoei and M. Vatanparast, *Phys. Chem. Chem. Phys.*, **2019**, 21, 623-630.

135. F. De Proft and P. Geerlings, *Chem. Rev.*, **2001**, 101, 1451-1464.
136. J. S. Murray and P. Politzer, *Chem. Phys. Lett.*, **1988**, 152, 364-370.
137. P. Politzer, G. P. Kirschenheuter and J. Alster, *J. Am. Chem. Soc.*, **1987**, 109, 1033-1037.
138. C. H. Suresh and S. R. Gadre, *J. Phys. Chem. A*, **2007**, 111, 710-714.
139. S. R. Gadre and C. Suresh, *J. Org. Chem.*, **1997**, 62, 2625-2627.
140. S. E. Wheeler, *J. Am. Chem. Soc.*, **2011**, 133, 10262-10274.
141. C. Suresh and S. R. Gadre, *J. Am. Chem. Soc.*, **1998**, 120, 7049-7055.
142. C. H. Suresh, *Inorg. Chem.*, **2006**, 45, 4982-4986.
143. M. Alipour and A. Mohajeri, *J. Phys. Org. Chem.*, **2012**, 25, 797-802.
144. D. Shin and Y. Jung, *Phys. Chem. Chem. Phys.*, **2022**, 24, 25740-25752.
145. F. B. Sayyed and C. H. Suresh, *J. Phys. Chem. A*, **2011**, 115, 5660-5664.
146. F. B. Sayyed, C. H. Suresh and S. R. Gadre, *J. Phys. Chem. A*, **2010**, 114, 12330-12333.
147. C. H. Suresh, P. Alexander, K. P. Vijayalakshmi, P. Sajith and S. R. Gadre, *Phys. Chem. Chem. Phys.*, **2008**, 10, 6492-6499.
148. F. B. Sayyed and C. H. Suresh, *Tetrahedron Lett.*, **2009**, 50, 7351-7354.
149. F. B. Sayyed and C. H. Suresh, *New J. Chem.*, **2009**, 33, 2465-2471.
150. R. F. W. Bader, *Acc. Chem. Res.*, **1985**, 18, 9-15.
151. R. Bader, *Clarendon: Oxford, UK*, **1990**.
152. R. F. Bader, *Chem. Rev.*, **1991**, 91, 893-928.
153. P. S. V. Kumar, V. Raghavendra and V. Subramanian, *J. Chem. Sci.*, **2016**, 128, 1527-1536.
154. C. F. Matta and R. J. Boyd, *The quantum theory of atoms in molecules: from solid state to DNA and drug design*, **2007**.
155. R. F. Bader, S. Johnson, T.-H. Tang and P. Popelier, *J. Phys. Chem.*, **1996**, 100, 15398-15415.
156. X. Fradera, M. A. Austen and R. F. Bader, *J. Phys. Chem. A*, **1999**, 103, 304-314.
157. R. F. Bader, J. Hernández-Trujillo and F. Cortés-Guzmán, *J. Comput. Chem.*, **2007**, 28, 4-14.
158. R. F. Bader and M. E. Stephens, *J. Am. Chem. Soc.*, **1975**, 97, 7391-7399.
159. R. Hilal, S. G. Aziz, A. O. Alyoubi and S. Elroby, *Procedia Comput. Sci.*, **2015**, 51, 1872-1877.
160. W. J. Huang, R. Momen, A. Azizi, T. Xu, S. R. Kirk, M. Filatov and S. Jenkins, *Int. J. Quantum Chem.*, **2018**, 118, e25768.
161. C. J. Cramer, *Essentials of computational chemistry: theories and models*. 2013: John Wiley & Sons.
162. E. Clementi. *Modern techniques in computational chemistry: Motecc*. 1989: Escom.
163. F. Jensen, *Introduction to computational chemistry*. 2017: John wiley & sons.
164. E. Schrödinger, *Ann. Phys.*, **1926**, 385, 437-490.
165. R. A. Friesner, *Proc.Natl. Acad. Sci.*, **2005**, 102, 6648-6653.
166. M. Born and R. Oppenheimer, *On the quantum theory of molecules*, in *Quantum Chemistry: Classic Scientific Papers*. 2000, World Scientific. p. 1-24.
167. M. Born and W. Heisenberg, *Original Scientific Papers Wissenschaftliche Originalarbeiten*, **1985**, 216-246.
168. A. Szabo and N. S. Ostlund, *Modern quantum chemistry: introduction to advanced electronic structure theory*. 2012: Courier Corporation.

169. A. Szabó and N. S. Ostlund, *Modern Quantum Chemistry: Introduction to Advanced Electronic Structure Theory*. 1982.
170. C. C. J. Roothaan, *Rev. Mod. Phys.*, **1951**, 23, 69-89.
171. G. G. Hall, *Proc. Royal Soc. A*, **1951**, 205, 541-552.
172. L. Visscher, *Post Dirac-Hartree-Fock methods-electron correlation*, in *Theoretical and Computational Chemistry*. 2002, Elsevier. p. 291-331.
173. *Post-Hartree–Fock Methods*, in *Methods of Molecular Quantum Mechanics*. 2009. p. 133-139.
174. W. Thiel, *Wiley Interdiscip. Rev. Comput. Mol. Sci.*, **2014**, 4, 145-157.
175. W. Thiel, *Tetrahedron*, **1988**, 44, 7393-7408.
176. J. Pople and D. Beveridge, **1970**.
177. I. N. Levine, D. H. Busch and H. Shull, *Quantum chemistry*. Vol. 6. 2009: Pearson Prentice Hall Upper Saddle River, NJ.
178. M. J. S. Dewar and W. Thiel, *J. Am. Chem. Soc.*, **1977**, 99, 4899-4907.
179. M. J. S. Dewar, E. G. Zoebisch, E. F. Healy and J. J. P. Stewart, *J. Am. Chem. Soc.*, **1985**, 107, 3902-3909.
180. J. J. P. Stewart, *J. Comput. Chem.*, **1989**, 10, 209-220.
181. J. J. P. Stewart, *J. Mol. Model.*, **2007**, 13, 1173-1213.
182. J. J. P. Stewart, *J. Mol. Model.*, **2013**, 19, 1-32.
183. P. O. Dral, X. Wu, L. Spörkel, A. Koslowski, W. Weber, R. Steiger, M. Scholten and W. Thiel, *J. Chem. Theory Comput.*, **2016**, 12, 1082-1096.
184. M. Orio, D. A. Pantazis and F. Neese, *Photosynth. Res.*, **2009**, 102, 443-453.
185. E. Engel, *Density functional theory*. 2011: Springer.
186. W. Kohn and L. Sham. *Density functional theory*. in *Conference proceedings-italian physical society*. 1996: Editrice compositori.
187. L. H. Thomas, *Math. Proc. Camb. Philos. Soc.*, **2008**, 23, 542-548.
188. E. Teller, *Rev. Mod. Phys.*, **1962**, 34, 627-631.
189. P. a. M. Dirac, *Math. Proc. Camb. Philos. Soc.*, **2008**, 26, 376-385.
190. W. Kohn and L. J. Sham, *Phys. Rev. *, **1965**, 140, A1133-A1138.
191. P. Hohenberg and W. Kohn, *Phys. Rev. *, **1964**, 136, B864-B871.
192. M. Gell-Mann and K. A. Brueckner, *Phys. Rev.*, **1957**, 106, 364.
193. M. Lewin, E. H. Lieb and R. Seiringer, *Pure Appl. Anal.*, **2019**, 2, 35-73.
194. M. Hofmann and H. F. Schaefer, *Computational Chemistry*, in *Encyclopedia of Physical Science and Technology (Third Edition)*, R.A. Meyers, Editor. 2003, Academic Press: New York. p. 487-506.
195. S. H. Vosko, L. Wilk and M. Nusair, *Can. J. Phys.*, **1980**, 58, 1200-1211.
196. D. M. Ceperley and B. J. Alder, *Phys. Rev. Lett.*, **1980**, 45, 566-569.
197. J. P. Perdew, K. Burke and M. Ernzerhof, *Phys. Rev. Lett.*, **1996**, 77, 3865.
198. K. Burke, J. P. Perdew and M. Ernzerhof, *Int. J. Quantum Chem.*, **1997**, 61, 287-293.
199. C. Lee, W. Yang and R. G. Parr, *Phys. Rev. B*, **1988**, 37, 785-789.
200. J. P. Perdew, *Phys. Rev. B*, **1986**, 33, 8822-8824.
201. J. P. Perdew, J. A. Chevary, S. H. Vosko, K. A. Jackson, M. R. Pederson, D. J. Singh and C. Fiolhais, *Phys. Rev. B*, **1992**, 46, 6671-6687.
202. J. P. Perdew, K. Burke and M. Ernzerhof, *Phys. Rev.Lett.*, **1996**, 77, 3865-3868.
203. J. P. Perdew, J. Tao, V. N. Staroverov and G. E. Scuseria, *J. Chem. Phys.*, **2004**, 120, 6898-6911.

204. Y. Zhao and D. G. Truhlar, *J. Phys. Chem. A*, **2004**, 108, 6908-6918.
205. Y. Zhao and D. G. Truhlar, *Theor. Chem. Account*, **2008**, 120, 215-241.
206. S. Grimme, *J. Comput. Chem.*, **2006**, 27, 1787-1799.
207. J. P. Perdew and K. Schmidt, *AIP Conf. Proc.*, **2001**, 577, 1-20.
208. J. P. Perdew, A. Ruzsinszky, J. Tao, V. N. Staroverov, G. E. Scuseria and G. I. Csonka, *J. Chem. Phys.*, **2005**, 123, 062201.
209. B. G. Janesko, *Int. J. Quantum Chem.*, **2013**, 113, 83-88.
210. E. R. Johnson, I. D. Mackie and G. A. Dilabio, *J. Phys. Org. Chem.*, **2009**, 22, 1127-1135.
211. S. Grimme, J. Antony, T. Schwabe and C. Muck-Lichtenfeld, *Org. Biomol. Chem.*, **2007**, 5, 741-758.
212. S. Grimme, *Wiley Interdiscip. Rev. Comput. Mol. Sci.*, **2011**, 1, 211-228.
213. S. Grimme, J. Antony, S. Ehrlich and H. Krieg, *J. Chem. Phys.*, **2010**, 132.
214. S. Grimme, *J. Comput. Chem.*, **2004**, 25, 1463-1473.
215. S. F. Boys and A. C. Egerton, *Proc. R. soc. Lond. Ser. A-Math. Phys.*, **1950**, 200, 542-554.
216. W. J. Hehre, R. F. Stewart and J. A. Pople, *J. Chem. Phys.*, **1969**, 51, 2657-2664.
217. J. S. Binkley, J. A. Pople and W. J. Hehre, *J. Am. Chem. Soc. *, **1980**, 102, 939-947.
218. M. S. Gordon, J. S. Binkley, J. A. Pople, W. J. Pietro and W. J. Hehre, *J. Am. Chem. Soc.*, **1982**, 104, 2797-2803.
219. W. J. Pietro, M. M. Francl, W. J. Hehre, D. J. Defrees, J. A. Pople and J. S. Binkley, *J. Am. Chem. Soc.*, **1982**, 104, 5039-5048.
220. W. J. Hehre, R. Ditchfield and J. A. Pople, *J. Chem. Phys.*, **1972**, 56, 2257-2261.
221. R. Ditchfield, W. J. Hehre and J. A. Pople, *J. Chem. Phys.*, **1971**, 54, 724-728.
222. T. H. Dunning Jr, *J. Chem. Phys.*, **1970**, 53, 2823-2833.
223. T. Dunning Jr, *Chem. Phys. Lett.*, **1970**, 7, 423-427.
224. P. C. Hariharan and J. A. Pople, *Theor. Chim. Acta*, **1973**, 28, 213-222.
225. D. J. Defrees, B. A. Levi, S. K. Pollack, W. J. Hehre, J. S. Binkley and J. A. Pople, *J. Am. Chem. Soc.*, **1979**, 101, 4085-4089.
226. G. W. Spitznagel, T. Clark, J. Chandrasekhar and P. V. R. Schleyer, *J. Comput. Chem.*, **1982**, 3, 363-371.
227. T. H. Dunning Jr, *J. Chem. Phys.*, **1989**, 90, 1007-1023.
228. R. A. Kendall, T. H. Dunning Jr and R. J. Harrison, *J. Chem. Phys.*, **1992**, 96, 6796-6806.
229. J. Zheng, X. Xu and D. G. Truhlar, *Theor. Chem. Acc.*, **2011**, 128, 295-305.
230. J. G. Hill, *Int. J. Quantum Chem.*, **2013**, 113, 21-34.
231. P. J. Hay and W. R. Wadt, *J. Chem. Phys.*, **1985**, 82, 270-283.
232. P. J. Hay and W. R. Wadt, *J. Chem. Phys.*, **1985**, 82, 270-283.
233. T. R. Cundari and W. J. Stevens, *J. Chem. Phys.*, **1993**, 98, 5555-5565.
234. M. Dolg, *Chapter 14 - Relativistic Effective Core Potentials*, in *Theor. Comput. Chem.*, P. Schwerdtfeger, Editor. 2002, Elsevier. p. 793-862.
235. C. E. Check, T. O. Faust, J. M. Bailey, B. J. Wright, T. M. Gilbert and L. S. Sunderlin, *J. Phys. Chem. A*, **2001**, 105, 8111-8116.
236. D. Geuenich, K. Hess, F. Köhler and R. Herges, *Chem. Rev.*, **2005**, 105, 3758-3772.
237. S. Shin, *Bull. Chem. Soc. Jpn.*, **1955**, 28, 450-453.

238. P. Johansson, S. P. Gejji, J. Tegenfeldt and J. Lindgren, *Electrochim. Acta*, **1998**, 43, 1375-1379.
239. S. Lorenz, A. Groß and M. Scheffler, *Chem. Phys. Lett.*, **2004**, 395, 210-215.
240. H. B. Schlegel, *J. Comput. Chem.*, **2003**, 24, 1514-1527.

Part A:

Electrostatic Topological Viewpoint of π-Conjugation and Aromaticity of Hydrocarbons

$$\sum_{i=1}^{3} \Delta\lambda_i$$

Aromatic
≤ 0.011

0.011 - 0.035
Nonaromatic
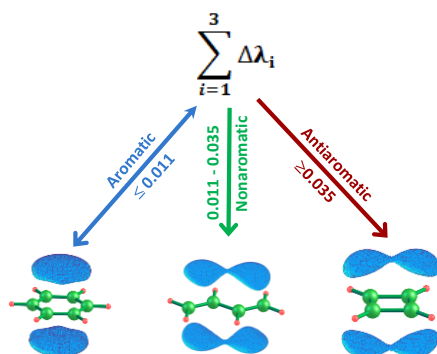
Antiaromatic
≥ 0.035

Part B:

Antiaromaticity-Aromaticity Interplay in Fused Benzenoid Systems using Molecular Electrostatic Potential Topology
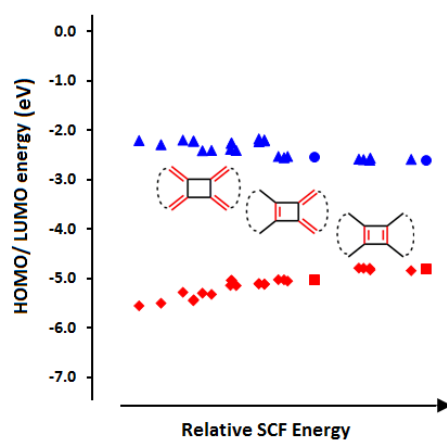
Part A

Electrostatic Topological Viewpoint of π-Conjugation and Aromaticity of Hydrocarbons

2.1 Abstract

A molecular electrostatic potential (MESP) topological study has been conducted for a variety of conjugated hydrocarbons at B3LYP/6-311+G(d,p) level of theory to understand their π-conjugation features and aromaticity. The value of MESP minimum (V_m) is related to the localized/delocalized distribution of π-electron density. The V_m are located interior to the rings in polycyclic benzenoid hydrocarbons (PBHs) whereas they lie outside the boundary of the rings in antiaromatic and in fused systems consisting of aromatic and antiaromatic moieties. The V_m points lie on top and bottom of the π-regions in linear polyenes and annulenes, while a degenerate distribution of CPs around the midpoint region of triple bonds is observed in alkynes. The eigenvalues λ_1, λ_2 and λ_3 of the Hessian matrix at V_m are used to define the aromatic character of the cyclic structures. The eigenvalues follow the trend $\lambda_1 \gg \lambda_2 > \lambda_3 \cong 0$ in PBHs, $\lambda_1 > \lambda_2 > \lambda_3 \cong 0$ in linear polyenes and $\lambda_1 > \lambda_2 > \lambda_3 \neq 0$ in antiaromatic systems. The difference in the aromatic character of PBHs from that of benzene is related with the deviations $\Delta\lambda_1$, $\Delta\lambda_2$ and $\Delta\lambda_3$. The total deviation $\sum_{i=1}^{3} \Delta\lambda_i$ is found to be ≤ 0.011 au for all aromatic systems and lies between 0.011 to 0.035 au for all nonaromatic systems. For antiaromatic systems its value is found to be above 0.035 au. Further, $\sum_{i=1}^{3} \Delta\lambda_i$ gives a direct interpretation of Clar's aromatic sextet structures for PBHs. In summary, MESP topology mapping is a powerful technique to quantify the localized and delocalized π-electron distribution in a variety of unsaturated hydrocarbon systems.

2.2 Introduction

"Aromaticity" is one of the most frequently used terms in chemistry since the discovery[1-4] of benzene in 1825. Though a rigorous definition of aromaticity is elusive,[5] some operational definitions exist for classifying molecules as aromatic, antiaromatic and nonaromatic.[6,7] In quantum chemical terms, aromaticity was defined and explained using Hückel's (4n+2) rule i.e. the conjugation of (4n+2)π-electrons over a planar monocyclic ring (where 'n' is a positive integer).[8-14] According to this rule, molecules other than aromatic are regarded as antiaromatic (4nπ-electrons) or nonaromatic based on certain criteria. Experimental and theoretical studies also enable classification of molecules into categories such as homoaromatic, heteroaromatic, pseudoaromatic,[15] metalloaromatic,[16] chelatoaromatic,[17] claromatic, hyperaromatic,[18] transition state aromatic, excited state aromatic,[19] *etc.* based on a variety of aromaticity criteria.[16,19-22] A general concept is that aromaticity is associated with the delocalization of π-electrons all along the series of bonds resulting in an aromatic ring.[23] Several aromaticity indices have been defined and used for estimating the aromatic character in terms of structural, magnetic, electronic and reactivity properties, *etc.* Among them some of the descriptors are just approximations, some are applicable to certain cases only and some are not good enough to give convincing results.[24-28]

The notion of aromaticity was first brought in for describing the benzene molecule, which is still considered as a paragon of aromaticity. Aromaticity in other π-systems was elucidated with Hückel's (4n+2) rule. Later, numerous studies on aromaticity were taken up. The Hückel's rule is strictly applicable only to the monocyclic conjugated systems, therefore attempts were made to expand the study on aromaticity to polycyclic systems also. Among them, one of the most successful was Clar's model,[29] which explained the stability shown by benzenoid species.[24,30-38] Polycyclic benzenoid hydrocarbons (PBHs), are a class of organic compounds consisting of two or more fused benzenoid rings, which is the most explored one for the study of aromaticity.[39-41] The aromaticity of a PBH is generally described for the individual benzenoid rings as local aromaticity and the average of all the local aromaticities is taken as the global aromaticity for the molecule.[27]

Many alternate ways were introduced to connect aromaticity with other molecular parameters. Schleyer *et al.*[42] stated that there is a linear relationship among the energetic, geometric, and magnetic criteria of aromaticity. Behrens *et al.*[43] demonstrated that the delocalization energy of π- electrons can be used as an index of aromaticity in PBHs. Giambiagi *et al.*[44] suggested that the quantum similarity theory can be used as the method to quantify concepts such as aromaticity. Bultinck *et al.*[18] used the electron density itself as a tool to study aromaticity of the individual benzenoid rings of a given PBH, quite similar to the original Polansky Index.[45] Suresh and Gadre attempted to explain the nature of aromaticity using topological features of the MESP.[46-48] The most interesting finding in their study was the distribution of critical points (CPs) of MESP topology, which could directly distinguish each ring of the PBH system. They obtained a strong correlation between MESP topology patterns and Clar's aromatic sextet theory. However, they did not provide a rigorous and general definition of aromaticity in terms of MESP topology of a large variety of molecules.

Numerous studies have shown that MESP topological analysis[49-53] is very useful for a quantitative interpretation of the localization/delocalization features of π-conjugated systems and lone pair-bearing molecules. Very recently, Gadre, Suresh and co-workers[54] proposed a definition for lone pairs from the characteristics of minima in MESP. The criterion was based upon the eigenvalues and eigenvectors of the Hessian where the largest eigenvalue and the corresponding eigenvector of lone pairs were found to be different from that of another kind of electron delocalization. Localized electron density in lone pair of atoms could be quantified using the negative minimum value of MESP at that region. It has been proposed that the magnitude of the eigenvalue at the CP that corresponds to the lone pair is numerically greater than 0.025 au and the eigenvector associated with it nearly points in the direction (angle ≤ 5°) of the atom on which it is localized. A clear-cut definition of lone pairs emerged in terms of MESP features[55] and that led to an easy interpretation of their interactive behavior with electron deficient π-regions in molecular systems.[56, 57] These studies also suggested that MESP topology features of π-bonded regions of molecules should be significantly different from that of non-bonded electron-localized regions such as lone pairs. The present work proposes an

MESP topology-based approach for a rigorous characterization of the π-regions of aromatic, antiaromatic and nonaromatic systems. We expect that such an MESP topology-based analysis will lead to a new definition of aromaticity as well as a new way to compare the local and global aromaticity values of a large variety of molecules.

2.3 Methodology

All the molecular systems investigated in the present work are optimized at the B3LYP/6-311+G(d,p) level of theory using Gaussian 09 program package,[58] with a check on the minimal nature by doing a frequency run and verifying that all the frequencies are real. At these geometries, MESP and MESP topology computation has been done using the recently developed DAMQT (deformed atoms in molecules quantum theory) package.[59-62] The DAMQT is based on the deformed atoms in molecules (DAM) method, for the analysis of the molecular electron density. The wave function constructed using B3LYP in conjunction with the valence triple-zeta level basis set and augumented with polarization and diffuse functions (6-311+G(d,p)) is expected to give a sufficiently accurate description of the electron density, $\rho(\mathbf{r})$. The values of MESP, its gradients and second derivatives are calculated while finding the CPs using DAM partition-expansion method.[59] Since the eigenvalues of the Hessian matrix describe the curvature of the function at the CP, we felt that such an information regarding the π-region of the molecule can bring out the extend of electron delocalization in the molecule. A very smooth even distribution is expected in cyclically conjugated electrons in aromatic molecules compared to other type of conjugations. In order to express this in terms of MESP topology, we chose the entity $\sum_{i=1}^{3} \Delta\lambda_i$ as it combines the information regarding all the three eigenvalues pertaining to a CP. Here DAMQT package is used for the MESP topology calculation and visualization. All the molecules selected for the present study are shown in Figure 2.1. Due to symmetry, CPs appearing only on one side of the molecular plane are discussed in the text.
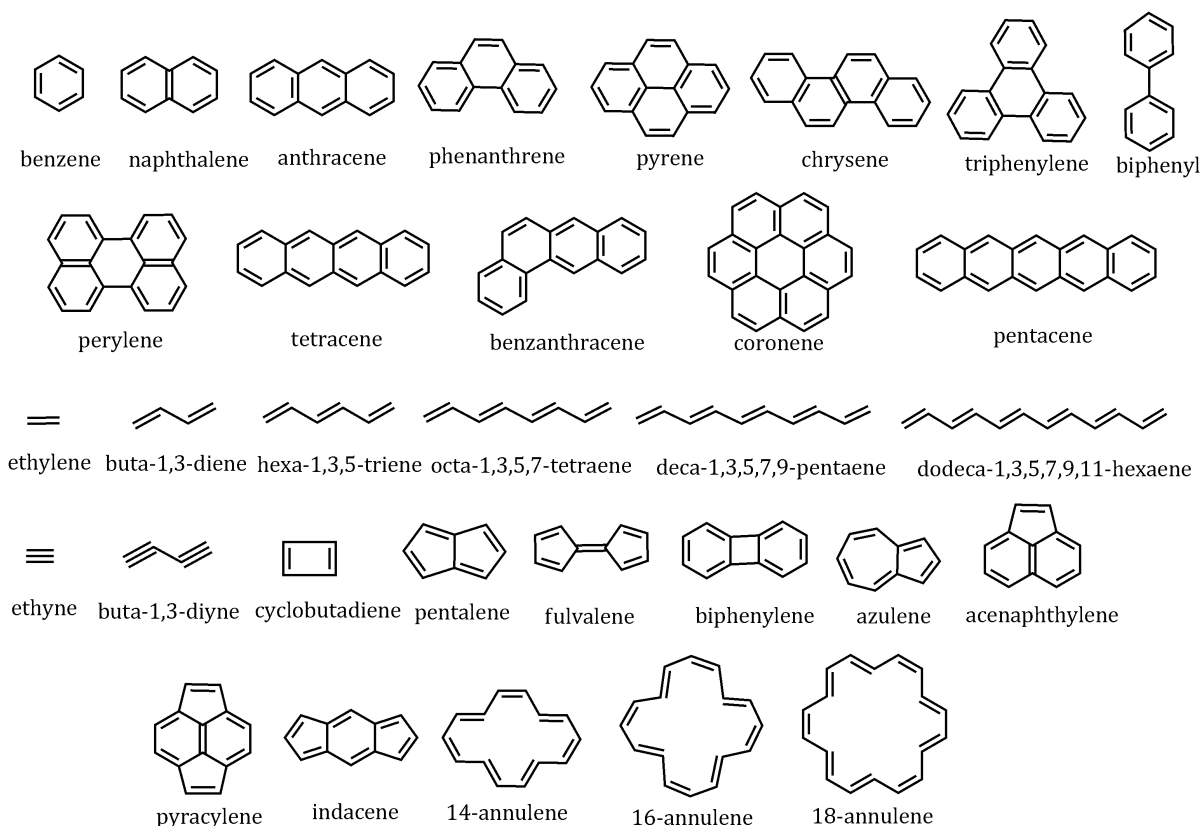
Figure 2.1 The selected set of molecules for exploring aromaticity, nonaromaticity and antiaromaticity

2.4 Results and Discussion

2.4.1 Benzene and Polycyclic Benzenoid Hydrocarbons

In the case of benzene, a set of six equivalent CPs appear on each side, around 1.89 Å vertically away from the molecular plane (Figure 2.2(a)). Each of these CPs is aligned at the mid-point region of the nearest CC bond but shifted towards the interior of the ring (Figure 2.2(b)). The (3, +3) CP is designated as V_m and the three eigenvalues of the Hessian matrix are denoted as λ_1, λ_2, and λ_3. In what follows, the symbol V_m stands for the minimum value of MESP as well as the corresponding CP. In benzene, V_m is -15.7 kcal/mol with λ_1, λ_2, and λ_3 being 0.0142, 0.0025 and 0.0005 au, respectively, showing the trend $\lambda_1 \gg \lambda_2 > \lambda_3 \cong 0$ for this perfectly aromatic molecule. The eigenvector (marked in red arrow in Figure 2.2) corresponding to the largest eigenvalue λ_1 shows an orientation

71

perpendicular to the π-bond. The eigenvectors corresponding to λ_2 (blue arrow) and λ_3 (green arrow) are aligned in a plane which is parallel to the ring plane.

(a)   (b)
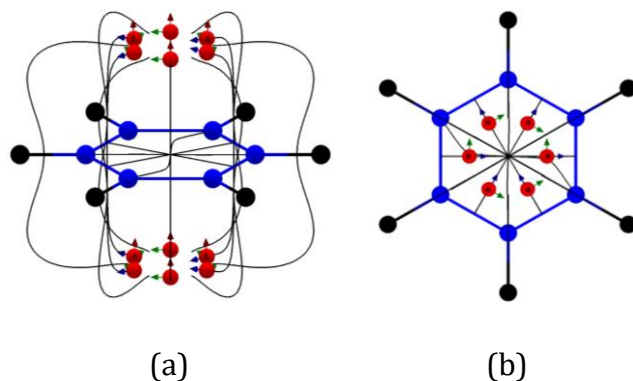
Figure 2.2 MESP topology of benzene. a) side view and b) top view of (3, +3) CPs embedded in gradient paths

The top view of the MESP topology of all the PBH systems studied in this work is shown in Figure 2.3. The V_m and eigenvalues of all these systems are given in Table 2.1. Non-degenerate V_m points appear in these systems are numbered as V_{m1}, V_{m2}, V_{m3}, *etc*. Similar to benzene, the direction of the eigenvector corresponding to the largest eigenvalue λ_1 for all other systems shows an orientation perpendicular to the π-bond, eigenvectors corresponding to λ_2 and λ_3 are aligned in a plane which is parallel to the ring plane. Unlike benzene, the number of V_m points seen in PBH is significantly less than the number of CC bonds. In benzene, the six equivalent CPs may be viewed as the signature of the perfect cyclic delocalization of 6π-electrons over six equal CC bonds while the reduction in CPs in other PBHs can be attributed to deviation from such a π-delocalization due to the presence of unequal CC bonds. In general, V_m points are seen to appear in the vicinity of CC bonds that are more localized. For instance, in the case of naphthalene, a set of four equivalent CPs (V_{m1}) and a fifth CP (V_{m2}) appear on one side of the molecular plane. V_{m1} CPs at -14.8 kcal/mol can be associated with symmetrically equivalent four CC bonds which are the shortest CC bonds of naphthalene, while V_{m2} at -12.7 kcal/mol can be

Figure 2.3 MESP topology of PBH systems (top). MESP isosurface plots (bottom) show the π-delocalization pattern. An appropriate MESP value in the range -0.018 to -0.020 au is selected for isosurface

assigned for the CC bond common for both the rings (Figure 2.3(a)). The λ_1, λ_2, and λ_3 corresponding to V_{m1} are 0.0152, 0.0049 and 0.0032 au and those of V_{m2} are 0.0086,

0.0004 and 0.0001 au, respectively. Eigenvalues corresponding to both the V_m follow the trend $\lambda_1 \gg \lambda_2 > \lambda_3 \cong 0$. The number of non-equivalent CPs are: two in anthracene (V_{m1}, V_{m2}), three in phenanthrene (V_{m1}, V_{m2}, V_{m3}), two in pyrene (V_{m1}, V_{m2}), three in chrysene (V_{m1}, V_{m2}, V_{m3}), one in triphenylene (V_{m1}), two in biphenyl (V_{m1}, V_{m2}), three in perylene (V_{m1}, V_{m2}, V_{m3}), two in tetracene (V_{m1}, V_{m2}), six in benzanthracene (V_{m1}, V_{m2}, V_{m3}, V_{m4}, V_{m5}, V_{m6}), two in coronene (V_{m1}, V_{m2}) and three in pentacene (V_{m1}, V_{m2}, V_{m3}). Here magnitude of $V_{m1} > V_{m2} > V_{m3} > V_{m4} > V_{m5} > V_{m6}$. The V_m and eigenvalues of all the systems are shown in Table 2.1. Among all the systems, the most negative V_{m1} -15.7 kcal/mol is observed in benzene, while for all the PBHs, V_{m1} lies in the range -13.4 to -14.8 kcal/mol.

In benzene, the number of π-electrons shared per CC bond is one, while this quantity is always less than one in a PBH as the number of CC bonds is greater than number of π-electrons. Hence MESP of PBHs is always less negative than benzene. Most of the V_m points as seen from top view show their location more towards the interior of the rings. In all PBH systems, $\lambda_1 \gg \lambda_2 > \lambda_3 \cong 0$ which means that their π-electron distribution as revealed by MESP topology is similar to that of benzene. Does it mean that their aromatic character is also similar to that of benzene? PBH systems are expected to be less aromatic than benzene due to imperfections in the cyclic π-delocalization. The deviation of λ values of a PBH from that of benzene, viz. $\Delta\lambda_1$, $\Delta\lambda_2$ and $\Delta\lambda_3$ can be used to understand the aromatic dilution of a PBH with respect to benzene. For instance, in the case of naphthalene, the deviations $\Delta\lambda_1$, $\Delta\lambda_2$ and $\Delta\lambda_3$ corresponding to the most negative potential V_{m1} are 0.0010, 0.0024 and 0.0027 au and that corresponding to V_{m2} are -0.0056, -0.0021 and -0.0004 au, respectively. These values are close to zero and indicate that the aromatic character of naphthalene is very similar to that of benzene. The total deviations $\sum_{i=1}^{3} \Delta\lambda_i$ (in au) of 0.0062 for V_{m1} and -0.0080 for V_{m2} as per Eq. 2.1 indicate the closeness of the aromatic character of naphthalene to that of benzene.

$$\sum_{i=1}^{3} \Delta\lambda_i = (\lambda_{1(sys)} - \lambda_{1(benz)}) + (\lambda_{2(sys)} - \lambda_{2(benz)}) + (\lambda_{3(sys)} - \lambda_{3(benz)})$$

Eq. 2.1

Table 2.1 MESP topology features (V_m in kcal/mol and the respective eigenvalues λ_1, λ_2, and λ_3 in au) of benzene and polycyclic benzenoid hydrocarbons at B3LYP/6-311+G(d,p) level of theory

Molecule	V_m Label	V_m	λ_1	λ_2	λ_3	$\sum_{i=1}^{3}\Delta\lambda_i$
benzene	V_{m1}	-15.7	0.0142	0.0025	0.0005	0.0000
naphthalene	V_{m1}	-14.8	0.0152	0.0049	0.0032	0.0062
	V_{m2}	-12.7	0.0086	0.0004	0.0001	-0.0080
anthracene	V_{m1}	-14.6	0.0158	0.0059	0.0041	0.0086
	V_{m2}	-12.6	0.0104	0.0035	0.0000	-0.0033
phenanthrene	V_{m1}	-14.5	0.0142	0.0042	0.0022	0.0034
	V_{m2}	-14.5	0.0141	0.0040	0.0024	0.0033
	V_{m3}	-14.3	0.0159	0.0068	0.0052	0.0107
pyrene	V_{m1}	-14.0	0.0156	0.0068	0.0052	0.0104
	V_{m2}	-13.9	0.0133	0.0044	0.0006	0.0011
chrysene	V_{m1}	-14.3	0.0141	0.0042	0.0027	0.0038
	V_{m2}	-14.0	0.0147	0.0058	0.0047	0.0080
	V_{m3}	-12.5	0.0081	0.0018	0.0008	-0.0065
triphenylene	V_{m1}	-14.3	0.0135	0.0036	0.0019	0.0018
biphenyl	V_{m1}	-14.8	0.0141	0.0031	0.0006	0.0006
	V_{m2}	-14.8	0.0140	0.0035	0.0008	0.0011
perylene	V_{m1}	-13.9	0.0140	0.0046	0.0028	0.0042
	V_{m2}	-13.3	0.0115	0.0040	0.0003	-0.0014
	V_{m3}	-12.1	0.0074	0.0005	0.0002	-0.0091
tetracene	V_{m1}	-14.4	0.0161	0.0065	0.0044	0.0098
	V_{m2}	-12.4	0.0106	0.0035	0.0015	-0.0016
benzanthracene	V_{m1}	-14.3	0.0153	0.0055	0.0038	0.0074
	V_{m2}	-14.3	0.0153	0.0055	0.0037	0.0073
	V_{m3}	-14.2	0.0138	0.0039	0.0018	0.0023
	V_{m4}	-14.1	0.0162	0.0076	0.0055	0.0121
	V_{m5}	-12.9	0.0103	0.0033	0.0017	-0.0019
	V_{m6}	-12.7	0.0104	0.0032	0.0012	-0.0024
coronene	V_{m1}	-13.4	0.0144	0.0050	0.0048	0.0070
	V_{m2}	-11.3	0.0074	0.0006	0.0003	-0.0089
pentacene	V_{m1}	-14.3	0.0162	0.0067	0.0045	0.0103
	V_{m2}	-12.3	0.0108	0.0037	0.0020	-0.0007
	V_{m3}	-11.8	0.0099	0.0036	0.0001	-0.0036

The total deviation in the eigenvalues, $\sum_{i=1}^{3}\Delta\lambda_i$ gives an overall idea about the proximity of the local aromatic character of the system to that of benzene. The $\sum_{i=1}^{3}\Delta\lambda_i$ corresponding to the most negative V_{m1} is positive for all the systems and falls in the range from 0.0006 to 0.0104 au. Along the linear polyacene series (naphthalene, anthracene, tetracene and pentacene), $\sum_{i=1}^{3}\Delta\lambda_i$ values for V_{m1} show a gradual increase in the positive character which can be attributed to a gradual change in character of the corresponding CC bond from a delocalized to a more localized double bond. In fact, higher polyacenes are susceptible for addition reactions due to the dilution of aromatic character as per Clar's theory.[38] In general, a positive value for $\sum_{i=1}^{3}\Delta\lambda_i$ can be assigned to a relatively more electron rich CC bond region in the molecule, whereas that corresponding to other V_m values shows both positive and negative deviations. The rings possessing small magnitude for $\sum_{i=1}^{3}\Delta\lambda_i$ may be regarded as more aromatic than the rings showing higher values (*cf.* Table 2.1). Among all the systems, the least deviation is shown by biphenyl[44] suggesting that the extent of aromaticity exhibited by each ring of this molecule is almost equal to that of benzene. A large deviation of $\sum_{i=1}^{3}\Delta\lambda_i$ from zero is a signature that the CC bond nearest to that CP is a more localized double bond. For instance, the magnitude of $\sum_{i=1}^{3}\Delta\lambda_i$ corresponding to the CC bond nearest to V_{m3} of phenanthrene (1.36 Å), V_{m1} of pyrene (1.36 Å), V_{m4} of benzanthracene (1.35 Å) and V_{m1} of pentacene (1.36 Å) is higher than 0.010, suggesting that they are the most localized (the shortest) among all the CC bonds studied herein. Also CPs of those V_m fall directly on top of the CC bond than the interior of the ring. Can we explain the aromatic sextet concept of Clar[63] using MESP topology? The MESP analysis would suggest that the perfect sextet representation is only possible for benzene whereas the most likely sextet representation of PBH systems[64-66] would require the combination of localized double bonds and sextets as well as their resonance forms.
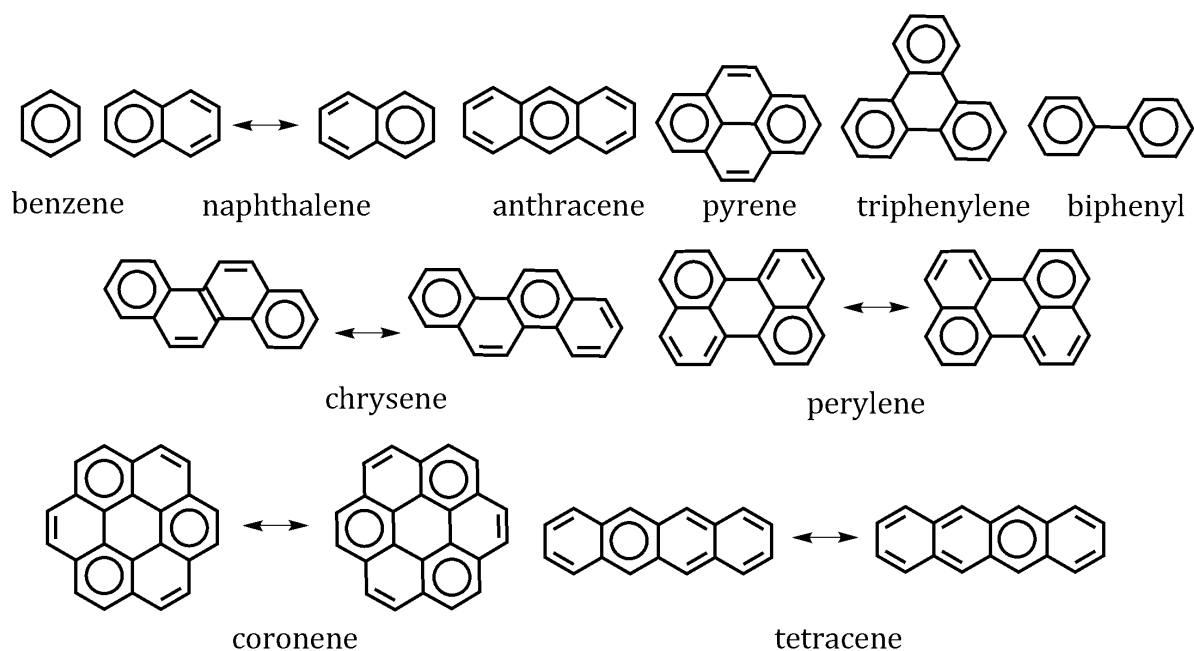
Figure 2.4 MESP topology-based Clar's aromatic sextets of polycyclic benzenoid systems

The ring that contains CPs showing numerically small deviation in the sum of eigenvalues constitutes an aromatic sextet. In naphthalene, the smallest $\sum_{i=1}^{3} \Delta\lambda_i$ is 0.0062 au and this value is identical for both the rings, due to symmetry. Hence, naphthalene may be represented as a resonance hybrid of two structures as shown in Figure 2.4. Similarly, perylene appears as a union of two naphthalene moieties and represented by two resonance forms whereas a single sextet representation is ideal for triphenylene. Also, a hybrid of two resonance forms can bring out the π-delocalization features of coronene. In perylene, triphenylene and coronene, less positive $\sum_{i=1}^{3} \Delta\lambda_i$ than naphthalene is seen, indicating that they are more aromatic than the latter. Moreover, the middle ring of perylene, triphenylene and coronene is devoid of π-character in the sextet representation which is regarded as an 'empty ring' in Clar's theory.[67, 68] Triphenylene is an example of a fully benzenoid hydrocarbon in Clar's theory as it can be described as a cyclically connected three benzene moieties. The ring represented with a sextet for pyrene has $\sum_{i=1}^{3} \Delta\lambda_i$ 0.0011 au and its CC bonds depicted as double bonds show $\sum_{i=1}^{3} \Delta\lambda_i$ 0.0104 au. Similar criteria are used for making the representation of chrysene and benzanthracene. For anthracene, the middle ring having $\sum_{i=1}^{3} \Delta\lambda_i = 0.0033$ au is proposed

for sextet representation while the peripheral rings show relatively more localized CC bonds.[38] As the number of rings increases in a linear way (linear polyacenes), the $\sum_{i=1}^{3} \Delta\lambda_i$ value of the terminal rings increases gradually (0.0098 au for tetracene and 0.0103 au for pentacene) indicating more localized character of the corresponding CC bonds. The $\sum_{i=1}^{3} \Delta\lambda_i$ values for the interior rings of tetracene and pentacene are negative and smaller in magnitude compared to the terminal rings suggesting the more delocalized but less electron dense features of them. The interior rings are considered more aromatic than the terminal ones on the basis of more delocalization of π-electrons and accordingly, the sextet representations given in Figures 2.5 are best suited for tetracene and pentacene,[38] respectively. Clar also proposed the 'aromatic dilution' concept for linear polyacene systems to describe the decreasing aromatic character of them with an increase in size. This occurs due to the possibility of drawing only one sextet for linear polyacenes and that sextet can be on any of the rings, while the rest of the rings are represented with alternate single and double bonds. Since one sextet is 'diluted' over several rings, aromatic dilution occurs as the size increases. The MESP-based analysis of aromatic character of linear polyacenes suggests that with the increase in the size of the system, the aromatic character of the terminal rings decreases significantly than the rest and the middle rings are more suitable for sextet representation.

2.4.2 Alkenes and Alkynes

MESP topology of ethylene and linear polyenes up to dodeca-1,3,5,7,9,11-hexaene is also studied as prototype nonaromatic systems. Ethylene possesses a localized π-bond while π-bonds show a delocalized character in the larger linear polyenes. As expected, the most localized π-bond of ethylene shows the most negative V_m at -18.6 kcal/mol, located over the midpoint of the CC bond, 1.73 Å away from the molecular plane. The alternate double and single CC bond distribution in polyenes is clearly seen in MESP topology wherein the V_m points are always located over the double bonds, while the formal CC single bonds are borne out to be devoid of a minimum in MESP (*cf.* Figure 2.5).

(a) ethylene

(b) buta-1,3-diene

(c) hexa-1,3,5-triene

(d) octa-1,3,5,7-tetraene

(e) deca-1,3,5,7,9-pentaene

(f) dodeca-1,3,5,7,9,11-hexaene
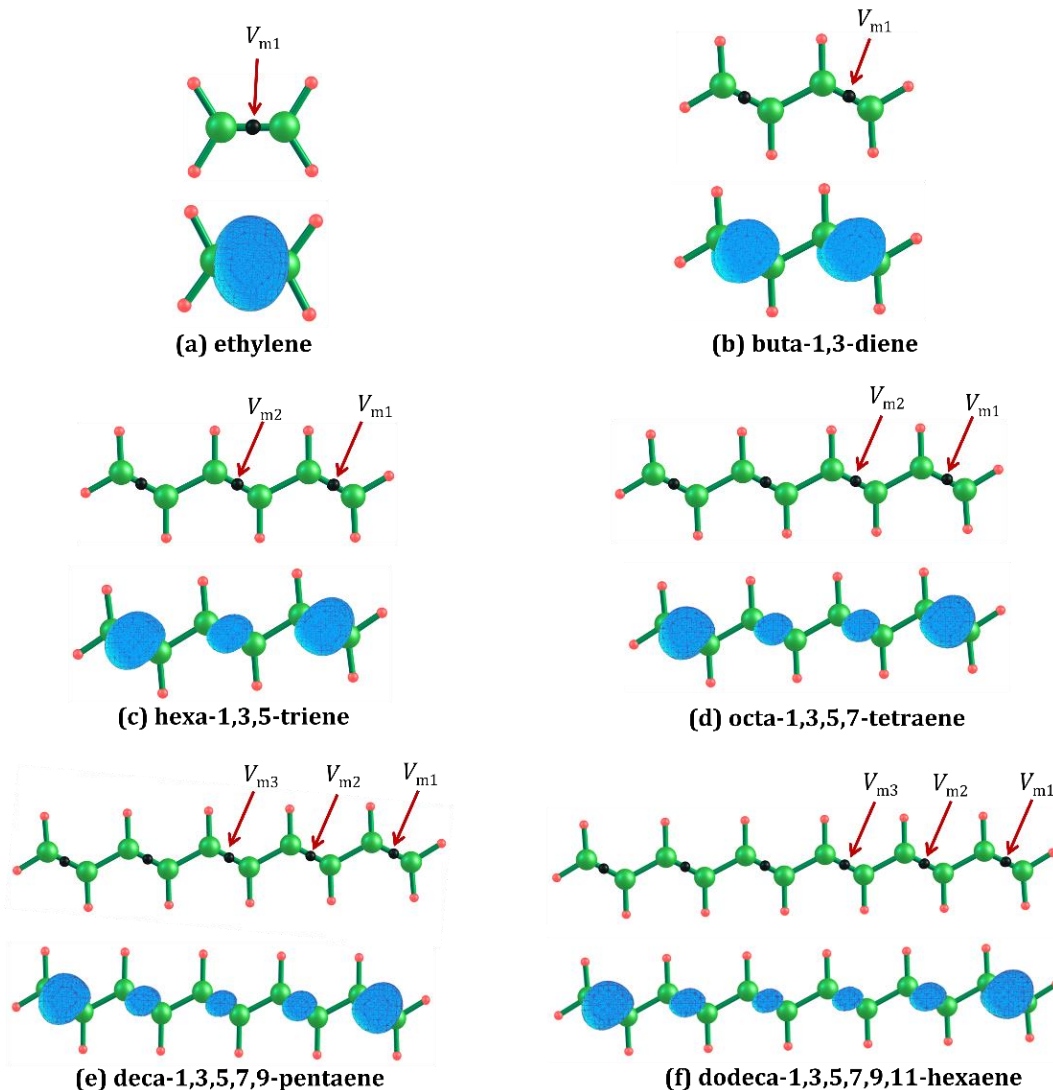
Figure 2.5 MESP topology of linear conjugated systems (top). MESP isosurface plots (bottom) show the π-delocalization pattern. Isosurface value is -0.02 au for all the systems.

In linear polyenes, the most negative V_m is always found on the terminal double bond while the negative character of V_m decreases towards the central region as the length of polyene increases (Table 2.2). The eigenvalues λ_1, λ_2, and λ_3 for the ethylene molecule are 0.0277, 0.0176 and 0.0073 au, respectively, which obey $\lambda_1 > \lambda_2 > \lambda_3 \cong 0$. Further, with respect to benzene V_m as a reference, the $\Delta\lambda_1$, $\Delta\lambda_2$, and $\Delta\lambda_3$ for ethylene are 0.0135, 0.0151

and 0.0068 au respectively, with $\sum_{i=1}^{3} \Delta\lambda_i$ being 0.0354 au. The high values of $\sum_{i=1}^{3} \Delta\lambda_i$ indicate the localized nature of the CC bond in ethylene. The $\sum_{i=1}^{3} \Delta\lambda_i$ value for all the linear polyenes falls in the range 0.027 to 0.013 au The smaller magnitude of $\sum_{i=1}^{3} \Delta\lambda_i$ than ethylene indicating the delocalized nature of the π-electrons in polyenes. In PBH systems, the most localized CC bonds show $\sum_{i=1}^{3} \Delta\lambda_i$ around 0.010 au and the smallest $\sum_{i=1}^{3} \Delta\lambda_i$ observed for linear polyene is higher than this value. Hence, we propose that irrespective of the nature of π-conjugation, $\sum_{i=1}^{3} \Delta\lambda_i$ value ≥ 0.011 au may be regarded as a largely localized (nonaromatic) double bond.

Table 2.2 MESP topology features (V_m in kcal/mol and the respective eigenvalues λ_1, λ_2, and λ_3 in au) of linear conjugated systems at B3LYP/6-311+G(d,p) level of theory

Molecule	V_m label	V_m	λ_1	λ_2	λ_3	$\sum_{i=1}^{3} \Delta\lambda_i$
ethylene	V_{m1}	-18.6	0.0277	0.0176	0.0073	0.0354
buta-1,3-diene	V_{m1}	-16.8	0.0232	0.0135	0.0071	0.0266
hexa-1,3,5-triene	V_{m1}	-16.7	0.0231	0.0131	0.0070	0.0260
	V_{m2}	-14.4	0.0176	0.0092	0.0060	0.0156
octa-1,3,5,7-tetraene	V_{m1}	-16.7	0.0232	0.0129	0.0070	0.0259
	V_{m2}	-14.1	0.0173	0.0089	0.0056	0.0146
deca-1,3,5,7,9-pentaene	V_{m1}	-16.8	0.0232	0.0129	0.0069	0.0258
	V_{m2}	-14.1	0.0173	0.0087	0.0055	0.0143
	V_{m3}	-13.7	0.0170	0.0085	0.0052	0.0135
dodeca-1,3,5,7,9,11-hexaene	V_{m1}	-16.9	0.0233	0.0128	0.0069	0.0258
	V_{m2}	-14.1	0.0173	0.0087	0.0054	0.0142
	V_{m3}	-13.7	0.0169	0.0084	0.0050	0.0131
ethyne	V_{m1}	-18.4	0.0290	0.0223	0.0000	0.0341
buta-1,3-diyne	V_{m1}	-12.1	0.0175	0.0126	0.0000	0.0129

The distribution of electron density and CPs in alkynes systems is different from that of alkenes. Ethyne and buta-1,3-diyne are the two systems we consider for the study. Ethyne consists of set of degenerate CPs located at -18.4 kcal/mol and distributed uniformly around the CC triple bond, in a circular manner (Figure 2.6). The eigenvalues

λ_1, λ_2, and λ_3 corresponding to V_{m1} are 0.0290, 0.0223 and 0.0000 au respectively and follow the trend $\lambda_1 > \lambda_2 > \lambda_3 = 0$. The $\sum_{i=1}^{3} \Delta\lambda_i$ for V_{m1} is 0.0341 au indicating the more localized electron density around the triple bond. Similarly, buta-1,3-diyne consists of equivalent CPs located at -12.1 kcal/mol and a circular distribution of CPs is seen around both the triple bonded regions. The λ_1, λ_2, and λ_3 values corresponding to V_{m1} are 0.0175, 0.0126 and 0.0000 au and follow the trend $\lambda_1 > \lambda_2 > \lambda_3 = 0$; the total deviation $\sum_{i=1}^{3} \Delta\lambda_i$ is 0.0129 au indicating significant reduction in the localized distribution of electron density when compared to ethyne.

(a) ethyne   **(b) buta-1,3-diyne**

Figure 2.6 The degenerate MESP isosurface plots depict the π-delocalization patterns. Isosurface value -18.0 kcal/mol for ethyne and -11.5 kcal/mol for buta-1,3 diyne

2.4.3 Antiaromatic and Non-benzenoid Hydrocarbons

The antiaromatic cyclobutadiene[69] is characterized by alternate CC single (1.57 Å) and double (1.33 Å) bonds. As expected, several V_m points with identical MESP minimum value are located for the CC double bonds with value -18.4 kcal/mol and distance of separation from the molecular plane 1.62 Å. The V_m value of cyclobutadiene is very similar to that of the localized CC bond of ethylene, while the bond distance is significantly shorter than that of ethylene. The eigenvalues λ_1, λ_2, and λ_3 are 0.0270, 0.0182 and 0.0102 au respectively, suggesting that $\lambda_1 > \lambda_2 > \lambda_3$ where λ_3 is not close to zero. The deviations $\Delta\lambda_1$, $\Delta\lambda_2$ and $\Delta\lambda_3$ with respect to benzene are 0.0128, 0.0157 and 0.0097 au, with the total deviation $\sum_{i=1}^{3} \Delta\lambda_i$ being 0.0382 au. Among all the molecules studied, the cyclobutadiene molecule exhibits the highest $\sum_{i=1}^{3} \Delta\lambda_i$ indicating the highly

localized nature of the π-bonds. The MESP topology of cyclobutadiene is shown in Figure 2.7(a) and the respective V_m and eigenvalues are listed in Table 2.3.
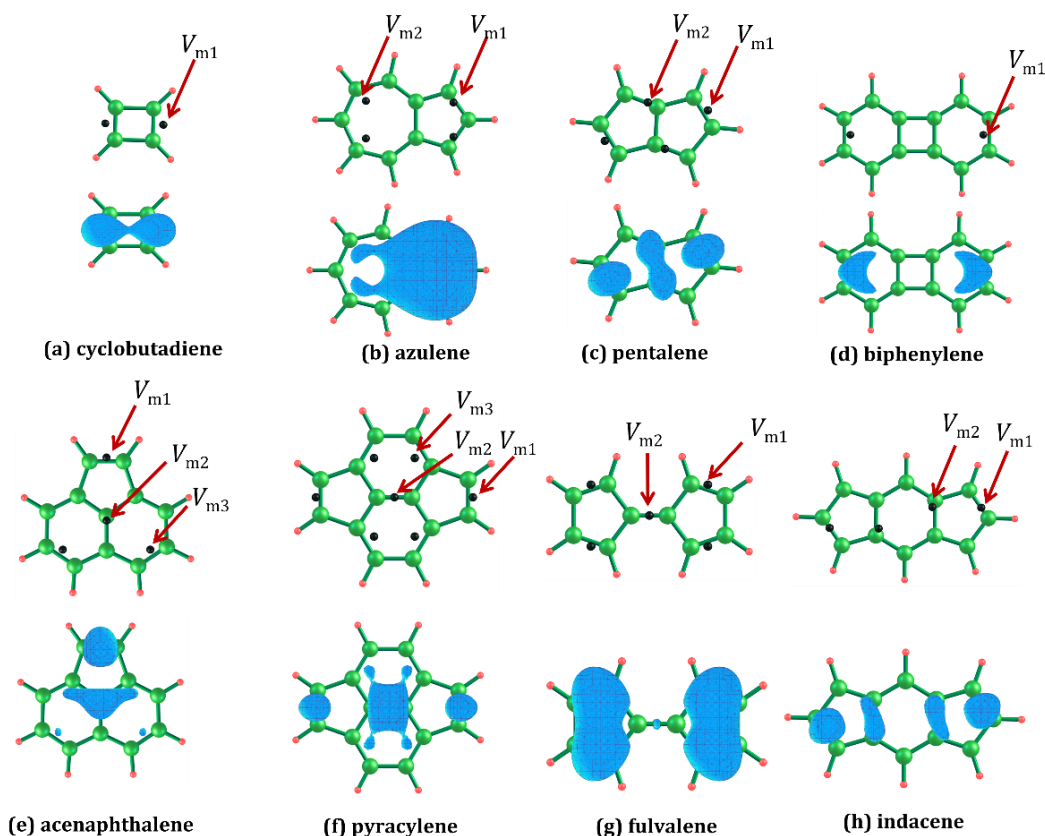
Figure 2.7 MESP topology of cyclobutadiene and other non-benzenoid systems (top). MESP isosurface plots (bottom) show the delocalization pattern. An appropriate MESP value in the range -0.017 to -0.023 au is selected for isosurface

Azulene consists of two non-equivalent CPs (V_{m1}, V_{m2}) on each side of the molecular plane. A set of two equivalent CPs (V_{m1}) located at -18.9 kcal/mol is associated with the five membered ring and another set of two degenerate CPs (V_{m2}) at -11.3 kcal/mol is associated with the seven membered ring of the molecule and CPs are aligned interior to the ring (Figure 2.7(b)). The λ_1, λ_2, and λ_3 eigenvalues corresponding to V_{m1} are 0.0198, 0.0059 and 0.0031 au and those of V_{m2} are 0.0103, 0.0029 and 0.0009 au respectively and they follow the trend $\lambda_1 \gg \lambda_2 > \lambda_3 \cong 0$ which is similar to PBHs. The $\Delta\lambda_1$, $\Delta\lambda_2$, and $\Delta\lambda_3$ values corresponding to V_{m1} are 0.0056, 0.0033 and 0.0026 au and that

corresponding to V_{m2} are -0.0038, 0.0004 and 0.0004 au, respectively. The $\sum_{i=1}^{3} \Delta\lambda_i$ for V_{m1} is 0.0116 au and that of V_{m2} is -0.0030 au which indicate that the five-membered ring possesses more localized electron density distribution similar to nonaromatic systems while the seven-membered ring has more delocalized electron density distribution similar to aromatic hydrocarbons. The $\sum_{i=1}^{3} \Delta\lambda_i$ based assessment of aromaticity fully support the conventional view[23] that the seven-membered ring of azulene is more aromatic than the five-membered one.

Table 2.3 MESP topology features of cyclobutadiene and other non-benzenoid systems (V_m in kcal/mol and the respective eigenvalues λ_1, λ_2, and λ_3 in au) at B3LYP/6-311+G(d,p) level of theory

Molecule	V_m label	V_m	λ_1	λ_2	λ_3	$\sum_{i=1}^{3} \Delta\lambda_i$
cyclobutadiene	V_{m1}	-18.4	0.0270	0.0182	0.0102	0.0382
azulene	V_{m1}	-18.9	0.0198	0.0059	0.0031	0.0116
	V_{m2}	-11.3	0.0103	0.0029	0.0009	-0.0030
pentalene	V_{m1}	-17.8	0.0230	0.0130	0.0074	0.0263
	V_{m2}	-15.0	0.0169	0.0057	0.0035	0.0088
biphenylene	V_{m1}	-15.1	0.0156	0.0038	0.0035	0.0057
acenaphthylene	V_{m1}	-17.6	0.0214	0.0111	0.0071	0.0224
	V_{m2}	-14.5	0.0112	0.0016	0.0012	-0.0032
	V_{m3}	-13.9	0.0139	0.0041	0.0029	0.0037
pyracylene	V_{m1}	-15.9	0.0204	0.0115	0.0072	0.0219
	V_{m2}	-14.4	0.0106	0.0022	0.0021	-0.0023
	V_{m3}	-13.2	0.0109	0.0023	0.0015	-0.0025
fulvalene	V_{m1}	-16.1	0.0211	0.0110	0.0071	0.0220
	V_{m2}	-10.8	0.0073	0.0015	0.0012	-0.0072
indacene	V_{m1}	-16.6	0.0194	0.0068	0.0048	0.0138
	V_{m2}	-14.8	0.0132	0.0024	0.0008	-0.0008

In pentalene, the CC bonds close to V_{m1} and V_{m2} show more double bond character (1.35 Å) than the rest (1.47 Å). V_{m1} is -17.8 kcal/mol and its eigenvalues λ_1, λ_2, and λ_3 are

0.0230, 0.0130 and 0.0074 au, respectively. Since $\lambda_1 > \lambda_2 > \lambda_3$ and $\sum_{i=1}^{3} \Delta\lambda_i = 0.0263$ au, olefinic character can be assigned to these bonds which are susceptible to addition reactions. The V_{m2} appears at -15.0 kcal/mol with eigenvalues 0.0169, 0.0057 and 0.0035 au. Here $\lambda_1 \gg \lambda_2 > \lambda_3$ and $\sum_{i=1}^{3} \Delta\lambda_i$ is 0.0088 au indicating the aromatic character of these bonds which may resist addition reactions. The $\sum_{i=1}^{3} \Delta\lambda_i$ based assessment suggests that aromatic character is limited only to very few CC bonds in pentalene[44] and the molecule can be considered as largely nonaromatic in nature. Biphenylene[44, 70] shows a V_m at -15.1 kcal/mol with eigenvalues, *viz.* 0.0156, 0.0038 and 0.0035 au showing the trend $\lambda_1 \gg \lambda_2 > \lambda_3 \cong 0$ and $\sum_{i=1}^{3} \Delta\lambda_i$ 0.0057 au indicating that the aromatic character of the molecule is very similar to that of benzene. Acenaphthylene[71, 72] shows three non-degenerate CPs $V_{m1,}$ $V_{m2,}$ V_{m3} at -17.6, -14.5 and -13.9 kcal/mol, respectively. The eigenvalues corresponding to V_{m1} show $\lambda_1 > \lambda_2 > \lambda_3 \cong 0$ and $\sum_{i=1}^{3} \Delta\lambda_i$ is 0.0224 au. The CC bond corresponding to V_{m1} is clearly a double bond and suggests nonaromatic character for the five-membered ring. The CP for this bond is located exterior to the ring and indicates the strain in the ring. The CPs of V_{m2} and V_{m3} are located over the six-membered rings and both follow the trend $\lambda_1 \gg \lambda_2 > \lambda_3 \cong 0$ with $\sum_{i=1}^{3} \Delta\lambda_i = -0.0032$ au for the former and 0.0037 au for the latter suggesting the strong aromatic character for the naphthalene-like region in the molecule. Very similar behaviour is observed in pyracylene[71, 73] wherein naphthalene-like moiety exhibits aromatic character whereas both the five membered rings show nonaromatic character due to the presence of a localized double bond.

Fulvalene consists of a set of four equivalent CPs (V_{m1}) at -16.1 kcal/mol, located near the π-region of the five-membered rings (above and below) and a set of equivalent CPs (V_{m2}), at -10.8 kcal/mol located exactly over the middle of the central bond that connects both the five-membered rings. The eigenvalues of V_{m1} follow the trend $\lambda_1 > \lambda_2 > \lambda_3 \cong 0$ and $\sum_{i=1}^{3} \Delta\lambda_i$ is 0.0220 au, indicating nonaromatic behaviour of the rings. Indacene is characterized by two non-equivalent CPs V_{m1} and V_{m2} at -16.6 and -14.8 kcal/mol on each side of the molecular plane. The eigenvalues of both CPs follow the trend $\lambda_1 \gg \lambda_2 > \lambda_3 \cong 0$, whereas $\sum_{i=1}^{3} \Delta\lambda_i$ is 0.0138 au for V_{m1} and -0.0008 au for V_{m2}. The $\sum_{i=1}^{3} \Delta\lambda_i$ value close to

zero for V_{m2} indicates strong aromatic character for the six-membered ring while the five-membered rings must behave as nonaromatic.

2.4.4 Annulenes

We extended the analysis to some higher annulenes[74, 75] in order to test the reliability of $\sum_{i=1}^{3} \Delta\lambda_i$ parameter in assessing aromaticity/nonaromaticity (Table 2.4) of the systems. The 14- and 18-annulenes are well known aromatic system while the 16-annulene is always regarded as nonaromatic. The 14-annulene shows three non-equivalent CPs (V_{m1}, V_{m2}, V_{m3}) on each side of the molecular plane (Figure 2.8). The V_{m1} points show value -13.3 kcal/mol and their eigenvalues λ_1, λ_2, and λ_3 are 0.0146, 0.0051, and 0.0018 au, respectively. V_{m2} is at -12.1 kcal/mol with eigenvalues 0.0138, 0.0056, and 0.0006 au These CPs are aligned slightly exterior to the ring boundary. V_{m3} is located at -10.8 kcal/mol with eigenvalues 0.0119, 0.0069, and 0.0002. These CPs are seen more towards the interior of the ring. The eigenvalues of V_{m1}, V_{m2} and V_{m3} follow the trend $\lambda_1 \gg \lambda_2 > \lambda_3 \cong 0$ which resembles that of PBHs. The $\sum_{i=1}^{3} \Delta\lambda_i$ for V_{m1}, V_{m2} and V_{m3} are 0.0043,

Table 2.4 MESP topology features (V_m in kcal/mol and the respective eigenvalues λ_1, λ_2, and λ_3 in au) of annulene systems at B3LYP/6-311+G(d,p) level of theory

Molecule	V_m label	V_m	λ_1	λ_2	λ_3	$\sum_{i=1}^{3} \Delta\lambda_i$
14-annulene	V_{m1}	-13.3	0.0146	0.0051	0.0018	0.0043
	V_{m2}	-12.1	0.0138	0.0056	0.0006	0.0027
	V_{m3}	-10.8	0.0119	0.0069	0.0002	0.0017
16-annulene	V_{m1}	-14.7	0.0195	0.0102	0.0055	0.0180
	V_{m2}	-14.6	0.0191	0.0093	0.0072	0.0184
	V_{m3}	-13.9	0.0177	0.0093	0.0042	0.0139
	V_{m4}	-12.1	0.0169	0.0093	0.0062	0.0152
18-annulene	V_{m1}	-12.7	0.0134	0.0055	0.0011	0.0027
	V_{m2}	-12.6	0.0137	0.0064	0.0005	0.0034

0.0017 and 0.0027 indicating more delocalized electron density distribution rather akin to PBHs. In 18-annulene there are two non-equivalent CPs (V_{m1}, V_{m2}) located at -12.7 and -12.6 kcal/mol and the eigenvalues corresponding to V_{m1} are 0.0134, 0.0055 and 0.0011 au and those corresponding to V_{m2} are 0.0137, 0.0064 and 0.0005 au, both following the trend $\lambda_1 \gg \lambda_2 > \lambda_3 \cong 0$. Also the $\sum_{i=1}^{3} \Delta\lambda_i$ for V_{m1} is 0.0027 au, and that for V_{m2} is 0.0034 au indicating the closeness of aromatic character of the molecule to that of benzene.[76, 77]
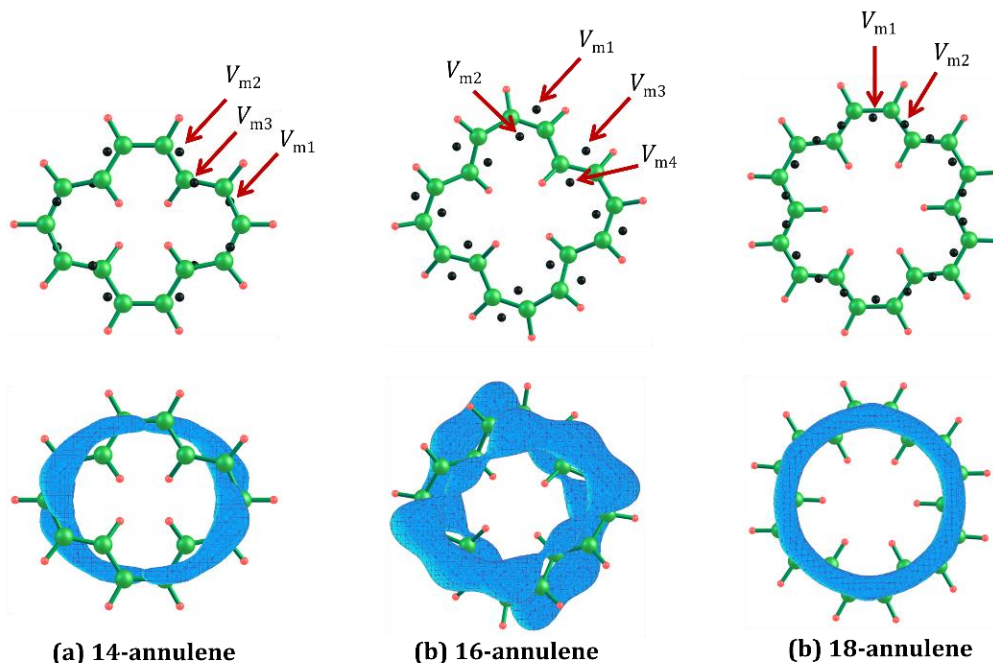
Figure 2.8 MESP topology of annulene systems (top). MESP isosurface plots (bottom) show the delocalization pattern. Isosurface value is -0.018 to -0.015 au for all the systems

In 16-annulene, four non-equivalent CPs (V_{m1}, V_{m2}, V_{m3}, V_{m4}) are located at -14.7, -14.6, -13.9 and -12.1 kcal/mol. The eigenvalues corresponding to these minima (in au) are as follows. V_{m1}: 0.0195, 0.0102, and 0.0055, V_{m2}: 0.0191, 0.0093 and 0.0072, V_{m3}: 0.0177, 0.0093 and 0.0042, and V_{m4}: 0.0169, 0.0093 and 0.0062. It is very clear that the trend in λ values ($\lambda_1 > \lambda_2 > \lambda_3 \cong 0$) is very similar to that of alkenes and significantly differs from that observed for 14- and 18-annulenes. Moreover, $\sum_{i=1}^{3} \Delta\lambda_i$ for 16-annulene is 0.0180 au for V_{m1}, 0.0184 au for V_{m2}, 0.0139 au for V_{m3} and 0.0152 au for V_{m4}. These values are greater than 0.01 au indicating the localized distribution of electron density over π-

regions. Thus, the classic nonaromatic character of the cyclic π-electrons in 16-annulene as pointed out in the literature[78] is clearly brought out by $\sum_{i=1}^{3} \Delta\lambda_i$.

To check the reliability of the B3LYP method, a benchmark study is also conducted with the DFT methods M06 (Table 2.5), and M06-2X (Table 2.7) and also with the *ab initio* method MP2 (Table 2.8) using the 6-311+G(d,p) basis set in all cases. Though the absolute values of MESP parameters differs to some extent, the relative order and the trend in values are almost identical in all the cases (Table 2.5 to Table 2.8). Hence, only the B3LYP/6-311+G(d,p) values are discussed in this work.

Table 2.5 MESP topology features (V_m in kcal/mol and eigenvalues in au) of all the molecules using M06/6-311+G(d,p) level of theory (continues…)

Molecule	V_m label	V_m	λ_1	λ_2	λ_3	$\sum_{i=1}^{3} \Delta\lambda_i$
benzene	V_{m1}	-15.7	0.0144	0.0025	0.0005	0.0000
naphthalene	V_{m1}	-14.8	0.0155	0.0049	0.0034	0.0065
	V_{m2}	-12.9	0.0092	0.0005	0.0003	-0.0074
anthracene	V_{m1}	-15.4	0.0179	0.0057	0.0046	0.0108
	V_{m2}	-13.7	0.0122	0.0039	0.0002	-0.0011
phenanthrene	V_{m1}	-15.2	0.0157	0.0041	0.0025	0.0050
	V_{m2}	-15.4	0.0180	0.0063	0.0056	0.0124
	V_{m3}	-15.2	0.0160	0.0042	0.0026	0.0054
pyrene	V_{m1}	-14.9	0.0176	0.0063	0.0056	0.0122
	V_{m2}	-14.6	0.0148	0.0043	0.0010	0.0027
	V_{m3}	-13.0	0.0083	0.0008	0.0002	-0.0080
chrysene	V_{m1}	-14.9	0.0158	0.0042	0.0029	0.0055
	V_{m2}	-14.8	0.0160	0.0043	0.0028	0.0057
	V_{m3}	-13.8	0.0095	0.0024	0.0009	-0.0045
triphenylene	V_{m1}	-14.9	0.0150	0.0036	0.0020	0.0033
biphenyl	V_{m1}	-15.4	0.0160	0.0036	0.0003	0.0025
perylene	V_{m1}	-14.6	0.0158	0.0045	0.0030	0.0059
	V_{m2}	-14.3	0.0128	0.0040	0.0017	0.0012
	V_{m3}	-13.2	0.0084	0.0009	0.0004	-0.0076
tetracene	V_{m1}	-15.2	0.0182	0.0061	0.0049	0.0119
	V_{m2}	-13.5	0.0123	0.0039	0.0015	0.0005

Table 2.5 MESP topology features (V_m in kcal/mol and eigenvalues in au) of all the molecules using M06/6-311+G(d,p) level of theory (continues…)

Molecule	V_m label	V_m	λ_1	λ_2	λ_3	$\sum_{i=1}^{3} \Delta\lambda_i$
benzanthracene	V_{m1}	-15.1	0.0183	0.0070	0.0059	0.0138
	V_{m2}	-15.0	0.0173	0.0053	0.0042	0.0094
	V_{m3}	-15.0	0.0172	0.0053	0.0041	0.0092
	V_{m4}	-14.8	0.0155	0.0039	0.0021	0.0042
	V_{m5}	-14.0	0.0119	0.0037	0.0018	0.0000
	V_{m6}	-13.8	0.0121	0.0035	0.0013	-0.0005
coronene	V_{m1}	-14.1	0.0162	0.0050	0.0046	0.0085
	V_{m2}	-12.3	0.0085	0.0008	0.0006	-0.0074
pentacene	V_{m1}	-15.0	0.0183	0.0063	0.0051	0.0124
	V_{m2}	-13.4	0.0126	0.0041	0.0020	0.0013
	V_{m3}	-12.8	0.0114	0.0039	0.0003	-0.0017
ethylene	V_{m1}	-18.6	0.0284	0.0182	0.0071	0.0364
buta-1,3-diene	V_{m1}	-18.0	0.0262	0.0123	0.0078	0.0289
hexa-1,3,5-triene	V_{m1}	-17.8	0.0259	0.0119	0.0077	0.0281
	V_{m2}	-15.9	0.0204	0.0087	0.0067	0.0184
octa-1,3,5,7-tetraene	V_{m1}	-17.8	0.0259	0.0117	0.0077	0.0279
	V_{m2}	-15.5	0.0199	0.0085	0.0063	0.0173
deca-1,3,5,7,9-pentaene	V_{m1}	-17.8	0.0259	0.0117	0.0077	0.0279
	V_{m2}	-15.5	0.0199	0.0084	0.0061	0.0170
	V_{m3}	-15.2	0.0195	0.0082	0.0058	0.0161
dodeca-1,3,5,7,9,11-hexaene	V_{m1}	-17.9	0.0259	0.0116	0.0076	0.0278
	V_{m2}	-15.5	0.0198	0.0083	0.0060	0.0169
	V_{m3}	-15.1	0.0193	0.0081	0.0056	0.0157
cyclobutadiene	V_{m1}	-18.6	0.0282	0.0192	0.0105	0.0406
azulene	V_{m1}	-19.2	0.0206	0.0060	0.0031	0.0124
	V_{m2}	-11.1	0.0102	0.0027	0.0010	-0.0035
pentalene	V_{m1}	-18.9	0.0258	0.0116	0.0080	0.0279
	V_{m2}	-16.7	0.0194	0.0058	0.0036	0.0115
biphenylene	V_{m1}	-14.5	0.0141	0.0037	0.0009	0.0014

Table 2.5 MESP topology features (V_m in kcal/mol and eigenvalues in au) of all the molecules using M06/6-311+G(d,p) level of theory

Molecule	V_m label	V_m	λ_1	λ_2	λ_3	$\sum_{i=1}^{3} \Delta\lambda_i$
fulvalene	V_{m1}	-17.0	0.0236	0.0096	0.0077	0.0235
	V_{m2}	-11.9	0.0086	0.0016	0.0013	-0.0058
acenaphthylene	V_{m1}	-19.1	0.0243	0.0100	0.0076	0.0246
	V_{m2}	-16.2	0.0137	0.0024	0.0020	0.0007
	V_{m3}	-14.6	0.0157	0.0041	0.0032	0.0056
pyracylene	V_{m1}	-17.1	0.0230	0.0104	0.0077	0.0237
	V_{m2}	-15.9	0.0127	0.0034	0.0021	0.0008
	V_{m3}	-14.0	0.0119	0.0026	0.0005	-0.0023
indacene	V_{m1}	-16.6	0.0158	0.0037	0.0009	0.0030
	V_{m2}	-18.1	0.0227	0.0067	0.0053	0.0173
14-annulene	V_{m1}	-13.8	0.0169	0.0065	0.0047	0.0108
	V_{m2}	-13.6	0.0166	0.0076	0.0027	0.0096
	V_{m3}	-13.4	0.0175	0.0077	0.0034	0.0111
	V_{m4}	-13.3	0.0159	0.0058	0.0044	0.0088
	V_{m5}	-13.0	0.0162	0.0066	0.0049	0.0103
	V_{m6}	-11.7	0.0142	0.0081	0.0026	0.0076
	V_{m7}	-11.5	0.0139	0.0080	0.0033	0.0078
16-annulene	V_{m1}	-14.9	0.0201	0.0105	0.0074	0.0206
	V_{m2}	-14.6	0.0205	0.0110	0.0053	0.0194
	V_{m3}	-14.0	0.0187	0.0098	0.0043	0.0155
	V_{m4}	-12.6	0.0180	0.0100	0.0071	0.0178
18-annulene	V_{m1}	-12.7	0.0134	0.0053	0.0010	0.0024
	V_{m2}	-12.6	0.0140	0.0062	0.0005	0.0033
ethyne	V_{m1}	-19.6	0.0319	0.0246	0.0000	0.0391
buta-1,3-diyne	V_{m1}	-13.5	0.0204	0.0148	0.0000	0.0178

Table 2.6 MESP topology features (V_m in kcal/mol and eigenvalues in au) of all the molecules at B3LYP/6-311+G(d,p) level of theory (continues..)

Molecule	V_m label	V_m	λ_1	λ_2	λ_3	$\sum_{i=1}^{3} \Delta\lambda_i$
benzene	V_{m1}	-15.7	0.0142	0.0025	0.0005	0.0000
naphthalene	V_{m1}	-14.8	0.0152	0.0049	0.0032	0.0061
	V_{m2}	-12.7	0.0086	0.0004	0.0001	-0.0081
anthracene	V_{m1}	-14.6	0.0158	0.0059	0.0041	0.0086
	V_{m2}	-12.6	0.0104	0.0035	0.0000	-0.0033
phenanthrene	V_{m1}	-14.5	0.0142	0.0042	0.0022	0.0034
	V_{m2}	-14.5	0.0141	0.0040	0.0024	0.0033
	V_{m3}	-14.3	0.0159	0.0068	0.0052	0.0107
pyrene	V_{m1}	-14.0	0.0156	0.0068	0.0052	0.0104
	V_{m2}	-13.9	0.0133	0.0044	0.0006	0.0011
chrysene	V_{m1}	-14.3	0.0141	0.0042	0.0027	0.0038
	V_{m2}	-14.0	0.0147	0.0058	0.0047	0.0080
	V_{m3}	-12.5	0.0081	0.0018	0.0008	-0.0065
triphenylene	V_{m1}	-14.3	0.0135	0.0036	0.0019	0.0018
biphenyl	V_{m1}	-14.8	0.0141	0.0031	0.0006	0.0006
perylene	V_{m1}	-13.9	0.0140	0.0046	0.0028	0.0042
	V_{m2}	-13.3	0.0115	0.0040	0.0003	-0.0014
	V_{m3}	-12.1	0.0074	0.0005	0.0002	-0.0091
tetracene	V_{m1}	-14.4	0.0161	0.0065	0.0044	0.0098
	V_{m2}	-12.4	0.0106	0.0035	0.0015	-0.0016
benzanthracene	V_{m1}	-14.3	0.0153	0.0055	0.0038	0.0074
	V_{m2}	-14.3	0.0153	0.0055	0.0037	0.0073
	V_{m3}	-14.2	0.0138	0.0039	0.0018	0.0023
	V_{m4}	-14.1	0.0162	0.0076	0.0055	0.0121
	V_{m5}	-12.9	0.0103	0.0033	0.0017	-0.0019
	V_{m6}	-12.7	0.0104	0.0032	0.0012	-0.0024
coronene	V_{m1}	-13.4	0.0144	0.0050	0.0048	0.0070
	V_{m2}	-11.3	0.0074	0.0006	0.0003	-0.0089
pentacene	V_{m1}	-14.3	0.0162	0.0067	0.0045	0.0102
	V_{m2}	-12.3	0.0108	0.0037	0.0020	-0.0007
	V_{m3}	-11.8	0.0099	0.0036	0.0001	-0.0036

Table 2.6 MESP topology features (V_m in kcal/mol and eigenvalues in au) of all the molecules at B3LYP/6-311+G(d,p) level of theory (continues..)

Molecule	V_m label	V_m	λ_1	λ_2	λ_3	$\sum_{i=1}^{3} \Delta\lambda_i$
ethylene	V_{m1}	-18.6	0.0277	0.0176	0.0073	0.0354
buta-1,3-diene	V_{m1}	-16.8	0.0232	0.0135	0.0071	0.0266
hexa-1,3,5-triene	V_{m1}	-16.7	0.0231	0.0131	0.0070	0.0260
	V_{m2}	-14.4	0.0176	0.0092	0.0060	0.0156
octa-1,3,5,7-tetraene	V_{m1}	-16.7	0.0232	0.0129	0.0070	0.0259
	V_{m2}	-14.1	0.0173	0.0089	0.0056	0.0146
deca-1,3,5,7,9-pentaene	V_{m1}	-16.8	0.0232	0.0129	0.0069	0.0258
	V_{m2}	-14.1	0.0173	0.0087	0.0055	0.0143
	V_{m3}	-13.7	0.0170	0.0085	0.0052	0.0135
dodeca-1,3,5,7,9,11-hexaene	V_{m1}	-16.9	0.0233	0.0128	0.0069	0.0258
	V_{m2}	-14.1	0.0173	0.0087	0.0054	0.0142
	V_{m3}	-13.7	0.0169	0.0084	0.0050	0.0131
cyclobutadiene	V_{m1}	-18.4	0.0270	0.0182	0.0102	0.0382
azulene	V_{m1}	-18.9	0.0198	0.0059	0.0031	0.0116
	V_{m2}	-11.3	0.0103	0.0029	0.0009	-0.0031
pentalene	V_{m1}	-17.8	0.0230	0.0130	0.0074	0.0262
	V_{m2}	-15.0	0.0169	0.0057	0.0035	0.0089
biphenylene	V_{m1}	-15.1	0.0156	0.0038	0.0035	0.0057
fulvalene	V_{m1}	-16.1	0.0211	0.0110	0.0071	0.0220
	V_{m2}	-10.8	0.0073	0.0015	0.0012	-0.0072
acenaphthylene	V_{m1}	-17.6	0.0214	0.0111	0.0071	0.0224
	V_{m2}	-14.5	0.0112	0.0016	0.0012	-0.0032
	V_{m3}	-13.9	0.0139	0.0041	0.0029	0.0037
pyracylene	V_{m1}	-15.9	0.0204	0.0115	0.0072	0.0219
	V_{m2}	-14.4	0.0106	0.0022	0.0021	-0.0023
	V_{m3}	-13.2	0.0109	0.0023	0.0015	-0.0025
indacene	V_{m1}	-14.8	0.0132	0.0024	0.0008	-0.0008
	V_{m2}	-16.6	0.0194	0.0068	0.0048	0.0138
14-annulene	V_{m1}	-13.3	0.0146	0.0051	0.0018	0.0043
	V_{m2}	-12.1	0.0138	0.0056	0.0006	0.0027
	V_{m3}	-10.8	0.0119	0.0069	0.0002	0.0017

Table 2.6 MESP topology features (V_m in kcal/mol and eigenvalues in au) of all the molecules at B3LYP/6-311+G(d,p) level of theory

Molecule	V_m label	V_m	λ_1	λ_2	λ_3	$\sum_{i=1}^{3} \Delta\lambda_i$
16-annulene	V_{m1}	-14.7	0.0195	0.0102	0.0055	0.0180
	V_{m2}	-14.6	0.0191	0.0093	0.0072	0.0184
	V_{m3}	-13.9	0.0177	0.0093	0.0042	0.0139
	V_{m4}	-12.1	0.0169	0.0093	0.0062	0.0152
18-annulene	V_{m1}	-12.7	0.0134	0.0055	0.0011	0.0027
	V_{m2}	-12.6	0.0137	0.0064	0.0005	0.0034
ethyne	V_{m1}	-18.4	0.0290	0.0223	0.0000	0.0341
but-1,3-yne	V_{m1}	-12.1	0.0175	0.0126	0.0000	0.0129

Table 2.7 MESP topology features (V_m in kcal/mol and eigenvalues in au) of all the molecules at M06-2X/6-311+G(d,p) level of theory (continues….)

Molecule	V_m label	V_m	λ_1	λ_2	λ_3	$\sum_{i=1}^{3} \Delta\lambda_i$
benzene	V_{m1}	-17.5	0.0171	0.0034	0.0007	0.0000
naphthalene	V_{m1}	-17.0	0.0183	0.0051	0.0040	0.0062
	V_{m2}	-15.5	0.0115	0.0015	0.0004	-0.0079
anthracene	V_{m1}	-16.7	0.0191	0.0061	0.0050	0.0091
	V_{m2}	-15.2	0.0130	0.0038	0.0004	-0.0040
phenanthrene	V_{m1}	-16.7	0.0192	0.0069	0.0058	0.0107
	V_{m2}	-16.5	0.0169	0.0042	0.0027	0.0027
	V_{m3}	-16.5	0.0167	0.0041	0.0027	0.0023
pyrene	V_{m1}	-16.3	0.0189	0.0070	0.0059	0.0106
	V_{m2}	-15.9	0.0156	0.0043	0.0009	-0.0004
	V_{m3}	-14.7	0.0096	0.0011	0.0002	-0.0103
chrysene	V_{m1}	-16.2	0.0167	0.0043	0.0031	0.0030
	V_{m2}	-16.1	0.0169	0.0044	0.0030	0.0031
	V_{m3}	-15.6	0.0110	0.0027	0.0015	-0.0059
	V_{m4}	-15.2	0.0110	0.0017	0.0003	-0.0083
triphenylene	V_{m1}	-16.2	0.0158	0.0036	0.0020	0.0002
	V_{m2}	-15.8	0.0111	0.0022	0.0003	-0.0075
biphenyl	V_{m1}	-16.7	0.0166	0.0035	0.0006	-0.0005

Table 2.7 MESP topology features (V_m in kcal/mol and eigenvalues in au) of all the molecules at M06-2X/6-311+G(d,p) level of theory (continues....)

Molecule	V_m label	V_m	λ_1	λ_2	λ_3	$\sum_{i=1}^{3} \Delta\lambda_i$
perylene	V_{m1}	-15.9	0.0167	0.0046	0.0033	0.0035
	V_{m2}	-15.8	0.0140	0.0042	0.0024	-0.0005
	V_{m3}	-14.9	0.0097	0.0011	0.0006	-0.0098
tetracene	V_{m1}	-16.5	0.0195	0.0068	0.0054	0.0105
	V_{m2}	-15.0	0.0134	0.0040	0.0018	-0.0019
	V_{m3}	-14.2	0.0115	0.0015	0.0000	-0.0081
benzanthracene	V_{m1}	-16.5	0.0196	0.0077	0.0063	0.0124
	V_{m2}	-16.3	0.0185	0.0056	0.0046	0.0075
	V_{m3}	-16.3	0.0184	0.0056	0.0045	0.0073
	V_{m4}	-16.1	0.0164	0.0039	0.0022	0.0013
	V_{m5}	-15.6	0.0130	0.0038	0.0020	-0.0023
	V_{m6}	-15.3	0.0130	0.0036	0.0015	-0.0030
coronene	V_{m1}	-15.4	0.0171	0.0052	0.0049	0.0060
	V_{m2}	-13.9	0.0091	0.0016	0.0005	-0.0100
pentacene	V_{m1}	-16.4	0.0198	0.0071	0.0056	0.0113
	V_{m2}	-14.9	0.0138	0.0043	0.0024	-0.0006
	V_{m3}	-14.2	0.0121	0.0039	0.0004	-0.0048
ethylene	V_{m1}	-20.6	0.0320	0.0163	0.0085	0.0355
buta-1,3-diene	V_{m1}	-19.1	0.0277	0.0132	0.0084	0.0280
hexa-1,3,5-triene	V_{m1}	-18.9	0.0274	0.0128	0.0083	0.0274
	V_{m2}	-17.3	0.0223	0.0099	0.0076	0.0186
octa-1,3,5,7-tetraene	V_{m1}	-18.9	0.0274	0.0128	0.0083	0.0273
	V_{m2}	-17.0	0.0220	0.0096	0.0073	0.0177
deca-1,3,5,7,9-pentaene	V_{m1}	-18.9	0.0274	0.0127	0.0083	0.0272
	V_{m2}	-17.0	0.0219	0.0095	0.0072	0.0174
	V_{m3}	-16.7	0.0215	0.0094	0.0069	0.0166
dodeca-1,3,5,7,9,11-hexaene	V_{m1}	-18.9	0.0274	0.0127	0.0083	0.0272
	V_{m2}	-17.0	0.0219	0.0095	0.0071	0.0174
	V_{m3}	-16.6	0.0214	0.0093	0.0068	0.0164
cyclobutadiene	V_{m1}	-19.5	0.0295	0.0150	0.0104	0.0337

Table 2.7 MESP topology features (V_m in kcal/mol and eigenvalues in au) of all the molecules at M06-2X/6-311+G(d,p) level of theory

Molecule	V_m label	V_m	λ_1	λ_2	λ_3	$\sum_{i=1}^{3} \Delta\lambda_i$
azulene	V_{m1}	-22.8	0.0253	0.0071	0.0033	0.0145
	V_{m2}	-12.7	0.0121	0.0030	0.0011	-0.0049
pentalene	V_{m1}	-19.6	0.0264	0.0120	0.0082	0.0254
	V_{m2}	-17.9	0.0212	0.0069	0.0048	0.0117
biphenylene	V_{m1}	-16.9	0.0186	0.0046	0.0039	0.0059
	V_{m2}	-15.9	0.0152	0.0040	0.0018	-0.0001
fulvalene	V_{m1}	-18.0	0.0245	0.0102	0.0080	0.0216
	V_{m2}	-13.4	0.0105	0.0027	0.0021	-0.0059
acenaphthylene	V_{m1}	-17.6	0.0214	0.0111	0.0071	0.0185
	V_{m2}	-14.5	0.0112	0.0016	0.0012	-0.0072
	V_{m3}	-13.9	0.0139	0.0041	0.0029	-0.0002
pyracylene	V_{m1}	-17.8	0.0236	0.0107	0.0078	0.0209
	V_{m2}	-17.7	0.0141	0.0036	0.0024	-0.0010
	V_{m3}	-15.6	0.0135	0.0031	0.0009	-0.0037
indacene	V_{m1}	-16.7	0.0170	0.0033	0.0026	0.0018
	V_{m2}	-16.9	0.0183	0.0050	0.0036	0.0057
	V_{m3}	-19.7	0.0253	0.0094	0.0074	0.0209
14-annulene	V_{m1}	-16.7	0.0237	0.0128	0.0061	0.0213
	V_{m2}	-16.2	0.0219	0.0116	0.0062	0.0185
	V_{m3}	-16.0	0.0215	0.0120	0.0050	0.0172
	V_{m4}	-15.9	0.0215	0.0117	0.0070	0.0191
	V_{m5}	-13.7	0.0188	0.0108	0.0068	0.0152
	V_{m6}	-13.6	0.0191	0.0113	0.0053	0.0145
16-annulene	V_{m1}	-17.0	0.0236	0.0130	0.0088	0.0242
	V_{m2}	-16.7	0.0238	0.0133	0.0063	0.0222
	V_{m3}	-16.4	0.0225	0.0121	0.0054	0.0189
	V_{m4}	-14.1	0.0223	0.0121	0.0090	0.0223
18-annulene	V_{m1}	-14.5	0.0152	0.0061	0.0013	0.0014
	V_{m2}	-14.4	0.0157	0.0072	0.0006	0.0023
ethyne	V_{m1}	-19.6	0.0319	0.0246	0.0000	0.0353
buta-1,3-diyne	V_{m1}	-13.5	0.0204	0.0148	0.0000	0.0140

Table 2.8 MESP topology features (V_m in kcal/mol and eigenvalues in au) of selected molecules at MP2/6-311+G(d,p) level of theory

Molecule	V_m label	V_m	λ_1	λ_2	λ_3	$\sum_{i=1}^{3}\Delta\lambda_i$
benzene	V_{m1}	-19.1	0.0173	0.0033	0.0007	0.0000
naphthalene	V_{m1}	-18.4	0.0193	0.0070	0.0050	0.0101
	V_{m2}	-16.1	0.0115	0.0011	0.0010	-0.0077
anthracene	V_{m1}	-14.6	0.0150	0.0052	0.0038	0.0027
	V_{m2}	-13.1	0.0103	0.0033	0.0001	-0.0075
phenanthrene	V_{m1}	-18.0	0.0207	0.0111	0.0072	0.0178
	V_{m2}	-18.0	0.0178	0.0053	0.0036	0.0054
	V_{m3}	-18.1	0.0176	0.0051	0.0038	0.0052
ethylene	V_{m1}	-18.5	0.0275	0.0174	0.0072	0.0309
butadiene	V_{m1}	-20.7	0.0293	0.0195	0.0096	0.0372
cyclobutadiene	V_{m1}	-23.1	0.0335	0.0250	0.0132	0.0505
azulene	V_{m1}	-24.6	0.0257	0.0081	0.0046	0.0172
	V_{m2}	-13.2	0.0128	0.0038	0.0020	-0.0026
pentalene	V_{m1}	-22.0	0.0288	0.0191	0.0100	0.0366
	V_{m2}	-20.1	0.0244	0.0117	0.0067	0.0215

2.4.5 (3, +1) Critical Points
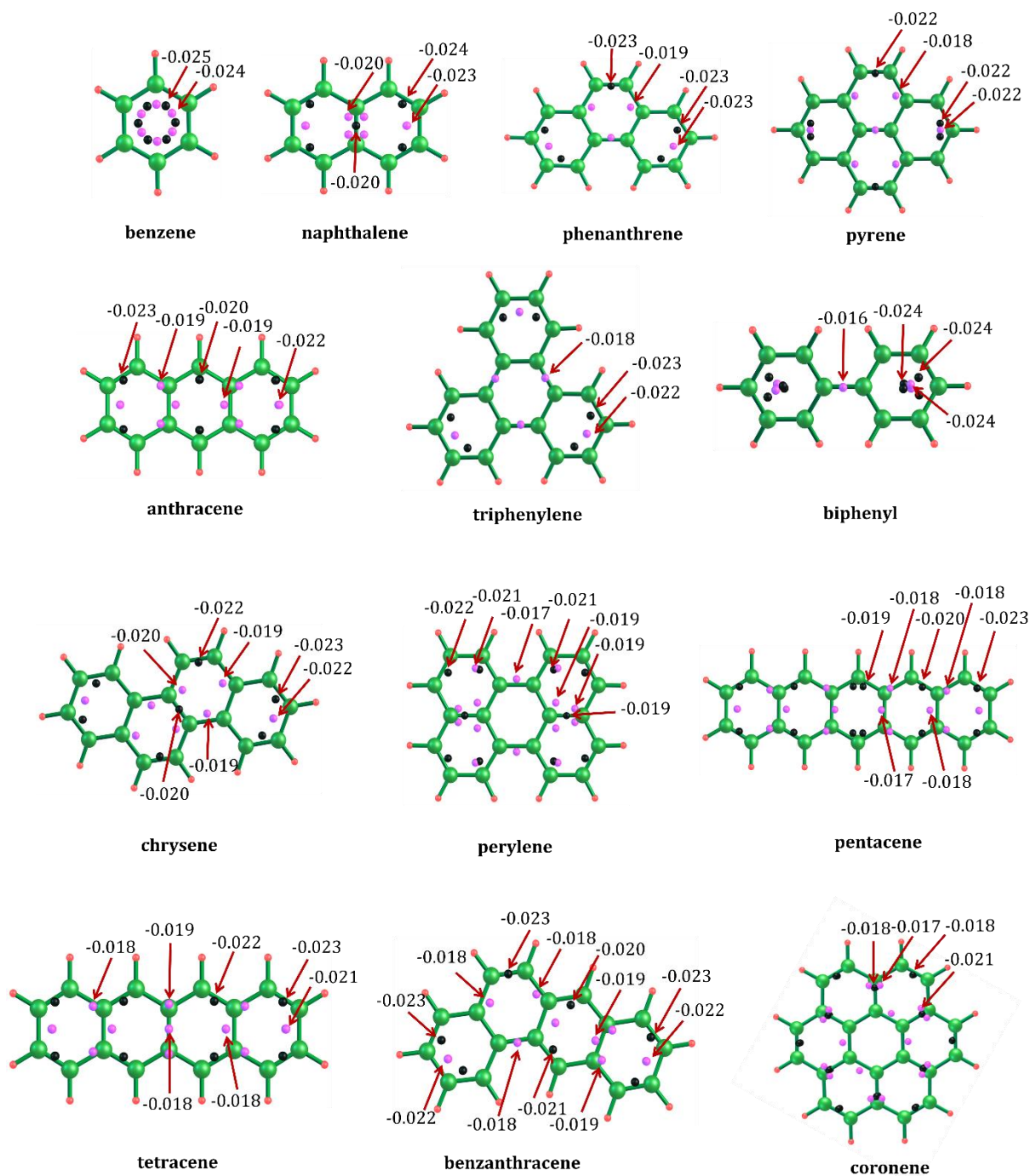
Figure 2.9 Topology of (3, +1) CPs in selected set of systems (values in kcal/mol)
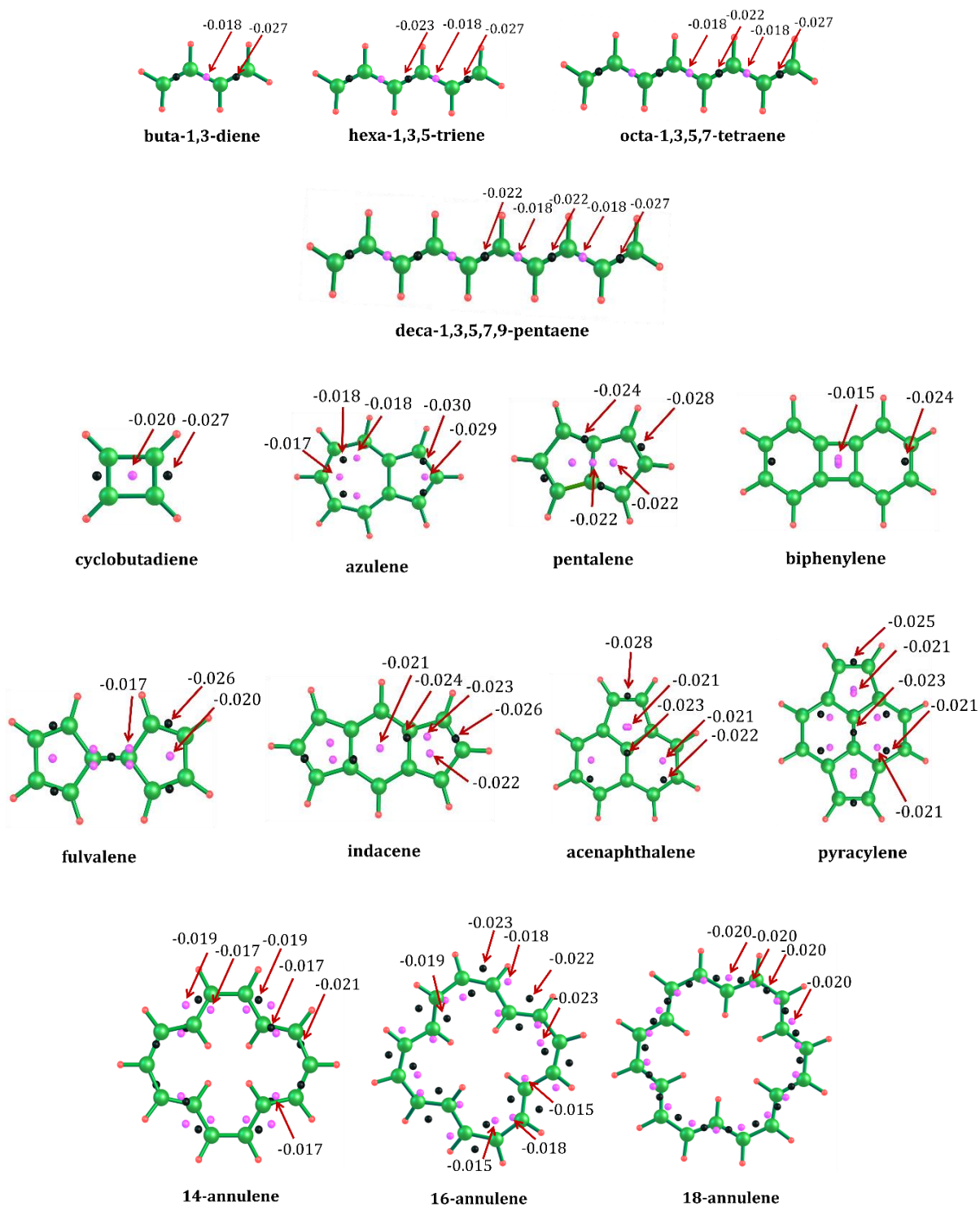
Figure 2.9 Topology of (3, +1) CPs in selected set of systems (values in kcal/mol)

So far the π-conjugation features have been addressed on the basis of the value of MESP minimum V_m and the respective eigenvalues. The V_m value gives information about the electron rich character of the molecular system at various locations while the eigenvalues provide a way to assess the localized/delocalized nature of the π-conjugation. In MESP topology, several (3, +1) CPs can be located in the π-region which normally appear in between two (3, +3) CPs. Some representative cases are shown in Figure 2.9. From the location of such (3, +1) CPs (saddle points), the function value increases in one direction and decreases in the other two directions of space. In aromatic systems such as benzene, naphthalene, phenanthrene and coronene, the MESP value of a (3, +1) CP is very close to that of the adjacent (3, +3) CP indicating a smooth, nearly uniform distribution of MESP over the ring. If two adjacent (3, +3) and (3, +1) CPs show more deviation in the values, it may indicate the decreasing delocalization effect as well as lower aromaticity at that region compared to other parts. For instance, in phenanthrene, the middle ring is less delocalized than the other two rings. Similarly, in 18-annulene, almost an even distribution of π-electron density is observed, while 16-annulene shows more localized distribution. Moreover, analysis of both types of CPs of azulene clearly indicates that seven membered ring has a uniform distribution of MESP. Though its five-membered ring features a similar data, the high magnitude of the CPs and $\sum_{i=1}^{3} \Delta\lambda_i$ of (3, +3) CP indicate the localized nature of the π-electron density. In olefins, a clear distinction between (3, +3) and (3, +1) CPs is possible on the basis of their MESP values. The significantly less negative (3, +1) CPs appear over the formally single-bonded region of the molecules (*cf.* Figure 2.9). A remarkable difference in (3, +3) and (3, +1) CP values is observed for the antiaromatic cyclobutadiene molecule indicating more localized nature of electron density, where (3, +1) CPs are located in the interior and (3, +3) CPs lie somewhat exterior to the ring.

2.5 Conclusions

MESP topology analysis has been carried out on a large variety of π-conjugated hydrocarbons using B3LYP/6-311+G(d,p) level theory. The negative regions observed in the MESP distribution correlate well with the delocalized/localized distribution of the π-

electrons in aromatic, antiaromatic, nonaromatic, annulenes and hybrid systems. In the case of PBH, MESP CPs are located interior to the six-membered rings whereas they lie exactly on top/bottom of the π-regions in linear polyenes. In strained systems, CPs lie outside the boundary of the ring. The eigenvalues follow the trend $\lambda_1 >> \lambda_2 > \lambda_3 \cong 0$ in PBH; $\lambda_1 > \lambda_2 > \lambda_3 \cong 0$ in linear polyenes (nonaromatic) and $\lambda_1 > \lambda_2 > \lambda_3 \neq 0$ in antiaromatic systems. Benzene is considered as a perfect aromatic system and the imperfection in the aromatic character of a PBH system is measured in terms of the deviations $\Delta\lambda_1$, $\Delta\lambda_2$ and $\Delta\lambda_3$ with respect to the corresponding eigenvalues of the benzene molecule. The eigenvalue analysis clearly shows that the total deviation $\sum_{i=1}^{3} \Delta\lambda_i$ very close to zero is an indicative of strong aromatic character of that region. PBH systems showed $\sum_{i=1}^{3} \Delta\lambda_i \leq$ 0.011 for most of the rings while cases such as phenanthrene, pyrene, benzanthracene and pentacene showed $\sum_{i=1}^{3} \Delta\lambda_i \geq 0.011$ au for rings containing localized CC bonds. Further, a clear distinction of the delocalized and localized regions of a PBH led to the identification of the most prominent Clar's aromatic sextet structures. The $\sum_{i=1}^{3} \Delta\lambda_i$ of all the alkenes and alkynes examined in the present work falls in the range 0.011 to 0.035 au, whereas antiaromatic systems such as cyclobutadiene showed $\sum_{i=1}^{3} \Delta\lambda_i \geq 0.035$ au. Since each molecule possesses unique distribution of π-electrons, the MESP eigenvalue based analysis of aromaticity is extended to study non-PBH systems consisting of strained CC bonds such as azulene, pentalene *etc*. The ring strain plays an important role in the distribution of CPs along the π-regions. They occupy positions outside the projected ring periphery. Most of these non-PBH systems show a hybrid character of aromaticity and nonaromaticity. For instance, in azulene, the seven-membered ring shows clearly aromatic character whereas the five membered ring is nonaromatic in nature. Likewise, a blend of aromatic and nonaromatic behavior is seen in some other hybrid systems. In the case of 14- and 18-annulenes, the eigenvalues and $\sum_{i=1}^{3} \Delta\lambda_i$ parameter are close to that of PBHs, indicating closeness of aromatic character of the system to that of benzene. However, in 16-annulene the eigenvalue sum parameter strongly supports its nonaromatic behavior. The dependence of $\sum_{i=1}^{3} \Delta\lambda_i$ parameter with aromatic character of molecules is illustrated schematically in Figure 2.10. Also the π-conjugation features of

the molecular systems have been related with the (3, +1) CP distribution. The localized nature of π-electron distribution is revealed when two adjacent (3, +3) and (3, +1) CPs show greater deviation in their MESP values whereas for aromatic systems, the MESP values of (3, +3) and (3, +1) CPs are more uniform.
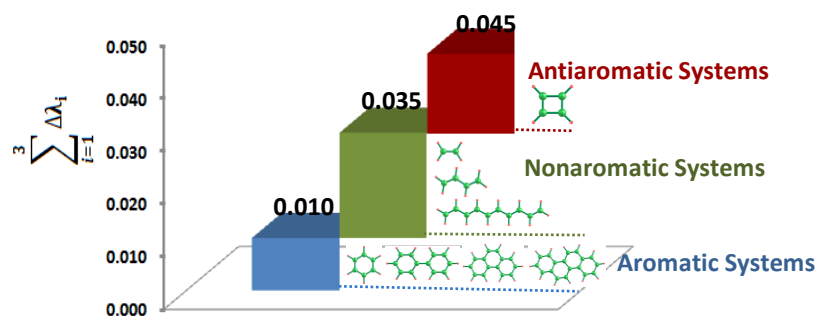
Figure 2.10 The variation of $\sum_{i=1}^{3} \Delta\lambda_i$ with aromaticity

Aromaticity is a multi-dimensional phenomenon, for which different explanations have been developed in terms of structural, magnetic, energetic, and electronic criteria due to various landmark studies. The electrostatic topological viewpoint of aromaticity elaborated in this work adds a new dimension to aromaticity. This viewpoint focusing on position and value of MESP minima, as well as the corresponding eigenvalues, is very simple and effective way to make a quick and general, in-depth assessment of localized or delocalized distribution of π-electrons in cyclic, acyclic and strained-cyclic unsaturated hydrocarbon systems.

Part B

Antiaromaticity–Aromaticity Interplay in Fused Benzenoid Systems using Molecular Electrostatic Potential Topology

2.6 Abstract

The phenomenon of antiaromaticity-aromaticity interplay in aromatic-antiaromatic (A-aA) fused systems is studied using MESP analysis, which clearly brings out the electron rich π-regions of molecular systems. Benzene, naphthalene, phenanthrene and pyrene are the aromatic units and cyclobutadiene and pentalene are the antiaromatic units considered to construct the A-aA fused systems. The fused system is seen to reduce the antiaromaticity by adopting a configuration containing least number of localized bonds over antiaromatic moieties. This is clearly observed in twenty-five isomers of fused system composed of three naphthalene and two cyclobutadiene units. Denoting the number of π-bonds in the cyclobutadiene rings by the notation (n, n′), the systems belonging to the class (0, 0) and (2, 2) turn out to be the most and least stable configurations respectively. The stability of the fused system depends on the empty π-character of antiaromatic ring, hence naphthalene and benzene prefer to fuse with cyclobutadiene in linear and angular fashion respectively. Generally, a configuration with maximum number of 'empty' rings (0, 0, 0, ...) is considered to be the most stable for the given A-aA system. The stability and aromatic/antiaromatic character of A-aA fused systems with pentalene is also interpreted in a similar way. MESP topology, clearly bringing out the distribution of double bonds in the fused systems, leads to a simple interpretation of the aromatic/antiaromatic character of them. Also it leads to powerful predictions on stable macrocyclic A-aA systems.

2.7 Introduction

Polycyclic aromatic-antiaromatic fused systems are emerging as novel molecules for applications in organic electronic devices due to their unique electronic and self-assembling properties.[79, 80] The incorporation of an antiaromatic moiety in PBHs brings about a change in the chemical and physical properties such as reactivity, conductivity, *etc*. It also results in a significant reduction in the aromatic character of benzenoid rings along with the dilution of the antiaromatic character of cyclobutadiene.[81] Antiaromatic systems exhibit a strong π-bond localization, while the aromatic systems favor dominant π-bond delocalization suggesting that aromatic-antiaromatic (A-aA) fusion leads to the dilution of both the properties. The fusion of an antiaromatic ring with an aromatic ring leads to a significant change in the bond order and C-C bond alternation within the molecule. Such a property provides useful hints for the design and synthesis of novel molecular frameworks.[82] Many fused systems have been synthesized by connecting benzenoid hydrocarbons with antiaromatic cyclobutadiene,[83-87] pentalene,[88-94] indacene[95-97], *etc*. These systems have been successfully applied for the design of various organo-electronic devices.[98-103] Cyclobutadiene, one of the classic antiaromatic organic molecules, has been used in the fused systems for modulating properties such as molecular conductivity, crystallization, segregation, and thin-film formation, *etc*.[104-108] The fused systems are also found to be appropriate for the development of semiconductor materials. Also, A-aA fusion is considered as a useful design strategy for the development of supramolecular structures. In general, the introduction of antiaromatic unit/s to polyacenes brings in a significant increase in conduction properties and is found suitable for the design of organic-photovoltaics.[109] The reactivity and the electronic properties of such systems are intimately connected to the unique molecular topology arising from the fusion patterns in the A-aA moieties. Hence, it is necessary to have a detailed investigation about the change in configuration, bond alternation and π-conjugation of fused systems over the isolated ones. The dilution in antiaromaticity in such fused systems could be brought in by adopting a stable configuration that avoids double bond localization within the antiaromatic rings. Theoretical studies[110, 111] on A-aA fused systems were mainly

focused on the energetic aspects of the π-conjugation,[112-115] ring current features,[116-118] and magnetic properties[119, 120] such as nuclear independent chemical shift (NICS). In these studies, the computed molecular descriptors were related to the local aromaticity, *i.e.*, the aromaticity expressed within a ring.[121-123]

The present study deals with the MESP topology-based characterization of the π-bond localization/delocalization features of a variety of A-aA systems. The MESP topology analysis is an important theoretical tool for characterizing the electron-rich π-regions of molecules. The topological analysis would also locate the MESP minimum (V_m) as a (3, +3) CP. Typically V_m points appear along the π-localized and lone-pair regions,[48, 52, 124] whereas the electron-deficient regions exhibit a positive potential. Previous studies on PBHs were useful for finding relationships between MESP topology and π-electron delocalization.[125] A simple and elegant interpretation of Clar's aromatic sextet theory was derived using the critical features of MESP. Clar's theory[63] described the aromaticity of a PBHs based on the maximum number of sextets (a sextet is defined as six π-electrons represented by a circle) drawn for a system. For the present study, the selected aromatic moieties are benzene, naphthalene, phenanthrene and pyrene; the selected antiaromatic moieties being cyclobutadiene and pentalene. The fusion between aromatic and antiaromatic moieties can be achieved in a linear or angular fashion. The notations BC, NC, PyC, PhC, BP and NP are used for representing the fused benzene-cyclobutadiene, naphthalene-cyclobutadiene, phenanthrene-cyclobutadiene, pyrene-cyclobutadiene, benzene-pentalene and naphthalene-pentalene systems, respectively. Among many possible resonance forms, a unique bond alternation pattern emerges for each A-aA system. The present study deals with identifying such a configuration using the MESP topology analysis.

2.8 Methodology

The selected systems are optimized at the B3LYP/6-311+G(d,p) level of density functional theory using Gaussian 09 program package.[58] The optimized structures were confirmed as energy minima by vibrational frequency analysis. The wave function

constructed using B3LYP in conjunction with the valence triple-zeta level basis set and augmented with polarization and diffuse functions (6-311+G(d, p)) is expected to give a sufficiently accurate description of the electron density, $\rho(\mathbf{r'})$, and the corresponding MESP.[51] The values of MESP, its gradients and second derivatives at the CPs are calculated after identifying the CPs using DAM partition-expansion method.[59, 61]

2.9 Results and Discussion

2.9.1 MESP Analysis of Benzenoid Systems, Cyclobutadiene and Pentalene

Figure 2.11 depicts the (3, +3) MESP minima (V_m) along with a suitable MESP isosurface observed for -12.5 kcal/mol. In benzene, a set of six symmetrically equivalent CPs can be located above and below the molecular plane in a uniform circular manner (only one side is illustrated in the Figure 2.11a). This suggests a perfect delocalization of the electron density in the system. Hence, a perfect aromatic sextet can be drawn for benzene, which can be regarded as representing a resonance hybrid of two Kekulé structures. The CC bond length in benzene is 1.39 Å, and V_m value is -15.7 kcal/mol. The benzenoid aromatic systems are likely to show a V_m value close to that of benzene due to sextet-type delocalization of π-electron within six-membered rings. Naphthalene consists of five CPs on each side of the molecular plane, only two out of which are symmetrically unequal (V_m1 and V_m2). This topology indicates an imperfection in the delocalization of electron density vis-à-vis that of benzene. The CC bond characterized by the location of V_m1 is more localized than other CC bonds, represented as double bonds with red color. The MESP topology immediately suggests the chemical formula given in Figure 2.11b as the most likely one for naphthalene. In contrast, the alternate, crossed-out structure shown below could be the least preferred one. Phenanthrene shows five (3, +3) CPs on each side of the molecular plane, three among them being symmetrically unequal ones. These are represented as V_m1, $V_\text{m2,}$ and V_m3. The location of the V_m positions suggests the chemical formula given in Figure 2.11c. It may be noted that among the seven double bonds required to represent the phenanthrene formula, two of them shown in blue color

104
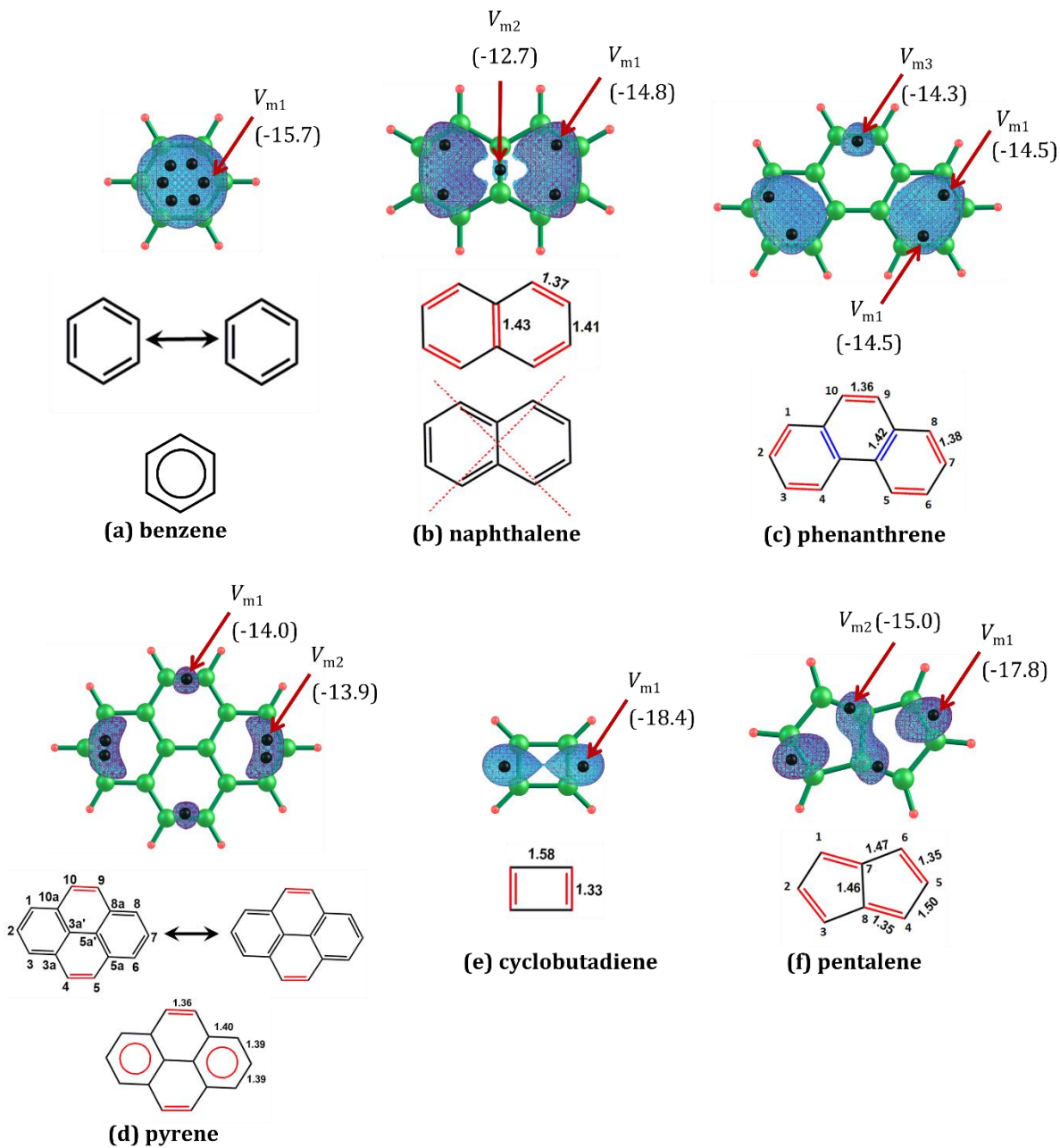
Figure 2.11 MESP topology patterns of benzene, naphthalene, phenanthrene, pyrene, cyclobutadiene and pentalene systems. The V_m positions associated with double bonds are given in red and remaining double bonded regions are given in blue color. V_m values are given in kcal/mol and bond length in Å

cannot be associated with a V_m position. However, a unique formula can be readily proposed as 'red' double bonds automatically fix the 'blue' ones. Pyrene system consists of a set of six (3, +3) CPs (on each side) in which two (*viz.* V_{m1} and V_{m2}) are unequal ones. V_{m1} is located directly on top of C4-C5 and C9-C10 bonds, whereas a pair of close lying V_{m2} appears close to C2 and C7 regions. Positions of V_{m2} suggest that C1-C2 and C2-C3 bonds are equivalent and similarly are C6-C7 and C7-C8 bonds. Therefore, the two Kekulé resonance forms used for pyrene to assign the Clar's sextet type delocalized structure as shown in Figure 2.11d. In cyclobutadiene, the two π-bonds are strongly localized with distance 1.33 Å and MESP topology detects this feature with V_m having value -18.4 kcal/mol at the top, midpoint region of the bonds. In pentalene, two types of CPs, *viz.* V_{m1} and V_{m2} are observed, having values -17.8 and -15.0 kcal/mol, respectively. The most negative V_{m1} shows localized electron density along the π-region, between C2-C3 and C5-C6 whereas V_{m2} indicates double bond nature for C1-C7 and C4-C8. In this system, lengths of both the double bonds corresponding to V_{m1} and V_{m2} are identical, *viz.* 1.35 Å. However, the V_m values suggest that the nature of localization is different in both regions. The V_{m1} value is close to that of cyclobutadiene, suggesting the antiaromatic character whereas V_{m2} values are close to that of benzene. The MESP isosurface corresponding to V_{m2} regions is indicative of a trans-1,3-butadiene-like conjugation along the middle region of pentalene. The MESP analysis suggests that pentalene is neither fully aromatic nor antiaromatic. However, the strong π-bond localization of C2-C3 and C5-C6 bonds indicates a high reactivity towards addition reaction to suggest a predominantly antiaromatic nature of it. The chemical formula given in Figure 2.11f, based on the MESP CPs, is recommended for pentalene.

2.9.2 Benzene–Cyclobutadiene Fused Systems

Figure 2.12 depicts the MESP topology of benzene-cyclobutadiene fused systems[126] (BC1 - BC4) and the corresponding representation of their chemical formula. In BC1, the benzene portion shows only one (3, +3) CP over each π-face (V_{m1} over the C3-C4 bond), suggesting that the ring fusion with the four-membered ring leads to a

substantial change in the MESP topology of benzene. The V_{m2} defines a double bond (C7-C8) for the four-membered ring. Although the C7-C8 bond is shorter than C3-C4, the latter has significantly more negative character (-19.1 kcal/mol) than the former (-10.7 kcal/mol) indicating that the fusion leads to charge transfer from four-membered to six-
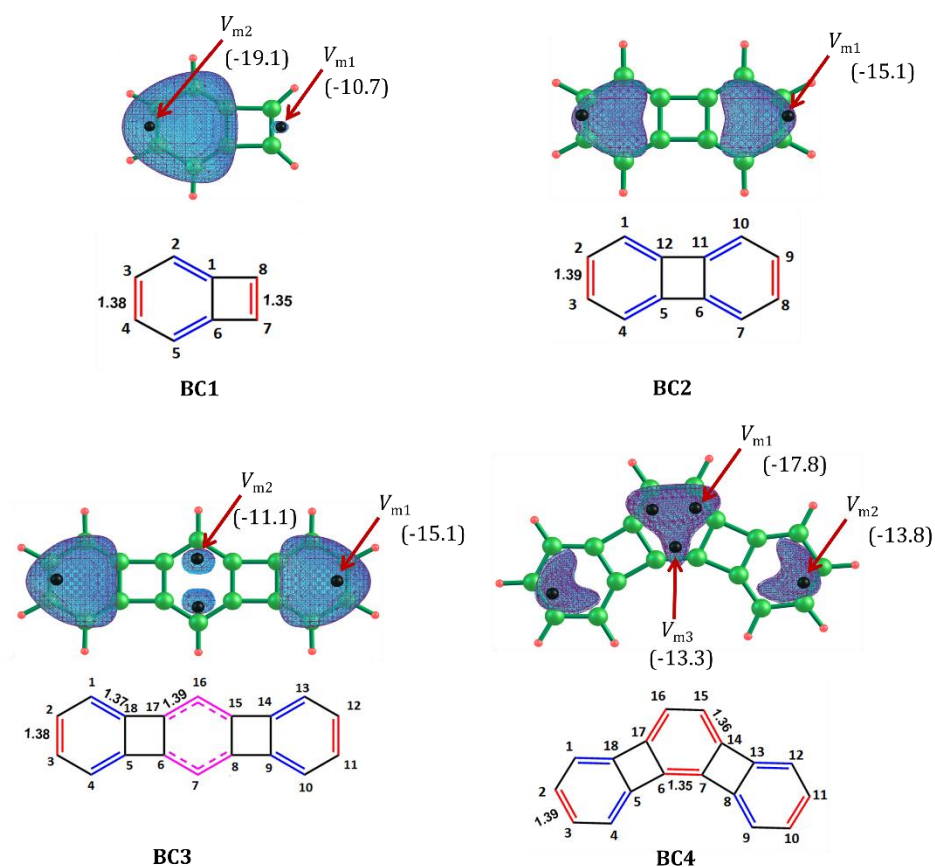
Figure 2.12 MESP CPs and isosurface patterns of benzene-cyclobutadiene fused systems. The V_m position associated double bonds are given in red and remaining double bonded regions are given in blue color. V_m values are given in kcal/mol and bond length in Å

membered ring. The electron rich C3-C4 bond suggests a reduction in the aromatic character as well as high reactivity for the system. Also, the V_m value of cyclobutadiene portion is increased 7.7 kcal/mol compared to cyclobutadiene suggesting a reduction in the localization of electron density over π-regions indicating dilution of its antiaromatic character. When a cyclobutadiene is inserted between two benzene rings (BC2), the CPs corresponding to the π-regions of the benzene rings show V_m value (-15.1 kcal/mol) very

similar to that of benzene suggesting more aromatic character than BC1. Two cyclobutadiene moieties could be connected to three benzene rings in a linear fashion (BC3) or they could be connected in an angular fashion (BC4). In BC3, most localized π-regions are observed at the end benzenoid rings with V_m value -15.1 kcal/mol indicating a benzene-type delocalization in the ring whereas a set of CP is appeared in the middle ring over the C7 and C16 atoms indicating that C6-C7 and C7-C8 bonds (1.39 Å) as well as C15-C16 and C16-C17 bonds are identical. The MESP isosurface images over these regions support the delocalization of the π-electrons over C6-C7-C8 and C15-C16-C17 bonds and the V_{m2} at this regions is -11.1 kcal/mol. To give a representation for such a delocalization, the pink-colored dotted line is used to draw the chemical formula for BC3 (Figure 2.12). In BC4, the middle benzene ring contains three CPs, out of which two are unequal ones (V_{m1} and V_{m2}) and distribution of CPs indicates the presence of three π-bonds in the ring. Each end ring consists of only one V_m, with an MESP value of -13.8 kcal/mol, representing the most localized π-bond in the corresponding ring. Based on this, the other π-regions can be defined (given in blue color, Figure 2.12). In BC3, the middle benzene ring has more electron-rich character than the terminal ones, whereas the cyclobutadiene rings are conspicuous by the absence of double bond localization. In BC4, the π-electron density over cyclobutadiene is shared with the neighboring six-membered rings and every six-membered ring may be represented as an aromatic one with 6π-electrons in it. This makes the isomer BC4 2.7 kcal/mol more stable than BC3. For all the cases, the distribution of CPs gives a clear view of the most appropriate single and double bond patterns. A chemical formula can be easily derived for all. No π-localization is observed in the cyclobutadiene rings, which act as empty rings between benzenoid rings. The 6π-electron delocalization within a benzene ring is seen in all the cases by avoiding π-localization within four-membered rings. In other words, the antiaromatic character of the four-membered rings is minimized by promoting the aromatic nature of the benzene rings. There are reports on the synthesis as well as for the crystallographic studies on the system BC3[127, 128] and BC4.[129, 130]

2.9.3 Benzene–Pentalene Fused Systems

Figure 2.13 represents MESP topology of benzene-pentalene (BP) fused systems (BP1 - BP3).[131] In BP1, there are a set of five unequal CPs appearing on each side of the molecular plane. Among the rings, the benzene moiety contains two unequal V_m points, V_{m3} and V_{m4} with values -15.3 and -14.8 kcal/mol, respectively indicating the π-electron delocalization in the ring to be similar to that for benzene. The V_m value of the middle five-membered ring is higher (-12.4 kcal/mol) than the other suggesting a decrease in the extent of π-electron delocalization over that ring, whereas the most localized π-region appears over the terminal five membered ring with V_m value of -17.6 kcal/mol, very close to that of the isolated pentalene suggesting antiaromatic character for that ring.
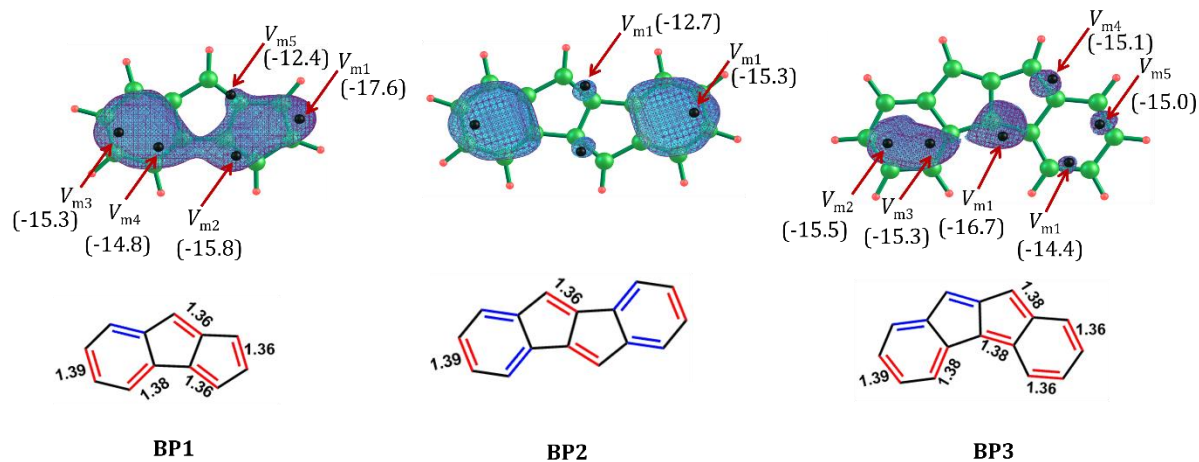
Figure 2.13 MESP topology patterns of benzene-pentalene fused systems. The V_m position associated double bonds are given in red and remaining double bonded regions are given in blue color. V_m values are given in kcal/mol and bond length in Å

In BP2,[90] aromatic character dominates due to the delocalization of the π-electrons within the benzene ring, while the pentalene portion shows only two localized double bonds with high V_m value -12.7 kcal/mol. BP3, an isomer of BP2 is less stable than the latter by 21.6 kcal/mol and also suggests that its aromatic stabilization is lower than that of BP2. The MESP feature shows the most negative V_m, -16.7 kcal/mol on the pentalene portion. Also the chemical formula of BP3 as per the MESP topology suggests only two localized π-bonds within one of the six membered rings indicating decrease in aromatic character.

This accounts for the instability due antiaromaticity of BP3 compared to BP2. Konishi *et al.* has demonstrated experimentally that BP3 type fusion shows enhanced antiaromatic character compared to BP2 type ring fusion.[132, 133] Stojanovic *et al.* has examined effect of two types of dibenzo-fusion of pentalene computationally, which well correlate with our topology analysis.[134, 135]

2.9.4 Naphthalene–Cyclobutadiene Fused Systems
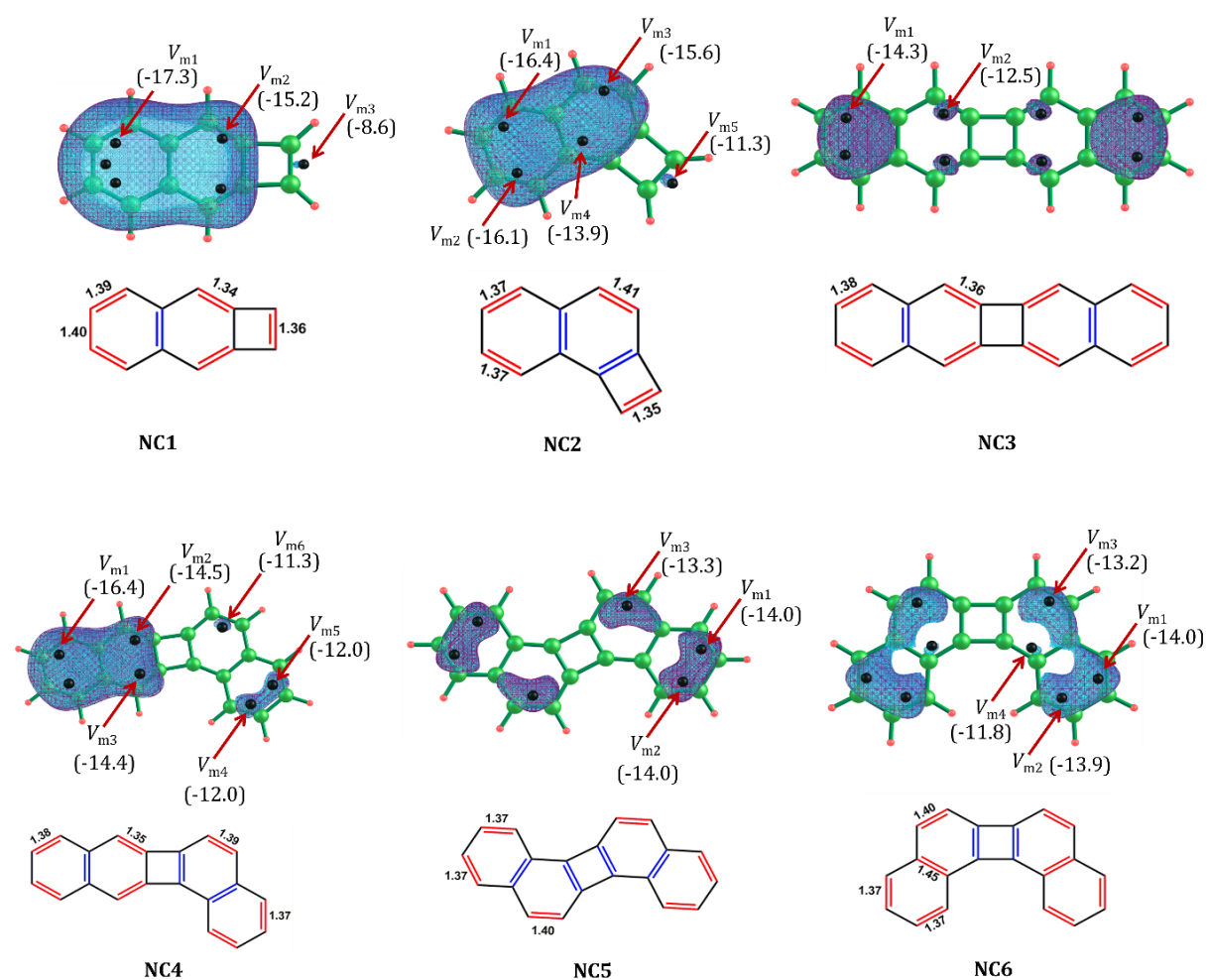
Figure 2.14 MESP topology patterns of naphthalene-cyclobutadiene fused systems. V_m values are in kcal/mol and bond length in Å

Two configurations are possible for the fusion of one naphthalene unit with cyclobutadiene, NC1 and NC2 (*cf.* Figure 2.14), with NC1 being more stable than NC2 by 12.0 kcal/mol. The MESP topology suggests that the fusion enhances the electron rich character of the naphthalene portion at the expense of the electron density from the cyclobutadiene portion. The four-membered ring is identified with the highest valued V_m point and the corresponding CC bond is the shortest. Though the naphthalene like π-electron distribution is dominating in both the cases, the π-bond distribution as per MESP topology suggests localization in the two double bonds of the four-membered ring of NC2 and only one for NC1. The tendency to hold 4π electrons in four membered ring support higher antiaromatic character for NC2 than NC1 which correlates to their relative stability. The V_m value observed over the four-membered ring showed significant increase compared to the V_m of cyclobutadiene (-18.4 kcal/mol). This suggests a dilution in antiaromatic character in both NC1 and NC2.

Two naphthalene rings fused to one cyclobutadiene give rise to four configurations, NC3- NC6 (*cf.* Figure 2.14). In all the isomers, the MESP features, in particular the (3, +3) CPs, appear prominently over the naphthalene moieties, while the four-membered ring is 'empty' with respect to the MESP minima. This indicates the tendency of the π-electrons to get delocalized over the naphthalene moieties. The MESP-based chemical formula suggests 0, 1, 2, and 2 double bonds for the four membered rings of NC3, NC4, NC5 and NC6, respectively indicating that antiaromatic character of cyclobutadiene is the minimum expressed in NC3, partially expressed in NC4 and strongly expressed in NC5 and NC6. NC4 is 4.0 kcal/mol higher in energy than NC3, while NC5 and NC6 are further up in the energy ladder by 12.3 and 12.8 kcal/mol which can be accounted to their higher antiaromatic character than others. Our suggested chemical formula for NC3 is in good agreement with the report by Kawai *et al.*, where they have studied the existence and stability of the radialene structure of NC3 isomer over its cyclobutadiene structure by high resolution atomic force microscopy.[136]

2.9.5 Three Naphthalene Moieties Fused with Two Cyclobutadienes
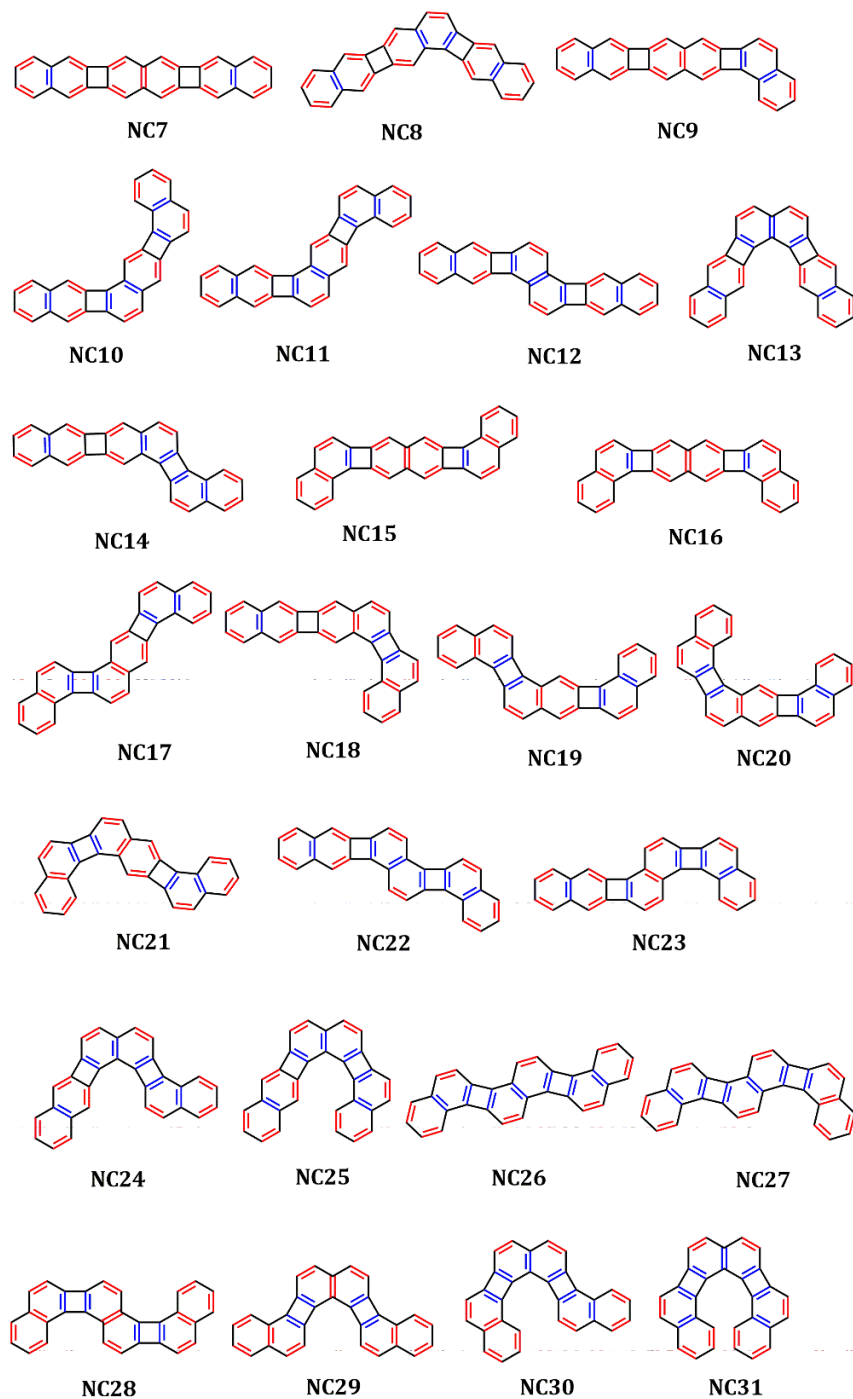
Figure 2.15 MESP CPs and isosurface-based chemical formulae for A-aA system of three naphthalene units fused with two cyclobutadiene moieties. The convention of 'blue' and 'red' double bonds as in the earlier figures

Table 2.9 The relative energies and number of double bonds (n, n') in cyclobutadiene rings in three naphthalene-two cyclobutadiene ring systems at B3LYP/6-311+G(d,p) level of theory

Fused Systems	(n, n')	Relative Energy (kcal/mol)	HOMO (eV)	LUMO (eV)	HOMO- LUMO Gap (eV)
NC7	(0, 0)	0.00	-5.55	-2.21	3.34
NC8	(0, 1)	2.37	-5.50	-2.30	3.21
NC9	(0, 1)	4.74	-5.28	-2.20	3.08
NC10	(1, 1)	5.86	-5.45	-2.23	3.22
NC11	(1, 1)	5.90	-5.43	-2.22	3.21
NC12	(1, 1)	6.84	-5.30	-2.42	2.88
NC13	(1, 1)	7.82	-5.32	-2.41	2.91
NC14	(0, 2)	9.87	-5.14	-2.39	2.75
NC15	(1, 1)	9.95	-5.04	-2.27	2.77
NC16	(1, 1)	10.01	-5.04	-2.26	2.78
NC17	(1, 2)	10.49	-5.14	-2.41	2.73
NC18	(1, 2)	12.94	-5.11	-2.18	2.93
NC19	(1, 2)	12.95	-5.10	-2.24	2.87
NC20	(1, 2)	13.53	-5.12	-2.20	2.92
NC21	(1, 2)	13.55	-5.11	-2.22	2.89
NC22	(1, 2)	15.04	-5.02	-2.53	2.49
NC23	(1, 2)	15.66	-5.03	-2.56	2.47
NC24	(1, 2)	16.04	-5.05	-2.53	2.52
NC25	(1, 2)	18.99	-5.04	-2.55	2.49
NC26	(2, 2)	23.73	-4.79	-2.59	2.20
NC27	(2, 2)	24.24	-4.79	-2.60	2.19
NC28	(2, 2)	24.91	-4.79	-2.61	2.18
NC29	(2, 2)	24.96	-4.83	-2.57	2.26
NC30	(2, 2)	29.38	-4.84	-2.59	2.25
NC31	(2, 2)	30.99	-4.81	-2.61	2.19

By fusing three naphthalene moieties with two cyclobutadienes, a total of twenty-five isomers, *viz*. NC7 - NC31 (*cf.* Figure 2.15). Here the structures showing fusion of two four-membered rings on one six-membered ring is not considered. The MESP based chemical

113

formula of all of them are presented in Figure 2.15. The MESP always exhibits minima over the naphthalene rings while the four membered rings appeared 'empty'. This indicates the presence of dominating naphthalene character over the cyclobutadiene character as well as dilution of antiaromaticity. For each chemical formula, the number of double bonds in four-membered rings is given in Table 2.9 as an ordered pair (n, n'); n for the left ring and the n' for the right ring. The relative energy of each isomer is also depicted in Table 2.9. On the basis of (n, n')-description, six categories of isomers can be defined, *viz.* (0, 0), (0, 1), (1, 1), (0, 2), (1, 2) and (2, 2). The linear one, *viz.* NC7, of the (0, 0) category is the most stable among all due to the least amount of π-character in the four- membered rings which suggests maximum dilution of antiaromaticity. The (0, 1)-category systems, NC8 and NC9 turn out to be less stable than NC7 by 2.37 and 4.74 kcal/mol, respectively indicating small destabilization due to the localization of one double bond in a four-membered ring. The destabilization is in the range 5.86-10.49 kcal/mol for the categories (1, 1) and (0, 2) wherein two bonds are localized for four-membered rings. The isomers NC17- NC25 contain total three localized bonds in four membered rings. This leads to further decrease in the stability as the antiaromatic character is expected to be high for the four-membered rings. The relative energy of these isomers is in the range 12.94 to 18.99 kcal/mol.
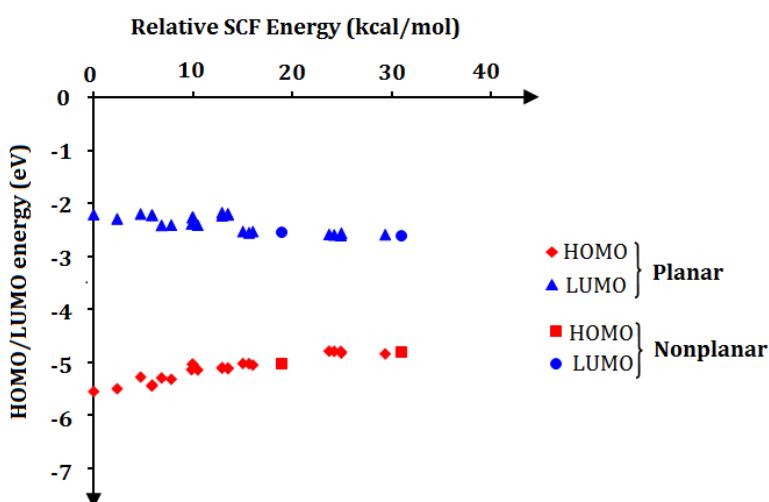
Figure 2.16 Trends in HOMO and LUMO energy with relative energy for three naphthalene-two cyclobutadiene ring systems

The isomers NC26-NC31 showing two double bonds in each four-membered rings are the most unstable with relative energies in the range 23.73 to 30.99 kcal/mol. Here the antiaromatic character is expressed from both the four-membered rings. For each category of molecules, the relative energy shows a small variation which can be attributed to the variation in strain energy at the curved portions as more curved structures are expected to show higher energy. In cases such as NC25 and NC31, a distortion from planarity occurs due to the steric effect from non-bonded C-H...H-C interactions arising from highly curved nature of the molecules. When the rings of two polycyclic systems can be incorporated into one-to-one correspondence, the corresponding ring currents are equal and are called equiaromatic.[137] As a result, the isomers NC7, NC12, NC13, NC15, NC16, NC26, NC28, NC29, and NC31 can be considered as equiaromatic. Table 2.9 also reports the HOMO, LUMO and the HOMO-LUMO gap using B3LYP/6-311+G(d, p) level of theory. The most stable isomer has the lowest HOMO and the highest LUMO energies and with the increase in the relative energy of the isomers, an increasing trend in HOMO energy and decreasing trend in LUMO energy are observed. This suggests that the chemical reactivity of the isomers increases with increase in the antiaromatic character as it reduces the HOMO-LUMO gap (Figure 2.16).

2.9.6 Naphthalene–Pentalene Fused Systems

Two configurations, NP1 and NP2 are possible for the fusion of naphthalene with one pentalene (Figure 2.17).[88] In both cases, the pentalene unit shows deeper negative potential than naphthalene. Also MESP V_m value distribution over the naphthalene in the fused system is similar to that of free naphthalene. The V_m points suggest a significant difference in the π-distribution within the pentalene portion of NP1 and NP2 as the former shows only three π-bonds whereas the latter shows four π-bonds meaning that the antiaromatic character of pentalene is more expressed in NP2 than NP1. This argument is supported by the relative energy values: NP1 is 5.5 kcal/mol more stable than NP2.
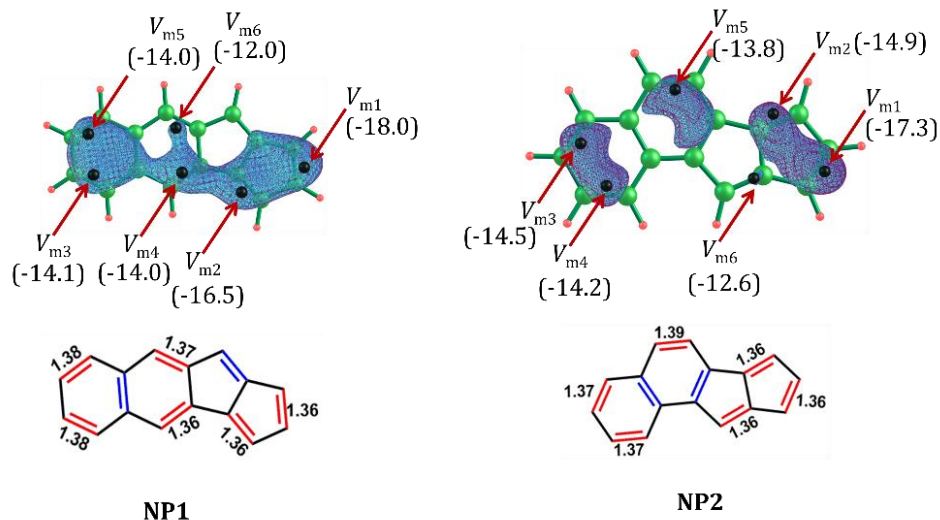
Figure 2.17 MESP CPs and isosurfaces for one naphthalene and one pentalene fused systems, along with MESP topology-based the representation of the double bonds in these systems. V_m values and bond length are in kcal/mol and Å, respectively

Similar observation is made for the two naphthalene-one pentalene fused systems (Figure 2.18), *viz.* NP3 through NP7. The NP3, NP4, NP5, NP6 and NP7 show respectively two, three, four, four and four π-bonds for the pentalene portion suggesting that antiaromaticity is the least expressed in NP3 followed by NP4 while NP5, NP6 and NP7 exhibit substantial antiaromatic character. The relative energies of NP3, NP4, NP5, NP6 and NP7 are 0.0, 3.1, 7.3, 7.4 and 7.5 kcal/mol, respectively. These kind of A-aA fused systems have found applications in the organic thin film transistors. Among them, NP3[90] and NP5[99] have been synthesized experimentally.
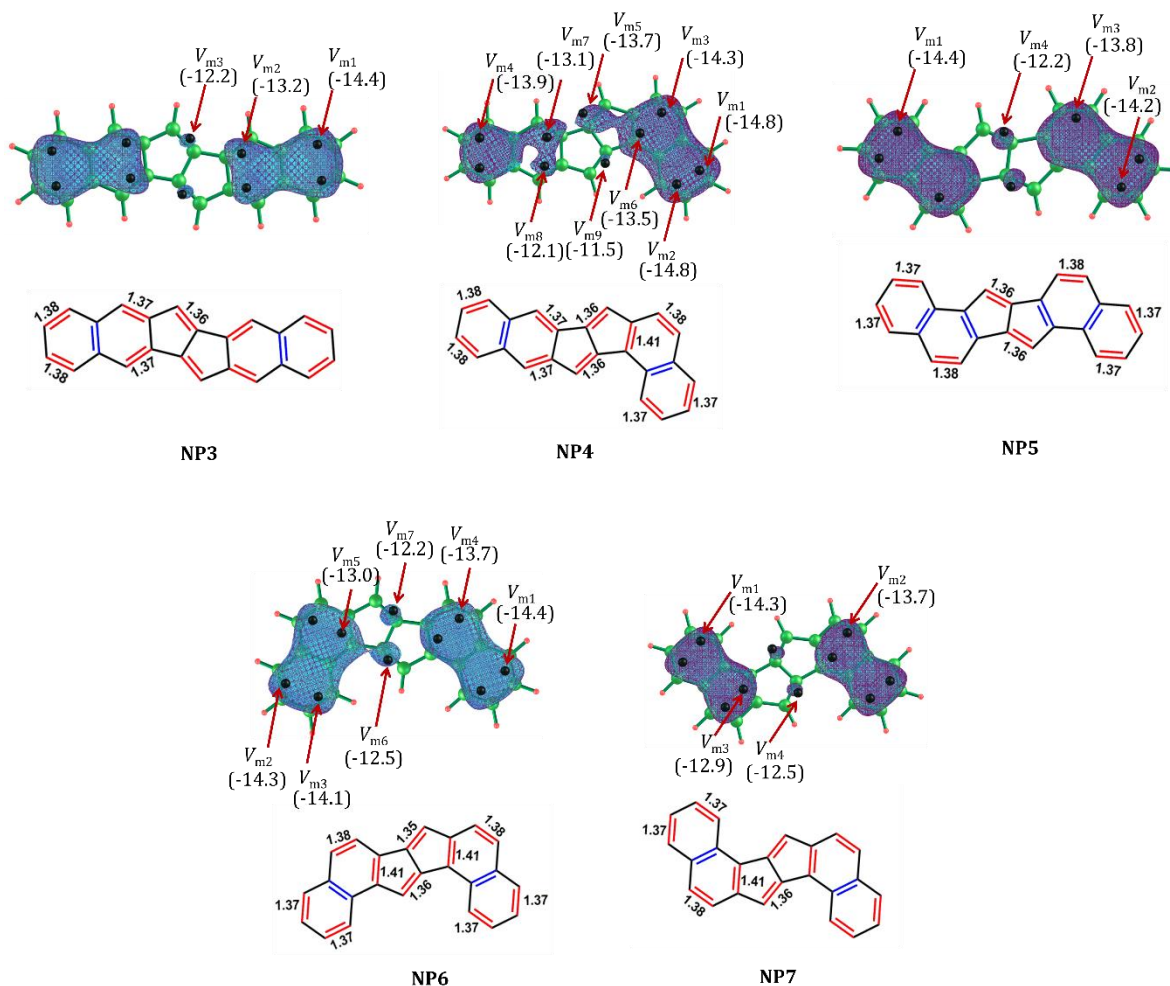
Figure 2.18 MESP CPs and isosurfaces for two naphthalene-one pentalene fused systems, along with MESP topology-based the representation of the double bonds in these systems. V_m values and bond length are in kcal/mol and Å, respectively

2.9.7 Cyclic Structures

The three benzene-two cyclobutadiene fused system BC4 having the (0, 0) angular configuration given in Figure 2.19 is more stable than the linear BC3 configuration. Extending this structure with more benzene and cyclobutadiene units can lead to a ring structure BC5 composed of six benzenes and six cyclobutadiene units. The MESP features suggest π-bond distribution within benzene rings and all the cyclobutadiene rings are 'empty'. In other words, a (0, 0, 0, 0, 0, 0) configuration can be assigned for BC5 to indicate
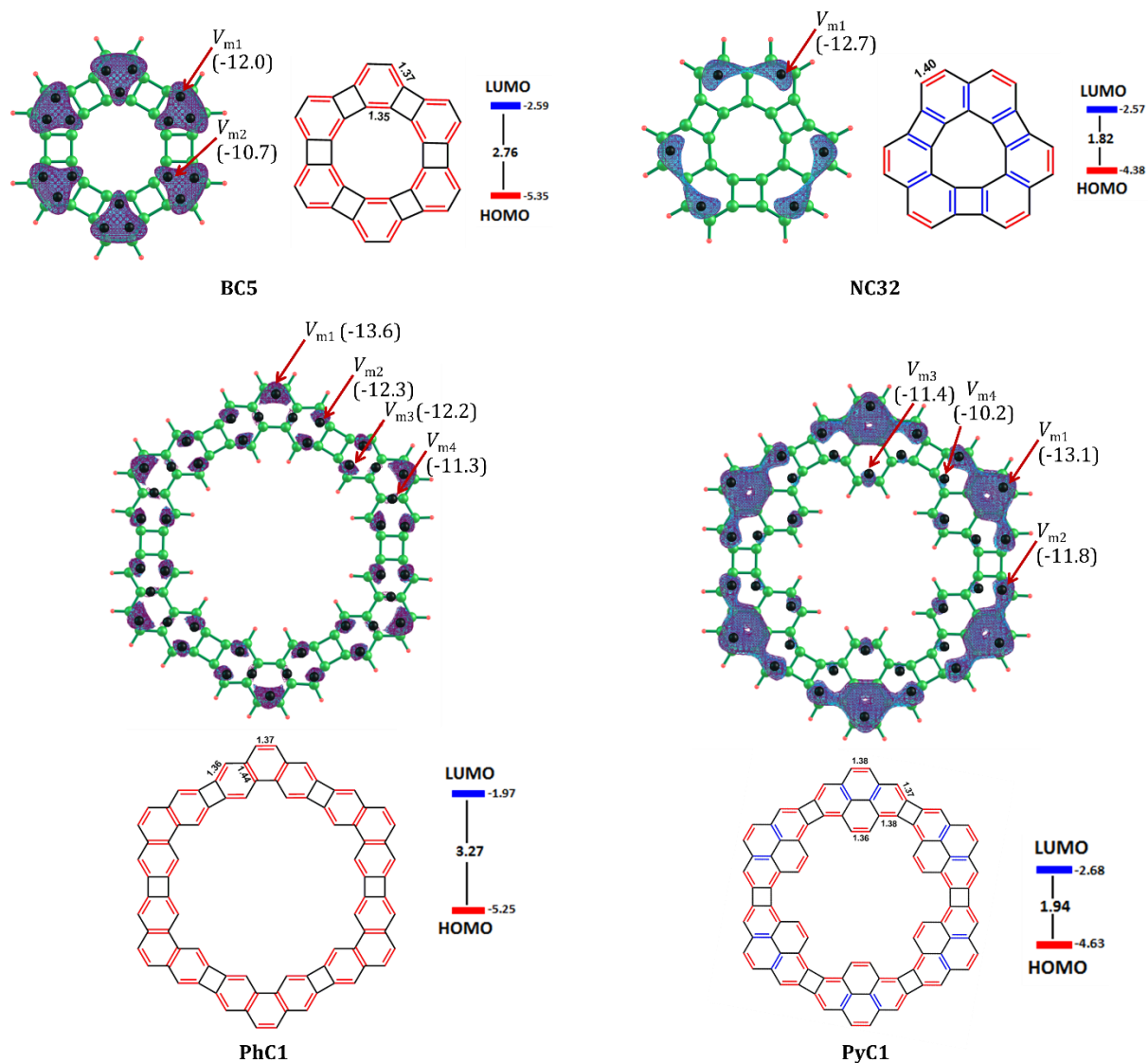
Figure 2.19 MESP CPs and isosurfaces for fused ring systems. HOMO- LUMO gap is given in eV

the absence of π-bond localization (Figure 2.19) in four-membered rings. Although six four-membered rings are present in BC5, MESP-based method suggests that the molecule may be stable and can be synthesized due to the dominance of aromatic character. In fact, the synthesis of BC5 is known in the literature, Vollhardt *et al.* had reported the total synthesis of the first helical phenylenes (heliphenes), angular [6]- and [7] phenylene, by double cobalt-catalyzed cyclotrimerization strategy and route for the preparation of such heliphene based metal complexes. [84, 138, 139] The cyclic structure for three naphthalene-

three cyclobutadiene fused system NC32 is shown in Figure 2.19. Here the MESP feature suggests a (2, 2, 2) configuration for the molecule which can be interpreted as a highly antiaromatic molecule. We predict that the synthesis of such a molecule may not be very easy. Figure 2.19 also depicts two more ring structures, one composed of six phenanthrene and six cyclobutadiene moieties (PhC1) and another one composed of six pyrene and six cyclobutadiene moieties (PyC1). We note that the aromatic moieties phenanthrene and pyrene prefer angular structures for fusion to yield 'empty' rings for cyclobutadienes. MESP topology suggest (0, 0, 0, 0, 0, 0) configuration for both PhC1 and PyC1. Hence such structures should behave as the most stable compared to any other isomers. Observed band gaps for the ring fused systems of naphthalene and pyrene with cyclobutadiene are 1.82 and 1.94 eV respectively, indicating the ease of conductivity associated with the ring fused systems compared to its linear ones. And we predict that such ring systems can be applied to better performing conducting materials due to the small band gap induced by the antiaromatic character of cyclobutadiene units. The continuous growth of biphenylene units reported by Gottfried, Liljeroth and co-workers can be explained based on our results.[140] The biphenylene network system consists of four-, six-, and eight-membered rings and this adopts a configuration containing the least number of double bonds in the four membered ring, *i.e.*, (1, 1, 1, 1, ...) configuration. This stable configuration plays a key role in the systematic growth as well as stability of the network system. It is also possible to explicate the dielectric properties of the network system based on the configuration. The findings of the work could be correlated with the Glidewell-Lloyd rule,[141, 142] which is extension of Clar's π-sextet rule. According to the former, total π-electrons in a conjugated polycyclic system tend to form the smallest 4n + 2 groups by avoiding smallest 4n group formation. The systems with smallest 4n + 2 groups describe the structural and electronic properties of these polycyclic conjugated hydrocarbons better.

El Bakouri *et al.* have examined[143] the scope of the Glidewell-Lloyd rule in 69 polycyclic hydrocarbons composed of various combinations of four-, six-, and eight-membered rings. According to them, conjugated polycyclic systems try to avoid the presence of double bonds at the ring junctions. This leads to stable Glidewell-Lloyd

structure that contains least number of double bonds in the four membered ring. These results well-correlate with our theory that A-aA fused systems try to reduce its antiaromaticity by adopting a configuration containing the least number of localized bonds over antiaromatic moieties. It could be seen that most of the structures that satisfy the Glidewell-Lloyd rule obey the MESP based interpretation of the π-bond distribution. Therefore, our present work could be considered as a manifestation of Glidewell–Lloyd rule in terms of MESP topology.

2.10 Conclusions

A detailed study on the design strategy of A-aA fused systems is very important, considering their potential applications in optoelectronic devices. Herein, MESP topology analysis has been carried out on a large variety of aromatic-antiaromatic fused systems using B3LYP/6-311+G(d, p) level of theory. The negative regions observed in the MESP analysis indicate the delocalization/localization of electron density in the aromatic/antiaromatic ring. The MESP topology studies clearly suggest that the double bond character in the antiaromatic rings of A-aA fused systems is getting diluted as they are in combination with aromatic rings. The stability of such systems correlates well with the number of localized bonds appearing in the antiaromatic moieties of the fused system. This correlation is clearly illustrated for twenty-five isomers of fused systems made up of three naphthalene and two cyclobutadiene units. They are divided into six different categories based on the number of π-bonds (n, n') observed in the cyclobutadiene rings. Among them, the most stable isomer is linear and belongs to (0, 0) category while the least stable isomers belong to (2, 2) category. The MESP distribution suggests a (2, 2, 2) configuration for a ring structure made up of three naphthalene and three cyclobutadiene units. This configuration predicts high antiaromatic character for the molecule due to the presence of two double bonds in each four-membered ring. MESP topology suggests angular structure as the most stable for benzene-cyclobutadiene fused systems. The ring structure made up of six benzene and six cyclobutadiene units shows 'empty' π-character for the cyclobutadiene rings indicating the lowest antiaromatic character or high stability for the structure. The synthesis of such a macrocycle is

achieved experimentally which can be supported by the inherent stability of the molecule due to the dominance of aromatic character from six benzene rings. In general, the (0, 0, 0, 0, ...) and (2, 2, 2, ...) configurations are expected to be the most stable and the least stable structures for a benzenoid aromatic-fused with cyclobutadiene moieties, respectively. Same trend is observed with A-aA fused systems of pentalene rings also as they try to keep a configuration that contains the least number of localized π-bonds in the pentalene ring. Any A-aA system with (0, 0, 0, 0, ...) configuration exhibits high HOMO-LUMO gap, indicating the high stability associated with it and one with (2, 2, 2, ...) configuration possesses small HOMO-LUMO gap, indicating its low stability or high reactivity. The π-bond distribution expressed using the MESP critical features provides a unique molecular formula for each system and also suggests a molecular design strategy for the creation of stable macrocycles with (0, 0, 0, 0, ...) configuration.

This systematic study on A-aA system clearly promotes MESP as a powerful tool for the analysis of π-bond distribution in conjugated cyclic hydrocarbons. This helps to attenuate the complexity of predicting the single and double bond distribution and suggests a unique structure for each molecule. Detailed study on MESP topology of a system furnishes the possibilities of designing molecules and predicting their properties and reactivity, based on the aromatic/antiaromatic character. The interpretation of molecular formula for a structure opens up to the concept of antiaromaticity-aromaticity interplay in A-aA fused systems. This also helps to predict the applications of such systems in the area of semiconducting materials due to the conducting properties induced by the antiaromatic moieties in combination with aromatic systems.

2.11 References

1.   T. Krygowski, M. Cyranski, Z. Czarnocki, G. Häfelinger and A. R. Katritzky, *Tetrahedron*, **2000**, 13, 1783-1796.
2.   M. K. Cyranski, T. M. Krygowski, A. R. Katritzky and P. V. R. Schleyer, *J. Org. Chem.*, **2002**, 67, 1333-1338.
3.   T. M. Krygowski and M. K. Cyrański, *Chem. Rev.*, **2001**, 101, 1385-1420.

4. P. V. R. Schleyer, *Chem. Rev.*, **2001**, 101, 1115-1118.

5. K. Jug and A. M. Köster, *J. Phys. Org. Chem.*, **1991**, 4, 163-169.

6. M. Glukhovtsev, *J. Chem. Educ.*, **1997**, 74, 132.

7. D. Klein and N. Trinajstic, *Pure Appl. Chem.*, **1989**, 61, 2107-2115.

8. A. Ciesielski, T. M. Krygowski, M. K. Cyrański and A. T. Balaban, *Phys. Chem. Chem. Phys.*, **2011**, 13, 3737-3747.

9. S. Kikuchi, *J. Chem. Educ.*, **1997**, 74, 194.

10. D. J. Klein and N. Trinajstic, *J. Am. Chem. Soc.*, **1984**, 106, 8050-8056.

11. J. Kruszewski and T. M. Krygowski, *Can. J. Chem.*, **1975**, 53, 945-951.

12. E. Miliordos, *Phys. Rev. A*, **2010**, 82, 062118.

13. N. Trinajstić, *Int. J. Quantum Chem.*, **1977**, 12, 469-477.

14. L. Zhao, R. Grande-Aztatzi, C. Foroutan-Nejad, J. M. Ugalde and G. Frenking, *ChemistrySelect*, **2017**, 2, 863-870.

15. J. J. Dannenberg and R. Rios, *J. Phys. Chem.*, **1994**, 98, 6714-6718.

16. H. Masui, *Coord. Chem. Rev.*, **2001**, 219-221, 957-992.

17. E. Kleinpeter and A. Koch, *Phys. Chem. Chem. Phys.*, **2011**, 13, 20593-20601.

18. J. S. Kudavalli, D. R. Boyd, D. Coyne, J. R. Keeffe, D. A. Lawlor, A. C. Maccormac, R. A. More O'ferrall, S. N. Rao and N. D. Sharma, *Org. Lett.*, **2010**, 12, 5550-5553.

19. P. B. Karadakov, *J. Phys. Chem. A*, **2008**, 112, 7303-7309.

20. R. V. Williams, *Chem. Rev.*, **2001**, 101, 1185-1204.

21. S. S. Shaik, P. C. Hiberty, J. M. Lefour and G. Ohanessian, *J. Am. Chem. Soc.*, **1987**, 109, 363-374.

22. K. K. Zborowski, M. Solà, J. Poater and L. M. Proniewicz, *J. Phys. Org. Chem.*, **2011**, 24, 499-506.

23. J. Dominikowska and M. Palusiak, *Struct. Chem.*, **2012**, 23, 1173-1183.

24. G. Portella, J. Poater and M. Sola, *J. Phys. Org. Chem.*, **2005**, 18, 785-791.

25. L. Schaad and B. Hess, *Pure Appl. Chem.*, **1982**, 54, 1097-1114.

26. J. Poater, X. Fradera, M. Duran and M. Sola, *Chem. Eur. J.*, **2003**, 9, 400-406.

27. P. Bultinck, R. Ponec, A. Gallegos, S. Fias, S. Van Damme and R. Carbó-Dorcaa, *Croat. Chem. Acta.*, **2006**, 79, 363-371.

28. P. Bultinck, R. Ponec and S. Van Damme, *J. Phys. Org. Chem.*, **2005**, 18, 706-718.

29. M. Solà, *Front. Chem.*, **2017**, 5.

30. M. Randić and A. T. Balaban, *Int. J. Quantum Chem.*, **2018**, e25657.

31. C. H. Suresh and M. J. Ajitha, *J. Org. Chem.*, **2013**, 78, 3918-3924.

32. M. Randić, A. T. Balaban and D. Plavšić, *Phys. Chem. Chem. Phys.*, **2011**, 13, 20644-20648.

33. J. I. Wu, M. Dobrowolski, M. Cyrański, B. Merner, G. Bodwell, Y. Mo and P. Schleyer, *Mol. Phys.*, **2009**, 107, 1177-1186.

34. J. Aihara, T. Ishida and H. Kanno, *Bull. Chem. Soc. Jpn.*, **2007**, 80, 1518-1521.

35. M. Antić, B. Furtula and S. Radenković, *J. Phys. Chem. A*, **2017**, 121, 3616-3626.

36. F. J. MartíN-MartíNez, S. Melchor and J. A. Dobado, *Org. Lett.*, **2008**, 10, 1991-1994.

37. C. H. Suresh and N. Koga, *J. Org. Chem.*, **2002**, 67, 1965-1968.

38. C. Suresh and S. R. Gadre, *J. Org. Chem.*, **1999**, 64, 2505-2512.

39. M. Müller, C. Kübel and K. Müllen, *Chem. Eur. J.*, **1998**, 4, 2099-2109.

40. P. Bultinck, *Faraday Discuss.*, **2007**, 135, 347-365.

41. K. P. Vijayalakshmi and C. H. Suresh, *New J. Chem.*, **2010**, 34, 2132-2138.

42. P. R. Von Schleyer and H. Jiao, *Pure Appl. Chem.*, **1996**, 68, 209-218.

43. S. Behrens, A. M. Koester and K. Jug, *J. Org. Chem.*, **1994**, 59, 2546-2551.

44. M. Giambiagi, M. S. De Giambiagi, C. D. Dos Santos Silva and A. P. De Figueiredo, *Phys. Chem. Chem. Phys.*, **2000**, 2, 3381-3392.

45. O. E. Polansky and G. Derflinger, *Int. J. Quantum Chem.*, **1967**, 1, 379-401.

46. S. R. Gadre and R. N. Shirsat, *Electrostatics of atoms and molecules*. 2000: Universities Press.

47. J. Mathew and C. H. Suresh, *Inorg. Chem.*, **2010**, 49, 4665-4669.

48. M. M. Deshmukh, S. R. Gadre, R. Tonner and G. Frenking, *Phys. Chem. Chem. Phys.*, **2008**, 10, 2298-2301.

49. S. R. Gadre, S. A. Kulkarni and I. H. Shrivastava, *J. Chem. Phys.*, **1992**, 96, 5253-5260.

50. S. R. Gadre and I. H. Shrivastava, *J. Chem. Phys.*, **1991**, 94, 4384-4390.

51. S. R. Gadre, S. A. Kulkarni, C. Suresh and I. H. Shrivastava, *Chem. Phys. Lett.*, **1995**, 239, 273-281.

52. S. R. Gadre and S. S. Pundlik, *J. Am. Chem. Soc.*, **1995**, 117, 9559-9563.

53. E. D. Jemmis, G. Subramanian, I. H. Srivastava and S. R. Gadre, *J. Phys. Chem.*, **1994**, 98, 6445-6451.

54. A. Kumar, S. R. Gadre, N. Mohan and C. H. Suresh, *J. Phys. Chem. A*, **2014**, 118, 526-532.

55. N. Mohan, C. H. Suresh, A. Kumar and S. R. Gadre, *Phys. Chem. Chem. Phys.*, **2013**, 15, 18401-18409.

56. S. R. Gadre and A. Kumar, *J. Chem. Sci.*, **2016**, 128, 1519-1526.

57. C. H. Suresh, N. Koga and S. R. Gadre, *Organometallics*, **2000**, 19, 3008-3015.

58. M. J. Frisch, G. W. Trucks, H. B. Schlegel, G. E. Scuseria, M. A. Robb, J. R. Cheeseman, G. Scalmani, V. Barone, B. Mennucci, G. A. Petersson, H. Nakatsuji, M. Caricato, X. Li, H. P. Hratchian, A. F. Izmaylov, J. Bloino, G. Zheng, J. L. Sonnenberg, M. Hada, M. Ehara, K. Toyota, R. Fukuda, J. Hasegawa, M. Ishida, T. Nakajima, Y. Honda, O. Kitao, H. Nakai, T. Vreven, J. A. Montgomery, J. E. Peralta, F. Ogliaro, M. Bearpark, J. J. Heyd, E. Brothers, K. N. Kudin, V. N. Staroverov, R. Kobayashi, J. Normand, K. Raghavachari, A. Rendell, J. C. Burant, S. S. Iyengar, J. Tomasi, M. Cossi, N. Rega, J. M. Millam, M. Klene, J. E. Knox, J. B. Cross, V. Bakken, C. Adamo, J. Jaramillo, R. Gomperts, R. E. Stratmann, O. Yazyev, A. J. Austin, R. Cammi, C. Pomelli, J. W. Ochterski, R. L. Martin, K. Morokuma, V. G. Zakrzewski, G. A. Voth, P. Salvador, J. J. Dannenberg, S. Dapprich, A. D. Daniels, Farkas, J. B. Foresman, J. V. Ortiz, J. Cioslowski and D. J. Fox, *Gaussian 09, Revision D.01*. 2013: Wallingford CT.

59. A. Kumar, S. D. Yeole, S. R. Gadre, R. López, J. F. Rico, G. Ramírez, I. Ema and D. Zorrilla, *J. Comput. Chem.*, **2015**, 36, 2350-2359.

60. R. López, J. F. Rico, G. Ramírez, I. Ema and D. Zorrilla, *Comput. Phys. Commun.*, **2009**, 180, 1654-1660.

61. R. López, J. F. Rico, G. Ramírez, I. Ema and D. Zorrilla, *Comput. Phys. Commun.*, **2015**, 192, 289-294.

62. R. López, J. F. Rico, G. Ramírez, I. Ema, D. Zorrilla, A. Kumar, S. D. Yeole and S. R. Gadre, *Comput. Phys. Commun.*, **2017**, 214, 207-215.

63. E. Clar, *The aromatic sextet*. 1972, London: Wiley-Interscience.

64.   A. T. Balaban, *Polycycl. Aromat. Compd.*, **2004**, 24, 83-89.

65.   I. Gutman and S. J. Cyvin, *Introduction to the theory of benzenoid hydrocarbons*. 2012: Springer Science & Business Media.

66.   S. J. Cyvin and I. Gutman, *Kekulé structures in benzenoid hydrocarbons*. Vol. 46. 2013: Springer Science & Business Media.

67.   T. K. Dickens and R. B. Mallion, *J. Phys. Chem. A*, **2018**, 122, 8858-8864.

68.   T. K. Dickens and R. B. Mallion, *J. Phys. Chem. A*, **2018**, 122, 8865-8873.

69.   T. Bally and S. Masamune, *Tetrahedron*, **1980**, 36, 343-370.

70.   M. J. Dewar, *Angew. Chem. Int. Ed.*, **1971**, 10, 761-776.

71.   H. P. Diogo, T. Kiyobayashi, M. E. Minas Da Piedade, N. Burlak, D. W. Rogers, D. Mcmasters, G. Persy, J. Wirz and J. F. Liebman, *J. Am. Chem. Soc.*, **2002**, 124, 2065-2072.

72.   S. Radenković, J. Đurđević and P. Bultinck, *Phys. Chem. Chem. Phys.*, **2012**, 14, 14067-14078.

73.   P. V. R. Schleyer, C. Maerker, A. Dransfeld, H. Jiao and N. J. Van Eikema Hommes, *J. Am. Chem. Soc.*, **1996**, 118, 6317-6318.

74.   J. Pople and K. Untch, *J. Am. Chem. Soc.*, **1966**, 88, 4811-4815.

75.   F. Sondheimer, *Acc. Chem. Res.*, **1972**, 5, 81-91.

76.   K. Jug and E. Fasold, *J. Am. Chem. Soc.*, **1987**, 109, 2263-2265.

77.   C. S. Wannere, K. W. Sattelmeyer, H. F. Schaefer Iii and P. V. R. Schleyer, *Angew. Chem. Int. Ed.*, **2004**, 43, 4200-4206.

78.   S. M. Johnson, I. C. Paul and G. S. D. King, *J. Chem. Soc. B: Phys. Org.*, **1970**, 643-649.

79.   P. J. Mayer, O. El Bakouri, T. Holczbauer, G. F. Samu, C. Janáky, H. Ottosson and G. London, *J. Org. Chem.*, **2020**, 85, 5158-5172.

80.   C. K. Frederickson, L. N. Zakharov and M. M. Haley, *J. Am. Chem. Soc.*, **2016**, 138, 16827-16838.

81.   B. D. Milanez, J. C. V. Chagas, M. Pinheiro Jr, A. J. A. Aquino, H. Lischka and F. B. C. Machado, *Theor. Chem. Acc.*, **2020**, 139, 113.

82.   A. Rajca, A. Safronov, S. Rajca, C. R. Ross and J. J. Stezowski, *J. Am. Chem. Soc.*, **1996**, 118, 7272-7279.

83. J. W. Barton, D. V. Lee and M. K. Shepherd, *J. Chem. Soc., Perkin Trans.*, **1985**, 1407-1411.

84. O. S. Miljanic, D. Holmes and K. P. C. Vollhardt, *Org. Lett.*, **2005**, 7, 4001-4004.

85. Z. Gu, G. B. Boursalian, V. Gandon, R. Padilla, H. Shen, T. V. Timofeeva, P. Tongwa, K. P. C. Vollhardt and A. A. Yakovenko, *Angew. Chem.*, **2011**, 123, 9585-9589.

86. D. Bruns, H. Miura, K. P. C. Vollhardt and A. Stanger, *Organic Lett.*, **2003**, 5, 549-552.

87. C. Eickmeier, D. Holmes, H. Junga, A. J. Matzger, F. Scherhag, M. Shim and K. P. C. Vollhardt, *Angew. Chem. Int. Ed.*, **1999**, 38, 800-804.

88. S.-I. Kato, S. Kuwako, N. Takahashi, T. Kijima and Y. Nakamura, *J. Org. Chem.*, **2016**, 81, 7700-7710.

89. A. Konishi, T. Fujiwara, N. Ogawa, Y. Hirao, K. Matsumoto, H. Kurata, T. Kubo, C. Kitamura and T. Kawase, *Chem. Lett.*, **2010**, 39, 300-301.

90. J. Shen, D. Yuan, Y. Qiao, X. Shen, Z. Zhang, Y. Zhong, Y. Yi and X. Zhu, *Org. Lett.*, **2014**, 16, 4924-4927.

91. G. Dai, J. Chang, W. Zhang, S. Bai, K. W. Huang, J. Xu and C. Chi, *Chem. Commun.*, **2015**, 51, 503-506.

92. J. Zheng, X. Zhuang, L. Qiu, Y. Xie, X. Wan and Z. Lan, *J. Phy. Chem. A*, **2015**, 119, 3762-3769.

93. G. Dai, J. Chang, X. Shi, W. Zhang, B. Zheng, K. W. Huang and C. Chi, *Chem. Eur. J.*, **2015**, 21, 2019-2028.

94. K. Niimi, M. J. Kang, E. Miyazaki, I. Osaka and K. Takimiya, *Org. Lett.*, **2011**, 13, 3430-3433.

95. J. L. Marshall, K. Uchida, C. K. Frederickson, C. Schütt, A. M. Zeidell, K. P. Goetz, T. W. Finn, K. Jarolimek, L. N. Zakharov and C. Risko, *Chem. Sci.*, **2016**, 7, 5547-5558.

96. B. S. Young, D. T. Chase, J. L. Marshall, C. L. Vonnegut, L. N. Zakharov and M. M. Haley, *Chem. Sci.*, **2014**, 5, 1008-1014.

97. D. T. Chase, B. D. Rose, S. P. Mcclintock, L. N. Zakharov and M. M. Haley, *Angew. Chem. Int. Ed.*, **2011**, 50, 1127-1130.

98. C. Wang, H. Dong, W. Hu, Y. Liu and D. Zhu, *Chem. Rev.*, **2012**, 112, 2208-2267.

99. T. Kawase, T. Fujiwara, C. Kitamura, A. Konishi, Y. Hirao, K. Matsumoto, H. Kurata, T. Kubo, S. Shinamura and H. Mori, *Angew. Chem. Int. Ed.*, **2010**, 49, 7728-7732.

100. T. Yamamoto, S. Shinamura, E. Miyazaki and K. Takimiya, *Bull.Chem.Soc.Jpn.*, **2010**, 83, 120-130.

101. B. Tylleman, C. M. Vande Velde, J.-Y. Balandier, S. Stas, S. Sergeyev and Y. H. Geerts, *Organic Lett.*, **2011**, 13, 5208-5211.

102. M. Mamada, H. Katagiri, M. Mizukami, K. Honda, T. Minamiki, R. Teraoka, T. Uemura and S. Tokito, *ACS Appl. Mater. Interfaces*, **2013**, 5, 9670-9677.

103. Z. B. Henson, K. Müllen and G. C. Bazan, *Nat. Chem.*, **2012**, 4, 699-704.

104. J. W. Barton, M. K. Shepherd and R. J. Willis, *J. Chem. Soc. Perkin Trans. 1*, **1986**, 967-971.

105. P. R. Buckland, N. P. Hacker and J. F. Mcomie, *J. Chem. Soc. Perkin Trans. 1*, **1983**, 1443-1448.

106. M. E. Cracknell, R. A. Kabli, J. F. Mcomie and D. H. Perry, *J. Chem. Soc. Perkin Trans. 1*, **1985**, 115-120.

107. D. T. Y. Bong, E. W. Chan, R. Diercks, P. I. Dosa, M. M. Haley, A. J. Matzger, O. Š. Miljanić, K. P. C. Vollhardt, A. D. Bond and S. J. Teat, *Organic Lett.*, **2004**, 6, 2249-2252.

108. C. Dosche, H. G. Löhmannsröben, A. Bieser, P. Dosa, S. Han, M. Iwamoto, A. Schleifenbaum and K. P. C. Vollhardt, *Phys. Chem. Chem. Phys.*, **2002**, 4, 2156-2161.

109. D. T. Chase, A. G. Fix, S. J. Kang, B. D. Rose, C. D. Weber, Y. Zhong, L. N. Zakharov, M. C. Lonergan, C. Nuckolls and M. M. Haley, *J. Am. Chem. Soc.*, **2012**, 134, 10349-10352.

110. S. Ito, T. Minami and M. Nakano, *J. Phy. Chem. C*, **2012**, 116, 19729-19736.

111. R. Firouzi, H. Shafie and H. Tohidnia, *ChemistrySelect*, **2017**, 2, 11526-11536.

112. R. Ayub, O. E. Bakouri, K. Jorner, M. Solà and H. Ottosson, *J. Org. Chem.*, **2017**, 82, 6327-6340.

113. V. Gineityte, *Monatsh. Chem.*, **2018**, 149, 1031-1044.

114. J. M. Schulman and R. L. Disch, *J. Phys. Chem. A*, **2007**, 111, 10010-10014.

115. J. M. Schulman and R. L. Disch, *J. Am. Chem. Soc.*, **1996**, 118, 8470-8474.

116. S. Radenkovic, J. Tošović, R. Havenith and P. Bultinck, *ChemPhysChem*, **2015**, 16, 216-222.

117. T. K. Dickens and R. B. Mallion, *Croat. Chem. Acta*, **2014**, 87, 221-232, 12 pp.

118. H. Figeys, N. Defay, R. Martin, J. Mcomie, B. Ayres and J. Chadwick, *Tetrahedron*, **1976**, 32, 2571-2578.

119. A. Ceulemans and A. G. Arvanitidis, *Bull. Chem. Soc. Jpn.*, **2015**, 88, 1553-1560.

120. J. M. Schulman, R. L. Disch, H. Jiao and P. V. R. Schleyer, *J. Phys. Chem. A*, **1998**, 102, 8051-8055.

121. A. T. Balaban, I. Gutman, S. Markovic, D. Simijonovic and J. Durdevic, *Polycyclic Aromat. Compd.*, **2011**, 31, 339-349.

122. R. Gershoni-Poranne, C. M. Gibson, P. W. Fowler and A. Stanger, *J. Org. Chem.*, **2013**, 78, 7544-7553.

123. I. Gutman, *South African J. Chem.*, **1994**, 47, 53-55.

124. C. H. Suresh and S. R. Gadre, *J. Am. Chem. Soc.*, **1998**, 120, 7049-7055.

125. P. K. Anjalikrishna, C. H. Suresh and S. R. Gadre, *J. Phys. Chem. A*, **2019**, 123, 10139-10151.

126. J. W. Barton and D. J. Rowe, *Tetrahedron*, **1985**, 41, 1323-1328.

127. A. Schleifenbaum, N. Feeder and K. P. C. Vollhardt, *Tetrahedron Lett.*, **2001**, 42, 7329-7332.

128. B. C. Berris, G. H. Hovakeemian, Y. H. Lai, H. Mestdagh and K. P. C. Vollhardt, *J. Am. Chem. Soc.*, **1985**, 107, 5670-5687.

129. J. W. Barton and R. B. Walker, *Tetrahedron Lett.*, **1978**, 19, 1005-1008.

130. R. Diercks and K. P. C. Vollhardt, *Angew. Chem. Int. Ed.*, **1986**, 25, 266-268.

131. M. Saito, *Symmetry*, **2010**, 2, 950-969.

132. A. Konishi, Y. Okada, M. Nakano, K. Sugisaki, K. Sato, T. Takui and M. Yasuda, *J. Am. Chem. Soc.*, **2017**, 139, 15284-15287.

133. A. Konishi, Y. Okada, R. Kishi, M. Nakano and M. Yasuda, *J. Am. Chem. Soc.*, **2019**, 141, 560-571.

134. M. Baranac-Stojanović and M. Stojanović, *Phys. Chem. Chem. Phys.*, **2019**, 21, 3250-3263.

135. M. Baranac-Stojanović, *Chem. Eur. J.*, **2019**, 25, 9747-9757.

136. S. Kawai, K. Takahashi, S. Ito, R. Pawlak, T. Meier, P. Spijker, F. F. Canova, J. Tracey, K. Nozaki and A. S. Foster, *ACS nano*, **2017**, 11, 8122-8130.

137. P. W. Fowler, S. Cotton, D. Jenkinson, W. Myrvold and W. H. Bird, *Chem. Phys. Lett.*, **2014**, 597, 30-35.

138. S. Han, A. D. Bond, R. L. Disch, D. Holmes, J. M. Schulman, S. J. Teat, K. P. C. Vollhardt and G. D. Whitener, *Angew. Chem., Int. Ed.*, **2002**, 41, 3223-3227.

139. D. L. Mohler, S. Kumaraswamy, A. Stanger and K. P. C. Vollhardt, *Synlett*, **2006**, 2981-2984.

140. Q. Fan, L. Yan, M. W. Tripp, O. Krejčí, S. Dimosthenous, S. R. Kachel, M. Chen, A. S. Foster, U. Koert and P. Liljeroth, *Science*, **2021**, 372, 852-856.

141. C. Glidewell and D. Lloyd, *Tetrahedron*, **1984**, 40, 4455-4472.

142. R. Pino-Rios and M. Solà, *J. Phy. Chem. A*, **2020**.

143. O. El Bakouri, J. Poater, F. Feixas and M. Solà, *Theo. Chem. Acc.*, **2016**, 135, 1-12.

Part A:

Electrostatic Potential for Exploring Electron Delocalization in Infinitenes, Circulenes, and Nanobelts

Electrostatic potential distribution of

infinitene   circulene   nanobelt
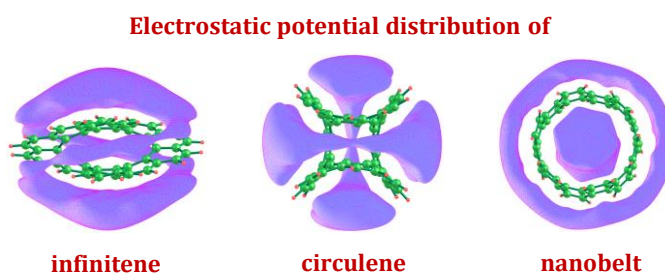
Part B:

Utilization of Through-Space Effect to Design Donor-Acceptor Systems without Donors and Acceptors
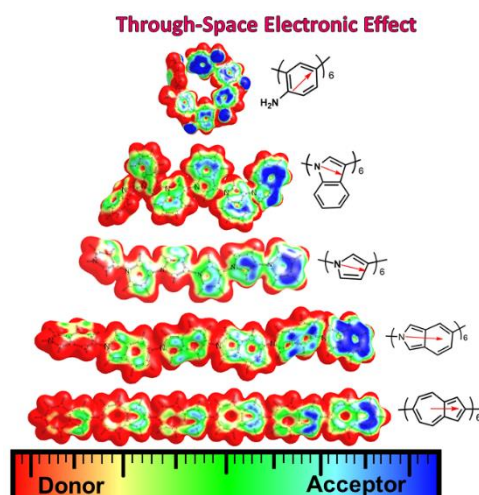
Part A

Electrostatic Potential for Exploring Electron Delocalization in Infinitenes, Circulenes, and Nanobelts

3.1 Abstract

The π-conjugation, aromaticity, and stability of the newly synthesized 12-infinitene, and of other infinitenes comprising 8-, 10-, 14- and 16-arene rings are investigated using density functional theory (DFT). The π-electron delocalization and aromatic character rooted in infinitenes are quantified in terms of molecular electrostatic potential (MESP) topology. Structurally, the infinitene bears a close resemblance of its helically twisted structure to the infinity symbol. The MESP topology shows that, infinitene possesses an infinity-shaped delocalization of the electron density that streams over the fused benzenoid rings. The parameter $\sum_{i=1}^{3} \Delta\lambda_i$, derived from the eigenvalues (λ_i) corresponding to the MESP minima, is used for quantifying the aromatic character of arene rings of infinitene. The structure, stability and MESP topology features of 8-, 10-, 12-, 14-, and 16-infinitenes are also compared with the corresponding isomeric circulenes and carbon nanobelts. Further, the strain in all such systems is evaluated by considering isomeric planar benzenoid hydrocarbons as reference systems. The 12-infinitene turns out to be the most aromatic and the least strained among all the systems examined.

3.2 Introduction

The ability to form different allotropes makes the carbon atom versatile, leading to the numerous new structures with unique physical, chemical, and biological properties.[1-4] In recent years, there have been significant advancements in the chemistry of nanocarbon structures, which have emerged as fascinating materials with potential applications in science and technology.[5] Among the various nanocarbon structures, cycloparaphenylene,[6, 7] cycloarenes, carbon nanobelt,[8-12] helical nanographene,[13, 14] graphene nanoribbon,[15, 16] and chiral π-conjugated macrocycle[17] have received significant attention. Furthermore, many attractive molecular carbon scaffolds[19-20] have been introduced, and subjected to theoretical and experimental investigations.[18] The unique helical structure and inherent chirality of helicenes are utilized in asymmetric catalysis, molecular machines, molecular recognition, molecular self-assemblies, organic functional materials, *etc*.[19-22] Circulenes have also been explored in detail due to their potential optoelectronic properties. However, molecules combining circulenes and helicenes are not yet known.

Krzeszewski *et al.*[23] recently synthesized a simple and unique helically twisted figure-eight carbon nanobelt, a condensed form of 12-benzene rings. The structure of this system can be viewed as a fusion of one homo-6-helicene unit with its chiral counterpart at their terminal rings and is regarded as "12-infinitene". Moreover, 12-infinitene belongs to the "$C_{48}H_{24}$" family and could be looked upon as a twisted helical isomer of 12-circulene. It was named infinitene due to its close resemblance of its helically twisted structure to the infinity symbol. This could be regarded as a new class of molecules in the history of carbon nanostructures.[11, 24-26] Christoph *et al.*[27] reported saddle-shaped 12-circulene created by the fusion of two 6-helicenes in head-to-head and tail-to-tail fashion. But 12-infinitene is the first example of a completely conjugated, helically twisted circulene, which has been successfully synthesized. Orozco-lc *et al.*[28] brought out the aromaticity of 12-infinitene using magnetically induced current density and the induced magnetic field analysis. Monaco *et al.*[29] studied the origin-independent current density induced by a perpendicular magnetic field in the infinitene molecule[29] that well-support the findings by Orozco-Ic *et al.* Further, the properties of infinitene have been explored by various research groups.[30]

Additionally, Fan *et al.*[30] synthesized chiral-twisted-figure-eight carbon nanobelts that could be used for material applications. The non-planarity of 12-infinitene raises a question regarding the distribution of 48π-electrons over 70 CC bonds for conserving its aromatic character. Also, there is a question whether the nature of aromaticity exhibited by the system is Hückel-type[31] or Möbius-type. Surprisingly, infinitene does not satisfy the Hückel or Möbius aromaticity criteria. Hence a detailed study is required for exploring its π-electron delocalization pathway and aromaticity.

An in-depth analysis of the electronic distribution in molecular systems helps to understand their chemical bonding, stability, reactivity, interactive behavior, aromatic character, and optoelectronic applications. The analysis based on MESP[32-34] is regarded as one of the most effective tools for understanding the localization/delocalization behavior of the electrons and predicting the chemical reactivity of the molecular systems. The MESP, $V(\mathbf{r})$, at any point in space, is a real physical quantity that shows the combined effect of nuclear and electronic charge distribution of molecular systems.[35, 36] The most negative, three-dimensional potential minimum (V_m) in MESP topology analysis indicates the electron-rich sites such as lone pairs and π-regions.[37] The present study uses MESP topology analysis for the systematic investigation to interpret the intrinsic π-electron distribution and aromatic character in infinity-shaped molecules and their isomeric counterparts, *viz.* benzenoid circulenes and benzenoid nanobelts.

3.3 Methodology

All the infinitene systems and other molecules explored in the study are optimized using DFT based B3LYP/6-311G(d,p) method[38, 39] as implemented in Gaussian16 program package.[40] The optimized geometries are checked for their minimal nature by doing a frequency run and verifying that all the harmonic frequencies are real. The DAMQT (Deformed Atoms in Molecules Quantum Theory) package is used to perform the MESP topology computation.[41-44] Among the (3, +3), (3, +1), (3, -1), and (3, -3) CPs of MESP, the present investigation has been focused on the characteristics of (3, +3) CPs, which appear at the electron-dense regions.[45] We use the notation V_m to represent the (3, +3) local minimum. Typically, V_m corresponds

to the most negative-valued $V(\mathbf{r})$. The total deviation of λ values of a given system from that for benzene, *viz.* $\Delta\lambda_1$, $\Delta\lambda_2$, and $\Delta\lambda_3$ (Eq. 3.1) has been proposed for distinguishing the aromatic, non-aromatic, and anti-aromatic C-C bonded π-regions in molecules.[53] The value of $\sum_{i=1}^{3} \Delta\lambda_i \leq 0.011$ au has recently been suggested for aromatic behaviour, while a value between 0.011 to 0.035 au is recommended for identifying the non-aromatic character, and a value above 0.035 au is proposed for anti-aromatic nature.[46]

$$\sum_{i=1}^{3} \Delta\lambda_i = (\lambda_{1(sys)} - \lambda_{1(benz)}) + (\lambda_{2(sys)} - \lambda_{2(benz)}) + (\lambda_{3(sys)} - \lambda_{3(benz)}) \qquad \text{Eq. 3.1}$$

3.4 Results and Discussion

3.4.1 12-Infinitene

The 12-infinitene system can be envisaged as a fused form of two 6-helicene units (6-helicene-*a* and 6-helicene-*b*) through ring fusions at the end portions. Figure 3.1 depicts its structure, wherein the two 6-helicene units are denoted using different color codes. In the top view of the structure (Figure 3.1a), a naphthalene unit (carbon centers C1 - C10) of 6-helicene-*a* appears as superimposed over another such unit from helicene-*b* (carbon centers C1' - C10'). The shortest distance of 3.00 Å is seen between C9 and C9' and between C10 and C10'. The longest groove distance, 3.67 Å, is noticed for C2...C2', C3...C3', C6...C6', and C7...C7'. The X-ray structure of this molecule showed C9...C9' and groove distances of 2.92 and 3.64 Å, respectively. This

(a)   (b)   (c)
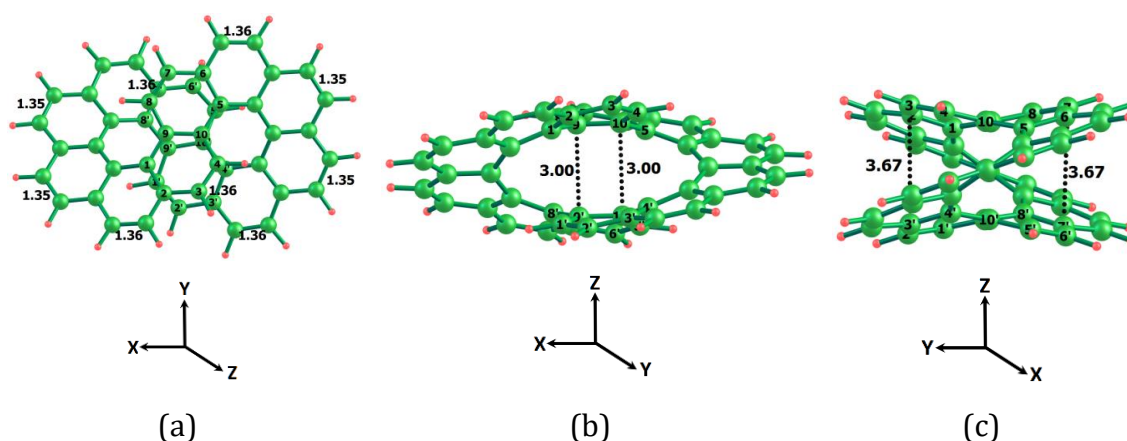
Figure 3.1 The optimized geometry of 12-infinitene at the B3LYP/6-311G(d,p) level. The distances between the carbon centers are given in Å
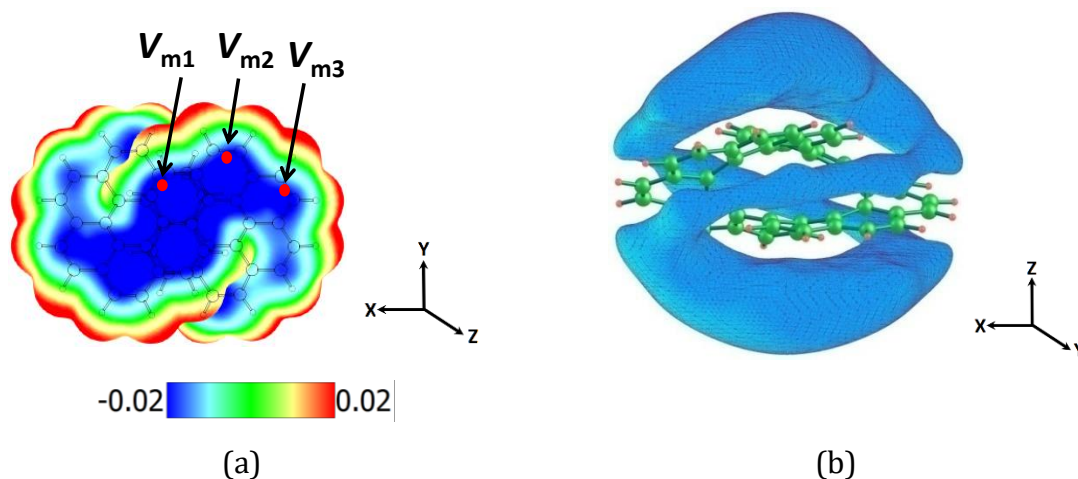
Figure 3.2 (a) MESP-textured electron density isosurface of value 0.001 au for 12-infinitene at the B3LYP/6-311G(d,p) level. Colour coding from blue to red indicates MESP values in the range −0.02 to 0.02 au and (b) The MESP isosurface is mapped at −0.01 au, where positions of MESP minima are denoted using red dots

is also borne out by the theoretical data.[23] The MESP textured on the 0.001 au (atomic unit) electron density isosurface in Figure 3.2(a) brings out the infinity-shape of the electron distribution over the aromatic rings. The MESP topology features of 12-infinitene in Figure 3.2(b) show three distinct MESP minima, V_{m1}, V_{m2}, and V_{m3}, appearing above the symmetrically dissimilar C-C bonds. The convex-armchair edges (K-regions) characterized by the presence of a V_m is more localized than others and is represented using double bonds with red color in Figure 3.1a (a total of 12 such bonds).[47] The armchair periphery in infinitene attributes more resonance stabilization for it.[48] The Clar's sextet-like electronic arrangement in armchair-edged systems reported by Rakhi and Suresh is well discernible here.[49] This feature is also evident from their bond lengths (1.35 to 1.36 Å), and other bond lengths, which lie in the range of 1.42 to 1.48 Å (Figure 3.1a). The X-ray crystal structure data show a range of 1.33 to 1.36 Å for the shorter C-C bonds and 1.40 to 1.48 Å for the longer ones. For a representation of the molecule using alternate single and double bonds, the positions of the red-colored double bonds automatically fix the position of other double bonds. Thus, MESP topology suggests a chemical formula for 12-infinitene as given in Figure 3.3a.[23] The 12-infinitene can also be represented as a resonance hybrid of two Clar's sextet structures (Figure 3.3b). Such a representation suggests

137

that the π-electrons of the C-C bond at the 6-6 ring fusion is almost equally shared by both the rings.

(a) (b)

Figure 3.3 (a) The MESP topology pattern and (b) resonance structures of 12-infinitene. The V_m positions associated with double bonds are shown in red

Table 3.1 MESP topology features of benzene and 12-infinitene at the B3LYP/6-311G(d,p) level (V_m values in kcal/mol and the eigenvalues in au)

| V_m type | MESP | eigenvalues | | | $\sum_{i=1}^{3} \Delta\lambda_i$ |
		λ_1	λ_2	λ_3	
$V_{m\text{-benzene}}$	-17.0	0.0166	0.0027	0.0005	0.0000
V_{m1}	-19.2	0.0180	0.0065	0.0049	0.0095
V_{m2}	-16.2	0.0166	0.0056	0.0042	0.0066
V_{m3}	-14.5	0.0170	0.0061	0.0047	0.0079

The three eigenvalues (λ_1, λ_2, and λ_3) for each V_m and the respective MESP values are given in Table 3.1. Among the three distinct V_m values of 12- infinitene, the V_{m1} corresponds to the most localized π-bond with a minimum value of -19.2 kcal/mol, which is more negative compared to the V_m of benzene, *viz*. -17.0 kcal/mol. But, V_{m2} and V_{m3} are less negative than that of benzene with minimum values of -16.2 and -14.5 kcal/mol, respectively. Similarly, the eigenvalues of V_{m1}, V_{m2} and V_{m3} show a small variation vis-à-vis the V_m value of benzene. The total deviation in the eigenvalues, $\sum_{i=1}^{3} \Delta\lambda_i$, reflects the resemblance of the aromatic character of the system to that of benzene. The previous study stipulated that the eigenvalue deviation parameter $\sum_{i=1}^{3} \Delta\lambda_i$ is ≤ 0.011 au for the all aromatic systems, lies between 0.011 to 0.035 au for all non-aromatic systems and above 0.035 au for anti-aromatic systems. In 12-infinitene, the $\sum_{i=1}^{3} \Delta\lambda_i$ values corresponding to each V_m is positive and they fall in the

range 0.0066 to 0.0095 au. This data clearly indicate that the extent of π-electron delocalization ingrained in each ring of infinitene is only slightly lower than that of benzene. Typically, polycyclic benzenoid hydrocarbons show a diminished aromatic character than that of benzene.[50-52] Further, the criterion of $\sum_{i=1}^{3} \Delta\lambda_i$ also supports Clar's representation of infinitene system (Figure 3.3b) wherein the ring with numerically small deviation in the sum of eigenvalues constitutes an aromatic sextet. The clockwise current density vector at the isosurface plotted at 0.025 au (Figure 3.4) using anisotropy-induced current density (ACID)[53] shows the diatropic ring current induced by the external magnetic field which confirms the aromatic character of 12-infinitene.[54] The 12-infinitene and the planar circulene system Kekulene are isomers wherein 12-infinitene is thermodynamically less stable than Kekulene[24] by 60.1 kcal/mol, which is equivalent to ~1.0 kcal/mol destabilization per C-C bond. Also, compared to the more strained isomeric [6, 6]-carbon nanobelt, 12-infinitene is more stable by 49.1 kcal/mol.

| 8- | 10- | 12- | 14- | 16- |
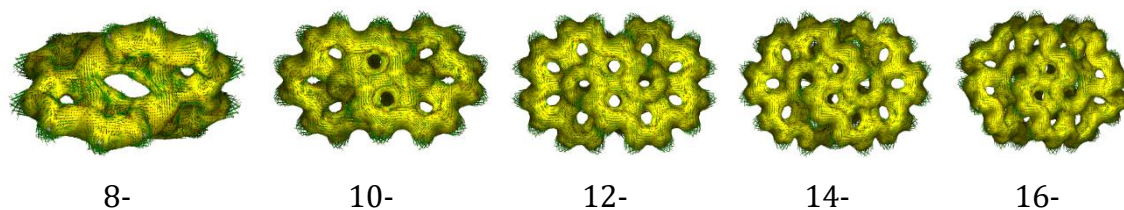
Figure 3.4 The ACID plot of infinitenes at isosurface value 0.025 au

3.4.2 8-, 10-, 14- and 16-Infinitenes: Structure and MESP topology

The infinitene-shaped molecules comprising of 8-, 10-, 14-, and 16- fused benzene rings are also analyzed for their structure, MESP topology features, π-electron distribution and aromatic character. In 8-infinitene, the shortest non-bonded distance of 3.13 Å is seen for C9...C9' and C10...C10' for the superimposed 'naphthalene-type' region as seen from the top. The longest groove distance of 4.82 Å is observed between C3...C1' and C4...C2' (Figure 3.5a). In 10-infinitene, the shortest CC distance (C9...C9' and C10...C10') and longest groove distance (C3...C2') are 2.96 and 4.08 Å, respectively.
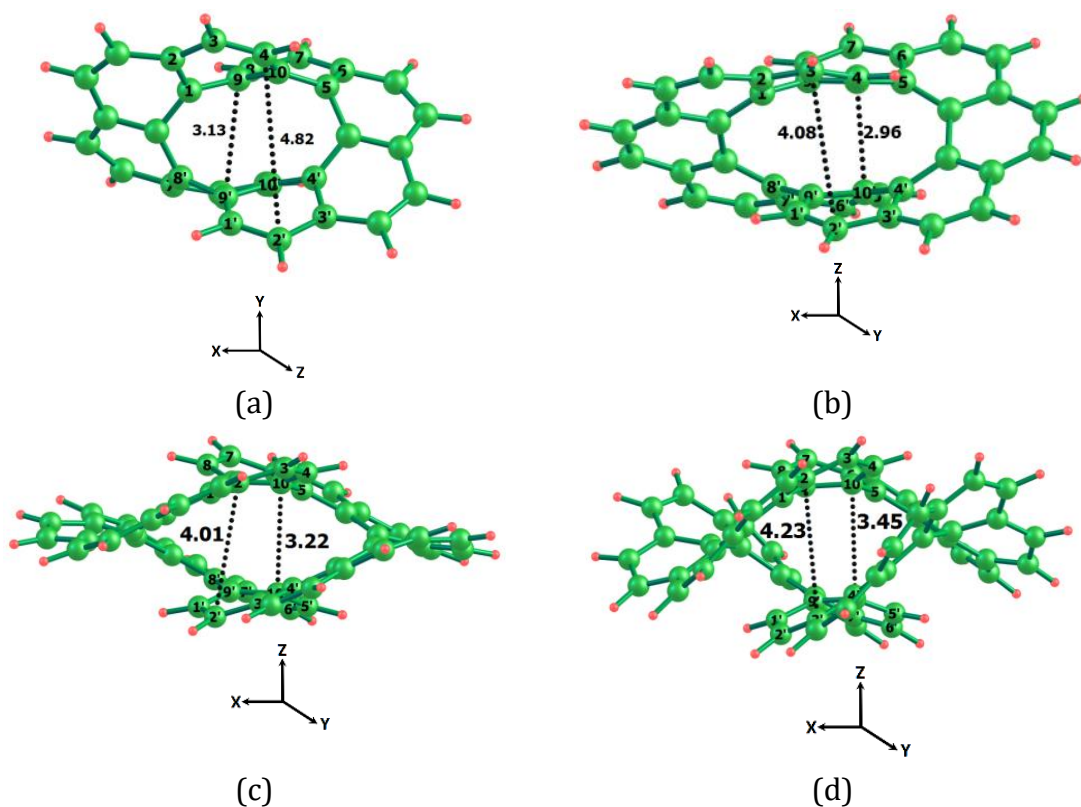
Figure 3.5 Optimized geometries of (a) 8- (b) 10-, (c) 14- and (d) 16-infinitene. The marked distances are in Å

Similarly, the shortest CC distance (C9...C9' and C10...C10') and longest groove distance (C2...C2') in 14-infinitene are 3.22 and 4.01 Å, respectively. The 16-infinitene appeared as the most twisted with shortest C...C distance of 3.45 Å and longest groove distance of 4.23 Å. The MESP data and trends in eigenvalues are displayed in Table 3.2. The MESP plotted on the 0.001-valued isodensity surface (Figure 3.6) clearly brings out the infinity-shape of the electron distribution in 8-, 10-, 14- and 16-infinitenes. The MESP analysis exhibits four MESP minima *viz.* V_{m1}, V_{m2}, V_{m3} and V_{m4} indicating symmetrically non-equivalent π-localized regions of C-C bonds in 8-infinitene. The bonds with considerable double bond character are ~1.39 Å in length, while the other bonds appear in the range 1.40 to 1.46 Å. The $\sum_{i=1}^{3} \Delta\lambda_i$ corresponding to the V_m suggest high non-aromatic character associated with the benzene rings. Similarly, in 10-infinitene, the V_{m1}, V_{m2}, and V_{m3} correspond to relatively more localized π-regions in the molecule with C-C bond lengths lying between 1.37 to 1.38 Å. The $\sum_{i=1}^{3} \Delta\lambda_i$ value

140

for both V_{m1} and V_{m3} is greater than the aromatic cut-off value 0.011 au, while very close to that for V_{m2}.

(a)

(b)

(c)

(d)

-0.02 ▮▮▮▮▮▮ 0.02
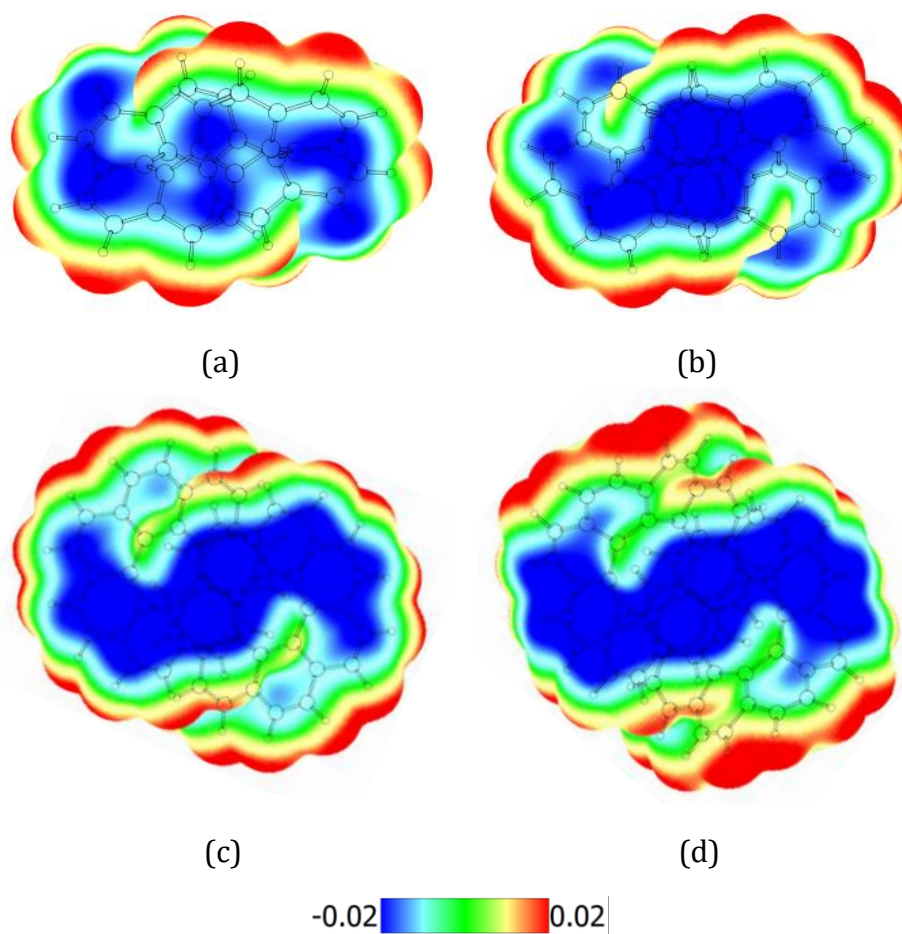
Figure 3.6 MESP textured on 0.001 au-valued electron density isosurface for (a) 8- (b) 10-, (c) 14- and (d) 16-infinitene at the B3LYP/6-311G(d,p) level. Colour coding from blue to red indicates MESP in the range −0.02 to 0.02 au

These data suggest the dominance of non-aromatic character over aromatic one for all the rings in 10-infinitene. Among the four distinct MESP minima *viz.* V_{m1}, V_{m2}, V_{m3} and V_{m4} observed for 14-infinitene, the $\sum_{i=1}^{3} \Delta\lambda_i$ data indicates an aromatic character for rings labeled with V_{m2}, V_{m3}, and V_{m4} and non-aromatic for other one. Similarly, in 16-infinitene, V_{m2} has the highest $\sum_{i=1}^{3} \Delta\lambda_i$ value which brings out the non-aromatic behaviour associated with the corresponding ring while rings embedded with V_{m1}, V_{m3}, and V_{m4} are expected to be aromatic. The non-aromatic V_m rings to be easily exposed for addition reactions and a few examples on transition state models for HCl

Table 3.2 Detailed MESP topology features of 8-, 10-, 12-, 14- and 16-infinitenes at the B3LYP/6-311G(d,p) level of theory (V_m values in kcal/mol and eigenvalues in au)

System	V_m type	MESP	eigenvalues			$\sum_{i=1}^{3} \Delta\lambda_i$
			λ_1	λ_2	λ_3	
8_infinitene	V_{m1}	-19.2	0.0180	0.0065	0.0049	0.0095
	V_{m2}	-17.6	0.0230	0.0087	0.0073	0.0190
	V_{m3}	-17.5	0.0234	0.0085	0.0075	0.0195
	V_{m4}	-17.3	0.0136	0.0056	0.0032	0.0025
	V_{m5}	-15.4	0.0200	0.0081	0.0066	0.0148
	V_{m6}	-14.8	0.0170	0.0074	0.0057	0.0102
	V_{m7}	-12.9	0.0267	0.0090	0.0071	0.0229
	V_{m8}	-11.0	0.0338	0.0160	0.0002	0.0302
10_infinitene	V_{m1}	-22.0	0.0167	0.0114	0.0053	0.0135
	V_{m2}	-17.4	0.0174	0.0063	0.0048	0.0086
	V_{m3}	-16.0	0.0183	0.0067	0.0054	0.0105
	V_{m4}	-14.5	0.0197	0.0071	0.0061	0.0130
	V_{m5}	-14.2	0.0100	0.0019	0.0005	-0.0075
	V_{m6}	-13.9	0.0226	0.0081	0.0067	0.0175
12-infinitene	V_{m1}	-19.2	0.0180	0.0065	0.0049	0.0095
	V_{m2}	-18.1	0.0387	0.0050	0.0036	0.0274
	V_{m3}	-16.2	0.0166	0.0056	0.0042	0.0066
	V_{m4}	-15.9	0.0100	0.0014	0.0007	-0.0079
	V_{m5}	-14.5	0.0170	0.0061	0.0047	0.0079
	V_{m6}	-13.1	0.0198	0.0072	0.0062	0.0133
14-infinitene	V_{m1}	-20.3	0.0185	0.0067	0.0053	0.0106
	V_{m2}	-18.8	0.0392	0.0040	0.0008	0.0242
	V_{m3}	-17.4	0.0178	0.0061	0.0049	0.0089
	V_{m4}	-16.7	0.0114	0.0020	0.0005	-0.0060
	V_{m5}	-15.6	0.0112	0.0016	0.0012	-0.0058
	V_{m6}	-14.6	0.0151	0.0048	0.0030	0.0030
	V_{m7}	-14.4	0.0170	0.0066	0.0046	0.0084
	V_{m8}	-12.1	0.0252	0.0086	0.0064	0.0203
16-infinitene	V_{m1}	-18.4	0.0189	0.0067	0.0056	0.0113
	V_{m2}	-17.7	0.0135	0.0026	0.0005	-0.0034
	V_{m3}	-17.4	0.0122	0.0019	0.0011	-0.0047
	V_{m4}	-16.4	0.0132	0.0027	0.0010	-0.0030
	V_{m5}	-16.0	0.0153	0.0048	0.0027	0.0029
	V_{m6}	-15.7	0.0154	0.0054	0.0033	0.0042
	V_{m7}	-13.8	0.0131	0.0037	0.0016	-0.0015
	V_{m8}	-12.3	0.0224	0.0090	0.0061	0.0176

Table 3.3 The bond length alternation (BLA in Å) for infinitenes at B3LYP/6-311G(d,p) level of theory

Infinitene	V_m point	V_m	longest CC	shortest CC	BLA
8-infinitene	V_{m1}	-17.5	1.46 1.44	1.39	0.06
	V_{m2}	-15.4	1.45 1.45	1.39	0.06
	V_{m3}	-14.8	1.45 1.45	1.39	0.07
	V_{m4}	-12.9	1.43 1.44	1.39	0.04
10-infinitene	V_{m1}	-22.0	1.43 1.43	1.37	0.06
	V_{m2}	-16.0	1.43 1.43	1.38	0.06
	V_{m3}	-14.5	1.43 1.43	1.38	0.05
12-infinitene	V_{m1}	-19.2	1.42 1.42	1.36	0.06
	V_{m2}	-16.2	1.42 1.42	1.36	0.06
	V_{m3}	-14.5	1.42 1.42	1.35	0.07
14-infinitene	V_{m1}	-20.3	1.42 1.42	1.36	0.06
	V_{m2}	-17.4	1.41 1.42	1.35	0.07
	V_{m3}	-14.6	1.41 1.42	1.35	0.07
	V_{m4}	-14.4	1.42 1.42	1.34	0.08
16-infinitene	V_{m1}	-23.3	1.41 1.42	1.36	0.05
	V_{m2}	-19.5	1.41 1.42	1.35	0.07
	V_{m3}	-16.0	1.41 1.42	1.35	0.07
	V_{m4}	-15.7	1.42 1.42	1.35	0.07

addition is given in Figure 3.7. Though all the systems showed infinity-shaped π-electron conjugation, the $\sum_{i=1}^{3} \Delta\lambda_i$ data clearly suggest non-aromatic character for many of the rings in them. The non-uniformity in the π-conjugation at C-C bonds in all the infinitene systems is clearly reflected in the bond length alternation (BLA) as well[30, 55] (Table 3.3). In general, BLA data support aromatic character for all the infinitenes.
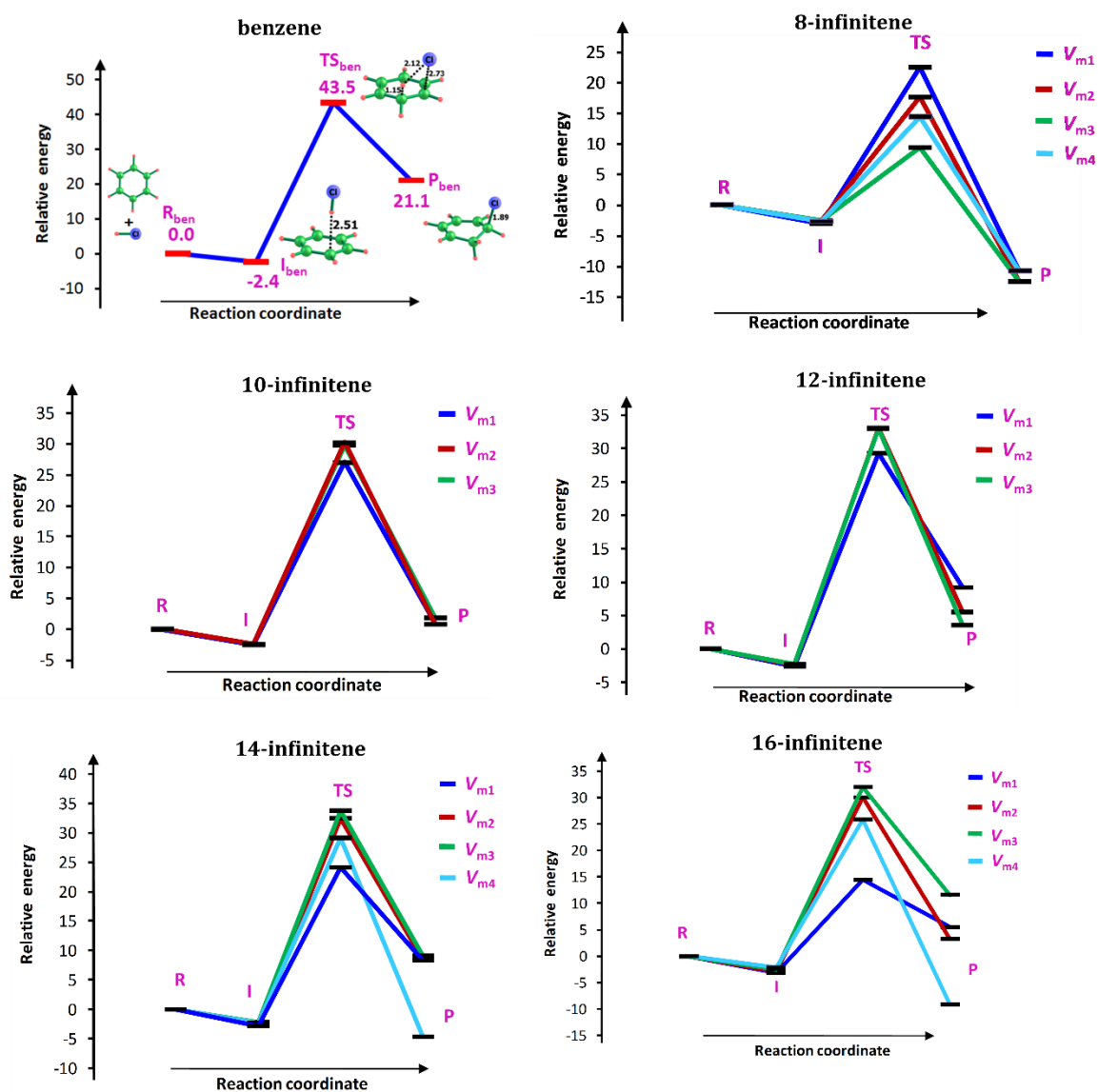
Figure 3.7 Energy profile for the addition of HCl across C=C bond in benzene, 8-, 10-, 12-, 14-, and 16-infinitene. The notations R, I, TS and P are used to denote the reactant, intermediate, transition state and product respectively. The royal blue, maroon, green and aqua blue respectively indicate the relative energy for the addition of HCl across the V_{m1}, V_{m2}, V_{m3} and V_{m4} associated double bonds. Energy values are given in kcal/mol.

144

3.4.3 Circulenes, Carbon Nanobelts and Infinitenes: Relative Stability

(a) Circulene
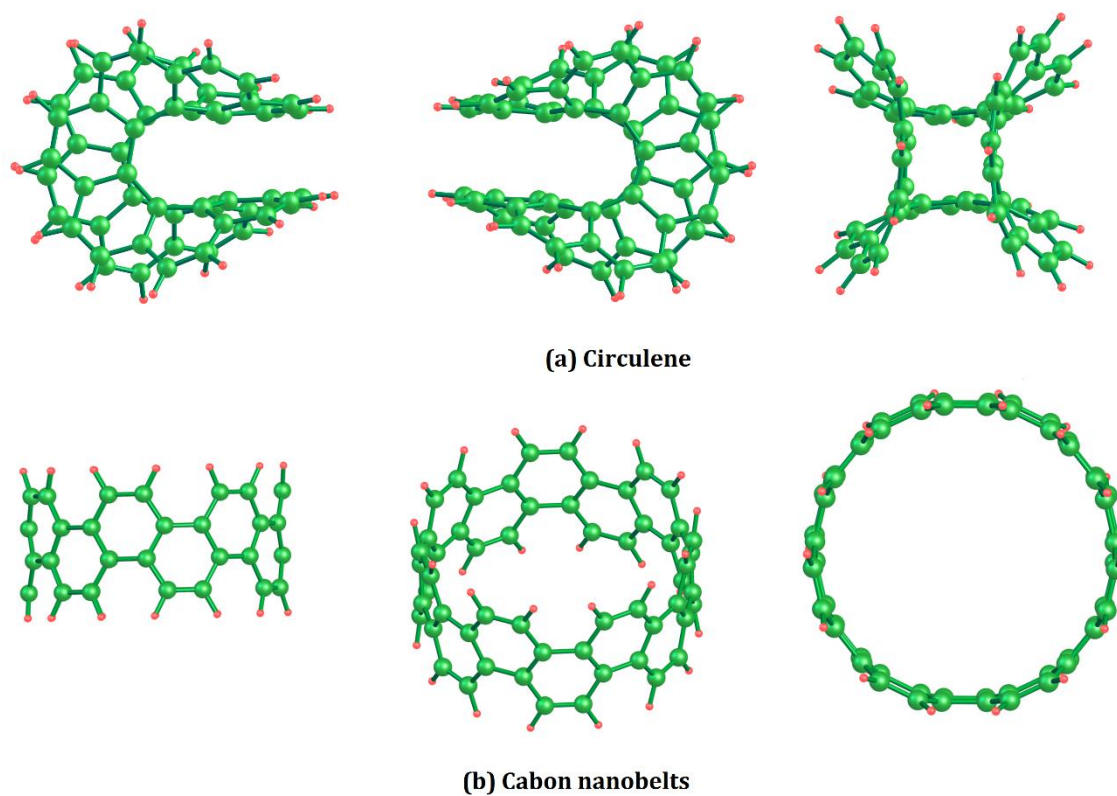
(b) Cabon nanobelts

Figure 3.8 (a) Optimized geometries of saddle-shaped 14-circulene and (b) 14-carbon nanobelts at the B3LYP/6-311G(d,p) level

Circulenes are macrocyclic arene systems for which the central n-sided ring is completely surrounded by benzenoids.[56] So far, the synthesis of different circulene systems consisting of 4-, 5-, 6-, 7- and 8- fused benzene rings has been reported by various research groups wherein only 5-, 6-, 7-circulenes have been synthesized without substituents.[57] Among them, 4-circulene (quadrannulene)[27, 58, 59] and 5-circulenes (corannulene)[60-62] appear bowl-shaped, while 6-circulene (coronene)[63] is endowed with a planar geometry. A saddle- shaped geometry is shown by 7- circulene (pleiadannulene)[25, 64, 65] and 8-circulenes.[66, 67] The 8-circulene is the largest circulene synthesized so far, and the synthesis of several of its derivatives is reported by different groups.[57, 66-71] Hopf and co-workers predicted the shape and strain energy of n-circulenes (where n = 3 to 20) based on a computational study.[27] According to them, the circulenes from n= 7 to 16 are saddle-shaped and those from n= 17 to 20 are

helics-shaped. The belt-shaped compounds, exclusively composed of fused benzene rings are regarded as carbon nanobelts (CNB) and have been used as a powerful gem for the synthesis of carbon nanotubes. A belt segment of armchair [6, 6]-CNT comprising of 12-arene rings (12-CNB) synthesized by Povie et al.[11] was the first member from the carbon nanobelt family. Later, higher members of CNBs of various sizes and shapes were reported by various research groups.[10, 13, 72-76]There are CNBs containing non-benzenoid rings[77-80] and hetero-atoms,[78, 81, 82] wherein the incorporation of hetero atoms radically alters the electronic properties of belts, leading to diverse applications in functional materials.
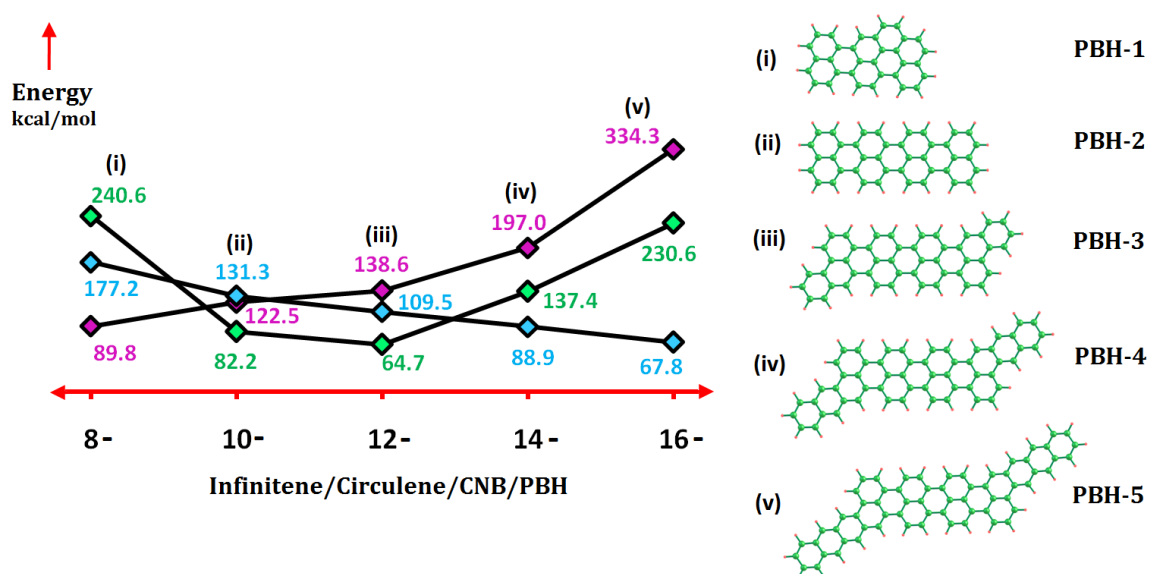
Figure 3.9 Energy of circulenes, belts and infinitenes relative to their planar PBH counterparts at the B3LYP/6-311G(d,p) level. Magenta, blue and green marks respectively indicate circulenes, belts and infinitenes

Circulenes, carbon nanobelts and infinitenes made up of n-benzenoid rings (represented with the molecular formula $C_{2n}H_n$) are isomers. They are expected to show π-electron distribution and aromaticity features characteristic to their unique structure. Circulenes show a saddle shape, with negative curvature and Figure 3.8 depicts the geometry of a representative example, 14-circulene. From 8-circulene to 16-circulene, the depth of the curved region increases, which indicates increasing strain effect in higher circulenes. A $C_{2n}H_n$ polycyclic benzenoid hydrocarbon (PBH) in

planar configuration is expected to be more stable than the isomeric circulene, CNB and infinitene mainly due to the least strain effect in planar state.
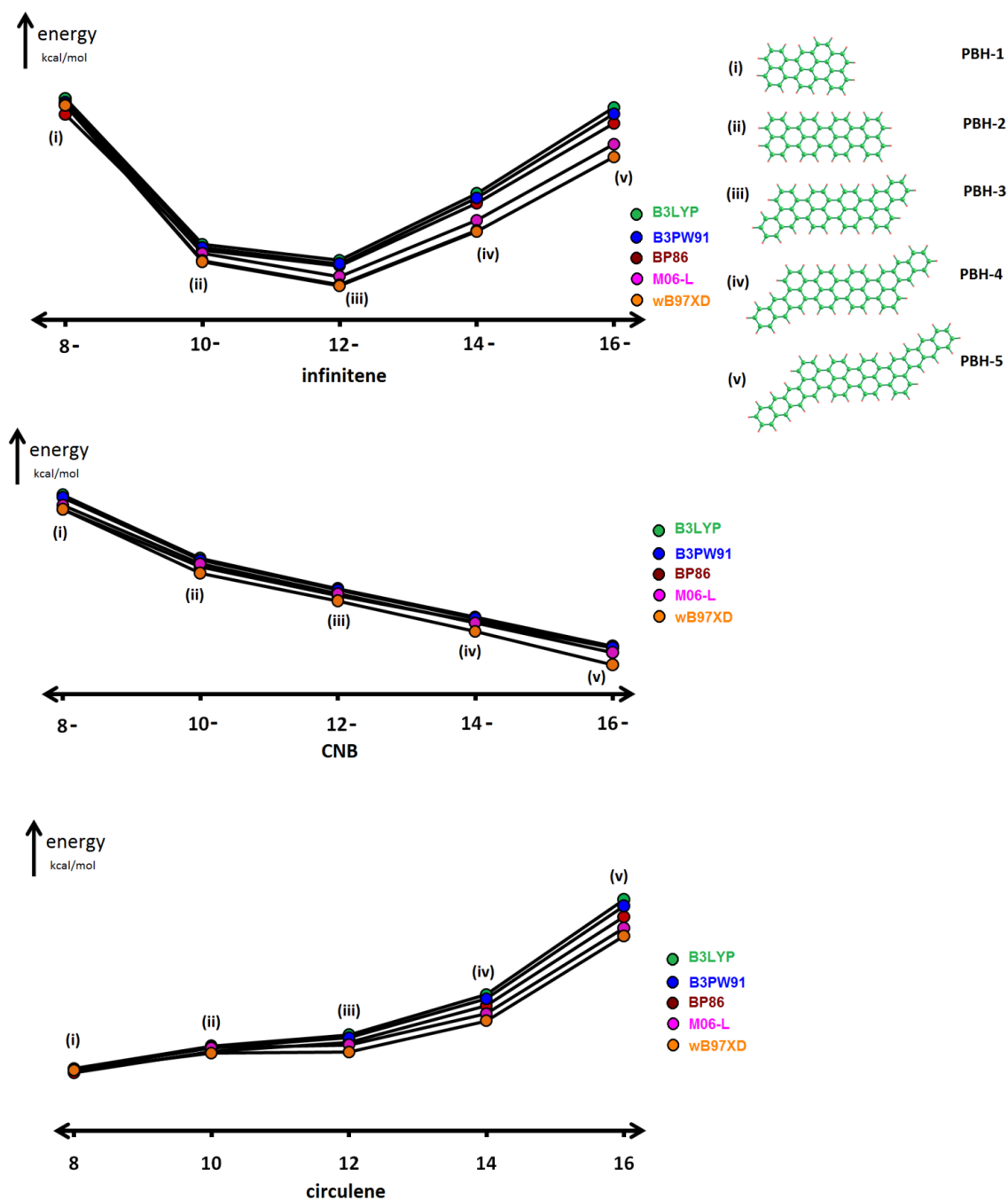
Figure 3.10 Energy of infinitenes, CNBs and circulenes relative to their planar PBH counterparts using different DFT methods

In Figure 3.9, the energies of 8-, 10-, 12-, 14- and 16-circulene/infinitene/nanobelts are compared relative to the energy of PBH systems,

viz. PBH-1, PBH-2, PBH-3, PBH-4 and PBH-5 which correspond to the molecular formulae $C_{32}H_{16}$, $C_{40}H_{20}$, $C_{48}H_{24}$, $C_{56}H_{28}$, and $C_{64}H_{32}$, respectively. The Figure 3.9 clearly shows that in the case of nanobelts, as the radius of the belt increases, stability of the system increases due to the decrease in strain energy. A strong linear trend in energy change is observed for this series. Exactly opposite trend in stability is observed for the n-circulenes as the strain effect increases substantially with increase in 'n'. In the case of infinitenes, the 8-infinitine shows the highest energy difference compared to the isomer PBH-1 whereas 12-infinitene shows the least energy difference compared to the isomer PBH-3. The relative energy data in Figure 3.9 also show that 10- and 12-infinitenes are significantly more stable than the corresponding nanobelts and circulenes whereas stability order for others is 8-infinitene < 8-CNB < 8-circulene; 14-circulene < 14-infinitene < 14-CNB and 16-circulene < 16-infinitene < 16-CNB. Among all the non-planar structures, 12-infinitene is the most stable one. Though the absolute values of the SCF energy and MESP parameters differ to some extent, the relative order and the trend in values are almost identical in all the cases (Figure 3.10). Hence, only the B3LYP/6-311G(d,p) values are discussed here.

3.4.4 Circulenes and Carbon Nanobelts: MESP Topology

Table 3.4 shows the MESP topology parameters such as the V_m value and eigenvalue parameter $\sum_{i=1}^{3} \Delta\lambda_i$ for circulenes and CNBs. The $\sum_{i=1}^{3} \Delta\lambda_i$ values indicate largely aromatic character for these systems, akin to that of benzene for all the benzenoid rings of circulenes. In 8-, 10- and 12-circulenes, V_m points showing $\sum_{i=1}^{3} \Delta\lambda_i > 0.01$ au are noticed at the curved regions. Since MESP at the curved region is influenced by π-regions of rings from above and below, high magnitude of $\sum_{i=1}^{3} \Delta\lambda_i$ need not necessarily indicate non-aromatic character as the CC bonds observed at these regions similar to those for the other regions. But, it can be attributed the localization of electron density between the two benzene rings at the curved regions.

Table 3.4 Detailed MESP topology features of 8-, 10-, 12-, 14- and 16-circulenes and CNBs at the B3LYP/6-311G(d,p) level (V_m values in kcal/mol and eigenvalues in au)

circulene	V_m type	MESP	$\sum_{i=1}^{3} \Delta\lambda_i$	CNB	V_m type	MESP	$\sum_{i=1}^{3} \Delta\lambda_i$
8-	V_{m1}	-17.6	-0.0120	8-	V_{m1}	-15.6	0.0160
	V_{m2}	-17.3	0.0063		V_{m2}	-15.2	-0.0087
	V_{m3}	-16.3	0.0087		V_{m3}	-13.7	0.0003
	V_{m4}	-14.0	0.0007				
10-	V_{m1}	-20.5	-0.0089	10-	V_{m1}	-13.1	0.0142
	V_{m2}	-20.1	0.0049		V_{m2}	-15.1	-0.0040
	V_{m3}	-19.0	0.0095		V_{m3}	-15.0	-0.0198
	V_{m4}	-18.3	0.0103		V_{m4}	-14.5	-0.0024
	V_{m5}	-16.9	0.0076				
	V_{m6}	-15.7	0.0039				
12-	V_{m1}	-21.7	0.0009	12-	V_{m1}	-15.0	-0.0023
	V_{m2}	-21.2	0.0232		V_{m2}	-14.8	0.0127
	V_{m3}	-19.8	0.0084		V_{m3}	-14.6	-0.0180
	V_{m4}	-18.9	0.0083		V_{m4}	-12.9	-0.0037
	V_{m5}	-18.0	0.0064				
	V_{m6}	-17.3	0.0053				
14-	V_{m1}	-22.2	0.0079	14-	V_{m1}	-15.0	-0.0010
	V_{m2}	-20.8	0.0036		V_{m2}	-14.6	0.0117
	V_{m3}	-20.0	-0.0081		V_{m3}	-14.4	-0.0166
	V_{m4}	-20.0	0.0068		V_{m4}	-12.7	-0.0046
	V_{m5}	-19.3	0.0063				
	V_{m6}	-18.4	0.0040				
	V_{m7}	-18.4	0.0030				
16-	V_{m1}	-22.8	0.0049	16-	V_{m1}	-14.8	0.0000
	V_{m2}	-21.7	-0.0056		V_{m2}	-14.4	0.0109
	V_{m3}	-21.2	0.0073		V_{m3}	-14.1	-0.0156
	V_{m4}	-20.9	0.0081		V_{m4}	-12.5	-0.0052
	V_{m5}	-19.7	0.0050				
	V_{m6}	-19.3	0.0018				
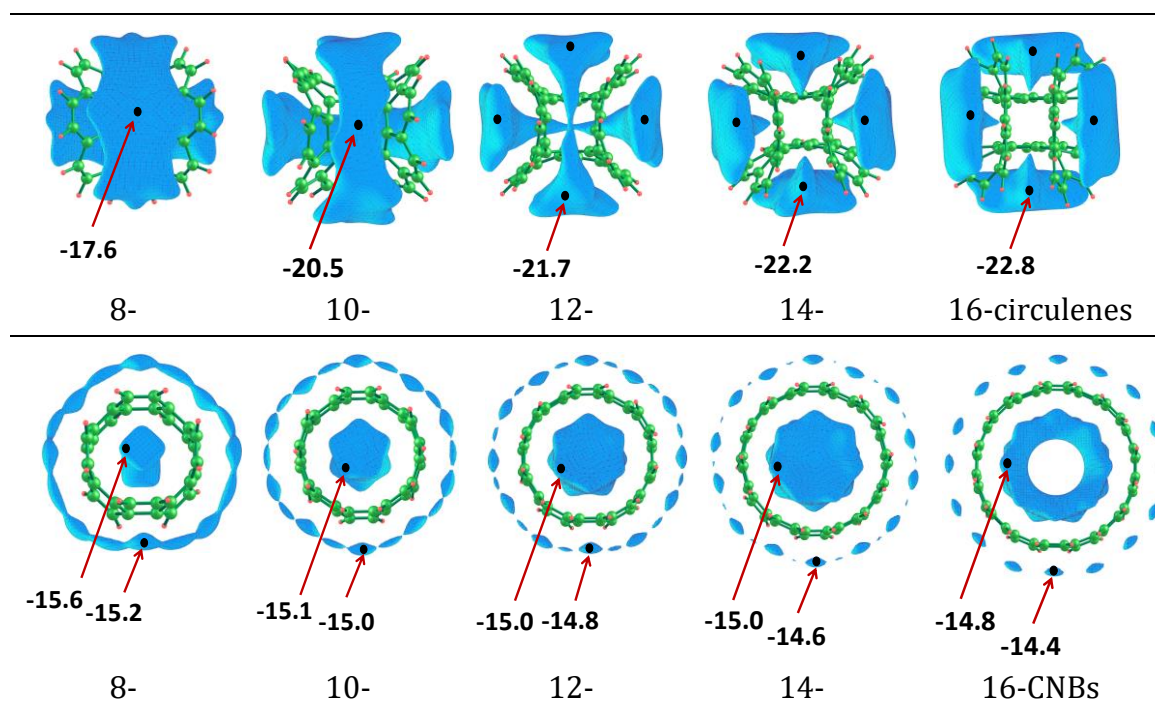
Figure 3.11 The MESP isosurfaces (value −0.02 au) of circulenes and CNBs. The most negative V_{m1} for circulenes and V_{m1} and V_{m2} values at the B3LYP/6-311G(d,p) level is given in kcal/mol

The $\sum_{i=1}^{3} \Delta\lambda_i$ data of CNBs clearly suggest that all the -HCCH- bonds of the CNB possess strong olefin character as the $\sum_{i=1}^{3} \Delta\lambda_i$ value of V_m observed at this region (inner/outer regions) is always higher than 0.01 au. Analysis of V_m values suggest that the MESP negative character gradually increases as the size of the circulene increases, whereas a slight decrease in the magnitude of MESP is observed with increase in the size of the CNBs. Further illustration of this MESP feature is evident from the MESP isosurface plots given in Figure 3.11. In circulenes, the curved-regions show accumulation of electron density and deeper is the curvature of the circulene, more localized and more negative is the MESP. In CNBs, the MESP distribution clearly distinguishes both the exterior and the interior regions. The interior MESP is more localized than the exterior one, whereas the absolute magnitudes of MESP at both the regions do not show significant deviations.

150

3.4.5 Infinitenes, Circulenes and Carbon Nanobelts: Distinction Based on Li⁺ Binding Affinity
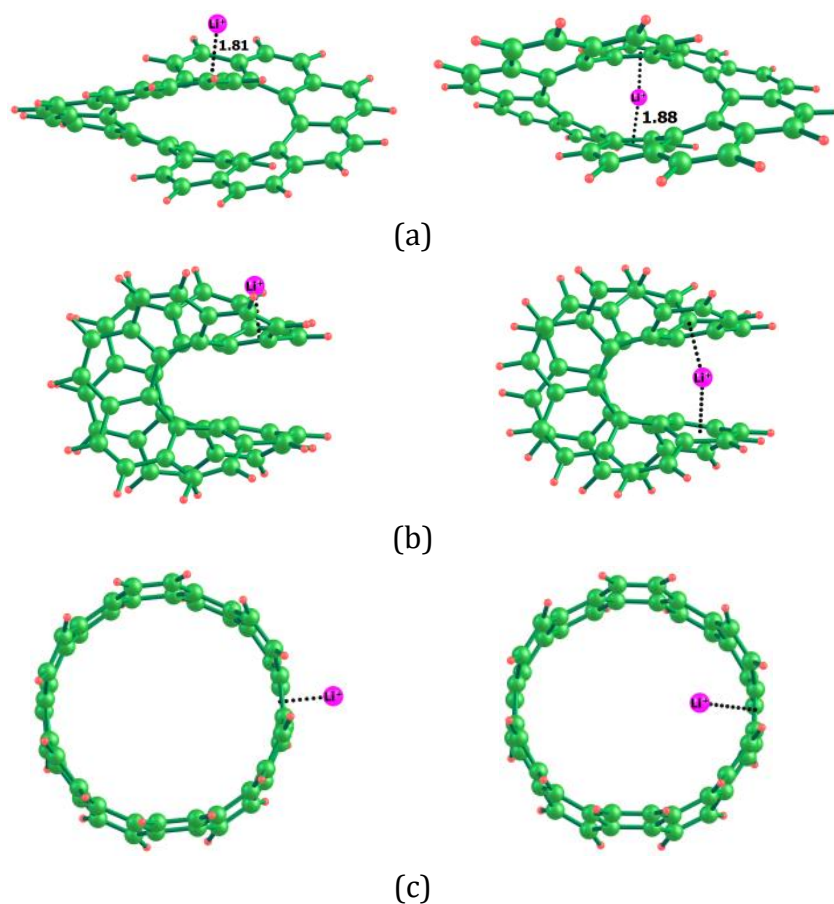
Figure 3.12 Binding of Li⁺ in the exterior- and interior- electron rich regions in (a) infinitene, (b) circulene and (c) CNB at the B3LYP/6-311G(d,p) level

The electron-rich characters of infinitene, circulene and CNB can be assessed by evaluating their strength of interaction with a cation such as Li⁺, since the electron rich sites are expected to show larger interaction than the other ones. The Li⁺ binding at the exterior (P1) and the interior (P2) electron rich regions in infinitene, circulene and CNB are depicted in Figure 3.12 and the binding energy data (B. E.) is given in Table 3.5. The Li⁺ complexes show significantly higher stability with infinitene-, circulene- and CNB-systems compared to aromatic systems such as benzene, naphthalene, anthracene, chrysene and pyrene. In all the cases, binding of cation at P2 is more stable wherein cation-π-interaction is supported by π-centers from multiple

rings whereas at P1, the binding is mostly directed towards one π-center. In infinitenes, the binding efficiency gradually increases with size of the system, whereas in circulenes, the binding strength increases up to 12-circulene and then decreases. In CNBs, the binding energy shows only a minor variation and their binding strength is significantly inferior to that of infintenes and circulenes. Among all the systems studied, the infinity-shaped systems appear as more effective for inducing cation-π interaction than others.

Table 3.5 Comparison of Li^+ binding in infinitene, circulene and CNB at exterior position (P1) and interior position (P2). Values are given in kcal/mol

system	B. E.	Infinitene/ Circulene/ CNB	B. E.					
			infinitene		circulene		CNB	
			P1	P2	P1	P2	P1	P2
benzene	-39.6	8	-52.2	-59.3	-53.8	-54.5	-49.6	-54.4
naphthalene	-42.3	10	-53.4	-63.9	-54.5	-67.5	-50.6	-51.8
anthracene	-44.7	12	-55.9	-66.0	-56.5	-69.3	-51.2	-50.9
chrysene	-45.9	14	-58.1	-69.3	-59.2	-70.2	-51.7	-52.3
pyrene	-45.8	16	-61.7	-72.5	-61.7	-64.0	-51.9	-52.4

3.5 Conclusions

The π-electron delocalization and aromatic character of recently synthesized 12-infinitene molecule is quantified in terms of MESP topology features. The MESP topology describes the double bond distribution in the system and provides a unique definition of the chemical formula that also supports Clar's aromatic sextet structure for each benzenoid ring. The possibility of other infinitenes containing 8-, 10-, 14- and 16- arene rings is also evaluated using DFT and the trend in π-electron delocalization as well as aromatic character is analyzed on the basis of the three eigenvalues (λ_i) of the Hessian matrix at the (3, +3) V_m critical points. Such a MESP topology-guided analysis confirms most of the benzene rings of infinitenes as aromatic, while non-aromatic localization is observed in a few. For all the cases, MESP distribution visualized in terms of isosurface plots clearly shows the infinity-shaped delocalization of the electron density that runs over all the fused benzene rings.

The eigenvalue parameter $\sum_{i=1}^{3} \Delta\lambda_i$ suggests that 12-infinitene to be highly aromatic while a strong localization of certain CC π-bonds induces slight non-aromatic character to other infinitenes. The stability of infinitenes is evaluated by comparing the energy of infinitenes relative to their isomeric planar PBH systems, circulenes and carbon nanobelts. The relative energy data reveals that 12-infinitene is not only the stable infinitene, but also the most stable system of all the systems, including nanobelts and circulenes. However, the stability order for other systems can be expressed as 8-infinitene < 8-CNB < 8-circulene; 10-infinitene < 10-circulene < 10-CNB; 14-circulene < 14-infinitene < 14-CNB and 16-circulene < 16-infinitene < 16-CNB. The MESP studies show that electron density is mostly accumulated at the curved-regions in circulenes and exterior regions in CNBs. The $\sum_{i=1}^{3} \Delta\lambda_i$ showed high aromatic character for all the benzenoid rings of circulenes, while all the -HCCH-bonds exhibit strong olefin character in CNBs. Also, the V_m data indicate that the MESP negative character gradually increases as the size of the circulene increases, while only a slight decrease in the magnitude of MESP is observed with increase in the size of the CNBs. Further, the electron-rich character of infinitene, circulene and CNB is evaluated by cation binding strength, wherein the infinity-shaped molecules were observed to possess greater cation-π interactions compared to circulenes and nanobelts. This study has brought out a MESP topological viewpoint of infinitenes, circulenes and nanobelts shedding light on the extent of π-conjugation, aromatic features and the stability ingrained in infinitenes compared to circulenes and nanobelts.

Part B

Utilization of Through-Space Effect to Design Donor-Acceptor Systems without Donors and Acceptors

3.6 Abstract

The MESP topology analysis reveals the underlying phenomenon of through-space effect (TSE), which imparts electron donor-acceptor properties to a wide range of chemical systems, including derivatives of pyrrole, indole, isoindole, azulene, and aniline. The TSE is inherent in pyrrole owing to strong polarization of electron density (PoED) from the formally positively charged N-center to the C_3C_4 bonding region. The $N \rightarrow C_3C_4$ directional nature of TSE has been effectively employed to design molecules with high electroni polarization, such as bipyrroles, polypyrroles, phenyl pyrroles, multi-pyrrolyl systems and N-doped nanographenes. In core-expanded structures, the direction of TSE from pyrrole units towards the core leads to highly electron-rich systems, while the opposite arrangement results in highly electron-deficient systems. Similarly, the MESP analysis reveals the presence of TSE in azulene, indole, isoindole, and aniline. Oligomeric chains of these systems are designed in such a way that the direction of TSE is consistent across each monomer, leading to substantial electronic polarization between the first and last monomer units. Notably, these designed systems exhibit strong donor-acceptor characteristics despite the absence of explicit donor and acceptor moieties, which is supported by FMO analysis, APT charge, NMR data and λ_{max}. Among the systems studied, the TSE of many experimentally known systems (bipyrroles, phenyl pyrroles, hexapyrrolylbenzene, octapyrrolylnaphthalene, decapyrrolylcorannulene, polyindole, polyazulene etc.) is unraveled for the first time, while numerous new systems (polypyrroles, polyisoindole, amino-substituted benzene polymer) are predicted as promising materials for the creation of donor-acceptor systems for optoelectronic applications. These findings demonstrate the potential of TSE in molecular design and provide new avenues for creating functional materials.

3.7 Introduction

When a molecule interacts with another one, or when it is excited, the electron density is transferred from the electron-rich molecule/site (donor, *D*) to the electron-deficient molecule/site (acceptor, *A*).[83-87] Typically, *D*s are conjugated molecules with high HOMO energy level, whereas *A*s are conjugated molecules with low LUMO energy level. A conjugated donor-acceptor (*D-A*) system is formed by linking *D* and *A* by a covalent bond or a spacer moiety.[88] *D-A* systems have found widespread applications in organic photovoltaic devices.[89] Many studies have recently been undertaken to characterize the mechanisms of *D-A* based charge-transfer processes in optoelectronic systems such as solar cells, light-emitting diodes (LEDs), organic photovoltaics (OPVs), field-effect transistors (FETs), conducting polymers, and so on.[90-92] Appropriate substitutions are used to fine-tune the donating effect of *D* and the accepting effect of *A*. Typical donors include +M/+I substituents such as -OH, -NH$_2$, -OR and -NR$_2$, or heterocyclic moiety such as thiophene, whereas typical acceptors include functional groups with -M/-I effects such as -NO$_2$, -CN, -CHO, -COOH, and their combinations.[93] N, N-dimethylamino- and nitro-/cyano- groups are the most potent *D* and *A* substituents, respectively.[94, 95] Planarization enhances the *D-A* effect by permitting effective conjugation (through-bond effect) between the *D* and *A* units.

Pyrrole (**P**), a five-membered aromatic N-heterocycle, is found in nearly all heterocyclic structures.[92] Pyrrole-derivatives have been widely used in the construction of organic semiconducting materials, conducting polymers, photovoltaics, fluorescent materials and FETs.[96-102] The six structural isomers of bipyrroles (²**P**) have been synthesized (Figure 3.13a).[102-119] Polypyrrole with C$_2$-C$_{2'}$ linkages (Figure 3.13b) is a well-known biocompatible conducting polymer,[106, 120] while polypyrroles constructed from C$_3$-N$_{1'}$ connections (Figure 3.13c) and C$_3$-C$_{2'}$ connections (Figure 3.13d) are yet to be reported. Due to their sterically bulky structure and exceptional optoelectric properties,[99, 121-127] a variety of multiple-pyrrolyl aromatic systems, such as hexapyrrolylbenzene[128, 129] (Figure 3.13e) and octapyrrolylnaphthalene,[129, 130] (Figure 3.13f) have been synthesized in the past and are considered as building blocks for bigger π-conjugated systems. Oki *et al.* recently reported the core-expanded, nonplanar, pyrrole-fused azacoronene with N-doped

heptagonal rings (Figure 3.13g, 3.13h) and presented a unique approach to synthesis N-doped nanographenes utilizing multiple-pyrrolyl polycyclic aromatic hydrocarbons.[125, 131] Xu *et al.* recently synthesized[132] decapyrrylcorannulene (Figure 3.13i) and demonstrated its application as a host for fullerenes.[133]
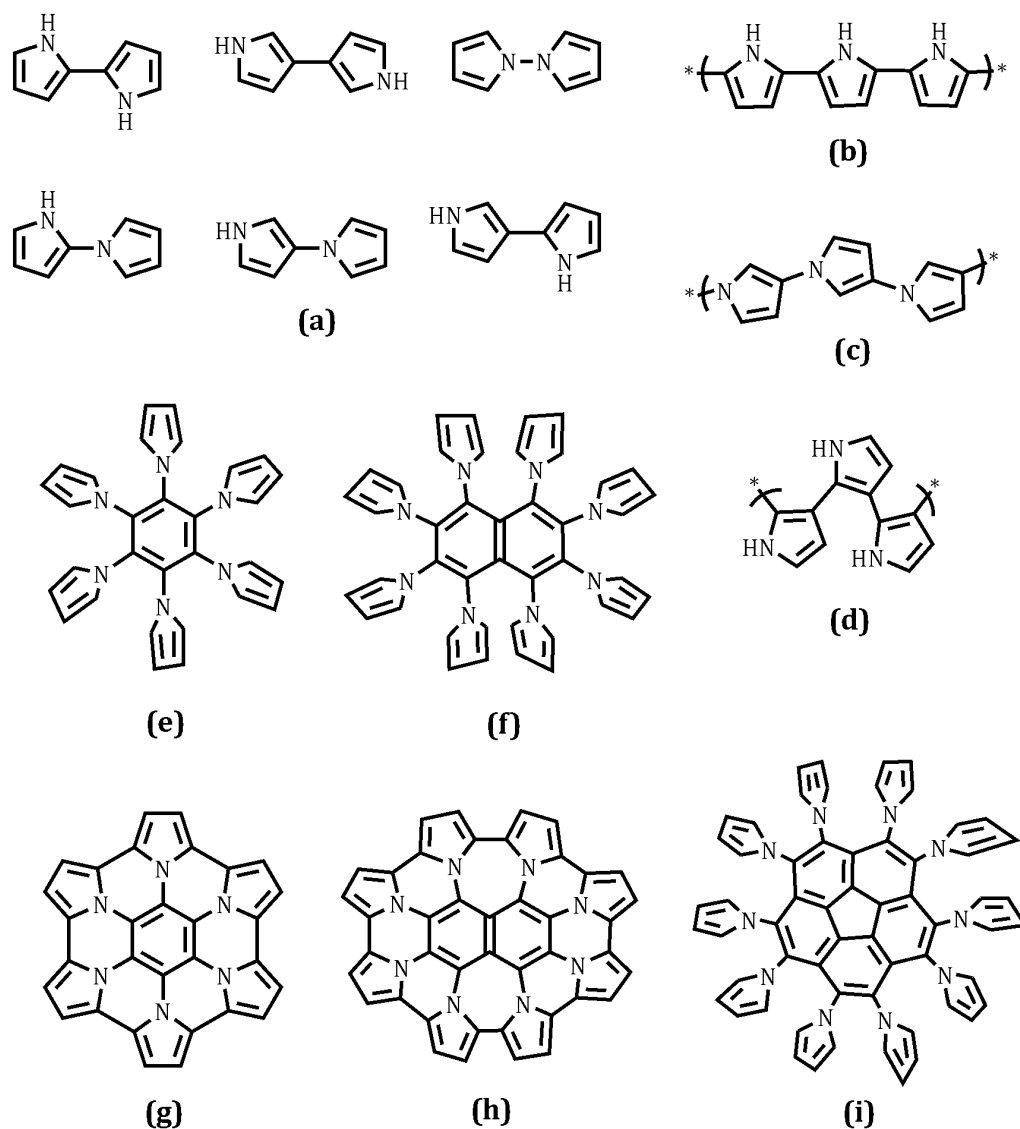
Figure 3.13 Oligomers of pyrrole and its poly-condensed/open forms on aromatic hydrocarbons

The synthesis of an azulene homopolymer with distinctive 2, 6'-connectivity[134, 135] paved the way for the development of novel azulene-based functional materials (Figure 3.14a).[136-140] Star-like azulene derivatives (Figure 3.14b) were used to create polyelectrochromic materials, multielectron redox catalysts and compounds capable

of multiple-electron transfer.[141, 142] Polyindoles with C_3-$N_{1'}$ (Figure 3.14d) and C_3-$C_{2'}$ (Figure 3.14e) linkages are conducting polymers that are excellent for electro-rheological fluids, energy storage devices, and corrosion inhibitors.[143-150] To yet, no polyisoindoles (Figure 3.14c) have been synthesized. Polyaniline is widely recognized as a conducting polymer,[151, 152] while the synthesis of amino-substituted benzene polymer remains an unexplored area of research, yet to be achieved (Figure 3.14f).

Electronic effect operating through the connected network of σ as well as π bonds are termed as through-bond effect (TBE) which include both resonance and inductive effects.[153] The TBE of a functional group can be either electron-withdrawing or electron-donating, and it is used to explain the mechanism of organic reactions.[154] More recent researches[155, 156] have demonstrated that the through-space effect (TSE)[157] or the polarization of a molecule through space predominates in many situations that were previously assumed to be produced primarily by TBE.[158, 159] Many attempts have been made in the past to evaluate TSE using a wide range of substituents.[160-167] The studies revealed that substituent effects in cation-π interactions are mostly caused by TSE rather than TBE.[168]
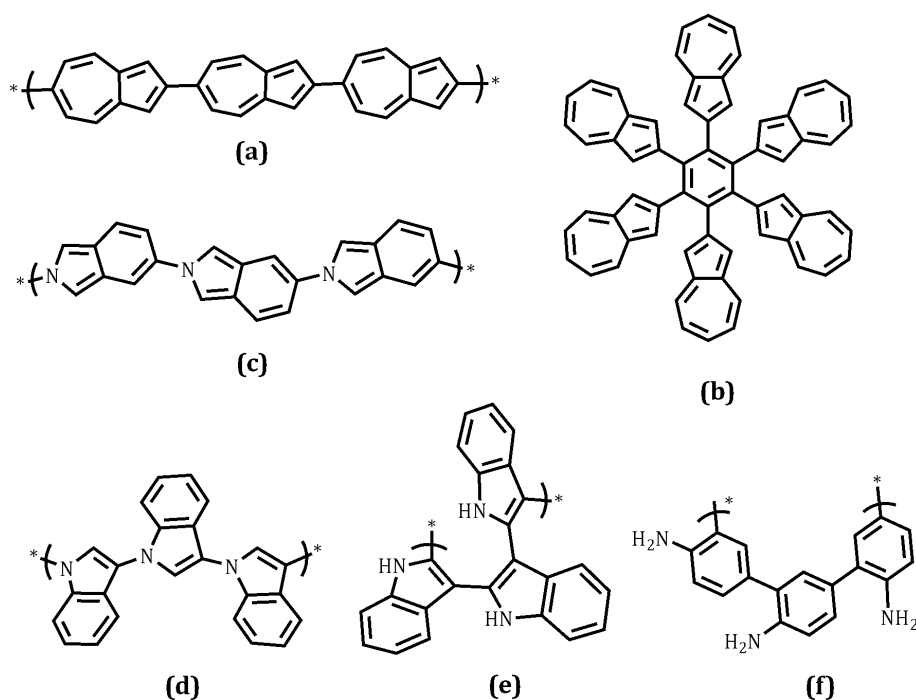
Figure 3.14 Oligomers of azulene, indole, isoindole, aniline and star-like azulene systems

The chain-type and core-expanded chemical systems depicted in Figures 3.13 and 3.14 are not like typical *D-A* systems, because they lack discrete *D* and *A* units. Using DFT, we investigate their structural characteristics, as well as those of several isomers.[169-172] Further, the MESP topology analysis has been performed to evaluate their electronic features. The MESP characteristics highlight the TSE phenomena in these systems, which results in substantial polarization of electron density (PoED) - from one end to the other for chain-type and from periphery to interior or interior to periphery for core-expanded structures.

3.8 Methodology

The DFT method M06-2X/6-311G+(d,p)[173-175] level using the standard protocols as implemented in Gaussian16 suite of programs[40] is used to optimize all the molecular structures considered for the study. The optimized structures were confirmed as energy minima by vibrational frequency analysis. The wave function constructed using global hybrid functional with 54% HF exchange in conjunction with 6-311G+(d, p) basis set is expected to give a sufficiently accurate description of the electron density, $\rho(\mathbf{r})$ and the corresponding MESP, $V(\mathbf{r})$. By employing the cubegen utility within the Gaussian 16 program, both the Vm values and the distribution of MESP on the isodensity surface are computed. The π-electron cloud of the molecule can be displayed by plotting a suitable negative-valued MESP isosurface. Further, Bader's quantum theory of atoms in molecules (QTAIM) analysis, based on the electron density distribution is carried out using AIMAll program package.[176] To check the reliability of the M06-2X method, a benchmark study is also conducted with the DFT methods B3LYP, M06-L, and wB97XD using the 6-311G+(d,p) basis set in all the cases.

3.9 Results and Discussion

3.9.1 MESP Topology of Pyrrole, Furan and Thiophene
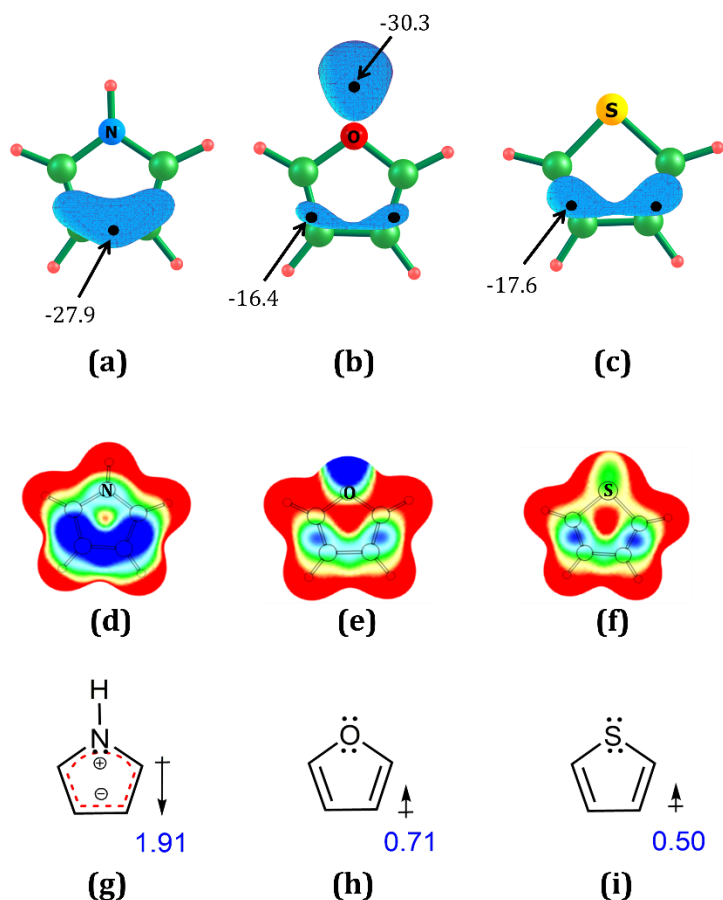
Figure 3.15 The MESP isosurface of (a) pyrrole, (b) furan and (c) thiophene systems plotted at -0.040, -0.025 and -0.025 au, respectively. The figures (d), (e) and (f) are the MESP mapped on to 0.01 au electron density isosurface and (g), (h) and (i) are the direction of dipole moment of pyrrole, furan and thiophene systems, respectively. Colour coding from blue to red indicates MESP values in the range −0.02 to 0.02 au. The V_m and dipole moment values are given in kcal/mol and Debye (D), respectively

The location and value of V_m in the pyrrole MESP structure varies greatly from those of furan and thiophene (Figure 3.15). The pyrrole V_m (-27.9 kcal/mol) is positioned over the C_3C_4, which has a greater single bond character (1.42 Å) than C_2C_3 and C_4C_5. Moreover, the N center lacks a V_m, indicating that the N lone pair is used for cyclic π-electron conjugation. The V_m is found over C_2C_3 and C_4C_5 bonds in furan and thiophene. The V_m points are also observed in the oxygen lone pair region, but the sulphur lone pair has no identifiable localization in the MESP topology, which may be

160

related to the diffused nature of its outermost electrons. The MESP distribution on the isodensity surface (Figure 3.15d) clearly demonstrates the high electronic polarization in pyrrole when compared to both furan and thiophene. Pyrrole has a large dipole moment, 1.91 D in the direction from N center to the midway region of C_3C_4 (Figure 3.15g), but furan and thiophene have a minor dipole moment in the direction from C_3C_4 to the hetero atom.[177] Consequently, MESP topology study validates the following intrinsic electronic features of pyrrole.

1) The pyrrole N center is electron deficient and positively charged.

2) Strong polarization of electron density (PoED) occurs in the direction from the N center to the C_3C_4 bonding region.

3.9.2 Bipyrroles
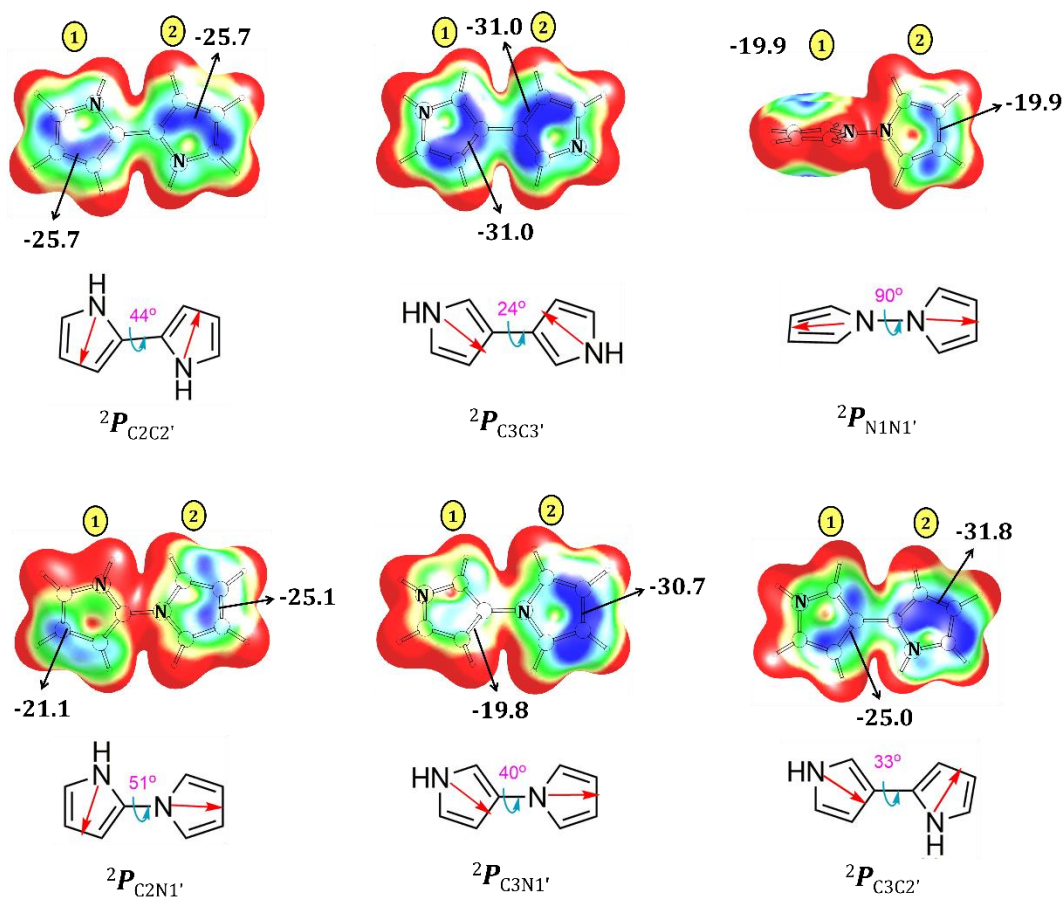
Figure 3.16 The MESP mapped on to 0.01 au electron density isosurface of bipyrroles (^2P), where colour coding from blue to red indicates MESP values in the range −0.03 to 0.03 au. The MESP minimum (V_m) corresponds to each ring is given in kcal/mol and the direction of TSE is denoted using red arrows

Figure 3.16 depicts the MESP distribution of six bipyrroles $^2P_{C2C2'}$, $^2P_{C3C3'}$, $^2P_{N1N1'}$, $^2P_{C2N1'}$, $^2P_{C3N1'}$ and $^2P_{C3C2'}$ wherein the subscript refers to the bonded atoms between the two rings. The PoED occurs in each pyrrole unit, from N_1 to C_3C_4 (for ring 1) or from $N_{1'}$ to $C_{3'}C_{4'}$ (for ring 2) which is depicted in the schematic diagrams (Figure 3.16). Compared to pyrrole, the bipyrroles show significant variation in the MESP distribution in each ring, which can be correlated with the ring-to-ring connectivity and the direction of the PoED. The MESP distribution in the bipyrroles can be easily assessed using the direction of PoED in each pyrrole unit (represented using arrows in Figure 3.16). When the arrows point inward ($\rightarrow\leftarrow$), as in $^2P_{C3C3'}$, the inner regions show higher negative MESP values than outer areas, and when they point outward ($\leftarrow\rightarrow$), as in $^2P_{N1N1'}$ and $^2P_{C2N1'}$, depletion of negative MESP from the interior is evident. The PoED effect is maximum when the arrows are oriented in the same direction (or at an acute angle) ($\rightarrow\rightarrow$), as in $^2P_{C3N1'}$ and $^2P_{C3C2'}$. The parallel orientation of arrows ($\overset{\rightarrow}{\leftarrow}$), as in $^2P_{C2C2'}$ has negligible impact on MESP distribution. The MESP results clearly show that depending on the atom to which the second pyrrole unit is coupled, the pyrrole unit acts as an electron donating (D) or as an electron withdrawing unit (A). For instance, the high negative V_m observed for $^2P_{C3C3'}$, compared to pyrrole suggest D character of pyrrole units whereas the less negative V_m seen in $^2P_{C2C2'}$ and $^2P_{C2N1'}$ indicate A character for the pyrrole units. In $^2P_{C3N1'}$ and $^2P_{C3C2'}$, the substantial reduction in the magnitude of V_m for the first ring and the remarkable enhancement in the V_m value of the second ring compared to pyrrole, suggesting donor-acceptor character for the systems. Despite the fact that the PoED in $^2P_{C3C2'}$ is not as powerful as that in $^2P_{C3N1'}$, the dipole moment 2.86 D found for the former indicates that the $C_3C_{2'}$ connection also leads to considerable PoED in a single direction. The twist angle (θ) between the pyrrole units in bipyrroles is high. The two pyrrole rings are arranged orthogonally in $^2P_{N1N1'}$, while θ the in other bipyrroles $^2P_{C2C2'}$, $^2P_{C3C3'}$, $^2P_{C2N1'}$, $^2P_{C3N1'}$ and $^2P_{C3C2'}$ are 44°, 24°, 51°, 40° and 33°, respectively. High θ values indicate minor levels of extended π-conjugation (TBE). Hence the polarization between the two pyrrole units can be attributed as a consequence of highly directional TSE.

3.9.3 Polypyrroles

(a) $^3P_{C3N1'}$

(b) $^3P_{C3C2'}$

(c) $^4P_{C3N1'}$

(d) $^4P_{C3C2'}$

(e) $^5P_{C3N1'}$

(f) $^5P_{C3C2'}$

(g) $^6P_{C3N1'}$

(h) $^6P_{C3C2'}$

(i) $^6P_{C3N1'}$

(j) $^6P_{C3C2'}$
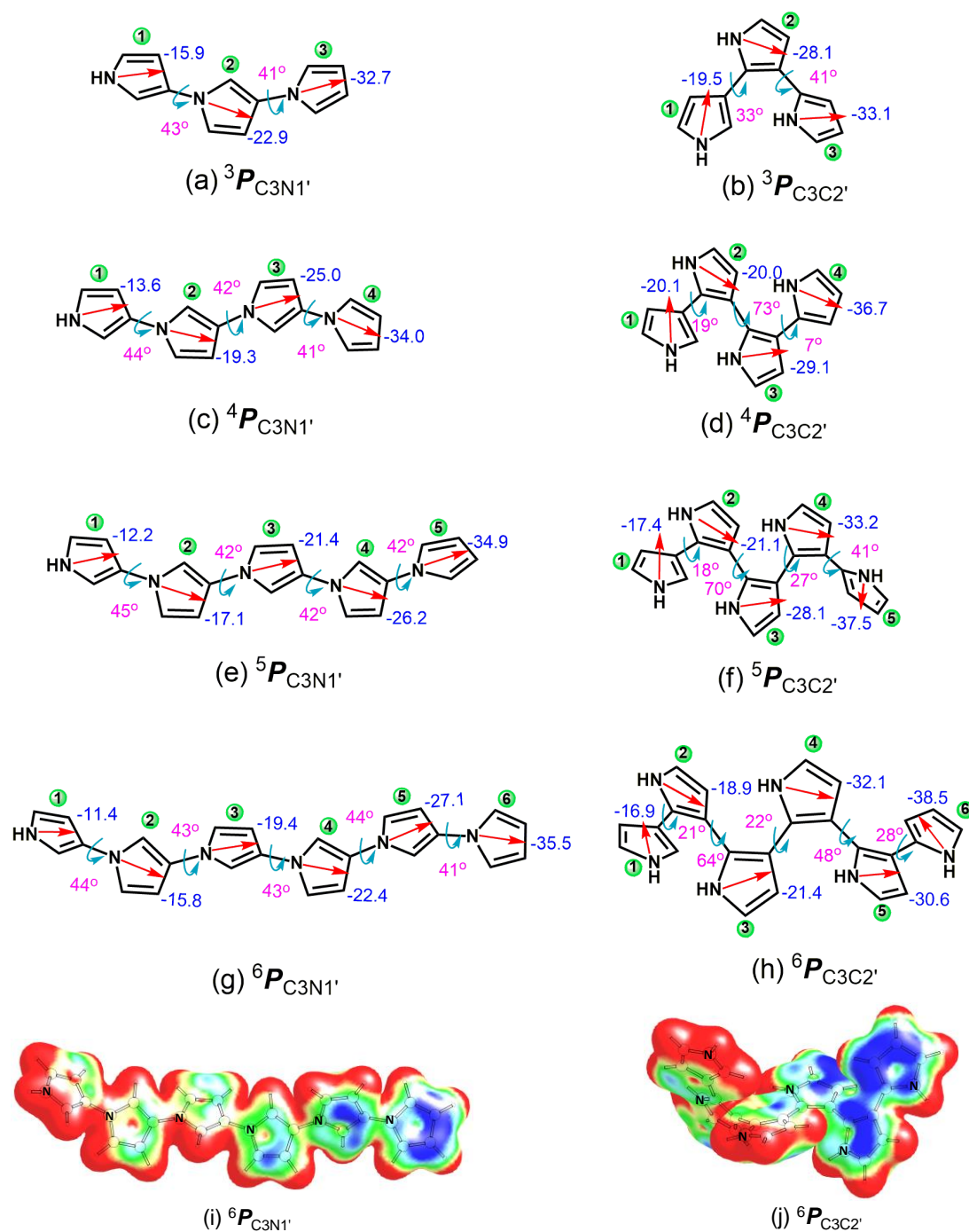
Figure 3.17 The direction of TSE and the variation in V_m values in each pyrrole ring in $C_3N_{1'}$ and $C_3C_{2'}$ connected polypyrroles. The V_m values are given in kcal/mol (blue font) and pyrrole rings from left to right are numbered from 1 to 6, respectively. The dihedral angle at the $C_3N_{1'}$ and $C_3C_{2'}$ junctions between the adjacent rings in $^nP_{C3N1'}$ and $^nP_{C3C2'}$ are given in pink font. The is MESP mapped on to 0.01 au electron density isosurface of (i) $^6P_{C3N1'}$ and (j) $^6P_{C3C2'}$ polypyrroles, where coding from blue to red indicates MESP values in the range −0.03 to 0.03 au

163

The MESP analysis of bipyrroles, $^2P_{C3N1'}$ and $^2P_{C3C2'}$ shows donor feature in one pyrrole unit and acceptor feature in the other. The ring that donates electron density becomes less negative in MESP while the other becomes more negative compared to pyrrole. The donor-to-acceptor electron flow can be extended through a chain of pyrrole units which are connected through either C_3-$N_{1'}$ or C_3-$C_{2'}$ connectivity. In polypyrroles, the extension of electron flow from one pyrrole unit to other is investigated further *viz.* $^nP_{C3N1'}$ and $^nP_{C3C2'}$ where n = 3 to 6. Unidirectional TSE from the first to the second and subsequent pyrrole rings is characterized in terms of V_m value in each ring. The magnitude of V_m in the first pyrrole ring (ring 1) in each system is significantly reduced when compared to pyrrole, showing its high electron deficient character, but the magnitude of V_m in the last ring is significantly enhanced suggesting its electron rich character (Table 3.6). This implies substantial polarization due to TSE from the first to the last pyrrole unit through the C_3-$N_{1'}$ or C_3-$C_{2'}$ connections. Figures 3.17(i) and 3.17(j) show a clear illustration of this phenomenon utilizing the MESP mapped on to a 0.01 au electron density surface. The depleted electron density in the first ring is evident as red regions, whereas the accumulated charge on the last ring is apparent as intense blue region. For instance, in $^6P_{C3N1'}$, the V_m is -11.4 kcal/mol for the first ring and -35.5 kcal/mol for the last ring. Similarly, in $^6P_{C3C2'}$, the first and sixth ring show V_m at -16.9 and -38.5 kcal/mol, respectively.

Table 3.6 The V_m values (in kcal/mol) of first and last pyrrole units in $^nP_{C3N1'}$ and $^nP_{C3C2'}$ polypyrroles at M06-2X/6-311G+(d,p) level of theory

Polypyrrole	V_m of first ring	V_m of last ring
$^3P_{C3N1'}$	-15.9	-32.7
$^4P_{C3N1'}$	-13.6	-34.0
$^5P_{C3N1'}$	-12.2	-34.9
$^6P_{C3N1'}$	-11.4	-35.5
$^3P_{C3C2'}$	-19.5	-33.1
$^4P_{C3C2'}$	-20.1	-36.7
$^5P_{C3C2'}$	-17.4	-37.5
$^6P_{C3C2'}$	-16.9	-38.5
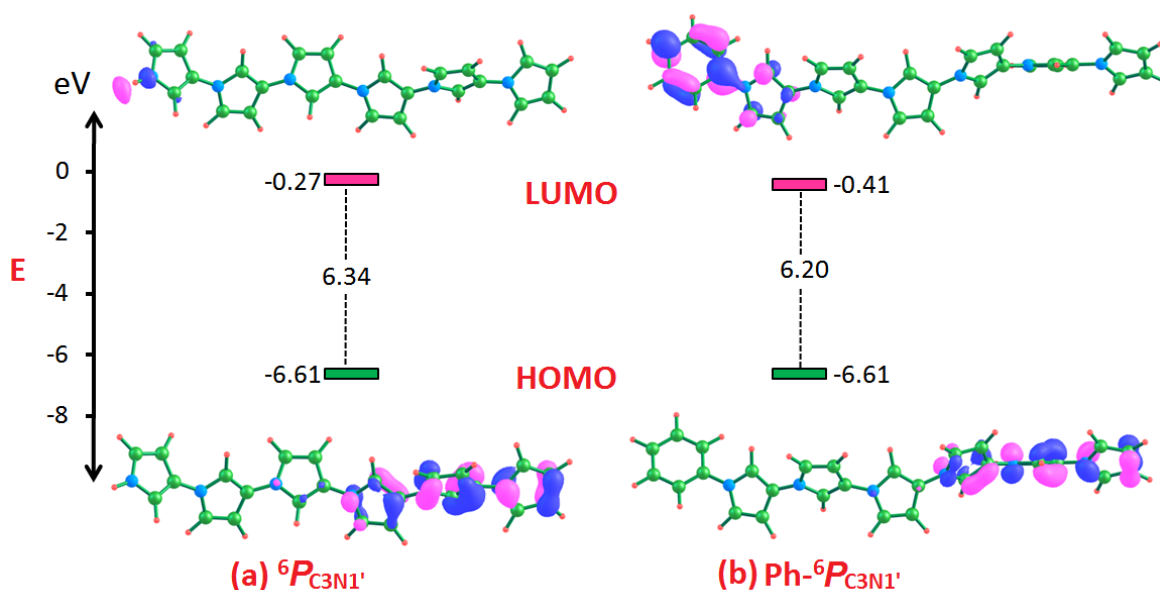
Figure 3.18 Schematic representation of electronic distributions observed in frontier molecular orbitals of representative (a) $^6P_{C3N1'}$ and (b) Ph-$^6P_{C3N1'}$ systems. The MO energy and band gap values in eV are also depicted.

In general, the magnitude of V_m progressively increases from the first to the last ring. The maximum negative character of MESP in the last ring as well as substantially decreased amount of negative MESP in all other rings suggest strong PoED in each pyrrole unit of polypyrroles with the C_3-$N_{1'}$ and C_3-$C_{2'}$ connections, which is reflected in their dipole moment too. For instance, when compared to the dipole moment of pyrrole, which is 1.91 D, the chain structures $^3P_{C3N1'}$, $^4P_{C3N1'}$, $^5P_{C3N1'}$, and $^6P_{C3N1'}$ show higher values, *viz.* 6.02, 8.28, 10.57, and 13.21 D, respectively. Similarly, the dipole moment is 4.22, 5.39, 6.35 and 6.28 D, respectively for $^3P_{C3C2'}$, $^4P_{C3C2'}$, $^5P_{C3C2'}$, and $^6P_{C3C2'}$. Figure 3.17 also depicts the dihedral angle (θ) at the C_3-$N_{1'}$ and C_3-$C_{2'}$ junctions in $^nP_{C3N1'}$ and $^nP_{C3C2'}$ systems, respectively. The θ of $^nP_{C3N1'}$ polypyrroles ranges from 41º to 45º, whereas that of $^nP_{C3C2'}$ polypyrroles extends from 25º to 64º. The $^nP_{C3C2'}$ systems have more twisted and zigzaggedly arranged pyrrole units than $^nP_{C3N1'}$ systems. The high θ values in both cases suggest extremely low degrees of extended π-conjugation (TBE) across the polypyrrole chain. The HOMO of all $^nP_{C3N1'}$ and $^nP_{C3C2'}$ is found at the most electron-rich pyrrole unit, but the LUMO is always found as the antibonding orbital of the N-H bond at the first pyrrole unit (Figure 3.18).

165

In the case of an N-phenyl substituted polypyrrole (Ph-$^6P_{C3N1'}$ in Figure 3.18), the HOMO is confined around the end pyrrole unit, while a π^* orbital localized on the phenyl ring is the LUMO. The HOMO and LUMO distributions clearly support the phenomenon of TSE.

(a)   (b)
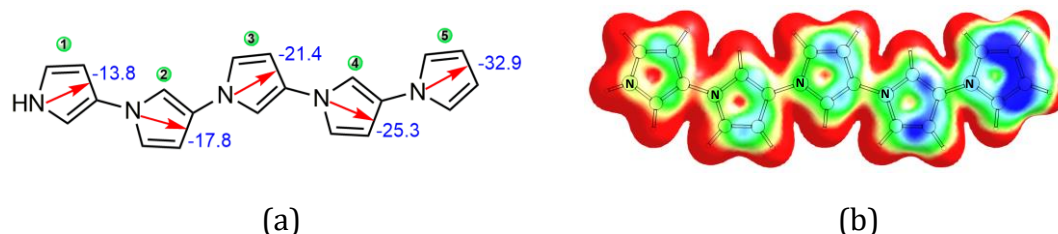
Figure 3.19 (a) The direction of PoED and the variation in V_m values in each pyrrole unit in $^{5'}P_{C3N1'}$ (b) The MESP mapped on to 0.01 au electron density isosurface of $^{5'}P_{C3N1'}$, where coding from blue to red indicates MESP values in the range −0.03 to 0.03 au

Since the monomeric units are significantly twisted in the oligomers, the TSE is considered more influential for the electronic polarization than the through bond resonance effect. A constrained optimization of $^5P_{C3N1'}$ at $\theta = 0°$ yields $^{5'}P_{C3N1'}$, a planar structure that is 4.4 kcal/mol, less stable than $^5P_{C3N1'}$ as shown in Figure 3.19. Though planarity improves the through bond resonance interaction, the electronic polarization is found to be significantly higher for the twisted structure than the planar suggesting that the TSE is dominating than TBE in the twisted system. To further demonstrate the directionality of TSE, a $(P_{C3N1'})_6$ cluster is constructed as shown in Figure 3.20a wherein the orientation of each pyrrole unit is fixed as per the structure of $^6P_{C3N1'}$ with a distance of separation $\cong 2.0$ Å between the adjacent pyrroles. The MESP distribution of $(P_{C3N1'})_6$ cluster shows steady enhancement in negative character from first to the last pyrrole and this pattern, very similar to $^6P_{C3N1'}$ confirms the directional nature of TSE. Similarly, $(P_{C3N1'})_n$ and $(P_{C3C2'})_n$ (Figure 3.20b) clusters showed MESP patterns very similar to $^nP_{C3N1'}$ and $^nP_{C3C2'}$ systems, respectively.
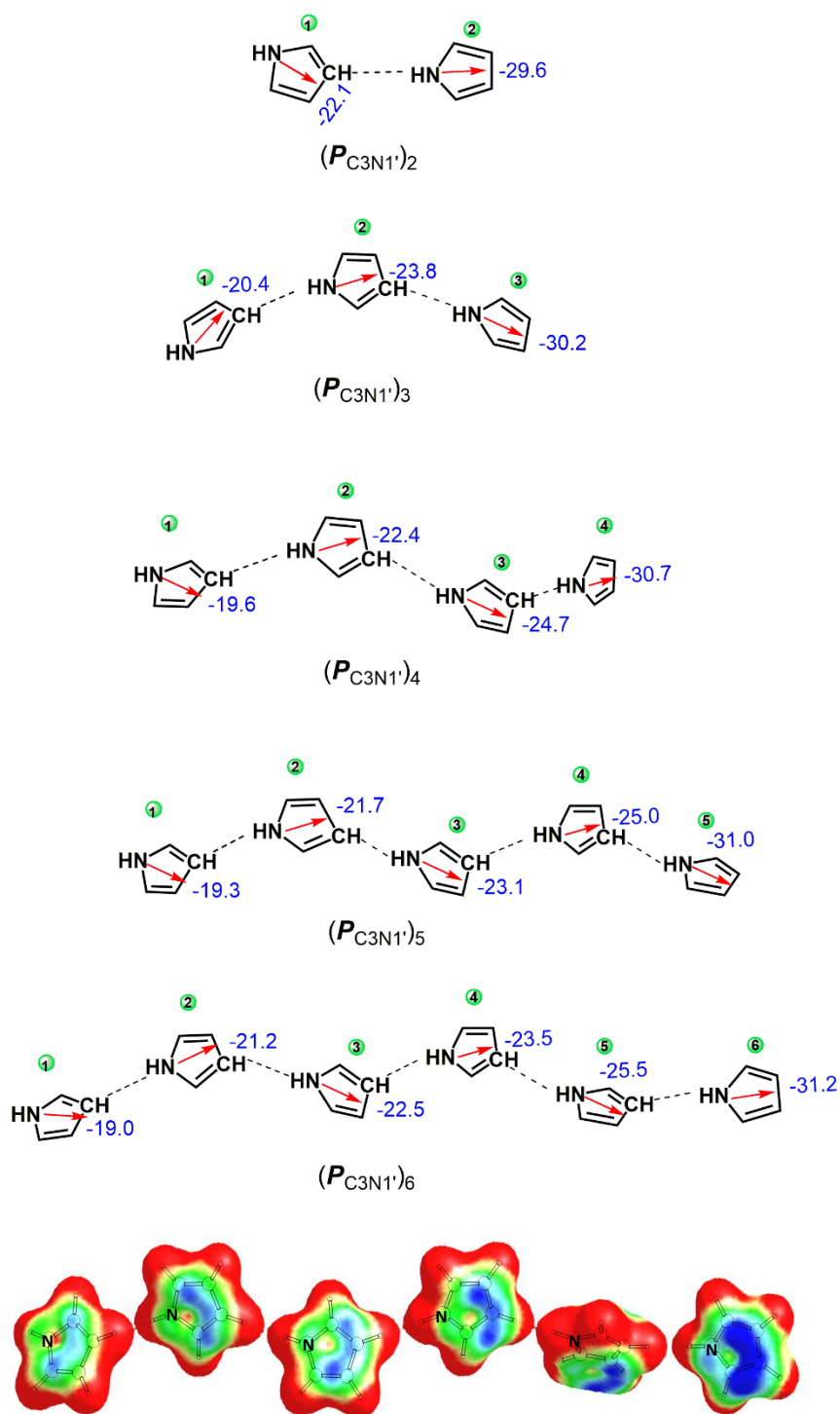
Figure 3.20a Illustration of the directional nature (red arrows) of TSE in $(P_{C3N1'})_6$ cluster. Pyrroles are numbered from 1 to 6 and V_m values of each ring is given in kcal/mol. The MESP of $(P_{C3N1'})_6$ is mapped on to 0.01 au electron density isosurface, where coding from blue to red indicates MESP values in the range −0.03 to 0.03 au.
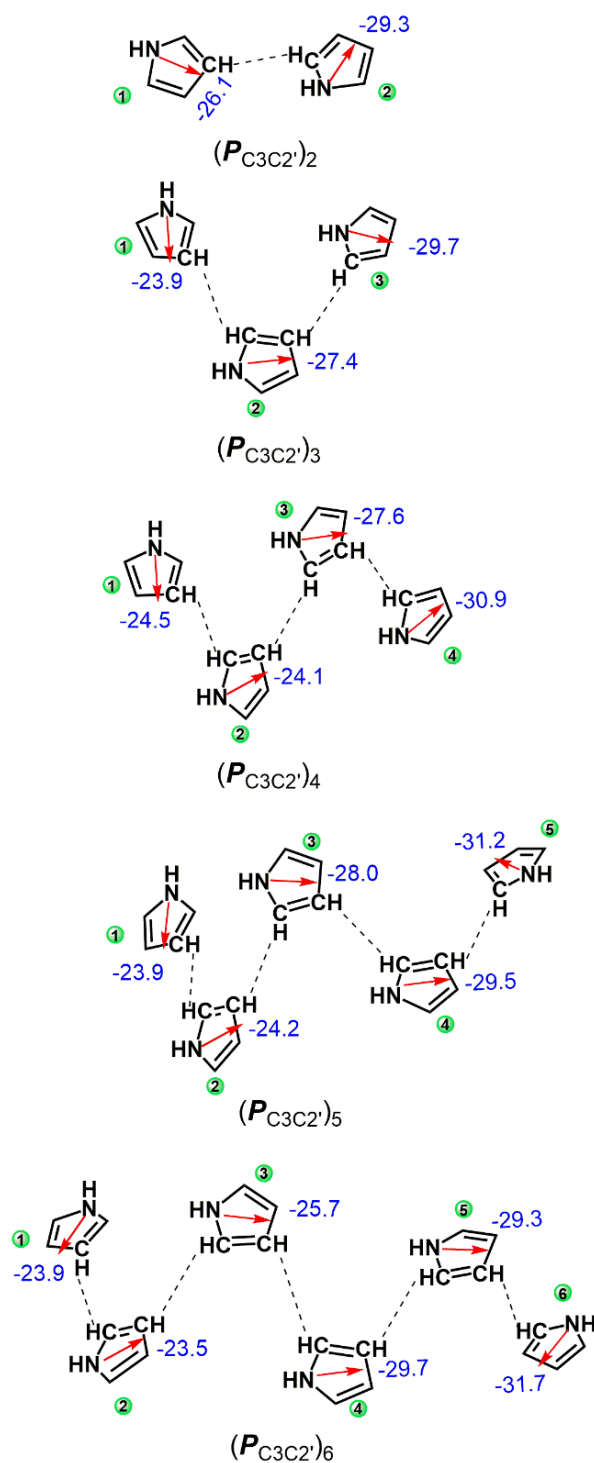
Figure 3.20b Illustration of the directional nature (red arrows) of TSE in $(\boldsymbol{P}_{C3C2'})_6$ cluster. Pyrroles are numbered from 1 to 6 and V_m values of each ring is given in kcal/mol.
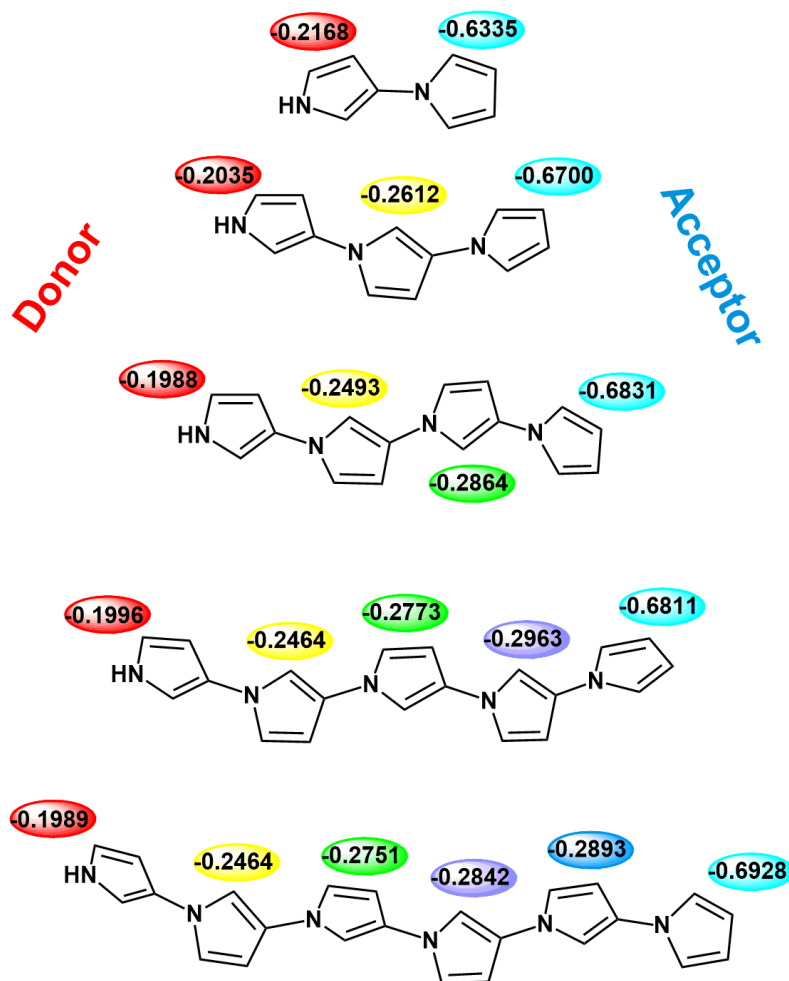
Figure 3.21 Atomic polar tensor (au) charges demonstrating the donor-acceptor feature of $^nP_{C3N1'}$ systems

In all cases, the TSE imparts donor character to the first pyrrole unit and acceptor character to the last one, despite the absence of an unambiguous donor or acceptor moiety. Further, the atomic polar tensor (APT)[178] charges offer compelling evidence for the donor characteristics of the first pyrrole unit and the acceptor characteristics of the last pyrrole unit in $^nP_{C3N1'}$ systems (Figure 3.21).

3.9.4 Phenyl Pyrrole Systems

The MESP distribution in 1-, 2-, and 3-phenyl pyrroles (1-***PhP***, 2-***PhP*** and 3-***PhP***) is depicted in Figure 3.22. The direct connection between the N center and the phenyl ring in 1-***PhP***[179-183] results in a significant reduction in the magnitude of V_m at

the phenyl ring (-10.2 kcal/mol), whereas V_m at the pyrrole ring is essentially unaffected due to the orthogonal orientation of the rings. The V_m at the phenyl and pyrrole moieties in 2-**PhP**[184-186] are close to those of benzene (-17.8 kcal/mol) and pyrrole (-27.9 kcal/mol), respectively demonstrating the null effect of phenyl-C_2 connection on electron distribution. The polarization direction in 3-**PhP** is from pyrrole to phenyl unit, which results in a considerable enhancement in V_m of the phenyl ring to -20.9 kcal/mol. Since the ring moieties in all **PhP**s are orthogonal, the polarization cannot be explained by resonance or the TBE between the linked moieties indicating that the polarization in such molecules is caused by the TSE.
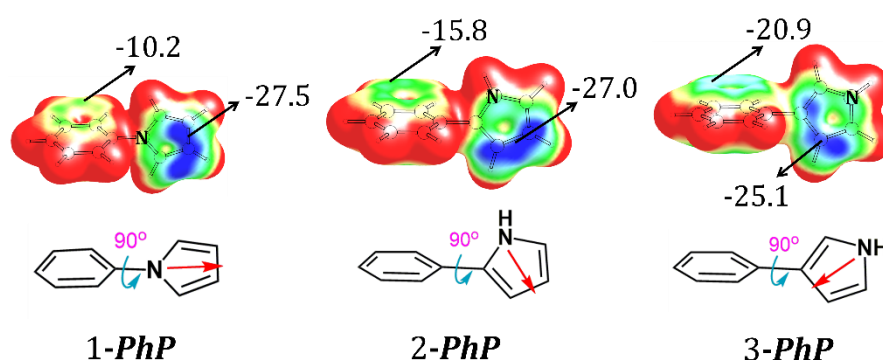
Figure 3.22 The MESP mapped on to 0.01 au electron density isosurface for 1-, 2- and 3-phenyl pyrroles (**PhP**). Colour coding from blue to red indicates MESP values in the range −0.03 to 0.03 au and the V_m values are given in kcal/mol

Highly directional nature of PoED in phenyldipyrroles (**PhDP**s), *viz.* (1, 1'-**PhDP)**, (2, 2'-**PhDP)**, (3, 3'-**PhDP)**, and (1, 3'-**PhDP)**, is obvious from the MESP distribution (Figure 3.23). The outwardly pointed arrows ($\leftarrow\rightarrow$) in 1, 1'-**PhDP** show a depletion in electron density on the phenyl ring, whereas the inwardly pointed arrows ($\rightarrow\leftarrow$) in 3, 3'-**PhDP** indicate an enhancement in electron density. The parallel orientation of arrows ($\overset{\rightarrow}{\leftarrow}$), in 2, 2'-**PhDP** suggests that pyrrole units have essentially minimal TSE effect on the phenyl ring, but the arrows in same direction ($\rightarrow\rightarrow$) in 1, 3'-**PhDP** propose a push-pull effect of electron density from the C-connected pyrrole unit to the N-connected one.
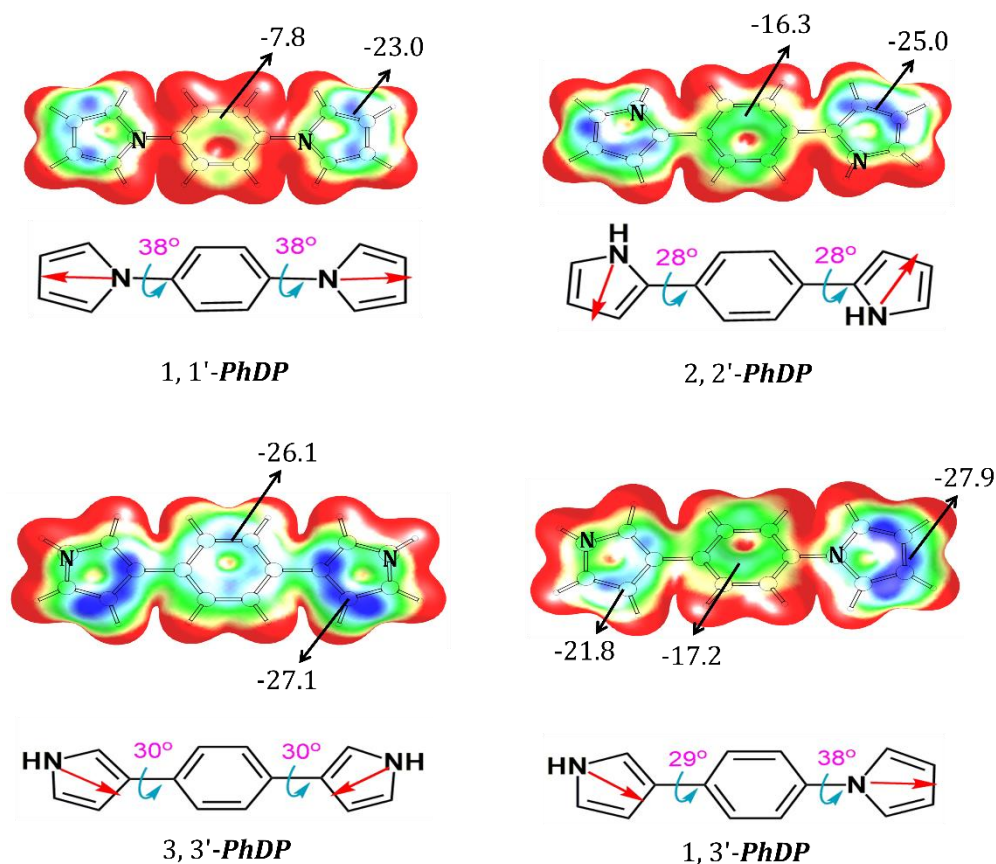
Figure 3.23 The MESP mapped on to 0.01 au electron density isosurface for phenyldipyrrole (*PhDP*) systems. Colour coding from blue to red indicates MESP values in the range −0.03 to 0.03 au and the V_m of each ring are given in kcal/mol. The red arrows represent the direction of TSE

The direction of electron flow in hexapyrrolylbenzene systems (*HPB*$_{N1}$, *HPB*$_{C2}$ and *HPB*$_{C3}$) is depicted in Figure 3.24, where *HPB*$_{N1}$ and *HPB*$_{C3}$ are experimentally known and *HPB*$_{C2}$ is yet to be synthesized.[187] The six arrows pointing outward in *HPB*$_{N1}$ indicate the maximum electron withdrawal effect at the core benzene ring, whereas the six arrows pointing inward in *HPB*$_{C3}$ indicate the flow of electron density from each pyrrole unit to the core unit. Their MESP distribution validates this hypothesis, since *HPB*$_{N1}$ and *HPB*$_{C3}$ show intense positive and negative MESP, respectively over the central arene ring. The arrows in *HPB*$_{C2}$ anticipate the PoED within the pyrrole rings and its impact on the central arene ring, where the TSE is expected to be the lowest.

171

HPB_{N1} HPB_{C2} HPB_{C3}
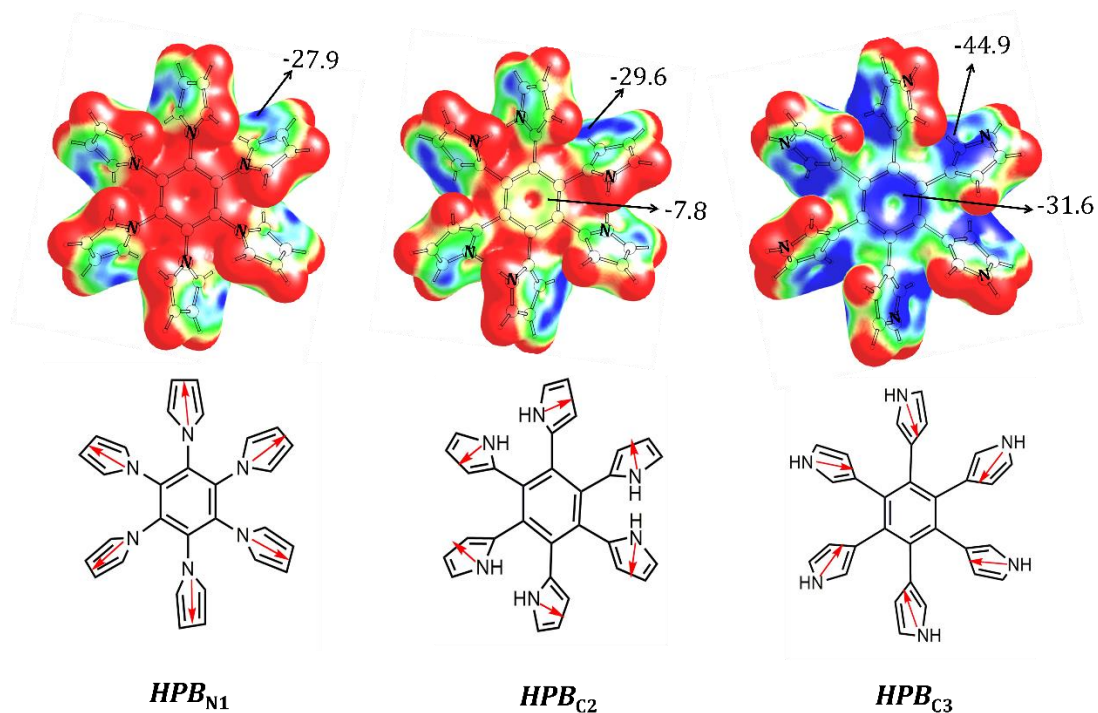
Figure 3.24 The direction of electron flow in hexapyrrolylbenzene (**HPB**) compounds is denoted using red arrows. The MESP mapped on to 0.01 au electron density isosurface shows colour coding from blue to red, which indicates MESP values in the range −0.03 to 0.03 au and the V_m values are given in kcal/mol.

OPN_{N1} OPN_{C3}
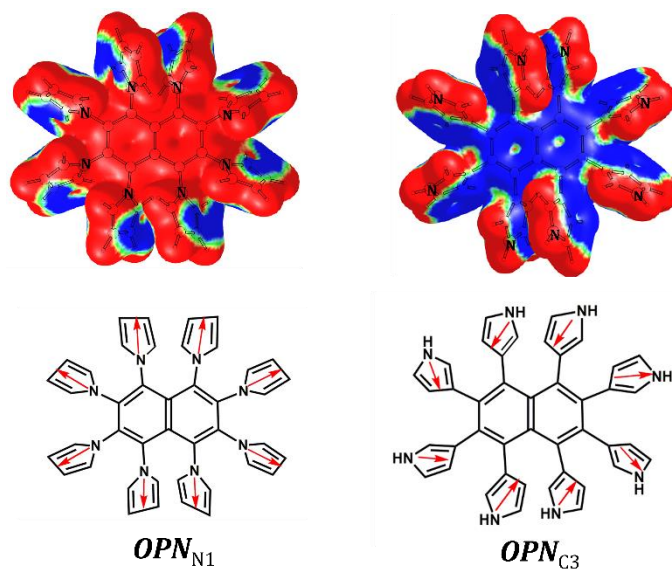
Figure 3.25 The MESP mapped on to 0.01 au electron density isosurface for intra-molecularly coupled octapyrrolylnaphthalene (**OPN**) systems. Colour coding from blue to red indicates MESP values in the range −0.01 to 0.01 au. The direction of electron flow is denoted using red arrows

172

Moreover, the PoED effect exhibited by pyrrole units is well discernible in experimentally known octapyrrolylnaphthalene (**OPN**$_{N1}$) and decapyrrolylcorannulene (**DPC**$_{N1}$) systems, where the core units (naphthalene or corannulene) are devoid of MESP minimum as eight/ten arrows are pointing outward (Figure 3.25/3.26). This implies a substantial electron withdrawal effect on the core, and the core might be rendered electron rich by linking it to the C$_3$ center of pyrrole units. In **OPN**$_{C3}$ and **DPC**$_{C3}$ systems, the eight/ten arrows representing the PoED effect from pyrrole units to core suggest highly electron rich character for the core region. In general, directionality of TSE can be considered as the basis for the strong polarization in all phenyl pyrrole systems.
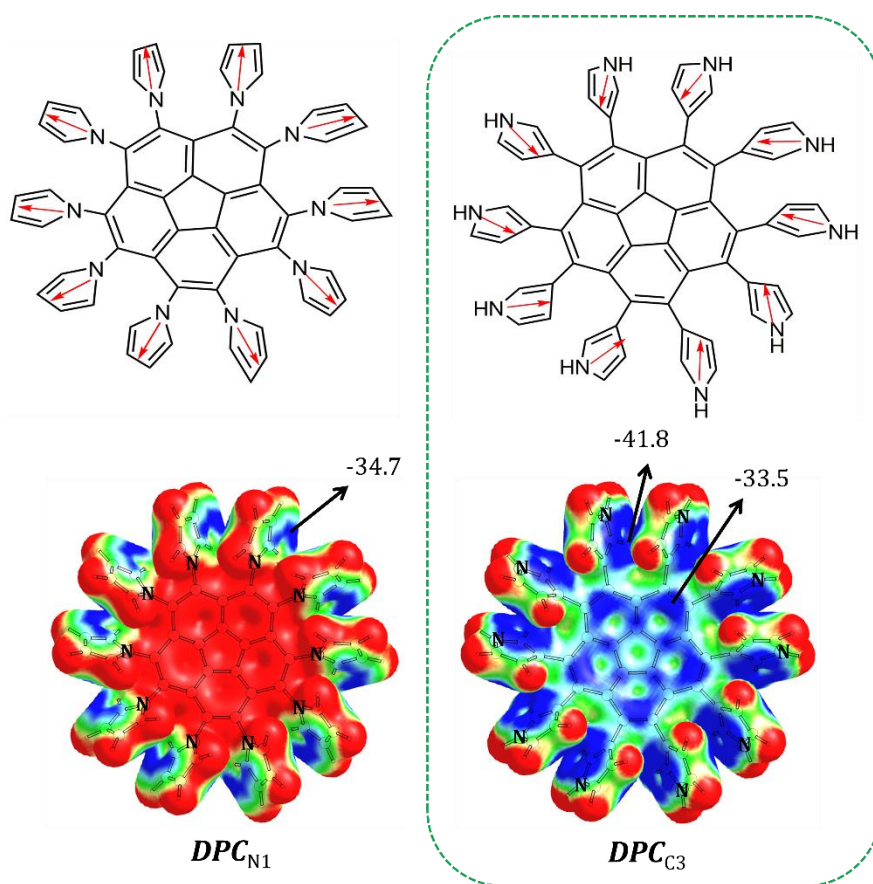
Figure 3.26 The MESP mapped on to 0.01 au electron density isosurface for intra-molecularly coupled decapyrrolylcorannulene (**DPC**) systems. Color coding from blue to red indicates MESP values in the range −0.03 to 0.03 au and the V_m of each ring are given in kcal/mol

3.9.5 N-doped Nanographene Systems
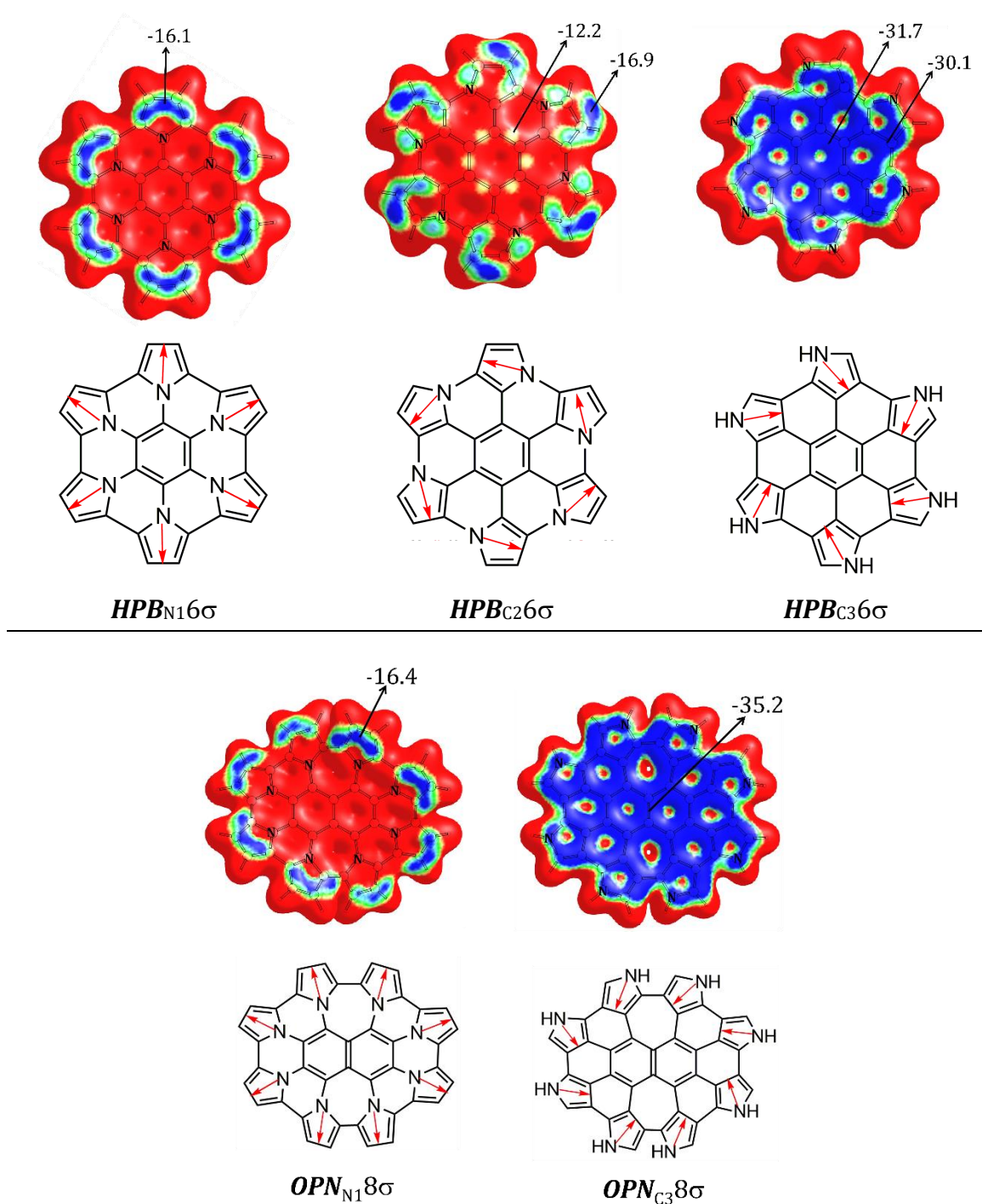
Figure 3.27 The direction of electron flow in intra-molecularly coupled hexapyrrolylbenzene (**HPB**6σ) and octapyrrolylnaphthalene (**OPN**8σ) compounds is denoted using red arrows. In the MESP mapped on to 0.01 au electron density isosurface colour coding from blue to red indicates MESP values in the range −0.01 to 0.01 au, respectively and V_m values are given in kcal/mol

The directionality of TSE as seen from MESP patterns can be used to interpret the electronic distribution in intra-molecularly coupled polypyrrolyl systems, commonly known as N-doped nanographenes (Figure 3.27). The arrow representations clearly brings out the electron density depletion at the core benzene/naphthalene ring in experimentally known $HPB_{N1}6\sigma$ and $OPN_{N1}8\sigma$, and the accumulation of electron density at the benzene/naphthalene core unit in $HPB_{C3}6\sigma$ and $OPN_{C3}8\sigma$. Moreover, as shown in Figure 3.26, the TSE on C_2 connected $HPB_{C2}6\sigma$ is negligible. In all systems, the MESP distribution perfectly corresponds with this prediction. Of the systems investigated here, **$HPB_{C2}6\sigma$**, **$HPB_{C3}6\sigma$** and **$OPN_{C3}8\sigma$** are yet to be synthesized. Analysis of MESP topology leads to smart molecular design strategies for the construction of both electron-rich and electron-deficient core-expanded structures.

3.9.6 Complementary Interactions in Dimers

Electrostatic complementarity plays a pivotal role when *D-A* molecules assemble to form dimer $(D\text{-}A)_2$ complexes. In this context, the *D* unit of the first monomer interacts with the *A* unit of the second monomer, and vice versa. For instance, pyrrole dimer shows dimerization energy (E_{dim}) of -7.6 kcal/mol. Additionally, E_{dim} values of polypyrroles exhibit consistent enhancement with an increase in the number of pyrrole units. As an example, when comparing $(^2\boldsymbol{P}_{C3N1'})_2$ with $(^6\boldsymbol{P}_{C3N1'})_2$, E_{dim} experiences a nearly two-fold increase, changing from -15.6 kcal/mol to -29.3 kcal/mol (Figure 3.28). This steady enhancement in E_{dim} can be attributed to the pronounced electronic polarization observed across multiple pyrrole units. In the case of core expanded systems, **$HPB_{C3}6\sigma$** can be paired with **$HPB_{N1}6\sigma$** to obtain electrostatic complementarity (Figure 3.29).[188] Such a complex **$HPB_{C3}6\sigma$**·····**$HPB_{N1}6\sigma$** show E_{dim} -40.4 kcal/mol. Similarly, the pair of **$OPN_{C3}6\sigma$** and **$OPN_{N1}6\sigma$** shows E_{dim} -52.8 kcal/mol due to the high electrostatic complementarity. The electrostatic complementarity observed in these core-expanded systems holds significant potential for the construction of charge transfer complexes, offering promising applications.[189]
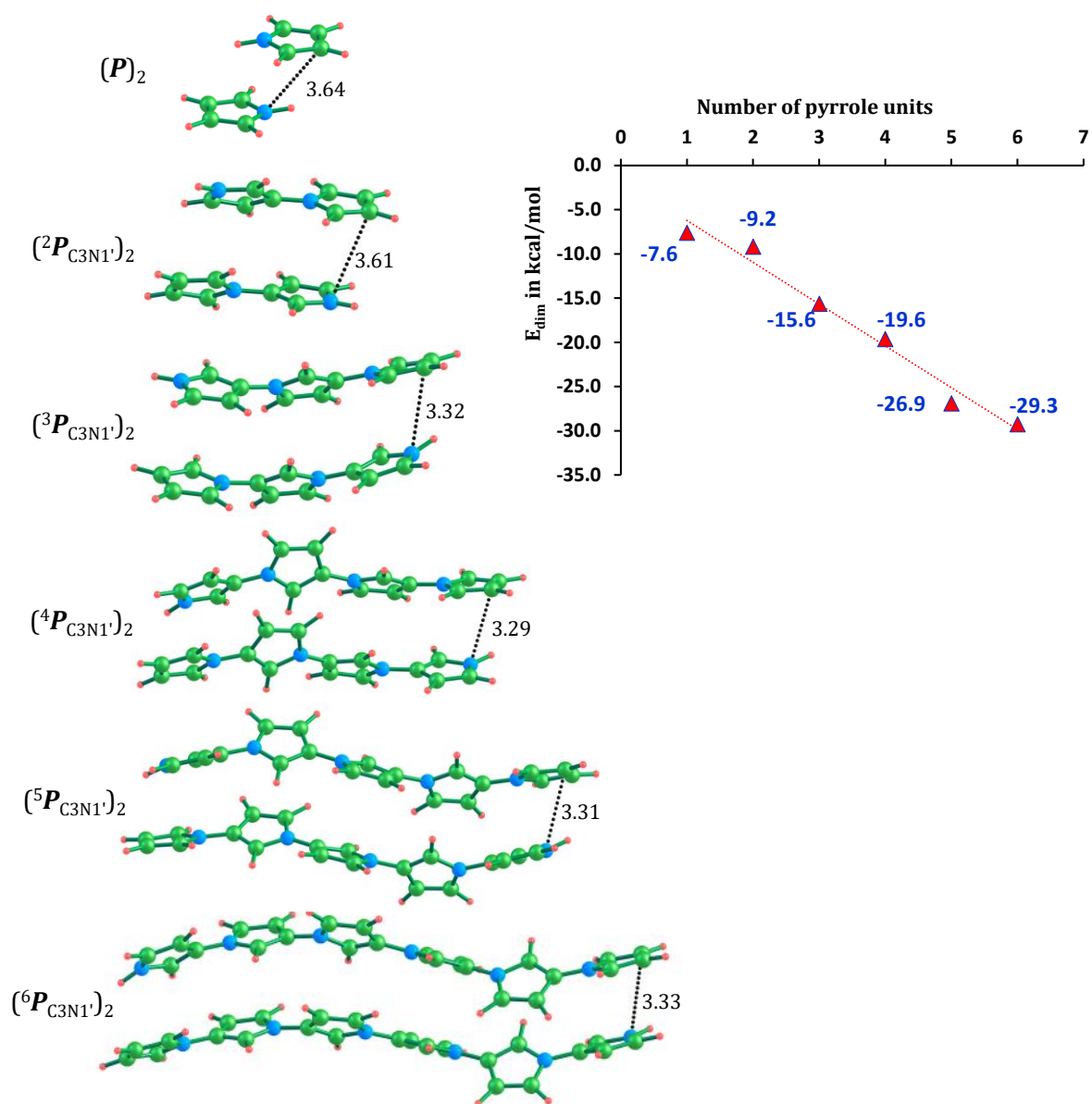
Figure 3.28 Complementary electrostatic interactions in the dimers of $^nP_{C3N1'}$. The intermolecular distances are given in Å
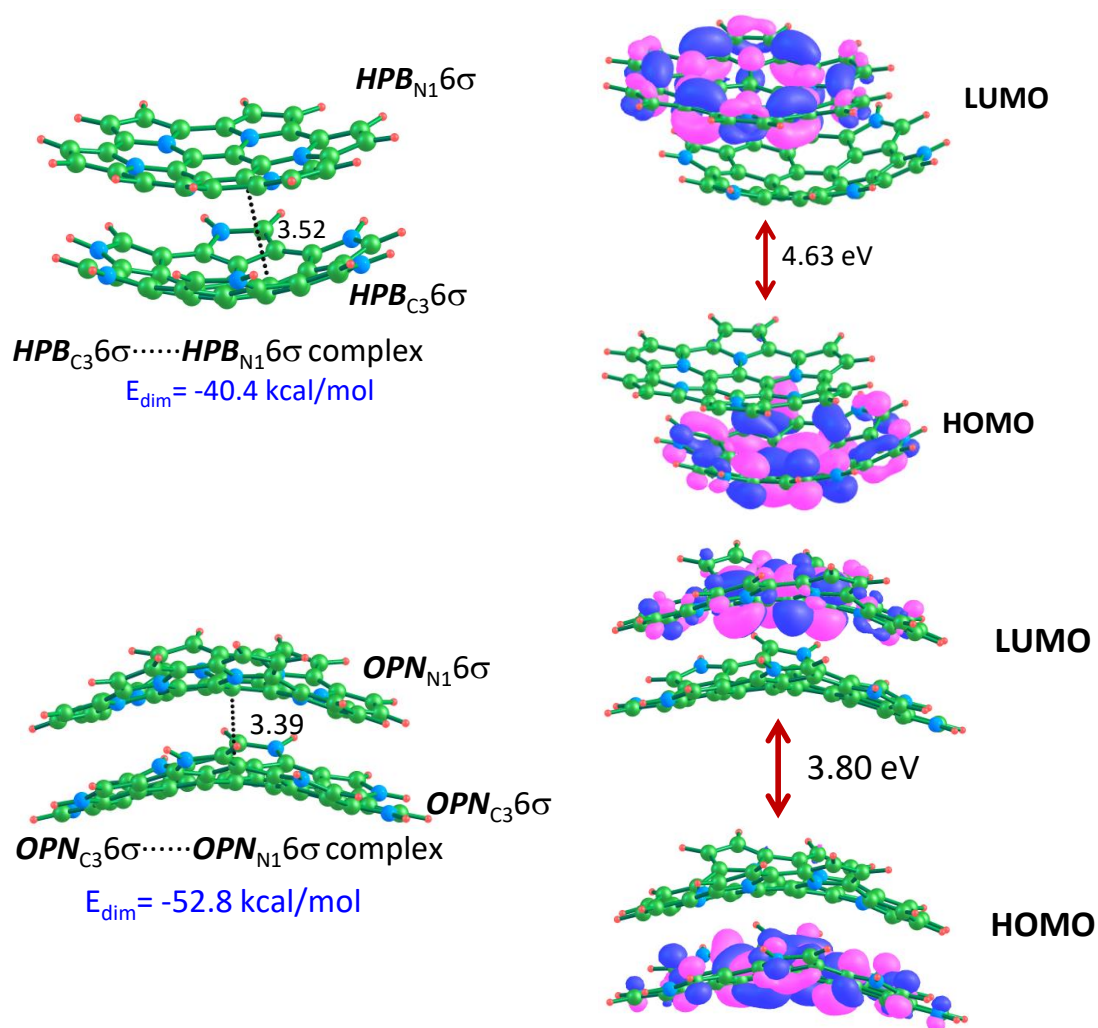
Figure 3.29 Complementary complexes of $HPB_{C3}6\sigma\cdots\cdots HPB_{N1}6\sigma$ and $OPN_{C3}6\sigma\cdots\cdots OPN_{N1}6\sigma$, respectively and electronic distributions observed in frontier molecular orbitals, wherein nearest non-covalent interatomic distances are given in Å

3.9.7 Indole, Isoindole, Azulene and Aniline

The MESP topology analysis has been performed on indole (*I*), isonidole (*iI*), azulene (*Az*), and aniline (*An*) systems to gain a better insight about PoED and the phenomenon of TSE. The *I* has two V_m points, -22.0 and -24.1 kcal/mol, which correspond to the five- and six-membered rings, respectively, whereas *iI* exhibits only one V_m, -25.8 kcal/mol, for the six-membered ring. The more negative V_m in *iI* compared to *I* can be attributed to the TSE which is directed from the N-center to the six-membered ring. In *Az*, the five-membered ring is electron richer than the seven-

membered ring. Consequently, seven-membered ring behaves as donor to the other ring, the acceptor. In **An**, the V_m of arene ring, (-23.1 kcal/mol) is observed near to the *para*-carbon C_4, indicating the directionality of TSE from amino group to the *para*-site.
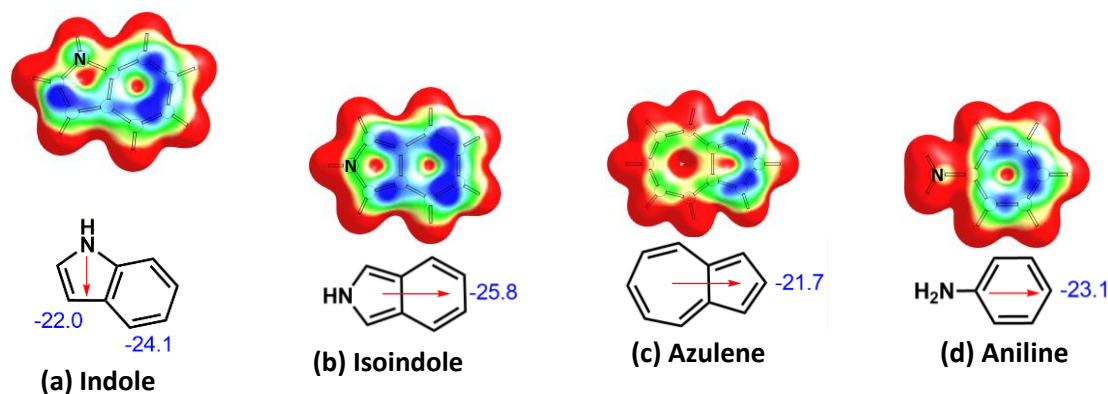
Figure 3.30 The MESP mapped on to 0.01 au electron density isosurface of indole (**I**), isoindole (**iI**), azulene (**Az**) and aniline (**An**) systems where colour coding from blue to red indicates MESP values in the range −0.02 to 0.02 au. The TSE in terms of V_m value (in kcal/mol) for a representative set of systems are also given. The red arrows represent the direction of TSE

The directional nature of TSE is utilized to design highly charge separated oligomers of **I** (^{n}**I**$_{C3N1'}$, ^{n}**I**$_{C3C2'}$ and ^{n}**I**$_{C6N1'}$), **iI** (^{n}**iI**$_{C5N1'}$), **Az** (^{n}**Az**$_{C1C6'}$), and **An** (^{n}**An**$_{C4C2'}$) where n = 2 to 6. The monomers are connected in a manner to get a unidirectional TSE for the oligomer. In all the cases, the last monomer unit exhibits a remarkable gain in the magnitude of V_m, while the first monomer exhibits a dramatic drop (Figure 3.31 to Figure 3.36). The distribution of V_m clearly suggest the strong donor-acceptor feature of the oligomers. The donor-acceptor aspect originating from the directional nature of the TSE is further confirmed by the MESP analysis of clusters of **I, iI, Az**, and **An** (Figure 3.37). In ^{n}**P**$_{C3N1'}$, ^{n}**P**$_{C3C2'}$, ^{n}**I**$_{C3N1'}$, ^{n}**I**$_{C3C2'}$, ^{n}**I**$_{C6N1'}$, ^{n}**iI**$_{C5N1'}$, ^{n}**Az**$_{C1C6'}$, and ^{n}**An**$_{C4C2'}$, the HOMO-LUMO gap decreases steadily with n moving from 1 to 6, in the range 1.1 – 2.0 eV (Table 3.7).
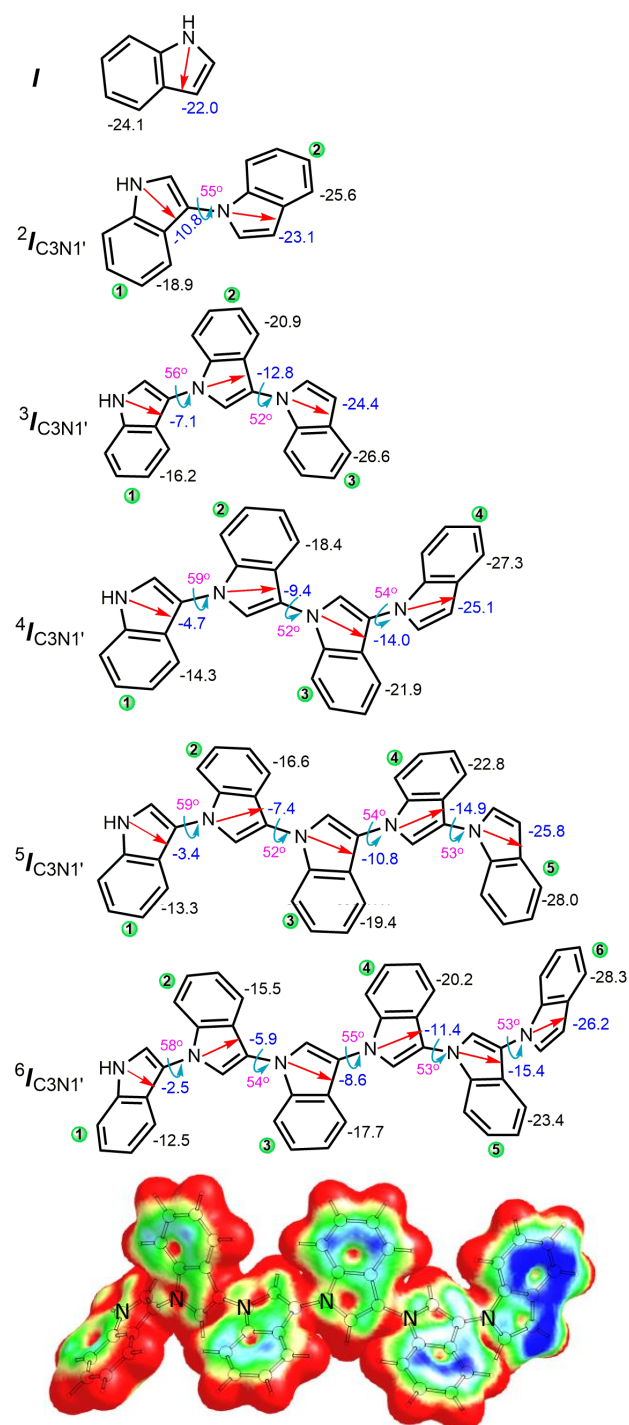
Figure 3.31 The direction of TSE and the variation in V_m values in 3, 1'-polyindoles (I to $^6I_{C3N1'}$). The V_m values of five- and six-membered rings are given in kcal/mol are represented in blue and black font respectively. The dihedral angle at the CCCC junctions between the adjacent rings are given in pink font. The MESP mapped on to 0.01 au electron density isosurface of $^6I_{C3N1'}$, where coding from blue to red indicates MESP values in the range −0.02 to 0.02 au

179
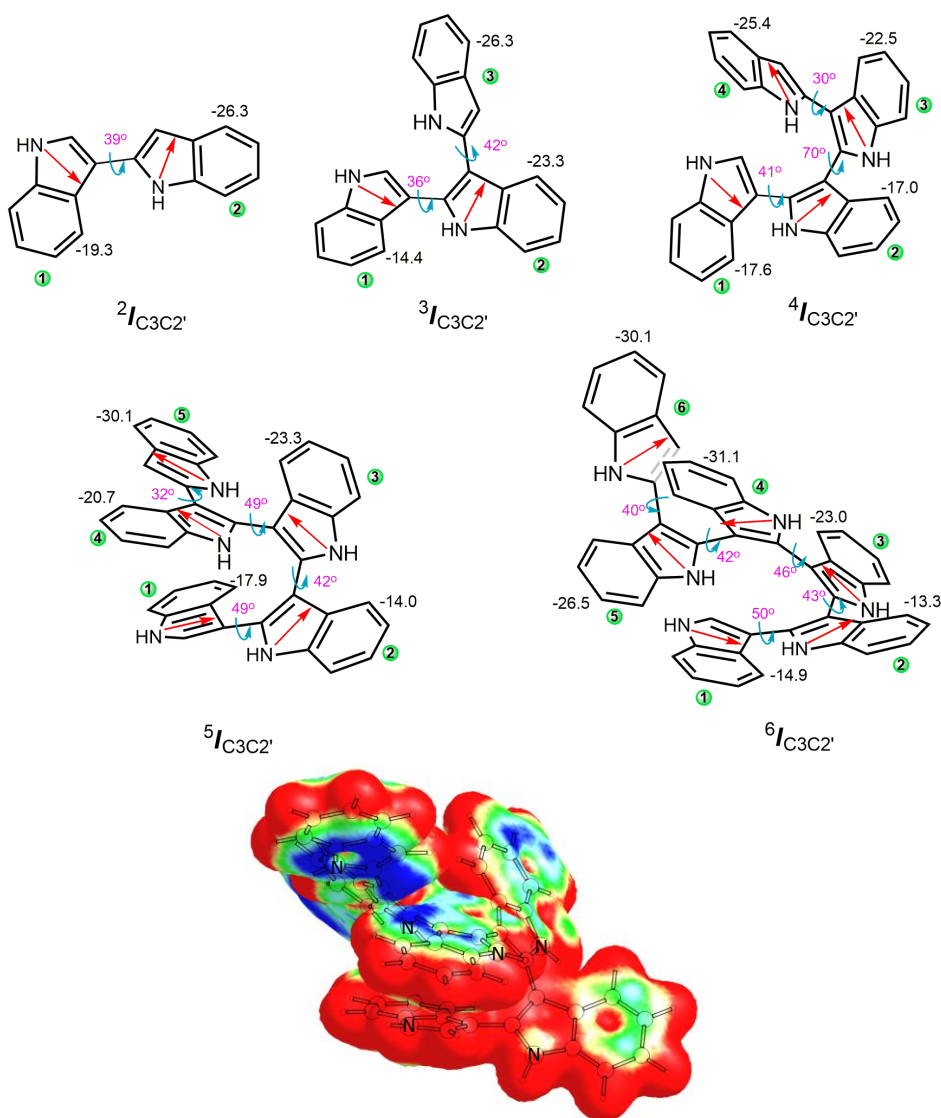
Figure 3.32 The direction of TSE and the variation in V_m values in 3, 2'-polyindoles ($^2I_{C3C2'}$ to $^6I_{C3C2'}$). The V_m values of six-membered rings are given in kcal/mol are represented in black font respectively. The dihedral angle at the CCCC junctions between the adjacent rings are given in pink font. The MESP mapped on to 0.01 au electron density isosurface of $^6I_{C3C2'}$, where coding from blue to red indicates MESP values in the range −0.02 to 0.02 au
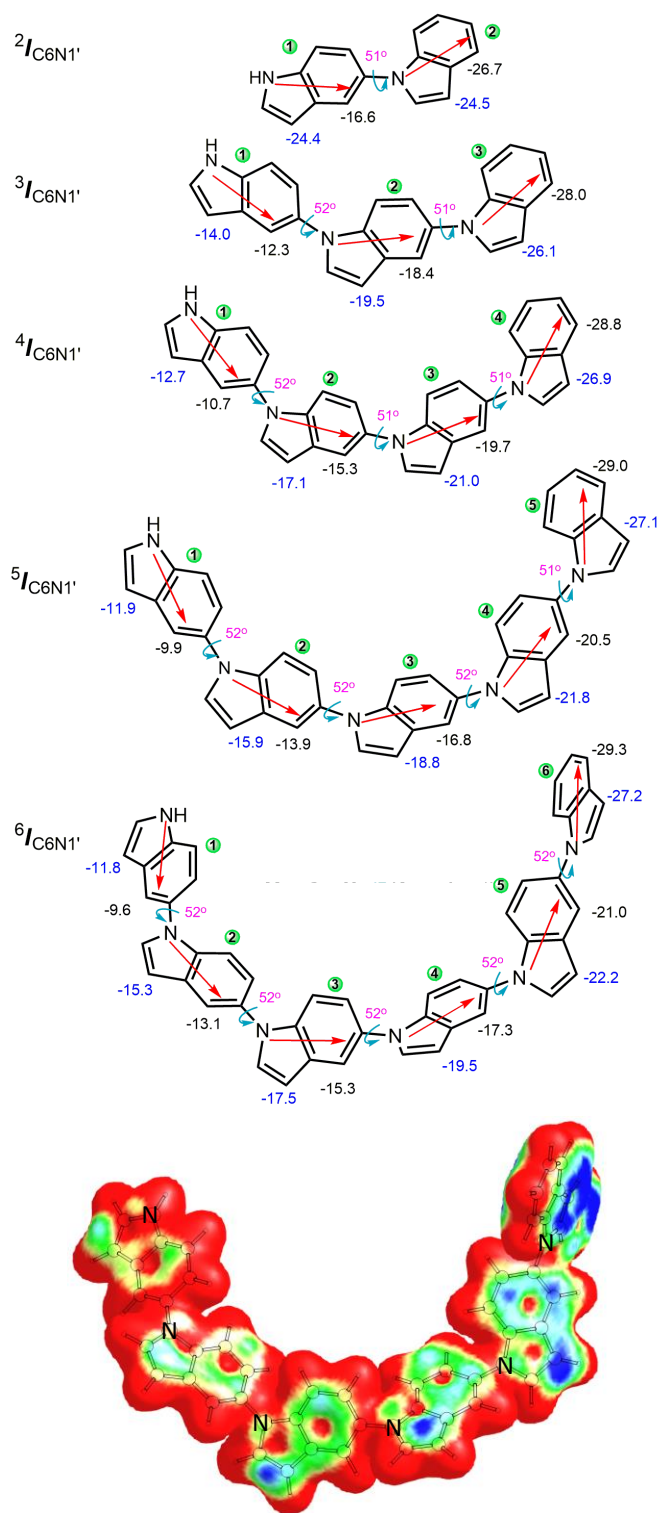
Figure 3.33 The direction of electron flow and the variation in V_m values in 6, 1'-polyindoles ($^2I_{C6N1'}$ to $^6I_{C6N1'}$). The V_m values of five- and six-membered rings are given in kcal/mol are represented in blue and black font respectively. The dihedral angle at the CCCC junctions between the adjacent rings are given in pink font. The MESP mapped on to 0.01 au electron density isosurface of $^6I_{C3N1'}$, where coding from blue to red indicates MESP values in the range −0.02 to 0.02 au
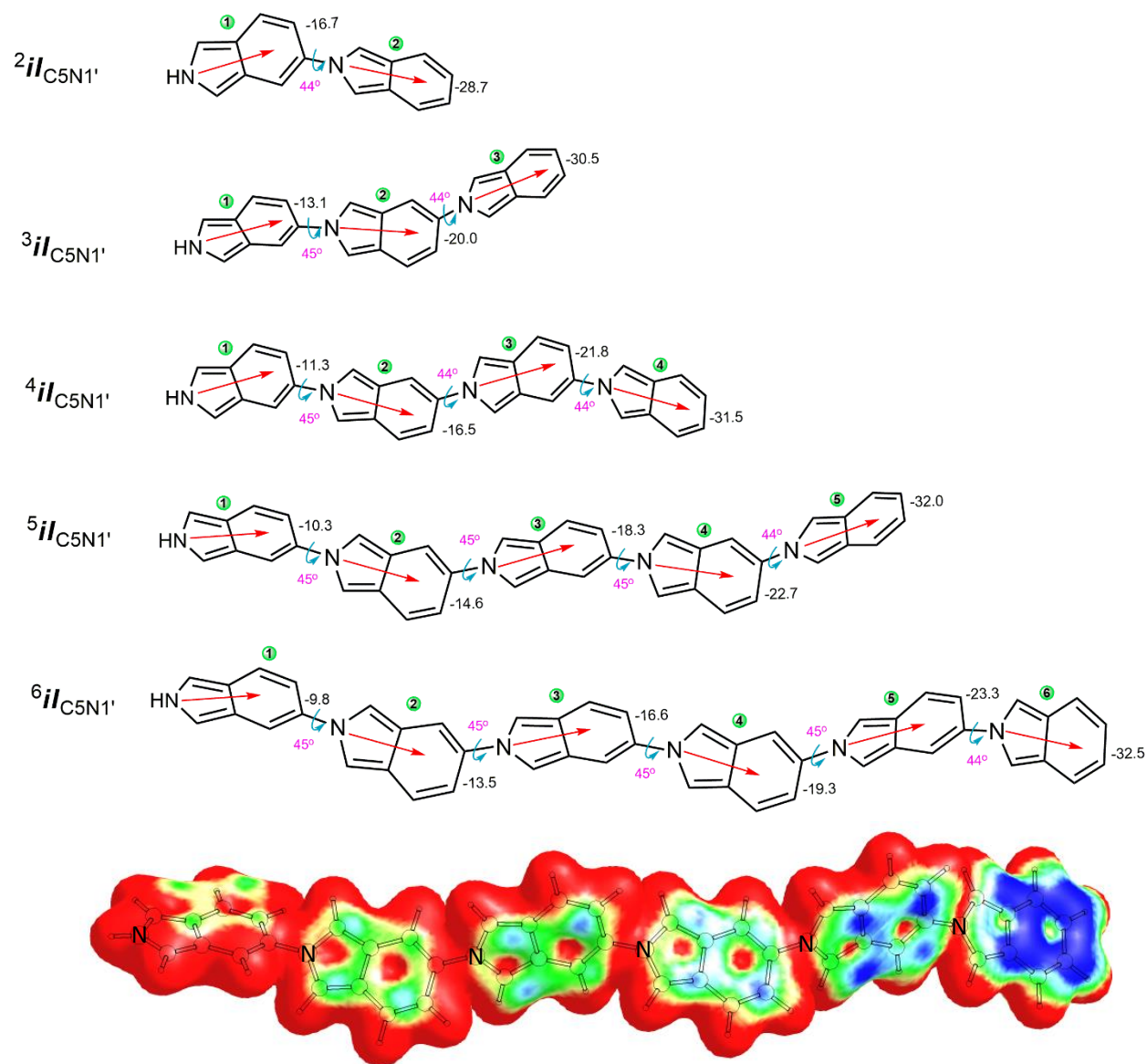
Figure 3.34 The direction of TSE and the variation in V_m values in polyisoindoles ($^2il_{C5N1'}$ to $^6il_{C5N1'}$). The V_m values are given in kcal/mol (black font) and the dihedral angle at the CCCC junctions between the adjacent rings are given in pink font. The MESP mapped on to 0.01 au electron density isosurface of $^6il_{C5N1'}$, where coding from blue to red indicates MESP values in the range −0.02 to 0.02 au
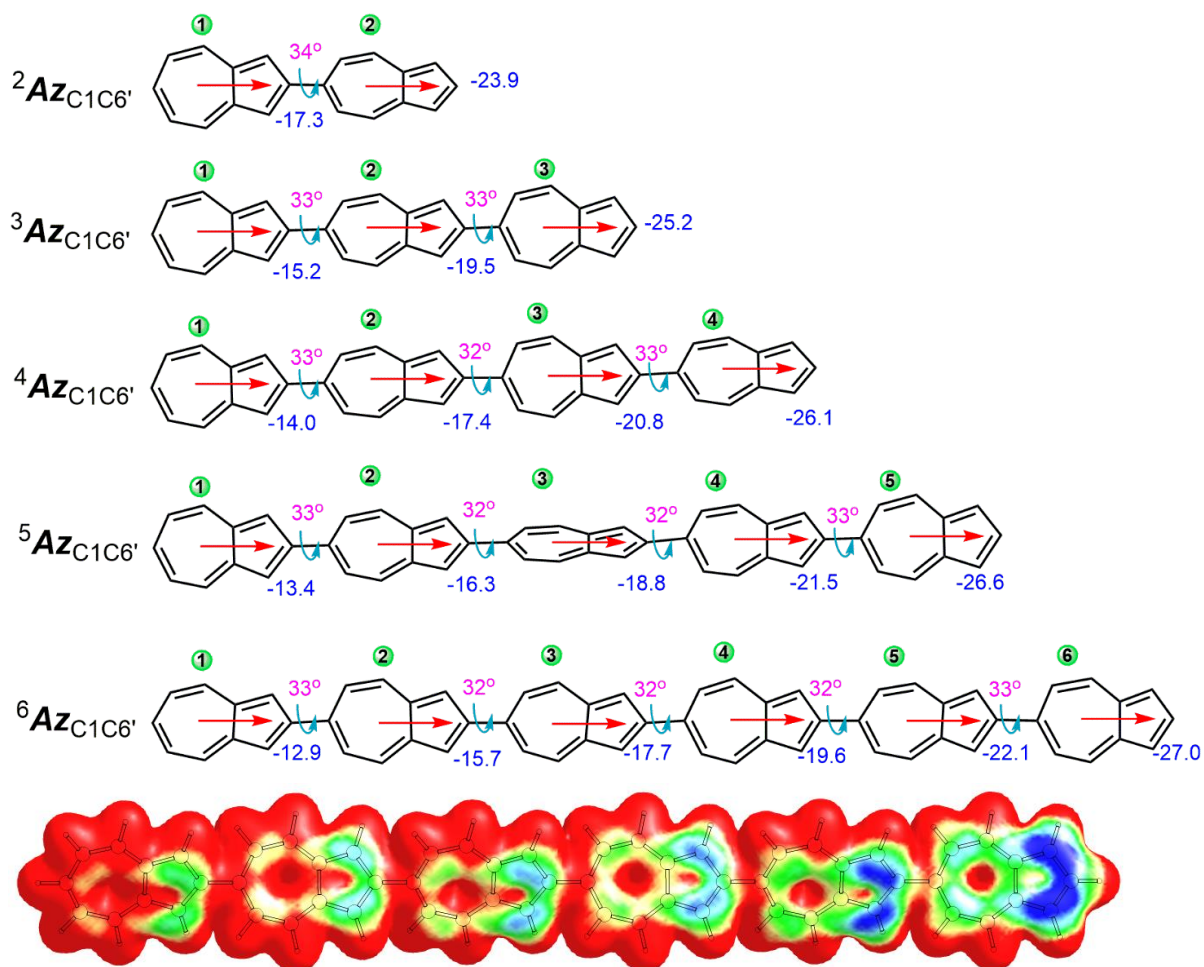
Figure 3.35 The direction of TSE and the variation in V_m values in polyazulenes ($^2Az_{C1C6'}$ to $^6Az_{C1C6'}$). The V_m values are given in kcal/mol (blue font) and azulene units from left to right are numbered from 1 to 6 respectively. The dihedral angle at the CCCC junctions between the adjacent units are given in pink font. The MESP mapped on to 0.01 au electron density isosurface of $^6Az_{C1C6'}$, where coding from blue to red indicates MESP values in the range −0.02 to 0.02 au
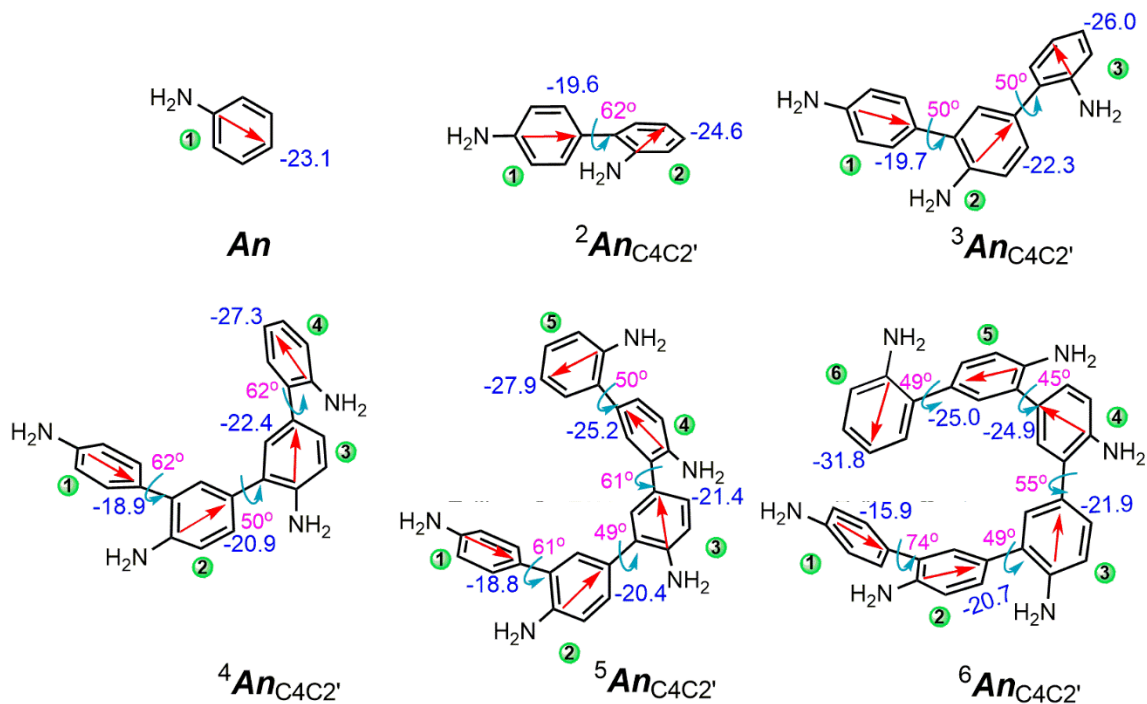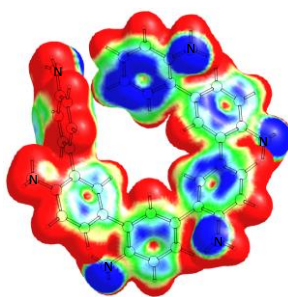
Figure 3.36 (a) The direction of TSE and the variation in V_m values in polyanilines (***An*** to ⁶***An***C4C2'). The V_m values are given in kcal/mol (blue font) and aniline rings from left to right are numbered from 1 to 6 respectively. The dihedral angle at the CCCC junctions between the adjacent rings are given in pink font. (b) The MESP mapped on to 0.01 au electron density isosurface of ⁶***An***C4C2', where coding from blue to red indicates MESP values in the range −0.03 to 0.03 au
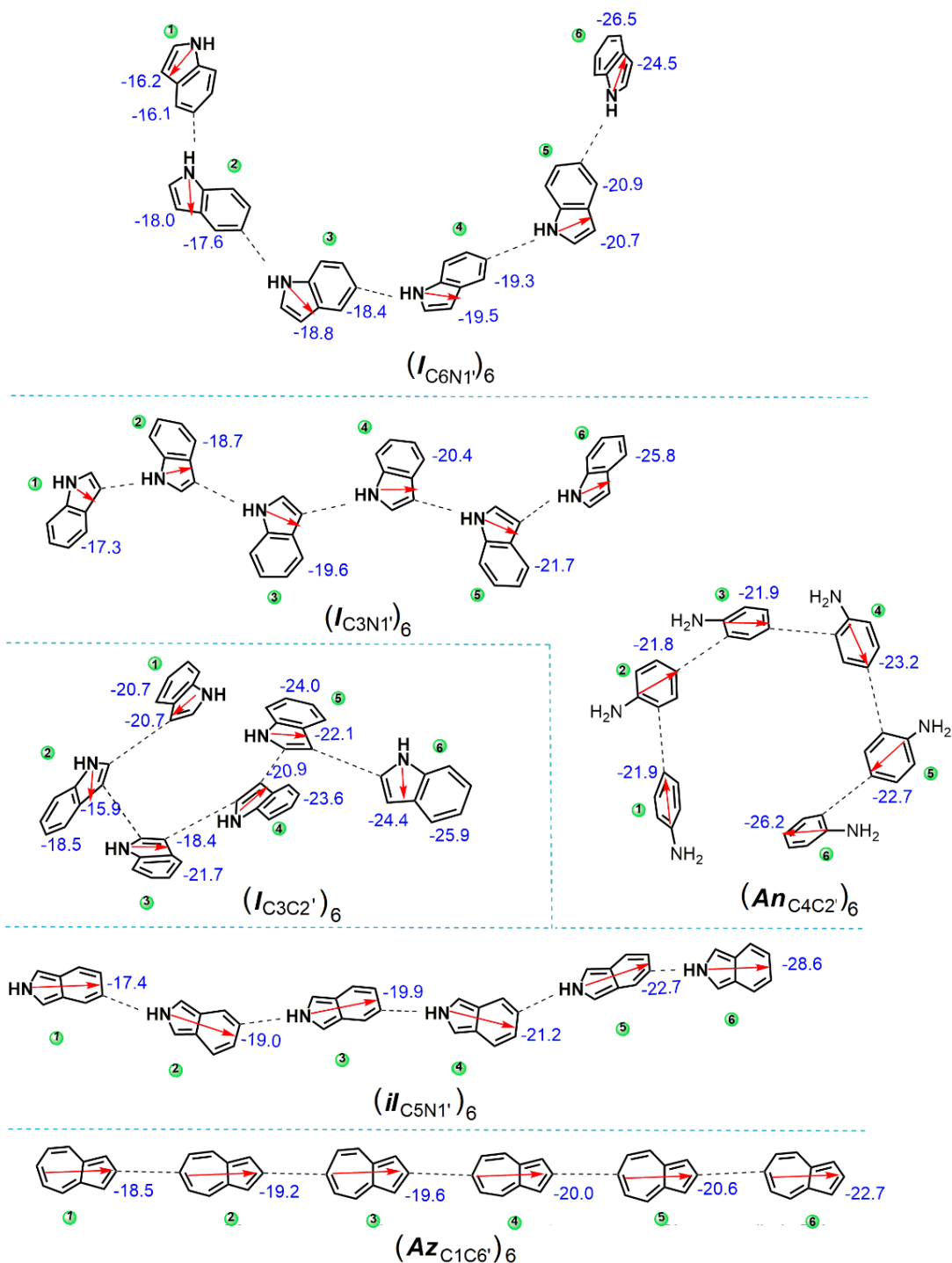
Figure 3.37 The direction of TSE in clusters of $I_{C3N1'}$, $I_{C3C2'}$, $I_{C6N1'}$, $iI_{C5N1'}$, $An_{C4C2'}$ and $Az_{C1C6'}$ systems and the V_m values are given in kcal/mol (Dotted lines represent H…..H distances $\cong 0$)

Table 3.7 The SCF energy, dipole moment, HOMO energy, LUMO energy and HOMO-LUMO gap (HLG) of all the systems at M06-2X/6-311+G(d, p) level of theory.

System	SCF energy (au)	Dipole moment (D)	HOMO (eV)	LUMO (eV)	HLG (eV)
pyrrole	-210.135113	1.91	-7.28	0.22	7.50
$^2P_{C2C2'}$	-419.092585	0.93	-6.46	0.10	6.56
$^2P_{C3C3'}$	-419.087658	0.47	-6.45	0.23	6.68
$^2P_{N1N1'}$	-419.037167	0.00	-7.53	0.38	7.91
$^2P_{C2N1'}$	-419.078019	1.81	-7.17	0.10	7.27
$^2P_{C3N1'}$	-419.077622	3.81	-7.12	-0.01	7.12
$^2P_{C3C2'}$	-419.090301	2.86	-6.42	0.09	6.51
$^3P_{C3N1'}$	-628.020696	6.03	-6.86	-0.12	6.74
$^4P_{C3N1'}$	-836.963995	8.28	-6.72	-0.19	6.53
$^5P_{C3N1'}$	-1045.907306	10.57	-6.68	-0.24	6.44
$^6P_{C3N1'}$	-1254.850791	13.21	-6.61	-0.27	6.34
$^3P_{C3C2'}$	-628.048771	4.22	-6.15	-0.03	6.11
$^4P_{C3C2'}$	-837.008796	5.39	-5.99	-0.10	5.90
$^5P_{C3C2'}$	-1045.964679	6.35	-5.85	-0.14	5.70
$^6P_{C3C2'}$	-1254.923696	6.28	-5.75	-0.17	5.58
1-*PhP*	-441.140786	2.28	-7.24	0.10	7.34
2-*PhP*	-441.149684	1.85	-7.19	0.18	7.37
3-*PhP*	-441.148589	2.12	-7.32	0.18	7.50
1, 1'-*PhDP*	-650.089131	0.00	-7.38	-0.28	7.10
2, 2'-*PhDP*	-650.110482	0.00	-6.47	-0.33	6.14
3, 3'-*PhDP*	-650.106479	6.34	-6.47	0.15	6.62
1, 3'-*PhDP*	-650.098642	4.24	-6.91	-0.01	6.90
HPB$_{N1}$	-1485.854932	0.00	-7.34	-0.85	6.48
HPB$_{C2}$	-1485.929707	0.02	-6.56	-0.42	6.13
HPB$_{C3}$	-1485.902467	4.48	-6.07	0.13	6.20
HPB$_{N16\sigma}$	-1478.755814	0.87	-5.82	-0.82	5.00
HPB$_{C26\sigma}$	-1478.711554	3.88	-5.98	-0.70	5.28
HPB$_{C36\sigma}$	-1478.787673	6.88	-5.33	-0.05	5.29

System	SCF energy (au)	Dipole moment (D)	HOMO (eV)	LUMO (eV)	HLG (eV)
OPN_{N1}	-2057.335592	0.04	-7.09	-1.86	5.23
$OPN_{N16\sigma}$	-2047.870308	0.00	-5.50	-1.51	3.99
$OPN_{C36\sigma}$	-2047.966596	0.03	-4.88	-0.26	4.61
DPC_{N1}	-2857.433340	0.29	-6.88	-2.03	4.85
DPC_{C3}	-2857.505526	4.60	-5.42	0.04	5.46
Indole	-363.756824	2.11	-7.06	0.11	7.17
$^2I_{C3N1'}$	-726.335890	3.63	-6.73	-0.13	6.60
$^3I_{C3N1'}$	-1088.887740	5.52	-6.54	-0.23	6.31
$^4I_{C3N1'}$	-1451.453493	7.48	-6.45	-0.30	6.15
$^5I_{C3N1'}$	-1814.019290	9.49	-6.40	-0.36	6.05
$^6I_{C3N1'}$	-2176.585098	11.22	-6.37	-0.39	5.97
$^2I_{C3C2'}$	-726.335890	3.63	-6.53	-0.12	6.41
$^3I_{C3C2'}$	-1088.918578	4.49	-6.54	-0.23	6.31
$^4I_{C3C2'}$	-1451.503285	3.30	-6.38	-0.32	6.06
$^5I_{C3C2'}$	-1814.101744	5.66	-6.09	-0.45	5.64
$^6I_{C3C2'}$	-2176.683402	7.09	-6.04	-0.51	5.52
$^2I_{C6N1'}$	-726.324788	4.57	-6.71	-0.10	6.61
$^3I_{C6N1'}$	-1088.893201	6.91	-6.59	-0.25	6.34
$^4I_{C6N1'}$	-1451.461808	8.64	-6.53	-0.32	6.21
$^5I_{C6N1'}$	-1814.030487	9.50	-6.51	-0.36	6.15
$^6I_{C6N1'}$	-2176.599293	9.98	-6.50	-0.37	6.13
isoindole	-363.741162	2.69	-6.38	0.07	6.45
^2iI	-726.294333	6.06	-6.20	-0.49	5.71
^3iI	-1088.847838	9.97	-6.11	-0.73	5.37
^4iI	-1451.401615	13.97	-6.05	-0.86	5.19
$^5\,iI$	-1813.955571	18.27	-6.02	-0.94	5.08
^6iI	-2176.509521	22.31	-6.00	-0.98	5.02

System	SCF energy (au)	Dipole moment (D)	HOMO (eV)	LUMO (eV)	HLG (eV)
Azulene	-385.754624	1.26	-6.68	-1.49	5.20
^2Az	-770.329854	3.34	-6.59	-2.08	4.52
^3Az	-1154.905556	5.94	-6.53	-2.35	4.18
^4Az	-1539.481290	8.86	-6.49	-2.50	3.99
^5Az	-1924.057144	11.92	-6.46	-2.59	3.88
^6Az	-2308.632953	15.14	-6.44	-2.65	3.80
Aniline	-287.553474	1.52	-7.10	0.31	7.42
^2An	-573.924979	2.82	-6.73	0.13	6.86
^3An	-860.299622	4.44	-6.52	0.13	6.65
^4An	-1146.669773	3.62	-6.43	0.05	6.49
^5An	-1433.042957	3.67	-6.33	0.02	6.35
^6An	-1719.417556	2.35	-6.25	0.04	6.29
$HAzB_{C1}$	-2539.639777	0.01	-6.31	-1.59	4.72
$HAzB_{C6}$	-2539.619065	0.00	-6.66	-1.93	4.72

Katagiri *et al.* reported the synthesis of $^3Az_{C1C6'}$ and other isomers, the terazulenes.[55] The excellent *n*-type behaviour exhibited by $^3Az_{C1C6'}$ as an organic field-effect transistor could be attributed to TSE which leads to the unidirectional flow of electron density. Also the electron-rich or deficient character of the central arene ring of the star-like azulene systems (*HAzB*) can be well described using the phenomenon of TSE (Figure 3.38). Connecting five-membered ring of *Az* to the arene pushes more electron density towards the core whereas the reverse effect occurs when the connection is made with the seven-membered ring.
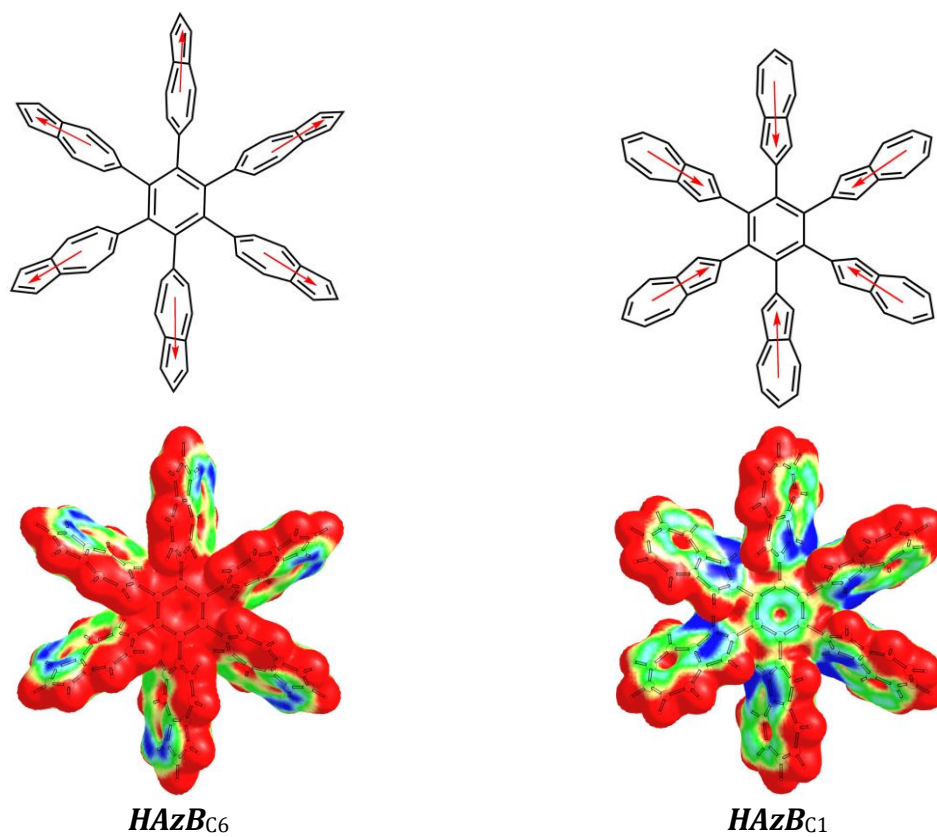
Figure 3.38 The MESP mapped on to 0.01 au electron density isosurface for **HAzB** systems, where coding from blue to red indicates MESP values in the range −0.02 to 0.02 au

3.9.8 NMR Data

The TSE phenomenon is also observed in the nuclear magnetic resonance (NMR) data. The correlation between the chemical shift at the C_3 center (δ_C) and the V_m value of the first and last pyrrole rings in $^nP_{C3N1'}$ is illustrated in Figure 3.39. In all cases, first rings show considerably high δ_C than the last ring, indicating the deshielded and shielded environment of the first and last rings, respectively. Thus the NMR data clearly support the donor nature of the first and acceptor nature of last pyrrole units. Similarly, the δ_H data also agrees to the donor-acceptor character of $^nP_{C3N1'}$. Furthermore, NMR analysis is conducted on other oligomeric systems, *viz.,* $^nP_{C3C2'}$, $^nI_{C3N1'}$, $^nI_{C3C2'}$, $^nI_{C6N1'}$, $^niI_{C5N1'}$, $^nAz_{C1C6'}$, and $^nAn_{C4C2'}$. In each case, a strong correlation is observed between the chemical shift at

189

the H, C, or N center and the MESP. The first monomer unit consistently exhibited significant deshielding, indicating their strong donor character. Conversely, the last monomer unit consistently demonstrated substantial shielding, indicating its strong acceptor character.
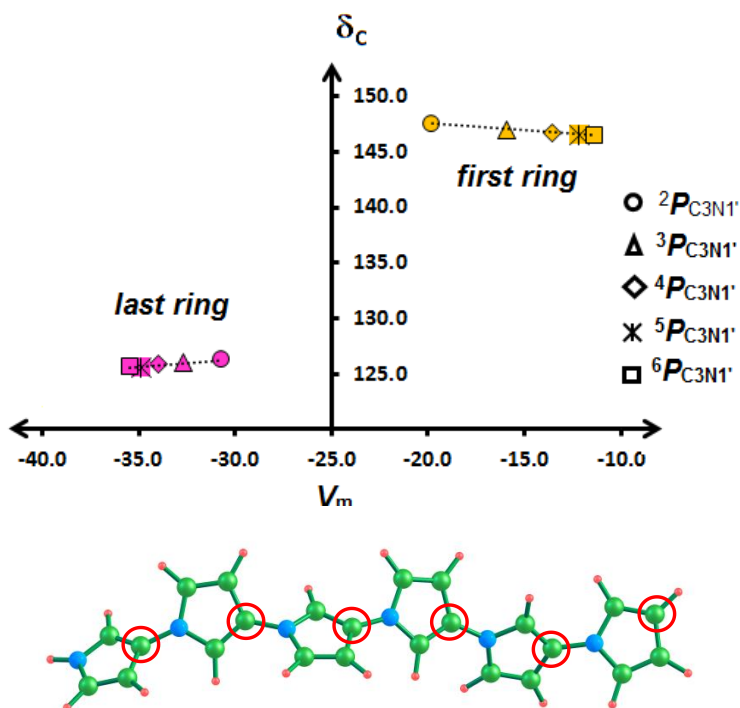
Figure 3.39 Relation between chemical shift, δ (in ppm) at the C_3 centers (represented using a red circle) and MESP V_m (in kcal/mol) at the first pyrrole ring (in yellow) and last pyrrole ring (in pink) in $^nP_{C3N1'}$ systems ($^2P_{C3N1'}$ to $^6P_{C3N1'}$).

3.9.9 Absorption Spectra

The theoretical λ_{max} of several known compounds is analysed in this study. The TSE induced electronic polarization phenomenon exhibited by molecular systems can be correlated with the absorption spectra of these molecules. Figure 3.40 illustrates the simulated absorption spectra of $^nP_{C3N1'}$, emphasizing the occurrence of a red shift from $^2P_{C3N1'}$ to $^6P_{C3N1'}$. This phenomenon can be attributed to the substantial increase in electron density in the last ring of $^nP_{C3N1'}$. Similar red shift in absorption spectra is observed for $^nP_{C3N1'}$, $^nP_{C3C2'}$, $^nI_{C3N1'}$, $^nI_{C3C2'}$, $^nI_{C6N1'}$, $^niI_{C5N1'}$, $^nAz_{C1C6'}$, and $^nAn_{C4C2'}$ systems indicating the strong *D-A* character of these molecules (Figure 3.41 to Figure 3.47).
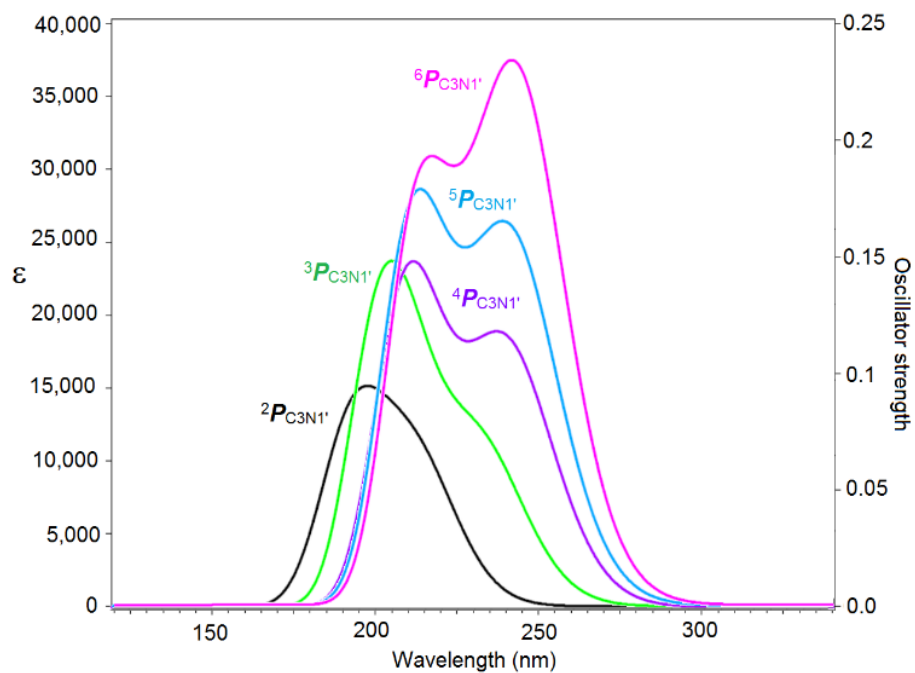
Figure 3.40 Simulated absorption spectra of $^nP_{C3N1'}$ systems (ε is given L mol^{-1} cm^{-1})
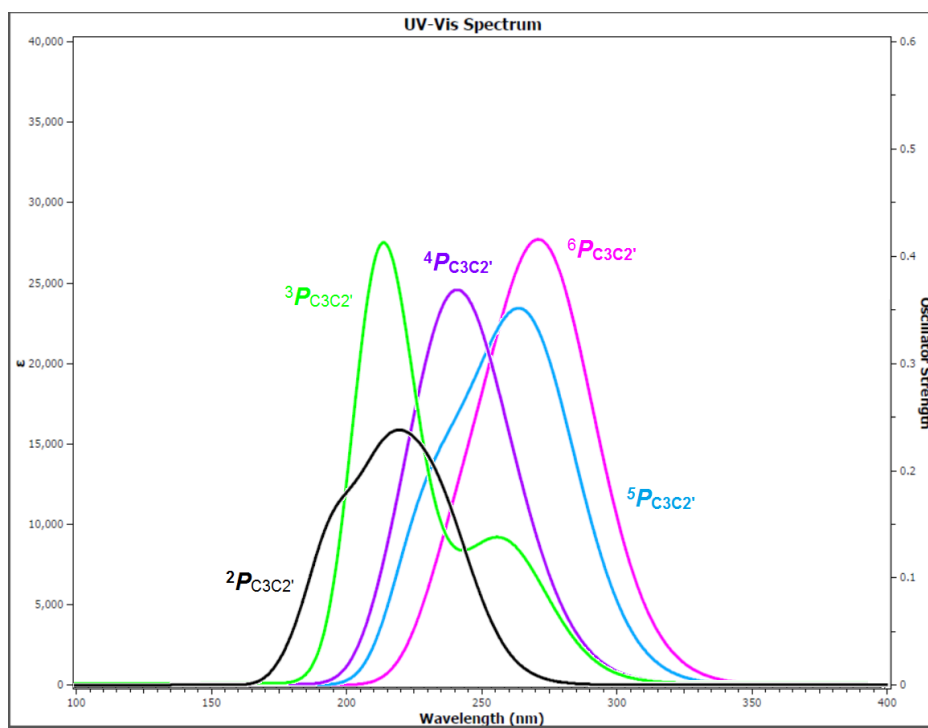
Figure 3.41 Simulated absorption spectra of $^nP_{C3C2'}$ where n = 2 to 6
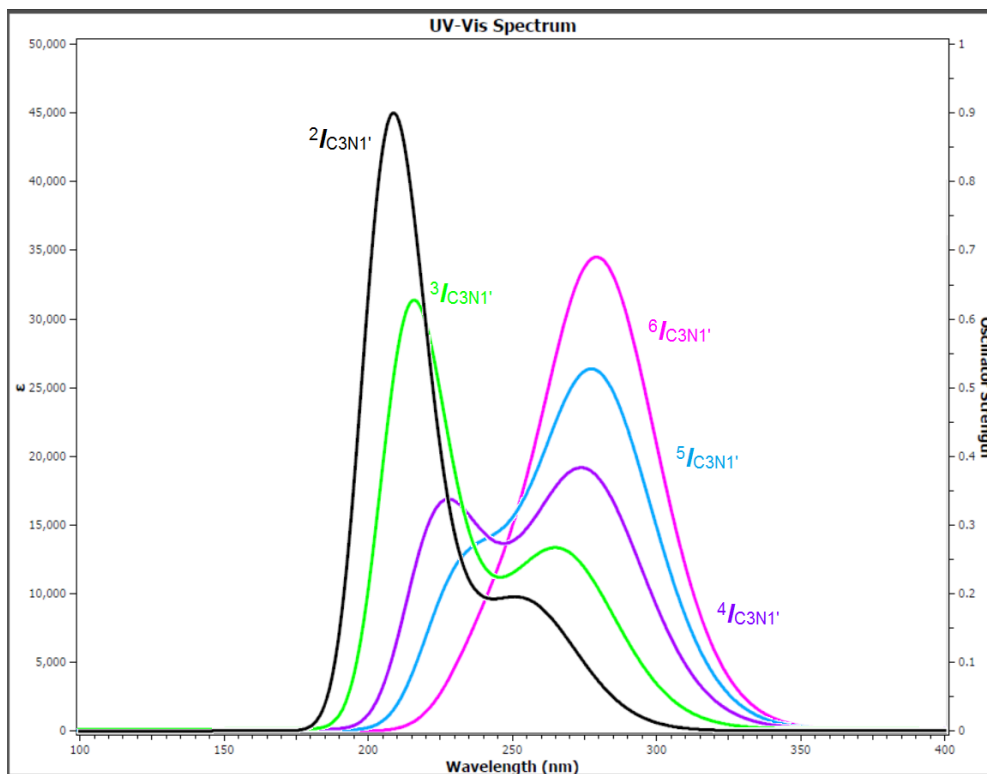
Figure 3.42 Simulated absorption spectra of $^{n}I_{C3N1'}$ where n = 2 to 6
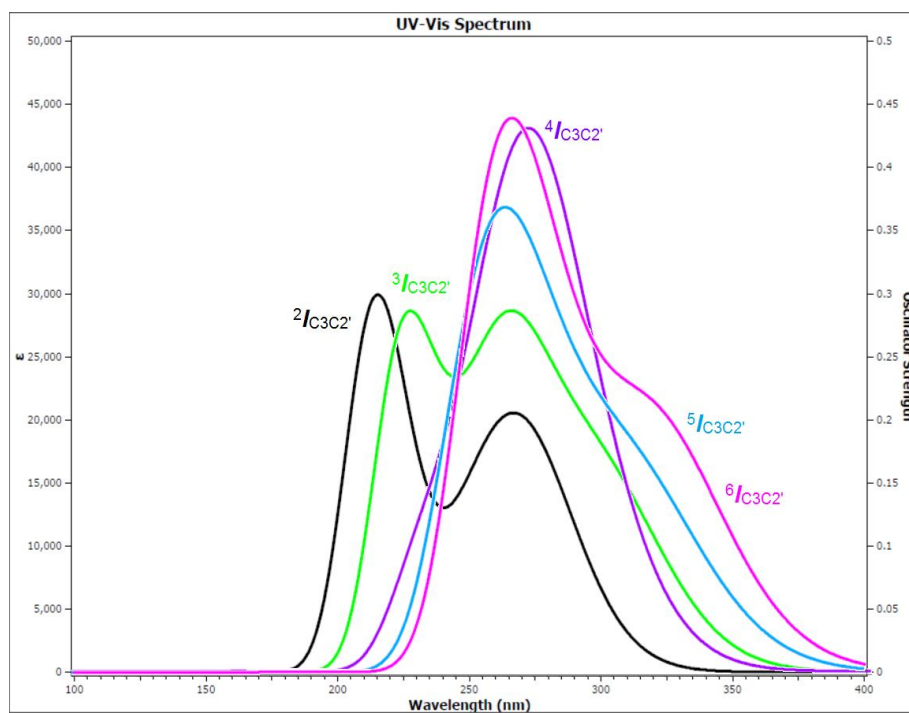
Figure 3.43 Simulated absorption spectra of $^{n}I_{C3C2'}$ where n = 2 to 6
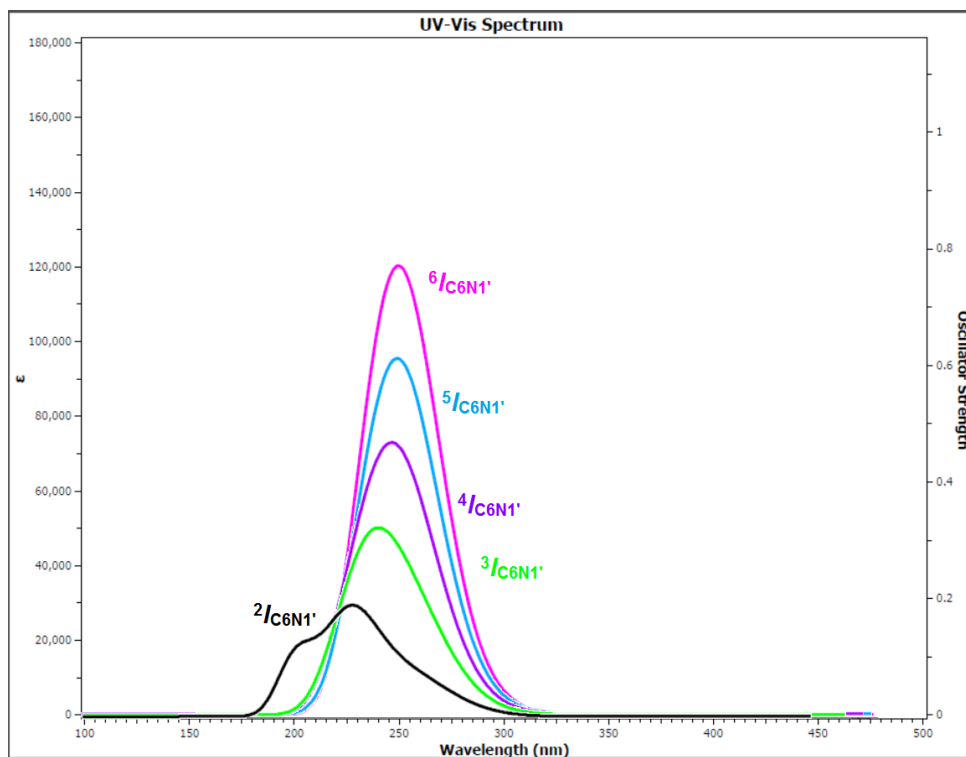
Figure 3.44 Simulated absorption spectra of $^nI_{C6N1'}$ where n = 2 to 6
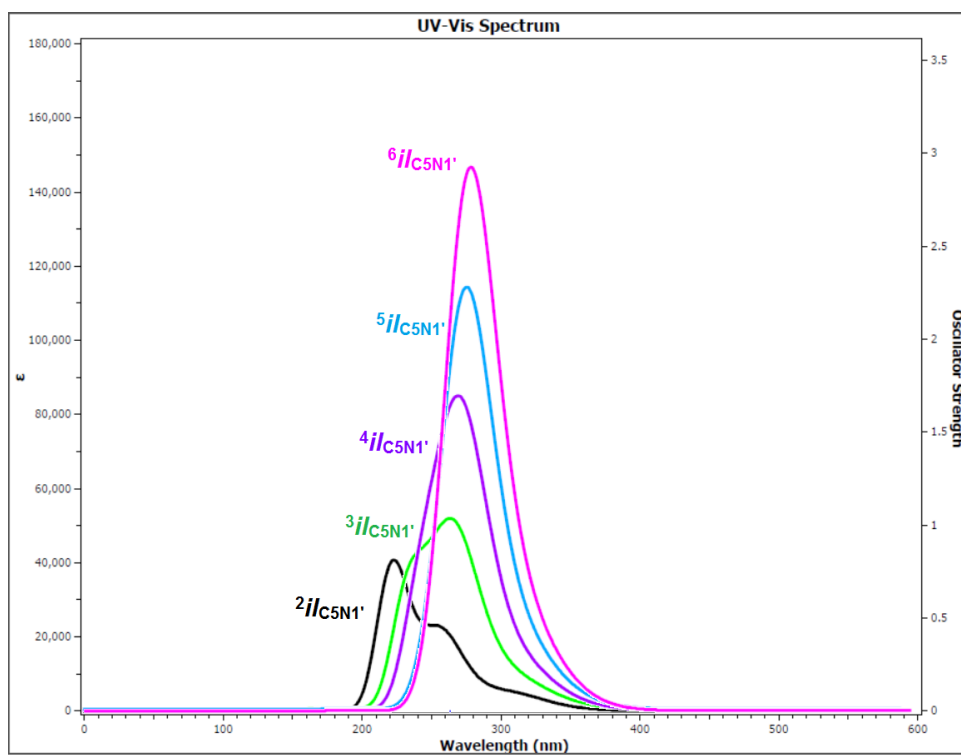
Figure 3.45 Simulated absorption spectra of $^niI_{C5N1'}$ where n = 2 to 6
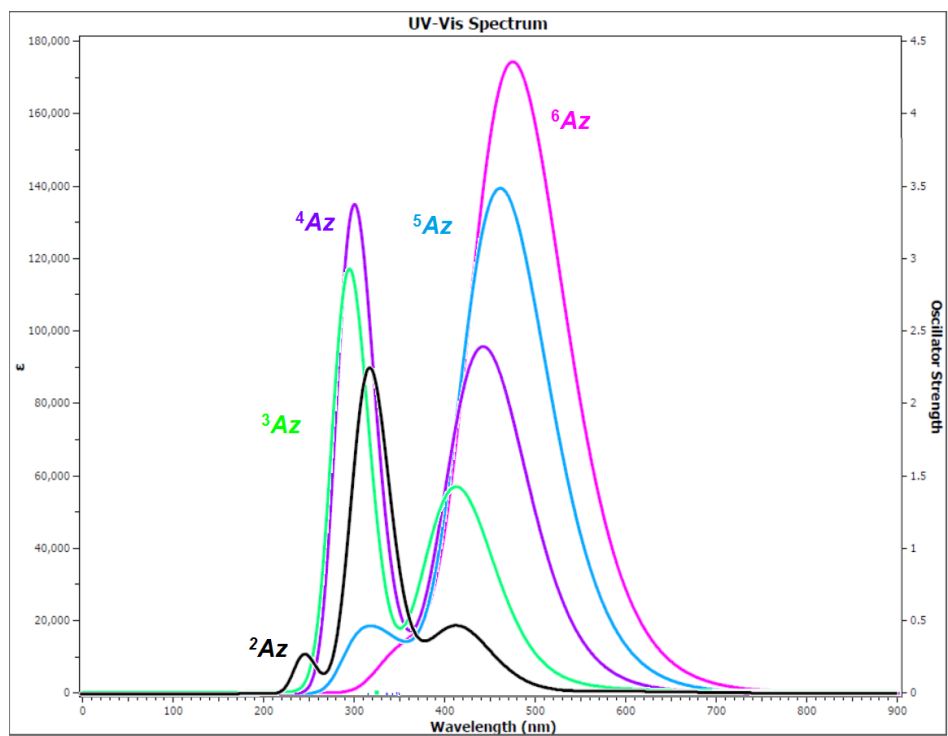
Figure 3.46 Simulated absorption spectra of ${}^{n}\textbf{\textit{Az}}$, where n = 2 to 6
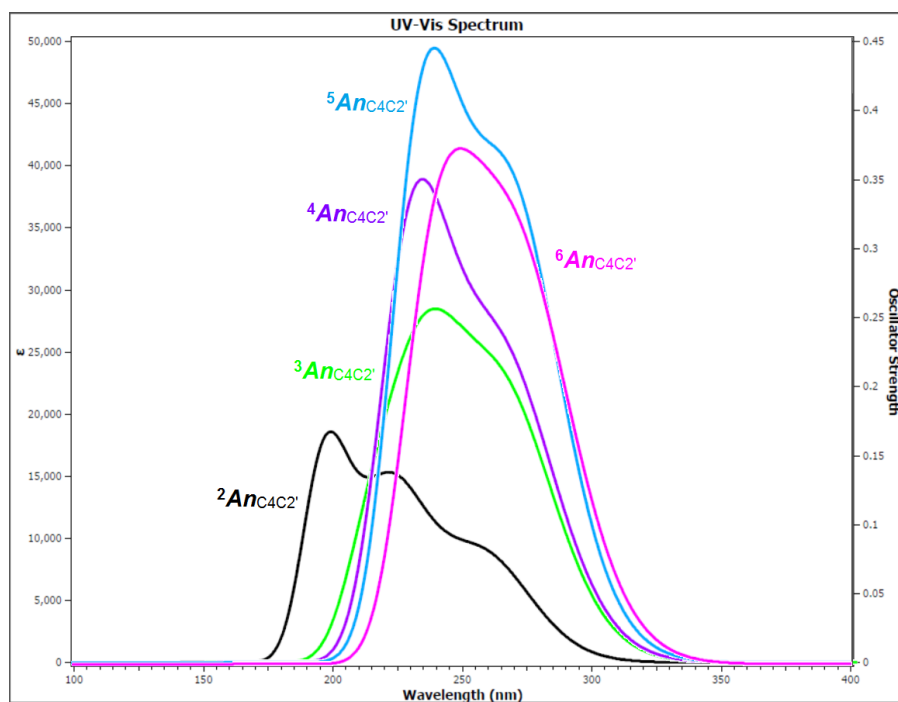
Figure 3.47 Simulated absorption spectra of ${}^{n}\textbf{\textit{An}}_{C4C2'}$, where n = 2 to 6

We have also applied Ciofini *et al.*'s procedure to compute the difference in total electron density between the ground and excited states of representative examples 1-*PhP* and *HPB*_{N1} (Figure 3.48) to verify the electronic polarization within these systems.[190]
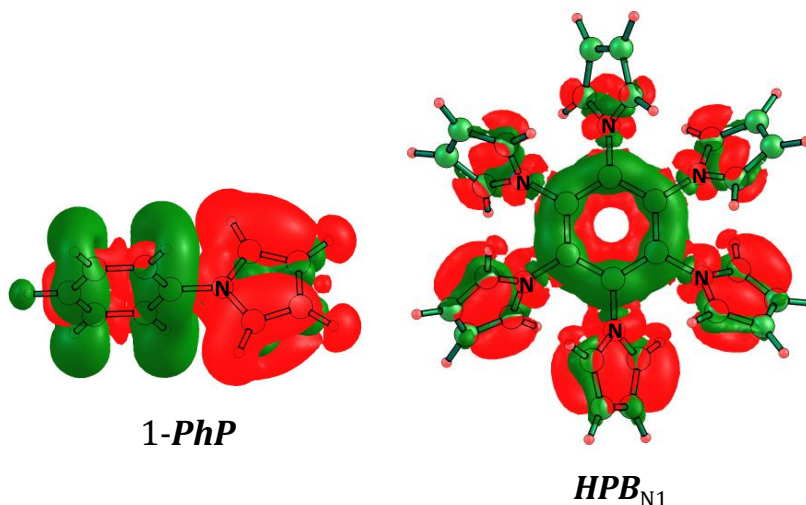
1-*PhP*

*HPB*_{N1}

Figure 3.48 The difference in total density computed for the ground and excited states of 1-*PhP* and *HPB*$_{N1}$ systems plotted at iso-contour value 0.001 au

The density maps unequivocally indicate that areas of electron density depletion are primarily localized around the pyrrole unit, whereas a noticeable augmentation in electron density is observed within the central benzene unit. This analysis underscores the distinct electronic behaviours in these molecules, shedding light on their unique polarization patterns and electronic structures.

3.10 Conclusions

The fundamental phenomenon of TSE is unraveled for a variety of molecular systems using MESP topology analysis which confirmed that it is highly directional in nature. Pyrrole exhibits strong TSE due to the presence of a highly electron deficient, N-center and extremely electron rich, C_3C_4 bonding region. By aligning the TSE of pyrrole units in the same direction, polypyrrole systems with high electronic polarization can be made. The TSE effect in polypyrrole is nearly unaffected by the twist angle between adjacent pyrrole units. Polypyrroles show strong donor-acceptor character from one end to the other due to TSE as the system is devoid of a specific donor or acceptor moieties.

Furthermore, TSE clearly explains the electron rich/deficient feature of experimentally known phenylpyrrole, hexapyrrolylbenzene, octapyrrolylnaphthalene, and decapyrrolylcorannulene systems as well as the newly designed core-expanded structures such as N-doped nanographenes. Highly directed TSE in azulene, indole, isoindole, and aniline is also disclosed here. The MESP-analysis of their oligomers, core-expanded structures and noncovalent clusters proved the predominance of TSE over TBE which creates strong donor-acceptor feature in all such systems. The data such as APT charge, NMR chemical shift, FMO and λ_{max} support the strong donor-acceptor character of the molecular systems. Tuning the directionality of TSE opens up a new molecular design strategy to construct donor-acceptor systems without specific donors and acceptors.

3.11 References

1. E. H. Falcao and F. Wudl, *J. Chem. Technol. Biotechnol.*, **2007**, 82, 524-531.
2. A. Hirsch, *Nat. Mater.*, **2010**, 9, 868-871.
3. N. Slepičková Kasálková, P. Slepička and V. Švorčík, *Nanomaterials*, **2021**, 11, 2368.
4. R. Rao, C. L. Pint, A. E. Islam, R. S. Weatherup, S. Hofmann, E. R. Meshot, F. Wu, C. Zhou, N. Dee, P. B. Amama, J. Carpena-Nuñez, W. Shi, D. L. Plata, E. S. Penev, B. I. Yakobson, P. B. Balbuena, C. Bichara, D. N. Futaba, S. Noda, H. Shin, K. S. Kim, B. Simard, F. Mirri, M. Pasquali, F. Fornasiero, E. I. Kauppinen, M. Arnold, B. A. Cola, P. Nikolaev, S. Arepalli, H.-M. Cheng, D. N. Zakharov, E. A. Stach, J. Zhang, F. Wei, M. Terrones, D. B. Geohegan, B. Maruyama, S. Maruyama, Y. Li, W. W. Adams and A. J. Hart, *ACS Nano*, **2018**, 12, 11756-11784.
5. V. P. Zhdanov, *Catal. Lett.*, **2022**.
6. R. Jasti, J. Bhattacharjee, J. B. Neaton and C. R. Bertozzi, *J. Am. Chem. Soc.*, **2008**, 130, 17646-17647.
7. E. Kayahara, V. K. Patel and S. Yamago, *J. Am. Chem. Soc.*, **2014**, 136, 2284-2287.
8. D. Eisenberg, R. Shenhar and M. Rabinovitz, *Chem. Soc. Rev.*, **2010**, 39, 2879-2890.
9. Y. Segawa, A. Yagi, K. Matsui and K. Itami, *Angew. Chem. Int. Ed.*, **2016**, 55, 5136-5158.
10. K. Y. Cheung, K. Watanabe, Y. Segawa and K. Itami, *Nat. Chem.*, **2021**, 13, 255-259.
11. G. Povie, Y. Segawa, T. Nishihara, Y. Miyauchi and K. Itami, *Science*, **2017**, 356, 172-175.
12. Y. Li, H. Kono, T. Maekawa, Y. Segawa, A. Yagi and K. Itami, *Mater. Res.*, **2021**, 2, 681-691.

13. K. Y. Cheung, C. K. Chan, Z. Liu and Q. Miao, *Angew. Chem. Int. Ed.*, **2017**, 56, 9003-9007.
14. Y. Sakamoto and T. Suzuki, *J. Am. Chem. Soc.*, **2013**, 135, 14074-14077.
15. Y. Gu, Z. Qiu and K. Müllen, *J. Am. Chem. Soc.*, **2022**.
16. V. Saraswat, R. M. Jacobberger and M. S. Arnold, *ACS Nano*, **2021**, 15, 3674-3708.
17. M. Hasegawa, Y. Nojima and Y. Mazaki, *ChemPhotoChem*, **2021**, 5, 1042-1058.
18. W. Zheng, T. Ikai, K. Oki and E. Yashima, *Nat. sci.*, **2022**, 2, e20210047.
19. M. S. Newman, *J. Am. Chem. Soc.*, **1940**, 62, 1683-1687.
20. M. S. Newman and W. B. Wheatley, *J. Am. Chem. Soc.*, **1948**, 70, 1913-1916.
21. Y. Shen and C.-F. Chen, *Chem. Rev.*, **2012**, 112, 1463-1535.
22. A. Urbano, *Angew. Chem. Int. Ed. Engl.*, **2003**, 42, 3986-3989.
23. M. Krzeszewski, H. Ito and K. Itami, *J. Am. Chem. Soc.*, **2022**, 144, 862-871.
24. C. Krieger, F. Diederich, D. Schweitzer and H. A. Staab, *Angew. Chem., Int. Ed. Engl.*, **1979**, 18, 699-701.
25. S. H. Pun, Y. Wang, M. Chu, C. K. Chan, Y. Li, Z. Liu and Q. Miao, *J. Am. Chem. Soc.*, **2019**, 141, 9680-9686.
26. Q.-H. Guo, Y. Qiu, M.-X. Wang and J. Fraser Stoddart, *Nat. Chem.*, **2021**, 13, 402-419.
27. H. Christoph, J. Grunenberg, H. Hopf, I. Dix, P. G. Jones, M. Scholtissek and G. Maier, *Chem. Eur. J.*, **2008**, 14, 5604-5616.
28. M. Orozco-Ic, R. R. Valiev and D. Sundholm, *Phys. Chem. Chem. Phys.*, **2022**, 24, 6404-6409.
29. G. Monaco, R. Zanasi and F. F. Summa, *J. Phys. Chem. A*, **2022**, 126, 3717-3723.
30. V. M. Freixas, S. Tretiak and S. Fernandez-Alberti, *J. Phys. Chem. Lett.*, **2022**, 13, 8495-8501.
31. P. V. R. Schleyer, *Chem. Rev.*, **2001**, 101, 1115-1118.
32. S. R. Gadre, S. V. Bapat, K. Sundararajan and I. H. Shrivastava, *Chem. Phys. Lett.*, **1990**, 175, 307-312.
33. S. R. Gadre, S. A. Kulkarni and I. H. Shrivastava, *J. Chem. Phys.*, **1992**, 96, 5253-5260.
34. E. Scrocco and J. Tomasi, *The electrostatic molecular potential as a tool for the interpretation of molecular properties*, in *New concepts II*. 1973, Springer. p. 95-170.
35. S. R. Gadre and R. K. Pathak. *Nonexistence of local maxima in molecular electrostatic potential maps*. in *Proc. Ind. Acad. Sci. (Chem. Sci.)*. 1990: Springer.
36. S. R. Gadre and I. H. Shrivastava, *J. Chem. Phys.*, **1991**, 94, 4384-4390.
37. R. N. Shirsat, S. V. Bapat and S. R. Gadre, *Chem. Phys. Lett.*, **1992**, 200, 373-378.
38. A. D. Becke, *J. Chem. Phys.*, **1993**, 98, 1372-1377.
39. A. D. Becke, *Phys. Rev. A*, **1988**, 38, 3098-3100.
40. M. J. Frisch, G. W. Trucks, H. B. Schlegel, G. E. Scuseria, M. A. Robb, J. R. Cheeseman, G. Scalmani, V. Barone, G. A. Petersson, H. Nakatsuji, X. Li, M. Caricato, A. V. Marenich, J. Bloino, B. G. Janesko, R. Gomperts, B. Mennucci, H. P. Hratchian, J. V. Ortiz, A. F. Izmaylov, J. L. Sonnenberg, D. Williams-Young, F. Ding, F. Lipparini, F. Egidi, J. Goings, B. Peng, A. Petrone, T. Henderson, D. Ranasinghe, V. G. Zakrzewski, J. Gao, N. Rega, G. Zheng, W. Liang, M. Hada, M. Ehara, K. Toyota, R. Fukuda, J. Hasegawa, M. Ishida, T. Nakajima, Y. Honda, O. Kitao, H. Nakai, T. Vreven, K.

Throssell, J. A. Montgomery Jr., J. E. Peralta, F. Ogliaro, M. J. Bearpark, J. J. Heyd, E. N. Brothers, K. N. Kudin, V. N. Staroverov, T. A. Keith, R. Kobayashi, J. Normand, K. Raghavachari, A. P. Rendell, J. C. Burant, S. S. Iyengar, J. Tomasi, M. Cossi, J. M. Millam, M. Klene, C. Adamo, R. Cammi, J. W. Ochterski, R. L. Martin, K. Morokuma, O. Farkas, J. B. Foresman and D. J. Fox, *Gaussian 16 Rev. A.03*. 2016: Wallingford, CT.

41. A. Kumar, S. D. Yeole, S. R. Gadre, R. López, J. F. Rico, G. Ramírez, I. Ema and D. Zorrilla, *J. Comput. Chem.*, **2015**, 36, 2350-2359.

42. R. López, J. F. Rico, G. Ramírez, I. Ema and D. Zorrilla, *Comput. Phys. Commun.*, **2009**, 180, 1654-1660.

43. R. López, J. F. Rico, G. Ramírez, I. Ema and D. Zorrilla, *Comput. Phys. Commun.*, **2015**, 192, 289-294.

44. R. López, J. F. Rico, G. Ramírez, I. Ema, D. Zorrilla, A. Kumar, S. D. Yeole and S. R. Gadre, *Comput. Phys. Commun.*, **2017**, 214, 207-215.

45. S. R. Gadre and R. D. Bendale, *Chem. Phys. Lett.*, **1986**, 130, 515-521.

46. P. K. Anjalikrishna, C. H. Suresh and S. R. Gadre, *J. Phys. Chem. A*, **2019**, 123, 10139-10151.

47. P. K. Anjalikrishna, S. R. Gadre and C. H. Suresh, *J. Phys. Chem. A*, **2021**, 125, 5999-6012.

48. R. Rieger and K. Müllen, *J. Phys. Org. Chem.*, **2010**, 23, 315-325.

49. R. Rakhi and C. H. Suresh, *ChemistrySelect*, **2021**, 6, 2760-2769.

50. K. P. Vijayalakshmi and C. H. Suresh, *New J. Chem.*, **2010**, 34, 2132-2138.

51. M. Solà, *Front. Chem.*, **2017**, 5.

52. C. Suresh and S. R. Gadre, *J. Org. Chem.*, **1999**, 64, 2505-2512.

53. R. Herges and D. Geuenich, *J. Phys. Chem. A*, **2001**, 105, 3214-3220.

54. C. Lu, P. Chen, H. Sheng, C. Li and J. Wang, *Spectrochim. Acta A Mol. Biomol. Spectrosc.*, **2022**, 282, 121674.

55. M. H. Garner, W. Bro-Jørgensen, P. D. Pedersen and G. C. Solomon, *J. Phys. Chem. C*, **2018**, 122, 26777-26789.

56. J. H. Dopper and H. Wynberg, *Tetrahedron Lett.*, **1972**, 13, 763-766.

57. T. Hensel, N. N. Andersen, M. Plesner and M. Pittelkow, *Synlett*, **2016**, 27, 498-525.

58. B. Kumar and B. T. King, *J. Org. Chem.*, **2012**, 77, 10617-10622.

59. Bharat, R. Bhola, T. Bally, A. Valente, M. K. Cyrański, Ł. Dobrzycki, S. M. Spain, P. Rempała, M. R. Chin and B. T. King, *Angew. Chem. Int. Ed.*, **2010**, 49, 399-402.

60. W. E. Barth and R. G. Lawton, *J. Am. Chem. Soc.*, **1966**, 88, 380-381.

61. L. T. Scott, M. M. Hashemi, D. T. Meyer and H. B. Warren, *J. Am. Chem. Soc.*, **1991**, 113, 7082-7084.

62. Y.-T. Wu and J. S. Siegel, *Chem. Rev.*, **2006**, 106, 4843-4867.

63. H.-C. Shen, J.-M. Tang, H.-K. Chang, C.-W. Yang and R.-S. Liu, *J. Org. Chem.*, **2005**, 70, 10113-10116.

64. K. Yamamoto, T. Harada, M. Nakazaki, T. Naka, Y. Kai, S. Harada and N. Kasai, *J. Am. Chem. Soc.*, **1983**, 105, 7171-7172.

65. K. Yamamoto, T. Harada, Y. Okamoto, H. Chikamatsu, M. Nakazaki, Y. Kai, T. Nakao, M. Tanaka, S. Harada and N. Kasai, *J. Am. Chem. Soc.*, **1988**, 110, 3578-3584.

66. C.-N. Feng, W.-C. Hsu, J.-Y. Li, M.-Y. Kuo and Y.-T. Wu, *Chem. Eur. J.*, **2016**, 22, 9198-9208.
67. C. N. Feng, M. Y. Kuo and Y. T. Wu, *Angew. Chem.*, **2013**, 125, 7945-7948.
68. R. W. Miller, A. K. Duncan, S. T. Schneebeli, D. L. Gray and A. C. Whalley, *Chem. Eur. J.*, **2014**, 20, 3705-3711.
69. B. Thulin and O. Wennerstrom, **1976**.
70. I. R. Márquez, S. Castro-Fernández, A. Millán and A. G. Campaña, *Chem. Comm.*, **2018**, 54, 6705-6718.
71. F. S. Dias and W. S. Machado, *Mol. Simul.*, **2021**, 47, 1002-1009.
72. G. Povie, Y. Segawa, T. Nishihara, Y. Miyauchi and K. Itami, *J. Am. Chem. Soc.*, **2018**, 140, 10054-10059.
73. A. Yagi, Y. Segawa and K. Itami, *Chem*, **2019**, 5, 746-748.
74. Y. Han, S. Dong, J. Shao, W. Fan and C. Chi, *Angew. Chem. Int. Ed.* , **2021**, 60, 2658-2662.
75. Z. Xia, S. H. Pun, H. Chen and Q. Miao, *Angew. Chem. Int. Ed.*, **2021**, 60, 10311-10318.
76. H. M. Bergman, G. R. Kiel, R. C. Handford, Y. Liu and T. D. Tilley, *J. Am. Chem. Soc.*, **2021**, 143, 8619-8624.
77. X.-S. Du, D.-W. Zhang, Y. Guo, J. Li, Y. Han and C.-F. Chen, *Angew. Chem. Int. Ed.*, **2021**, 60, 13021-13028.
78. J. Xie, X. Li, S. Wang, A. Li, L. Jiang and K. Zhu, *Nat. Commun.*, **2020**, 11, 3348.
79. H. Chen, S. Gui, Y. Zhang, Z. Liu and Q. Miao, *CCS Chem.*, **2021**, 3, 613-619.
80. Q. Zhang, Y.-E. Zhang, S. Tong and M.-X. Wang, *J. Am. Chem. Soc.*, **2020**, 142, 1196-1199.
81. M.-L. Tan, Q.-H. Guo, X.-Y. Wang, T.-H. Shi, Q. Zhang, S.-K. Hou, S. Tong, J. You and M.-X. Wang, *Angew. Chem. Int. Ed.* , **2020**, 59, 23649-23658.
82. J. Wang and Q. Miao, *Org. Lett.*, **2019**, 21, 10120-10124.
83. A. B. Parusel, *Phys. Chem. Chem. Phys.*, **2000**, 2, 5545-5552.
84. J. Jortner, *J. Chem. Phys.*, **1976**, 64, 4860-4867.
85. G. Zerza, M. C. Scharber, C. J. Brabec, N. S. Sariciftci, R. Gomez, J. L. Segura, N. Martín and V. I. Srdanov, *J. Phys. Chem. A*, **2000**, 104, 8315-8322.
86. W. U. Huynh, J. J. Dittmer, W. C. Libby, G. L. Whiting and A. P. Alivisatos, *Adv. Funct. Mater.*, **2003**, 13, 73-79.
87. J. J. Dittmer, E. A. Marseglia and R. H. Friend, *Adv. Mater.,* **2000**, 12, 1270-1274.
88. D. Zhang and M. Heeney, *Organic Donor–Acceptor Systems*. 2020, Wiley Online Library. p. 1251-1251.
89. J. Singh, M. R. Nagar, C. P. Sharma, N. M. Gupta, A. Choudhury, K. S. Rawat, R. P. Vats, S. Gupta, J.-H. Jou and A. Goel, *ACS Appl. Opt. Mater.*, **2022**.
90. G. Pourtois, D. Beljonne, J. Cornil, M. A. Ratner and J. L. Brédas, *J. Am. Chem. Soc.*, **2002**, 124, 4436-4447.
91. M. Cyr, S. Brixi, A. Ganguly, B. H. Lessard and J. L. Brusso, *Dyes Pigm.*, **2023**, 210, 110964.
92. A. Gomez-Zavaglia and R. Fausto, *J. Phys. Chem. A*, **2004**, 108, 6953-6967.
93. B. Albinsson, M. P. Eng, K. Pettersson and M. U. Winters, *Phys. Chem. Chem. Phys.*, **2007**, 9, 5847-5864.

94.   O. V. Kuznetsova, A. N. Egorochkin and O. V. Novikova, *Russ. J. Gen. Chem.*, **2006**, 76, 554-562.
95.   F. Bureš, *RSC Adv.*, **2014**, 4, 58826-58851.
96.   D. Ateh, H. Navsaria and P. Vadgama, *J. R. Soc. Interface*, **2006**, 3, 741-752.
97.   C. Bulumulla, R. Gunawardhana, P. L. Gamage, J. T. Miller, R. N. Kularatne, M. C. Biewer and M. C. Stefan, *ACS Appl. Mater. Interfaces*, **2020**, 12, 32209-32232.
98.   J. Du, C. Bulumulla, I. Mejia, G. T. Mccandless, M. C. Biewer and M. C. Stefan, *Polym. Chem.*, **2017**, 8, 6181-6187.
99.   M. Lazerges, K. I. Chane-Ching, S. Aeiyach, S. Chelli, B. Peppin-Donnat, M. Billon, C. Lombard, F. Maurel and M. Jouini, *J. Solid State Electrochem.*, **2009**, 13, 231-238.
100. X. Zou, S. Cui, J. Li, X. Wei and M. Zheng, *Front. Chem.*, **2021**, 9, 671294.
101. H. Wu, Y. Wang, X. Qiao, D. Wang, X. Yang and H. Li, *Chem. Mater.*, **2018**, 30, 6992-6997.
102. S. K. Dey and D. A. Lightner, *J. Org. Chem.*, **2007**, 72, 9395-9397.
103. Y. Tan and K. Ghandi, *Synth. Met.*, **2013**, 175, 183-191.
104. H. Rapoport and N. Castagnoli, *J. Am. Chem. Soc.*, **1962**, 84, 2178-2181.
105. W. Flitsch and F.-J. Lüttig, *Liebigs Ann. Chem.*, **1987**, 1987, 893-894.
106. T. Jarosz and P. Ledwon, *Mater. Sci. Eng. C*, **2021**, 14, 281.
107. S. Maity, A. Dubey and S. Chakraborty, *J. Ind. Text.*, **2021**, 51, 152-173.
108. S. Ahmad, *Polym. Eng. Sci.*, **2009**, 49, 916-921.
109. R. Gleiter and J. Ritter, *Tetrahedron*, **1996**, 52, 10383-10388.
110. M. Wang, *Polymers*, **2016**, 8, 373.
111. J. G. Andino, S. Mazumder, K. Pal and K. G. Caulton, *Angew. Chem., Int. Ed.*, **2013**, 52, 4726-4732.
112. F. Heidarizadeh and S. Asadipour, *Iran. Chem. Commun.*, **2015**, 3, 187-198.
113. E. Orti, F. Tomas and J. Sanchez-Marin, *J. Mol. Struct.: Theochem.*, **1983**, 104, 197-206.
114. A. Cihaner, O. Mert and A. S. Demir, *Electrochim. Acta*, **2009**, 54, 1333-1338.
115. M. Farnier, S. Soth and P. Fournari, *Can. J. Chem.*, **1976**, 54, 1083-1086.
116. C. C. Hughes, A. Prieto-Davo, P. R. Jensen and W. Fenical, *Org. Lett.*, **2008**, 10, 629-631.
117. L. Fu and G. W. Gribble, *Tetrahedron Lett.*, **2008**, 49, 3545-3548.
118. A. A. Kanakis and V. Sarli, *Org. Lett.*, **2010**, 12, 4872-4875.
119. L. Goldenberg, R. Lyubovskaya, I. Nazarova and O. Roschupkina, *Synth. Met.*, **1991**, 40, 393-396.
120. K. Maksymiuk, *Electroanalysis*, **2006**, 18, 1537-1551.
121. H. Biemans, C. Zhang, P. Smith, H. Kooijman, W. Smeets, A. Spek and E. Meijer, *J. Org. Chem.*, **1996**, 61, 9012-9015.
122. M. Lazerges, M. Jouini, P. Hapiot, P. Guiriec and P.-C. Lacaze, *J. Phys. Chem. A*, **2003**, 107, 5042-5048.
123. M. Jouini, M. Lazerges, S. Chelly, M. Billon, C. Lombard, B. Pepin-Donat and C. Pernelle, *Synth. Met.*, **2008**, 158, 681-683.
124. K. Hrnčariková, Á. Szöllősy and D. Végh, *Arkivoc*, **2006**, 2, 124-129.
125. K. Oki, M. Takase, N. Kobayashi and H. Uno, *J. Org. Chem.*, **2021**, 86, 5102-5109.

126. Y. Sasaki, M. Takase, N. Kobayashi, S. Mori, K. Ohara, T. Okujima and H. Uno, *J. Org. Chem.*, **2021**, 86, 4290-4295.
127. F. Wu, K. Oki, J. Xue, S. Mori, M. Takase, Z. Shen and H. Uno, *Org. Lett.*, **2022**, 24, 80-84.
128. M. Navakouski, H. Zhylitskaya, P. J. Chmielewski, M. Żyła-Karwowska and M. Stępień, *J. Org. Chem.*, **2020**, 85, 187-194.
129. X. Qiao, M. A. Padula, D. M. Ho, N. J. Vogelaar, C. E. Schutt and R. A. Pascal, *J. Am. Chem. Soc.*, **1996**, 118, 741-745.
130. X. Zhou, Z. Li, H. Wang, M. Kitamura, K.-I. Kanno, K. Nakajima and T. Takahashi, *J. Org. Chem.*, **2004**, 69, 4559-4562.
131. K. Oki, M. Takase, S. Mori, A. Shiotari, Y. Sugimoto, K. Ohara, T. Okujima and H. Uno, *J. Am. Chem. Soc.*, **2018**, 140, 10430-10434.
132. Y.-Y. Xu, H.-R. Tian, S.-H. Li, Z.-C. Chen, Y.-R. Yao, S.-S. Wang, X. Zhang, Z.-Z. Zhu, S.-L. Deng and Q. Zhang, *Nat. Commun.*, **2019**, 10, 1-9.
133. Y. Zhang, R. Guan, M. Chen, Y. Shen, Q. Pan, Y. Lian and S. Yang, *Inorg. Chem.*, **2021**, 60, 1462-1471.
134. T. Morita and K. Takase, *Bull. Chem. Soc. Jpn.*, **1982**, 55, 1144-1152.
135. Q. Sun, I. C.-Y. Hou, K. Eimre, C. A. Pignedoli, P. Ruffieux, A. Narita and R. Fasel, *Chem. Commun.*, **2019**, 55, 13466-13469.
136. Y. Yamaguchi, M. Takubo, K. Ogawa, K.-I. Nakayama, T. Koganezawa and H. Katagiri, *J. Am. Chem. Soc.*, **2016**, 138, 11335-11343.
137. J. Huang, S. Huang, Y. Zhao, B. Feng, K. Jiang, S. Sun, C. Ke, E. Kymakis and X. Zhuang, *Small Methods*, **2020**, 4, 2000628.
138. Q. Fan, D. Martin-Jimenez, D. Ebeling, C. K. Krug, L. Brechmann, C. Kohlmeyer, G. Hilt, W. Hieringer, A. Schirmeisen and J. M. Gottfried, *J. Am. Chem. Soc.*, **2019**, 141, 17713-17720.
139. J. R. Dias, *J. Phys. Org. Chem.*, **2007**, 20, 395-409.
140. J. Xiang, W. L. Tan, J. Zhang, Y. Wang, C. Duan, C. R. Mcneill, X. Yang, C. Ge and X. Gao, *Macromolecules*, **2022**, 55, 8074-8083.
141. S. Ito, M. Ando, A. Nomura, N. Morita, C. Kabuto, H. Mukai, K. Ohta, J. Kawakami, A. Yoshizawa and A. Tajiri, *J. Org. Chem.*, **2005**, 70, 3939-3949.
142. K. Nakagawa, T. Yokoyama, K. Toyota, N. Morita, S. Ito, S. Tahata, M. Ueda, J. Kawakami, M. Yokoyama and Y. Kanai, *Tetrahedron*, **2010**, 66, 8304-8312.
143. A. Thadathil, J. Kavil, G. R. Kovummal, C. P. Jijil and P. Periyat, *ACS omega*, **2022**, 7, 11473-11490.
144. A. K. Singh and R. Prakash. *Conduction mechanism in electronic polymers: Effect of morphology*. in *2008 2nd National Workshop on Advanced Optoelectronic Materials and Devices*. 2008: IEEE.
145. B. Sari, N. Yavas, M. Makulogullari, O. Erol and H. I. Unal, *React. Funct. Polym.*, **2009**, 69, 808-815.
146. T. Plachý, J. Žitka, M. Mrlík, P. Bažant, M. Kadlečková, M. Trchová and J. Stejskal, *Polymer*, **2021**, 217, 123448.
147. B. Purty, R. B. Choudhary, A. Biswas and G. Udayabhanu, *Polym. Bull.*, **2019**, 76, 1619-1640.
148. C. J. Verma, A. S. Keshari, P. Dubey and R. Prakash, *Vacuum*, **2020**, 177, 109363.

149. M. B. Gómez Costa, J. M. Juárez, M. L. Martínez, J. Cussa and O. A. Anunziata, *Microporous Mesoporous Mater.*, **2012**, 153, 191-197.
150. T. Tüken, B. Yazıcı and M. Erbil, *Surf. Coat. Technol.*, **2006**, 200, 4802-4809.
151. A. H. Majeed, L. A. Mohammed, O. G. Hammoodi, S. Sehgal, M. A. Alheety, K. K. Saxena, S. A. Dadoosh, I. K. Mohammed, M. M. Jasim and N. U. Salmaan, *Int. J. Polym. Sci.*, **2022**, 2022, 9047554.
152. V. Babel and B. L. Hiran, *Polym. Compos.*, **2021**, 42, 3142-3157.
153. S. E. Galembeck, R. P. Orenha, R. M. Madeira, L. B. Peixoto and R. L. Parreira, *J. Braz. Chem. Soc.*, **2021**, 32, 1447-1455.
154. E. Brodskaya, G. V. F. Ratovskii and M. G. Voronkov, *Russ. Chem. Rev.*, **1993**, 62, 919.
155. R. Hoffmann, *Acc. Chem. Res.*, **1971**, 4, 1-9.
156. F. B. Sayyed and C. H. Suresh, *J. Phys. Chem. A*, **2011**, 115, 5660-5664.
157. F. Cozzi, R. Annunziata, M. Benaglia, M. Cinquini, L. Raimondi, K. K. Baldridge and J. S. Siegel, *Org. Biomol. Chem.*, **2003**, 1, 157-162.
158. S. Puhl, T. Steenbock, C. Herrmann and J. Heck, *Angew. Chem. Int. Ed.*, **2020**, 59, 2407-2413.
159. M. Saraswat and S. Venkataramani, *Phys. Chem. Chem. Phys.*, **2018**, 20, 4386-4395.
160. Q. Zhang, H. Lei, H. Guo, Y. Wang, Y. Gao, W. Zhang and R. Cao, *ChemSusChem*, **2022**, 15, e202200086.
161. E. M. Nolan and R. Linck, *J. Am. Chem.Soc.*, **2000**, 122, 11497-11506.
162. I. Azcarate, C. Costentin, M. Robert and J.-M. Savéant, *J. Am. Chem. Soc.*, **2016**, 138, 16639-16644.
163. K. Bowden and E. J. Grubbs, *Chem. Soc. Rev.*, **1996**, 25, 171-177.
164. W. Adcock and N. A. Trout, *Chem. Rev.*, **1999**, 99, 1415-1436.
165. R. J. Burns, I. K. Mati, K. B. Muchowska, C. Adam and S. L. Cockroft, *Angew. Chem.*, **2020**, 132, 16860-16867.
166. J. Simó Padial, J. Poater, D. T. Nguyen, P. Tinnemans, F. M. Bickelhaupt and J. Mecinović, *J. Org. Chem.*, **2017**, 82, 9418-9424.
167. S. E. Wheeler and K. N. Houk, *J. Chem. Theory Comput.*, **2009**, 5, 2301-2312.
168. S. E. Wheeler and K. N. Houk, *J. Am. Chem. Soc.*, **2009**, 131, 3126-3127.
169. A. Becke, *Chem. Phys*, 98, 5648.
170. R. Parr and W. Yang, *Density Functional Theory of Atoms and Molecules, New York: Oxford Univ.* 1989, Press.
171. C. Lee, W. Yang and R. G. Parr, *Phys. Rev. B*, **1988**, 37, 785.
172. R. G. Parr. *Density Functional Theory of Atoms and Molecules*. 1980. Dordrecht: Springer Netherlands.
173. Y. Zhao and D. G. Truhlar, *Theor. Chem. Acc.*, **2008**, 120, 215-241.
174. E. G. Hohenstein, S. T. Chill and C. D. Sherrill, *J. Chem. Theory Comput.*, **2008**, 4, 1996-2000.
175. R. Ditchfield, W. J. Hehre and J. A. Pople, *J. Chem. Phys.*, **1971**, 54, 724-728.
176. P. S. V. Kumar, V. Raghavendra and V. Subramanian, *J. Chem. Sci.*, **2016**, 128, 1527-1536.
177. G. Marino, *J. Heterocycl. Chem.*, **1972**, 9, 817-819.
178. J. Cioslowski, *J. Am. Chem. Soc.*, **1989**, 111, 8333-8336.

179. K. Meindl, J. Henn, N. Kocher, D. Leusser, K. A. Zachariasse, G. M. Sheldrick, T. Koritsanszky and D. Stalke, *J. Phys. Chem. A*, **2009**, 113, 9684-9691.
180. H.-C. Ma and X.-Z. Jiang, *J. Org. Chem.*, **2007**, 72, 8943-8946.
181. A. F. L. O. M. Santos and M. a. V. Ribeiro Da Silva, *J. Chem. Thermodyn.*, **2010**, 42, 734-741.
182. S. Murali and W. Rettig, *J. Phys. Chem. A*, **2006**, 110, 28-37.
183. T. Yoshihara, V. A. Galievsky, S. I. Druzhinin, S. Saha and K. A. Zachariasse, *Photochem. Photobiol. Sci.*, **2003**, 2, 342-353.
184. C. A. Figueira and P. T. Gomes, *Catal. Lett.*, **2015**, 145, 762-768.
185. J. Wen, R.-Y. Zhang, S.-Y. Chen, J. Zhang and X.-Q. Yu, *J. Org. Chem.*, **2012**, 77, 766-771.
186. R. D. Rieth, N. P. Mankad, E. Calimano and J. P. Sadighi, *Org. Lett.*, **2004**, 6, 3981-3.
187. F. Ammon, S. T. Sauer, R. Lippert, D. Lungerich, D. Reger, F. Hampel and N. Jux, *Org. Chem. Front.*, **2017**, 4, 861-870.
188. C. H. Suresh and S. Anila, *Acc. Chem. Res.*, **2023**, 56, 1884-1895.
189. A. Sosorev, D. Dominskiy, I. Chernyshov and R. Efremov, *Int. J. Mol. Sci.*, **2020**, 21, 5654.
190. T. Le Bahers, C. Adamo and I. Ciofini, *J. Chem. Theory Comput.*, **2011**, 7, 2498-2506.

Topology of Electrostatic Potential and Electron Density Reveals Covalent to Non-Covalent Carbon-Carbon Bond Continuum
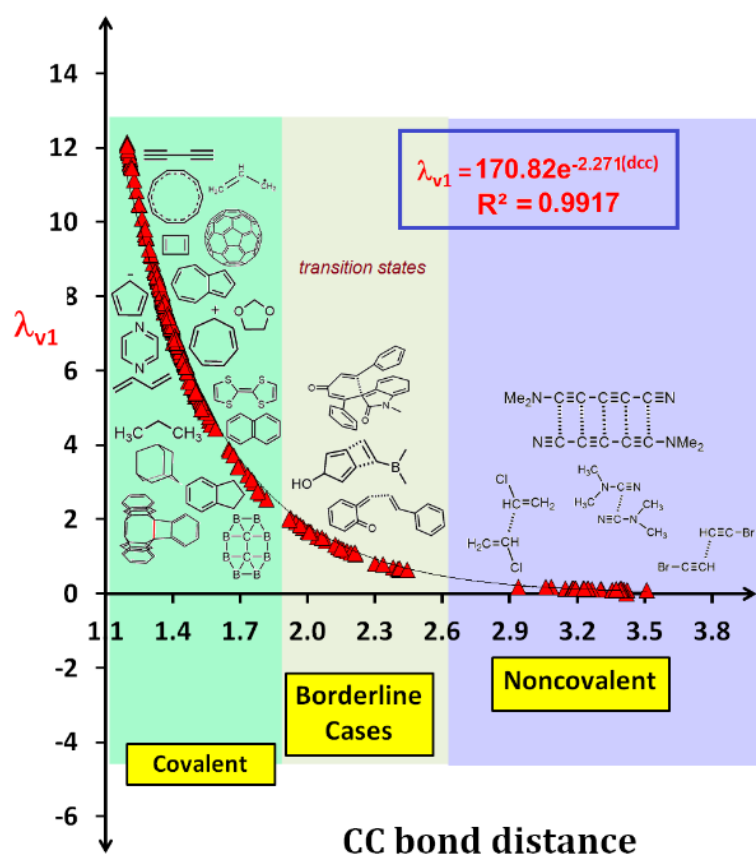
Topology of Electrostatic Potential and Electron Density Reveals Covalent to Non-Covalent Carbon-Carbon Bond Continuum

4.1 Abstract

The covalent and non-covalent nature of carbon-carbon (CC) interactions in a wide range of molecular systems can be characterized using various methods, including the analysis of molecular electrostatic potential (MESP), represented as $V(\mathbf{r})$, and the molecular electron density (MED), represented as $\rho(\mathbf{r})$. These techniques provide valuable insights into the bonding between carbon atoms in different molecular environments. By uncovering a fundamental exponential relationship between the distance of the CC bond and the highest eigenvalue (λ_{v1}) of $V(\mathbf{r})$ at the bond critical point (BCP), this study establishes the continuum model for all types of CC interactions, including transition states. The continuum model is further delineated into three distinct regions, namely covalent, borderline cases, and non-covalent, based on the gradient, λ'_{v1} with the bond distance of the CC interaction. For covalent interactions, this parameter exhibits a more negative value than -5.0 au/Å, while for non-covalent interactions, it is less negative than -1.0 au/Å. Borderline cases, which encompass transition state structures, fall within the range of -1.0 to -5.0 au/Å. Furthermore, this study expands upon Popelier's analysis of the Laplacian of the MED, denoted as $\nabla^2\rho$, to encompass the entire spectrum of covalent, non-covalent, and borderline cases of CC interactions. Therefore, the study presents compelling evidence supporting the concept of a continuum model for CC bonds in chemistry. Additionally, this continuum model is further explored within the context of C-N, C-O, C-S, N-N, O-O, and S-S interactions, albeit with a limited dataset.

4.2 Introduction

With regard to the possibility of creating large networks of covalent connections with itself and other elements, the carbon atom stands out amid all the chemical elements. The supremacy of the carbon-carbon (CC) bond is well-known among all the other linkages observed in organic molecules.[1] Since the carbon atom is neither a highly electropositive nor an electronegative, electrons are more likely to be shared between two carbon atoms to yield a covalent bond. The single bond between the carbon atoms, known as a σ-bond, is commonly described to be formed by the interactions of sp^3-hybridized orbitals. Carbon atoms can also form a π-bond under sp^2-hybridized state or two π-bonds under sp-hybridized state. Some CC linkages are also regarded as aromatic or antiaromatic ones, depending on the nature of the π-conjugation. The carbon-carbon non-covalent bonding scenario describes weak attractive interaction between carbon centers saturated by either σ-bonds or by both σ- and π-bonds. The typical single bond (C_{sp3}–C_{sp3}) to triple bond (C_{sp}≡C_{sp}) distance lies in the range 1.54 to 1.20 Å, while the non-covalent C···C distance is around 3.0 Å. Hounshell *et al.* reported[2] that one of the C–C bond in hexaphenylethane is significantly longer compared to the normal C–C one, due to the steric repulsion between six phenyl groups present in it. To learn more about the atypical covalent bonds (long bonds, strained bonds, or short bonds), many attempts have been made in the past[3-16] which led to the discovery of many bulky systems with substantially elongated C–C bonds. The CC bond formation reactions are one of the most actively explored topics in organic chemistry. The discovery of new methodologies for effective CC bond formation has gained prominence, as evidenced by the recent Nobel awards in chemistry.[17] The CC bond formation is the prime step in most of the organic synthesis reactions for the development of the carbon framework of organic compounds.[18] Carbonaceous clusters are important in many fields of study, including astrochemistry, material science, structural chemistry, *etc.*[19] Special structural and electrical properties of multiple bonds reveal intriguing chemical characteristics of the system under study. The strong CC bonds create a huge variety of molecular structures, many of which are crucial components of the basic life framework.[20]

Bonds and related entities, such as bond length, bond strength, bond order *etc.*, have been the most frequently used for the interpretation of many chemical phenomena.[21] To comprehend the chemical reactivity and the properties of a molecular system, one must have a quantitative understanding of the electronic influence on an atom in that system.[22] Each atom in a molecular system is strongly influenced by the electrons as well as nuclei of the neighboring atoms. For exploring the basic features of molecular structure and reactivity,[23] a detailed understanding of molecular scalar fields is found to be useful. The MESP has been widely used for exploring the electronic structure, chemical bonding in covalent and noncovalent contexts, and the interaction between atomic and molecular systems.[24-29] By employing a trustworthy *ab initio* or DFT method to solve the Schrödinger equation, it is possible to calculate the MED,[30, 31] as well as MESP of the system under study with high accuracy. Almost all current quantum chemistry programs provide MESP and MED computing modules at different levels of theory, but they do not generally offer MESP topology analysis tools. Politzer and co-workers pioneered the systematic application of MESP to forecast the molecular regions susceptible to electrophilic and nucleophilic attack.[32-35] Later, Gadre, Suresh, and others made fundamental contributions to the understanding of the topological characteristics of MESP and also developed the algorithms and software for the MESP topology analysis.[23, 25, 36-38]

The MESP and MED topology analyses are considered as a powerful tools to analyze the electronic distribution in σ-, π-, non-covalently bonded and non-bonded regions in molecules. Recently developed DAMQT (deformed atoms in molecules quantum theory) software[39, 40] also offers the MESP topology computation.[41-44] DAMQT is a package for the analysis and visualization of MED and MESP in atoms and molecules, and related properties such as deformation density, as well as the critical points (CPs) of MESP and MED. It is based on the principle of least deformation criterion previously described in the DAM partitioning of the electron density into atomic fragments.[45] In the DAM partition, the electron density of every atomic fragment is expanded in products of radial factors times regular spherical harmonics centered at its nucleus. The electron density of the full molecule is thus represented as a set of atomic expansions in terms of effective multipoles, which are functions of the distance to the corresponding nuclei. The radial factors of the effective multipoles

are piecewise expanded in terms of exponentials times polynomials of variable, **r**. This representation is used for the rapid evaluation of the MESP.

In the present study, topology analysis using MESP and MED is carried out on a wide variety of molecular systems containing different types of CC bonds (such as C–C, C=C, C≡C). We also examine strained, sterically crowded, aromatic systems as well as those incorporating non-covalent interactions. The topology of the MED and MESP reveals a CC bond continuum and suggests a MESP-based relation that connects the CC distance and eigenvalue of the highest magnitude (λ_{v1}). The continuum may be divided into three regions using MESP topology analysis, *viz.* covalent, non-covalent, and borderline cases. By defining borderline cases between covalent and non-covalent bonds, we attempt to give a new dimension to the analysis based on the Laplacian, $\nabla^2\rho$ reported by Popelier.[46, 47]

4.3 Methodology

The topology analysis of MESP and MED has been carried out on a large variety of molecular systems consisting of σ-, π-, and non-covalently bonded CC regions to characterize the nature of BCPs and to introduce an ideal covalent to non-covalent regime. All molecular systems explored in the present study are optimized using M06-2X/6-311G(d,p) level of theory[48] implemented in Gaussian 16 program package,[49] with a check on the minimal nature by doing a vibrational frequency run and verifying that all the frequencies are real for all systems, except for the transition state structures. The MESP topology computations on molecular geometries have been carried out using DAMQT package[42-44, 50] to locate and characterize the (3, -1) MESP CPs. Bader's quantum theory of atoms in molecules (QTAIM) analysis, based on the MED, $\rho(\mathbf{r})$, distribution is carried out for locating (3, -1) CPs between interacting atoms using AIMAII package.[51-53] Based on the MED value at the respective BCPs, atom-atom interactions are characterized as covalent or noncovalent. The three eigenvalues of Hessian matrix correspond to electrostatic potential are designated as λ_{v1}, λ_{v2}, and λ_{v3} while that of electron density are represented as $\lambda_{\rho1}$, $\lambda_{\rho2}$, and $\lambda_{\rho3}$. In MESP, the direction of the eigenvector corresponding to the largest eigenvalue λ_{v1} is always perpendicular to the CC bond while, the eigenvectors associated with λ_{v2} and λ_{v3} are oriented parallel to the CC bond plane.

4.4 Results and Discussion

4.4.1 MESP Topology Analysis

4.4.1.1 Covalent CC Bonds in Hydrocarbons and Carbon Clusters

(a)   (b)   (c)   (d)
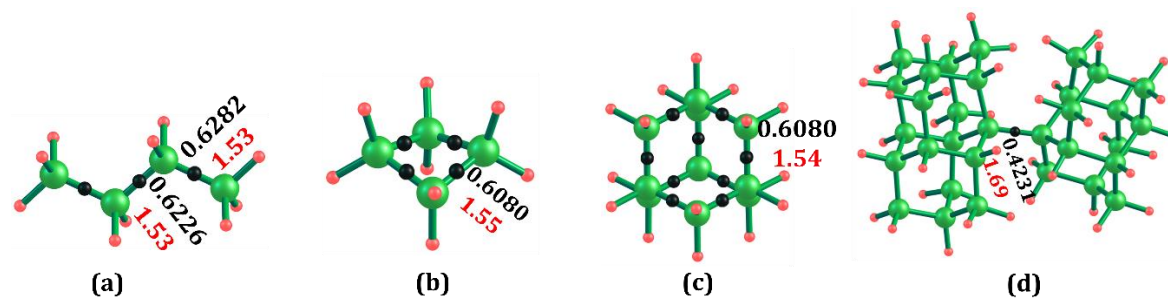
Figure 4.1 The MESP (3, -1) CP distribution in selected set of systems bearing C–C bonds. The MESP value at the BCP (in au) and bond length (in Å) are represented in black and red fonts, respectively

The MESP topology showing the (3, -1) CPs observed for a representative set of C–C single bonded systems such as typical alkanes, strained cycloalkanes, caged structures, and sterically crowded structures are depicted in Figure 4.1, while the topological features of all other saturated structures are given in Table 4.2 and Table 4.3. In general, $V(\mathbf{r})$ value at the CP decreases with increase in the length of the C–C bond. For the alkane series, the $V(\mathbf{r})$ is observed in a narrow range 0.623 to 0.631 au. The elongation in C–C bond length in strained cycloalkane and caged structure is clearly reflected in the $V(\mathbf{r})$ value (Table 4.4). Significantly long C–C bond distances, d_{CC} (1.65 to 1.82 Å) in sterically bulky structures is evident from the smaller $V(\mathbf{r})$ ranging from 0.381 to 0.503 au (Figure 4.2) compared to other saturated systems. Figure 4.3 depicts the distribution of (3, -1) CPs in a representative set of systems containing C=C and aromatic bonds. The BCP in ethylene is located at the midpoint of C=C bond with high $V(\mathbf{r})$ of 1.021 au (Figure 4.3a). Generally, BCP values corresponding to formal CC double ($C_{sp2}=C_{sp2}$) and formal CC single ($C_{sp2}–C_{sp2}$) bonds in alkenes appear in the vicinity of 1.10 and 0.70 au, respectively (Figure 4.3b). The terminal double bond always shows a high $V(\mathbf{r})$ than the interior ones (Table 4.5). Due to the symmetry, benzene has only one type of BCP, 0.886 au located at the midpoint

of each CC bond (Figure 4.3c), whereas as per the symmetry, naphthalene shows four types of nonequivalent BCPs (Figure 4.3d). Among the four BCPs of naphthalene, the

3,4:7,8:9,10:11,12:13,14-Pentabenzotetracyclo(4.2.2.2^{1,2}.2^{2,5}) tetradeca-3,5,7,9,11,13-hexaene (Pbtth)

2-(Pentacyclo[7.3.1.1^{4,12}.0^{2,7}.0^{6,11}] tetradec-1-yl)heptacyclo [7.7.1.1^{3,15}.0^{1,12}.0^{2,7}.0^{4,13}.0^{6,11}]octadecane (Ptho)

1,1'-Bi(pentacyclo[7.3.1.1^{4,12}.0^{2,7}.0^{6,11}] tetradecane) (Bptd)

2-(Adamantan-1-yl)heptacyclo [7.7.1.1^{3,15}.0^{1,12}.0^{2,7}.0^{4,13}.0^{6,11}] octadecane (Ahod)

10,10''-Dimethyl-5',6'-dihydro-10H,10''H-dispiro [acridine-9,1'-cyclopenta[fg] acenaphthylene-2',9''-acridine] (Dddcpa)

1,1,2,2-tetrakis(4-(2-methyl-2-propanyl)phenyl)-1,2,5,6-tetrahydrocyclopenta[fg]acenaphthylene (Ttca)

5',6'-dihydrodispiro[dibenzo[a,d][7]annulene-5,1'-cyclopenta[fg]acenaphthylene-2',5''-dibenzo[a,d][7]annulene] (Dddcada)

hexakis(3,5-di-t-Butylphenyl)ethane (Hdbec)

1,1,2,2-tetrakis(3,5-dimethylphenyl)-1,2,5,6-tetrahydrocyclopenta[fg]acenaphthylene (Tdtca)

1,2-diamino-*o*-carborane-1

1,2-diamino-*o*-carborane-2

Figure 4.2 The MESP (3, -1) CP distribution of long C-C bonds in sterically crowded systems where values of BCP in au and CC distance in Å

largest and smallest BCP values stand for the shortest and longest CC bonds, respectively. In general, due to the inherent conjugation effect, the CC bond length of polycyclic benzenoid hydrocarbons (PBH) appears in the range between 1.36 to 1.51 Å, which are characterized by $V(\mathbf{r})$ ranging from 0.722 to 0.950 au (Table 4.6).
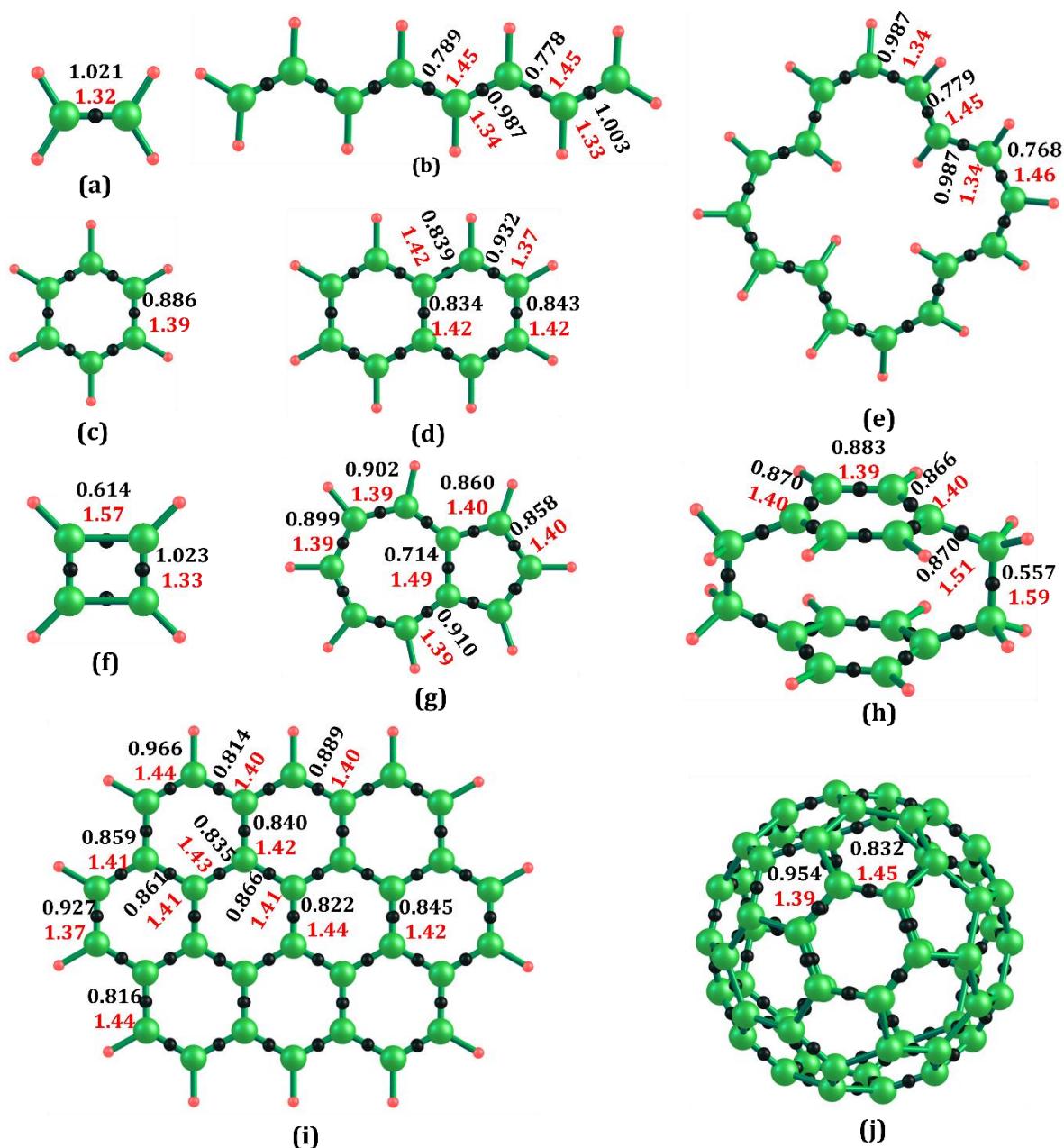
Figure 4.3 The MESP (3, -1) CP distribution in selected set of systems containing C=C bonds. The MESP value at the CP (in au) and bond length (in Å) are represented in black and red fonts, respectively

Table 4.1 The general trend in the MESP value of (3, -1) BCP for different types of systems at M06-2X/6-311G(d,p) level of theory

Type of system	Bond type	d_{CC} in Å	$V(\mathbf{r})$ in au
Alkane	C–C	1.53	0.623 – 0.631
Cycloalkane	C–C	1.50 – 1.55	0.743 – 0.609
Cage	C–C	1.54 – 1.56	0.608 – 0.593
Sterically crowded	C–C	1.56 – 1.82	0.503 – 0.381
Olefin	C–C	1.32 – 1.34	1.025 – 0.987
Olefin	C=C	1.45 – 1.46	0.789 – 0.762
PBH	$C_{aromatic}$–$C_{aromatic}$	1.39	0.886 – 0.888
PBH	C–C	1.42 – 1.51	0.722 – 0.844
PBH	C=C	1.36 – 1.38	0.950 – 0.904
Antiaromatic (cyclobutadiene)	C–C	1.57	0.614
Antiaromatic (cyclobutadiene)	C=C	1.33	1.023
Azulene	$C_{aromatic}$–$C_{aromatic}$	1.39 – 1.40	0.910 – 0.858
Azulene	C–C	1.49	0.714
Cyclophane	$C_{aromatic}$–$C_{aromatic}$	1.39 – 1.40	0.895 – 0.886
Cyclophane	C–C	1.50 – 1.59	0.682 – 0.557
Annulene	C–C	1.44 – 1.46	0.799 – 0.768
Annulene	C=C	1.34 – 1.36	0.987 – 0.960
Fullerene	C–C	1.45	0.832
Fullerene	C=C	1.39	0.954
Carbon nanotube	C–C	1.45	0.805
Carbon nanotube	$C_{aromatic}$–$C_{aromatic}$	1.41	0.878 – 0.877
Graphene	$C_{aromatic}$–$C_{aromatic}$	1.40 – 1.41	0.889 – 0.866
Graphene	C–C	1.41 – 1.44	0.861 – 0.814
Graphene	C=C	1.36 – 1.37	0.966 – 0.927
Heterocyclic	$C_{aromatic}$–$C_{aromatic}$	1.39 – 1.40	0.923 – 0.882
Heterocyclic	C–C	1.39 - 1.55	1.086 – 0.596
Heterocyclic	C=C	1.33 – 1.40	1.062 – 0.910
Carbon rings	C–C	1.36 – 1.39	1.031 – 1.071
Carbon rings	C=C	1.28 – 1.32	1.167 – 1.229
Carbon rings	C≡C	1.22 – 1.30	1.398 – 1.241
Carbon subsulfides/subchalcogenides	C=C	1.26 – 1.29	1.308 – 1.202
Carbon subsulfides/subchalcogenides	C–C	1.38	1.043
Alkynes	C–C	1.35 – 1.38	1.078 – 1.004
Alkynes	C≡C	1.20 – 1.22	1.416 – 1.395
Mixed	$C_{aromatic}$–$C_{aromatic}$	1.38 – 1.39	0.900 – 0.854
Mixed	C–C	1.43 - 1.54	0.864 – 0.613
Mixed	C=C	1.33 – 1.34	1.022 – 0.975
Mixed	C≡C	1.20 – 1.21	1.397 – 1.370

The BCP distribution also detects the alternate single and double bond feature of olefinic systems in terms of the low and high values of $V(\mathbf{r})$, respectively. Typically, the difference between the $V(\mathbf{r})$ of the formal CC single and CC double bond in olefins ($\Delta V(\mathbf{r})$) is 0.225 au. In antiaromatic cyclobutadiene, the $\Delta V(\mathbf{r})$ = 0.410 au is significantly larger than the olefins. The $\Delta V(\mathbf{r})$ of annulene is 0.219 au and that of fullerene is 0.122 au, suggesting more delocalized CC bond distribution in the latter than the former (Table 4.7). Three nonequivalent $V(\mathbf{r})$ of seven membered ring in azulene 0.910, 0.902 and 0.899 au are very close to that of benzene indicating that it has stronger aromatic character than the five membered ring, which is characterized by two nonequivalent $V(\mathbf{r})$ 0.858 and 0.860 au. In cyclophanes, the $V(\mathbf{r})$ between 0.895 and 0.886 au, very close to that of benzene indicates more aromatic character for the CC bonds in rings, while the bridged $C_{sp3}-C_{sp3}$ bonds are characterized by smaller $V(\mathbf{r})$. The $V(\mathbf{r})$ data given in Table 4.1 clearly reveal the presence of C–C and $C_{aromatic}-C_{aromatic}$ bonds in carbon nanotubes and C–C, C=C and $C_{aromatic}-C_{aromatic}$ bonds in graphene sheets (Table 4.8).
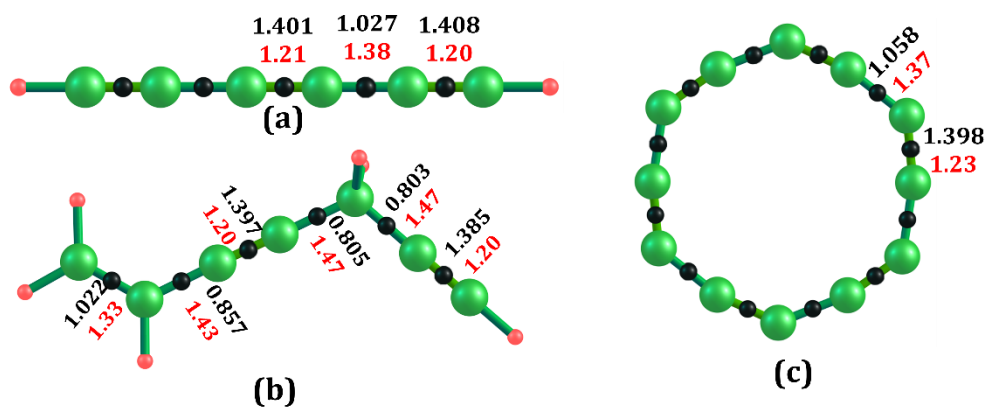
Figure 4.4 The MESP (3, -1) CP distribution in selected set of systems containing C≡C bonds. The MESP value at the CP (in au) and bond length (in Å) are represented in black and red fonts, respectively

The distribution of (3, -1) CPs in a representative set of systems containing C≡C bonds is illustrated in Figure 4.4. Alkynes (or polyynes[54]) always exhibit very high $V(\mathbf{r})$ values compared to alkanes and alkenes. The $C_{sp}\equiv C_{sp}$ bond in acetylene is characterized by the $V(\mathbf{r})$ value of 1.402 au. For formal CC single and formal CC triple bonds in alkynes, the $V(\mathbf{r})$ values appear in the vicinity of 1.00 and 1.42 au, respectively and they show

large $\Delta V(\mathbf{r})$, 0.412 au between the $V(\mathbf{r})$ of $C_{sp} \equiv C_{sp}$ and $C_{sp}-C_{sp}$ (Table 4.9). Large $V(\mathbf{r})$ value of 1.241 au observed for C2 molecule signifies its triple bond character.
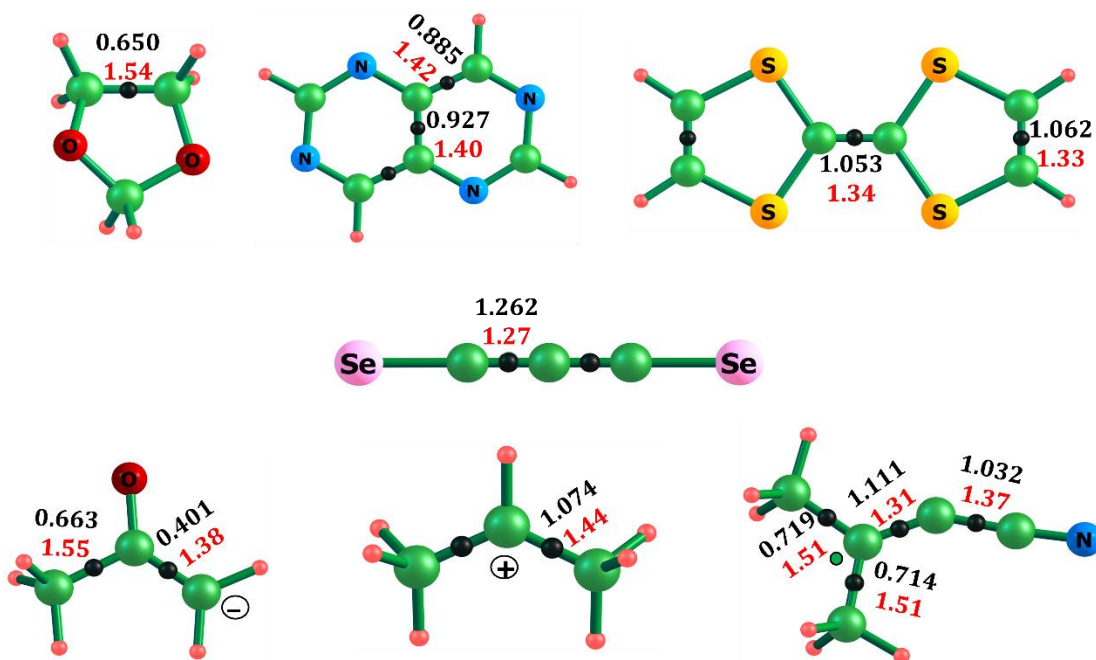
Figure 4.5 The MESP (3, -1) CP distribution in different types of CC bond of heterocyclic, anionic, cationic and radical systems. The MESP value at the CP (in au) and bond length (in Å) are represented in black and red fonts, respectively

Further, the (3, -1) CP distribution in selected set of carbon rings is given in Table 4.10 *viz.* C_6, C_8, C_{10}, C_{12}, *etc.*[55] The uniform $V(\mathbf{r})$ shows cumulenic character anticipated for the structure of a carbon rings (C_n) with bond angle alternation if n = 4N+2, while two types of BCP with $\Delta V(\mathbf{r})$, 0.367 au supports the acetylenic character with bond length alternation if n = 4N. In heterocyclic systems containing N, O and S, the $V(\mathbf{r})$ ranging between 0.923 and 0.882 au, 1.086 and 0.596 au and 1.062 and 0.910 au represent $C_{aromatic}-C_{aromatic}$, C−C and C=C bonds, respectively (Table 4.11).

The $V(\mathbf{r})$ values clearly suggest the double bond character exhibited by most of the carbon subsulfides[12] and carbon subchalcogenides (Table 4.12).[19, 56-60] Further, the MESP topology study is conducted on anionic, cationic, radical systems and some neutral molecules (Figure 4.5) containing multiple type of bonds such as C−C, C=C, C≡C, aromatic bonds *etc.* The $V(\mathbf{r})$ observed for such systems are given in Table 4.13. The distribution

of (3, -1) CPs in a representative set of organometallic[61] and hypervalent carbon compounds[62] containing different CC bonds is shown in Figure 4.6. For CC bonds ranging from 1.38 to 1.53 Å containing Li, Si, Ge, Cr, Fe, *etc.* the $V(\mathbf{r})$ value falls between 1.073 to 0.613 au (Table 4.14).

ferrocene η^6-CrO$_3$ Ge$_2$C$_5$H$_2$ C$_6$Li$_6$
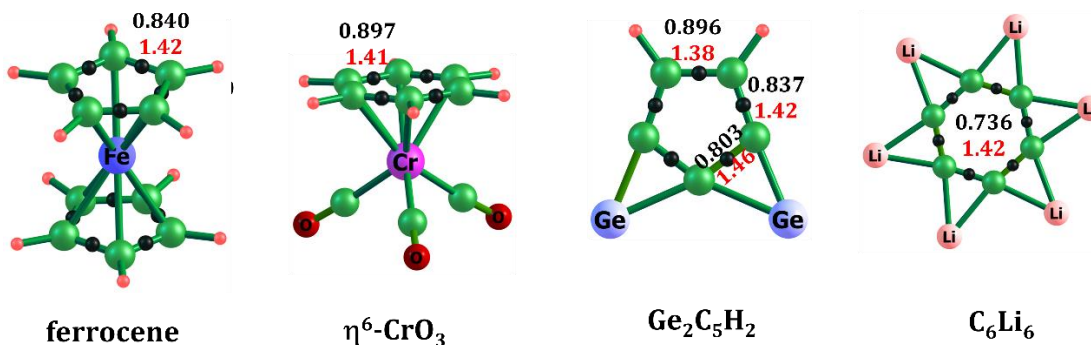
Figure 4.6 The MESP (3, -1) CP distribution in representative set of organometallic and hypervalent systems. The MESP value at the CP (in au) and bond length (in Å) are represented in black and red fonts, respectively

Table 4.2 The CC bond distance (Å) and the MESP data V_{bnp}, V_ρ, $V(\mathbf{r})$ and eigenvalues (in au) of alkanes at M06-2X/6-311G(d,p) level of theory

system	d_{CC}	V_{bnp}	V_ρ	$V(\mathbf{r})$	λ_{v1}	λ_{v2}	λ_{v3}	λ'_{v1}
ethane	1.53	10.376	-9.746	0.630	5.174	-1.094	-1.094	-12.100
propane	1.53	12.302	-11.675	0.627	5.177	-1.089	-1.077	-12.096
	1.53	12.302	-11.675	0.627	5.177	-1.089	-1.077	-12.096
butane	1.53	13.538	-12.910	0.628	5.183	-1.091	-1.080	-12.111
	1.53	13.538	-12.910	0.628	5.183	-1.091	-1.080	-12.111
	1.53	14.216	-13.594	0.623	5.175	-1.081	-1.058	-12.082
decane	1.53	17.061	-16.434	0.628	5.180	-1.091	-1.080	-12.105
	1.53	17.061	-16.434	0.628	5.180	-1.091	-1.080	-12.105
	1.53	19.389	-18.764	0.625	5.184	-1.086	-1.065	-12.105
	1.53	19.389	-18.764	0.625	5.184	-1.086	-1.065	-12.105
	1.53	19.793	-19.168	0.625	5.182	-1.085	-1.065	-12.100
	1.53	19.793	-19.168	0.625	5.181	-1.085	-1.065	-12.100
	1.53	19.918	-19.293	0.625	5.181	-1.085	-1.065	-12.100
	1.53	18.588	-17.965	0.623	5.178	-1.083	-1.062	-12.091
	1.53	18.588	-17.965	0.623	5.178	-1.083	-1.062	-12.091

Table 4.3 The CC bond distance (Å) and the MESP data V_{bnp}, V_ρ, $V(\mathbf{r})$ and eigenvalues (in au) of cycloalkanes at M06-2X/6-311G(d,p) level of theory

system	d_{CC}	V_{bnp}	V_ρ	$V(\mathbf{r})$	λ_{v1}	λ_{v2}	λ_{v3}	λ'_{v1}
cyclopropane	1.50	12.837	-12.093	0.743	5.311	-1.221	-1.172	-12.820
cyclobutane	1.55	14.205	-13.596	0.609	4.878	-1.013	-0.986	-11.567
cyclohexane	1.53	16.826	-16.208	0.618	5.130	-1.066	-1.052	-11.989
adamentane	1.54	22.306	-21.698	0.608	5.058	-1.034	-1.029	-11.828
cubane	1.56	20.022	-19.429	0.593	4.643	-0.949	-0.902	-11.153

Table 4.4 The CC bond distance (Å) and the MESP data V_{bnp}, V_ρ, $V(\mathbf{r})$ and eigenvalues (in au) of sterically crowded systems at M06-2X/6-311G(d,p) level of theory

system	d_{CC}	V_{bnp}	V_ρ	$V(\mathbf{r})$	λ_{v1}	λ_{v2}	λ_{v3}	λ'_{v1}
Pbtth	1.69	43.655	-43.180	0.475	3.428	-0.664	-0.613	-8.351
Ptho	1.69	43.655	-43.180	0.475	3.428	-0.664	-0.613	-8.351
Bptd	1.65	41.323	-40.857	0.467	3.889	-0.740	-0.736	-9.172
Ahod	1.66	41.302	-40.843	0.459	3.836	-0.726	-0.721	-9.042
Dddcpa	1.70	50.370	-49.937	0.433	3.407	-0.628	-0.605	-8.112
Ttca	1.73	55.861	-55.454	0.407	3.194	-0.573	-0.559	-7.588
Dddcada	1.76	49.381	-49.000	0.381	2.980	-0.517	-0.511	-7.081
Hdbec	1.67	80.666	-80.191	0.475	3.709	-0.700	-0.700	-8.735
Tdtca	1.75	52.219	-51.831	0.389	3.061	-0.543	-0.529	-7.275
1,2-diamino-o-carborane-1	1.79	35.917	-35.415	0.503	2.693	-0.501	-0.455	-6.626
1,2-diamino-o-carborane-2	1.82	40.123	-39.649	0.474	2.536	-0.464	-0.405	-6.265

Table 4.5 The CC bond distance (Å) and the MESP data V_{bnp}, V_ρ, $V(\mathbf{r})$ and eigenvalues (in au) of alkenes

system	d_{CC}	V_{bnp}	V_ρ	$V(\mathbf{r})$	λ_{v1}	λ_{v2}	λ_{v3}	λ'_{v1}
ethene	1.32	10.966	-9.946	1.021	8.637	-2.256	-2.060	-19.170
butadiene	1.33	13.780	-12.773	1.007	8.470	-2.194	-1.996	-18.842
	1.33	13.780	-12.773	1.007	8.470	-2.194	-1.996	-18.842
	1.46	13.664	-12.902	0.762	6.098	-1.356	-1.320	-14.066
hexatriene	1.33	15.230	-14.227	1.004	8.431	-2.181	-1.985	-18.768
	1.33	15.230	-14.227	1.004	8.431	-2.181	-1.985	-18.768
	1.34	16.586	-15.595	0.991	8.275	-2.121	-1.926	-18.461
	1.45	15.629	-14.855	0.775	6.190	-1.390	-1.345	-14.261
	1.45	15.629	-14.855	0.775	6.190	-1.390	-1.345	-14.261
octatetraene	1.33	16.209	-15.207	1.003	8.418	-2.176	-1.982	-18.742
	1.33	16.209	-15.207	1.003	8.418	-2.176	-1.982	-18.742
	1.34	18.035	-17.048	0.987	8.225	-2.104	-1.912	-18.363
	1.34	18.035	-17.048	0.987	8.225	-2.104	-1.912	-18.363
	1.45	17.604	-16.815	0.789	6.301	-1.431	-1.376	-14.495
	1.45	16.813	-16.035	0.778	6.214	-1.399	-1.352	-14.312
	1.45	16.813	-16.035	0.778	6.214	-1.399	-1.352	-14.312
decapentaene	1.33	16.948	-15.946	1.002	8.412	-2.174	-1.980	-18.732
	1.33	16.948	-15.946	1.002	8.412	-2.174	-1.980	-18.732
	1.34	19.013	-18.028	0.985	8.206	-2.097	-1.907	-18.327
	1.34	19.013	-18.028	0.985	8.206	-2.097	-1.907	-18.327
	1.35	19.484	-18.501	0.982	8.169	-2.084	-1.896	-18.254
	1.45	18.791	-17.998	0.793	6.333	-1.442	-1.385	-14.563
	1.45	18.791	-17.998	0.793	6.333	-1.442	-1.385	-14.563
	1.45	17.661	-16.882	0.779	6.223	-1.402	-1.354	-14.330
	1.45	17.661	-16.882	0.779	6.223	-1.402	-1.354	-14.330

Table 4.6 The CC bond distance (Å) and the MESP data V_{bnp}, V_ρ, $V(\mathbf{r})$ and eigenvalues (in au) of polycyclic benzenoid hydrocarbons at M06-2X/6-311G(d,p) level of theory (continues..)

system	d_{CC}	V_{bnp}	V_ρ	$V(\mathbf{r})$	λ_{v1}	λ_{v2}	λ_{v3}	λ'_{v1}
benzene	1.39	15.598	-14.713	0.886	7.272	-1.764	-1.638	-16.489
naphthalene	1.37	19.961	-19.029	0.932	7.697	-1.914	-1.757	-17.335
	1.37	19.961	-19.029	0.932	7.697	-1.914	-1.757	-17.335
	1.37	19.961	-19.029	0.932	7.697	-1.914	-1.757	-17.335
	1.37	19.961	-19.029	0.932	7.697	-1.914	-1.757	-17.335
	1.42	19.361	-18.517	0.843	6.833	-1.616	-1.517	-15.601
	1.42	19.361	-18.517	0.843	6.833	-1.616	-1.517	-15.601
	1.42	20.978	-20.140	0.839	6.772	-1.591	-1.490	-15.472
	1.42	20.978	-20.140	0.839	6.772	-1.591	-1.490	-15.472
	1.42	20.978	-20.144	0.839	6.772	-1.591	-1.490	-15.472
	1.42	20.978	-20.140	0.839	6.772	-1.591	-1.490	-15.472
	1.42	22.113	-21.279	0.834	6.725	-1.575	-1.463	-15.373
biphenyl	1.39	21.193	-20.302	0.891	7.300	-1.775	-1.646	-16.547
	1.39	21.193	-20.302	0.891	7.300	-1.775	-1.646	-16.547
	1.39	21.193	-20.302	0.891	7.300	-1.775	-1.646	-16.547
	1.39	21.193	-20.302	0.891	7.300	-1.775	-1.646	-16.547
	1.39	20.385	-19.497	0.888	7.272	-1.763	-1.638	-16.489
	1.39	20.385	-19.497	0.888	7.272	-1.763	-1.638	-16.489
	1.39	20.385	-19.497	0.888	7.272	-1.763	-1.638	-16.489
	1.39	20.385	-19.497	0.888	7.272	-1.763	-1.638	-16.489
	1.40	22.803	-21.926	0.877	7.142	-1.725	-1.596	-16.224
	1.40	22.803	-21.926	0.877	7.142	-1.725	-1.596	-16.224
	1.40	22.803	-21.926	0.877	7.142	-1.725	-1.596	-16.224
	1.40	22.803	-21.926	0.877	7.142	-1.725	-1.596	-16.224
	1.48	22.857	-22.128	0.730	5.762	-1.253	-1.213	-13.351

Table 4.6 The CC bond distance (Å) and the MESP data V_{bnp}, V_ρ, $V(\mathbf{r})$ and eigenvalues (in of polycyclic benzenoid hydrocarbons at M06-2X/6-311G(d,p) level of theory

system	d_{CC}	V_{bnp}	V_ρ	$V(\mathbf{r})$	λ_{v1}	λ_{v2}	λ_{v3}	λ'_{v1}
anthracene	1.36	22.131	-21.169	0.950	7.860	-1.972	-1.803	-17.656
	1.36	22.131	-21.169	0.950	7.860	-1.972	-1.803	-17.656
	1.36	22.131	-21.169	0.950	7.860	-1.972	-1.803	-17.656
	1.36	22.131	-21.169	0.950	7.860	-1.972	-1.803	-17.656
	1.39	24.480	-23.601	0.886	7.199	-1.738	-1.609	-16.338
	1.39	24.480	-23.601	0.886	7.199	-1.738	-1.609	-16.338
	1.39	24.480	-23.601	0.886	7.199	-1.738	-1.609	-16.338
	1.39	24.480	-23.601	0.886	7.199	-1.738	-1.609	-16.338
	1.43	21.276	-20.449	0.821	6.584	-1.527	-1.439	-15.086
	1.43	21.276	-20.449	0.821	6.584	-1.527	-1.439	-15.086
	1.43	23.518	-22.705	0.821	6.584	-1.527	-1.439	-15.086
	1.43	23.518	-22.705	0.821	6.584	-1.527	-1.439	-15.086
	1.43	23.518	-22.705	0.821	6.584	-1.527	-1.439	-15.086
	1.43	23.518	-22.705	0.821	6.584	-1.527	-1.439	-15.086
	1.43	25.040	-24.197	0.814	6.509	-1.503	-1.405	-14.928
	1.43	25.040	-24.197	0.814	6.509	-1.503	-1.405	-14.928
biphenylene	1.37	22.290	-21.341	0.949	7.710	-1.933	-1.789	-17.387
	1.37	22.290	-21.341	0.949	7.710	-1.933	-1.789	-17.387
	1.37	22.290	-21.341	0.949	7.710	-1.933	-1.789	-17.387
	1.37	22.290	-21.341	0.949	7.710	-1.933	-1.789	-17.387
	1.38	20.393	-19.489	0.904	7.419	-1.827	-1.680	-16.775
	1.38	20.393	-19.489	0.904	7.419	-1.827	-1.680	-16.775
	1.42	20.603	-19.759	0.844	6.819	-1.625	-1.512	-15.567
	1.42	20.603	-19.759	0.844	6.819	-1.625	-1.512	-15.567
	1.42	20.603	-19.758	0.844	6.819	-1.625	-1.512	-15.567
	1.42	20.602	-19.758	0.844	6.819	-1.625	-1.512	-15.567
	1.42	23.714	-22.873	0.840	6.772	-1.577	-1.405	-15.535
	1.42	23.714	-22.873	0.840	6.772	-1.577	-1.405	-15.535
	1.51	22.862	-22.140	0.722	5.301	-1.194	-1.147	-12.624
	1.51	22.861	-22.139	0.722	5.301	-1.194	-1.147	-12.624

Table 4.7 The CC bond distance (Å) and the MESP data V_{bnp}, V_ρ, $V(\mathbf{r})$ and eigenvalues (in au) of annulenes at M06-2X/6-311G(d,p) level of theory

system	d_{CC}	V_{bnp}	V_ρ	$V(\mathbf{r})$	λ_{v1}	λ_{v2}	λ_{v3}	λ'_{v1}
14-annulene	1.35	23.116	-22.141	0.975	8.081	-2.056	-1.883	-18.086
	1.35	23.116	-22.141	0.975	8.081	-2.056	-1.883	-18.086
	1.35	23.159	-22.188	0.971	8.054	-2.053	-1.875	-18.036
	1.35	23.159	-22.188	0.971	8.054	-2.053	-1.875	-18.036
	1.35	22.424	-21.460	0.965	8.012	-2.038	-1.849	-17.943
	1.36	22.056	-21.095	0.960	7.933	-2.017	-1.840	-17.796
	1.36	22.056	-21.095	0.960	7.933	-2.017	-1.840	-17.796
	1.44	22.508	-21.709	0.799	6.384	-1.459	-1.406	-14.673
	1.44	22.508	-21.762	0.799	6.384	-1.459	-1.406	-14.673
	1.45	22.561	-21.779	0.782	6.232	-1.416	-1.361	-14.355
	1.45	22.561	-20.799	0.782	6.232	-1.416	-1.361	-14.355
	1.46	21.582	-20.804	0.777	6.177	-1.404	-1.347	-14.236
	1.46	21.582	-21.177	0.777	6.177	-1.404	-1.347	-14.236
	1.46	21.955	-21.739	0.769	6.140	-1.388	-1.329	-14.151
16-anuulene	1.34	24.266	-23.279	0.987	8.216	-2.107	-1.919	-18.350
	1.34	24.266	-23.279	0.987	8.216	-2.107	-1.919	-18.350
	1.34	24.266	-23.279	0.987	8.216	-2.107	-1.919	-18.350
	1.34	24.266	-23.279	0.987	8.216	-2.107	-1.919	-18.350
	1.34	23.259	-22.272	0.987	8.198	-2.111	-1.920	-18.321
	1.34	23.259	-22.272	0.987	8.198	-2.111	-1.920	-18.321
	1.34	23.259	-22.272	0.987	8.198	-2.111	-1.920	-18.321
	1.34	23.259	-22.272	0.987	8.198	-2.111	-1.920	-18.321
	1.45	23.607	-22.828	0.779	6.210	-1.404	-1.356	-14.308
	1.45	23.607	-22.828	0.779	6.210	-1.404	-1.356	-14.308
	1.45	23.607	-22.828	0.779	6.210	-1.404	-1.356	-14.308
	1.45	23.607	-22.828	0.779	6.210	-1.404	-1.356	-14.308
	1.46	22.676	-21.908	0.768	6.097	-1.369	-1.326	-14.072
	1.46	22.676	-21.908	0.768	6.097	-1.369	-1.326	-14.072
	1.46	22.676	-21.908	0.768	6.097	-1.369	-1.326	-14.072
	1.46	22.676	-21.908	0.768	6.097	-1.369	-1.326	-14.072

Table 4.8 The CC bond distance (Å) and the MESP data V_{bnp}, V_ρ, $V(\mathbf{r})$ and eigenvalues (in au) of fullerene, graphene, cyclophane and carbon nanotube systems at M06-2X/6-311G(d,p) level of theory (continues…)

system	d_{CC}	V_{bnp}	V_ρ	$V(\mathbf{r})$	λ_{v1}	λ_{v2}	λ_{v3}	λ'_{v1}
fullerene	1.39	53.132	-52.178	0.954	7.370	-1.819	-1.670	-16.687
	1.39	53.132	-52.178	0.954	7.370	-1.819	-1.670	-16.687
	1.45	52.960	-52.128	0.832	6.241	-1.450	-1.335	-14.399
	1.45	52.960	-52.128	0.832	6.241	-1.450	-1.335	-14.399
ovalene	1.36	31.916	-30.950	0.966	7.965	-2.012	-1.833	-17.863
	1.36	31.916	-30.950	0.966	7.965	-2.012	-1.833	-17.863
	1.36	31.916	-30.950	0.966	7.965	-2.012	-1.833	-17.863
	1.36	31.916	-30.950	0.966	7.965	-2.012	-1.833	-17.863
	1.37	31.371	-30.445	0.927	7.579	-1.875	-1.724	-17.103
	1.37	31.371	-30.445	0.927	7.579	-1.875	-1.724	-17.103
	1.40	34.551	-33.662	0.889	7.183	-1.735	-1.604	-16.305
	1.40	34.551	-33.662	0.889	7.183	-1.735	-1.604	-16.305
	1.40	34.551	-33.662	0.889	7.183	-1.735	-1.604	-16.305
	1.40	34.551	-33.662	0.889	7.183	-1.735	-1.604	-16.305
	1.41	38.875	-38.009	0.866	6.917	-1.641	-1.518	-15.771
	1.41	38.875	-38.009	0.866	6.917	-1.641	-1.518	-15.771
	1.41	38.875	-38.009	0.866	6.917	-1.641	-1.518	-15.771
	1.41	38.875	-38.009	0.866	6.917	-1.641	-1.518	-15.771
	1.41	36.042	-35.181	0.861	6.901	-1.634	-1.512	-15.735
	1.41	36.042	-35.181	0.861	6.901	-1.634	-1.512	-15.735
	1.41	36.042	-35.181	0.861	6.901	-1.634	-1.512	-15.735
	1.41	36.042	-35.181	0.861	6.901	-1.634	-1.512	-15.735
	1.41	32.735	-31.876	0.859	6.913	-1.640	-1.530	-15.760
	1.41	32.735	-31.876	0.859	6.913	-1.640	-1.530	-15.760
	1.41	32.735	-31.876	0.859	6.913	-1.640	-1.530	-15.760
	1.41	32.735	-31.876	0.859	6.913	-1.640	-1.530	-15.760
	1.42	37.592	-36.748	0.845	6.726	-1.578	-1.466	-15.382
	1.42	37.592	-36.748	0.845	6.726	-1.578	-1.466	-15.382
	1.42	36.937	-36.097	0.840	6.696	-1.566	-1.456	-15.316
	1.42	36.937	-36.097	0.840	6.696	-1.566	-1.456	-15.316
	1.42	36.937	-36.097	0.840	6.696	-1.566	-1.456	-15.316
	1.42	36.937	-36.097	0.840	6.696	-1.566	-1.456	-15.316
	1.43	37.883	-37.047	0.835	6.634	-1.546	-1.441	-15.193
	1.43	37.883	-37.047	0.835	6.634	-1.546	-1.441	-15.193
	1.43	37.883	-37.047	0.835	6.634	-1.546	-1.441	-15.193
	1.43	37.883	-37.047	0.835	6.634	-1.546	-1.441	-15.193

Table 4.8 The CC bond distance (Å) and the MESP data V_{bnp}, V_ρ, $V(\mathbf{r})$ and eigenvalues (in a
of fullerene, graphene, cyclophane and carbon nanotube systems at M06-2X/6-311G(d,p)
level of theory (continues…)

system	d_{CC}	V_{bnp}	V_ρ	$V(\mathbf{r})$	λ_{v1}	λ_{v2}	λ_{v3}	λ'_{v1}
	1.44	39.329	-38.507	0.822	6.494	-1.499	-1.403	-14.904
	1.44	32.748	-31.931	0.816	6.498	-1.500	-1.416	-14.908
	1.44	32.748	-31.931	0.816	6.498	-1.500	-1.416	-14.908
	1.44	32.748	-31.931	0.816	6.498	-1.500	-1.416	-14.908
	1.44	32.748	-31.931	0.816	6.498	-1.500	-1.416	-14.908
	1.44	33.446	-32.632	0.814	6.476	-1.492	-1.409	-14.862
	1.44	33.446	-32.632	0.814	6.476	-1.492	-1.409	-14.862
	1.44	33.446	-32.632	0.814	6.476	-1.492	-1.409	-14.862
	1.44	33.446	-32.632	0.814	6.476	-1.492	-1.409	-14.862
cyclophane_$C_{13}H_{18}$	1.39	24.795	-23.901	0.895	7.340	-1.804	-1.670	-16.646
	1.39	24.454	-23.570	0.884	7.249	-1.781	-1.645	-16.458
	1.39	25.302	-24.428	0.875	7.221	-1.742	-1.615	-16.380
	1.39	25.302	-24.428	0.875	7.221	-1.742	-1.615	-16.380
	1.40	25.092	-24.224	0.868	7.145	-1.723	-1.599	-16.228
	1.40	25.092	-24.224	0.868	7.145	-1.723	-1.599	-16.228
	1.50	23.764	-23.083	0.682	5.474	-1.176	-1.156	-12.752
	1.50	23.764	-23.083	0.682	5.474	-1.176	-1.156	-12.752
	1.55	23.456	-22.863	0.593	4.948	-1.032	-1.009	-11.588
	1.55	23.456	-22.863	0.593	4.948	-1.032	-1.009	-11.588
	1.55	22.661	-22.069	0.591	4.886	-1.002	-0.999	-11.442
	1.55	22.661	-22.069	0.591	4.886	-1.002	-0.999	-11.442
	1.56	22.335	-21.749	0.586	4.759	-0.983	-0.966	-11.172
	1.56	22.335	-21.749	0.586	4.759	-0.983	-0.966	-11.172
cyclophane_$C_{16}H_{16}$	1.39	26.835	-25.952	0.883	7.284	-1.789	-1.651	-16.527
	1.39	26.835	-25.952	0.883	7.284	-1.789	-1.651	-16.526
	1.39	26.835	-25.952	0.883	7.283	-1.789	-1.651	-16.525
	1.39	26.835	-25.951	0.883	7.283	-1.789	-1.651	-16.525
	1.39	27.427	-26.557	0.870	7.196	-1.740	-1.609	-16.331
	1.39	27.427	-26.557	0.870	7.196	-1.739	-1.609	-16.331
	1.39	27.427	-26.557	0.870	7.196	-1.739	-1.609	-16.330
	1.39	27.427	-26.557	0.870	7.196	-1.739	-1.609	-16.329
	1.40	27.393	-26.527	0.866	7.173	-1.733	-1.601	-16.281
	1.40	27.393	-26.527	0.866	7.172	-1.733	-1.601	-16.281
	1.40	27.393	-26.527	0.866	7.172	-1.733	-1.601	-16.280
	1.40	27.393	-26.527	0.866	7.172	-1.733	-1.601	-16.280

Table 4.8 The CC bond distance (Å) and the MESP data V_{bnp}, V_ρ, $V(\mathbf{r})$ and eigenvalues (in au) of fullerene, graphene, cyclophane and carbon nanotube systems at M06-2X/6-311G(d,p) level of theory

system	d_{CC}	V_{bnp}	V_ρ	$V(\mathbf{r})$	λ_{v1}	λ_{v2}	λ_{v3}	λ'_{v1}
	1.51	25.820	-25.150	0.670	5.377	-1.143	-1.131	-12.528
	1.51	25.820	-25.150	0.670	5.377	-1.143	-1.131	-12.527
	1.51	25.820	-25.150	0.670	5.377	-1.143	-1.131	-12.527
	1.51	25.820	-25.150	0.670	5.376	-1.143	-1.131	-12.525
	1.59	24.258	-23.701	0.557	4.427	-0.906	-0.884	-10.439
	1.59	24.258	-23.701	0.557	4.427	-0.906	-0.884	-10.438
CNT_C24H12	1.41	32.013	-31.135	0.878	6.898	-1.684	-1.547	-15.744
	1.41	32.013	-31.135	0.878	6.898	-1.684	-1.546	-15.744
	1.41	32.013	-31.135	0.878	6.898	-1.684	-1.546	-15.744
	1.41	32.013	-31.135	0.878	6.898	-1.684	-1.546	-15.744
	1.41	32.013	-31.135	0.878	6.897	-1.684	-1.546	-15.744
	1.41	32.013	-31.135	0.878	6.897	-1.684	-1.546	-15.744
	1.41	32.013	-31.135	0.878	6.897	-1.684	-1.546	-15.744
	1.41	32.013	-31.135	0.878	6.897	-1.684	-1.546	-15.744
	1.41	32.012	-31.135	0.878	6.896	-1.684	-1.546	-15.744
	1.41	32.012	-31.135	0.878	6.896	-1.684	-1.546	-15.744
	1.41	37.377	-31.135	0.878	6.895	-1.684	-1.546	-15.744
	1.41	32.011	-31.134	0.878	6.895	-1.684	-1.546	-15.744
	1.41	32.012	-31.134	0.877	6.895	-1.684	-1.546	-15.744
	1.41	32.012	-36.500	0.877	6.895	-1.684	-1.546	-15.744
	1.41	32.012	-31.134	0.877	6.895	-1.684	-1.546	-15.744
	1.41	32.012	-31.135	0.877	6.895	-1.684	-1.546	-15.744
	1.41	32.011	-31.135	0.877	6.895	-1.683	-1.546	-15.744
	1.41	32.011	-31.135	0.877	6.895	-1.683	-1.546	-15.744
	1.41	32.011	-31.135	0.877	6.895	-1.683	-1.546	-15.744
	1.41	32.011	-31.134	0.877	6.895	-1.683	-1.546	-15.744
	1.41	32.012	-31.134	0.877	6.894	-1.683	-1.545	-15.744
	1.41	32.012	-31.134	0.877	6.894	-1.683	-1.545	-15.744
	1.41	32.012	-31.134	0.877	6.893	-1.683	-1.545	-15.744
	1.41	32.012	-31.134	0.877	6.893	-1.683	-1.545	-15.744
	1.45	32.755	-31.134	0.805	6.298	-1.425	-1.347	-14.475
	1.45	32.755	-31.134	0.805	6.298	-1.425	-1.347	-14.475
	1.45	32.754	-31.134	0.805	6.296	-1.424	-1.347	-14.475
	1.45	32.754	-31.950	0.805	6.296	-1.424	-1.347	-14.475
	1.45	32.755	-31.950	0.805	6.295	-1.424	-1.347	-14.475
	1.45	32.755	-31.949	0.805	6.295	-1.424	-1.347	-14.475

Table 4.9 The CC bond distance (Å) and the MESP data V_{bnp}, V_ρ, $V(\mathbf{r})$ and eigenvalues (in au) of alkynes at M06-2X/6-311G(d,p) level of theory (continues..)

system	d_{CC}	V_{bnp}	V_ρ	$V(\mathbf{r})$	λ_{v1}	λ_{v2}	λ_{v3}	λ'_{v1}
acetylene	1.20	11.255	-9.853	1.402	12.151	-3.500	-3.500	-25.649
diacetylene	1.20	13.612	-12.206	1.406	11.951	-3.435	-3.435	-25.310
	1.20	13.612	-12.206	1.406	11.951	-3.435	-3.435	-25.310
	1.38	12.938	-11.934	1.004	7.447	-1.844	-1.844	-16.996
triacetylene	1.20	14.806	-13.398	1.408	11.898	-3.414	-3.414	-25.218
	1.20	14.806	-13.398	1.408	11.898	-3.414	-3.414	-25.218
	1.21	15.963	-14.562	1.401	11.697	-3.348	-3.348	-24.872
	1.37	14.588	-13.560	1.027	7.597	-1.894	-1.894	-17.290
	1.37	14.588	-13.560	1.027	7.597	-1.894	-1.894	-17.290
tetraacetylene	1.20	15.610	-14.200	1.411	11.883	-3.408	-3.408	-25.191
	1.20	15.610	-14.200	1.411	11.883	-3.408	-3.408	-25.191
	1.21	17.152	-15.753	1.399	11.620	-3.319	-3.319	-24.738
	1.21	17.152	-15.753	1.399	11.620	-3.319	-3.319	-24.738
	1.36	16.250	-15.198	1.051	7.775	-1.954	-1.954	-17.642
	1.37	15.567	-14.532	1.035	7.637	-1.907	-1.907	-17.370
	1.37	15.567	-14.532	1.035	7.637	-1.907	-1.907	-17.370
pentaacetylene	1.20	16.217	-14.805	1.412	11.878	-3.405	-3.405	-25.183
	1.20	16.217	-14.805	1.412	11.878	-3.405	-3.405	-25.183
	1.21	17.955	-16.556	1.400	11.595	-3.309	-3.309	-24.695
	1.21	17.955	-16.556	1.400	11.595	-3.309	-3.309	-24.695
	1.21	18.341	-16.946	1.395	11.535	-3.286	-3.286	-24.590
	1.36	17.234	-16.175	1.060	7.827	-1.971	-1.971	-17.744
	1.36	17.234	-16.175	1.060	7.827	-1.971	-1.971	-17.744
	1.37	16.266	-15.227	1.039	7.653	-1.912	-1.912	-17.400
	1.37	16.266	-15.227	1.039	7.653	-1.912	-1.912	-17.400
hexaacetylene	1.20	16.704	-15.291	1.414	11.876	-3.404	-3.404	-25.193
	1.20	16.704	-15.291	1.414	11.876	-3.404	-3.404	-25.193
	1.21	18.562	-17.161	1.401	11.585	-3.305	-3.305	-24.683
	1.21	18.562	-17.161	1.401	11.585	-3.305	-3.305	-24.683
	1.22	19.143	-17.748	1.395	11.505	-3.275	-3.275	-24.515
	1.22	19.143	-17.748	1.395	11.505	-3.275	-3.275	-24.515
	1.36	18.221	-17.153	1.068	7.884	-1.990	-1.990	-17.838
	1.36	17.935	-16.872	1.064	7.848	-1.978	-1.978	-17.798
	1.36	17.935	-16.872	1.064	7.848	-1.978	-1.978	-17.798
	1.37	16.809	-15.768	1.042	7.659	-1.914	-1.914	-17.398
	1.37	16.809	-15.768	1.042	7.659	-1.914	-1.914	-17.398
heptaacetylene	1.20	17.111	-15.697	1.415	11.876	-3.404	-3.404	-25.193
	1.20	17.111	-15.696	1.415	11.876	-3.404	-3.404	-25.193
	1.21	19.049	-17.647	1.402	11.582	-3.304	-3.304	-24.683

Table 4.9 The CC bond distance (Å) and the MESP data V_{bnp}, V_ρ, $V(\mathbf{r})$ and eigenvalues (in a of alkynes at M06-2X/6-311G(d,p) level of theory

system	d_{CC}	V_{bnp}	V_ρ	$V(\mathbf{r})$	λ_{v1}	λ_{v2}	λ_{v3}	λ'_{v1}
	1.21	19.049	-17.647	1.402	11.582	-3.304	-3.304	-24.683
	1.22	19.750	-18.354	1.396	11.494	-3.271	-3.271	-24.515
	1.22	19.750	-18.354	1.396	11.494	-3.271	-3.271	-24.515
	1.22	19.946	-18.551	1.395	11.474	-3.263	-3.263	-24.460
	1.36	18.923	-17.851	1.072	7.906	-1.997	-1.997	-17.879
	1.36	18.923	-17.851	1.072	7.906	-1.997	-1.997	-17.879
	1.36	18.480	-17.413	1.066	7.856	-1.981	-1.981	-17.798
	1.36	18.480	-17.413	1.066	7.856	-1.981	-1.981	-17.798
	1.37	17.254	-16.211	1.043	7.662	-1.915	-1.915	-17.438
	1.37	17.254	-16.211	1.043	7.662	-1.915	-1.915	-17.438
octaacetylene	1.20	17.461	-16.045	1.416	11.876	-3.404	-3.404	-25.193
	1.20	17.461	-16.045	1.416	11.876	-3.404	-3.404	-25.193
	1.21	19.456	-18.054	1.403	11.580	-3.303	-3.303	-24.683
	1.21	19.456	-18.054	1.403	11.580	-3.303	-3.303	-24.683
	1.22	20.237	-18.840	1.397	11.489	-3.269	-3.269	-24.515
	1.22	20.237	-18.840	1.397	11.489	-3.269	-3.269	-24.515
	1.22	20.552	-19.156	1.395	11.462	-3.258	-3.258	-24.460
	1.22	20.552	-19.156	1.395	11.462	-3.258	-3.258	-24.460
	1.35	19.625	-18.549	1.076	7.929	-2.005	-2.005	-17.960
	1.35	19.468	-18.393	1.074	7.916	-2.000	-2.000	-17.920
	1.35	19.468	-18.393	1.074	7.916	-2.000	-2.000	-17.920
	1.36	18.925	-17.857	1.068	7.860	-1.982	-1.982	-17.798
	1.36	18.925	-17.857	1.068	7.860	-1.982	-1.982	-17.798
	1.37	17.631	-16.586	1.045	7.664	-1.915	-1.915	-17.438
	1.37	17.631	-16.586	1.045	7.664	-1.915	-1.915	-17.438
nonaacetylene	1.20	17.767	-16.351	1.416	11.876	-3.404	-3.404	-25.193
	1.20	17.767	-16.351	1.416	11.876	-3.404	-3.404	-25.193
	1.21	19.806	-18.402	1.403	11.580	-3.303	-3.303	-24.683
	1.21	19.806	-18.402	1.403	11.580	-3.303	-3.303	-24.683
	1.22	20.644	-19.246	1.398	11.487	-3.268	-3.268	-24.515
	1.22	20.644	-19.246	1.398	11.487	-3.268	-3.268	-24.515
	1.22	21.039	-19.643	1.396	11.457	-3.256	-3.256	-24.460
	1.22	21.039	-19.643	1.396	11.457	-3.256	-3.256	-24.460
	1.22	21.158	-19.762	1.395	11.449	-3.253	-3.253	-24.460
	1.35	20.170	-19.092	1.078	7.939	-2.008	-2.008	-17.960
	1.35	19.913	-18.838	1.076	7.920	-2.002	-2.002	-17.920
	1.35	19.913	-18.838	1.076	7.920	-2.002	-2.002	-17.920
	1.36	19.302	-18.233	1.069	7.862	-1.983	-1.983	-17.798
	1.37	17.958	-16.912	1.045	7.665	-1.916	-1.916	-17.438

Table 4.10 The CC bond distance (Å) and the MESP data V_{bnp}, V_ρ, $V(\mathbf{r})$ and eigenvalues (in au) of C_2 and carbon rings at M06-2X/6-311G(d,p) level of theory

system	d_{CC}	V_{bnp}	V_ρ	$V(\mathbf{r})$	λ_{v1}	λ_{v2}	λ_{v3}	λ'_{v1}
C_2	1.30	9.745	-8.504	1.241	9.118	-2.691	-2.337	-20.108
C_6	1.32	16.221	-15.054	1.167	8.651	-2.322	-2.215	-19.276
	1.32	16.222	-15.055	1.167	8.651	-2.322	-2.215	-19.276
	1.32	16.221	-15.054	1.167	8.651	-2.322	-2.215	-19.276
	1.32	16.221	-15.054	1.167	8.651	-2.322	-2.215	-19.276
	1.32	16.221	-15.054	1.167	8.651	-2.322	-2.215	-19.276
	1.32	16.221	-15.054	1.167	8.651	-2.322	-2.215	-19.276
C_8	1.39	18.043	-17.012	1.031	7.320	-1.863	-1.831	-16.678
	1.39	18.043	-17.012	1.031	7.320	-1.863	-1.831	-16.678
	1.39	18.043	-17.012	1.031	7.320	-1.863	-1.831	-16.678
	1.39	18.043	-17.012	1.031	7.320	-1.863	-1.831	-16.678
	1.25	17.242	-15.924	1.317	10.483	-2.944	-2.777	-22.642
	1.25	17.242	-15.924	1.317	10.483	-2.944	-2.777	-22.642
	1.25	17.242	-15.924	1.317	10.483	-2.944	-2.777	-22.642
	1.25	17.242	-15.924	1.317	10.483	-2.944	-2.777	-22.642
C_{10}	1.28	18.905	-17.675	1.229	9.572	-2.593	-2.583	-21.055
C_{12}	1.23	20.161	-18.794	1.366	11.121	-3.141	-3.075	-23.823
	1.37	19.258	-18.200	1.058	7.656	-1.958	-1.931	-17.383
C_{14}	1.28	20.629	-19.385	1.244	9.668	-2.620	-2.612	-21.247
C_{16}	1.22	21.622	-20.224	1.398	11.480	-3.262	-3.254	-24.486
	1.37	20.611	-19.555	1.057	7.656	-1.950	-1.934	-17.409

Table 4.11 The CC bond distance (Å) and the MESP data V_{bnp}, V_ρ, $V(\mathbf{r})$ and eigenvalues (in au) of heterocyclic systems at M06-2X/6-311G(d,p) level of theory (continues..)

system	d_{CC}	V_{bnp}	V_ρ	$V(\mathbf{r})$	λ_{v1}	λ_{v2}	λ_{v3}	λ'_{v1}
pyrazine	1.39	16.922	-16.005	0.917	7.268	-1.734	-1.598	-16.445
	1.39	16.922	-16.005	0.917	7.268	-1.734	-1.598	-16.445
pyrrole	1.37	15.970	-15.060	0.910	7.611	-1.941	-1.692	-17.189
	1.37	15.970	-15.060	0.910	7.611	-1.941	-1.692	-17.189
	1.42	15.626	-14.820	0.806	6.683	-1.633	-1.463	-15.347
furan	1.35	16.240	-15.267	0.973	7.998	-2.063	-1.787	-17.933
	1.35	16.240	-15.267	0.973	7.998	-2.063	-1.787	-17.933
	1.43	15.683	-14.871	0.812	6.469	-1.562	-1.413	-14.921
thiophene	1.36	17.600	-16.640	0.960	7.849	-2.016	-1.798	-17.647
	1.36	17.600	-16.640	0.960	7.849	-2.016	-1.798	-17.647
	1.43	17.021	-16.198	0.823	6.621	-1.578	-1.447	-15.188
tetrahydro pyran	1.53	17.246	-16.608	0.638	5.218	-1.075	-1.031	-12.146
	1.53	17.246	-16.608	0.638	5.218	-1.075	-1.031	-12.146
	1.53	17.023	-16.395	0.629	5.126	-1.067	-1.051	-11.988
	1.53	17.023	-16.395	0.629	5.126	-1.067	-1.051	-11.988
THF	1.53	16.005	-15.363	0.643	5.173	-1.072	-1.017	-12.078
	1.53	16.004	-15.362	0.642	5.172	-1.071	-1.017	-12.078
	1.53	15.882	-15.241	0.641	5.120	-1.075	-1.054	-12.011
thiozolidine	1.52	17.584	-16.919	0.665	5.235	-1.097	-1.053	-12.200
thioxanthene	1.39	25.760	-24.858	0.902	7.244	-1.776	-1.627	-16.428
	1.39	25.760	-24.858	0.902	7.244	-1.776	-1.627	-16.428
	1.39	23.450	-22.554	0.896	7.295	-1.781	-1.646	-16.539
	1.39	23.450	-22.554	0.896	7.295	-1.781	-1.646	-16.539
	1.39	25.359	-24.463	0.895	7.251	-1.770	-1.630	-16.447
	1.39	25.359	-24.463	0.895	7.251	-1.770	-1.630	-16.447
	1.40	27.272	-26.379	0.893	7.155	-1.740	-1.590	-16.240
	1.40	27.272	-26.379	0.893	7.155	-1.740	-1.590	-16.240
	1.39	23.312	-22.419	0.893	7.280	-1.771	-1.639	-16.507
	1.39	23.312	-22.419	0.893	7.280	-1.771	-1.639	-16.507
	1.39	22.726	-21.836	0.891	7.273	-1.767	-1.638	-16.492
	1.39	22.726	-21.836	0.891	7.273	-1.767	-1.638	-16.492
	1.51	25.658	-24.964	0.694	5.421	-1.164	-1.126	-12.633
	1.51	25.658	-24.964	0.694	5.421	-1.164	-1.126	-12.633
piperazine	1.52	17.325	-16.688	0.638	5.252	-1.078	-1.038	-12.217
	1.52	17.325	-16.688	0.638	5.252	-1.078	-1.038	-12.217
pyrrolidine	1.54	15.774	-15.157	0.616	5.052	-1.042	-1.002	-11.819
	1.55	15.598	-15.002	0.596	4.876	-1.007	-0.981	-11.452

Table 4.11 The CC bond distance (Å) and the MESP data V_{bnp}, V_ρ, $V(\mathbf{r})$ and eigenvalues (in au) of heterocyclic systems at M06-2X/6-311G(d,p) level of theory (continues..)

system	d_{CC}	V_{bnp}	V_ρ	$V(\mathbf{r})$	λ_{v1}	λ_{v2}	λ_{v3}	λ'_{v1}
dioxolane	1.54	16.358	-15.708	0.650	5.075	-1.035	-0.944	-11.846
DBN	1.52	20.956	-20.287	0.669	5.339	-1.111	-1.060	-12.432
	1.53	19.861	-19.215	0.646	5.182	-1.082	-1.043	-12.098
	1.53	19.596	-18.955	0.641	5.081	-1.054	-1.008	-11.961
	1.54	19.461	-18.828	0.633	5.067	-1.058	-1.027	-11.880
	1.54	19.469	-18.844	0.625	5.128	-1.063	-1.030	-11.880
benzonitrile	1.39	18.225	-17.303	0.923	7.329	-1.781	-1.654	-16.588
	1.39	18.225	-17.302	0.923	7.329	-1.781	-1.654	-16.588
	1.39	19.021	-18.104	0.917	7.163	-1.742	-1.596	-16.475
	1.39	19.021	-18.104	0.917	7.163	-1.742	-1.596	-16.475
	1.40	17.875	-16.962	0.913	7.259	-1.754	-1.635	-16.252
	1.40	17.875	-16.962	0.913	7.259	-1.754	-1.635	-16.252
	1.44	18.060	-17.173	0.887	6.421	-1.507	-1.461	-14.841
porphyrin	1.36	27.976	-27.003	0.972	8.086	-2.071	-1.868	-17.879
	1.36	27.976	-27.003	0.972	8.086	-2.071	-1.868	-17.879
	1.37	27.941	-26.987	0.954	7.760	-1.965	-1.766	-17.478
	1.37	27.941	-26.987	0.954	7.760	-1.964	-1.766	-17.478
	1.39	29.973	-29.051	0.922	7.326	-1.795	-1.654	-16.588
	1.39	29.973	-29.051	0.922	7.326	-1.795	-1.654	-16.588
	1.39	29.973	-29.052	0.922	7.326	-1.795	-1.654	-16.588
	1.39	29.973	-29.051	0.922	7.326	-1.795	-1.653	-16.588
	1.39	29.980	-29.084	0.896	7.215	-1.746	-1.615	-16.364
	1.39	29.980	-29.084	0.896	7.215	-1.746	-1.615	-16.364
	1.39	29.980	-29.084	0.896	7.215	-1.746	-1.615	-16.364
	1.39	29.980	-29.084	0.896	7.214	-1.746	-1.615	-16.364
	1.43	29.154	-28.323	0.830	6.530	-1.526	-1.381	-14.977
	1.43	29.154	-28.323	0.830	6.530	-1.526	-1.381	-14.977
	1.43	29.154	-28.324	0.830	6.530	-1.526	-1.381	-14.977
	1.43	29.154	-28.324	0.830	6.530	-1.526	-1.381	-14.977
	1.46	29.030	-28.265	0.765	6.115	-1.385	-1.277	-14.118
	1.46	29.030	-28.265	0.765	6.115	-1.385	-1.276	-14.118
	1.46	29.030	-28.265	0.765	6.115	-1.385	-1.276	-14.118
	1.46	29.030	-28.265	0.765	6.115	-1.385	-1.276	-14.118
aziridine	1.48	13.253	-12.447	0.806	5.558	-1.326	-1.247	-13.411
cyanogen	1.39	13.183	-12.097	1.086	7.258	-1.783	-1.783	-16.648
pyramid-	1.40	22.956	-22.029	0.927	7.113	-1.675	-1.535	-16.142
pyramidine	1.42	21.593	-20.709	0.885	6.744	-1.537	-1.446	-15.390

Table 4.11 The CC bond distance (Å) and the MESP data V_{bnp}, V_ρ, $V(\mathbf{r})$ and eigenvalues (in au) of heterocyclic systems at M06-2X/6-311G(d,p) level of theory

system	d_{CC}	V_{bnp}	V_ρ	$V(\mathbf{r})$	λ_{v1}	λ_{v2}	λ_{v3}	λ'_{v1}
oxirane	1.47	13.663	-12.802	0.861	5.712	-1.414	-1.274	-13.837
ethylene-carbonate	1.53	17.322	-16.621	0.702	5.180	-1.067	-0.964	-12.070
furfural	1.36	18.033	-17.052	0.981	7.850	-2.001	-1.742	-17.637
	1.36	19.243	-18.266	0.977	7.816	-1.984	-1.734	-17.557
	1.42	17.852	-16.999	0.854	6.653	-1.608	-1.464	-15.286
	1.46	18.148	-17.342	0.805	6.107	-1.342	-1.255	-14.022
ethylene glycol	1.51	14.946	-14.283	0.664	5.405	-1.122	-1.023	-12.505
tetrathia-fulvalene	1.33	24.712	-23.650	1.062	8.534	-2.285	-2.017	-18.966
	1.33	24.712	-23.650	1.062	8.534	-2.285	-2.017	-18.966
	1.34	29.224	-28.172	1.053	8.313	-2.265	-1.934	-18.541
Dithiano-dithiine	1.52	30.311	-29.605	0.706	5.324	-1.133	-1.111	-12.404
	1.52	30.311	-29.605	0.706	5.324	-1.133	-1.111	-12.404
	1.53	39.159	-38.475	0.684	5.113	-1.056	-1.017	-11.891
thiirane	1.48	15.175	-14.384	0.791	5.710	-1.289	-1.245	-13.465
thietane	1.54	16.072	-15.429	0.643	5.026	-1.045	-0.995	-11.803
	1.54	16.072	-15.429	0.643	5.026	-1.045	-0.995	-11.803
thiane	1.53	18.478	-17.831	0.647	5.198	-1.086	-1.070	-12.126
	1.53	18.478	-17.831	0.647	5.198	-1.086	-1.070	-12.126
	1.53	18.145	-17.513	0.632	5.132	-1.067	-1.053	-11.993
	1.53	18.145	-17.513	0.632	5.132	-1.067	-1.053	-11.993
thiaindans	1.39	22.292	-21.384	0.908	7.314	-1.801	-1.657	-16.626
	1.39	21.852	-20.948	0.904	7.343	-1.804	-1.662	-16.588
	1.39	20.065	-19.178	0.887	7.269	-1.769	-1.636	-16.475
	1.39	23.459	-22.572	0.887	7.147	-1.733	-1.576	-16.401
	1.39	20.566	-19.680	0.887	7.234	-1.765	-1.629	-16.364
	1.40	20.389	-19.506	0.882	7.211	-1.753	-1.621	-16.216
	1.51	21.450	-20.761	0.689	5.401	-1.157	-1.113	-12.602
	1.53	20.384	-19.727	0.657	5.134	-1.078	-1.043	-11.988
SeC$_3$Se	1.27	24.341	-23.080	1.261	9.808	-2.649	-2.649	-21.481
SC$_3$S	1.27	17.942	-16.680	1.262	9.803	-2.654	-2.654	-21.491
C$_5$S	1.26	16.805	-15.497	1.308	10.094	-2.742	-2.742	-22.027
	1.28	17.152	-15.880	1.272	9.587	-2.571	-2.571	-21.087
	1.29	15.909	-14.691	1.219	9.279	-2.446	-2.446	-20.534
	1.28	14.708	-13.506	1.202	9.803	-2.537	-2.537	-21.352
NCCP	1.38	14.783	-13.741	1.043	7.422	-1.828	-1.828	-16.916

Table 4.12 The CC bond distance (Å) and the MESP data V_{bnp}, V_ρ, $V(\mathbf{r})$ and eigenvalues (in au) of anions, cations and radical systems at M06-2X/6-311G(d,p) level of theory (continues..)

system	d_{CC}	V_{bnp}	V_ρ	$V(\mathbf{r})$	λ_{v1}	λ_{v2}	λ_{v3}	λ'_{v1}
acetylene cation	1.19	10.970	-9.053	1.914	12.212	-3.951	-3.951	-25.883
cycloprop-enyl cation	1.36	12.989	-11.640	1.349	7.554	-2.000	-1.726	-17.665
	1.36	12.989	-11.640	1.349	7.554	-2.000	-1.726	-17.665
	1.36	12.989	-11.640	1.349	7.554	-2.000	-1.726	-17.665
cycloheptatrienylcation	1.39	17.274	-16.163	1.110	7.237	-1.703	-1.654	-16.403
	1.39	17.274	-16.163	1.110	7.236	-1.703	-1.653	-16.402
	1.39	17.274	-16.163	1.110	7.236	-1.703	-1.653	-16.402
	1.39	17.274	-16.163	1.110	7.236	-1.703	-1.653	-16.401
	1.39	17.273	-16.163	1.110	7.236	-1.703	-1.653	-16.400
	1.39	17.273	-16.163	1.110	7.235	-1.703	-1.653	-16.400
	1.39	17.273	-16.163	1.110	7.235	-1.703	-1.653	-16.399
benzene-1-ylium	1.32	16.839	-15.477	1.362	8.708	-2.343	-2.097	-19.377
	1.32	16.839	-15.477	1.362	8.708	-2.343	-2.097	-19.377
	1.39	16.411	-15.292	1.119	7.311	-1.776	-1.638	-16.549
	1.39	16.411	-15.292	1.119	7.311	-1.776	-1.638	-16.549
	1.43	16.151	-15.052	1.100	6.567	-1.645	-1.517	-15.120
	1.43	16.151	-15.052	1.100	6.567	-1.645	-1.517	-15.120
propan-1-ylium	1.39	13.237	-12.049	1.188	7.179	-1.710	-1.704	-16.404
	1.69	12.075	-11.270	0.805	3.406	-0.780	-0.667	-8.295
	1.78	11.915	-11.161	0.754	2.753	-0.624	-0.465	-6.814
propan-2-ylium	1.44	12.486	-11.412	1.074	6.497	-1.451	-1.391	-14.850
2-methyl propan-2-ylium	1.46	14.341	-13.324	1.017	6.170	-1.348	-1.297	-14.170
	1.46	14.323	-13.308	1.015	6.156	-1.346	-1.292	-14.140
	1.46	14.317	-13.305	1.012	6.130	-1.338	-1.284	-14.085
ethen-1-ylium	1.25	11.139	-9.569	1.570	10.449	-2.933	-2.571	-22.521

Table 4.12 The CC bond distance (Å) and the MESP data V_{bnp}, V_ρ, $V(\mathbf{r})$ and eigenvalues (in au) of anions, cations and radical systems at M06-2X/6-311G(d,p) level of theory

system	d_{CC}	V_{bnp}	V_ρ	$V(\mathbf{r})$	λ_{v1}	λ_{v2}	λ_{v3}	λ'_{v1}
cyclopenta dienylanion	1.41	15.315	-14.712	0.603	6.912	-1.734	-1.530	-15.802
	1.41	15.313	-14.711	0.602	6.902	-1.731	-1.527	-15.783
	1.41	15.311	-14.709	0.602	6.898	-1.730	-1.526	-15.774
acetate	1.57	14.006	-13.630	0.376	4.715	-0.928	-0.924	-11.014
benzen-1-ide	1.39	16.265	-15.577	0.688	7.207	-1.766	-1.620	-16.365
	1.39	16.265	-15.577	0.688	7.207	-1.766	-1.620	-16.365
	1.40	16.208	-15.547	0.661	7.120	-1.726	-1.598	-16.174
	1.40	16.208	-15.547	0.661	7.120	-1.726	-1.598	-16.174
	1.42	15.870	-15.284	0.585	6.759	-1.564	-1.563	-15.417
	1.42	15.870	-15.284	0.585	6.759	-1.564	-1.563	-15.417
ethyn-1-ide	1.24	10.567	-9.607	0.960	10.842	-2.979	-2.979	-23.281
ethen-1-ide	1.35	10.413	-9.741	0.671	8.027	-2.043	-1.934	-17.951
2-oxopropan-1-ide	1.38	14.515	-13.853	0.663	7.498	-1.912	-1.679	-16.898
	1.55	13.799	-13.398	0.401	4.942	-1.003	-0.992	-11.543
ethan-1-ide	1.54	9.947	-9.605	0.342	5.031	-1.146	-1.055	-11.767
benzene radical	1.37	16.293	-15.353	0.940	7.600	-1.883	-1.761	-17.148
	1.37	16.293	-15.353	0.940	7.600	-1.883	-1.761	-17.148
	1.39	16.331	-15.441	0.889	7.247	-1.760	-1.629	-16.434
	1.40	16.255	-15.369	0.886	7.140	-1.742	-1.616	-16.235
	1.40	16.255	-15.369	0.886	7.140	-1.742	-1.616	-16.235
3-methylbut-2-enenitrile radical	1.31	17.036	-15.925	1.111	8.884	-2.380	-2.172	-19.654
	1.37	15.995	-14.963	1.032	7.614	-1.906	-1.894	-17.302
	1.51	15.317	-14.598	0.719	5.460	-1.173	-1.156	-12.711
	1.51	15.494	-14.781	0.714	5.392	-1.160	-1.147	-12.573
allyl_radical	1.38	12.348	-11.443	0.905	7.469	-1.836	-1.710	-16.876
vinyl_radical	1.30	10.749	-9.662	1.087	9.087	-2.429	-2.229	-20.033

Table 4.13 The CC bond distance (Å) and the MESP data V_{bnp}, V_ρ, $V(\mathbf{r})$ and eigenvalues (in au) of systems containing multiple types of bonds at M06-2X/6-311G(d,p) level of theory (continues..)

system	d_{CC}	V_{bnp}	V_ρ	$V(\mathbf{r})$	λ_{v1}	λ_{v2}	λ_{v3}	λ'_{v1}
cyclobutadiene	1.33	14.365	-13.342	1.023	8.514	-2.252	-1.978	-19.006
	1.33	14.365	-13.342	1.023	8.514	-2.252	-1.978	-19.006
	1.57	13.322	-12.708	0.614	4.546	-0.996	-0.911	-10.956
	1.57	13.322	-12.708	0.614	4.546	-0.996	-0.911	-10.956
hexa_1,5_dien _3_yne	1.21	16.771	-15.401	1.370	11.776	-3.394	-3.359	-25.012
	1.33	14.865	-13.847	1.019	8.434	-2.191	-1.989	-18.774
	1.33	14.865	-13.847	1.019	8.434	-2.191	-1.989	-18.774
	1.43	15.119	-14.256	0.864	6.616	-1.563	-1.528	-15.216
	1.43	15.119	-14.256	0.864	6.616	-1.563	-1.528	-15.216
hexpta_1_en_ 3,6_diyne	1.20	16.081	-16.203	1.397	12.099	-3.499	-3.496	-25.567
	1.20	17.600	-13.995	1.385	11.930	-3.450	-3.435	-25.279
	1.33	15.380	-14.707	1.022	8.466	-2.203	-1.999	-18.837
	1.43	15.728	-15.069	0.857	6.557	-1.544	-1.511	-15.097
	1.47	15.926	-14.701	0.805	5.993	-1.373	-1.350	-13.909
	1.47	15.506	-14.200	0.803	5.972	-1.363	-1.339	-13.862
2-pentene	1.33	15.003	-14.002	1.001	8.549	-2.236	-2.013	-18.990
	1.50	13.648	-12.965	0.682	5.534	-1.196	-1.179	-12.875
	1.50	15.117	-14.441	0.675	5.517	-1.178	-1.163	-12.829
	1.53	14.169	-13.543	0.626	5.110	-1.078	-1.064	-11.956
isoprene	1.33	15.250	-14.245	1.005	8.464	-2.195	-1.997	-18.833
	1.34	15.694	-14.699	0.995	8.400	-2.171	-1.964	-18.697
	1.47	15.526	-14.781	0.744	5.958	-1.313	-1.274	-13.765
	1.50	14.997	-14.313	0.684	5.476	-1.172	-1.155	-12.745

Table 4.13 The CC bond distance (Å) and the MESP data V_{bnp}, V_ρ, $V(\mathbf{r})$ and eigenvalues (in of systems containing multiple types of bonds at M06-2X/6-311G(d,p) level of theory

system	d_{CC}	V_{bnp}	V_ρ	$V(\mathbf{r})$	λ_{v1}	λ_{v2}	λ_{v3}	λ'_{v1}
indene	1.34	19.317	-18.330	0.988	8.295	-2.141	-1.920	-18.511
	1.38	20.332	-19.432	0.900	7.383	-1.812	-1.678	-16.721
	1.39	20.264	-19.377	0.888	7.270	-1.769	-1.643	-16.495
	1.39	19.170	-18.291	0.879	7.242	-1.764	-1.629	-16.428
	1.39	18.887	-18.012	0.875	7.215	-1.752	-1.622	-16.372
	1.39	19.175	-18.300	0.874	7.192	-1.747	-1.616	-16.328
	1.40	21.365	-20.512	0.854	7.029	-1.669	-1.524	-15.997
	1.47	19.801	-19.052	0.749	5.966	-1.342	-1.271	-13.830
	1.51	19.610	-18.927	0.683	5.420	-1.160	-1.121	-12.655
	1.51	18.481	-17.801	0.680	5.412	-1.164	-1.116	-12.625
dihydroindene	1.39	20.604	-19.715	0.889	7.319	-1.786	-1.658	-16.591
	1.39	20.604	-19.715	0.889	7.319	-1.786	-1.658	-16.591
	1.39	19.110	-18.234	0.876	7.240	-1.759	-1.629	-16.423
	1.39	19.414	-18.539	0.875	7.219	-1.755	-1.624	-16.383
	1.39	19.414	-18.539	0.875	7.219	-1.755	-1.624	-16.383
	1.40	21.724	-20.859	0.865	7.177	-1.720	-1.574	-16.292
	1.51	19.908	-19.240	0.668	5.363	-1.142	-1.109	-12.526
	1.51	19.908	-19.240	0.668	5.363	-1.142	-1.109	-12.526
	1.54	18.657	-18.044	0.613	4.974	-1.030	-1.001	-11.664
	1.54	18.657	-18.044	0.613	4.974	-1.030	-1.001	-11.664
cyclopentadiene	1.34	15.835	-14.859	0.975	8.249	-2.127	-1.909	-18.428
	1.34	15.835	-14.859	0.975	8.249	-2.127	-1.909	-18.428
	1.47	15.180	-14.444	0.736	5.945	-1.346	-1.264	-13.778
	1.50	15.058	-14.375	0.683	5.501	-1.192	-1.142	-12.824
	1.50	15.058	-14.375	0.683	5.501	-1.192	-1.142	-12.824

Table 4.14 The CC bond distance (Å) and the MESP data V_{bnp}, V_{ρ}, $V(\mathbf{r})$ and eigenvalues (in au) of organometallic and hypervalent carbon complexes at M06-2X/6-311G(d,p) level of theory

system	d_{CC}	V_{bnp}	V_{ρ}	$V(\mathbf{r})$	λ_{v1}	λ_{v2}	λ_{v3}	λ'_{v1}
ferrocene	1.42	26.987	-26.147	0.840	6.744	-1.643	-1.481	-15.477
bis(benzene) chromium(0)	1.41	28.355	-27.503	0.852	6.851	-1.663	-1.522	-15.643
η^3-CrCl$_3$	1.40	27.583	-26.511	1.073	6.765	-1.762	-1.525	-16.089
metallacyclobutane	1.42	27.389	-26.389	1.001	6.789	-1.651	-1.505	-15.572
C$_3$H$_4$Li$_2$	1.50	13.348	-12.690	0.658	5.379	-1.232	-1.215	-12.825
	1.53	13.290	-12.677	0.613	4.976	-1.227	-1.084	-12.042
C$_6$H$_6$-CrCO$_3$	1.41	28.150	-27.253	0.897	6.929	-1.670	-1.546	-15.809
Si$_2$C$_5$H$_2$	1.38	19.190	-18.274	0.916	7.520	-1.874	-1.689	-16.981
	1.42	19.612	-18.764	0.848	6.733	-1.613	-1.516	-15.417
	1.42	19.612	-18.764	0.848	6.732	-1.613	-1.516	-15.415
	1.46	21.248	-20.440	0.808	5.973	-1.446	-1.315	-13.948
	1.46	21.246	-20.439	0.807	5.964	-1.444	-1.313	-13.930
Ge$_2$C$_5$H$_2$	1.38	24.399	-23.502	0.896	7.441	-1.855	-1.668	-16.826
	1.42	25.794	-24.956	0.837	6.731	-1.624	-1.523	-15.417
	1.42	25.794	-24.956	0.837	6.731	-1.624	-1.523	-15.417
	1.46	29.716	-28.913	0.803	6.103	-1.475	-1.342	-14.185
	1.46	29.716	-28.913	0.802	6.102	-1.474	-1.341	-14.185
C$_6$Li$_6$	1.42	18.138	-17.402	0.736	6.764	-1.600	-1.584	-15.451
C$_2$B$_8$	1.50	18.849	-18.020	0.829	5.426	-1.248	-1.233	-12.719

4.4.1.2 Transition State Structures as Borderline Cases

A transition state (TS) in a chemical reaction is essentially a configuration attained by reactants during complex formation where a local maximum value of the potential energy is obtained. Michael addition,[63-66] cycloaddition[67-69] and rearrangement[70-72] (Claisen,[73] Cope,[74] Wittig[70, 75] *etc*.) reactions usually exhibit TS that involve significant

236
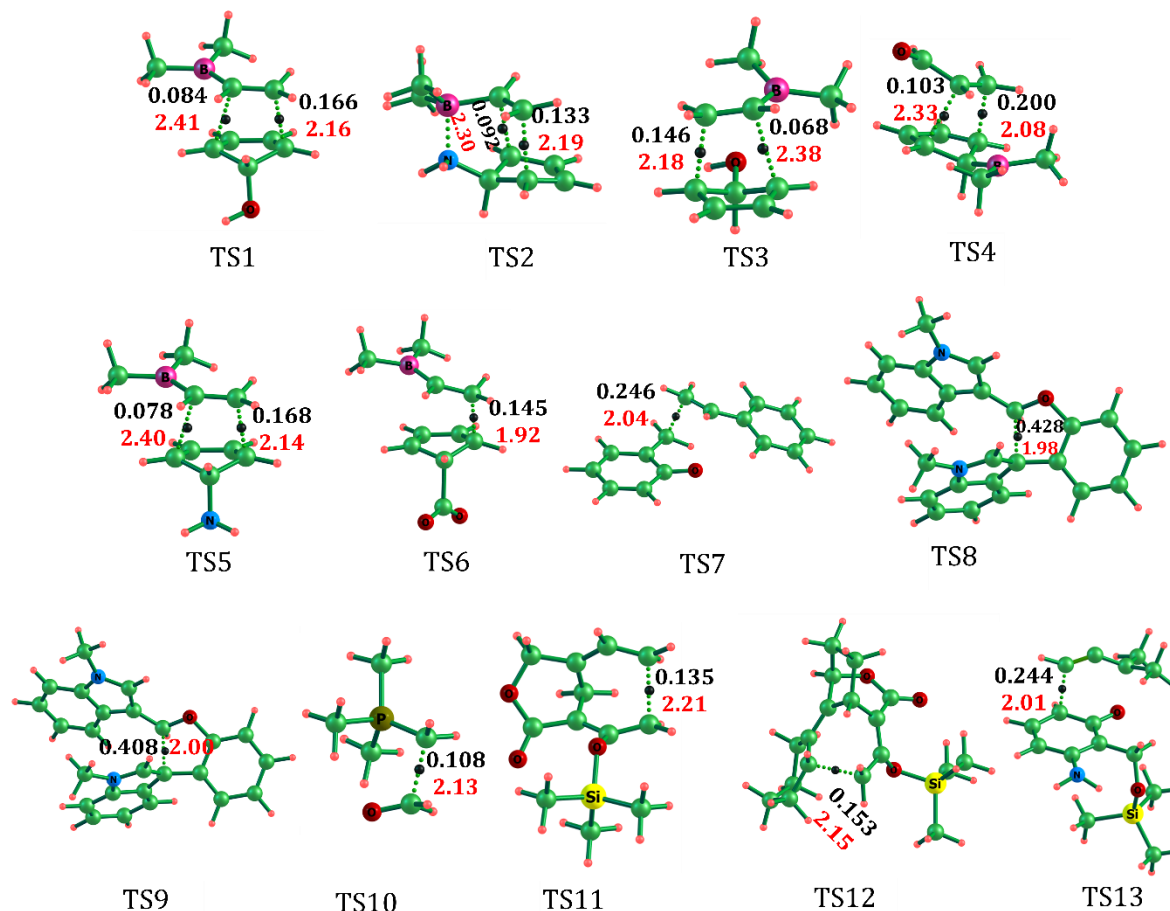
Figure 4.7 The MESP (3, -1) CP distribution at the longest/weak CC interaction in a transition state model from cycloaddition (TS1-TS7), ring closure (TS8-TS9), Wittig (TS10), Cope (TS11-TS12) and Claisen (TS13) rearrangement reactions. The MESP value at the CP (in au) and bond length (in Å) are represented in black and red fonts, respectively

interaction between carbon atoms of reactants. Cycloaddition is a pericyclic chemical reaction in which two or more independent π-systems combine with cyclic electron movement, culminating in the formation of a ring with a net decrease in bond multiplicity. The reaction facilitates the strongest carbon-carbon bond formation in a single step without using specific nucleophile or electrophile moieties. If the carbon skeleton of a molecule is rearranged to produce a structural isomer of the original molecule or a substituent frequently moves from one atom to another within the same molecule is termed as a rearrangement reaction. The majority of rearrangement processes involve the breaking and/or formation of C–C, C–O, or C–N bonds (Figure 4.7).

The addition of a nucleophile (or a carbanion) to an α, β-unsaturated carbonyl compound that contains a functional group which is electron-withdrawing in nature, is known as the Michael Addition. It belongs to a class of reactions that are extremely useful for facilitating the formation of new carbon-carbon bonds (Figure 4.8).
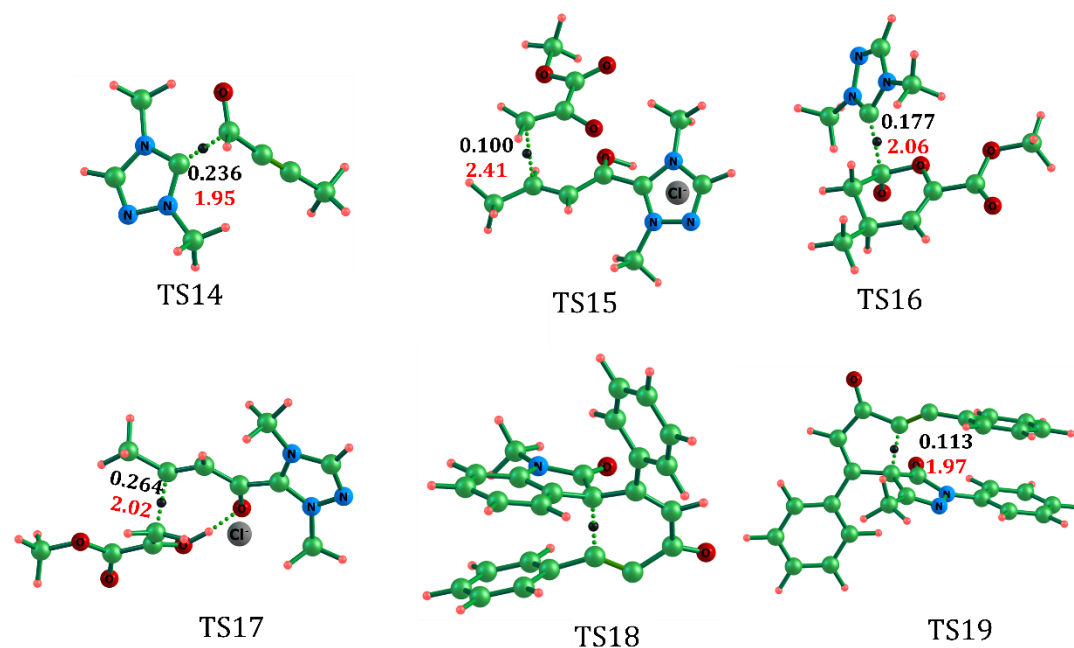
Figure 4.8 The MESP (3, -1) CP distribution at the longest/weak CC interaction in a transition state model from Michael addition reactions. The MESP value at the CP (in au) and bond length (in Å) are represented in black and red fonts, respectively

The highest d_{CC} in the chemical systems so far investigated in the present study is 1.82 Å, while longer CC bonds are seen in TS structures. The d_{CC} values observed in TS structures prompt the question of whether the CC interaction is covalent or non-covalent. Therefore, a detailed investigation is required for exploring the bond character and the trend in eigenvalues. A selected set of such TS structures involving formation, rearrangement, cleavage[76] or activation[77] of CC bonds from various organic reactions are considered for the study and the nature of CC interaction is quantified using MESP. The $V(\mathbf{r})$ value -0.099 to 0.428 au in TS structures indicates weak interactions between CC centers at a distance ranging between 2.45 to 1.92 Å. The d_{CC} and $V(\mathbf{r})$ data show that CC interactions observed in TS structures are regarded as borderline case. The detailed MESP topology of various TS corresponding to different reactions is given in Table 4.15.

Table 4.15 The CC bond distance (Å) and the MESP data V_{bnp}, V_ρ, $V(\mathbf{r})$ and eigenvalues (in au) of transition states at M06-2X/6-311G(d,p) level of theory

system	d_{CC}	V_{bnp}	V_ρ	$V(\mathbf{r})$	λ_{v1}	λ_{v2}	λ_{v3}	λ'_{v1}
TS1	2.16	20.036	-19.869	0.166	1.186	-0.222	-0.204	-2.882
	2.41	20.848	-20.764	0.084	0.641	-0.102	-0.064	-1.633
TS2	2.19	18.789	-18.657	0.133	1.096	-0.184	-0.173	-2.673
	2.30	20.191	-20.099	0.092	0.807	-0.130	-0.087	-2.085
TS3	2.18	20.237	-20.091	0.146	1.141	-0.207	-0.191	-2.773
	2.38	21.077	-21.009	0.068	0.707	-0.108	-0.085	-1.741
TS4	2.08	19.788	-19.588	0.200	1.408	-0.262	-0.244	-3.422
	2.33	19.330	-19.227	0.103	0.788	-0.122	-0.099	-1.934
TS5	2.14	18.414	-18.246	0.168	1.244	-0.231	-0.215	-3.020
	2.40	19.529	-19.451	0.078	0.657	-0.103	-0.071	-1.654
TS6	1.92	20.566	-20.420	0.145	2.021	-0.395	-0.384	-4.910
TS7	1.98	36.002	-35.573	0.428	1.782	-0.353	-0.307	-4.298
TS8	2.00	36.648	-36.239	0.408	1.678	-0.324	-0.269	-4.127
TS9	2.04	22.873	-22.627	0.246	1.534	-0.312	-0.310	-3.738
TS10	2.13	17.407	-17.299	0.108	1.312	-0.202	-0.180	-3.111
TS11	2.21	23.836	-23.701	0.135	1.051	-0.184	-0.158	-2.547
TS12	2.15	30.785	-30.632	0.153	1.214	-0.216	-0.185	-2.945
TS13	2.01	27.393	-27.149	0.244	1.662	-0.337	-0.314	-4.065
TS14	1.95	22.124	-21.888	0.236	1.928	-0.315	-0.292	-4.640
TS15	2.41	27.666	-27.566	0.101	0.683	-0.117	-0.101	-1.638
TS16	2.06	29.557	-29.380	0.177	1.496	-0.237	-0.209	-3.583
TS17	2.02	30.036	-29.772	0.264	1.647	-0.331	-0.304	-3.975
TS18	1.97	37.351	-37.238	0.113	1.831	-0.333	-0.314	-4.467
TS19	1.92	37.721	-37.564	0.157	1.998	-0.376	-0.334	-4.967
TS20	2.45	20.002	-20.101	-0.099	0.637	-0.080	-0.073	-1.504
TS21	2.21	20.840	-20.775	0.065	1.096	-0.144	-0.121	-2.554

4.4.1.3 Non-Covalent C···C Interactions
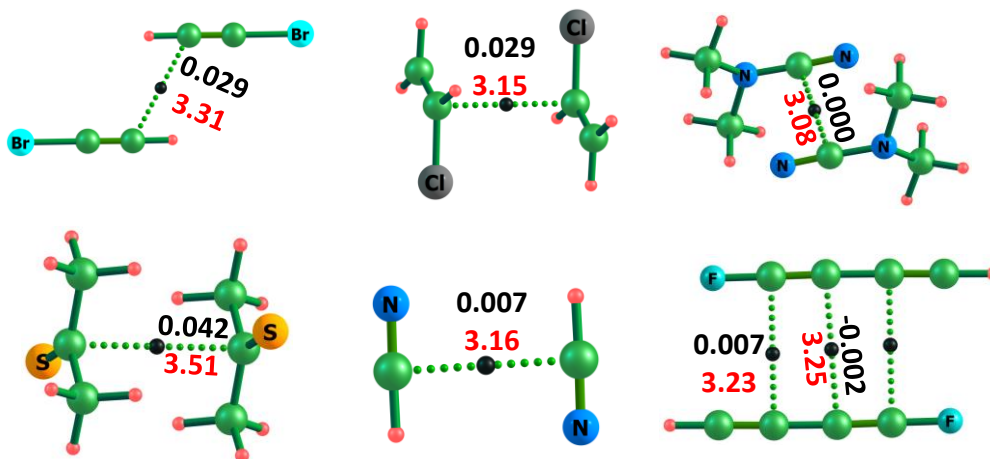
Figure 4.9 The MESP (3, -1) CP distribution corresponding to non-covalent C···C interaction in dimers. The MESP value at the CP (in au) and bond length (in Å) are represented in black and red fonts, respectively

Temporary fluctuations in electronic distribution occur within molecules when they come close to each other. These fluctuations give rise to attractive interactions known as van der Waals forces, which are generally weaker compared to ionic or covalent bonds. In this study, we focused on examining van der Waals C···C interactions in various dimeric molecules using the MESP topology. The C···C interactions were observed at distances ranging from 3.06 to 3.51 Å, as shown in Figure 4.9. The associated $V(\mathbf{r})$, varied between 0.842 to -0.028 au, as shown in table 4.16. Furthermore, we investigated the non-covalent C···C interactions within an encapsulated system by optimizing the endohedral complex $C_2@C_{60}$, where the C_2 unit possesses triplet character (Table 4.16). In this system, C_2 is stabilized by 24.8 kcal/mol and displays six BCPs. The C···C distances corresponding to these BCPs fall within the range 2.95 – 3.11 Å, and the corresponding $V(\mathbf{r})$ values are within the range 0.072 – 0.066 au.

Table 4.16 The CC bond distance (Å) and the MESP data V_{bnp}, V_ρ, $V(\mathbf{r})$ and eigenvalues (in au) of π-conjugated dimers at M06-2X/6-311G(d,p) level of theory (continues..)

system	d_{CC}	V_{bnp}	V_ρ	$V(\mathbf{r})$	λ_{v1}	λ_{v2}	λ_{v3}	λ'_{v1}
acetylene bromide dimer	1.20	23.498	-22.072	1.426	12.060	-3.520	-3.517	-25.492
	1.20	23.498	-22.072	1.426	12.060	-3.520	-3.517	-25.492
	3.31	16.206	-16.177	0.029	0.102	-0.023	-0.004	-0.212
acetonitrile dimer	1.46	14.949	-14.106	0.843	6.096	-1.404	-1.398	-14.157
	1.46	14.949	-14.106	0.842	6.096	-1.404	-1.398	-14.157
	3.25	11.858	-11.854	0.004	0.120	-0.015	-0.015	-0.244
acetylene dimer	3.30	7.449	-7.425	0.024	0.104	-0.024	-0.005	-0.213
vinylchloride dimer	3.15	15.711	-15.682	0.029	0.140	-0.030	-0.009	-0.306
diyne dimer	3.42	11.457	-11.466	-0.009	0.009	-0.004	-0.003	-0.165
	3.42	11.451	-11.459	-0.009	0.084	-0.013	-0.012	-0.164
	3.41	12.322	-12.350	-0.028	0.083	-0.008	-0.001	-0.169
diyneflouride dimer	3.23	15.217	-15.210	0.007	0.135	-0.024	-0.020	-0.254
	3.23	15.217	-15.210	0.007	0.135	-0.024	-0.020	-0.254
	3.27	15.625	-15.627	-0.002	0.109	-0.016	-0.009	-0.232
diynecyanide dimer	3.25	14.505	-14.474	0.031	0.122	-0.021	-0.020	-0.243
	3.25	14.505	-14.474	0.031	0.122	-0.021	-0.020	-0.243
	3.39	16.031	-16.003	0.028	0.094	-0.015	-0.013	-0.177
	3.36	15.720	-15.693	0.027	0.098	-0.015	-0.011	-0.190
	3.36	15.720	-15.693	0.027	0.098	-0.015	-0.011	-0.190
C$_{12}$ dimer	3.18	24.677	-24.642	0.034	0.133	-0.018	-0.014	-0.283
	3.18	24.677	-24.643	0.034	0.133	-0.018	-0.014	-0.283
	3.18	24.678	-24.644	0.034	0.133	-0.018	-0.014	-0.283
	3.18	24.678	-24.644	0.034	0.133	-0.018	-0.014	-0.283
	3.18	24.677	-24.643	0.034	0.133	-0.018	-0.014	-0.283
	3.18	24.676	-24.643	0.034	0.132	-0.018	-0.014	-0.282
	3.19	24.508	-24.476	0.032	0.124	-0.017	-0.014	-0.275

Table 4.16 The CC bond distance (Å) and the MESP data V_{bnp}, V_ρ, $V(\mathbf{r})$ and eigenvalues (in of π-conjugated dimers at M06-2X/6-311G(d,p) level of theory

system	d_{CC}	V_{bnp}	V_ρ	$V(\mathbf{r})$	λ_{v1}	λ_{v2}	λ_{v3}	λ'_{v1}
	3.19	24.509	-24.477	0.032	0.124	-0.017	-0.014	-0.274
	3.19	24.509	-24.477	0.032	0.124	-0.017	-0.014	-0.274
	3.19	24.509	-24.477	0.032	0.125	-0.017	-0.014	-0.275
	3.19	24.509	-24.477	0.032	0.124	-0.017	-0.014	-0.274
	3.19	24.511	-24.479	0.032	0.124	-0.017	-0.014	-0.274
diyne_CN_NMe2 dimer	3.23	21.075	-21.073	0.002	0.126	-0.022	-0.015	-0.252
	3.40	21.243	-21.260	-0.017	0.087	-0.009	-0.008	-0.171
dimethyl cynamide dimer	3.08	18.108	-18.108	0.000	0.169	-0.036	-0.017	-0.353
thioacetone dimer	3.51	18.449	-18.407	0.042	0.080	-0.015	-0.010	-0.134
vinylfluoride dimer	3.06	13.235	-13.195	0.040	0.180	-0.051	-0.030	-0.371
diyneCF3 dimer	3.40	20.805	-20.767	0.039	0.131	-0.037	-0.021	-0.173
	3.40	20.802	-20.763	0.038	0.131	-0.037	-0.021	-0.173
	3.39	21.577	-21.560	0.017	0.094	-0.016	-0.015	-0.175
	3.37	21.558	-21.542	0.015	0.101	-0.016	-0.007	-0.182
	3.37	21.557	-21.541	0.015	0.101	-0.016	-0.007	-0.182
C2@C60	2.95	57.258	-57.186	0.072	0.168	-0.009	-0.003	-0.481
	2.95	57.258	-57.186	0.071	0.167	-0.009	-0.003	-0.479
	3.10	57.127	-57.061	0.067	0.120	-0.012	-0.006	-0.338
	3.11	57.126	-57.059	0.066	0.119	-0.011	-0.006	-0.336
	3.10	57.122	-57.056	0.066	0.119	-0.010	-0.005	-0.342
	3.10	57.122	-57.056	0.066	0.119	-0.010	-0.005	-0.342

4.4.1.4 Analysis of MESP Topology Parameters

(a)

(b)
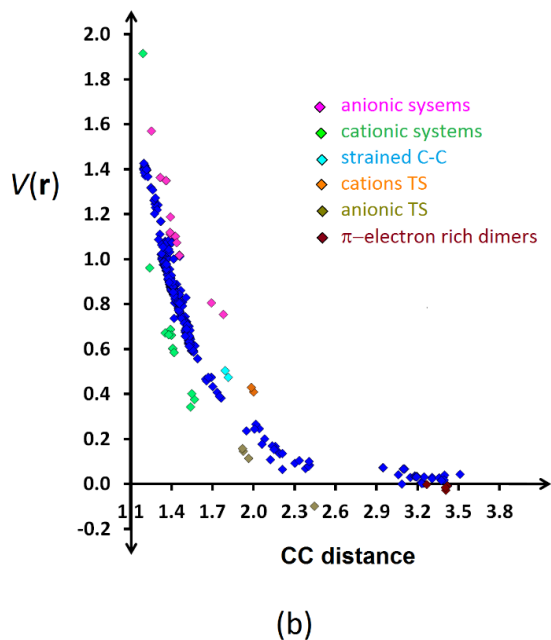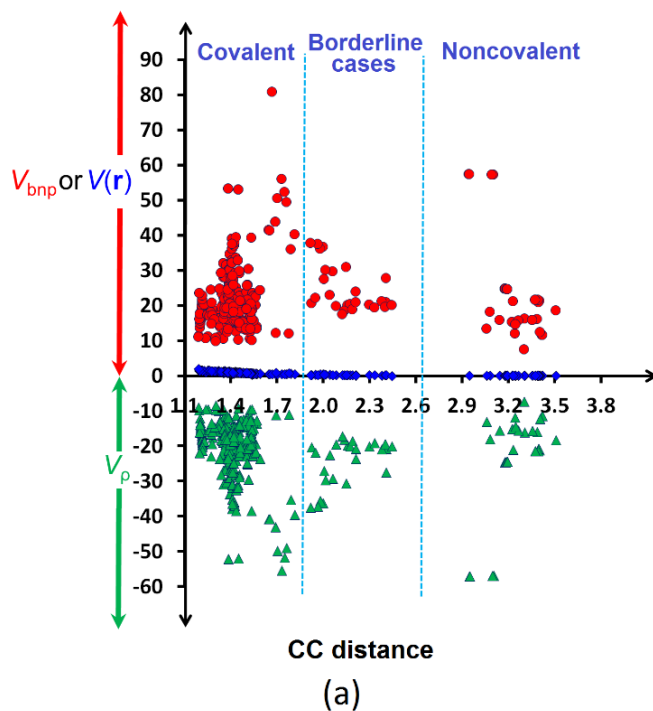
Figure 4.10 Distribution of nuclear (V_{bnp}), electronic (V_ρ) and total MESP ($V(\mathbf{r})$) at bond CP, with respect to CC bond distances (MESP data in au and bond lengths in Å). The red, blue and green marks indicate V_{bnp}, $V(\mathbf{r})$ and V_ρ, respectively

The data of $V(\mathbf{r})$, V_{bnp} and V_ρ at the BCP, plotted against the d_{CC} for all the CC interactions considered in the study is depicted in Figure 4.10a. Both V_{bnp} and V_ρ show a random distribution while $V(\mathbf{r})$ shows mostly a decreasing exponential trend with the d_{CC} as shown in Figure 4.10b. Thus, the relation between $V(\mathbf{r})$ and d_{CC} suggests a CC bond continuum, irrespective of the nature of the CC bond whether it is covalent, non-covalent or borderline. In Figure 4.10b, some points deviate from the general exponential trend which represent electron deficient systems such as cations and electron rich systems such as anions or π-systems with CC triple bonds. Negative $V(\mathbf{r})$ value is observed for highly electron rich systems such as diyne dimer. At the equilibrium CC bonding distance, the V_{bnp} balances with the V_ρ for the lowest $V(\mathbf{r})$. The eigenvalues λ_{v1}, λ_{v2} and λ_{v3} plotted against d_{CC} are shown in Figure 4.11. For all the systems, the magnitude of the positive eigenvalue λ_{v1} appears very large compared to the magnitude of both the negative eigenvalues, *viz.* λ_{v2} and λ_{v3}. Also values of λ_{v2} and λ_{v3} are very close to each other (Table 4.17). Hence, λ_{v1} is considered as the most sensitive eigenvalue parameter to define the CC bond character.

The plots in Figure 4.11 display the variations in the three eigenvalues with respect to the d_{CC}. An exponential function fits almost perfectly ($R^2 = 0.9917$) to define a correlation between the d_{CC} and λ_{v1}. The correlation predicts that CC bond interaction is a continuum, irrespective of the nature of the CC bond, whether it is covalent, non-covalent or borderline case. The CC bond continuum observed at the M06-2X/6-311G(d,p) level of theory gives the following fit.

$$\lambda_{v1} = 170.82\ e^{(-2.271 d_{CC})} \qquad \text{Eq. 4.4}$$

where d_{CC} is the CC bond distance in Å. Therefore,

$$d_{CC} = \frac{\ln(170.82/\lambda_{v1})}{2.271} \qquad \text{Eq. 4.5}$$

The prediction of d_{CC} using Eq. 4.5 is near perfect. The slope of Eq. 4.5, $\lambda'_{v1} = \frac{d(\lambda_{v1})}{d(d_{CC})}$ is in the range -25.88 to -0.13 au/Å for the d_{CC} range 1.20 to 3.51 Å. For d_{CC} around 3.0 Å, λ_{v1} value is close to zero while λ'_{v1} is less negative than -1.0 au/Å. Here, we propose d_{CC}

in the range 2.95 to 3.51 Å in non-covalent category wherein λ'_{v1} is less negative than -1.0 au/Å. In all TSs, the d_{CC} corresponding to bond formation shows λ'_{v1} in the range -1.52 to -4.97 au/Å. As a generalization, we propose λ'_{v1} in the range -1.0 to -5.0 au/Å as borderline cases between non-covalent and covalent interactions and this corresponds to d_{CC} in the range 1.92 to 2.63 Å. All d_{CC} corresponding to λ'_{v1} more negative than -5.0 au/Å are selected in the covalent category. For instance, the longest covalent CC bond in the data set is 1.82 Å having λ'_{v1} = -6.26 au/Å, while the shortest one is 1.20 Å having λ'_{v1} = -25.88 au/Å. Figure 4.11 also depicts the covalent, non-covalent and borderline cases.
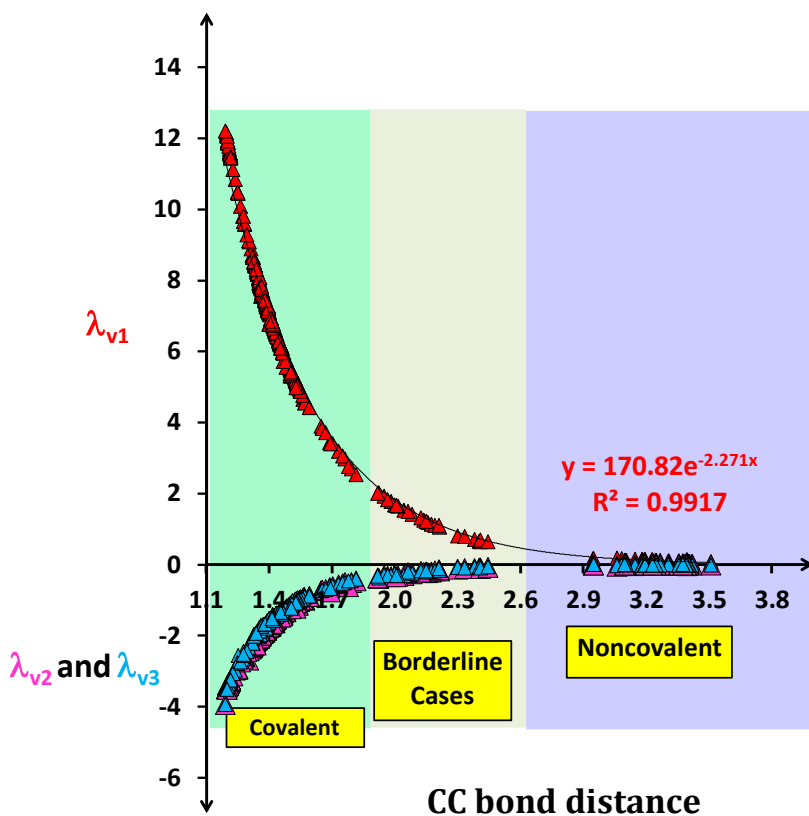
Figure 4.11 The exponential variation of λ_{v1}, λ_{v2} and λ_{v3} (in au) with CC bond distances (Å)

A benchmark analysis is also performed with the DFT techniques M06-L, wB97XD and B3LYP for a large variety of representative systems to assess the reliability of the M06-2X approach. Figure 4.12 depicts the correlation between the largest positive

eigenvalue and the CC bond distance. In all cases, a near perfect exponential relationship is obtained. The correlation at M06-L is nearly identical to M06-2X level in terms of the coefficient and exponent in the equation. Compared to these two levels, wB97XD level results show slightly smaller magnitude for both coefficient and exponent. The correlation at B3LYP level is notable for the significantly smaller magnitude of coefficient. The results from the first three methods are considered as superior considering the in-built dispersion effect in such methods.
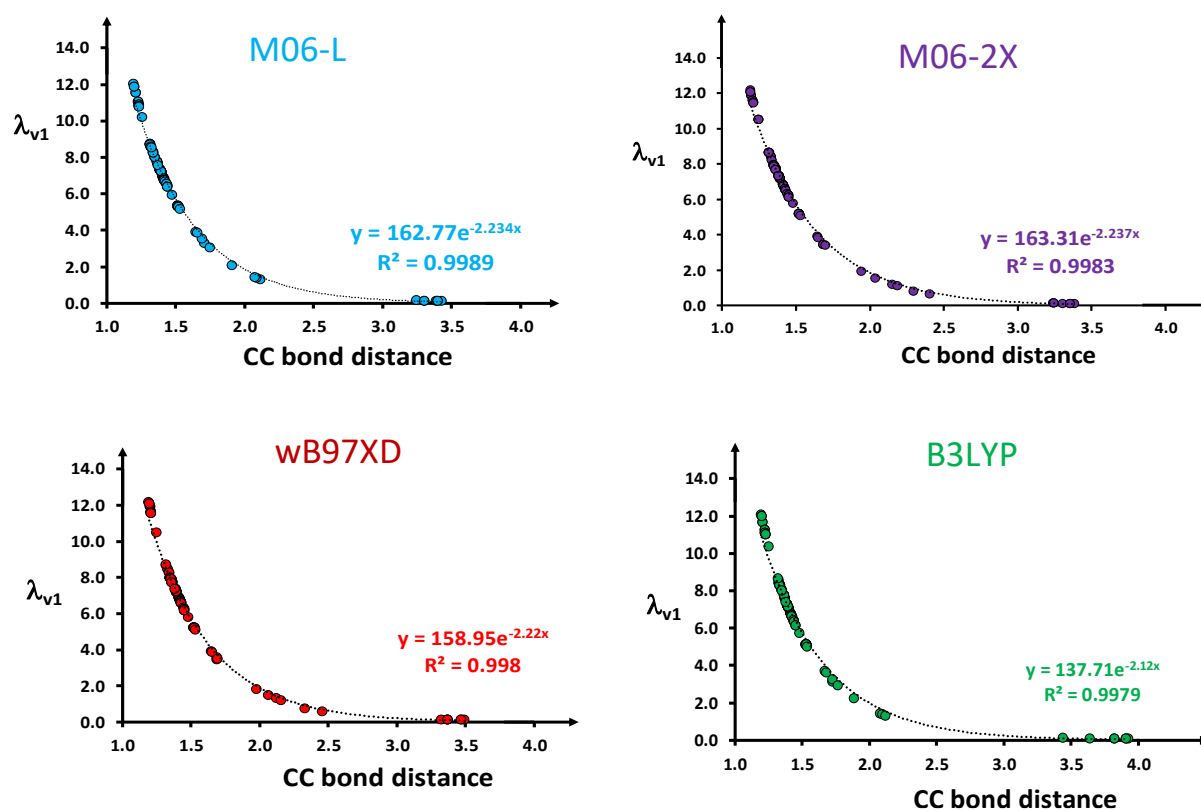
Figure 4.12 The exponential variation of λ_{v1} (in au) with CC bond distances (Å) using different levels of theory

4.4.2 QTAIM Analysis

The concept of "Atoms in Molecules" (AIM) has evolved as a consequence of the fact that molecules may be partitioned into atoms whose energies can be precisely computed using quantum mechanics.[78] The quantum theory of AIM (QTAIM) has developed over the past few decades into a tool to connect the *ab initio* wave functions with chemical understanding.[79] The key parameters used in QTAIM theory are the MED, $\rho(\mathbf{r})$ at the BCP and the Laplacian of $\rho(\mathbf{r})$, *viz.* $\nabla^2\rho(\mathbf{r})$, at that point. The $\nabla^2\rho(\mathbf{r})$ distinguishes between two major categories of bonds.[47] If $\nabla^2\rho(\mathbf{r}) > 0$, the bond is referred to as a closed-shell interaction, which includes ionic bonds, hydrogen bonds, van der Waals interactions, *etc*. If $\nabla^2\rho(\mathbf{r}) < 0$, the bond is a shared interaction, such as covalent and polar bonds. The $\nabla^2\rho(\mathbf{r})$ can be negative only if the first two eigenvalues $\lambda_{\rho 1}$ and $\lambda_{\rho 2}$ dominate over third

Figure 4.13 The MED (3, -1) CP distribution in selected set of systems. The $\rho(\mathbf{r})$ value at the BCP and $\nabla^2\rho$ (in au) are represented in black and blue fonts, respectively

eigenvalue $\lambda_{\rho 3}$, indicating that ρ is concentrated toward the BCP. If $\lambda_{\rho 3}$ dominates over $\lambda_{\rho 1}$ and $\lambda_{\rho 2}$, the $\nabla^2\rho = \lambda_{\rho 1} + \lambda_{\rho 2} + \lambda_{\rho 3}$ (or $\lambda_{\rho total}$) becomes positive, where $\rho(\mathbf{r})$ increases rapidly away from the BCP.[46, 80] To validate the non-covalent interactions among atoms in molecules, Popelier's $\nabla^2\rho$ theory has been utilized in several studies.[46, 80-85] A QTAIM study focusing only on a particular bonding interaction, including both covalent and non-covalent interactions of a large variety of systems is yet to be reported. Here, we conduct such a study on CC bonding interactions based on Popelier's $\nabla^2\rho$ theory.

Further, QTAIM analysis is carried out to reveal the covalent to non-covalent CC bond continuum in terms of the electron density. The covalent CC bonds from wide variety of molecular systems such as alkanes, strained systems, alkenes, alkynes, carbon clusters, heterocyclic systems, PBHs *etc.* show $\rho(\mathbf{r})$ values ranging from 0.133 to 0.410 au with corresponding $\nabla^2\rho$ ranges between -1.228 and -0.009 au (Table 4.17 to Table 4.31). The $\rho(\mathbf{r})$ value for non-covalent CC bonds ranges from 0.004 to 0.009 au, while their $\nabla^2\rho$ is between 0.032 and 0.013 au. The $\rho(\mathbf{r})$ at the weakest CC bond of TS structures from diverse organic reactions is seen to lie between 0.0271 to 0.1023 au with $\nabla^2\rho$ between -0.025 to 0.054 au. A representative set of examples is shown in Figure 4.13. Figure 4.14a depicts the plot of $\rho(\mathbf{r})$ against the d_{CC} of all the molecules. Irrespective of the nature of the CC interactions, the $\rho(\mathbf{r})$ shows an exponential decay with increase in d_{CC}. This data again confirms the CC bond continuum in chemistry. The variation of $\lambda_{\rho i}$ at BCP with d_{CC} shows that the negative eigenvalues, $\lambda_{\rho 1}$ and $\lambda_{\rho 2}$ show very similar values for all the systems (Figure 4.14b). In the case of the positive eigenvalue $\lambda_{\rho 3}$, from very short CC to the typical CC single bond distance, the value rises sharply and thereafter, decreases exponentially. The shape of d_{CC} versus $\lambda_{\rho 3}$ curve suggests that the $\lambda_{\rho 3}$ can attain same value for a short as well as long CC distance. For instance, in tetraacetylene, $\lambda_{\rho 3}$ correspond to a C≡C with distance 1.21 Å is 0.113 au whereas the TS structure with d_{CC} 2.41 Å also shows a similar value for $\lambda_{\rho 3}$, 0.116 au. Hence, it is difficult to differentiate the nature of CC bond based only on the eigenvalues.
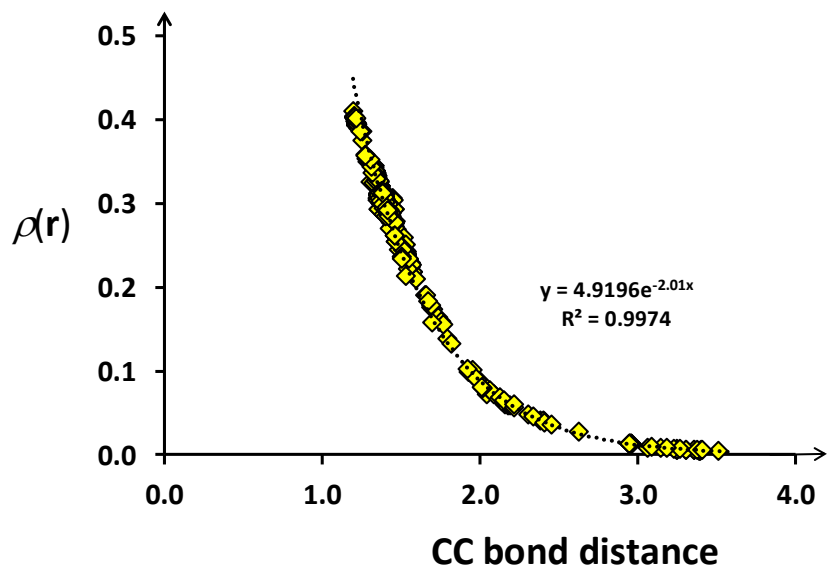
(a)
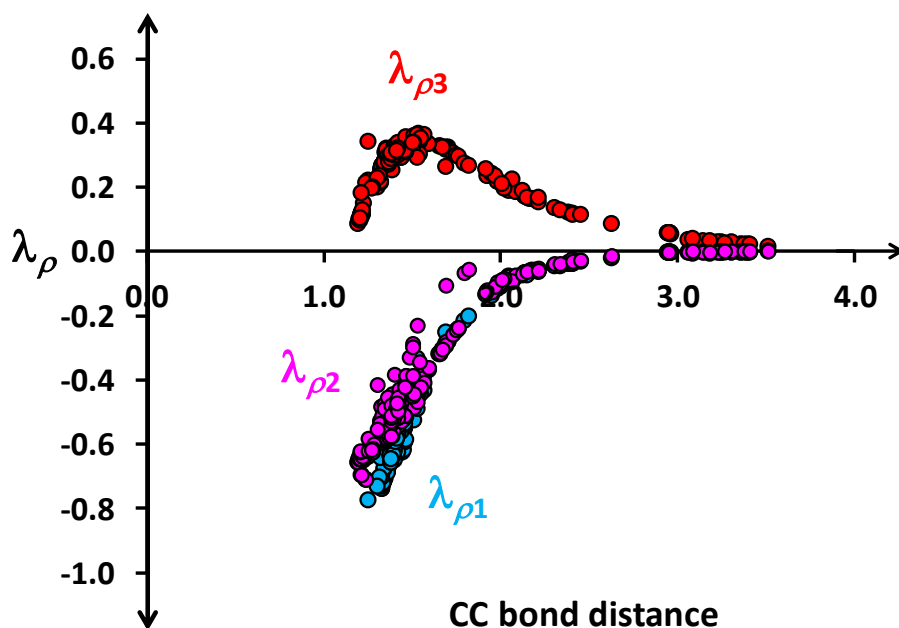
(b)

Figure 4.14 (a) Relationship between electron density, $\rho(\mathbf{r})$ (au) and CC bond distances (Å). (b) Variation of eigenvalues (in au) with CC bond distances (Å)
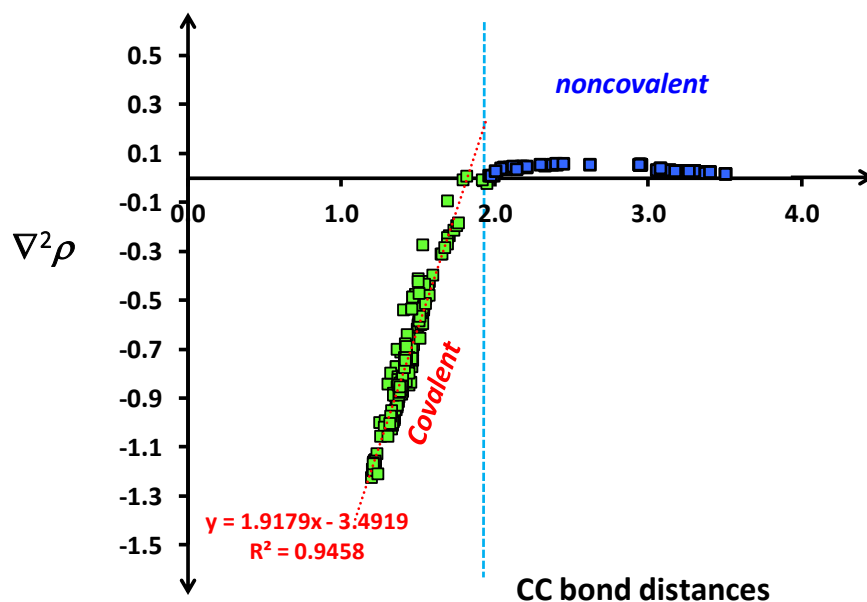
Figure 4.15 Correlation between $\nabla^2\rho$ value (in au) at the BCP and the CC bond distance (Å)

Figure 4.15 illustrates the Popelier's $\nabla^2\rho$ theory. Here $\nabla^2\rho$ is plotted against d_{CC} and as per Popelier's criterion, the negative $\nabla^2\rho$ values correspond to a covalent bond and the remaining ones indicate non-covalent bonds. As shown in Figure 4.15, all the negative $\nabla^2\rho$ can be fitted on a straight line with $R^2 = 0.9458$. This suggests that the highest negative $\nabla^2\rho$ corresponds to the shortest CC bond, while a negative value close to zero points to one of the weakest covalent CC bonds. Here, d_{CC} value 1.94 Å observed in a TS is regarded as the weakest covalent CC bond on the basis of the lowest negative $\nabla^2\rho$ value, -0.013. Majority of the d_{CC} in TSs showed positive $\nabla^2\rho$ very close to zero. Though the magnitude of the three eigenvalues are significantly greater than zero for all the TSs, the close to 'zero' behaviour of $\nabla^2\rho$ is observed for them due to $\lambda_{\rho3} \cong - (\lambda_{\rho1} + \lambda_{\rho2})$. In the case of systems showing d_{CC} around 3.0 Å or higher, the $\nabla^2\rho$ is positive and close to zero because all the three eigenvalues are close to zero. Such cases clearly fall under the category of non-covalent CC interactions. It may be noted that the borderline cases of TS cannot be clearly distinguished from the non-covalent cases using only the $\nabla^2\rho$ criterion. For borderline cases, $\nabla^2\rho$ is close to zero with the condition that the magnitude of all the three eigenvalues are significantly higher than zero.

Table 4.17 The CC bond distance (Å) and the AIM data $\rho(\mathbf{r})$ and eigenvalues (in au) of alkanes at M06-2X/6-311G(d,p) level of theory

system	d_{cc}	$\rho(\mathbf{r})$	$\lambda_{\rho 1}$	$\lambda_{\rho 2}$	$\lambda_{\rho 3}$	$\nabla^2\rho$
ethane	1.53	0.238	-0.433	-0.433	0.336	-0.530
propane	1.53	0.240	-0.441	-0.437	0.340	-0.537
	1.53	0.240	-0.441	-0.437	0.340	-0.537
butane	1.53	0.242	-0.447	-0.440	0.344	-0.543
	1.53	0.240	-0.440	-0.437	0.339	-0.538
	1.53	0.240	-0.440	-0.437	0.339	-0.537
decane	1.53	0.241	-0.445	-0.440	0.343	-0.542
	1.53	0.241	-0.446	-0.440	0.343	-0.542
	1.53	0.241	-0.446	-0.440	0.344	-0.542
	1.53	0.241	-0.445	-0.440	0.343	-0.542
	1.53	0.241	-0.445	-0.440	0.343	-0.542
	1.53	0.241	-0.446	-0.440	0.343	-0.542
	1.53	0.241	-0.446	-0.440	0.344	-0.542
	1.53	0.240	-0.439	-0.437	0.339	-0.537
	1.53	0.240	-0.439	-0.437	0.339	-0.537

Table 4.18 The CC bond distance (Å) and the AIM data $\rho(\mathbf{r})$ and eigenvalues (in au) of cycloalkanes at M06-2X/6-311G(d,p) level of theory

system	d_{cc}	$\rho(\mathbf{r})$	$\lambda_{\rho 1}$	$\lambda_{\rho 2}$	$\lambda_{\rho 3}$	$\nabla^2\rho$
cyclopropane	1.50	0.236	-0.440	-0.288	0.314	-0.413
cyclobutane	1.55	0.233	-0.420	-0.417	0.344	-0.493
cyclohexane	1.53	0.240	-0.439	-0.437	0.343	-0.533
adamentane	1.54	0.238	-0.433	-0.433	0.344	-0.523
cubane	1.56	0.229	-0.410	-0.409	0.349	-0.470

Table 4.19 The CC bond distance (Å) and the AIM data $\rho(\mathbf{r})$ and eigenvalues (in au) of sterically crowded systems

system	d_{cc}	$\rho(\mathbf{r})$	$\lambda_{\rho 1}$	$\lambda_{\rho 2}$	$\lambda_{\rho 3}$	$\nabla^2\rho$
Pbtth	1.69	0.176	-0.288	-0.280	0.324	-0.244
Ptho	1.69	0.179	-0.294	-0.292	0.316	-0.270
Bptd	1.65	0.191	-0.320	-0.318	0.327	-0.312
Ahod	1.66	0.191	-0.320	-0.318	0.327	-0.312
Dddcpa	1.70	0.173	-0.280	-0.280	0.322	-0.238
Ttca	1.73	0.164	-0.261	-0.259	0.306	-0.214
Dddcada	1.76	0.156	-0.243	-0.240	0.297	-0.186
Hdbec	1.67	0.184	-0.305	-0.305	0.323	-0.287
Tdtca	1.75	0.159	-0.248	-0.247	0.299	-0.196
1,2-diamino-o-carborane-1	1.79	0.138	-0.215	-0.067	0.273	-0.009
1,2-diamino-o-carborane-2	1.82	0.133	-0.204	-0.056	0.267	-0.007

Table 4.20 The CC bond distance (Å) and the AIM data $\rho(\mathbf{r})$ and eigenvalues (in au) of alkenes at M06-2X/6-311G(d,p) level of theory

system	d_{cc}	$\rho(\mathbf{r})$	$\lambda_{\rho 1}$	$\lambda_{\rho 2}$	$\lambda_{\rho 3}$	$\nabla^2\rho$
ethene	1.32	0.344	-0.734	-0.550	0.256	-1.028
butadiene	1.33	0.341	-0.727	-0.549	0.264	-1.011
	1.46	0.272	-0.541	-0.501	0.335	-0.707
hexatriene	1.33	0.339	-0.723	-0.548	0.266	-1.005
	1.34	0.336	-0.716	-0.548	0.274	-0.990
	1.45	0.275	-0.547	-0.503	0.333	-0.717
octatetraene	1.33	0.339	-0.722	-0.547	0.266	-1.003
	1.34	0.335	-0.712	-0.547	0.276	-0.984
	1.45	0.278	-0.555	-0.505	0.331	-0.730
	1.45	0.276	-0.549	-0.504	0.333	-0.720
decapentaene	1.33	0.339	-0.722	-0.547	0.266	-1.003
	1.34	0.335	-0.711	-0.547	0.276	-0.981
	1.35	0.333	-0.708	-0.546	0.278	-0.976
	1.45	0.279	-0.558	-0.506	0.330	-0.734
	1.45	0.276	-0.550	-0.504	0.333	-0.721

Table 4.21 The CC bond distance (Å) and the AIM data $\rho(\mathbf{r})$ and eigenvalues (in au) of polycyclic benzenoid hydrocarbons at M06-2X/6-311G(d,p) level of theory

system	d_{cc}	$\rho(\mathbf{r})$	$\lambda_{\rho 1}$	$\lambda_{\rho 2}$	$\lambda_{\rho 3}$	$\nabla^2 \rho$
benzene	1.39	0.308	-0.635	-0.531	0.308	-0.858
naphthalene	1.37	0.320	-0.669	-0.540	0.295	-0.915
	1.37	0.320	-0.669	-0.540	0.295	-0.915
	1.37	0.320	-0.669	-0.540	0.295	-0.915
	1.37	0.320	-0.669	-0.540	0.295	-0.915
	1.42	0.295	-0.598	-0.518	0.320	-0.796
	1.42	0.295	-0.598	-0.518	0.320	-0.796
	1.42	0.294	-0.596	-0.519	0.324	-0.792
	1.42	0.294	-0.596	-0.519	0.324	-0.792
	1.42	0.294	-0.595	-0.516	0.328	-0.783
	1.42	0.294	-0.596	-0.519	0.324	-0.792
	1.42	0.294	-0.596	-0.519	0.324	-0.792
anthracene	1.36	0.325	-0.682	-0.543	0.289	-0.936
	1.39	0.307	-0.631	-0.530	0.312	-0.849
	1.43	0.288	-0.581	-0.511	0.324	-0.768
	1.43	0.288	-0.581	-0.513	0.328	-0.766
	1.43	0.287	-0.576	-0.508	0.332	-0.752
biphenyl	1.39	0.309	-0.636	-0.531	0.307	-0.860
	1.39	0.308	-0.635	-0.532	0.308	-0.858
	1.40	0.304	-0.624	-0.522	0.314	-0.832
	1.48	0.262	-0.513	-0.482	0.343	-0.653
biphenylene	1.37	0.318	-0.659	-0.538	0.292	-0.904
	1.38	0.311	-0.643	-0.524	0.303	-0.864
	1.42	0.293	-0.593	-0.507	0.320	-0.780
	1.42	0.304	-0.633	-0.538	0.336	-0.835
	1.51	0.243	-0.447	-0.433	0.349	-0.530

Table 4.22 The CC bond distance (Å) and the AIM data $\rho(\mathbf{r})$ and eigenvalues (in au) of annulenes at M06-2X/6-311G(d,p) level of theory

system	d_{cc}	$\rho(\mathbf{r})$	$\lambda_{\rho 1}$	$\lambda_{\rho 2}$	$\lambda_{\rho 3}$	$\nabla^2\rho$
14-annulene	1.35	0.306	-0.627	-0.527	0.308	-0.846
	1.35	0.304	-0.619	-0.525	0.309	-0.835
	1.35	0.293	-0.594	-0.499	0.321	-0.772
	1.36	0.293	-0.594	-0.498	0.318	-0.774
	1.44	0.306	-0.627	-0.527	0.308	-0.846
	1.45	0.304	-0.619	-0.525	0.309	-0.835
	1.46	0.293	-0.594	-0.498	0.318	-0.774
	1.46	0.293	-0.594	-0.499	0.321	-0.772
16-annulene	1.34	0.333	-0.706	-0.540	0.276	-0.971
	1.34	0.332	-0.703	-0.535	0.277	-0.961
	1.45	0.275	-0.545	-0.499	0.332	-0.712
	1.46	0.271	-0.534	-0.494	0.334	-0.695

Table 4.23 The CC bond distance (Å) and the AIM data $\rho(\mathbf{r})$ and eigenvalues (in au) of carbon clusters at M06-2X/6-311G(d,p) level of theory

system	d_{cc}	$\rho(\mathbf{r})$	$\lambda_{\rho 1}$	$\lambda_{\rho 2}$	$\lambda_{\rho 3}$	$\nabla^2\rho$
ovalene	1.40	0.306	-0.630	-0.529	0.312	-0.846
	1.43	0.290	-0.586	-0.514	0.328	-0.772
	1.44	0.285	-0.573	-0.510	0.329	-0.754
	1.41	0.299	-0.610	-0.524	0.321	-0.812
	1.42	0.292	-0.592	-0.516	0.327	-0.781
	1.44	0.285	-0.572	-0.509	0.329	-0.752
	1.42	0.293	-0.593	-0.517	0.326	-0.784
	1.44	0.286	-0.574	-0.510	0.331	-0.753
	1.41	0.299	-0.609	-0.523	0.322	-0.811
	1.41	0.298	-0.608	-0.522	0.320	-0.810
	1.37	0.317	-0.659	-0.537	0.298	-0.897
	1.36	0.328	-0.691	-0.543	0.285	-0.949
C_{60}	1.45	0.276	-0.543	-0.478	0.336	-0.686
	1.39	0.309	-0.631	-0.518	0.305	-0.844

Table 4.24 The CC bond distance (Å) and the AIM data $\rho(\mathbf{r})$ and eigenvalues (in au) of alkynes at M06-2X/6-311G(d,p) level of theory (continues....)

system	d_{cc}	$\rho(\mathbf{r})$	$\lambda_{\rho1}$	$\lambda_{\rho2}$	$\lambda_{\rho3}$	$\nabla^2\rho$
acetylene	1.20	0.410	-0.657	-0.657	0.085	-1.228
diacetylene	1.20	0.404	-0.646	-0.646	0.099	-1.193
	1.38	0.299	-0.570	-0.570	0.293	-0.848
triacetylene	1.20	0.403	-0.647	-0.647	0.102	-1.193
	1.21	0.398	-0.636	-0.636	0.108	-1.163
	1.37	0.303	-0.575	-0.575	0.288	-0.863
tetracetylene	1.20	0.403	-0.648	-0.648	0.103	-1.193
	1.21	0.396	-0.637	-0.637	0.113	-1.161
	1.36	0.308	-0.581	-0.581	0.284	-0.877
	1.37	0.304	-0.577	-0.577	0.287	-0.867
pentaacetylene	1.36	0.309	-0.583	-0.583	0.282	-0.883
	1.21	0.396	-0.637	-0.637	0.114	-1.161
	1.20	0.403	-0.649	-0.649	0.103	-1.194
	1.37	0.305	-0.578	-0.578	0.287	-0.869
	1.21	0.395	-0.638	-0.638	0.117	-1.159
	1.36	0.309	-0.583	-0.583	0.282	-0.883
	1.21	0.396	-0.637	-0.637	0.114	-1.161
	1.37	0.305	-0.578	-0.578	0.287	-0.869
	1.20	0.403	-0.649	-0.649	0.103	-1.194
hexaacetylene	1.22	0.394	-0.638	-0.638	0.119	-1.158
	1.36	0.310	-0.583	-0.583	0.282	-0.885
	1.21	0.396	-0.638	-0.638	0.115	-1.161
	1.36	0.311	-0.585	-0.585	0.281	-0.889
	1.37	0.305	-0.578	-0.578	0.287	-0.870
	1.20	0.403	-0.649	-0.649	0.103	-1.194
	1.22	0.394	-0.638	-0.638	0.119	-1.158
	1.36	0.310	-0.583	-0.583	0.282	-0.885
	1.21	0.396	-0.638	-0.638	0.115	-1.161
	1.37	0.305	-0.578	-0.578	0.287	-0.870
	1.20	0.403	-0.649	-0.649	0.103	-1.194
heptaacetylene	1.22	0.394	-0.639	-0.639	0.121	-1.157
	1.35	0.311	-0.586	-0.586	0.280	-0.891
	1.22	0.394	-0.639	-0.639	0.120	-1.157
	1.36	0.310	-0.584	-0.584	0.282	-0.886
	1.35	0.311	-0.586	-0.586	0.280	-0.891
	1.22	0.394	-0.639	-0.639	0.120	-1.157

Table 4.24 The CC bond distance (Å) and the AIM data $\rho(\mathbf{r})$ and eigenvalues (in au) of alkynes at M06-2X/6-311G(d,p) level of theory

system	d_{cc}	$\rho(\mathbf{r})$	$\lambda_{\rho 1}$	$\lambda_{\rho 2}$	$\lambda_{\rho 3}$	$\nabla^2 \rho$
	1.36	0.310	-0.584	-0.584	0.282	-0.886
	1.21	0.396	-0.638	-0.638	0.115	-1.161
	1.37	0.305	-0.578	-0.578	0.287	-0.870
	1.20	0.403	-0.649	-0.649	0.103	-1.195
	1.21	0.396	-0.638	-0.638	0.115	-1.161
	1.37	0.305	-0.578	-0.578	0.287	-0.870
	1.20	0.403	-0.649	-0.649	0.103	-1.195
octaacetylene	1.22	0.394	-0.639	-0.639	0.122	-1.157
	1.35	0.312	-0.586	-0.586	0.280	-0.892
	1.22	0.394	-0.639	-0.639	0.120	-1.158
	1.35	0.312	-0.587	-0.587	0.279	-0.894
	1.36	0.310	-0.584	-0.584	0.281	-0.887
	1.22	0.396	-0.638	-0.638	0.115	-1.161
	1.22	0.394	-0.639	-0.639	0.122	-1.157
	1.35	0.312	-0.586	-0.586	0.280	-0.892
	1.22	0.394	-0.639	-0.639	0.120	-1.158
	1.36	0.310	-0.584	-0.584	0.281	-0.887
	1.22	0.396	-0.638	-0.638	0.115	-1.161
	1.37	0.305	-0.579	-0.579	0.287	-0.871
	1.20	0.403	-0.649	-0.649	0.103	-1.195
	1.37	0.305	-0.579	-0.579	0.287	-0.871
	1.20	0.403	-0.649	-0.649	0.103	-1.195
nonaacetylene	1.22	0.393	-0.639	-0.639	0.122	-1.156
	1.35	0.312	-0.587	-0.587	0.279	-0.895
	1.22	0.393	-0.639	-0.639	0.122	-1.157
	1.35	0.312	-0.586	-0.586	0.280	-0.893
	1.35	0.312	-0.587	-0.587	0.279	-0.895
	1.22	0.393	-0.639	-0.639	0.122	-1.157
	1.35	0.312	-0.586	-0.586	0.280	-0.893
	1.22	0.394	-0.639	-0.639	0.120	-1.158
	1.36	0.310	-0.584	-0.584	0.281	-0.887
	1.21	0.396	-0.638	-0.638	0.115	-1.161
	1.37	0.305	-0.579	-0.579	0.287	-0.871
	1.20	0.403	-0.649	-0.649	0.103	-1.195
	1.22	0.394	-0.639	-0.639	0.120	-1.158
	1.36	0.310	-0.584	-0.584	0.281	-0.887
	1.21	0.396	-0.638	-0.638	0.115	-1.161
	1.37	0.305	-0.579	-0.579	0.287	-0.871
	1.20	0.403	-0.649	-0.649	0.103	-1.195

Table 4.25 The CC bond distance (Å) and the AIM data $\rho(\mathbf{r})$ and eigenvalues (in au) of carbon rings at M06-2X/6-311G(d,p) level of theory

system	d_{cc}	$\rho(\mathbf{r})$	$\lambda_{\rho 1}$	$\lambda_{\rho 2}$	$\lambda_{\rho 3}$	$\nabla^2 \rho$
C_2	1.30	0.325	-0.629	-0.415	0.198	-0.846
C_6	1.32	0.325	-0.531	-0.483	0.213	-0.801
C_8	1.25	0.375	-0.640	-0.582	0.221	-1.001
	1.39	0.287	-0.521	-0.443	0.251	-0.713
C_{10}	1.28	0.350	-0.605	-0.601	0.211	-0.995
C_{12}	1.23	0.389	-0.651	-0.627	0.149	-1.129
	1.37	0.300	-0.556	-0.530	0.272	-0.814
C_{14}	1.28	0.353	-0.618	-0.614	0.212	-1.020
C_{16}	1.37	0.301	-0.558	-0.554	0.285	-0.827
	1.22	0.396	-0.651	-0.641	0.126	-1.166
C_{20}	1.36	0.306	-0.570	-0.567	0.283	-0.855
	1.22	0.394	-0.645	-0.640	0.127	-1.158

Table 4.26 The CC bond distance (Å) and the AIM data $\rho(\mathbf{r})$ and eigenvalues (in au) of heterocyclic systems at M06-2X/6-311G(d,p) level of theory (continues..)

system	d_{cc}	$\rho(\mathbf{r})$	$\lambda_{\rho 1}$	$\lambda_{\rho 2}$	$\lambda_{\rho 3}$	$\nabla^2 \rho$
DBN	1.53	0.243	-0.454	-0.445	0.345	-0.554
	1.53	0.242	-0.448	-0.442	0.349	-0.541
	1.53	0.240	-0.447	-0.439	0.347	-0.539
	1.53	0.237	-0.432	-0.429	0.341	-0.520
	1.52	0.252	-0.489	-0.465	0.353	-0.601
porphyrin	1.43	0.289	-0.586	-0.505	0.331	-0.760
	1.39	0.307	-0.642	-0.535	0.314	-0.863
	1.39	0.309	-0.642	-0.532	0.305	-0.870
	1.46	0.276	-0.550	-0.488	0.346	-0.693
	1.39	0.307	-0.642	-0.535	0.314	-0.863
	1.46	0.276	-0.550	-0.488	0.346	-0.693
	1.39	0.309	-0.642	-0.532	0.305	-0.870
	1.35	0.331	-0.690	-0.538	0.281	-0.948
	1.36	0.321	-0.664	-0.525	0.292	-0.898

Table 4.26 The CC bond distance (Å) and the AIM data $\rho(\mathbf{r})$ and eigenvalues (in au) heterocyclic systems at M06-2X/6-311G(d,p) level of theory

system	d_{cc}	$\rho(\mathbf{r})$	$\lambda_{\rho 1}$	$\lambda_{\rho 2}$	$\lambda_{\rho 3}$	$\nabla^2\rho$
aziridine	1.48	0.245	-0.463	-0.331	0.318	-0.476
cynogen	1.39	0.294	-0.575	-0.575	0.298	-0.851
pyramidopyramidine	1.40	0.311	-0.649	-0.550	0.327	-0.873
	1.42	0.299	-0.627	-0.545	0.338	-0.834
benzonitrile	1.44	0.273	-0.528	-0.499	0.293	-0.734
	1.40	0.304	-0.628	-0.521	0.312	-0.837
	1.39	0.310	-0.640	-0.535	0.306	-0.868
	1.39	0.308	-0.634	-0.534	0.309	-0.860
furfural	1.42	0.286	-0.562	-0.483	0.321	-0.725
	1.36	0.326	-0.688	-0.532	0.290	-0.930
	1.36	0.327	-0.690	-0.524	0.285	-0.930
	1.46	0.279	-0.587	-0.516	0.354	-0.748
ethylene glycol	1.51	0.259	-0.527	-0.488	0.360	-0.655
tetrathiafulavalene	1.33	0.337	-0.705	-0.512	0.264	-0.953
	1.34	0.327	-0.679	-0.475	0.272	-0.883
thiaindans	1.39	0.308	-0.633	-0.527	0.308	-0.852
	1.39	0.306	-0.627	-0.522	0.308	-0.840
	1.40	0.305	-0.622	-0.521	0.317	-0.826
	1.39	0.307	-0.628	-0.522	0.306	-0.844
	1.39	0.305	-0.627	-0.524	0.309	-0.842
	1.39	0.309	-0.634	-0.524	0.306	-0.852
	1.53	0.240	-0.439	-0.436	0.343	-0.532
	1.51	0.249	-0.471	-0.455	0.343	-0.582
dithianodithiine	1.52	0.245	-0.453	-0.451	0.346	-0.558
	1.34	0.329	-0.677	-0.489	0.277	-0.890
	1.53	0.242	-0.451	-0.443	0.366	-0.528
thiatane	1.54	0.239	-0.438	-0.436	0.342	-0.532
thiane	1.53	0.242	-0.445	-0.443	0.344	-0.544
	1.53	0.240	-0.440	-0.437	0.343	-0.534
SeC₃Se	1.27	0.358	-0.628	-0.628	0.199	-1.057
SC₃S	1.27	0.357	-0.617	-0.617	0.195	-1.040
NCCP	1.38	0.299	-0.577	-0.577	0.289	-0.866
C₅S	1.29	0.346	-0.623	-0.623	0.213	-1.034
	1.26	0.366	-0.635	-0.635	0.185	-1.084
	1.28	0.353	-0.620	-0.620	0.205	-1.036

Table 4.27 The CC bond distance (Å) and the AIM data $\rho(\mathbf{r})$ and eigenvalues (in au) of cation, anion and radical systems at M06-2X/6-311G(d,p) level of theory

system	d_{cc}	$\rho(\mathbf{r})$	$\lambda_{\rho 1}$	$\lambda_{\rho 2}$	$\lambda_{\rho 3}$	$\nabla^2\rho$
cyclopropenyl cation	1.36	0.314	-0.540	-0.456	0.294	-0.703
tropellium cation	1.39	0.309	-0.638	-0.559	0.312	-0.884
benzene-1-ylium	1.32	0.337	-0.643	-0.548	0.217	-0.974
	1.43	0.270	-0.506	-0.431	0.296	-0.642
	1.39	0.310	-0.637	-0.533	0.304	-0.866
propan-1-ylium	1.39	0.305	-0.616	-0.535	0.298	-0.852
	1.69	0.158	-0.251	-0.107	0.263	-0.095
propan-2-ylium	1.44	0.288	-0.562	-0.528	0.292	-0.799
2-methylpropan-2-ylium	1.46	0.278	-0.541	-0.513	0.309	-0.745
	1.46	0.278	-0.539	-0.512	0.309	-0.742
	1.46	0.277	-0.536	-0.511	0.309	-0.738
acetylene cation	1.19	0.342	-0.340	-0.340	0.144	-0.536
ethen-1-ylium	1.25	0.385	-0.775	-0.623	0.340	-1.058
cyclopentadienyl anion	1.41	0.291	-0.584	-0.467	0.315	-0.736
	1.41	0.291	-0.585	-0.468	0.315	-0.738
benzen-1-ide	1.42	0.287	-0.528	-0.518	0.298	-0.747
	1.40	0.302	-0.614	-0.512	0.309	-0.817
	1.39	0.304	-0.626	-0.517	0.310	-0.833
acetate	1.57	0.227	-0.434	-0.410	0.363	-0.481
ethylene carbonate	1.53	0.251	-0.490	-0.470	0.363	-0.596
ethyn-1-ide	1.24	0.385	-0.712	-0.712	0.212	-1.212
ethan-1-ide	1.54	0.222	-0.392	-0.346	0.302	-0.436
2-oxopropan-1-ide	1.38	0.311	-0.658	-0.481	0.299	-0.840
	1.55	0.234	-0.445	-0.425	0.354	-0.516
benzene_radical	1.37	0.315	-0.637	-0.542	0.291	-0.889
	1.40	0.301	-0.612	-0.511	0.310	-0.812
	1.39	0.307	-0.632	-0.527	0.309	-0.851
3-methylbut-2-enenitrile radical	1.31	0.344	-0.705	-0.535	0.236	-1.005
	1.37	0.303	-0.570	-0.554	0.276	-0.847
	1.51	0.249	-0.471	-0.453	0.338	-0.586
	1.51	0.245	-0.459	-0.444	0.338	-0.565
allyl_radical	1.38	0.312	-0.647	-0.531	0.299	-0.879
vinyl_radical	1.30	0.352	-0.732	-0.555	0.228	-1.059

Table 4.28 The CC bond distance (Å) and the AIM data $\rho(\mathbf{r})$ and eigenvalues (in au) of systems with multiple types of CC bonds at M06-2X/6-311G(d,p) level of theory

system	d_{cc}	$\rho(\mathbf{r})$	$\lambda_{\rho 1}$	$\lambda_{\rho 2}$	$\lambda_{\rho 3}$	$\nabla^2\rho$
dihydroindene	1.39	0.309	-0.634	-0.530	0.307	-0.856
	1.39	0.306	-0.628	-0.524	0.309	-0.842
	1.40	0.309	-0.637	-0.532	0.318	-0.851
	1.39	0.307	-0.630	-0.526	0.309	-0.848
	1.39	0.306	-0.628	-0.524	0.309	-0.842
	1.39	0.309	-0.634	-0.530	0.307	-0.856
	1.51	0.248	-0.465	-0.452	0.344	-0.572
	1.51	0.248	-0.465	-0.452	0.344	-0.572
	1.54	0.234	-0.425	-0.424	0.343	-0.505
	1.54	0.234	-0.425	-0.424	0.343	-0.505
isoprene	1.34	0.339	-0.724	-0.543	0.268	-0.999
	1.47	0.268	-0.531	-0.492	0.340	-0.683
	1.33	0.340	-0.723	-0.547	0.264	-1.006
	1.50	0.251	-0.474	-0.460	0.339	-0.595
2-pentene	1.50	0.251	-0.476	-0.460	0.336	-0.600
	1.33	0.342	-0.732	-0.537	0.262	-1.006
	1.50	0.253	-0.479	-0.465	0.340	-0.604
	1.53	0.236	-0.431	-0.427	0.339	-0.520
hex_1_ene_3_yne	1.43	0.278	-0.539	-0.511	0.306	-0.745
	1.33	0.339	-0.725	-0.541	0.264	-1.002
	1.20	0.401	-0.640	-0.625	0.097	-1.167
	1.46	0.261	-0.484	-0.480	0.308	-0.656
	1.53	0.235	-0.432	-0.424	0.339	-0.518
hexa_1,5_dien_3_yne	1.43	0.280	-0.543	-0.513	0.303	-0.753
	1.33	0.339	-0.723	-0.542	0.265	-1.000
	1.21	0.400	-0.654	-0.621	0.104	-1.171
	1.43	0.280	-0.543	-0.513	0.303	-0.753
	1.33	0.339	-0.723	-0.542	0.265	-1.000

Table 4.29 The CC bond distance (Å) and the AIM data $\rho(\mathbf{r})$ and eigenvalues (in au) of organometallic and hypervalent carbon compounds at M06-2X/6-311G(d,p) level of theory

system	d_{cc}	$\rho(\mathbf{r})$	$\lambda_{\rho 1}$	$\lambda_{\rho 2}$	$\lambda_{\rho 3}$	$\nabla^2 \rho$
η^3-CrCl$_3$	1.40	0.285	-0.456	-0.384	0.298	-0.542
metallacyclobutane	1.42	0.289	-0.510	-0.480	0.310	-0.680
ferrocene	1.42	0.289	-0.574	-0.456	0.314	-0.717
Bis(benzene)chromium(0)	1.41	0.292	-0.585	-0.474	0.311	-0.747
C$_3$H$_4$Li$_2$	1.50	0.236	-0.441	-0.299	0.317	-0.423
	1.53	0.214	-0.334	-0.232	0.293	-0.273
(C$_6$H$_6$)Cr(CO)$_3$	1.41	0.296	-0.595	-0.491	0.311	-0.775
Si$_2$C$_5$H$_2$	1.38	0.315	-0.657	-0.518	0.302	-0.873
	1.42	0.287	-0.565	-0.498	0.320	-0.744
	1.42	0.287	-0.565	-0.498	0.320	-0.744
	1.46	0.254	-0.408	-0.389	0.309	-0.487
	1.46	0.254	-0.408	-0.389	0.309	-0.487
Ge$_2$C$_5$H$_2$	1.38	0.312	-0.648	-0.511	0.305	-0.854
	1.42	0.286	-0.559	-0.489	0.319	-0.729
	1.42	0.286	-0.559	-0.489	0.319	-0.729
	1.46	0.261	-0.427	-0.423	0.314	-0.537
	1.46	0.261	-0.427	-0.423	0.314	-0.537
C$_6$Li$_6$	1.42	0.285	-0.512	-0.498	0.319	-0.691
C$_2$B$_8$	1.50	0.234	-0.421	-0.388	0.337	-0.472

Table 4.30 The CC bond distance (Å) and the AIM data $\rho(\mathbf{r})$ and eigenvalues (in au) of transition states at M06-2X/6-311G(d,p) level of theory

system	d_{cc}	$\rho(\mathbf{r})$	$\lambda_{\rho 1}$	$\lambda_{\rho 2}$	$\lambda_{\rho 3}$	$\nabla^2 \rho$
TS1	2.16	0.061	-0.064	-0.061	0.164	0.039
	2.41	0.040	-0.038	-0.024	0.116	0.054
TS2	2.30	0.048	-0.045	-0.040	0.135	0.050
	2.19	0.059	-0.060	-0.058	0.161	0.043
TS3	2.18	0.059	-0.062	-0.058	0.163	0.043
	2.38	0.041	-0.038	-0.033	0.119	0.049
TS4	2.33	0.046	-0.045	-0.038	0.130	0.047
	2.08	0.072	-0.082	-0.076	0.186	0.029
TS5	2.14	0.064	-0.068	-0.065	0.170	0.037
	2.40	0.041	-0.039	-0.025	0.117	0.053
TS6	1.92	0.099	-0.127	-0.121	0.235	-0.013
	2.63	0.027	-0.022	-0.013	0.084	0.049
TS7	1.98	0.089	-0.117	-0.096	0.217	0.004
TS8	2.00	0.087	-0.110	-0.099	0.214	0.005
TS9	2.04	0.073	-0.080	-0.078	0.190	0.032
TS10	2.13	0.068	-0.076	-0.071	0.188	0.041
TS11	2.21	0.057	-0.061	-0.053	0.152	0.038
TS12	2.15	0.065	-0.074	-0.065	0.169	0.030
TS13	2.01	0.080	-0.095	-0.090	0.209	0.024
TS14	1.95	0.102	-0.140	-0.128	0.244	-0.025
TS15	2.41	0.038	-0.033	-0.031	0.114	0.051
TS16	2.06	0.077	-0.096	-0.091	0.225	0.038
TS17	2.02	0.080	-0.095	-0.085	0.196	0.016
TS19	1.97	0.093	-0.118	-0.111	0.234	0.005
TS20	1.92	0.102	-0.135	-0.128	0.255	-0.008
TS21	2.45	0.036	-0.031	-0.028	0.114	0.054
TS22	2.21	0.060	-0.063	-0.060	0.166	0.043

Table 4.31 The CC bond distance (Å) and the AIM data $\rho(\mathbf{r})$ and eigenvalues (in au) of π-conjugate dimers at M06-2X/6-311G(d,p) level of theory

system	d_{cc}	$\rho(\mathbf{r})$	$\lambda_{\rho 1}$	$\lambda_{\rho 2}$	$\lambda_{\rho 3}$	$\nabla^2 \rho$
acetylenebromide dimer	3.31	0.006	-0.004	-0.001	0.026	0.021
acetonitrile dimer	3.25	0.007	-0.005	-0.002	0.029	0.023
diyne cyanide dimer	3.39	0.005	-0.003	-0.001	0.020	0.016
	3.36	0.006	-0.003	-0.001	0.021	0.017
	3.36	0.006	-0.003	-0.001	0.021	0.017
	3.25	0.006	-0.004	-0.002	0.026	0.020
	3.25	0.006	-0.004	-0.002	0.026	0.020
acetylene dimer	3.30	0.006	-0.004	-0.001	0.027	0.022
vinylchloride dimer	3.15	0.008	-0.005	-0.002	0.034	0.027
diyne flouride dimer	3.23	0.007	-0.004	-0.002	0.028	0.021
	3.27	0.007	-0.004	-0.001	0.026	0.021
C_{12} dimer	3.18	0.008	-0.005	-0.002	0.031	0.024
	3.19	0.008	-0.004	-0.001	0.029	0.024
diyne_CN_NMe$_2$_dimer	3.40	0.006	-0.003	0.000	0.021	0.018
vinyl fluoride dimer	3.06	0.008	-0.004	-0.003	0.035	0.028
dimethyl cyanide dimer	3.08	0.009	-0.006	-0.001	0.040	0.033
thiacetone dimer	3.51	0.004	0.000	0.000	0.014	0.013
diyne_CF$_3$_dimer	3.39	0.005	-0.003	0.000	0.019	0.016
	3.37	0.006	-0.003	-0.002	0.021	0.016
diyne_dimer	3.41	0.006	-0.003	-0.001	0.022	0.017
C_2 @C_{60}	2.95	0.013	-0.005	-0.003	0.057	0.048
	2.95	0.013	-0.005	-0.003	0.056	0.048
	2.95	0.013	-0.005	-0.003	0.055	0.047
	2.95	0.013	-0.005	-0.003	0.057	0.048
	2.96	0.013	-0.005	-0.003	0.055	0.047
	2.96	0.013	-0.005	-0.003	0.055	0.047
	2.96	0.013	-0.005	-0.003	0.055	0.047
	2.95	0.013	-0.005	-0.003	0.056	0.047
	2.95	0.013	-0.005	-0.003	0.057	0.048
	2.95	0.013	-0.005	-0.003	0.056	0.048

4.4.3 Beyond CC Interactions

Among all types of covalent and noncovalent atom-atom bonding interactions, the CC interaction is the most unique as it shows the largest variation in the nature and strength, across millions of carbon compounds. The exponential relation in Eq. 4.4 describes the entire world of CC interaction in chemistry and it emerges as a fundamental relationship in chemical bonding theory. The exponent -2.271 and coefficient 170.82 of Eq. 4.4 is unique to the level of DFT used, M06-2X/6-311G(d,p). Similar exponential relationships may exist for bonding between other atoms. However, screening of all types of atom-atom interactions is a herculean task. Moreover, unlike CC interactions, a large variety of bonding type may not be available for all other atoms for a trustworthy derivation of the equation. For a limited set of data, an exploratory MESP topology analysis is conducted for atom-atom interactions such as C–N, C–O, C–S, N–N, O–O, and S–S, in molecules from diverse experimental and theoretical investigations.[86-92] The study takes into account the covalent, non-covalent, and borderline cases. In all cases, the magnitude of the positive eigenvalue λ_{v1} showed relatively large value compared to the magnitude of both λ_{v2} and λ_{v3}, wherein $\lambda_{v2} \cong \lambda_{v3}$ (Table 4.32 – Table 4.37). The plot of bond distance versus the positive eigenvalue showed strong exponential relationship in all cases (Figure 4.16 - Figure 4.21). Thus, the elaborate study of CC interactions and the limited study of other interactions clearly support that chemical bonding scenario fits in to a continuum model across covalent, non-covalent and borderline cases.
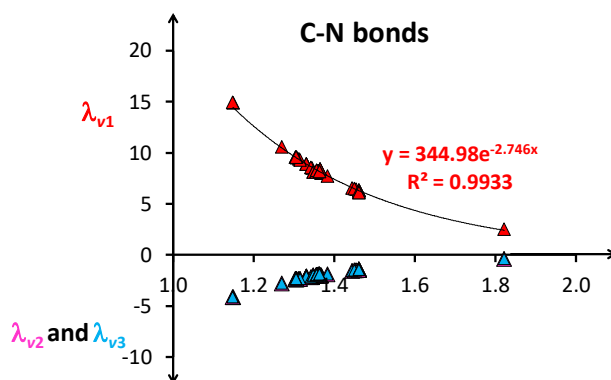
Figure 4.16 The exponential variation of $\lambda_{v1}, \lambda_{v2}$ and λ_{v3} (in au) with C-N bond distances (Å) from selected set of systems.

Table 4.32 MESP topology of selected set of systems containing C-N bonds at M06-2X/6-311G(d,p) level of theory. The C-N bond distance is given in Å and the MESP data V_{bnp}, V_ρ, $V(\mathbf{r})$ and eigenvalues are given in au (continues…)

system	d_{CN}	V_{bnp}	V_ρ	$V(\mathbf{r})$	λ_{v1}	λ_{v2}	λ_{v3}
pyrrole	1.37	16.521	-15.565	0.955	7.995	-2.039	-1.786
	1.37	16.521	-15.565	0.955	7.995	-2.039	-1.786
pyrazine	1.33	17.584	-16.534	1.050	8.911	-2.168	-2.145
	1.33	17.584	-16.534	1.050	8.911	-2.168	-2.145
	1.33	17.584	-16.534	1.050	8.911	-2.168	-2.145
	1.33	17.584	-16.534	1.050	8.911	-2.168	-2.145
quinazoline	1.31	21.216	-20.110	1.107	9.532	-2.374	-2.323
	1.31	21.315	-20.210	1.105	9.570	-2.393	-2.321
	1.36	20.580	-19.602	0.977	8.216	-1.941	-1.937
	1.36	24.817	-23.839	0.977	8.200	-1.947	-1.938
piperazine	1.46	17.945	-17.211	0.735	6.305	-1.464	-1.323
	1.46	17.945	-17.211	0.735	6.305	-1.464	-1.323
	1.46	17.944	-17.210	0.734	6.303	-1.464	-1.323
	1.46	17.944	-17.210	0.734	6.303	-1.464	-1.323
pyrrolidine	1.46	16.584	-15.852	0.732	6.288	-1.458	-1.312
	1.46	16.584	-15.852	0.732	6.288	-1.458	-1.312
thiozolidine	1.46	18.314	-17.541	0.772	6.409	-1.503	-1.347
triazole	1.31	17.118	-16.032	1.086	9.378	-2.364	-2.207
	1.32	17.168	-16.096	1.072	9.302	-2.350	-2.103
	1.35	17.135	-16.084	1.051	8.516	-2.187	-1.900
	1.36	16.833	-15.866	0.967	8.233	-1.995	-1.881
tetrazole	1.31	17.330	-16.206	1.124	9.540	-2.407	-2.204
	1.34	17.278	-16.191	1.087	8.571	-2.204	-1.933

Table 4.32 MESP topology of selected set of systems containing C-N bonds at M06-2X/6-311G(d,p) level of theory. The C-N bond distance is given in Å and the MESP data V_{bnp}, V_ρ, $V(\mathbf{r})$ and eigenvalues are given in au

system	d_{CN}	V_{bnp}	V_ρ	$V(\mathbf{r})$	λ_{v1}	λ_{v2}	λ_{v3}
DBN	1.27	22.891	-21.731	1.160	10.564	-2.791	-2.617
	1.38	23.424	-22.511	0.913	7.703	-1.917	-1.676
	1.45	21.871	-21.078	0.793	6.557	-1.557	-1.406
	1.45	21.736	-20.953	0.783	6.465	-1.534	-1.366
	1.46	20.429	-19.703	0.726	6.290	-1.408	-1.399
benzonitrile	1.15	18.485	-16.913	1.572	14.886	-4.143	-4.142
porphyrin	1.35	32.253	-31.269	0.984	8.100	-2.035	-1.810
	1.35	32.253	-31.269	0.984	8.100	-2.035	-1.810
	1.36	32.253	-31.269	0.984	8.100	-2.035	-1.810
	1.36	32.253	-31.269	0.983	8.100	-2.035	-1.809
	1.37	32.300	-31.341	0.960	8.365	-2.050	-1.925
	1.37	32.300	-31.340	0.960	8.364	-2.050	-1.925
	1.37	32.300	-31.340	0.960	8.364	-2.050	-1.925
	1.37	32.300	-31.340	0.960	8.363	-2.050	-1.924
aziridine	1.46	13.557	-12.744	0.813	6.086	-1.469	-1.305
	1.46	13.557	-12.744	0.813	6.086	-1.469	-1.305
cyanogen	1.15	14.790	-13.142	1.647	14.956	-4.172	-4.172
pyramido pyramidine	1.31	21.251	-20.119	1.131	9.572	-2.383	-2.340
	1.31	21.250	-20.119	1.131	9.571	-2.383	-2.339
	1.31	21.400	-20.274	1.126	9.552	-2.386	-2.313
	1.31	21.400	-20.274	1.126	9.550	-2.385	-2.313
	1.36	22.289	-21.275	1.013	8.299	-1.980	-1.969
	1.36	22.288	-21.275	1.013	8.298	-1.980	-1.969
	1.36	20.653	-19.660	0.993	8.152	-1.923	-1.916
	1.36	20.652	-19.660	0.993	8.150	-1.923	-1.915
TS$_{C-N}$	1.82	23.157	-1.450	0.372	2.531	-0.421	-0.390
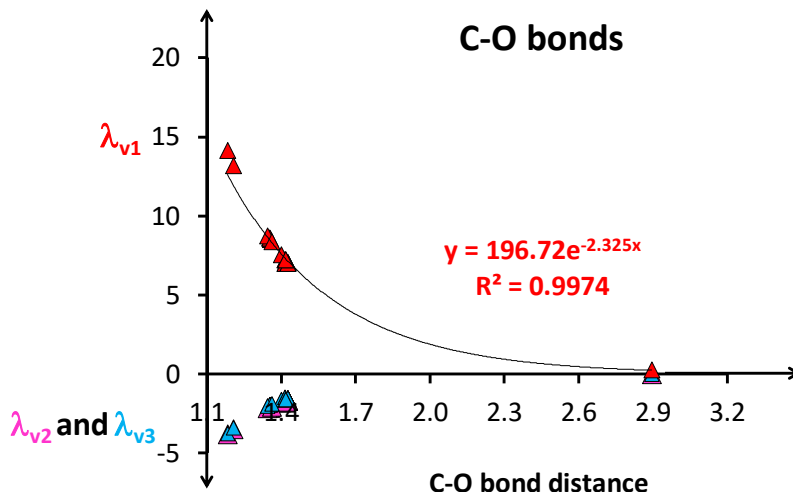
Figure 4.17 The exponential variation of $\lambda_{v1}, \lambda_{v2}$ and λ_{v3} (in au) with C-O bond distances (Å) from selected set of systems.

Table 4.33 MESP topology of selected set of systems containing C-O bonds at M06-2X/6-311G(d,p) level of theory. The C-O bond distance is given in Å and the MESP data V_{bnp}, V_{ρ}, $V(\mathbf{r})$ and eigenvalues are given in au

system	d_{CO}	V_{bnp}	V_{ρ}	$V(\mathbf{r})$	λ_{v1}	λ_{v2}	λ_{v3}
furan	1.35	17.148	-16.152	0.996	8.513	-2.127	-1.948
	1.35	17.148	-16.152	0.996	8.513	-2.127	-1.948
tetrahydropyran	1.41	18.643	-17.824	0.820	7.221	-1.743	-1.607
	1.41	18.643	-17.824	0.820	7.221	-1.743	-1.607
THF	1.42	17.243	-16.445	0.798	7.028	-1.700	-1.542
	1.42	17.243	-16.445	0.798	7.027	-1.700	-1.541
dioxolone	1.40	17.883	-17.006	0.877	7.556	-1.828	-1.643
	1.42	17.497	-16.677	0.820	7.036	-1.711	-1.547
oxirane	1.41	14.329	-13.432	0.898	6.974	-1.804	-1.486
	1.41	14.329	-13.431	0.898	6.971	-1.803	-1.485
ethylene carbonate	1.18	20.205	-18.726	1.480	14.132	-3.802	-3.787
	1.35	20.041	-19.010	1.032	8.575	-2.123	-1.939
	1.35	20.040	-19.009	1.031	8.573	-2.122	-1.938
	1.42	18.672	-17.803	0.868	7.012	-1.672	-1.540
	1.42	18.671	-17.803	0.868	7.009	-1.672	-1.539
furfural	1.20	18.935	-17.549	1.385	13.155	-3.511	-3.431
	1.34	19.311	-18.268	1.043	8.738	-2.193	-2.015
	1.36	20.107	-19.101	1.006	8.354	-2.078	-1.897
ethylene glycol	1.42	15.347	-14.523	0.825	7.198	-1.753	-1.605
	1.42	15.347	-14.522	0.825	7.198	-1.753	-1.605
NNDMAacetylCl	2.90	16.630	-16.680	-0.050	0.243	-0.025	-0.010

267
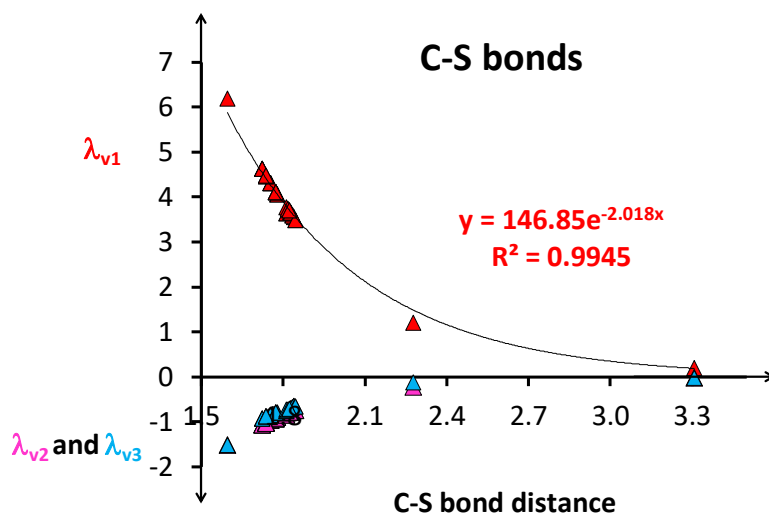
Figure 4.18 The exponential variation of $\lambda_{v1}, \lambda_{v2}$ and λ_{v3} (in au) with C-S bond distances (Å) from selected set of systems.

Table 4.34 MESP topology of selected set of systems containing C-S bonds at M06-2X/6-311G(d,p) level of theory. The C-S bond distance is given in Å and the MESP data V_{bnp}, V_ρ, $V(\mathbf{r})$ and eigenvalues are given in au (continues...)

system	d_{CS}	V_{bnp}	V_ρ	$V(\mathbf{r})$	λ_{v1}	λ_{v2}	λ_{v3}
thiophene	1.72	18.667	-17.945	0.723	4.641	-1.056	-0.917
	1.72	18.667	-17.945	0.723	4.641	-1.056	-0.917
thioxathene	1.78	27.181	-26.539	0.642	4.073	-0.882	-0.785
	1.78	27.181	-26.539	0.642	4.073	-0.882	-0.785
	1.83	17.804	-17.246	0.559	3.609	-0.764	-0.674
thiozolidine	1.84	17.804	-17.253	0.552	3.558	-0.744	-0.639
tetrathiafulvalene	1.75	25.759	-25.064	0.694	4.312	-0.963	-0.835
	1.75	25.759	-25.064	0.694	4.312	-0.963	-0.835
	1.75	25.759	-25.064	0.694	4.312	-0.963	-0.835
	1.75	25.759	-25.064	0.694	4.312	-0.963	-0.835
	1.77	28.322	-27.649	0.674	4.122	-0.929	-0.787
	1.77	28.322	-27.649	0.674	4.122	-0.929	-0.787
	1.77	28.322	-27.649	0.674	4.122	-0.929	-0.787
	1.77	28.322	-27.649	0.674	4.122	-0.929	-0.787

Table 4.34 MESP topology of selected set of systems containing C-S bonds at M06-2X/6-311G(d,p) level of theory. The C-S bond distance is given in Å and the MESP data V_{bnp}, V_ρ, $V(\mathbf{r})$ and eigenvalues are given in au

system	d_{CS}	V_{bnp}	V_ρ	$V(\mathbf{r})$	λ_{v1}	λ_{v2}	λ_{v3}
benzoyl isothiocyanate	1.59	21.146	-20.188	0.958	6.201	-1.508	-1.507
thiaindans	1.77	23.101	-22.459	0.642	4.123	-0.900	-0.789
	1.84	21.553	-20.988	0.566	3.591	-0.752	-0.669
thiirane	1.81	15.950	-15.297	0.652	3.655	-0.840	-0.747
	1.81	15.950	-15.297	0.652	3.655	-0.840	-0.747
lenthionine	1.81	26.066	-25.444	0.621	3.784	-0.792	-0.724
	1.82	25.982	-25.361	0.621	3.743	-0.797	-0.722
	1.83	25.949	-25.339	0.610	3.670	-0.779	-0.703
	1.83	26.170	-25.564	0.606	3.663	-0.764	-0.696
thietane	1.84	17.219	-16.667	0.552	3.489	-0.736	-0.649
	1.84	17.219	-16.667	0.552	3.489	-0.736	-0.649
thiane	1.82	19.781	-19.215	0.566	3.709	-0.776	-0.706
	1.82	19.781	-19.215	0.566	3.709	-0.776	-0.706
terthienyl	1.72	26.013	-25.284	0.729	4.634	-1.056	-0.915
	1.72	26.013	-25.284	0.729	4.634	-1.056	-0.915
	1.74	30.044	-29.331	0.713	4.477	-1.014	-0.868
	1.74	30.044	-29.331	0.713	4.477	-1.014	-0.868
	1.74	28.371	-27.659	0.713	4.490	-1.016	-0.872
	1.74	28.371	-27.658	0.713	4.490	-1.016	-0.872
CO_2....H_2S complex	3.31	11.710	-11.693	0.018	0.201	-0.017	-0.014
TS_{C-S}	2.28	15.521	-15.218	0.304	1.208	-0.225	-0.110
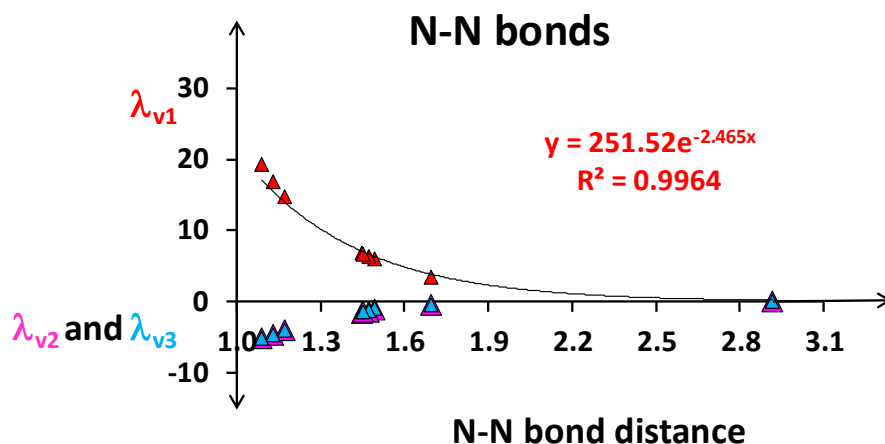
Figure 4.19 The exponential variation of $\lambda_{v1}, \lambda_{v2}$ and λ_{v3} (in au) with N-N bond distances (Å) from selected set of systems.

Table 4.35 MESP topology of selected set of systems containing N-N bonds at M06-2X/6-311G(d,p) level of theory. The N-N bond distance is given in Å and the MESP data V_{bnp}, V_ρ, $V(\mathbf{r})$ and eigenvalues are given in au

system	d_{NN}	V_{bnp}	V_ρ	$V(\mathbf{r})$	λ_{v1}	λ_{v2}	λ_{v3}
N_2	1.09	13.593	-11.683	1.910	19.221	-5.267	-5.267
N_2F_4	1.50	21.362	-20.526	0.836	5.982	-1.249	-1.038
N_2O_4	1.70	18.722	-18.165	0.556	3.426	-0.599	-0.547
N_3CH_3_dimer	2.92	16.322	-16.250	0.072	0.206	-0.054	-0.048
N_3H	1.13	15.433	0.072	1.776	16.844	-4.811	-4.811
	1.17	0.000	0.072	1.637	14.681	-4.177	-4.177
hydrazine	1.47	11.590	15.433	0.722	6.334	-1.500	-1.329
aminimide_1	1.45	39.776	-38.956	0.820	6.721	-1.596	-1.495
aminimide_2	1.45	34.614	-33.806	0.808	6.618	-1.565	-1.460
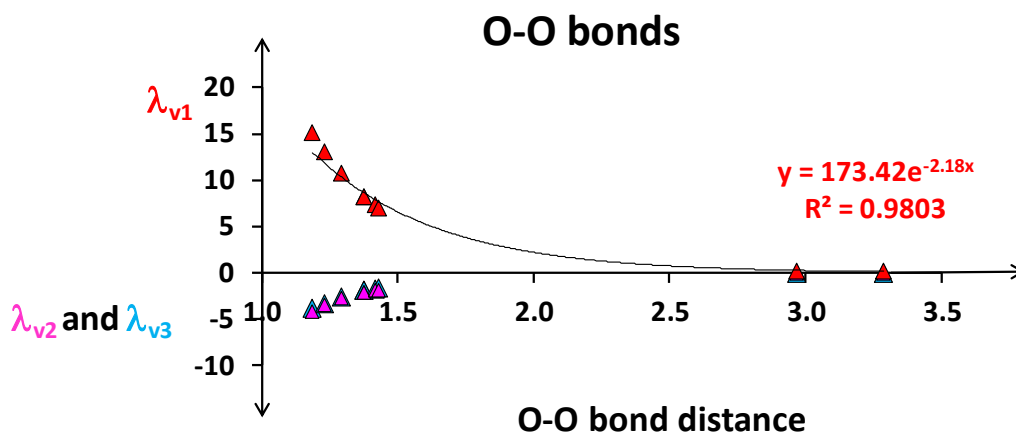
Figure 4.20 The exponential variation of λ_{v1}, λ_{v2} and λ_{v3} (in au) with O-O bond distances (Å) from selected set of systems.

Table 4.36 MESP topology of selected set of systems containing O-O bonds at M06-2X/6-311G(d,p) level of theory. The O-O bond distance is given in Å and the MESP data V_{bnp}, V_{ρ}, $V(\mathbf{r})$ and eigenvalues are given in au

system	d_{OO}	V_{bnp}	V_{ρ}	$V(\mathbf{r})$	λ_{v1}	λ_{v2}	λ_{v3}
CH$_3$COO_dimer	2.97	20.343	-20.341	0.002	0.163	-0.016	-0.012
CrO$_5$	1.38	24.809	-23.803	1.006	8.247	-2.165	-1.838
	1.38	24.806	-23.800	1.006	8.242	-2.164	-1.836
H$_2$S$_2$O$_8$	1.42	30.159	-29.230	0.929	7.384	-1.840	-1.739
O$_2$	1.19	14.253	-12.709	1.544	15.084	-4.178	-3.776
O$_2$F$_2$	1.30	18.614	-17.361	1.252	10.756	-2.687	-2.644
O$_2$H$_2$	1.43	12.639	-11.847	0.793	7.055	-1.828	-1.573
O$_3$	1.23	16.356	-14.928	1.428	13.062	-3.395	-3.327
cyclopentanone dimer	3.29	21.649	-21.607	0.042	0.208	-0.045	-0.035
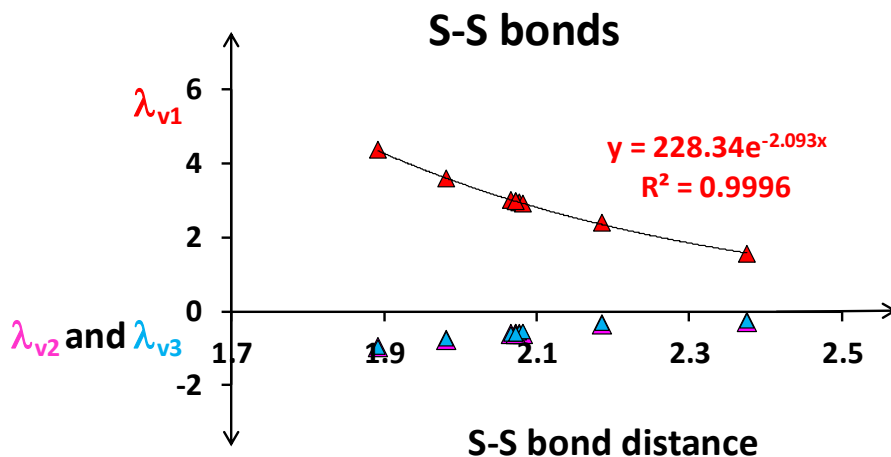
Figure 4.21 The exponential variation of λ_{v1}, λ_{v2} and λ_{v3} (in au) with SS bond distances (Å) from selected set of systems.

Table 4.37 MESP topology of selected set of systems containing S-S bonds at M06-2X/6-311G(d,p) level of theory. The S-S bond distance is given in Å and the MESP data V_{bnp}, V_{ρ}, $V(\mathbf{r})$ and eigenvalues are given in au

system	d_{SS}	V_{bnp}	V_{ρ}	$V(\mathbf{r})$	λ_{v1}	λ_{v2}	λ_{v3}
lenthionine	2.08	27.490	-26.889	0.601	2.938	-0.610	-0.586
S_2Cl_2	1.98	24.137	-23.380	0.757	3.596	-0.766	-0.754
$[(CH_3)_3P^+-SCH_3...CH_3S^-...H_2O$	2.07	26.309	-25.731	0.578	2.970	-0.614	-0.597
$H_2S_2O_3$	1.89	24.283	-23.422	0.861	4.373	-0.957	-0.954
$H_2S_2O_6$	2.19	28.356	-27.791	0.565	2.387	-0.342	-0.329
DHS_{red}	2.08	24.730	-24.152	0.579	2.918	-0.624	-0.560
$C_4H_{10}S_2O_2$	2.07	24.410	-23.814	0.596	3.009	-0.626	-0.614
$H_2O...(CH_3)_3P...CH_3SSCH_3...H2O$	2.07	27.050	-26.473	0.577	2.972	-0.614	-0.597
TS_{S-S}	2.38	29.428	-29.152	0.276	1.576	-0.297	-0.267

4.5 Conclusions

MESP topology analysis has been carried out on a large variety of molecular systems containing various types of CC interactions using M06-2X/6-311G(d,p) level of theory as well as using a benchmark set of DFT methods. The $V(\mathbf{r})$ value is observed in

different ranges for different types of CC bond interactions *viz.* single, double, triple, aromatic, π-conjugated, organometallics, strained, sterically crowded, transition states, non-covalent *etc*. The relationship between the MESP $V(\mathbf{r})$ at BCP and CC distance suggests a CC bond continuum in chemistry which encompasses all kinds of covalent, non-covalent and borderline cases such as transition states. At the equilibrium CC bonding distance, the V_{bnp} balances with the V_ρ for the lowest $V(\mathbf{r})$. An exponential function fits almost perfectly to define a fundamental correlation between the CC distance and the highest eigenvalue λ_{v1} of the MESP bond critical point. This relationship confirms the continuum nature of CC bonds in chemistry. The slope of the exponential function, λ'_{v1} suggests the demarcation of the continuum in three regions *viz.* covalent, non-covalent and borderline cases. The λ'_{v1} more negative than -5.0 au/Å for covalent and less negative than -1.0 au/Å for non-covalent CC bonds, while λ'_{v1} between -1.0 and -5.0 au/Å defines the borderline cases between non-covalent as well as covalent CC interactions. The CC bond continuum is further supported by the MED value at the BCP. For the first time, Popelier's $\nabla^2\rho$ analysis on chemical bonding is tested exclusively for a single variety of bonding interaction–the CC interaction. The $\nabla^2\rho$ theory applies to all covalent interactions and non-covalent interactions whereas borderline cases such as transition states can be addressed by invoking the nature of all the three eigenvalues of the BCP. For the borderline cases, the magnitude of all three eigenvalues is significantly larger than zero whereas their sum, the $\nabla^2\rho$ is close to zero. We extend our analysis to explore the validity of these concepts in the context of other atom-atom interactions, specifically focusing on C-N, C-O, C-S, N-N, O-O, and S-S bonds, although with a limited dataset. By conducting a comprehensive examination of CC interactions and an initial exploration of other interactions, our findings unequivocally demonstrate the existence of a bond continuum within the realm of chemistry.

4.6 References

1.   A. S. Goldman, *Nature*, **2010**, 463, 435-436.
2.   W. D. Hounshell, D. A. Dougherty, J. P. Hummel and K. Mislow, *J. Am. Chem. Soc.*, **1977**, 99, 1916-1924.

3. Y. Ishigaki, T. Shimajiri, T. Takeda, R. Katoono and T. Suzuki, *Chem*, **2018**, 4, 795-806.

4. T. Takeda, H. Kawai, R. Herges, E. Mucke, Y. Sawai, K. Murakoshi, K. Fujiwara and T. Suzuki, *Tetrahedron Lett.*, **2009**, 50, 3693-3697.

5. S. Kammermeier, R. Herges and P. G. Jones, *Angew. Chem., Int. Ed. Engl.*, **1997**, 36, 1757-1760.

6. P. R. Schreiner, L. V. Chernish, P. A. Gunchenko, E. Y. Tikhonchuk, H. Hausmann, M. Serafin, S. Schlecht, J. E. Dahl, R. M. Carlson and A. A. Fokin, *Nature*, **2011**, 477, 308-311.

7. K. Tanaka, N. Takamoto, Y. Tezuka, M. Kato and F. Toda, *Tetrahedron*, **2001**, 57, 3761-3767.

8. B. Kahr, D. Van Engen and K. Mislow, *J. Am. Chem. Soc.*, **1986**, 108, 8305-8307.

9. A. A. Fokin, L. V. Chernish, P. A. Gunchenko, E. Y. Tikhonchuk, H. Hausmann, M. Serafin, J. E. Dahl, R. M. Carlson and P. R. Schreiner, *J. Am. Chem. Soc.*, **2012**, 134, 13641-13650.

10. A. a. A. Delgado, A. Humason, R. Kalescky, M. Freindorf and E. Kraka, *Molecules*, **2021**, 26, 950.

11. E. J. J. Korpela, J. R. Carvalho, H. Lischka and M. Kertesz, *J. Phys. Chem. A*, **2023**.

12. T. Kubo, Y. Suga, D. Hashizume, H. Suzuki, T. Miyamoto, H. Okamoto, R. Kishi and M. Nakano, *J. Am. Chem. Soc.*, **2021**, 143, 14360-14366.

13. H. Kawai, T. Takeda, K. Fujiwara, T. Inabe and T. Suzuki, *Cryst. Growth Des.*, **2005**, 5, 2256-2260.

14. J. Li, R. Pang, Z. Li, G. Lai, X.-Q. Xiao and T. Müller, *Angew. Chem. Int. Ed.*, **2019**, 58, 1397-1401.

15. F. Toda, K. Tanaka, Z. Stein and I. Goldberg, *Acta Crystallographica Section C: Crystal Structure Communications*, **1996**, 52, 177-180.

16. S. Grimme and P. R. Schreiner, *Angew. Chem. Int. Ed.*, **2011**, 50, 12639-12642.

17. M. Rueping and I. Atodiresei, *C–C Bond Formation: Cascade or Domino Reaction*, in *Comprehensive Chirality*, E.M. Carreira and H. Yamamoto, Editors. 2012, Elsevier: Amsterdam. p. 345-373.

18. N. G. Schmidt, E. Eger and W. Kroutil, *ACS Catal.*, **2016**, 6, 4286-4311.

19.   M. Agúndez, J. Cernicharo and M. Guélin, *Astron. Astrophys.*, **2014**, 570, A45.

20.   L. Di Costanzo and S. Geremia, *Molecules*, **2020**, 25, 3555.

21.   S. Shahbazian, *Chem. Eur. J.*, **2018**, 24, 5401-5405.

22.   C. H. Suresh and N. Koga, *J. Am. Chem. Soc.,* **2002**, 124, 1790-1797.

23.   S. R. Gadre, S. A. Kulkarni and I. H. Shrivastava, *J. Chem. Phys.*, **1992**, 96, 5253-5260.

24.   C. H. Suresh, G. S. Remya and P. K. Anjalikrishna, *Wiley Interdiscip. Rev. Comput. Mol. Sci.*, **2022**, 12, e1601.

25.   S. R. Gadre, C. H. Suresh and N. Mohan, *Molecules*, **2021**, 26, 3289.

26.   R. Bonaccorsi, E. Scrocco and J. Tomasi, *J. Chem. Phys.*, **1970**, 52, 5270-5284.

27.   E. Scrocco and J. Tomasi, *The electrostatic molecular potential as a tool for the interpretation of molecular properties*, in *New concepts II*. 1973, Springer. p. 95-170.

28.   E. Scrocco and J. Tomasi, *Electronic molecular structure, reactivity and intermolecular forces: an euristic interpretation by means of electrostatic molecular potentials*, in *Advances in quantum chemistry*. 1978, Elsevier. p. 115-193.

29.   A. Pullman and B. Pullman, *Q. Rev. Biophys.*, **1981**, 14, 289-380.

30.   R. F. W. Bader, *Acc. Chem. Res.*, **1985**, 18, 9-15.

31.   R. Bader, *Clarendon: Oxford, UK*, **1990**.

32.   P. Politzer and D. G. Truhlar, *Chemical applications of atomic and molecular electrostatic potentials: reactivity, structure, scattering, and energetics of organic, inorganic, and biological systems*. 2013: Springer Science & Business Media.

33.   P. Politzer, K. C. Daiker and R. A. Donnelly, *Cancer Lett.*, **1976**, 2, 17-23.

34.   P. Politzer, R. A. Donnelly and K. C. Daiker, *J. Chem. Soc., Chem. Commun.*, **1973**, 617-618.

35.   J. S. Murray and P. Politzer, *Wiley Interdiscip. Rev. Comput. Mol. Sci.*, **2011**, 1, 153-163.

36.   R. K. Pathak and S. R. Gadre, *J. Chem. Phys.*, **1990**, 93, 1770-1773.

37.   S. R. Gadre and R. K. Pathak. *Nonexistence of local maxima in molecular electrostatic potential maps*. in *Proc. Indian Ac. Sci. Chem. Sci.* 1990: Springer.

38.   S. R. Gadre and R. N. Shirsat, *Electrostatics of atoms and molecules*. 2000: Universities Press.

39. A. Kumar, R. López, F. Martínez, G. Ramírez, I. Ema, D. Zorrilla, S. D. Yeole and S. R. Gadre, *Comput. Phys. Commun.*, **2022**, 279, 108460.

40. R. López, I. Ema, G. Ramírez, D. Zorrilla, S. R. Gadre, A. Kumar and S. D. Yeole. *DAMQT 3.2*. 2020.

41. A. Kumar, S. D. Yeole, S. R. Gadre, R. López, J. F. Rico, G. Ramírez, I. Ema and D. Zorrilla, *DAMQT 2.1. 0: A New Version of the DAMQT Package Enabled with the Topographical Analysis of Eelectron Density and Electrostatic Potential in Molecules*. 2015, Wiley Online Library.

42. R. López, J. F. Rico, G. Ramírez, I. Ema and D. Zorrilla, *Comput. Phys. Commun.*, **2015**, 192, 289-294.

43. R. López, J. F. Rico, G. Ramírez, I. Ema, D. Zorrilla, A. Kumar, S. D. Yeole and S. R. Gadre, *Comput. Phys. Commun.*, **2017**, 214, 207-215.

44. R. López, J. F. Rico, G. Ramírez, I. Ema and D. Zorrilla, *Comput. Phys. Commun.*, **2009**, 180, 1654-1660.

45. J. F. Rico, R. Lopez, I. Ema and G. Ramirez, *J. Mol. Struct.: THEOCHEM*, **2005**, 727, 115-121.

46. P. L. A. Popelier, *J. Phys. Chem. A*, **1999**, 103, 2883-2890.

47. P. L. Popelier, *J. Mol. Model.*, **2022**, 28, 276.

48. Y. Zhao and D. G. Truhlar, *Theor. Chem. Account.*, **2008**, 120, 215-241.

49. M. J. Frisch, G. W. Trucks, H. B. Schlegel, G. E. Scuseria, M. A. Robb, J. R. Cheeseman, G. Scalmani, V. Barone, G. A. Petersson, H. Nakatsuji, X. Li, M. Caricato, A. V. Marenich, J. Bloino, B. G. Janesko, R. Gomperts, B. Mennucci, H. P. Hratchian, J. V. Ortiz, A. F. Izmaylov, J. L. Sonnenberg, D. Williams-Young, F. Ding, F. Lipparini, F. Egidi, J. Goings, B. Peng, A. Petrone, T. Henderson, D. Ranasinghe, V. G. Zakrzewski, J. Gao, N. Rega, G. Zheng, W. Liang, M. Hada, M. Ehara, K. Toyota, R. Fukuda, J. Hasegawa, M. Ishida, T. Nakajima, Y. Honda, O. Kitao, H. Nakai, T. Vreven, K. Throssell, J. A. Montgomery Jr., J. E. Peralta, F. Ogliaro, M. J. Bearpark, J. J. Heyd, E. N. Brothers, K. N. Kudin, V. N. Staroverov, T. A. Keith, R. Kobayashi, J. Normand, K. Raghavachari, A. P. Rendell, J. C. Burant, S. S. Iyengar, J. Tomasi, M. Cossi, J. M. Millam, M. Klene, C. Adamo, R. Cammi, J. W. Ochterski, R. L. Martin, K. Morokuma,

O. Farkas, J. B. Foresman and D. J. Fox, *Gaussian 16 Rev. A.03*. 2016: Wallingford, CT.

50. A. Kumar, S. D. Yeole, S. R. Gadre, R. López, J. F. Rico, G. Ramírez, I. Ema and D. Zorrilla, *J. Comput. Chem.*, **2015**, 36, 2350-2359.

51. Á. M. Pendás and C. Gatti, *Complementary Bonding Analysis*, **2021**, 43.

52. C. Gatti, *Computational Materials Discovery*, **2018**, 117.

53. F. Jensen, *WIREs Comput. Mol. Sci.*, **2013**, 3, 273-295.

54. K. Remya and C. H. Suresh, *Phys. Chem. Chem. Phys.*, **2015**, 17, 27035-27044.

55. K. Remya and C. H. Suresh, *RSC adv.*, **2016**, 6, 44261-44271.

56. T. Salomon, J. B. Dudek, Y. Chernyak, J. Gauss and S. Thorwirth, *J. Mol. Spectrosc.*, **2021**, 378, 111456.

57. S. Thorwirth, T. Salomon, S. Fanghänel, J. Kozubal and J. Dudek, *Chem. Phys. Lett.*, **2017**, 684, 262-266.

58. B. A. Mcguire, M.-A. Martin-Drumel, K. L. K. Lee, J. F. Stanton, C. A. Gottlieb and M. C. Mccarthy, *Phys. Chem. Chem. Phys.*, **2018**, 20, 13870-13889.

59. M. C. Mccarthy, J. H. Baraban, P. B. Changala, J. F. Stanton, M.-A. Martin-Drumel, S. Thorwirth, C. A. Gottlieb and N. J. Reilly, *J. Phys. Chem. Lett.*, **2015**, 6, 2107-2111.

60. J. B. Dudek, T. Salomon, S. Fanghänel and S. Thorwirth, *Int. J. Quantum Chem.*, **2017**, 117, e25414.

61. P. R. Remya and C. H. Suresh, *Dalton Trans.*, **2015**, 44, 17660-17672.

62. P. Das and P. K. Chattaraj, *Chemistry*, **2022**, 4, 1723-1756.

63. L. R. Domingo, J. A. Sáez and M. Arnó, *Org. Biomol. Chem.*, **2014**, 12, 895-904.

64. M. J. Sarma, S. Jindani, B. Ganguly, S. Pabbaraja and G. Mehta, *J. Org. Chem.*, **2022**, 87, 884-891.

65. J. A. Izzo, Y. Myshchuk, J. S. Hirschi and M. J. Vetticatt, *Org. Biomol. Chem.*, **2019**, 17, 3934-3939.

66. S. Thiyagarajan, R. V. Sankar, P. K. Anjalikrishna, C. H. Suresh and C. Gunanathan, *ACS Catal.*, **2022**, 12, 2191-2204.

67. H. Wang, Y. Wang, K.-L. Han and X.-J. Peng, *J. Org. Chem.*, **2005**, 70, 4910-4917.

68. D. Taherinia and A. Fattahi, *Sci. Rep.*, **2022**, 12, 22225.

69. D. Svatunek, R. P. Pemberton, J. L. Mackey, P. Liu and K. N. Houk, *J. Org. Chem.*, **2020**, 85, 3858-3864.

70. S. R. Nath and K. A. Joshi, *Phys. Chem. Chem. Phys.*, **2018**, 20, 21457-21473.

71. V. Cachatra, A. Almeida, J. Sardinha, S. D. Lucas, A. Gomes, P. D. Vaz, M. H. Florêncio, R. Nunes, D. Vila-Viçosa, M. J. Calhorda and A. P. Rauter, *Org. Lett.*, **2015**, 17, 5622-5625.

72. M. J. Sarma, S. Jindani, B. Ganguly, S. Pabbaraja and G. Mehta, *J. Org. Chem.* , **2021**, 87, 884-891.

73. M. Ramirez, V. Vece, S. Hanessian and K. N. Houk, *J. Org. Chem.*, **2021**, 86, 17955-17964.

74. C. W. Lee, B. L. H. Taylor, G. P. Petrova, A. Patel, K. Morokuma, K. N. Houk and B. M. Stoltz, *J. Am. Chem. Soc.*, **2019**, 141, 6995-7004.

75. R. Robiette, J. Richardson, V. K. Aggarwal and J. N. Harvey, *J. Am. Chem. Soc.*, **2006**, 128, 2394-2409.

76. A. Asha, J. Ravindran, S. Suma, C. H. Suresh and R. S. Lankalapalli, *ChemistrySelect*, **2020**, 5, 2545-2550.

77. C. Challa, S. Varughese, C. H. Suresh and R. S. Lankalapalli, *Org. Lett.*, **2017**, 19, 4219-4222.

78. R. F. Bader and P. Beddall, *J. Chem. Phys.*, **1972**, 56, 3320-3329.

79. P. L. A. Popelier, F. Aicken and S. O'brien, *Atoms in molecules*. Vol. 188. 2000: Prentice Hall Manchester.

80. P. L. A. Popelier, *The QTAIM Perspective of Chemical Bonding*, in *The Chemical Bond*. 2014. p. 271-308.

81. T. J. Mooibroek, *Molecules*, **2019**, 24, 3370.

82. A. Bauzá, T. J. Mooibroek and A. Frontera, *Chem. Eur. J.*, **2014**, 20, 10245-10248.

83. V. Georgakilas, M. Otyepka, A. B. Bourlinos, V. Chandra, N. Kim, K. C. Kemp, P. Hobza, R. Zboril and K. S. Kim, *Chem. Rev.*, **2012**, 112, 6156-6214.

84. S. J. Grabowski, W. A. Sokalski, E. Dyguda and J. Leszczyński, *J. Phys. Chem. B*, **2006**, 110, 6444-6446.

85. J. Dutta, D. K. Sahoo, S. Jena, K. D. Tulsiyan and H. S. Biswal, *Phys. Chem. Chem. Phys.*, **2020**, 22, 8988-8997.

86. L. Maestre, R. Dorel, Ó. Pablo, I. Escofet, W. M. C. Sameera, E. Álvarez, F. Maseras, M. M. Díaz-Requejo, A. M. Echavarren and P. J. Pérez, *J. Am. Chem. Soc.*, **2017**, 139, 2216-2223.

87. Y.-Y. Jiang, T.-T. Liu, X. Sun, Z.-Y. Xu, X. Fan, L. Zhu and S. Bi, *Org. Biomol. Chem.*, **2018**, 16, 5808-5815.

88. A. Frontera, *C*, **2020**, 6, 60.

89. V. R. Mundlapati, D. K. Sahoo, S. Bhaumik, S. Jena, A. Chandrakar and H. S. Biswal, *Angew. Chem. Int. Ed.*, **2018**, 57, 16496-16500.

90. J. Baltrusaitis, E. V. Patterson and C. Hatch, *J. Phys. Chem. A*, **2012**, 116, 9331-9339.

91. K. Arai, M. Noguchi, B. G. Singh, K. I. Priyadarsini, K. Fujio, Y. Kubo, K. Takayama, S. Ando and M. Iwaoka, *FEBS Open Bio.*, **2013**, 3, 55-64.

92. O. Dmitrenko, C. Thorpe and R. D. Bach, *J. Org. Chem.*, **2007**, 72, 8298-8307.

ABSTRACT

Name of the Student: Anjali Krishna P. K.

Faculty of Study: Chemical Sciences

AcSIR academic centre/CSIR Lab: CSIR - National Institute For Interdisciplinary Science and Technology (NIIST)

Registration No. : 10CC18A39002

Year of Submission: 2023

Name of the Supervisor: Dr. C. H. Suresh

Title of the thesis: Exploration of Aromaticity, Through-Space Effect, and Nature of CC Bonds in Chemistry using Molecular Electrostatic Potential Analysis

Molecular Electrostatic Potential (MESP) analysis is a powerful computational technique utilized in theoretical chemistry to explore the electrostatic properties of molecules. The thesis strives to elucidate the diverse applications of MESP analysis. Its objective is to highlight the capability of MESP in providing a unified perspective on the electrostatic properties of molecules and carbon-carbon (CC) bonds within the field of chemistry using Density Functional Theory (DFT).

Chapter 1 presents a comprehensive overview of MESP, covering discrete charge electrostatic field and potential, electrostatic theorems, historical development, topology concepts, applications, and a general comparison with the concept of molecular electron density (MED). Additionally, it provides an overview of the computational methodologies employed throughout the thesis.

Chapter 2 explores a topological study of MESP applied to various conjugated hydrocarbons. The objective is to comprehend their π-conjugation features, aromatic character and to investigate the interplay of aromaticity and antiaromaticity in fused aromatic-antiaromatic (A-aA) systems through MESP analysis. This study effectively delineates the electron-rich π-regions of molecular systems.

Chapter 3 delves into the π-conjugation, aromaticity, and stability of the recently synthesized 12-infinitene, as well as other infinitenes incorporating 8-, 10-, 14-, and 16-arene rings. This investigation employs DFT and explores the underlying phenomenon of the through-space effect (TSE) which imparts electron donor-acceptor properties to a diverse array of chemical systems, including derivatives of pyrrole, indole, isoindole, azulene, and aniline.

Chapter 4 explores the covalent and non-covalent nature of CC interactions in a diverse array of molecular systems. This characterization achieved through the topology analysis of MESP and MED offer valuable insights into the bonding between carbon atoms in different molecular environments.

DETAILS OF PUBLICATIONS EMANATING FROM THE THESIS WORK

1. **Anjalikrishna, P. K.**; Suresh, C. H.; Gadre, S. R., Electrostatic Topographical Viewpoint of π-Conjugation and Aromaticity of Hydrocarbons. *J. Phys. Chem. A* **2019,** 123, 10139-10151.

2. **Anjalikrishna, P. K.**; Gadre, S. R.; Suresh, C. H., Antiaromaticity–Aromaticity Interplay in Fused Benzenoid Systems using Molecular Electrostatic Potential Topology. *J. Phys. Chem. A* **2021,** 125, 5999-6012.

3. **Anjalikrishna, P. K**.; Gadre, S. R.; Suresh, C. H., Electrostatic Potential for Exploring Electron Delocalization in Infinitenes, Circulenes, and Nanobelts. *J. Org. Chem.* **2023**, 88, 7, 4123–4133.

4. **Anjalikrishna, P. K**.; Gadre, S. R.; Suresh, C. H., Topology of Electrostatic Potential and Electron Density Reveals a Covalent to Non-covalent Carbon–Carbon Bond Continuum. *Phys. Chem. Chem. Phys.* **2023**, 25, 25191-25204 [HOT ARTICLE].

5. **Anjalikrishna, P. K**.; Suresh, C. H., Utilization of Through-Space Effect to Design Donor-Acceptor Systems of Pyrrole, Indole, Isoindole, Azulene and Aniline. *Phys. Chem. Chem. Phys.,* **2024**, 26, 1340-1351.

Contributions to Academic Conferences

1. Presented a poster entitled '*Electrostatic Topographical Viewpoint of π-Conjugation and Aromaticity of Hydrocarbons*' at the national conference on New Frontiers in Chemistry-from Fundamentals to Applications-III (NFCFA2019) held on December 20-22, 2019 at BITS Pilani, K K Birla Goa Campus.

    Abstract: A molecular electrostatic potential (MESP) topographical study has been conducted for a variety of conjugated hydrocarbons at B3LYP/6-311+G(d,p) level of theory to understand their π-conjugation features and aromaticity. The value of MESP minimum (V_m) is related to the localized and delocalized distribution of π-electron density. The V_m values are located interior to the rings in polycyclic benzenoid hydrocarbons (PBHs), whereas they lie outside the boundary of the rings in antiaromatic and in fused systems consisting of aromatic and antiaromatic moieties. The V_m points lie on top and bottom of the π-regions in linear polyenes and annulenes, while a degenerate distribution of CPs around the midpoint region of triple bonds is observed in alkynes. The eigenvalues λ_1, λ_2, and λ_3 of the Hessian matrix at V_m (MESP minima) are used to define the aromatic character of the cyclic structures. The eigenvalues follow the trend $\lambda_1 \gg \lambda_2 > \lambda_3 \cong 0$ in PBHs, $\lambda_1 > \lambda_2 > \lambda_3 \cong 0$ in linear polyenes, and $\lambda_1 > \lambda_2 > \lambda_3 \neq 0$ in antiaromatic systems. The difference in the aromatic character of PBHs from that of benzene is related to the deviations $\Delta\lambda_1$, $\Delta\lambda_2$, and $\Delta\lambda_3$. The total deviation $\sum_{i=1}^{3}\Delta\lambda_i$ is found to be ≤ 0.011 au for all aromatic systems and lies between 0.011 and 0.035 au for all nonaromatic systems. For antiaromatic systems, its value is found to be above 0.035 au. Further, $\sum_{i=1}^{3}\Delta\lambda_i$ gives a direct interpretation of Clar's aromatic sextet structures for PBHs. In summary, MESP topography mapping is a powerful technique to quantify the localized and delocalized π-electron distribution in a variety of unsaturated hydrocarbon systems.

2. Presented a poster entitled '*Antiaromaticity–Aromaticity Interplay in Fused Benzenoid Systems using Molecular Electrostatic Potential Topology*' at Theoretical Chemistry Symposium (TCS 2021) held on December 11-14, 2021 organized by IISER Kolkata,

285

IACS Kolkata, Kalyani University and S.N. Bose National Centre for Basic Sciences Kolkata.

Abstract: The phenomenon of antiaromaticity–aromaticity interplay in aromatic–antiaromatic (A–aA)-fused systems is studied using molecular electrostatic potential (MESP) analysis, which clearly brings out the electron-rich π-regions of molecular systems. Benzene, naphthalene, phenanthrene, and pyrene are the aromatic units and cyclobutadiene and pentalene are the antiaromatic units considered to construct the A–aA-fused systems. The fused system is seen to reduce the antiaromaticity by adopting a configuration containing the least number of localized bonds over antiaromatic moieties. This is clearly observed in 25 isomers of a fused system composed of three naphthalene and two cyclobutadiene units. Denoting the number of π-bonds in the cyclobutadiene rings by the notation (n, n′), the systems belonging to the class (0, 0) and (2, 2) turn out to be the most and least stable configurations, respectively. The stability of the fused system depends on the empty π-character of the antiaromatic ring, hence naphthalene and benzene prefer to fuse with cyclobutadiene in a linear and angular fashion, respectively. Generally, a configuration with the maximum number of 'empty' rings (0, 0, 0, …) is considered to be the most stable for the given A–aA system. The stability and aromatic/antiaromatic character of A–aA-fused systems with pentalene is also interpreted in a similar way. MESP topology, clearly bringing out the distribution of double bonds in the fused systems, leads to a simple interpretation of the aromatic/antiaromatic character of them. Also, it leads to powerful predictions on stable macrocyclic A–aA systems.

3. Presented a poster entitled '*Antiaromaticity–Aromaticity Interplay in Fused Benzenoid Systems using Molecular Electrostatic Potential Topology*' at DAE-BRNS Symposium on Current Trends in Theoretical Chemistry (CTTC-2022) held on September 22-24, 2022 at DAE Convention Centre, Anushaktinagar, Mumbai. [Best poster]

Abstract: The phenomenon of antiaromaticity–aromaticity interplay in aromatic–antiaromatic (A–aA)-fused systems is studied using molecular electrostatic potential

(MESP) analysis, which clearly brings out the electron-rich π-regions of molecular systems. Benzene, naphthalene, phenanthrene, and pyrene are the aromatic units and cyclobutadiene and pentalene are the antiaromatic units considered to construct the A–aA-fused systems. The fused system is seen to reduce the antiaromaticity by adopting a configuration containing the least number of localized bonds over antiaromatic moieties. This is clearly observed in 25 isomers of a fused system composed of three naphthalene and two cyclobutadiene units. Denoting the number of π-bonds in the cyclobutadiene rings by the notation (n, n'), the systems belonging to the class (0, 0) and (2, 2) turn out to be the most and least stable configurations, respectively. The stability of the fused system depends on the empty π-character of the antiaromatic ring, hence naphthalene and benzene prefer to fuse with cyclobutadiene in a linear and angular fashion, respectively. Generally, a configuration with the maximum number of 'empty' rings (0, 0, 0, ...) is considered to be the most stable for the given A–aA system. The stability and aromatic/antiaromatic character of A–aA-fused systems with pentalene is also interpreted in a similar way. MESP topology, clearly bringing out the distribution of double bonds in the fused systems, leads to a simple interpretation of the aromatic/antiaromatic character of them. Also, it leads to powerful predictions on stable macrocyclic A–aA systems.

SCI PUBLICATIONS

Electrostatic Topographical Viewpoint of π-Conjugation and Aromaticity of Hydrocarbons

Published as part of The Journal of Physical Chemistry virtual special issue "Paul Geerlings Festschrift".

Puthannur K. Anjalikrishna,[†,‡] Cherumuttathu H. Suresh,[*,†,‡] and Shridhar R. Gadre[*,§]
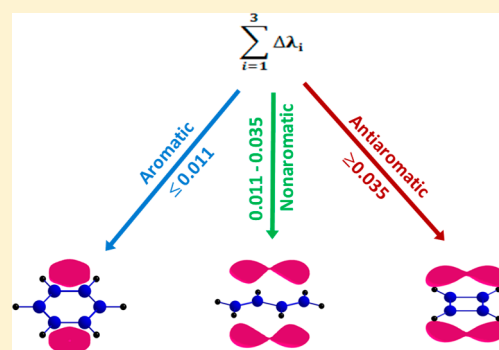
[†]Chemical Sciences and Technology Division, CSIR-National Institute for Interdisciplinary Science and Technology, Thiruvananthapuram, Kerala 695019, India

[‡]Academy of Scientific and Innovative Research (AcSIR), Ghaziabad 201002, India

[§]Interdisciplinary School of Scientific Computing, Savitribai Phule Pune University, Pune 411007, India

Ⓢ *Supporting Information*

ABSTRACT: A molecular electrostatic potential (MESP) topographical study has been conducted for a variety of conjugated hydrocarbons at B3LYP/6-311+G(d,p) level of theory to understand their π-conjugation features and aromaticity. The value of MESP minimum (V_m) is related to the localized and delocalized distribution of π-electron density. The V_m values are located interior to the rings in polycyclic benzenoid hydrocarbons (PBHs), whereas they lie outside the boundary of the rings in antiaromatic and in fused systems consisting of aromatic and antiaromatic moieties. The V_m points lie on top and bottom of the π-regions in linear polyenes and annulenes, while a degenerate distribution of CPs around the midpoint region of triple bonds is observed in alkynes. The eigenvalues λ_1, λ_2, and λ_3 of the Hessian matrix at V_m(MESP minima) are used to define the aromatic character of the cyclic structures. The eigenvalues follow the trend $\lambda_1 \gg \lambda_2 > \lambda_3 \cong 0$ in PBHs, $\lambda_1 > \lambda_2 > \lambda_3 \cong 0$ in linear polyenes, and $\lambda_1 > \lambda_2 > \lambda_3 \neq 0$ in antiaromatic systems. The difference in the aromatic character of PBHs from that of benzene is related to the deviations $\Delta\lambda_1$, $\Delta\lambda_2$, and $\Delta\lambda_3$. The total deviation $\sum_{i=1}^{3}\Delta\lambda_i$ is found to be ≤ 0.011 au for all aromatic systems and lies between 0.011 and 0.035 au for all nonaromatic systems. For antiaromatic systems, its value is found to be above 0.035 au. Further, $\sum_{i=1}^{3}\Delta\lambda_i$ gives a direct interpretation of Clar's aromatic sextet structures for PBHs. In summary, MESP topography mapping is a powerful technique to quantify the localized and delocalized π-electron distribution in a variety of unsaturated hydrocarbon systems.

INTRODUCTION

"Aromaticity" is one of the most frequently used terms in chemistry since the discovery[1−4] of benzene in 1825. Though a rigorous definition of aromaticity is elusive,[5] some operational definitions exist for classifying molecules as aromatic, antiaromatic, and nonaromatic.[6,7] In quantum chemical terms, aromaticity was defined and explained using Hückel's $(4n + 2)$ rule. that is, the conjugation of $(4n + 2)\pi$-electrons over a planar monocyclic ring (where n is a positive integer).[8−14] According to this rule, molecules other than aromatic are regarded as antiaromatic ($4n\pi$-electrons) or nonaromatic based on certain criteria. Experimental and theoretical studies also enable classification of molecules into categories such as homoaromatic, heteroaromatic, pseudoaromatic,[15] metalloaromatic,[16] chelatoaromatic,[17] claromatic, hyperaromatic,[18] transition state aromatic, excited state aromatic,[19] etc. based on a variety of aromaticity criteria.[16,19−22] A general concept is that aromaticity is associated with the delocalization of π-electrons all along the series of bonds resulting in an aromatic ring.[23] Several aromaticity indices have been defined and used for estimating the aromatic character in terms of structural, magnetic, electronic, and reactivity properties. Among them some of the descriptors are just approximations, some are applicable to certain cases only, and some are not good enough to give convincing results.[24−28]

The notion of aromaticity was first brought in for describing the benzene molecule, which is still considered as a paragon of aromaticity. Aromaticity in other π-systems was elucidated with Hückel's $(4n + 2)$ rule. Later, numerous studies on aromaticity were taken up. The Hückel's rule is strictly applicable only to the monocyclic conjugated systems; therefore attempts were made to expand the study on aromaticity to polycyclic systems also. Among them, one of the most successful was Clar's model,[29] which explained the stability shown by benzenoid species.[24,30−38] Polycyclic benzenoid hydrocarbons (PBHs), are a class of organic compounds consisting of two or more fused benzenoid rings, which is the most explored one for the study of

aromaticity.[39−42] The aromaticity of a PBH is generally described for the individual benzenoid rings as local aromaticity, and the average of all the local aromaticities is taken as the global aromaticity for the molecule.[27] Many alternate ways were introduced to connect aromaticity with other molecular parameters. von Schleyer and Jiao[43] stated that there is a linear relationship among the energetic, geometric, and magnetic criteria of aromaticity. Behrens et al.[44] demonstrated that the delocalization energy of π-electrons can be used as an index of aromaticity in PBHs. Giambiagi et al.[45] suggested that the quantum similarity theory can be used as the method to quantify concepts such as aromaticity. Bultinck et al.[28] used the electron density itself as a tool to study aromaticity of the individual benzenoid rings of a given PBH, quite similar to the original Polansky Index.[46] Suresh and Gadre attempted to explain the nature of aromaticity using topographical features of the molecular electrostatic potential (MESP).[47−49] The most interesting finding in their study was the distribution of critical points (CPs) of MESP topography, which could directly distinguish each ring of the PBH system. They obtained a strong correlation between MESP topography patterns and Clar's aromatic sextet theory. However, they did not provide a rigorous and general definition of aromaticity in terms of MESP topography of a large variety of molecules.

Numerous studies have shown that MESP topographical analysis[50−54] is very useful for a quantitative interpretation of the localization and delocalization features of π-conjugated systems and lone pair-bearing molecules. Very recently, Gadre, Suresh, and co-workers[55] proposed a definition of lone pairs from the characteristics of minima in MESP. The criterion was based upon the eigenvalues and eigenvectors of the Hessian where the largest eigenvalue and the corresponding eigenvector of lone pairs were found to be different from that of another kind of electron delocalization. Localized electron density in a lone pair of atoms could be quantified using the negative minimum value of MESP at that region. It has been proposed that the magnitude of the eigenvalue at the CP that corresponds to the lone pair is numerically greater than 0.025 au and the eigenvector associated with it nearly points in the direction (angle ≤ 5°) of the atom on which it is localized. A clear-cut definition of lone pairs emerged in terms of MESP features[56] and that led to an easy interpretation of their interactive behavior with electron deficient π-regions in molecular systems.[57,58] These studies also suggested that MESP topography features of π-bonded regions of molecules should be significantly different from those of nonbonded electron-localized regions such as lone pairs. The present work proposes a MESP topography-based approach for a rigorous characterization of the π-regions of aromatic, antiaromatic, and nonaromatic systems. We expect that such a MESP topography-based analysis will lead to a new definition of aromaticity as well as a new way to compare the local and global aromaticity values of a large variety of molecules.

■ METHODOLOGY

All the molecular systems investigated in the present work are optimized at the B3LYP/6-311+G(d,p) level of theory using Gaussian 09 program[59] package, with a check on the minimal nature by doing a frequency run and verifying that all the frequencies are real. At these geometries, MESP and MESP topography computation has been done using the recently developed DAMQT package.[60−63] DAMQT is based on the deformed atoms in molecules (DAM) method for the analysis

of the molecular electron density. The wave function constructed using B3LYP in conjunction with the valence triple-ζ level basis set and augmented with polarization and diffuse functions (6-311+G(d,p)) is expected to give a sufficiently accurate description of the electron density, ρ. The values of MESP and its gradients and second derivatives are calculated while finding the CPs using DAM partition-expansion method.[60]

The MESP function $V(\mathbf{r})$ at any point in the space (position vector $\mathbf{r}$) can be calculated using eq 1, where $\rho(\mathbf{r})$ is a continuous electron density and Z_A is the charge on the nucleus of atom A located at a distance $\mathbf{R}_A$.[47,64,65]

$$V(\mathbf{r}) = \sum_A^N \frac{Z_A}{|\mathbf{r} - \mathbf{R}_A|} - \int \frac{\rho(\mathbf{r}')\, d^3\mathbf{r}'}{|\mathbf{r} - \mathbf{r}'|} \tag{1}$$

The topographical features of the scalar function $V(\mathbf{r})$ can be extracted from its first and second order partial derivatives. At the CP, all the first derivatives of $V(\mathbf{r})$ vanish meaning that $\nabla V(\mathbf{r}) = 0$. The nature of the CP at $\mathbf{r}_c$ is decided by the signs of the three eigenvalues of the corresponding 3 × 3 Hessian matrix $\mathbf{A}$, the elements of which are defined by

$$A_{ij} = \left(\frac{\partial^2 V(\mathbf{r})}{\partial x_i \partial x_j} \right)_{\mathbf{r}=\mathbf{r}_c} \tag{2}$$

The eigenvalues indicate the curvature of the function at the CP and the eigenvector signifies the axis of the curvature.[55] A nondegenarate CP is represented by an ordered pair (R, σ) where R gives the rank of the CP, the number of nonzero eigenvalues of the Hessian matrix, while σ represents the signature, the algebraic sum of the sign of the eigenvalues.

The (R, σ) representations for the four types of non-degenerate CPs typically observed in MESP distribution are (3, +3), (3, +1), (3, −1) and (3, −3). The (3, +3) CP corresponds to a local minimum with MESP rising in all the directions toward it while a (3, −3) CP designates a local maximum, the nuclear positions. The (3, −1) and (3, +1) type CPs are called saddle points.[66−68] The CP distribution of ethylene is depicted in Figure 1 as an illustrative example. Here the red and pink dots represent (3, +3) and (3, −1) critical points, and the arrows in red, blue, and green display the eigenvectors
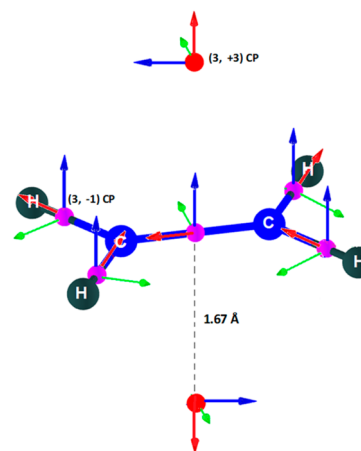

Figure 1. Distribution of MESP CPs with the directions of corresponding eigenvectors for the ethylene molecule. See text for details.
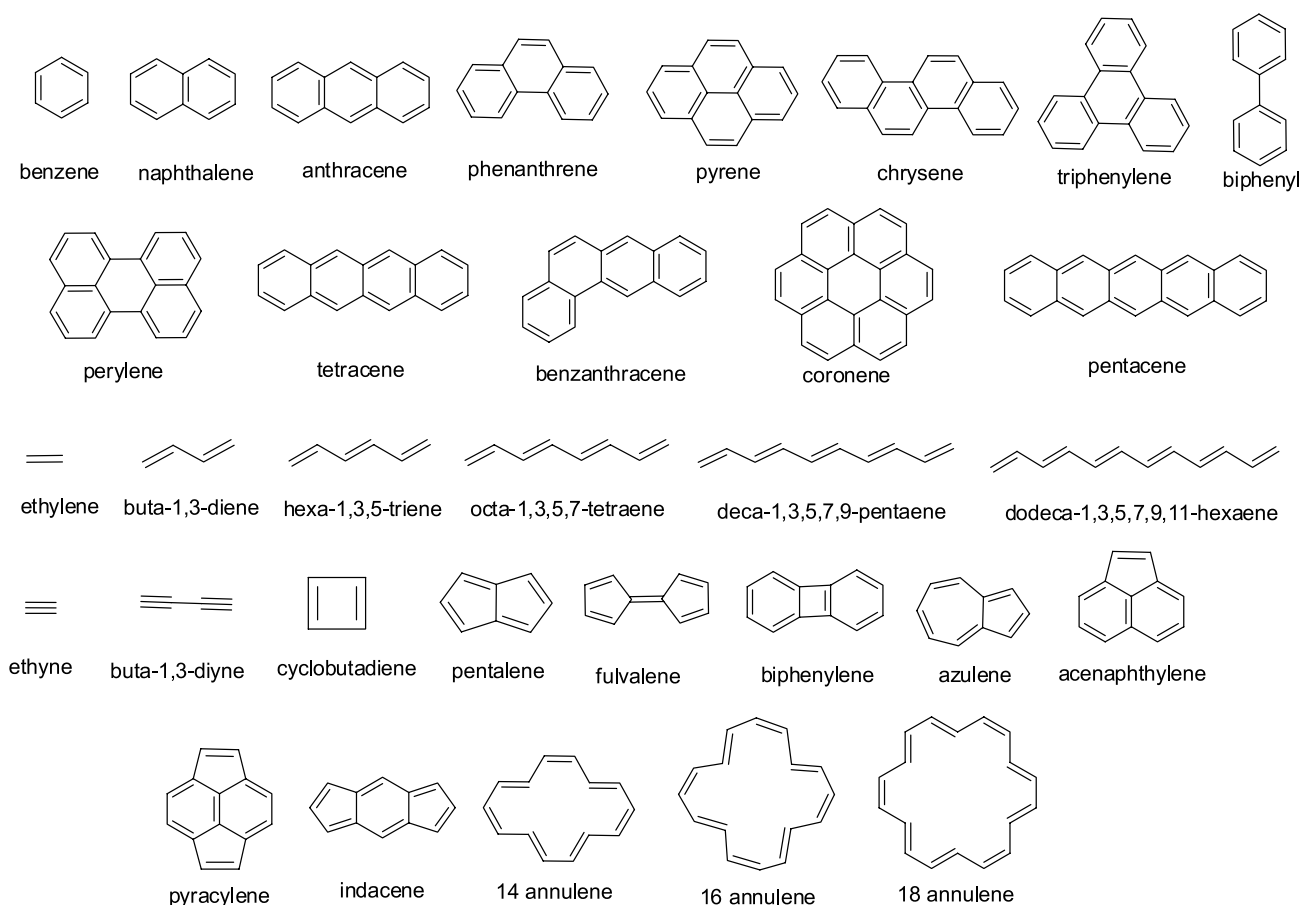
Figure 2. Selected set of molecules for exploring aromaticity, nonaromaticity, and antiaromaticity.

corresponding to the numerically highest, intermediate, and lowest eigenvalues. In ethylene, at the (3, +3) position, the most negative-valued MESP (V_m) is observed ca. 1.67 Å away from the midpoint of the CC bond. In molecules containing "ring" moieties, a (3, +1) CP is observed around the middle region of the ring.

Since the eigenvalues describe the curvature of the function at the critical point, we felt that such information regarding the π-region of the molecule can bring out the extent of electron delocalization in the molecule. A very smooth even distribution is expected in cyclically conjugated electrons in aromatic molecules compared to other type of conjugations. In order to express this in terms of MESP topography, we chose the entity $\sum_{i=1}^{3} \Delta \lambda_i$ as it combines the information regarding all three eigenvalues pertaining to a critical point.

Here DAMQT package is used for the MESP topography calculation and visualization. All the molecules selected for the present study are shown in Figure 2. Due to symmetry, CPs appearing only on one side of the molecular plane are discussed in the text. To check the reliability of the B3LYP method, a benchmark study is also conducted with the DFT methods M06 and M06-2X and also with the *ab initio* method MP2 using the 6-311+G(d,p) basis set in all cases. Though the absolute values of MESP parameters differs to some extent, the relative order and the trend in values are almost identical in all the cases (Supporting Information). Hence, only the B3LYP/6-311+G(d,p) values are discussed hereafter in the text.

■ RESULTS AND DISCUSSION

Benzene and Polycyclic Benzenoid Hydrocarbons. In the case of benzene, a set of six equivalent CPs appear on each side, around 1.89 Å vertically away from the molecular plane (Figure 3a). Each of these CPs is aligned at the midpoint
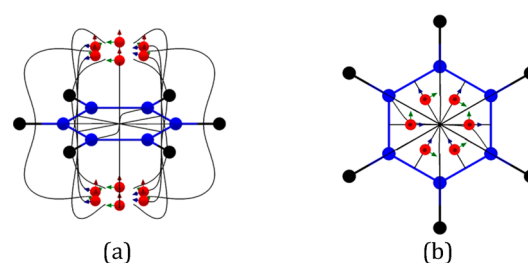

Figure 3. MESP topography of benzene: (a) side view and (b) top view of (3, +3) CPs embedded in gradient paths. See text for details.

region of the nearest CC bond but shifted toward the interior of the ring (Figure 3b). The (3, +3) CP is designated as V_m, and the three eigenvalues of the Hessian matrix are denoted as λ_1, λ_2, and λ_3. In what follows, the symbol V_m stands for the minimum value of MESP as well as the corresponding CP.

In benzene, V_m is −15.7 kcal/mol with λ_1, λ_2, and λ_3 being 0.0142, 0.0025, and 0.0005 au respectively, showing the trend $\lambda_1 \gg \lambda_2 > \lambda_3 \cong 0$ for this perfectly aromatic molecule. The eigenvector (marked in red arrow in Figure 3) corresponding to the largest eigenvalue λ_1 shows an orientation perpendicular to the π-bond. The eigenvectors corresponding to λ_2 (blue
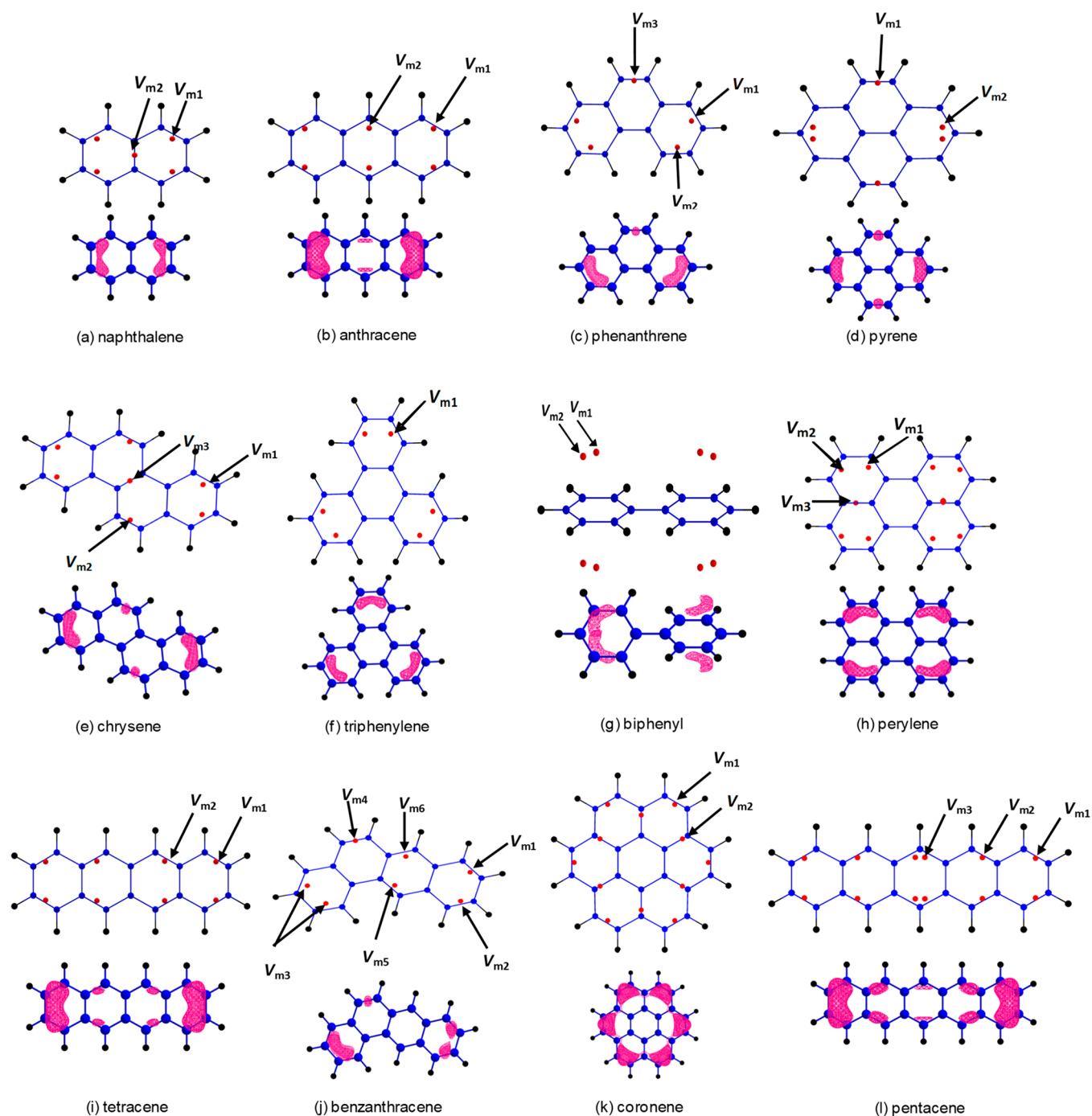
Figure 4. MESP topography of PBH systems (top). MESP isosurface plots (bottom) show the π-delocalization pattern. An appropriate MESP value in the range -11.0 to -14.5 kcal/mol is selected for isosurface. See text for details.

arrow) and λ_3 (green arrow) are aligned in a plane that is parallel to the ring plane. The top view of the MESP topography of all the PBH systems studied in this work is shown in Figure 4. The V_m and eigenvalues of all these systems are given in Table 1. Nondegenerate V_m points appearing in these systems are numbered as V_{m1}, V_{m2}, V_{m3}, etc. Similar to benzene, the direction of the eigenvector corresponding to the largest eigenvalue λ_1 for all other systems shows an orientation perpendicular to the π-bond, eigenvectors corresponding to λ_2 and λ_3 are aligned in a plane that is parallel to the ring plane. Unlike benzene, the number of V_m points seen in PBHs is significantly less than the number of CC bonds. In benzene,

the six equivalent CPs may be viewed as the signature of the perfect cyclic delocalization of 6π-electrons over six equal CC bonds while the reduction in CPs in other PBHs can be attributed to deviation from such a π-delocalization due to the presence of unequal CC bonds. In general, V_m points are seen to appear in the vicinity of C–C bonds that are more localized.

For instance, in the case of naphthalene, a set of four equivalent CPs (V_{m1}) and a fifth CP (V_{m2}) appear on one side of the molecular plane. V_{m1} CPs at -14.8 kcal/mol can be associated with symmetrically equivalent four CC bonds, which are the shortest CC bonds of naphthalene, while V_{m2} at -12.7 kcal/mol can be assigned for the CC bond common for

Table 1. MESP Topography Features[a] of Benzene and Polycyclic Benzenoid Hydrocarbons

molecule	V_m label	V_m	λ_1	λ_2	λ_3	$\sum_{i=1}^{3}\Delta\lambda_i$
benzene	V_{m1}	−15.7	0.0142	0.0025	0.0005	0.0000
naphthalene	V_{m1}	−14.8	0.0152	0.0049	0.0032	0.0062
	V_{m2}	−12.7	0.0086	0.0004	0.0001	−0.0080
anthracene	V_{m1}	−14.6	0.0158	0.0059	0.0041	0.0086
	V_{m2}	−12.6	0.0104	0.0035	0.0000	−0.0033
phenanthrene	V_{m1}	−14.5	0.0142	0.0042	0.0022	0.0034
	V_{m2}	−14.5	0.0141	0.0040	0.0024	0.0033
	V_{m3}	−14.3	0.0159	0.0068	0.0052	0.0107
pyrene	V_{m1}	−14.0	0.0156	0.0068	0.0052	0.0104
	V_{m2}	−13.9	0.0133	0.0044	0.0006	0.0011
chrysene	V_{m1}	−14.3	0.0141	0.0042	0.0027	0.0038
	V_{m2}	−14.0	0.0147	0.0058	0.0047	0.0080
	V_{m3}	−12.5	0.0081	0.0018	0.0008	−0.0065
triphenylene	V_{m1}	−14.3	0.0135	0.0036	0.0019	0.0018
biphenyl	V_{m1}	−14.8	0.0141	0.0031	0.0006	0.0006
	V_{m2}	−14.8	0.0140	0.0035	0.0008	0.0011
perylene	V_{m1}	−13.9	0.0140	0.0046	0.0028	0.0042
	V_{m2}	−13.3	0.0115	0.0040	0.0003	−0.0014
	V_{m3}	−12.1	0.0074	0.0005	0.0002	−0.0091
tetracene	V_{m1}	−14.4	0.0161	0.0065	0.0044	0.0098
	V_{m2}	−12.4	0.0106	0.0035	0.0015	−0.0016
benzanthracene	V_{m1}	−14.3	0.0153	0.0055	0.0038	0.0074
	V_{m2}	−14.3	0.0153	0.0055	0.0037	0.0073
	V_{m3}	−14.2	0.0138	0.0039	0.0018	0.0023
	V_{m4}	−14.1	0.0162	0.0076	0.0055	0.0121
	V_{m5}	−12.9	0.0103	0.0033	0.0017	−0.0019
	V_{m6}	−12.7	0.0104	0.0032	0.0012	−0.0024
coronene	V_{m1}	−13.4	0.0144	0.0050	0.0048	0.0070
	V_{m2}	−11.3	0.0074	0.0006	0.0003	−0.0089
pentacene	V_{m1}	−14.3	0.0162	0.0067	0.0045	0.0103
	V_{m2}	−12.3	0.0108	0.0037	0.0020	−0.0007
	V_{m3}	−11.8	0.0099	0.0036	0.0001	−0.0036

[a]V_m in kcal/mol and the respective eigenvalues λ_1, λ_2, and λ_3 in au. See text for details.

both the rings (Figure 4a). The λ_1, λ_2, and λ_3 corresponding to V_{m1} are 0.0152, 0.0049, and 0.0032 au and those of V_{m2} are 0.0086, 0.0004, and 0.0001 au, respectively. Eigenvalues corresponding to both the V_m values follow the trend $\lambda_1 \gg \lambda_2 > \lambda_3 \cong 0$. The number of nonequivalent CPs are two in anthracene (V_{m1}, V_{m2}), three in phenanthrene (V_{m1}, V_{m2}, V_{m3}), two in pyrene (V_{m1}, V_{m2}), three in chrysene (V_{m1}, V_{m2}, V_{m3}), one in triphenylene (V_{m1}), two in biphenyl (V_{m1}, V_{m2}), three in perylene (V_{m1}, V_{m2}, V_{m3}), two in tetracene (V_{m1}, V_{m2}), six in benzanthracene (V_{m1}, V_{m2}, V_{m3}, V_{m4}, V_{m5}, V_{m6}), two in coronene (V_{m1}, V_{m2}), and three in pentacene (V_{m1}, V_{m2}, V_{m3}). Here magnitudes follow the progression $V_{m1} > V_{m2} > V_{m3} > V_{m4} > V_{m5} > V_{m6}$. The V_m values and eigenvalues of all the systems are shown in Table 1. Among all the systems, the most negative V_{m1} −15.7 kcal/mol is observed in benzene while for all the PBHs, V_{m1} lies in the range −13.4 to −14.8 kcal/mol. In benzene, the number of π-electrons shared per CC bond is one, while this quantity is always less than one in a PBH as the number of CC bonds is greater than the number of π-electrons. Hence MESP of PBHs is always less negative than that of benzene. Most of the V_m points as seen from top view show their location more toward the interior of the rings.

In all PBH systems, $\lambda_1 \gg \lambda_2 > \lambda_3 \cong 0$, which means that their π-electron distribution as revealed by MESP topography is similar to that of benzene. Does it mean that their aromatic character is also similar to that of benzene? PBH systems are

expected to be less aromatic than benzene due to imperfections in the cyclic π-delocalization. The deviation of λ values of a PBH from that of benzene, namely, $\Delta\lambda_1$, $\Delta\lambda_2$, and $\Delta\lambda_3$, can be used to understand the aromatic dilution of a PBH with respect to benzene. For instance, in the case of naphthalene, the deviations $\Delta\lambda_1$, $\Delta\lambda_2$, and $\Delta\lambda_3$ corresponding to the most negative potential V_{m1} are 0.0010, 0.0024, and 0.0027 au and those corresponding to V_{m2} are −0.0056, −0.0021, and −0.0004 au, respectively. These values are close to zero and indicate that the aromatic character of naphthalene is very similar to that of benzene. The total deviations, $\sum_{i=1}^{3}\Delta\lambda_i$ (in au), of 0.0062 for V_{m1} and −0.0080 for V_{m2} as per eq 3 indicate the closeness of the aromatic character of naphthalene to that of benzene.

$$\sum_{i=1}^{3} \Delta\lambda_i = (\lambda_{1(system)} - \lambda_{1(benzene)})$$
$$+ (\lambda_{2(system)} - \lambda_{2(benzene)})$$
$$+ (\lambda_{3(system)} - \lambda_{3(benzene)}) \quad (3)$$

The total deviation in the eigenvalues, $\sum_{i=1}^{3}\Delta\lambda_i$, gives an overall idea about the proximity of the local aromatic character of the system to that of benzene.

The $\sum_{i=1}^{3}\Delta\lambda_i$ corresponding to the most negative V_{m1} is positive for all the systems and falls in the range from 0.0006 to
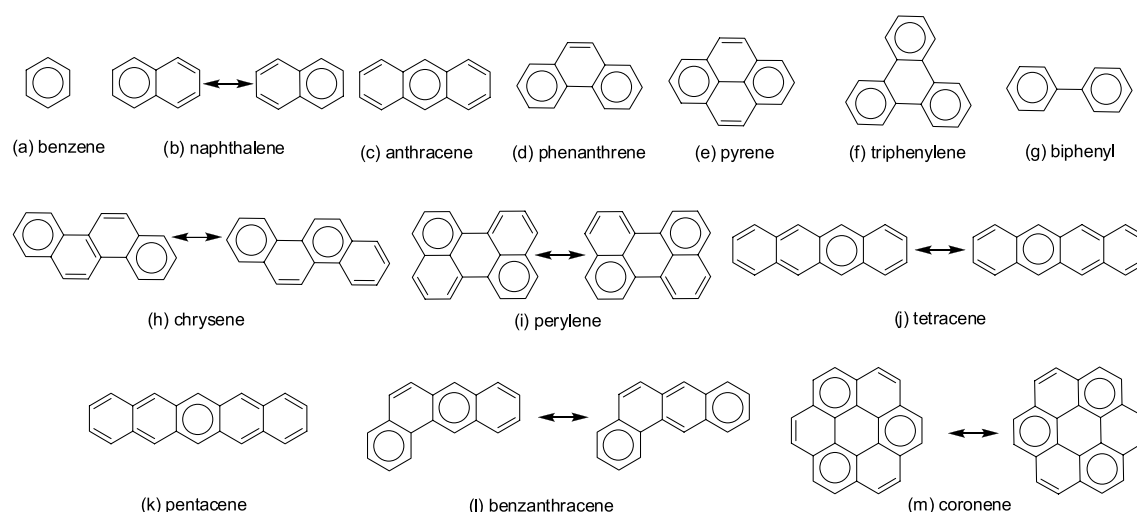
Figure 5. MESP topography-based Clar's aromatic sextets of polycyclic aromatic systems. See text for details.

0.0104 au. Along the linear polyacene series (naphthalene, anthracene, tetracene, and pentacene), $\sum_{i=1}^{3}\Delta\lambda_i$ values for V_{m1} show a gradual increase in the positive character, which can be attributed to a gradual change in character of the corresponding CC bond from a delocalized to a more localized double bond. In fact, higher polyacenes are susceptible to addition reactions due to the dilution of aromatic character as per Clar's theory.[30] In general, a positive value for $\sum_{i=1}^{3}\Delta\lambda_i$ can be assigned to a relatively more electron-rich CC bond region in the molecule, whereas that corresponding to other V_m values shows both positive and negative deviations. The rings possessing small magnitude for $\sum_{i=1}^{3}\Delta\lambda_i$ may be regarded as more aromatic than the rings showing higher values (cf. Table 1). Among all the systems, the least deviation is shown by biphenyl[45] suggesting that the extent of aromaticity exhibited by each ring of this molecule is almost equal to that of benzene. A large deviation of $\sum_{i=1}^{3}\Delta\lambda_i$ from zero is a signature that the CC bond nearest to that CP is a more localized double bond. For instance, the magnitude of $\sum_{i=1}^{3}\Delta\lambda_i$ corresponding to the CC bond nearest to V_{m3} of phenanthrene (1.36 Å), V_{m1} of pyrene (1.36 Å), V_{m4} of benzanthracene (1.35 Å), and V_{m1} of pentacene (1.36 Å) is higher than 0.010, suggesting that they are the most localized (the shortest) among all the CC bonds studied herein. Also CPs of those V_m fall directly on top of the CC bond rather than in the interior of the ring. Can we explain the aromatic sextet concept of Clar[69] using MESP topography? The MESP analysis would suggest that the perfect sextet representation is only possible for benzene whereas the most likely sextet representation of PBH systems[70−72] would require the combination of localized double bonds and sextets as well as their resonance forms. The ring that contains CPs showing numerically small deviation in the sum of eigenvalues constitutes an aromatic sextet. In naphthalene, the smallest $\sum_{i=1}^{3}\Delta\lambda_i$ is 0.0062 au, and this value is identical for both the rings, due to symmetry. Hence, naphthalene may be represented as a resonance hybrid of two structures as shown in Figure 5b. Similarly, perylene appears as a union of two naphthalene moieties and is represented by two resonance forms, whereas a single sextet representation is ideal for triphenylene. Also, a hybrid of two resonance forms (Figure 5m) can bring out the π-delocalization features of coronene. In perylene, triphenylene, and coronene, less positive $\sum_{i=1}^{3}\Delta\lambda_i$ than naphthalene is seen, indicating that they are more

aromatic than the latter. Moreover, the middle ring of perylene, triphenylene, and coronene is devoid of π-character in the sextet representation, which is regarded as an "empty ring" in Clar's theory.[73,74] Triphenylene is an example of a fully benzenoid hydrocarbon in Clar's theory as it can be described as cyclically connected three benzene moieties. The ring represented with a sextet for pyrene has $\sum_{i=1}^{3}\Delta\lambda_i$ = 0.0011 au and its CC bonds depicted as double bonds show $\sum_{i=1}^{3}\Delta\lambda_i$ = 0.0104 au (Figure 5e). Similar criteria are used for making the representation of chrysene and benzanthracene. For anthracene, the middle ring having $\sum_{i=1}^{3}\Delta\lambda_i$ = 0.0033 au is proposed for sextet representation, while the peripheral rings show relatively more localized CC bonds (Figure 5c).[30] As the number of rings increases in a linear way (linear polyacenes), the $\sum_{i=1}^{3}\Delta\lambda_i$ value of the terminal rings increases gradually (0.0098 au for tetracene and 0.0103 au for pentacene) indicating more localized character of the corresponding CC bonds. The $\sum_{i=1}^{3}\Delta\lambda_i$ values for the interior rings of tetracene and pentacene are negative and smaller in magnitude compared to the terminal rings suggesting more delocalized but less electron dense features of them. The interior rings are considered more aromatic than the terminal ones on the basis of more delocalization of π-electrons, and accordingly, the sextet representations given in Figure 5j,k are best suited for tetracene and pentacene,[30] respectively. Clar also proposed the "aromatic dilution" concept for linear polyacene systems to describe the decreasing aromatic character of them with an increase in size. This occurs due to the possibility of drawing only one sextet for linear polyacenes and that sextet can be on any of the rings while the rest of the rings are represented with alternate single and double bonds. Since one sextet is "diluted" over several rings, aromatic dilution occurs as the size increases. The MESP-based analysis of aromatic character of linear polyacenes suggests that with the increase in the size of the system, the aromatic character of the terminal rings decreases more significantly than the rest and the middle rings are more suitable for sextet representation.

Alkenes and Alkynes. MESP topography of ethylene and linear polyenes up to dodeca-1,3,5,7,9,11-hexaene is also studied as prototype nonaromatic systems. Ethylene possesses a localized π-bond while π-bonds show a delocalized character in the larger linear polyenes. As expected, the most localized π-bond of ethylene shows the most negative V_m at −18.6 kcal/

mol, located over the midpoint of the CC bond, 1.73 Å away from the molecular plane. The alternate double and single CC bond distribution in polyenes is clearly seen in MESP topography, wherein the V_m points are always located over the double bonds while the formal CC single bonds are borne out to be devoid of a minimum in MESP (cf. Figure 6). In
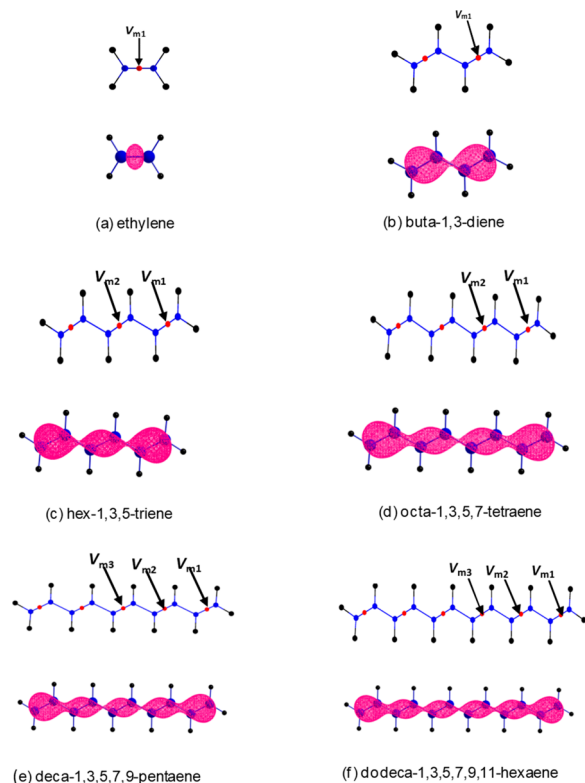

Figure 6. MESP topography of linear conjugated systems (top). MESP isosurface plots (bottom) show the π-delocalization pattern. Isosurface value is −13.0 kcal/mol for ethylene and −11.0 kcal/mol for all others. See text for details.

linear polyenes, the most negative V_m is always found on the terminal double bond while the negative character of V_m decreases toward the central region as the length of polyene increases (Table 2). The eigenvalues λ_1, λ_2, and λ_3 for the ethylene molecule are 0.0277, 0.0176, and 0.0073 au, respectively, which obeys $\lambda_1 > \lambda_2 > \lambda_3 \cong 0$. Further, with respect to benzene V_m as a reference, the $\Delta\lambda_1$, $\Delta\lambda_2$, and $\Delta\lambda_3$ for ethylene are 0.0135, 0.0151, and 0.0068 au, respectively, with $\sum_{i=1}^3 \Delta\lambda_i$ being 0.0354 au. The high values of $\sum_{i=1}^3 \Delta\lambda_i$ indicate the localized nature of the CC bond in ethylene. The $\sum_{i=1}^3 \Delta\lambda_i$ value for all the linear polyenes falls in the range 0.027 to 0.013 au. The smaller magnitude of $\sum_{i=1}^3 \Delta\lambda_i$ than ethylene indicating the delocalized nature of the π-electrons in polyenes. In PBH systems, the most localized CC bonds show $\sum_{i=1}^3 \Delta\lambda_i$ around 0.010 au and the smallest $\sum_{i=1}^3 \Delta\lambda_i$ observed for linear polyenes is higher than this value. Hence, we propose that irrespective of the nature of π-conjugation, $\sum_{i=1}^3 \Delta\lambda_i$ value $\geq$ 0.011 au may be regarded as a largely localized (nonaromatic) double bond.

The distribution of electron density and critical points in alkyne systems is different from that of alkenes. Ethyne and buta-1,3-diyne are the two systems we consider for the study. Ethyne consists of set of degenerate CPs located at −18.4 kcal/mol and distributed uniformly around the CC triple bond in a circular manner (Figure 7). The eigenvalues λ_1, λ_2, and λ_3

Table 2. MESP Topography Features[a] of Linear Conjugated Systems

molecule	V_m label	V_m	λ_1	λ_2	λ_3	$\sum_{i=1}^3 \Delta\lambda_i$
ethylene	V_{m1}	−18.6	0.0277	0.0176	0.0073	0.0354
buta-1,3-diene	V_{m1}	−16.8	0.0232	0.0135	0.0071	0.0266
hexa-1,3,5-triene	V_{m1}	−16.7	0.0231	0.0131	0.0070	0.0260
	V_{m2}	−14.4	0.0176	0.0092	0.0060	0.0156
octa-1,3,5,7-tetraene	V_{m1}	−16.7	0.0232	0.0129	0.0070	0.0259
	V_{m2}	−14.1	0.0173	0.0089	0.0056	0.0146
deca-1,3,5,7,9-pentaene	V_{m1}	−16.8	0.0232	0.0129	0.0069	0.0258
	V_{m2}	−14.1	0.0173	0.0087	0.0055	0.0143
	V_{m3}	−13.7	0.0170	0.0085	0.0052	0.0135
dodeca-1,3,5,7,9,11-hexaene	V_{m1}	−16.9	0.0233	0.0128	0.0069	0.0258
	V_{m2}	−14.1	0.0173	0.0087	0.0054	0.0142
	V_{m3}	−13.7	0.0169	0.0084	0.0050	0.0131
ethyne	V_{m1}	−18.4	0.0290	0.0223	0.0000	0.0341
buta-1,3-diyne	V_{m1}	−12.1	0.0175	0.0126	0.0000	0.0129

[a] V_m in kcal/mol and the respective eigenvalues λ_1, λ_2, and λ_3 in au. See text for details.
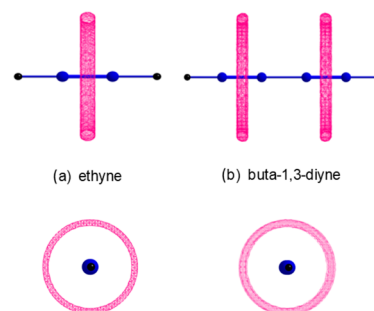

Figure 7. Degenerate MESP isosurface plots depict the π-delocalization patterns. Isosurface value −18.0 kcal/mol for ethyne and −11.5 for buta-1,3-diyne. See text for details.

corresponding to V_{m1} are 0.0290, 0.0223, and 0.0000 au, respectively and follow the trend $\lambda_1 > \lambda_2 > \lambda_3 = 0$. The $\sum_{i=1}^3 \Delta\lambda_i$ for V_{m1} is 0.0341 au indicating the more localized electron density around the triple bond. Similarly, buta-1,3-diyne consists of equivalent CPs located at −12.1 kcal/mol and a circular distribution of CPs is seen around both the triple bonded regions. The λ_1, λ_2, and λ_3 values corresponding to V_{m1} are 0.0175, 0.0126, and 0.0000 au and follow the trend $\lambda_1 > \lambda_2 > \lambda_3 = 0$; the total deviation $\sum_{i=1}^3 \Delta\lambda_i$ is 0.0129 au indicating significant reduction in the localized distribution of electron density when compared to ethyne.

Antiaromatic and Non-benzenoid Hydrocarbons. The antiaromatic cyclobutadiene[75] is characterized by alternate CC single (1.57 Å) and double (1.33 Å) bonds. As expected, several V_m points with identical MESP minimum value are located for the CC double bonds with value −18.4 kcal/mol and distance of separation from the molecular plane 1.62 Å. The V_m value of cyclobutadiene is very similar to that of the localized CC bond of ethylene while the bond distance is significantly shorter than that in ethylene. The eigenvalues λ_1,
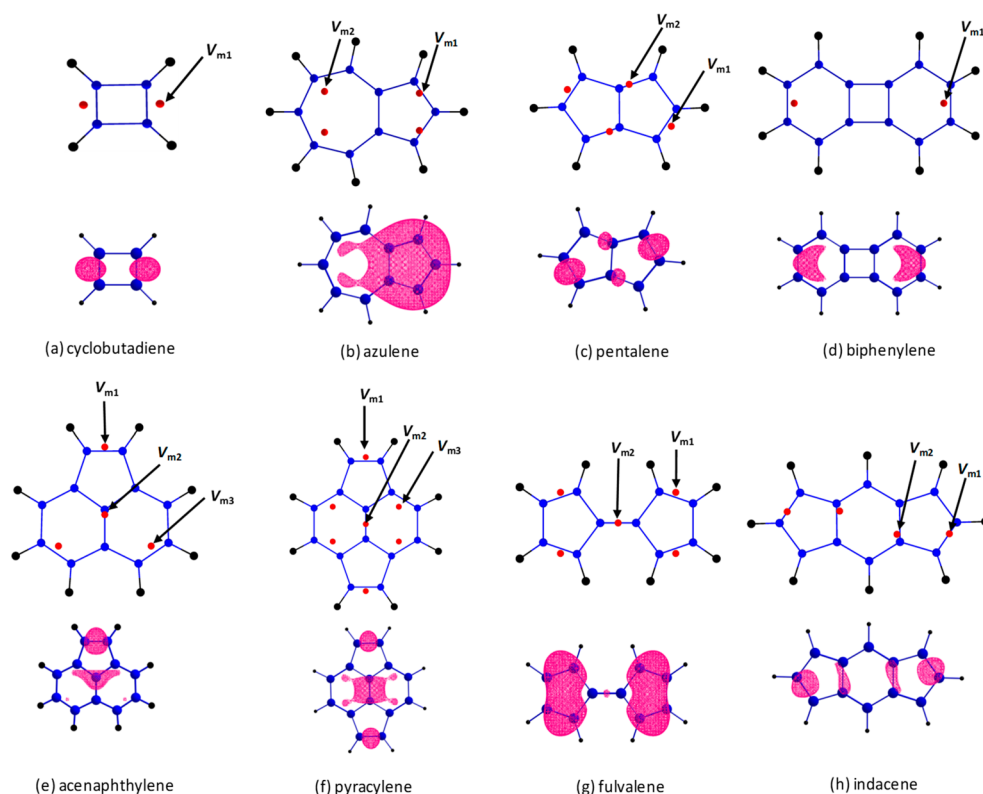
Figure 8. MESP topography of cyclobutadiene and other non-benzenoid systems (top). MESP isosurface plots (bottom) show the delocalization pattern. An appropriate MESP value in the range −11.0 to −14.5 kcal/mol is selected for isosurface. See text for details.

Table 3. MESP Topography Features of Cyclobutadiene and Other Non-benzenoid Systems[a]

molecule	V_m label	V_m	λ_1	λ_2	λ_3	$\sum_{i=1}^{3}\Delta\lambda_i$
cyclobutadiene	V_{m1}	−18.4	0.0270	0.0182	0.0102	0.0382
azulene	V_{m1}	−18.9	0.0198	0.0059	0.0031	0.0116
	V_{m2}	−11.3	0.0103	0.0029	0.0009	−0.0030
pentalene	V_{m1}	−17.8	0.0230	0.0130	0.0074	0.0263
	V_{m2}	−15.0	0.0169	0.0057	0.0035	0.0088
biphenylene	V_{m1}	−15.1	0.0156	0.0038	0.0035	0.0057
acenaphthylene	V_{m1}	−17.6	0.0214	0.0111	0.0071	0.0224
	V_{m2}	−14.5	0.0112	0.0016	0.0012	−0.0032
	V_{m3}	−13.9	0.0139	0.0041	0.0029	0.0037
pyracylene	V_{m1}	−15.9	0.0204	0.0115	0.0072	0.0219
	V_{m2}	−14.4	0.0106	0.0022	0.0021	−0.0023
	V_{m3}	−13.2	0.0109	0.0023	0.0015	−0.0025
fulvalene	V_{m1}	−16.1	0.0211	0.0110	0.0071	0.0220
	V_{m2}	−10.8	0.0073	0.0015	0.0012	−0.0072
indacene	V_{m1}	−16.6	0.0194	0.0068	0.0048	0.0138
	V_{m2}	−14.8	0.0132	0.0024	0.0008	−0.0008

[a]V_m in kcal/mol and the respective eigenvalues λ_1, λ_2, and λ_3 in au. See text for details.

λ_2, and λ_3 are 0.0270, 0.0182, and 0.0102 au, respectively, suggesting that $\lambda_1 > \lambda_2 > \lambda_3$ where λ_3 is not close to zero. The deviations $\Delta\lambda_1$, $\Delta\lambda_2$, and $\Delta\lambda_3$ with respect to benzene are 0.0128, 0.0157, and 0.0097 au, with the total deviation $\sum_{i=1}^{3}\Delta\lambda_i$ being 0.0382 au. Among all the molecules studied, the cyclobutadiene molecule exhibits the highest $\sum_{i=1}^{3}\Delta\lambda_i$ indicating the highly localized nature of the π-bonds. The MESP topography of cyclobutadiene is shown in Figure 8a, and the respective V_m and eigenvalues are listed in Table 3.

Azulene consists of two nonequivalent CPs (V_{m1}, V_{m2}) on each side of the molecular plane. A set of two equivalent CPs (V_{m1}) located at −18.9 kcal/mol is associated with the five-

membered ring and another set of two degenerate CPs (V_{m2}) at −11.3 kcal/mol is associated with the seven-membered ring of the molecule and CPs are aligned interior to the ring (Figure 8b). The λ_1, λ_2, and λ_3 eigenvalues corresponding to V_{m1} are 0.0198, 0.0059, and 0.0031 au and those of V_{m2} are 0.0103, 0.0029, and 0.0009 au, respectively, and they follow the trend $\lambda_1 \gg \lambda_2 > \lambda_3 \cong 0$, which is similar to PBHs. The $\Delta\lambda_1$, $\Delta\lambda_2$, and $\Delta\lambda_3$ values corresponding to V_{m1} are 0.0056, 0.0033, and 0.0026 au and those corresponding to V_{m2} are −0.0038, 0.0004, and 0.0004 au, respectively. The $\sum_{i=1}^{3}\Delta\lambda_i$ for V_{m1} is 0.0116 au and that of V_{m2} is −0.0030 au, which indicate that the five-membered ring possesses more localized electron

density distribution similar to nonaromatic systems while the seven-membered ring has more delocalized electron density distribution similar to aromatic hydrocarbons. The $\sum_{i=1}^{3}\Delta\lambda_i$ based assessment of aromaticity fully supports the conventional view[23] that the seven-membered ring of azulene is more aromatic than the five-membered one.

In pentalene, the CC bonds close to V_{m1} and V_{m2} show more double bond character (1.35 Å) than the rest (1.47 Å). V_{m1} is −17.8 kcal/mol and its eigenvalues λ_1, λ_2, and λ_3 are 0.0230, 0.0130, and 0.0074 au, respectively. Since $\lambda_1 > \lambda_2 > \lambda_3$ and $\sum_{i=1}^{3}\Delta\lambda_i$ = 0.0263 au, olefinic character can be assigned to these bonds, which are susceptible to addition reactions. The V_{m2} appears at −15.0 kcal/mol with eigenvalues 0.0169, 0.0057, and 0.0035 au. Here $\lambda_1 \gg \lambda_2 > \lambda_3$ and $\sum_{i=1}^{3}\Delta\lambda_i$ is 0.0088 au indicating the aromatic character of these bonds, which may resist addition reactions. The $\sum_{i=1}^{3}\Delta\lambda_i$ based assessment suggests that aromatic character is limited only to very few CC bonds in pentalene,[45] and the molecule can be considered as largely nonaromatic in nature. Biphenylene[45,76] shows a V_m at −15.1 kcal/mol with eigenvalues 0.0156, 0.0038, and 0.0035 au showing the trend $\lambda_1 \gg \lambda_2 > \lambda_3 \cong 0$ and $\sum_{i=1}^{3}\Delta\lambda_i$ 0.0057 au indicating that the aromatic character of the molecule is very similar to that of benzene.

Acenaphthylene[77,78] shows three nondegenerate CPs, V_{m1}, V_{m2}, and V_{m3}, at −17.6, −14.5, and −13.9 kcal/mol, respectively. The eigenvalues corresponding to V_{m1} show $\lambda_1 > \lambda_2 > \lambda_3 \cong 0$ and $\sum_{i=1}^{3}\Delta\lambda_i$ is 0.0224 au. The CC bond corresponding to V_{m1} is clearly a double bond and suggests nonaromatic character for the five-membered ring. The CP for this bond is located exterior to the ring and indicates the strain in the ring. The CPs of V_{m2} and V_{m3} are located over the six-membered rings and both follow the trend $\lambda_1 \gg \lambda_2 > \lambda_3 \cong 0$ with $\sum_{i=1}^{3}\Delta\lambda_i$ = −0.0032 au for the former and 0.0037 au for the latter suggesting the strong aromatic character for the naphthalene-like region in the molecule. Very similar behavior is observed in pyraclene[77,79] wherein the naphthalene-like moiety exhibits aromatic character whereas both the five membered rings show nonaromatic character due to the presence of a localized double bond.

Fulvalene consists of a set of four equivalent CPs (V_{m1}) at −16.1 kcal/mol, located near the π-region of the five-membered rings (above and below) and a set of equivalent CPs (V_{m2}) at −10.8 kcal/mol located exactly over the middle of the central bond that connects both five-membered rings. The eigenvalues of V_{m1} follow the trend $\lambda_1 > \lambda_2 > \lambda_3 \cong 0$ and $\sum_{i=1}^{3}\Delta\lambda_i$ is 0.0220 au, indicating nonaromatic behavior of the rings. Indacene is characterized by two nonequivalent CPs V_{m1} and V_{m2} at −16.6 and −14.8 kcal/mol on each side of the molecular plane. The eigenvalues of both CPs follow the trend $\lambda_1 \gg \lambda_2 > \lambda_3 \cong 0$ whereas $\sum_{i=1}^{3}\Delta\lambda_i$ is 0.0138 au for V_{m1} and −0.0008 au for V_{m2}. The $\sum_{i=1}^{3}\Delta\lambda_i$ value close to zero for V_{m2} indicates strong aromatic character for the six-membered ring, while the five-membered rings must behave as nonaromatic.

Annulenes. We extended the analysis to some higher annulenes[80,81] in order to test the reliability of the $\sum_{i=1}^{3}\Delta\lambda_i$ parameter to assess aromaticity or nonaromaticity (Table 4). The 14- and 18-annulenes are well-known aromatic systems, while the 16-annulene is always regarded as nonaromatic. The 14-annulene shows three nonequivalent CPs (V_{m1}, V_{m2}, V_{m3}) on each side of the molecular plane (Figure 9). The V_{m1} points show value −13.3 kcal/mol, and their eigenvalues λ_1, λ_2, and λ_3 are 0.0146, 0.0051, and 0.0018 au, respectively. V_{m2} is at −12.1 kcal/mol with eigenvalues 0.0138, 0.0056, and 0.0006 au.

Table 4. MESP Topography Features[a] of Annulene Systems

molecule	V_m label	V_m	λ_1	λ_2	λ_3	$\sum_{i=1}^{3}\Delta\lambda_i$
14-annulene	V_{m1}	−13.3	0.0146	0.0051	0.0018	0.0043
	V_{m2}	−12.1	0.0138	0.0056	0.0006	0.0027
	V_{m3}	−10.8	0.0119	0.0069	0.0002	0.0017
16-annulene	V_{m1}	−14.7	0.0195	0.0102	0.0055	0.0180
	V_{m2}	−14.6	0.0191	0.0093	0.0072	0.0184
	V_{m3}	−13.9	0.0177	0.0093	0.0042	0.0139
	V_{m4}	−12.1	0.0169	0.0093	0.0062	0.0152
18-annulene	V_{m1}	−12.7	0.0134	0.0055	0.0011	0.0027
	V_{m2}	−12.6	0.0137	0.0064	0.0005	0.0034

[a]V_m in kcal/mol and the respective eigenvalues λ_1, λ_2, and λ_3 in au. See text for details.
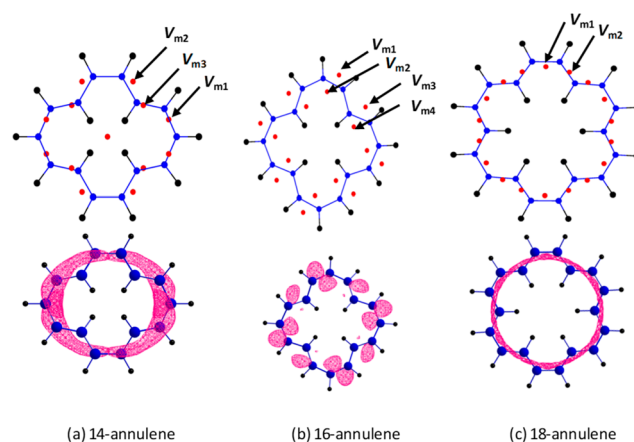

Figure 9. MESP topography of annulene systems (top). MESP isosurface plots (bottom) show the delocalization pattern. Isosurface value is −11.0 kcal/mol for all the systems. See text for details.

These CPs are aligned slightly exterior to the ring boundary. V_{m3} is located at −10.8 kcal/mol with eigenvalues 0.0119, 0.0069, and 0.0002. These CPs are seen more toward the interior of the ring. The eigenvalues of V_{m1}, V_{m2}, and V_{m3} follow the trend $\lambda_1 \gg \lambda_2 > \lambda_3 \cong 0$, which resembles that of PBHs. The $\sum_{i=1}^{3}\Delta\lambda_i$ values for V_{m1}, V_{m2}, and V_{m3} are 0.0043, 0.0017, and 0.0027 indicating more delocalized electron density distribution rather akin to PBHs. In 18-annulene, there are two nonequivalent CPs (V_{m1}, V_{m2}) located at −12.7 and −12.6 kcal/mol, and the eigenvalues corresponding to V_{m1} are 0.0134, 0.0055, and 0.0011 au and those corresponding to V_{m2} are 0.0137, 0.0064, and 0.0005 au, both following the trend $\lambda_1 \gg \lambda_2 > \lambda_3 \cong 0$. Also the $\sum_{i=1}^{3}\Delta\lambda_i$ for V_{m1} is 0.0027 au and that for V_{m2} is 0.0034 au indicating the closeness of aromatic character of the molecule to that of benzene.[82,83]

In 16-annulene, four nonequivalent CPs (V_{m1}, V_{m2}, V_{m3}, V_{m4}) are located at −14.7, −14.6, −13.9, and −12.1 kcal/mol. The eigenvalues corresponding to these minima (in au) are as follows. V_{m1}, 0.0195, 0.0102, and 0.0055; V_{m2}, 0.0191, 0.0093, and 0.0072; V_{m3}, 0.0177, 0.0093, and 0.0042; and V_{m4}, 0.0169, 0.0093, and 0.0062. It is very clear that the trend in λ values ($\lambda_1 > \lambda_2 > \lambda_3 \cong 0$) is very similar to that of alkenes and significantly differs from that observed for 14- and 18-annulenes. Moreover, $\sum_{i=1}^{3}\Delta\lambda_i$ for 16-annulene is 0.0180 au for V_{m1}, 0.0184 au for V_{m2}, 0.0139 au for V_{m3}, and 0.0152 au for V_{m4}. These values are greater than 0.01 au indicating the localized distribution of electron density over π-regions. Thus, the classic nonaromatic character of the cyclic π-electrons in
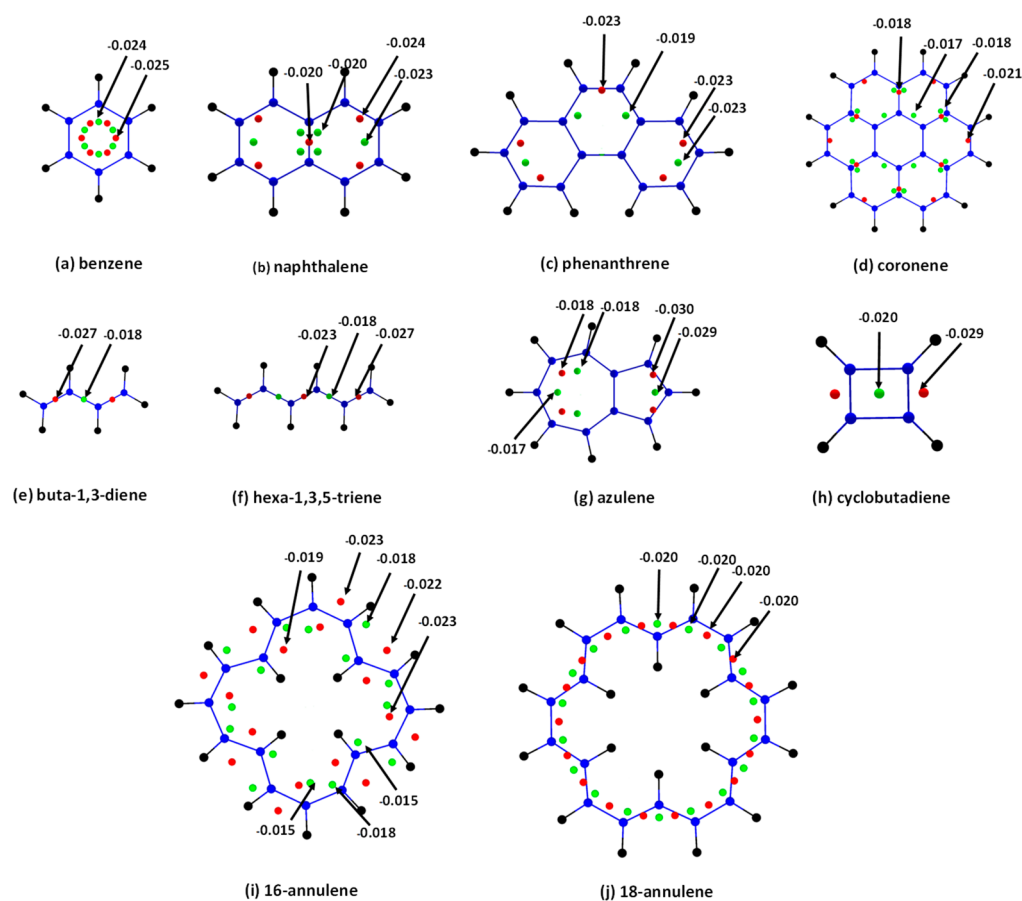
Figure 10. Topography of (3, +1) critical points in selected set of systems. See text for details.

16-annulene as pointed out in the literature[84] is clearly brought out by $\sum_{i=1}^{3}\Delta\lambda_i$.

(3, +1) Critical Points. So far the π-conjugation features have been addressed on the basis of the value of MESP minimum V_m and the respective eigenvalues. The V_m value gives information about the electron rich character of the molecular system at various locations, while the eigenvalues provide a way to assess the localized and delocalized nature of the π-conjugation. In MESP topography, several (3, +1) CPs can be located in the π-region, which normally appear in between two (3, +3) CPs. Some representative cases are shown in Figure 10. From the location of such (3, +1) CPs (saddle points), the function value increases in one direction and decreases in the other two directions of space. In aromatic systems such as benzene, naphthalene, phenanthrene, and coronene, the MESP value of a (3, +1) CP is very close to that of the adjacent (3, +3) CP indicating a smooth, nearly uniform distribution of MESP over the ring. If two adjacent (3, +3) and (3, +1) CPs show more deviation in the values, it may indicate the decreasing delocalization effect as well as lower aromaticity at that region compared to other parts. For instance, in phenanthrene, the middle ring is less delocalized than the other two rings. Similarly, in 18-annulene, almost an even distribution of π-electron density is observed, while 16-annulene shows more localized distribution. Moreover, analysis of both types of CPs of azulene clearly indicates that the seven membered ring has a uniform distribution of MESP. Though its five-membered ring features similar data, the high magnitude of the CPs and $\sum_{i=1}^{3}\Delta\lambda_i$ of (3, +3) CP indicate the localized nature of the π-electron density. In olefins, a clear

distinction between (3, +3) and (3, +1) CPs is possible on the basis of their MESP values. The significantly less negative (3, +1) CPs appear over the formally single-bonded region of the molecules (cf. Figure 10). A remarkable difference in (3, +3) and (3, +1) CP values is observed for the antiaromatic cyclobutadiene molecule indicating more localized nature of electron density, where (3, +1) CPs are located in the interior and (3, +3) CPs lie somewhat exterior to the ring.

■ CONCLUDING REMARKS

MESP topography analysis has been carried out on a large variety of π-conjugated hydrocarbons using B3LYP/6-311+G-(d,p) level theory. The negative regions observed in the MESP distribution correlate well with the delocalized and localized distribution of the π-electrons in aromatic, antiaromatic, nonaromatic, annulene, and hybrid systems. In the case of polycyclic benzenoid hydrocarbons (PBHs), MESP CPs are located interior to the six-membered rings, whereas they lie exactly on top and bottom of the π-regions in linear polyenes. In strained systems, CPs lie outside the boundary of the ring. The eigenvalues follow the trend $\lambda_1 \gg \lambda_2 > \lambda_3 \cong 0$ in PBHs, $\lambda_1 > \lambda_2 > \lambda_3 \cong 0$ in linear polyenes (nonaromatic), and $\lambda_1 > \lambda_2 > \lambda_3 \neq 0$ in antiaromatic systems. Benzene is considered as a perfect aromatic system, and the imperfection in the aromatic character of a PBH system is measured in terms of the deviations $\Delta\lambda_1$, $\Delta\lambda_2$, and $\Delta\lambda_3$ with respect to the corresponding eigenvalues of the benzene molecule. The eigenvalue analysis clearly shows that the total deviation $\sum_{i=1}^{3}\Delta\lambda_i$ very close to zero is an indicative of strong aromatic character of that region. PBH systems showed $\sum_{i=1}^{3}\Delta\lambda_i \leq$

0.011 for most of the rings, while cases such as phenanthrene, pyrene, benzanthracene, and pentacene showed $\sum_{i=1}^{3}\Delta\lambda_i \geq$ 0.011 au for rings containing localized CC bonds. Further, a clear distinction of the delocalized and localized regions of a PBH led to the identification of the most prominent Clar's aromatic sextet structures. The $\sum_{i=1}^{3}\Delta\lambda_i$ values of all the alkenes and alkynes examined in the present work fall in the range 0.011 to 0.035 au, whereas antiaromatic systems such as cyclobutadiene showed $\sum_{i=1}^{3}\Delta\lambda_i \geq 0.035$ au. Since each molecule possesses a unique distribution of π-electrons, the MESP eigenvalue based analysis of aromaticity is extended to study non-PBH systems consisting of strained CC bonds such as azulene, pentalene, etc. The ring strain plays an important role in the distribution of CPs along the π-regions. They occupy positions outside the projected ring periphery. Most of these non-PBH systems show a hybrid character of aromaticity and nonaromaticity. For instance, in azulene, the seven-membered ring shows clearly aromatic character, whereas the five membered ring is nonaromatic in nature. Likewise, a blend of aromatic and nonaromatic behavior is seen in some other hybrid systems. In the case of 14- and 18-annulenes, the eigenvalues and $\sum_{i=1}^{3}\Delta\lambda_i$ parameter are close to that of PBHs, indicating closeness of aromatic character of the system to that of benzene. However, in 16-annulene, the eigenvalue sum parameter strongly supports its nonaromatic behavior. The dependence of the $\sum_{i=1}^{3}\Delta\lambda_i$ parameter on aromatic character of molecules is illustrated schematically in Figure 11.
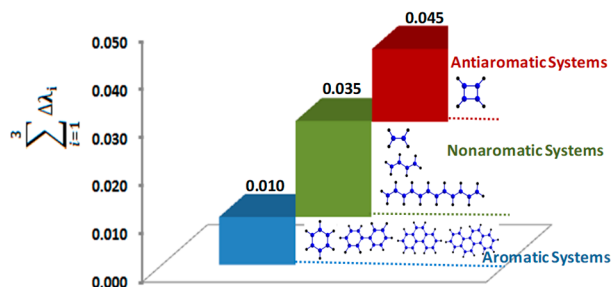

Figure 11. Variation of $\sum_{i=1}^{3}\Delta\lambda_i$ with aromaticity.

Also the π-conjugation features of the molecular systems have been related to the (3, +1) CP distribution. The localized nature of π-electron distribution is revealed when two adjacent (3, +3) and (3, +1) CPs show greater deviation in their MESP values, whereas for aromatic systems, the MESP values of (3, +3) and (3, +1) CPs are more uniform.

Aromaticity is a multidimensional phenomenon, for which different explanations have been developed in terms of structural, magnetic, energetic, and electronic criteria due to various landmark studies. The electrostatic topographical viewpoint of aromaticity elaborated in this work adds a new dimension to aromaticity. This viewpoint focusing on position and value of MESP minima, as well as the corresponding eigenvalues, is a very simple and effective way to make a quick and general, in-depth assessment of localized or delocalized distribution of π-electrons in cyclic, acyclic, and strained-cyclic unsaturated hydrocarbon systems.

ASSOCIATED CONTENT

Ⓢ Supporting Information

The Supporting Information is available free of charge on the ACS Publications website at DOI: 10.1021/acs.jpca.9b09056.

Detailed MESP topographical features from different methods and Cartesian coordinates of all the systems (PDF)

AUTHOR INFORMATION

Corresponding Authors
*S.R.G. E-mail: gadre@unipune.ac.in.
*C.H.S. E-mail: sureshch@niist.res.in. Tel: +91-471-2515472. Homepage: http://www.niist.res.in/chsuresh.

ORCID Ⓞ
Cherumuttathu H. Suresh: 0000-0001-7237-6638
Shridhar R. Gadre: 0000-0003-3234-3959

Notes
The authors declare no competing financial interest.

REFERENCES

(1) Krygowski, T.; Cyranski, M.; Czarnocki, Z.; Häfelinger, G.; Katritzky, A. R. Aromaticity: a theoretical concept of immense practical importance. *Tetrahedron* **2000**, *56*, 1783−1796.

(2) Cyranski, M. K.; Krygowski, T. M.; Katritzky, A. R.; Schleyer, P. v. R. To what extent can aromaticity be defined uniquely? *J. Org. Chem.* **2002**, *67*, 1333−1338.

(3) Krygowski, T. M.; Cyrański, M. K. Structural aspects of aromaticity. *Chem. Rev.* **2001**, *101*, 1385−1420.

(4) Schleyer, P. v. R. Introduction: Aromaticity. *Chem. Rev.* **2001**, *101*, 1115−1118.

(5) Jug, K.; Köster, A. M. Aromaticity as a multi-dimensional phenomenon. *J. Phys. Org. Chem.* **1991**, *4*, 163−169.

(6) Glukhovtsev, M. Aromaticity Today: Energetic and Structural Criteria. *J. Chem. Educ.* **1997**, *74*, 132.

(7) Klein, D.; Trinajstic, N. Foundations of conjugated circuit models. *Pure Appl. Chem.* **1989**, *61*, 2107−2115.

(8) Ciesielski, A.; Krygowski, T. M.; Cyrański, M. K.; Balaban, A. T. Defining rules of aromaticity: a unified approach to the Hückel, Clar and Randić concepts. *Phys. Chem. Chem. Phys.* **2011**, *13*, 3737−3747.

(9) Kikuchi, S. A History of the Structural Theory of Benzene - The Aromatic Sextet Rule and Hückel's Rule. *J. Chem. Educ.* **1997**, *74*, 194.

(10) Klein, D. J.; Trinajstic, N. Hückel rules and electron correlation. *J. Am. Chem. Soc.* **1984**, *106*, 8050−8056.

(11) Kruszewski, J.; Krygowski, T. M. An Extension of the Hückel 4N+2 Rule to Polycyclic Non-alternant Conjugated Hydrocarbons. *Can. J. Chem.* **1975**, *53*, 945−951.

(12) Miliordos, E. Hückel versus Mobius aromaticity: The particle in a cylinder versus a Mobius strip. *Phys. Rev. A: At., Mol., Opt. Phys.* **2010**, *82*, 062118.

(13) Trinajstić, N. New developments in Hückel theory. *Int. J. Quantum Chem.* **1977**, *12*, 469−477.

(14) Zhao, L.; Grande-Aztatzi, R.; Foroutan-Nejad, C.; Ugalde, J. M.; Frenking, G. Aromaticity, the Hückel 4n+2 rule and magnetic current. *ChemistrySelect* **2017**, *2*, 863−870.

(15) Dannenberg, J. J.; Rios, R. Theoretical Study of the Enolic Forms of Acetylacetone. How Strong Is the Hydrogen Bond? *J. Phys. Chem.* **1994**, *98*, 6714−6718.

(16) Masui, H. Metalloaromaticity. *Coord. Chem. Rev.* **2001**, *219−221*, 957−992.

(17) Kleinpeter, E.; Koch, A. Chelatoaromaticity—existing: yes or no? An answer given by spatial magnetic properties (through space NMR shieldings—TSNMRS). *Phys. Chem. Chem. Phys.* **2011**, *13*, 20593−20601.

(18) Kudavalli, J. S.; Boyd, D. R.; Coyne, D.; Keeffe, J. R.; Lawlor, D. A.; MacCormac, A. C.; More O'Ferrall, R. A.; Rao, S. N.; Sharma, N. D. Hyperaromatic Stabilization of Arenium Ions. *Org. Lett.* **2010**, *12*, 5550−5553.

(19) Karadakov, P. B. Ground- and Excited-State Aromaticity and Antiaromaticity in Benzene and Cyclobutadiene. *J. Phys. Chem. A* **2008**, *112*, 7303−7309.

(20) Williams, R. V. Homoaromaticity. *Chem. Rev.* **2001**, *101*, 1185−1204.

(21) Shaik, S. S.; Hiberty, P. C.; Lefour, J. M.; Ohanessian, G. Is delocalization a driving force in chemistry? Benzene, allyl radical, cyclobutadiene, and their isoelectronic species. *J. Am. Chem. Soc.* **1987**, *109*, 363−374.

(22) Zborowski, K. K.; Solà, M.; Poater, J.; Proniewicz, L. M. Theoretical studies on aromaticity of selected hydroxypyrones. Part 3#. Chelatoaromaticity phenomenon in metalcomplexes of hydroxypyrones. *J. Phys. Org. Chem.* **2011**, *24*, 499−506.

(23) Dominikowska, J.; Palusiak, M. EL: the new aromaticity measure based on one-electron density function. *Struct. Chem.* **2012**, *23*, 1173−1183.

(24) Portella, G.; Poater, J.; Sola, M. Assessment of Clar's aromatic π-sextet rule by means of PDI, NICS and HOMA indicators of local aromaticity. *J. Phys. Org. Chem.* **2005**, *18*, 785−791.

(25) Schaad, L.; Hess, B. A comparison of recent theoretical aromaticity indices. *Pure Appl. Chem.* **1982**, *54*, 1097−1114.

(26) Poater, J.; Fradera, X.; Duran, M.; Sola, M. The delocalization index as an electronic aromaticity criterion: application to a series of planar polycyclic aromatic hydrocarbons. *Chem. - Eur. J.* **2003**, *9*, 400−406.

(27) Bultinck, P.; Ponec, R.; Gallegos, A.; Fias, S.; Van Damme, S.; Carbó-Dorcaa, R. Generalized Polansky Index as an aromaticity measure in polycyclic aromatic hydrocarbons. *Croat. Chem. Acta.* **2006**, *79*, 363−371.

(28) Bultinck, P.; Ponec, R.; Van Damme, S. Multicenter bond indices as a new measure of aromaticity in polycyclic aromatic hydrocarbons. *J. Phys. Org. Chem.* **2005**, *18*, 706−718.

(29) Solà, M. Forty years of Clar's aromatic π-sextet rule. *Front. Chem.* **2013**, *1*, 22.

(30) Suresh, C.; Gadre, S. R. Clar's aromatic sextet theory revisited via molecular electrostatic potential topography. *J. Org. Chem.* **1999**, *64*, 2505−2512.

(31) Randić, M.; Balaban, A. T. Local aromaticity and aromatic sextet theory beyond Clar. *Int. J. Quantum Chem.* **2018**, *118*, e25657.

(32) Suresh, C. H.; Ajitha, M. J. DFT Prediction of Multitopic N-Heterocyclic Carbenes Using Clar's Aromatic Sextet Theory. *J. Org. Chem.* **2013**, *78*, 3918−3924.

(33) Randić, M.; Balaban, A. T.; Plavšić, D. Applying the conjugated circuits method to Clar structures of [n] phenylenes for determining resonance energies. *Phys. Chem. Chem. Phys.* **2011**, *13*, 20644−20648.

(34) Wu, J. I.; Dobrowolski, M.; Cyrański, M.; Merner, B.; Bodwell, G.; Mo, Y.; Schleyer, P. On the aromatic stabilization energy of the 4N π electron pyrene. *Mol. Phys.* **2009**, *107*, 1177−1186.

(35) Aihara, J.; Ishida, T.; Kanno, H. Bond resonance energy as an indicator of local aromaticity. *Bull. Chem. Soc. Jpn.* **2007**, *80*, 1518−1521.

(36) Antic, M.; Furtula, B.; Radenkovic, S. Aromaticity of Nonplanar Fully Benzenoid Hydrocarbons. *J. Phys. Chem. A* **2017**, *121*, 3616−3626.

(37) Martin-Martinez, F. J.; Melchor, S.; Dobado, J. A. Clar−Kekule′ structuring in armchair carbon nanotubes. *Org. Lett.* **2008**, *10*, 1991−1994.

(38) Suresh, C. H.; Koga, N. Accurate calculation of aromaticity of benzene and antiaromaticity of cyclobutadiene: new homodesmotic reactions. *J. Org. Chem.* **2002**, *67*, 1965−1968.

(39) Müller, M.; Kübel, C.; Müllen, K. Giant polycyclic aromatic hydrocarbons. *Chem. - Eur. J.* **1998**, *4*, 2099−2109.

(40) Behrens, S.; Koester, A. M.; Jug, K. Delocalization Energy of π Electrons as an Index for Aromaticity of Polycyclic Hydrocarbons. *J. Org. Chem.* **1994**, *59*, 2546−2551.

(41) Bultinck, P. Critical analysis of the local aromaticity concept in polyaromatic hydrocarbons. *Faraday Discuss.* **2007**, *135*, 347−365.

(42) Vijayalakshmi, K. P.; Suresh, C. H. Pictorial representation and validation of Clar's aromatic sextet theory using molecular electrostatic potentials. *New J. Chem.* **2010**, *34*, 2132−2138.

(43) von Schleyer, P. R.; Jiao, H. What is aromaticity? *Pure Appl. Chem.* **1996**, *68*, 209−218.

(44) Behrens, S.; Koester, A. M.; Jug, K. Delocalization Energy of π-Electrons as an Index for Aromaticity of Polycyclic Hydrocarbons. *J. Org. Chem.* **1994**, *59*, 2546−2551.

(45) Giambiagi, M.; Segre de Giambiagi, M.; dos Santos Silva, C. D.; Paiva de Figueiredo, A. P. Multicenter bond indices as a measure of aromaticity. *Phys. Chem. Chem. Phys.* **2000**, *2*, 3381−3392.

(46) Polansky, O. E.; Derflinger, G. Zur Clar'schen Theorie lokaler benzoider Gebiete in kondensierten Aromaten. *Int. J. Quantum Chem.* **1967**, *1*, 379−401.

(47) Gadre, S. R.; Shirsat, R. N. *Electrostatics of atoms and molecules*; Universities Press: 2000.

(48) Deshmukh, M. M.; Gadre, S. R.; Tonner, R.; Frenking, G. Molecular electrostatic potentials of divalent carbon (0) compounds. *Phys. Chem. Chem. Phys.* **2008**, *10*, 2298−2301.

(49) Mathew, J.; Suresh, C. H. Use of molecular electrostatic potential at the carbene carbon as a simple and efficient electronic parameter of N-heterocyclic carbenes. *Inorg. Chem.* **2010**, *49*, 4665−4669.

(50) Gadre, S. R.; Kulkarni, S. A.; Shrivastava, I. H. Molecular electrostatic potentials: A topographical study. *J. Chem. Phys.* **1992**, *96*, 5253−5260.

(51) Gadre, S. R.; Shrivastava, I. H. Shapes and sizes of molecular anions via topographical analysis of electrostatic potential. *J. Chem. Phys.* **1991**, *94*, 4384−4390.

(52) Gadre, S. R.; Kulkarni, S. A.; Suresh, C.; Shrivastava, I. H. Basis set dependence of the molecular electrostatic potential topography. A case study of substituted benzenes. *Chem. Phys. Lett.* **1995**, *239*, 273−281.

(53) Gadre, S. R.; Pundlik, S. S. Topographical analysis of electron density and molecular electrostatic potential for cyclopropa- and cyclobutabenzenes. *J. Am. Chem. Soc.* **1995**, *117*, 9559−9563.

(54) Jemmis, E. D.; Subramanian, G.; Srivastava, I. H.; Gadre, S. R. Closo-boranes,-carboranes, and-silaboranes: a topographical study using electron density and molecular electrostatic potential. *J. Phys. Chem.* **1994**, *98*, 6445−6451.

(55) Kumar, A.; Gadre, S. R.; Mohan, N.; Suresh, C. H. Lone Pairs: An Electrostatic Viewpoint. *J. Phys. Chem. A* **2014**, *118*, 526−532.

(56) Mohan, N.; Suresh, C. H.; Kumar, A.; Gadre, S. R. Molecular electrostatics for probing lone pair−π interactions. *Phys. Chem. Chem. Phys.* **2013**, *15*, 18401−18409.

(57) Gadre, S. R.; Kumar, A. Bonding and Reactivity Patterns from Electrostatic Landscapes of Molecules. *J. Chem. Sci.* **2016**, *128*, 1519−1526.

(58) Suresh, C. H.; Koga, N.; Gadre, S. R. Molecular Electrostatic Potential and Electron Density Topography: Structure and Reactivity of (substituted arene)Cr(CO)$_3$ Complexes. *Organometallics* **2000**, *19*, 3008−3015.

(59) Frisch, M. J.; Trucks, G. W.; Schlegel, H. B.; Scuseria, G. E.; Robb, M. A.; Cheeseman, J. R.; Scalmani, G.; Barone, V.; Mennucci, B.; Petersson, G. A.; Nakatsuji, H.; Caricato, M.; Li, X.; Hratchian, H. P.; Izmaylov, A. F.; Bloino, J.; Zheng, G.; Sonnenberg, J. L.; Hada, M.; Ehara, M.; Toyota, K.; Fukuda, R.; Hasegawa, J.; Ishida, M.; Nakajima, T.; Honda, Y.; Kitao, O.; Nakai, H.; Vreven, T.; Montgomery, J. A., Jr.; Peralta, J. E.; Ogliaro, F.; Bearpark, M.; Heyd, J. J.; Brothers, E.; Kudin, K. N.; Staroverov, V. N.; Kobayashi, R.; Normand, J.; Raghavachari, K.; Rendell, A.; Burant, J. C.; Iyengar, S. S.; Tomasi, J.; Cossi, M.; Rega, N.; Millam, J. M.; Klene, M.; Knox, J. E.; Cross, J. B.; Bakken, V.; Adamo, C.; Jaramillo, J.; Gomperts, R.; Stratmann, R. E.; Yazyev, O.; Austin, A. J.; Cammi, R.; Pomelli, C.; Ochterski, J. W.; Martin, R. L.; Morokuma, K.; Zakrzewski, V. G.; Voth, G. A.; Salvador, P.; Dannenberg, J. J.; Dapprich, S.; Daniels, A.

D.; Farkas, O.; Foresman, J. B.; Ortiz, J. V.; Cioslowski, J.; Fox, D. J. *Gaussian 09*, revision D.01; Gaussian, Inc.: Wallingford, CT, 2009.

(60) Kumar, A.; Yeole, S. D.; Gadre, S. R.; López, R.; Rico, J. F.; Ramírez, G.; Ema, I.; Zorrilla, D. DAMQT 2.1. 0: a new version of the DAMQT package enabled with the topographical analysis of electron density and electrostatic potential in molecules. *J. Comput. Chem.* **2015**, *36*, 2350−2359.

(61) López, R.; Rico, J. F.; Ramírez, G.; Ema, I.; Zorrilla, D. DAMQT: A package for the analysis of electron density in molecules. *Comput. Phys. Commun.* **2009**, *180*, 1654−1660.

(62) López, R.; Rico, J. F.; Ramírez, G.; Ema, I.; Zorrilla, D. DAMQT 2.0: A new version of the DAMQT package for the analysis of electron density in molecules. *Comput. Phys. Commun.* **2015**, *192*, 289−294.

(63) López, R.; Rico, J. F.; Ramírez, G.; Ema, I.; Zorrilla, D.; Kumar, A.; Yeole, S. D.; Gadre, S. R. Topology of molecular electron density and electrostatic potential with DAMQT. *Comput. Phys. Commun.* **2017**, *214*, 207−215.

(64) Bader, R. F.; Tal, Y.; Anderson, S. G.; Nguyen-Dang, T. T. Quantum topology: theory of molecular structure and its change. *Isr. J. Chem.* **1980**, *19*, 8−29.

(65) Gejji, S. P.; Suresh, C. H.; Babu, K.; Gadre, S. R. Ab Initio Structure and Vibrational Frequencies of $(CF_3SO_2)_2N-Li^+$ Ion Pairs. *J. Phys. Chem. A* **1999**, *103*, 7474−7480.

(66) Yeole, S. D.; Gadre, S. R. Topography of scalar fields: molecular clusters and π-conjugated systems. *J. Phys. Chem. A* **2011**, *115*, 12769−12779.

(67) Bijina, P. V.; Suresh, C. H.; Gadre, S. R. Electrostatics for probing lone pairs and their interactions. *J. Comput. Chem.* **2018**, *39*, 488−499.

(68) Phukan, A. K.; Kalagi, R. P.; Gadre, S. R.; Jemmis, E. D. Structure, reactivity and aromaticity of acenes and their BN analogues: A density functional and electrostatic investigation. *Inorg. Chem.* **2004**, *43*, 5824−5832.

(69) Clar, E. *The aromatic sextet*; Wiley-Interscience: London, 1972.

(70) Balaban, A. T. Clar formulas: How to draw and how not to draw formulas of polycyclic aromatic hydrocarbons. *Polycyclic Aromat. Compd.* **2004**, *24*, 83−89.

(71) Gutman, I.; Cyvin, S. J. *Introduction to the theory of benzenoid hydrocarbons*; Springer Science & Business Media: 2012.

(72) Cyvin, S. J.; Gutman, I. *Kekulé structures in benzenoid hydrocarbons*; Springer Science & Business Media: 2013; Vol. *46*.

(73) Dickens, T. K.; Mallion, R. B. Topological Ring-Currents and Clar Sextets in Fully Benzenoid Hydrocarbons I. Structures with Fewer than 18 Rings. *J. Phys. Chem. A* **2018**, *122*, 8858−8864.

(74) Dickens, T. K.; Mallion, R. B. Topological Ring-Currents and Clar Sextets in Fully Benzenoid Hydrocarbons. II. Large Structures Containing More than 18 Rings. *J. Phys. Chem. A* **2018**, *122*, 8865−8873.

(75) Bally, T.; Masamune, S. Cyclobutadiene. *Tetrahedron* **1980**, *36*, 343−370.

(76) Dewar, M. J. Aromaticity and pericyclic reactions. *Angew. Chem., Int. Ed. Engl.* **1971**, *10*, 761−776.

(77) Diogo, H. P.; Kiyobayashi, T.; Minas da Piedade, M. E.; Burlak, N.; Rogers, D. W.; McMasters, D.; Persy, G.; Wirz, J.; Liebman, J. F. The aromaticity of pyracylene: An experimental and computational study of the energetics of the hydrogenation of acenaphthylene and pyracylene. *J. Am. Chem. Soc.* **2002**, *124*, 2065−2072.

(78) Radenković, S.; Đurđević, J.; Bultinck, P. Local aromaticity of the five-membered rings in acenaphthylene derivatives. *Phys. Chem. Chem. Phys.* **2012**, *14*, 14067−14078.

(79) Schleyer, P. v. R.; Maerker, C.; Dransfeld, A.; Jiao, H.; van Eikema Hommes, N. J. Nucleus-independent chemical shifts: a simple and efficient aromaticity probe. *J. Am. Chem. Soc.* **1996**, *118*, 6317−6318.

(80) Pople, J.; Untch, K. Induced paramagnetic ring currents. *J. Am. Chem. Soc.* **1966**, *88*, 4811−4815.

(81) Sondheimer, F. Annulenes. *Acc. Chem. Res.* **1972**, *5*, 81−91.

(82) Jug, K.; Fasold, E. Structure and aromaticity of 14-annulene and 18-annulene. *J. Am. Chem. Soc.* **1987**, *109*, 2263−2265.

(83) Wannere, C. S.; Sattelmeyer, K. W.; Schaefer, H. F., III; Schleyer, P. v. R. Aromaticity: The Alternating C-C Bond Length Structures of [14]-,[18]-, and [22]-Annulene. *Angew. Chem., Int. Ed.* **2004**, *43*, 4200−4206.

(84) Johnson, S. M.; Paul, I. C.; King, G. S. D. [16]Annulene: the crystal and molecular structure. *J. Chem. Soc. B* **1970**, 643−649.

Article

Antiaromaticity−Aromaticity Interplay in Fused Benzenoid Systems Using Molecular Electrostatic Potential Topology

Puthannur K. Anjalikrishna, Shridhar R. Gadre, and Cherumuttathu H. Suresh*

Cite This: J. Phys. Chem. A 2021, 125, 5999−6012
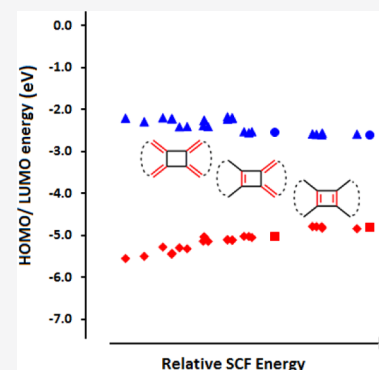
Read Online

ACCESS | Metrics & More | Article Recommendations | Supporting Information

ABSTRACT: The phenomenon of antiaromaticity−aromaticity interplay in aromatic−antiaromatic (A−aA)-fused systems is studied using molecular electrostatic potential (MESP) analysis, which clearly brings out the electron-rich π-regions of molecular systems. Benzene, naphthalene, phenanthrene, and pyrene are the aromatic units and cyclobutadiene and pentalene are the antiaromatic units considered to construct the A−aA-fused systems. The fused system is seen to reduce the antiaromaticity by adopting a configuration containing the least number of localized bonds over antiaromatic moieties. This is clearly observed in 25 isomers of a fused system composed of three naphthalene and two cyclobutadiene units. Denoting the number of π-bonds in the cyclobutadiene rings by the notation (n, n'), the systems belonging to the class $(0, 0)$ and $(2, 2)$ turn out to be the most and least stable configurations, respectively. The stability of the fused system depends on the empty π-character of the antiaromatic ring, hence naphthalene and benzene prefer to fuse with cyclobutadiene in a linear and angular fashion, respectively. Generally, a configuration with the maximum number of 'empty' rings $(0, 0, 0, ...)$ is considered to be the most stable for the given A−aA system. The stability and aromatic/antiaromatic character of A−aA-fused systems with pentalene is also interpreted in a similar way. MESP topology, clearly bringing out the distribution of double bonds in the fused systems, leads to a simple interpretation of the aromatic/antiaromatic character of them. Also, it leads to powerful predictions on stable macrocyclic A−aA systems.

INTRODUCTION

Polycyclic aromatic−antiaromatic (A−aA)-fused systems are emerging as novel molecules for applications in organic electronic devices due to their unique electronic and self-assembling properties.[1,2] The incorporation of an antiaromatic moiety into polycyclic benzenoid hydrocarbons (PBHs) brings about a change in the chemical and physical properties such as reactivity, conductivity, and so forth. It also results in a significant reduction in the aromatic character of benzenoid rings along with the dilution of the antiaromatic character of cyclobutadiene.[3] Antiaromatic systems exhibit a strong π-bond localization, while the aromatic systems favor dominant π-bond delocalization suggesting that A−aA fusion leads to the dilution of both the properties. The fusion of an antiaromatic ring with an aromatic ring leads to a significant change in the bond order and C−C bond alternation within the molecule. Such a property provides useful hints for the design and synthesis of novel molecular frameworks.[4] Many fused systems have been synthesized by connecting benzenoid hydrocarbons with antiaromatic cyclobutadiene,[5−9] pentalene,[10−16] indacene,[17−19] and so forth. These systems have been successfully applied for the design of various organo-electronic devices.[20−25] Cyclo-butadiene, one of the classic antiaromatic organic molecules, has been used in the fused systems for modulating properties such as molecular conductivity, crystallization, segregation, thin-film formation, and so forth.[26−30] The fused systems are also found

to be appropriate for the development of semiconductor materials. Also, A−aA fusion is considered as a useful design strategy for the development of supramolecular structures. In general, the introduction of antiaromatic unit/s to polyacenes brings in a significant increase in conduction properties and is found to be suitable for the design of organic-photovoltaics.[31] The reactivity and the electronic properties of such systems are intimately connected to the unique molecular topology arising from the fusion patterns in the A−aA moieties. Hence, it is necessary to have a detailed investigation about the change in the configuration, bond alternation, and π-conjugation of fused systems over the isolated ones. The dilution in antiaromaticity in such fused systems could be brought in by adopting a stable configuration that avoids double bond localization within the antiaromatic rings. Theoretical studies[32,33] on A−aA fused systems were mainly focused on the energetic aspects of the π-conjugation,[34−37] ring current features,[38−40] and magnetic properties[41,42] such as nuclear-independent chemical shift. In
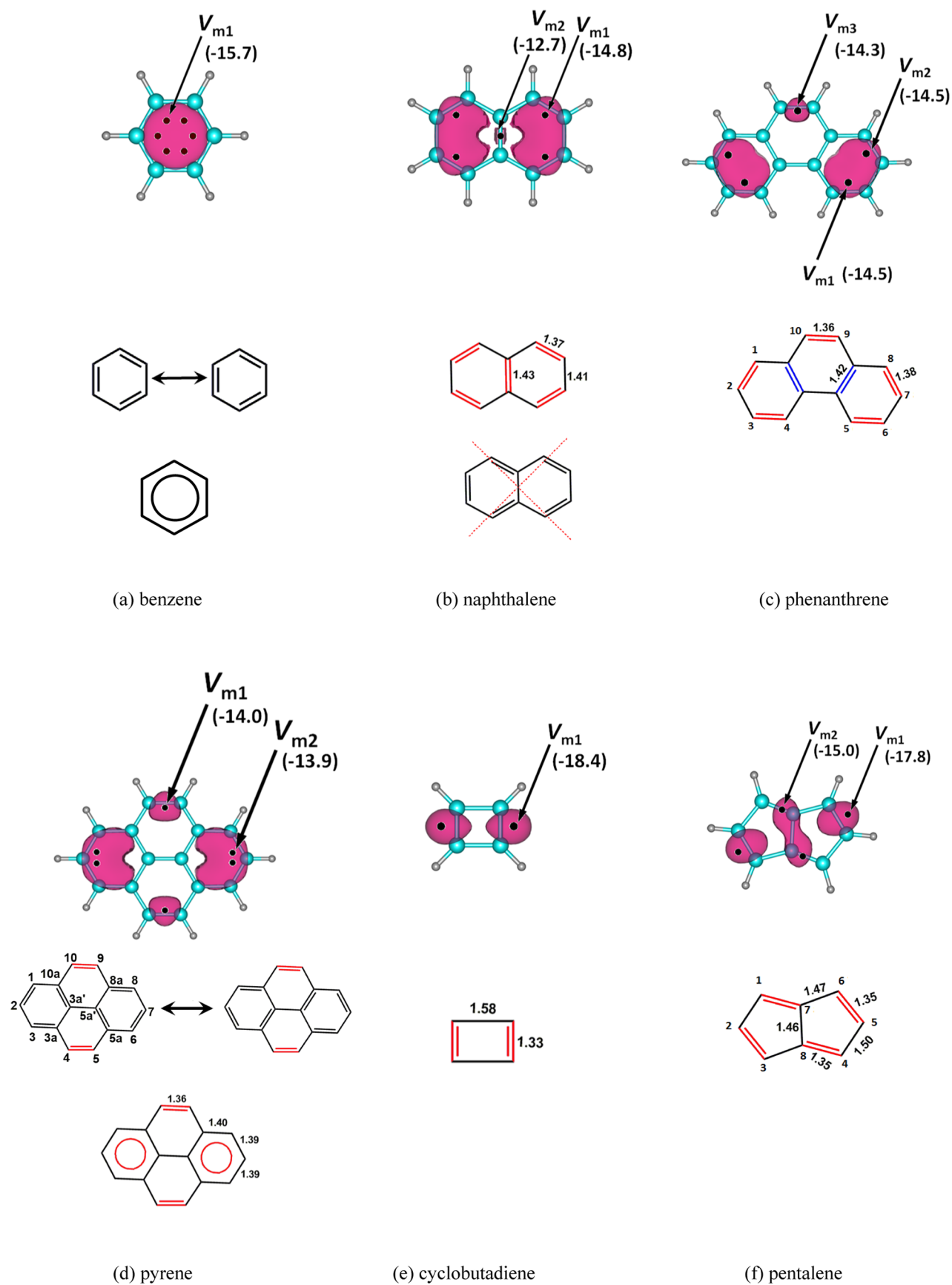
Figure 1. MESP topology patterns of benzene, naphthalene, phenanthrene, pyrene, cyclobutadiene, and pentalene systems. The V_m positions associated with double bonds are given in red and remaining double-bonded regions are given in blue color.

these studies, the computed molecular descriptors were related to the local aromaticity, that is, the aromaticity expressed within a ring.[43−45]

The present study deals with the molecular electrostatic potential (MESP) topology-based characterization of the π-bond localization/delocalization features of a variety of A—aA systems. The MESP topology analysis is an important theoretical tool for characterizing the electron-rich π-regions of molecules. The expression for MESP is given in eq 1. The first term on the r.h.s. of this equation is the bare nuclear potential. Here, Z_A is the nuclear charge of an atom A positioned at $\mathbf{R}_A$; N being the number of nuclei. The integration term on the r.h.s. is the potential generated by the continuous molecular electron density, $\rho(\mathbf{r}')$. If this term dominates over the nuclear one in a region of space, the MESP, $V(\mathbf{r})$, in that region would attain negative values. The π-electron cloud of the molecule can be displayed by plotting a suitable negative-valued MESP isosurface. The topological analysis would also locate the MESP minimum (V_m) as a (3, +3) critical point (CP). Typically, V_m points appear along the π-localized and lone-pair regions,[46−48] whereas the electron-deficient regions exhibit a positive potential.

$$V(\mathbf{r}) = \sum_A^N \frac{Z_A}{|\mathbf{r} - \mathbf{R}_A|} - \int \frac{\rho(\mathbf{r}')\mathrm{d}^3\mathbf{r}'}{|\mathbf{r} - \mathbf{r}'|} \tag{1}$$

Previous studies on PBHs were useful for finding relationships between MESP topology and π-electron delocalization.[49] A simple and elegant interpretation of Clar's aromatic sextet theory was derived using the critical features of MESP. Clar's theory[50] described the aromaticity of PBHs based on the maximum number of sextets (a sextet is defined as six π-electrons represented by a circle) drawn for a system. For the present study, the selected aromatic moieties are benzene, naphthalene, phenanthrene, and pyrene; the selected antiaromatic moieties (aA) being cyclobutadiene and pentalene. The fusion between aromatic and antiaromatic moieties can be achieved in a linear or angular fashion. The notations BC, NC, PyC, PhC, BP, and NP are used for representing the fused benzene—cyclobutadiene, naphthalene—cyclobutadiene, phenanthrene—cyclobutadiene, pyrene—cyclobutadiene, benzene—pentalene, and naphthalene—pentalene systems, respectively. Among many possible resonance forms, a unique bond alternation pattern emerges for each A—aA system. The present study deals with identifying such a configuration using the MESP topology analysis.

METHODOLOGY

The selected systems are optimized at the B3LYP/6-311+G(d, p) level of density functional theory using the Gaussian 09 program[51] package. The optimized structures were confirmed as energy minima by vibrational frequency analysis. The wave function constructed using B3LYP in conjunction with the valence triple-zeta level basis set and augmented with polarization and diffuse functions (6-311+G(d, p)) is expected to give a sufficiently accurate description of the electron density, $\rho(\mathbf{r})$, and the corresponding MESP.[52]

In the topology description, a CP is usually represented as an ordered pair of (R, σ). Here, R is the rank of the CP, that is the number of nonzero eigenvalues of the Hessian matrix and σ is the signature, that is, the algebraic sum of the sign of the eigenvalues. There are four types of nondegenerate CPs of rank three.[53] A (3, +3)-type CP denotes a local minimum and a (3,

−3)-type CP denotes a local maximum. Among the saddle points, a (3, −1) CP is called the bond CP and a (3, +1) CP is termed as the ring CP. The values of MESP, its gradients, and second derivatives at the CPs are calculated after identifying the CPs using the DAM partition−expansion method.[54,55]

RESULTS AND DISCUSSION

MESP Analysis of Benzenoid Systems, Cyclobutadiene, and Pentalene. Figure 1 depicts the (3, +3) MESP minima (V_m) along with a suitable MESP isosurface observed for −12.5 kcal/mol. In benzene, a set of six symmetrically equivalent CPs can be located above and below the molecular plane in a uniform circular manner (only one side is illustrated in Figure 1a). This suggests a perfect delocalization of the electron density in the system. Hence, a perfect aromatic sextet can be drawn for benzene, which can be regarded as representing a resonance hybrid of two Kekulé structures. The C—C bond length in benzene is 1.39 Å, and the V_m value is −15.7 kcal/mol. The benzenoid aromatic systems are likely to show a V_m value close to that of benzene due to sextet-type delocalization of the π-electron within six-membered rings. Naphthalene consists of five CPs on each side of the molecular plane, only two out of which are symmetrically unequal $(V_{m1}$ and $V_{m2})$. This topology indicates an imperfection in the delocalization of electron density vis-à-vis that of benzene. The C—C bond characterized by the location of V_{m1} is more localized than other C—C bonds, represented as double bonds with red color. The MESP topology immediately suggests the chemical formula given in Figure 1b as the most likely one for naphthalene. In contrast, the alternate, crossed-out structure shown below could be the least preferred one.

Phenanthrene shows five (3, +3) CPs on each side of the molecular plane, three among them being symmetrically unequal ones. These are represented as V_{m1}, V_{m2}, and V_{m3}. The location of the V_m positions suggests the chemical formula given in Figure 1c. It may be noted that among the seven double bonds required to represent the phenanthrene formula, two of them shown in blue color cannot be associated with a V_m position. However, a unique formula can be readily proposed as "red" double bonds automatically fix the "blue" ones. The pyrene system consists of a set of six (3, +3) CPs (on each side) in which two (viz. V_{m1} and V_{m2}) are unequal ones. V_{m1} is located directly on top of C4—C5 and C9—C10 bonds, whereas a pair of close lying V_{m2} appears close to C2 and C7 regions. Positions of V_{m2} suggest that C1—C2 and C2—C3 bonds are equivalent and similarly are C6—C7 and C7—C8 bonds. Therefore, the two Kekulé resonance forms used for pyrene to assign the Clar's sextet-type delocalized structure are shown in Figure 1d.

In cyclobutadiene, the two π-bonds are strongly localized with a distance of 1.33 Å and the MESP topology detects this feature with a V_m value of −18.4 kcal/mol at the top, midpoint region of the bonds. In pentalene, two types of CPs, viz. V_{m1} and V_{m2}, are observed, having values −17.8 and −15.0 kcal/mol, respectively. The most negative V_{m1} shows localized electron density along the π-region, between C2—C3 and C5—C6, whereas V_{m2} indicates double bond nature for C1—C7 and C4—C8. In this system, lengths of both the double bonds corresponding to V_{m1} and V_{m2} are identical, viz. 1.35 Å. However, the V_m values suggest that the nature of localization is different in both regions. The V_{m1} value is close to that of cyclobutadiene, suggesting the antiaromatic character, whereas V_{m2} values are close to that of benzene. The MESP isosurface corresponding to V_{m2} regions is indicative of a *trans*-1,3-butadiene-like conjugation along the
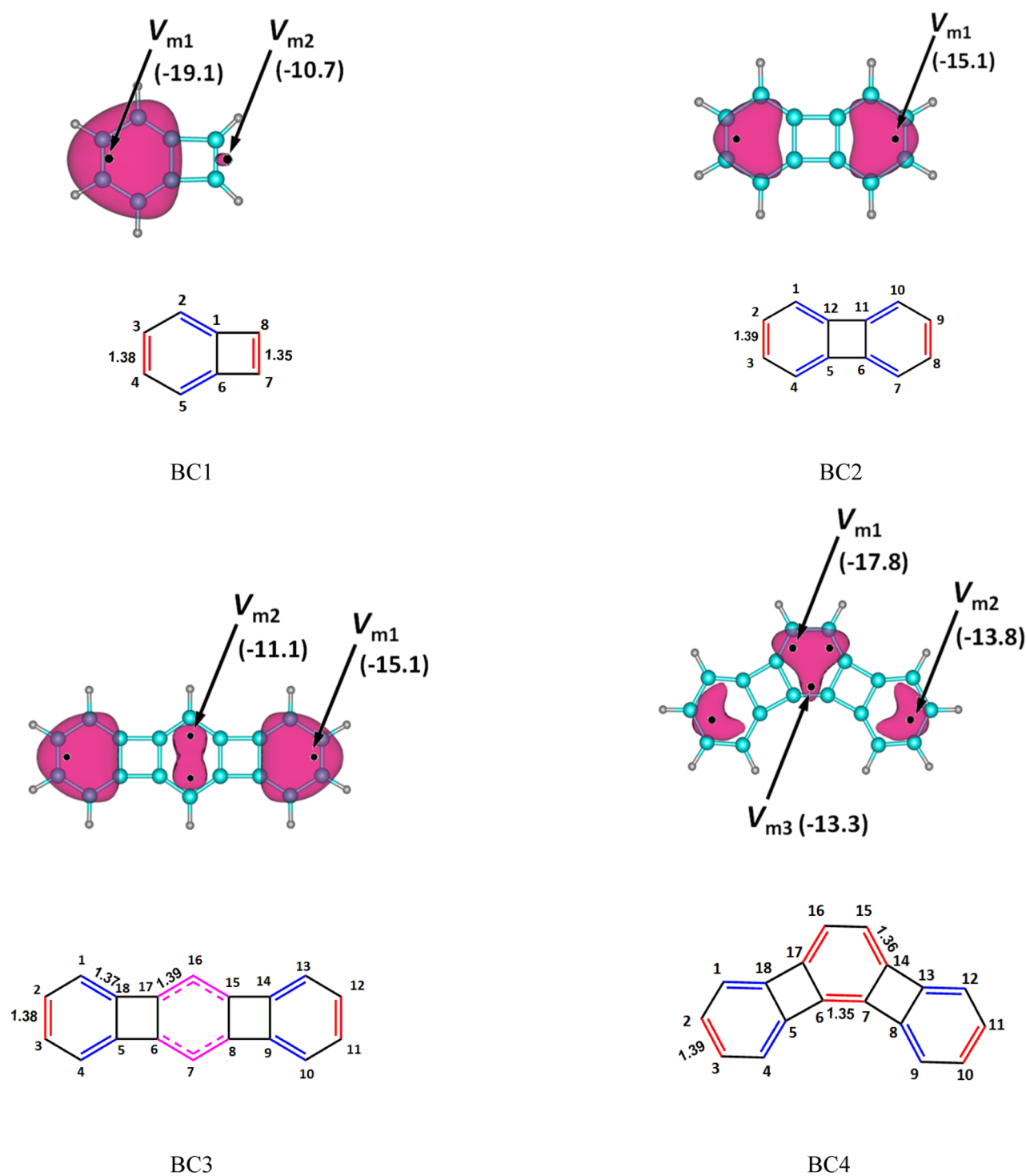
Figure 2. MESP CPs and isosurface patterns of benzene−cyclobutadiene-fused systems. See the text for details. The V_m position-associated double bonds are given in red and remaining double bonded regions are given in blue color.

middle region of pentalene. The MESP analysis suggests that pentalene is neither fully aromatic nor antiaromatic. However, the strong π-bond localization of C2−C3 and C5−C6 bonds indicates a high reactivity toward addition reaction to suggest a predominantly antiaromatic nature of it. The chemical formula given in Figure 1f, based on the MESP CPs, is recommended for pentalene.

Benzene−Cyclobutadiene-Fused Systems. Figure 2 depicts the MESP topology of benzene−cyclobutadiene-fused systems[56] (BC1−BC4) and the corresponding representation of

their chemical formula. In BC1, the benzene portion shows only one (3, +3) CP over each π-face (V_{m1} over the C3−C4 bond), suggesting that the ring fusion with the four-membered ring leads to a substantial change in the MESP topology of benzene. V_{m2} defines a double bond (C7−C8) for the four-membered ring. Although the C7−C8 bond is shorter than C3−C4, the latter has significantly more negative character (−19.1 kcal/mol) than the former (−10.7 kcal/mol) indicating that the fusion leads to charge transfer from the four-membered to six-membered ring. The electron-rich C3−C4 bond suggests a
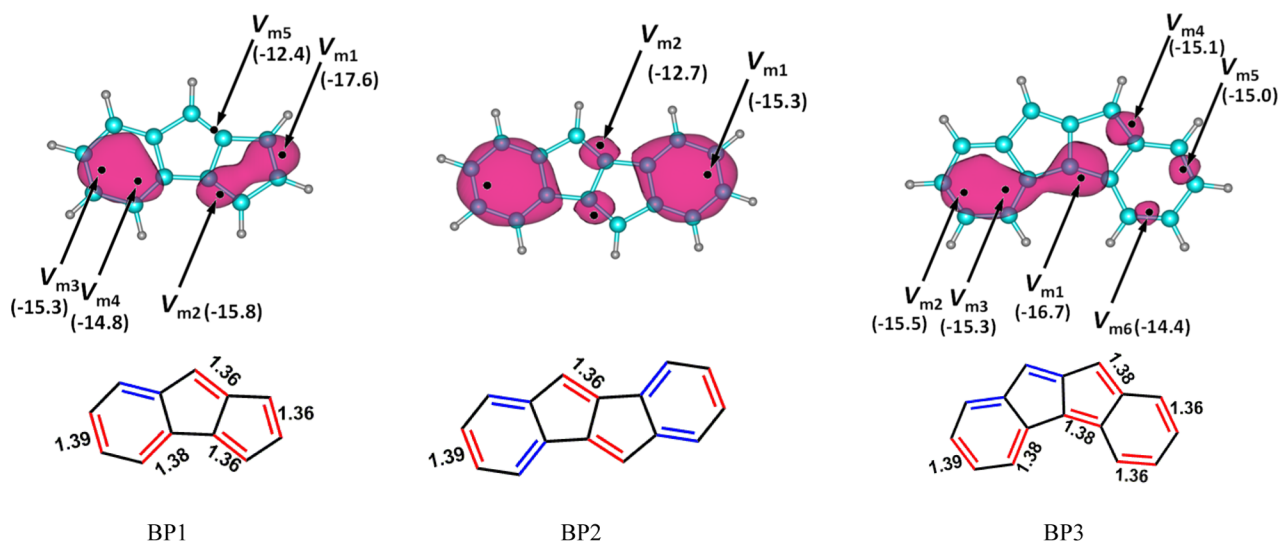
Figure 3. MESP topology patterns of benzene−pentalene-fused systems. The V_m position-associated double bonds are given in red and remaining double-bonded regions are given in blue color.

reduction in the aromatic character as well as high reactivity for the system. Also, the V_m value of cyclobutadiene portion is increased by 7.7 kcal/mol compared to that of cyclobutadiene suggesting a reduction in the localization of electron density over π-regions indicating dilution of its antiaromatic character. When a cyclobutadiene is inserted between two benzene rings (BC2), the CPs corresponding to the π-regions of the benzene rings show a V_m value (−15.1 kcal/mol) very similar to that of benzene suggesting more aromatic character than BC1. Two cyclobutadiene moieties could be connected to three benzene rings in a linear fashion (BC3) or they could be connected in an angular fashion (BC4). In BC3, most localized π-regions are observed at the end benzenoid rings with a V_m value of −15.1 kcal/mol indicating a benzene-type delocalization in the ring, whereas a set of CP appears in the middle ring over the C7 and C16 atoms indicating that C6−C7 and C7−C8 bonds (1.39 Å) as well as C15−C16 and C16−C17 bonds are identical. The MESP isosurface images over these regions support the delocalization of the π-electrons over C6−C7−C8 and C15−C16−C17 bonds and V_{m2} at this regions is −11.1 kcal/mol. To give a representation for such a delocalization, the pink-colored dotted line is used to draw the chemical formula for BC3 (Figure 2). In BC4, the middle benzene ring contains three CPs, out of which two are unequal ones (V_{m1} and V_{m2}) and distribution of CPs indicates the presence of three π-bonds in the ring. Each end ring consists of only one V_m, with an MESP value of −13.8 kcal/mol, representing the most localized π-bond in the corresponding ring. Based on this, the other π-regions can be defined (given in blue color, Figure 2). In BC3, the middle benzene ring has more electron-rich character than the terminal ones, whereas the cyclobutadiene rings are conspicuous by the absence of double bond localization. In BC4, the π-electron density over cyclobutadiene is shared with the neighboring six-membered rings and every six-membered ring may be represented as an aromatic one with 6π-electrons in it. This makes the isomer BC4 2.7 kcal/mol more stable than BC3. For all the cases, the distribution of CPs gives a clear view of the most appropriate single- and double-bond patterns. A chemical formula can be easily derived for all. No π-localization is observed in the cyclobutadiene rings, which act as empty rings between benzenoid rings. The 6π-electron delocalization within

a benzene ring is seen in all the cases by avoiding π-localization within four-membered rings. In other words, the antiaromatic character of the four-membered rings is minimized by promoting the aromatic nature of the benzene rings. There are reports on the synthesis as well as on the crystallographic studies on the systems BC3[57,58] and BC4.[59,60]

Benzene−Pentalene-Fused Systems. Figure 3 represents the MESP topology of benzene−pentalene (BP)-fused systems (BP1−BP3).[61] In BP1, there are a set of five unequal CPs appearing on each side of the molecular plane. Among the rings, the benzene moiety contains two unequal V_m points, V_{m3} and V_{m4} with values −15.3 and −14.8 kcal/mol, respectively, indicating the π-electron delocalization in the ring to be similar to that for benzene. The V_m value of the middle five-membered ring is higher (−12.4 kcal/mol) than those of the others suggesting a decrease in the extent of π-electron delocalization over that ring, whereas the most localized π-region appears over the terminal five-membered ring with a V_m value of −17.6 kcal/mol, very close to that of the isolated pentalene suggesting antiaromatic character for that ring. In BP2,[12] aromatic character dominates due to the delocalization of the π-electrons within the benzene ring, while the pentalene portion shows only two localized double bonds with a high V_m value of −12.7 kcal/mol. BP3, an isomer of BP2, is less stable than the latter by 21.6 kcal/mol and also suggests that its aromatic stabilization is lower than that of BP2. The MESP feature shows the most negative V_m −16.7 kcal/mol on the pentalene portion. Also, the chemical formula of BP3 as per the MESP topology suggests only two localized π-bonds within one of the six-membered rings indicating a decrease in aromatic character. This accounts for the instability due to antiaromaticity of BP3 compared to BP2. Konishi et al. have demonstrated experimentally that the BP3-type fusion shows enhanced antiaromatic character compared to the BP2-type ring fusion.[62,63] Stojanovic et al. have examined the effect of two types of dibenzo-fusion of pentalene computationally, which well correlate with our topology analysis.[64,65]

Naphthalene−Cyclobutadiene-Fused Systems. Two configurations are possible for the fusion of one naphthalene unit with cyclobutadiene, NC1 and NC2 (cf. Figure 4), with NC1 being more stable than NC2 by 12.0 kcal/mol. The MESP topology suggests that the fusion enhances the electron-rich
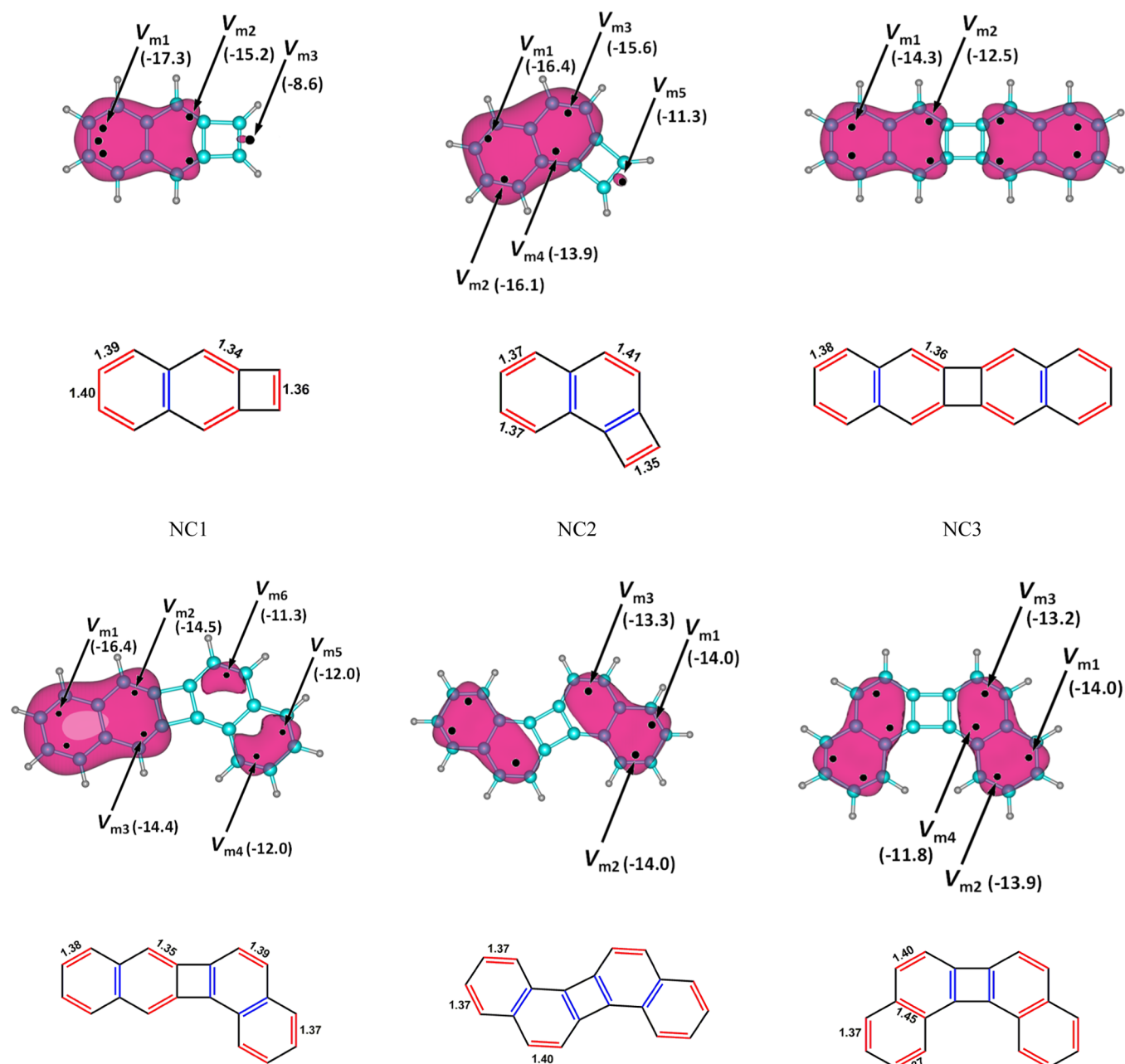
Figure 4. MESP topology patterns of naphthalene−cyclobutadiene-fused systems. See the text for details.

character of the naphthalene portion at the expense of the electron density from the cyclobutadiene portion. The four-membered ring is identified with the highest valued V_m point and the corresponding CC bond is the shortest. Though the naphthalene-like π-electron distribution is dominating in both the cases, the π-bond distribution as per MESP topology suggests localization in the two double bonds of the four-membered ring of NC2 and only one for NC1. The tendency to hold 4π electrons in the four-membered ring supports higher antiaromatic character for NC2 than NC1, which correlates with their relative stability. The V_m value observed over the four-membered ring showed a significant increase compared to the V_m value of cyclobutadiene (−18.4 kcal/mol). This suggests a dilution in antiaromatic character in both NC1 and NC2.

Two naphthalene rings fused to one cyclobutadiene give rise to four configurations, NC3−NC6 (*cf.* Figure 4). In all the

isomers, the MESP features, in particular the (3, +3) CPs, appear prominently over the naphthalene moieties, while the four-membered ring is 'empty' with respect to the MESP minima. This indicates the tendency of the π-electrons to get delocalized over the naphthalene moieties. The MESP-based chemical formula suggests 0, 1, 2, and 2 double bonds for the four-membered rings of NC3, NC4, NC5, and NC6, respectively, indicating that antiaromatic character of cyclobutadiene is the minimum expressed in NC3, partially expressed in NC4, and strongly expressed in NC5 and NC6. NC4 is 4.0 kcal/mol higher in energy than NC3, while NC5 and NC6 are further up in the energy ladder by 12.3 and 12.8 kcal/mol, which can be accounted to their higher antiaromatic character than others. Our suggested chemical formula for NC3 is in good agreement with the report by Kawai et al., where they have studied the existence and stability of the radialene structure of the NC3
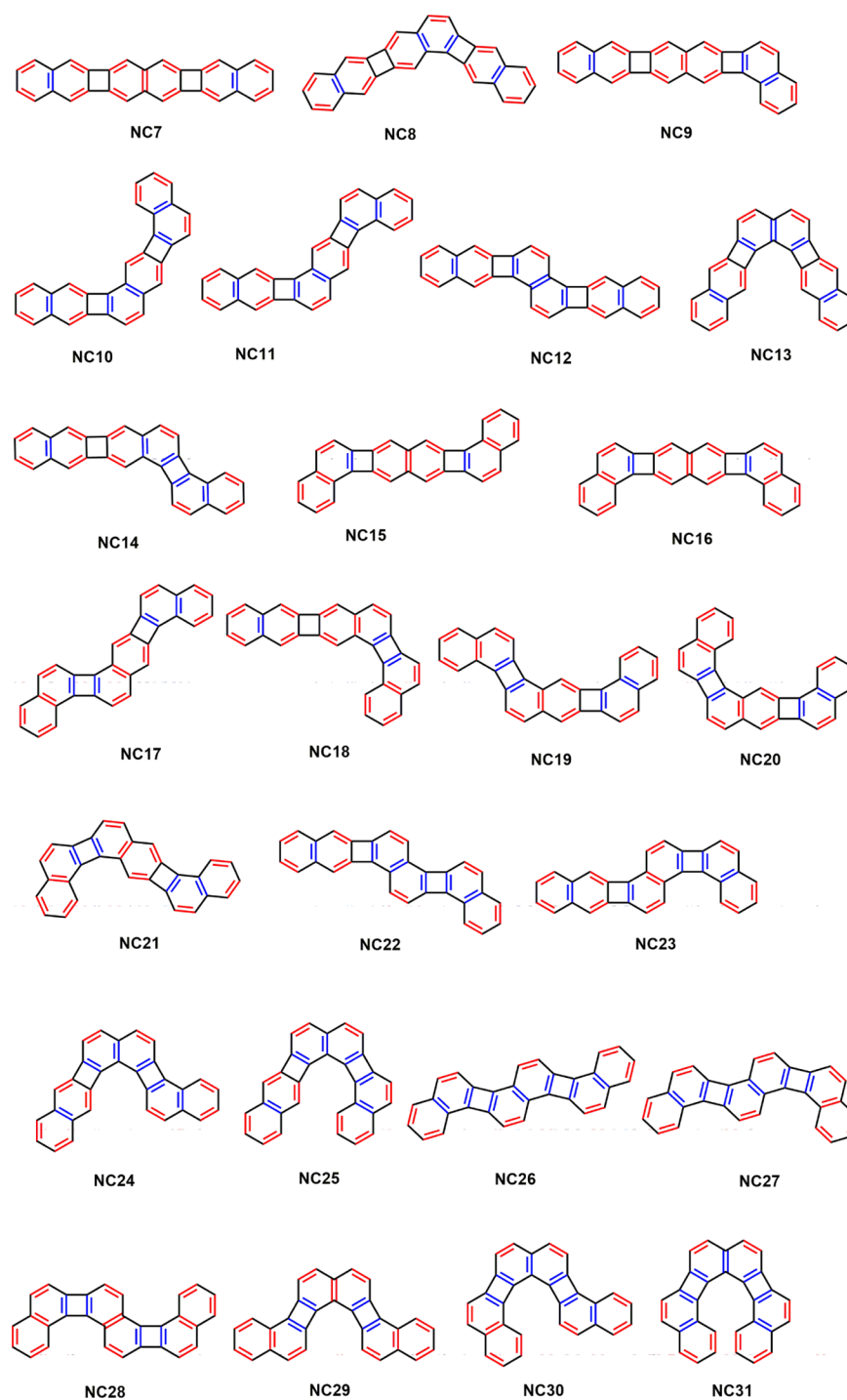
Figure 5. MESP CPs and isosurface-based chemical formulae for the A–aA systems of three naphthalene units fused with two cyclobutadiene moieties. The convention of "blue" and "red" double bonds as in the earlier figures. See the text for details.

isomer over its cyclobutadiene structure by high-resolution atomic force microscopy.[66]

Three Naphthalene Moieties Fused with Two Cyclobutadienes. By fusing three naphthalene moieties with two cyclobutadienes, a total of 25 isomers, viz. NC7–NC31, were obtained (*cf.* Figure 5). Here, the structures showing fusion of two four-membered rings on one six-membered ring is not considered. The MESP features of all of them are given in Supporting Information (Figure S1), while the MESP-based chemical formula is presented in Figure 6. The MESP always exhibits minima over the naphthalene rings while the four-

membered rings appeared 'empty'. This indicates the presence of dominating naphthalene character over the cyclobutadiene character as well as dilution of antiaromaticity. For each chemical formula, the number of double bonds in four-membered rings is given in Table 1 as an ordered pair (n, n'); n for the left ring and the n' for the right ring. The relative energy of each isomer is also depicted in Table 1. On the basis of (n, n')-description, six categories of isomers can be defined, viz. $(0, 0)$, $(0, 1)$, $(1, 1)$, $(0, 2)$, $(1, 2)$, and $(2, 2)$.

The linear one, viz. NC7, of the $(0, 0)$ category is the most stable among all due to the least amount of π-character in the
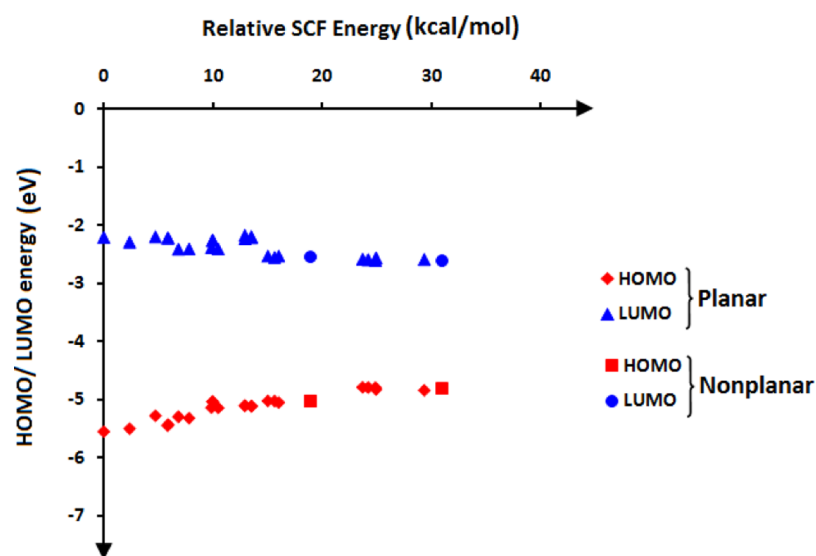
Figure 6. Trends in HOMO and LUMO energy with relative energy for three naphthalene−two cyclobutadiene ring systems. See the text for details.

Table 1. Relative Energies and the Number of Double Bonds (n, n') in Cyclobutadiene Rings in Three Naphthalene−Two Cyclobutadiene Ring Systems[a]

fused systems	(n, n')	relative energy (kcal/mol)	HOMO (eV)	LUMO (eV)	HOMO− LUMO gap (eV)
NC7	(0, 0)	0.00	−5.55	−2.21	3.34
NC8	(0, 1)	2.37	−5.50	−2.30	3.21
NC9	(0, 1)	4.74	−5.28	−2.20	3.08
NC10	(1, 1)	5.86	−5.45	−2.23	3.22
NC11	(1, 1)	5.90	−5.43	−2.22	3.21
NC12	(1, 1)	6.84	−5.30	−2.42	2.88
NC13	(1, 1)	7.82	−5.32	−2.41	2.91
NC14	(0, 2)	9.87	−5.14	−2.39	2.75
NC15	(1, 1)	9.95	−5.04	−2.27	2.77
NC16	(1, 1)	10.01	−5.04	−2.26	2.78
NC17	(1, 2)	10.49	−5.14	−2.41	2.73
NC18	(1, 2)	12.94	−5.11	−2.18	2.93
NC19	(1, 2)	12.95	−5.10	−2.24	2.87
NC20	(1, 2)	13.53	−5.12	−2.20	2.92
NC21	(1, 2)	13.55	−5.11	−2.22	2.89
NC22	(1, 2)	15.04	−5.02	−2.53	2.49
NC23	(1, 2)	15.66	−5.03	−2.56	2.47
NC24	(1, 2)	16.04	−5.05	−2.53	2.52
NC25	(1, 2)	18.99	−5.04	−2.55	2.49
NC26	(2, 2)	23.73	−4.79	−2.59	2.20
NC27	(2, 2)	24.24	−4.79	−2.60	2.19
NC28	(2, 2)	24.91	−4.79	−2.61	2.18
NC29	(2, 2)	24.96	−4.83	−2.57	2.26
NC30	(2, 2)	29.38	−4.84	−2.59	2.25
NC31	(2, 2)	30.99	−4.81	−2.61	2.19

[a]See the text for details.

four-membered rings, which suggests the maximum dilution of antiaromaticity. The (0, 1)-category systems, NC8 and NC9, turn out to be less stable than NC7 by 2.37 and 4.74 kcal/mol, respectively, indicating small destabilization due to the localization of one double bond in a four-membered ring. The destabilization is in the range 5.86−10.49 kcal/mol for the categories (1, 1) and (0, 2), wherein two bonds are localized for four-membered rings. The isomers NC17−NC25 contain

totally three localized bonds in four-membered rings. This leads to a further decrease in the stability as the antiaromatic character is expected to be high for the four-membered rings. The relative energy of these isomers is in the range 12.94 to 18.99 kcal/mol. The isomers NC26−NC31 showing two double bonds in each four-membered ring are the most unstable with relative energies in the range 23.73−30.99 kcal/mol. Here, the antiaromatic character is exhibited by both the four-membered rings. For each category of molecules, the relative energy shows a small variation, which can be attributed to the variation in strain energy at the curved portions as more curved structures are expected to show higher energy. In cases such as NC25 and NC31, a distortion from planarity occurs due to the steric effect from nonbonded C−H···H−C interactions arising from highly curved nature of the molecules. When the rings of two polycyclic systems can be incorporated into one-to-one correspondence, the corresponding ring currents are equal and are called equiaromatic.[67] As a result, the isomers NC7, NC12, NC13, NC15, NC16, NC26, NC28, NC29, and NC31 can be considered as equiaromatic. Table 1 also shows the HOMO, LUMO, and the HOMO−LUMO gap calculated using B3LYP/6-311+G(d, p) level of theory. The most stable isomer has the lowest HOMO and the highest LUMO energies and with the increase in the relative energy of the isomers, an increasing trend in HOMO energy and a decreasing trend in LUMO energy are observed. This suggests that the chemical reactivity of the isomers increases with the increase in the antiaromatic character as it reduces the HOMO−LUMO gap (Figure 6).

Naphthalene−Pentalene-Fused Systems. Two configurations, NP1 and NP2, are possible for the fusion of naphthalene with one pentalene (Figure 7).[10] In both cases, the pentalene unit shows deeper negative potential than naphthalene. Also, the MESP V_m value distribution over the naphthalene in the fused system is similar to that of free naphthalene. The V_m points suggest a significant difference in the π-distribution within the pentalene portion of NP1 and NP2 as the former shows only three π-bonds, whereas the latter shows four π-bonds meaning that the antiaromatic character of pentalene is more expressed in NP2 than NP1. This argument is supported by the relative energy values: NP1 is 5.5 kcal/mol more stable than NP2. A similar observation is made for the two
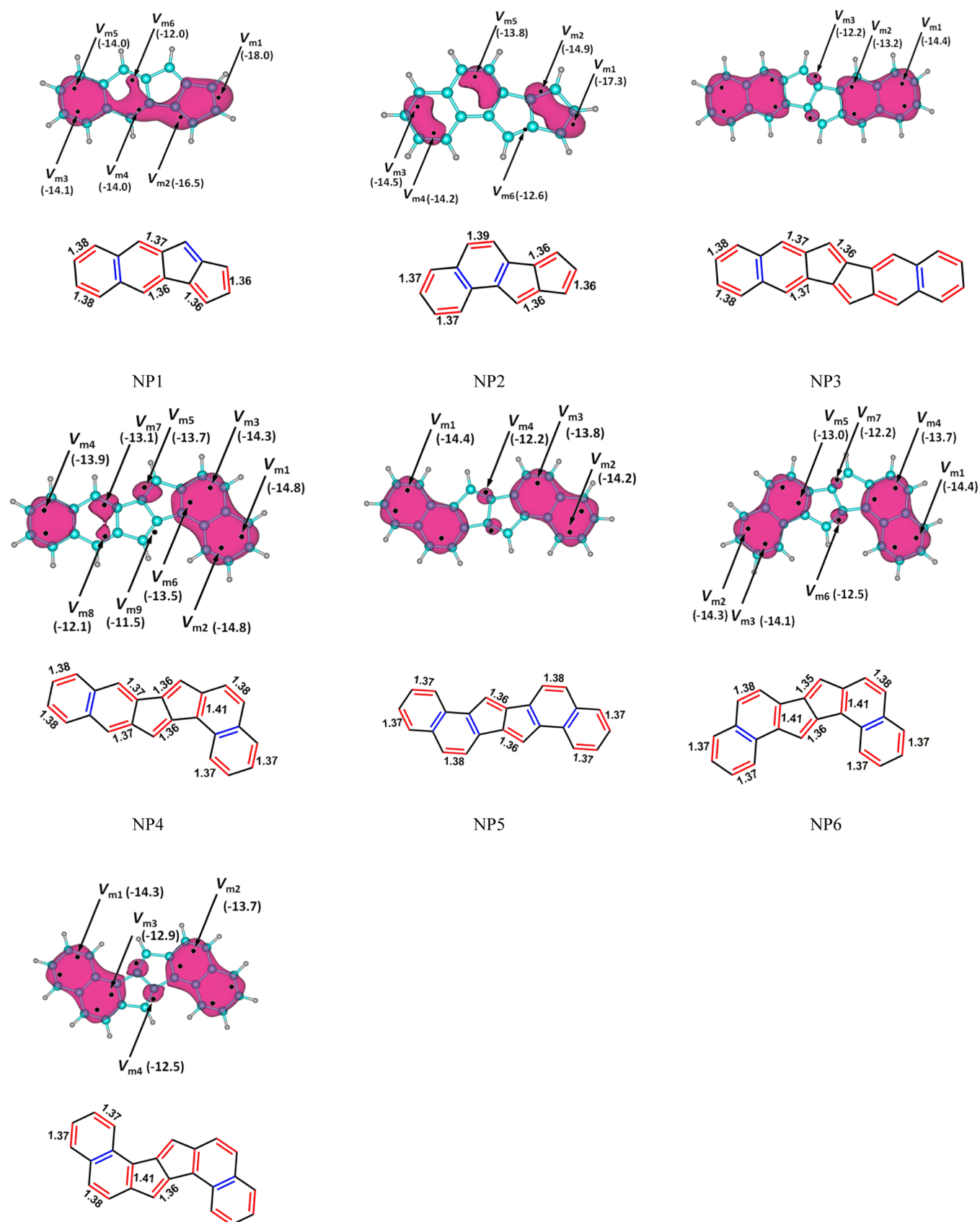
Figure 7. MESP CPs and isosurfaces for naphthalene−pentalene-fused systems, along with the MESP topology-based representation of the double bonds in these systems. See the text for details.

naphthalene−one pentalene-fused systems, viz. NP3 through NP7. NP3, NP4, NP5, NP6, and NP7 show, respectively, two,

three, four, four, and four π-bonds for the pentalene portion suggesting that antiaromaticity is the least expressed in NP3,
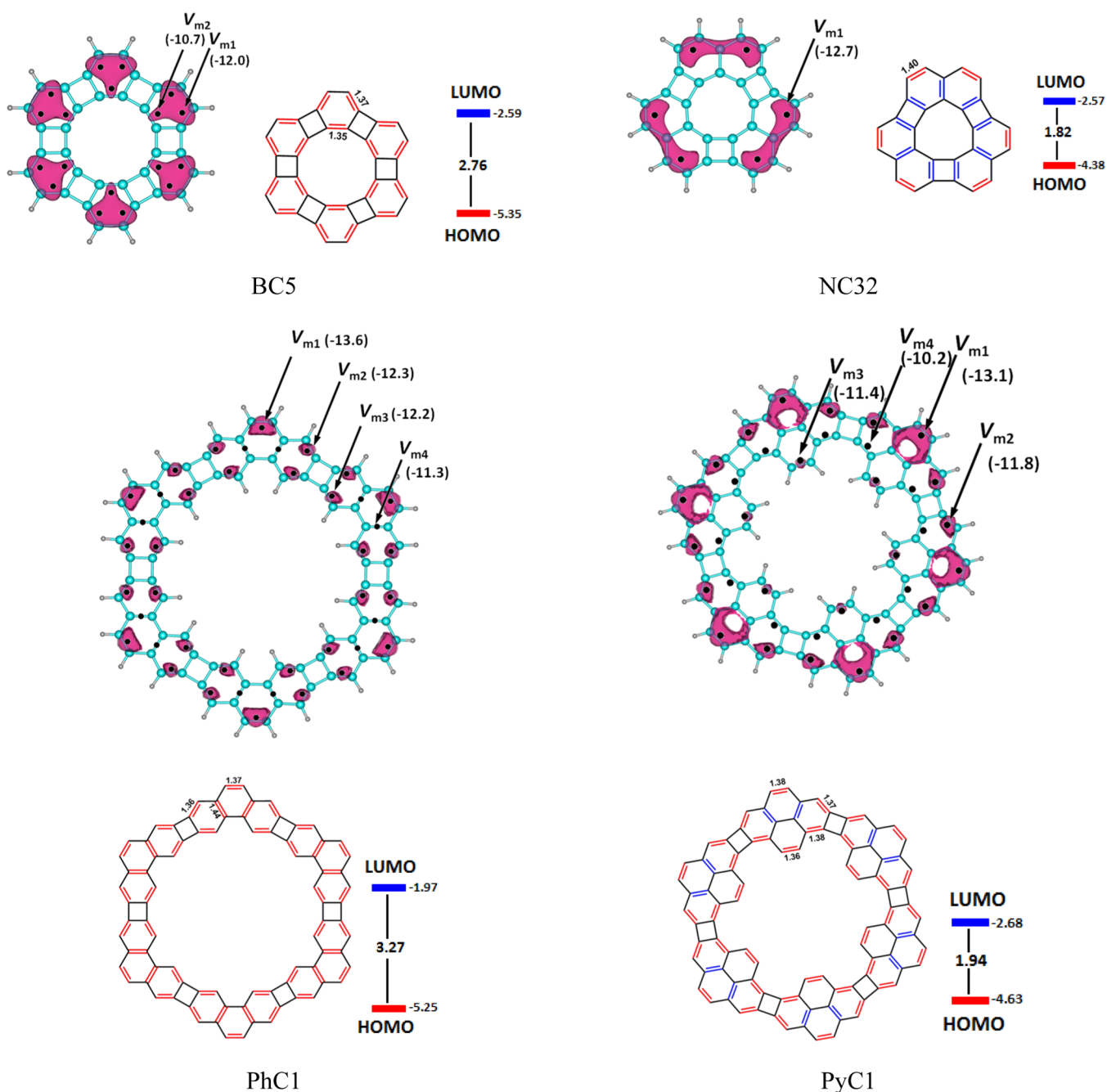
Figure 8. MESP CPs and isosurfaces for fused ring systems. The HOMO−LUMO gap is given in eV. Details of double bonds are as given in the captions of the earlier figures. See the text for details.

followed by NP4, while NP5, NP6, and NP7 exhibit substantial antiaromatic character. The relative energies of NP3, NP4, NP5, NP6, and NP7 are 0.0, 3.1, 7.3, 7.4, and 7.5 kcal/mol, respectively. These kinds of A−aA-fused systems have found applications in the organic thin film transistors. Among them, NP3[12] and NP5[21] have been synthesized experimentally. The three benzene−two cyclobutadiene-fused system BC4 having the (0, 0) angular configuration (Figure 2) is more stable than the linear BC3 configuration. Extending this structure with more benzene and cyclobutadiene units can lead to a ring structure BC5 composed of six benzene and six cyclobutadiene units.

The MESP features suggest π-bond distribution within benzene rings and all the cyclobutadiene rings are "empty". In other words, a (0, 0, 0, 0, 0, 0) configuration can be assigned for

BC5 to indicate the absence of π-bond localization (Figure 8) in four-membered rings. Although six four-membered rings are present in BC5, the MESP-based method suggests that the molecule may be stable and can be synthesized due to the dominance of aromatic character. In fact, the synthesis of BC5 is known in the literature, Vollhardt et al. had reported the total synthesis of the first helical phenylenes (heliphenes), angular [6]- and [7]-phenylene, using a double cobalt-catalyzed cyclotrimerization strategy and a route for the preparation of such heliphene-based metal complexes.[6,68,69]

The cyclic structure for three naphthalene−three cyclobutadiene-fused system NC32 is shown in Figure 8. Here, the MESP feature suggests a (2, 2, 2) configuration for the molecule that can be interpreted as a highly antiaromatic molecule. We

predict that the synthesis of such a molecule may not be very easy. Figure 8 also depicts two more ring structures, one composed of six phenanthrene and six cyclobutadiene moieties (PhC1) and another one composed of six pyrene and six cyclobutadiene moieties (PyC1). We note that the aromatic moieties phenanthrene and pyrene prefer angular structures for fusion to yield "empty" rings for cyclobutadienes. MESP topology suggests a $(0, 0, 0, 0, 0, 0)$ configuration for both PhC1 and PyC1. Hence, such structures should behave as the most stable compared to any other isomers. Observed band gaps for the ring-fused systems of naphthalene and pyrene with cyclobutadiene are 1.82 and 1.94 eV, respectively, indicating the ease of conductivity associated with the ring-fused systems compared to their linear ones. We predict that such ring systems can be applied to better performing conducting materials due to the small band gap induced by the antiaromatic character of cyclobutadiene units. The continuous growth of biphenylene units reported by Gottfried, Liljeroth, and co-workers can be explained based on our results.[70] The biphenylene network system consists of four-, six-, and eight-membered rings and this adopts a configuration containing the least number of double bonds in the four-membered ring, that is, the $(1, 1, 1, 1, ...)$ configuration. This stable configuration plays a key role in the systematic growth as well as stability of the network system. It is also possible to explicate the dielectric properties of the network system based on the configuration.

The findings of the work could be correlated with the Glidewell–Lloyd rule,[71,72] which is the extension of Clar's π-sextet rule. According to the former, total π-electrons in a conjugated polycyclic system tend to form the smallest $4n + 2$ groups by avoiding smallest $4n$ group formation. The systems with smallest $4n + 2$ groups describe the structural and electronic properties of these polycyclic conjugated hydrocarbons better.

El Bakouri et al. have examined[73] the scope of the Glidewell–Lloyd rule in 69 polycyclic hydrocarbons composed of various combinations of four-, six-, and eight-membered rings. According to them, conjugated polycyclic systems try to avoid the presence of double bonds at the ring junctions. This leads to a stable Glidewell–Lloyd structure that contains the least number of double bonds in the four-membered ring.

These results well correlate with our theory that A—aA-fused systems try to reduce their antiaromaticity by adopting a configuration containing the least number of localized bonds over antiaromatic moieties. It could be seen that most of the structures that satisfy the Glidewell–Lloyd rule obey the MESP-based interpretation of the π-bond distribution. Therefore, our present work could be considered as a manifestation of the Glidewell–Lloyd rule in terms of MESP topology.

■ CONCLUSIONS

A detailed study on the design strategy of A—aA-fused systems is very important, considering their potential applications in optoelectronic devices. Herein, MESP topology analysis has been carried out on a large variety of A—aA-fused systems using the B3LYP/6-311+G(d, p) level of theory. The negative regions observed in the MESP analysis indicate the delocalization/localization of electron density in the aromatic/antiaromatic ring. The MESP topology studies clearly suggest that the double bond character in the antiaromatic rings of A—aA-fused systems is getting diluted as they are in combination with aromatic rings. The stability of such systems correlates well with the number of localized bonds appearing in the antiaromatic moieties of the fused system. This correlation is clearly illustrated for 25 isomers

of fused systems made up of three naphthalene and two cyclobutadiene units. They are divided into six different categories based on the number of π-bonds (n, n') observed in the cyclobutadiene rings. Among them, the most stable isomer is linear and belongs to the $(0, 0)$ category, while the least stable isomers belong to the $(2, 2)$ category. The MESP distribution suggests a $(2, 2, 2)$ configuration for a ring structure made up of three naphthalene and three cyclobutadiene units. This configuration predicts high antiaromatic character for the molecule due to the presence of two double bonds in each four-membered ring. MESP topology suggests an angular structure as the most stable for benzene—cyclobutadiene-fused systems. The ring structure made up of six benzene and six cyclobutadiene units shows 'empty' π-character for the cyclobutadiene rings indicating the lowest antiaromatic character or high stability for the structure. The synthesis of such a macrocycle is achieved experimentally, which can be supported by the inherent stability of the molecule due to the dominance of aromatic character from six benzene rings. In general, the $(0, 0, 0, 0, ...)$ and $(2, 2, 2, ...)$ configurations are expected to be the most stable and the least stable structures for a benzenoid aromatic-fused with cyclobutadiene moieties, respectively. The same trend is observed with A—aA-fused systems of pentalene rings also as they try to keep a configuration that contains the least number of localized π-bonds in the pentalene ring. Any A—aA system with a $(0, 0, 0, 0, ...)$ configuration exhibits a high HOMO–LUMO gap, indicating the high stability associated with it and one with a $(2, 2, 2, ...)$ configuration possesses a small HOMO–LUMO gap, indicating its low stability or high reactivity. The π-bond distribution expressed using the MESP critical features provides a unique molecular formula for each system and also suggests a molecular design strategy for the creation of stable macrocycles with a $(0, 0, 0, 0, ...)$ configuration.

This systematic study on A—aA systems clearly promotes MESP as a powerful tool for the analysis of π-bond distribution in conjugated cyclic hydrocarbons. This helps to attenuate the complexity of predicting the single- and double-bond distribution and suggests a unique structure for each molecule. A detailed study on the MESP topology of a system furnishes the possibilities of designing molecules and predicting their properties and reactivity, based on the aromatic/antiaromatic character. The interpretation of the molecular formula for a structure opens up to the concept of antiaromaticity—aromaticity interplay in A—aA-fused systems. This also helps to predict the applications of such systems in the area of semiconducting materials due to the conducting properties induced by the antiaromatic moieties in combination with aromatic systems.

■ ASSOCIATED CONTENT

ⓈI Supporting Information

The Supporting Information is available free of charge at https://pubs.acs.org/doi/10.1021/acs.jpca.1c04286.

> Detailed MESP topographical features, Cartesian coordinates, SCF energy, HOMO energy, LUMO energy, and HOMO–LUMO gap of all the systems (PDF)

■ AUTHOR INFORMATION

Corresponding Author

Cherumuttathu H. Suresh − Chemical Sciences and Technology Division, CSIR-National Institute for Interdisciplinary Science and Technology,

Thiruvananthapuram, Kerala 695019, India; Academy of Scientific and Innovative Research (AcSIR), Ghaziabad 201002, India; ● orcid.org/0000-0001-7237-6638; Phone: +91-471-2515472; Email: sureshch@niist.res.in; http://www.niist.res.in/chsuresh

Authors

     Puthannur K. Anjalikrishna — *Chemical Sciences and Technology Division, CSIR-National Institute for Interdisciplinary Science and Technology, Thiruvananthapuram, Kerala 695019, India; Academy of Scientific and Innovative Research (AcSIR), Ghaziabad 201002, India*

     Shridhar R. Gadre — *Department of Scientific Computing, Modelling and Simulation, SavitribaiPhule Pune University, Pune 411007, India;* ● orcid.org/0000-0003-3234-3959

Complete contact information is available at:
https://pubs.acs.org/10.1021/acs.jpca.1c04286

Author Contributions

This manuscript was written through contributions of all authors. All authors have given approval to the final version of the manuscript.

Notes

The authors declare no competing financial interest.

■ REFERENCES

(1) Mayer, P. J.; El Bakouri, O.; Holczbauer, T.; Samu, G. F.; Janáky, C.; Ottosson, H.; London, G. Structure−Property Relationships in Unsymmetric Bis(antiaromatics): Who Wins the Battle between Pentalene and Benzocyclobutadiene? *J. Org. Chem.* **2020**, *85*, 5158.

(2) Frederickson, C. K.; Zakharov, L. N.; Haley, M. M. Modulating Paratropicity Strength in Diareno-Fused Antiaromatics. *J. Am. Chem. Soc.* **2016**, *138*, 16827.

(3) Milanez, B. D.; Chagas, J. C. V.; Pinheiro Jr, M., Jr; Aquino, A. J. A.; Lischka, H.; Machado, F. B. C. Effects on the aromaticity and on the biradicaloid nature of acenes by the inclusion of a cyclobutadiene linkage. *Theor. Chem. Acc.* **2020**, *139*, 113.

(4) Rajca, A.; Safronov, A.; Rajca, S.; Ross, C. R.; Stezowski, J. J. Biphenylene Dimer. Molecular Fragment of a Two-Dimensional Carbon Net and Double-Stranded Polymer. *J. Am. Chem. Soc.* **1996**, *118*, 7272.

(5) Barton, J. W.; Lee, D. V.; Shepherd, M. K. Benzocyclo-octenes. part 4. Benzo- and dibenzo[a,e]-cycle-octene synthesis via benzocyclobutene. *J. Chem. Soc., Perkin Trans. 1* **1985**, 1407.

(6) Miljanić, O. S.; Holmes, D.; Vollhardt, K. P. C. 1,3,6,9,12,14,17,20-Octaethynyltetrabenz[a,b,f,j,k,o]-4,5,10,11,15,16,21,22- octadehydro[18]annulene: A Carbon-Rich Hydrocarbon. *Org. Lett.* **2005**, *7*, 4001.

(7) Gu, Z.; Boursalian, G. B.; Gandon, V.; Padilla, R.; Shen, H.; Timofeeva, T. V.; Tongwa, P.; Vollhardt, K. P. C.; Yakovenko, A. A. Activated phenacenes from phenylenes by nickel-catalyzed alkyne cycloadditions. *Angew. Chem.* **2011**, *123*, 9585.

(8) Bruns, D.; Miura, H.; Vollhardt, K. P. C.; Stanger, A. En Route to Archimedene: Total Synthesis of C$_{3h}$-Symmetric [7] Phenylene. *Org. Lett.* **2003**, *5*, 549.

(9) Eickmeier, C.; Holmes, D.; Junga, H.; Matzger, A. J.; Scherhag, F.; Shim, M.; Vollhardt, K. P. C. A Novel Phenylene Topology: Total Syntheses of Zigzag [4]- and [5] Phenylene. *Angew. Chem., Int. Ed.* **1999**, *38*, 800.

(10) Kato, S.-i.; Kuwako, S.; Takahashi, N.; Kijima, T.; Nakamura, Y. Benzo-and naphthopentalenes: syntheses, structures, and properties. *J. Org. Chem.* **2016**, *81*, 7700.

(11) Konishi, A.; Fujiwara, T.; Ogawa, N.; Hirao, Y.; Matsumoto, K.; Kurata, H.; Kubo, T.; Kitamura, C.; Kawase, T. Pentaleno [1, 2-c: 4, 5-c′] dithiophene Derivatives: First Synthesis, Properties, and a Molecular Structure. *Chem. Lett.* **2010**, *39*, 300.

(12) Shen, J.; Yuan, D.; Qiao, Y.; Shen, X.; Zhang, Z.; Zhong, Y.; Yi, Y.; Zhu, X. Diaceno [a, e] pentalenes from Homoannulations of o-Alkynylaryliodides Utilizing a Unique Pd(OAc)$_2$/n-Bu$_4$NOAc Catalytic Combination. *Org. Lett.* **2014**, *16*, 4924.

(13) Dai, G.; Chang, J.; Zhang, W.; Bai, S.; Huang, K.-W.; Xu, J.; Chi, C. Dianthraceno [a, e] pentalenes: synthesis, crystallographic structures and applications in organic field-effect transistors. *Chem. Commun.* **2015**, *51*, 503.

(14) Zheng, J.; Zhuang, X.; Qiu, L.; Xie, Y.; Wan, X.; Lan, Z. Antiaromatic characteristic analysis of 1, 4-diazapentalene derivatives: a theoretical study. *J. Phys. Chem. A* **2015**, *119*, 3762.

(15) Dai, G.; Chang, J.; Shi, X.; Zhang, W.; Zheng, B.; Huang, K.-W.; Chi, C. Thienoacene-Fused Pentalenes: Syntheses, Structures, Physical Properties and Applications for Organic Field-Effect Transistors. *Chem.—Eur. J.* **2015**, *21*, 2019.

(16) Niimi, K.; Kang, M. J.; Miyazaki, E.; Osaka, I.; Takimiya, K. General Synthesis of Dinaphtho[2,3-b:2′,3′-f]thieno[3,2-b]thiophene (DNTT) Derivatives. *Org. Lett.* **2011**, *13*, 3430.

(17) Marshall, J. L.; Uchida, K.; Frederickson, C. K.; Schütt, C.; Zeidell, A. M.; Goetz, K. P.; Finn, T. W.; Jarolimek, K.; Zakharov, L. N.; Risko, C.; Herges, R.; Jurchescu, O. D.; Haley, M. M. Indacenodibenzothiophenes: synthesis, optoelectronic properties and materials applications of molecules with strong antiaromatic character. *Chem. Sci.* **2016**, *7*, 5547.

(18) Young, B. S.; Chase, D. T.; Marshall, J. L.; Vonnegut, C. L.; Zakharov, L. N.; Haley, M. M. Synthesis and properties of fully-conjugated indacenedithiophenes. *Chem. Sci.* **2014**, *5*, 1008.

(19) Chase, D. T.; Rose, B. D.; McClintock, S. P.; Zakharov, L. N.; Haley, M. M. Indeno [1, 2-b] fluorenes: fully conjugated antiaromatic analogues of acenes. *Angew. Chem., Int. Ed.* **2011**, *50*, 1127.

(20) Wang, C.; Dong, H.; Hu, W.; Liu, Y.; Zhu, D. Semiconducting π-Conjugated Systems in Field-Effect Transistors: A Material Odyssey of Organic Electronics. *Chem. Rev.* **2012**, *112*, 2208.

(21) Kawase, T.; Fujiwara, T.; Kitamura, C.; Konishi, A.; Hirao, Y.; Matsumoto, K.; Kurata, H.; Kubo, T.; Shinamura, S.; Mori, H.; Miyazaki, E.; Takimiya, K. Dinaphthopentalenes: Pentalene Derivatives for Organic Thin-Film Transistors. *Angew. Chem., Int. Ed.* **2010**, *49*, 7728.

(22) Yamamoto, T.; Shinamura, S.; Miyazaki, E.; Takimiya, K. Three structural isomers of dinaphthothieno [3, 2-b] thiophenes: elucidation of physicochemical properties, crystal structures, and field-effect transistor characteristics. *Bull. Chem. Soc. Jpn.* **2010**, *83*, 120.

(23) Tylleman, B.; Vande Velde, C. M. L.; Balandier, J.-Y.; Stas, S.; Sergeyev, S.; Geerts, Y. H. Synthesis of Isomerically Pure anti-Anthradithiophene Derivatives. *Org. Lett.* **2011**, *13*, 5208.

(24) Mamada, M.; Katagiri, H.; Mizukami, M.; Honda, K.; Minamiki, T.; Teraoka, R.; Uemura, T.; Tokito, S. syn-/anti-Anthradithiophene Derivative Isomer Effects on Semiconducting Properties. *ACS Appl. Mater. Interfaces* **2013**, *5*, 9670.

(25) Henson, Z. B.; Müllen, K.; Bazan, G. C. Design strategies for organic semiconductors beyond the molecular formula. *Nat. Chem.* **2012**, *4*, 699.

(26) Barton, J. W.; Shepherd, M. K.; Willis, R. J. Polycyclic biphenylenes. Part 6. Direct routes to benzo [b] biphenylene and related systems via cycloaddition reactions. *J. Chem. Soc., Perkin Trans. 1* **1986**, 967.

(27) Buckland, P. R.; Hacker, N. P.; McOmie, J. F. W. Biphenylenes. Part 32. A new, general synthesis of mono-and poly-benzobiphenylenes from substituted benzocyclobutene-1, 2-diones and ortho-bis (cyanomethyl) arenes. *J. Chem. Soc., Perkin Trans. 1* **1983**, 1443.

(28) Cracknell, M. E.; Kabli, R. A.; McOmie, J. F. W.; Perry, D. H. Biphenylenes. Part 33. Synthesis of bisbenzo [3, 4] cyclobuta [1, 2-b; 1′, 2′-h]-and bisbenzo [3, 4] cyclobuta [1, 2-c; 1′, 2′-g]-phenanthrene, and attempts to prepare planar derivatives of cyclo-octatetraene. *J. Chem. Soc., Perkin Trans. 1* **1985**, 115.

(29) Bong, D. T.-Y.; Chan, E. W. L.; Diercks, R.; Dosa, P. I.; Haley, M. M.; Matzger, A. J.; Miljanić, O. Š.; Vollhardt, K. P. C.; Bond, A. D.; Teat, S. J.; Stanger, A. Syntheses of syn and anti doublebent [5] phenylene. *Org. Lett.* **2004**, 6, 2249.

(30) Dosche, C.; Löhmannsröben, H.-G.; Bieser, A.; Dosa, P. I.; Han, S.; Iwamoto, M.; Schleifenbaum, A.; Vollhardt, K. P. C. Photophysical properties of [N] phenylenes. *Phys. Chem. Chem. Phys.* **2002**, 4, 2156.

(31) Chase, D. T.; Fix, A. G.; Kang, S. J.; Rose, B. D.; Weber, C. D.; Zhong, Y.; Zakharov, L. N.; Lonergan, M. C.; Nuckolls, C.; Haley, M. M. 6, 12-Diarylindeno [1, 2-b] fluorenes: syntheses, photophysics, and ambipolar OFETs. *J. Am. Chem. Soc.* **2012**, 134, 10349.

(32) Ito, S.; Minami, T.; Nakano, M. Diradical Character Based Design for Singlet Fission of Condensed-Ring Systems with 4nπ Electrons. *J. Phys. Chem. C* **2012**, 116, 19729.

(33) Firouzi, R.; Shafie, H.; Tohidnia, H. Characterization of Local Aromaticity in Polycyclic Conjugated Hydrocarbons Based on Anisotropy of π-Electron Density. *ChemistrySelect* **2017**, 2, 11526.

(34) Ayub, R.; Bakouri, O. E.; Jorner, K.; Solà, M.; Ottosson, H. Can Baird's and Clar's Rules Combined Explain Triplet State Energies of Polycyclic Conjugated Hydrocarbons with Fused 4nπ- and (4n + 2)π-Rings? *J. Org. Chem.* **2017**, 82, 6327.

(35) Gineityte, V. An extension of the Fries rule to non-benzenoid hydrocarbons having four-atomic rings. *Monatsh. Chem.* **2018**, 149, 1031.

(36) Schulman, J. M.; Disch, R. L. A Theoretical Study of Large Planar [N]Phenylenes. *J. Phys. Chem. A* **2007**, 111, 10010.

(37) Schulman, J. M.; Disch, R. L. Theoretical studies of the [N] phenylenes. *J. Am. Chem. Soc.* **1996**, 118, 8470.

(38) Radenković, S.; Tošović, J.; Havenith, R.; Bultinck, P. Ring currents in benzo-And benzocyclobutadieno-annelated biphenylene derivatives. *ChemPhysChem* **2015**, 16, 216.

(39) Dickens, T. K.; Mallion, R. B. Ring-current assessment of the annulene-within-an-annulene model for some large coupled super-ring conjugated-systems. *Croat. Chem. Acta* **2014**, 87, 221.

(40) Figeys, H. P.; Defay, N.; Martin, R. H.; McOmie, J. F. W.; Ayres, B. E.; Chadwick, J. B. Experimental and theoretical study of the induced paramagnetic ring-current in the 4-membered ring of biphenylene and related hydrocarbons. *Tetrahedron* **1976**, 32, 2571.

(41) Ceulemans, A.; Arvanitidis, A. G. Directed graphs and induced magnetic multipoles in polycyclic hydrocarbons. *Bull. Chem. Soc. Jpn.* **2015**, 88, 1553.

(42) Schulman, J. M.; Disch, R. L.; Jiao, H.; Schleyer, P. v. R. Chemical shifts of the [N] phenylenes and related compounds. *J. Phys. Chem. A* **1998**, 102, 8051.

(43) Balaban, A. T.; Gutman, I.; Marković, S.; Simijonović, D.; Đurđević, J. Local Aromaticity in Benzo- and Benzocyclobutadieno-Annelated Phenanthrenes. *Polycyclic Aromat. Compd.* **2011**, 31, 339.

(44) Gershoni-Poranne, R.; Gibson, C. M.; Fowler, P. W.; Stanger, A. Concurrence between current density, nucleus-independent chemical shifts, and aromatic stabilization energy: the case of isomeric [4]-and [5] phenylenes. *J. Org. Chem.* **2013**, 78, 7544.

(45) Gutman, I. Cyclic conjugation in phenylenes. *S. Afr. J. Chem.* **1994**, 47, 53.

(46) Suresh, C. H.; Gadre, S. R. A Novel Electrostatic Approach to Substituent Constants: Doubly Substituted Benzenes. *J. Am. Chem. Soc.* **1998**, 120, 7049.

(47) Gadre, S. R.; Pundlik, S. S. Topographical Analysis of Electron Density and Molecular Electrostatic Potential for Cyclopropa- and Cyclobutabenzenes. *J. Am. Chem. Soc.* **1995**, 117, 9559.

(48) Deshmukh, M. M.; Gadre, S. R.; Tonner, R.; Frenking, G. Molecular electrostatic potentials of divalent carbon(0) compounds. *Phys. Chem. Chem. Phys.* **2008**, 10, 2298.

(49) Anjalikrishna, P. K.; Suresh, C. H.; Gadre, S. R. Electrostatic Topographical Viewpoint of π-Conjugation and Aromaticity of Hydrocarbons. *J. Phys. Chem. A* **2019**, 123, 10139.

(50) Clar, E. *The Aromatic Sextet*; Wiley-Interscience: London, 1972.

(51) Frisch, M. J.; Trucks, G. W.; Schlegel, H. B.; Scuseria, G. E.; Robb, M. A.; Cheeseman, J. R.; Scalmani, G.; Barone, V.; Mennucci, B.; Petersson, G. A.; Nakatsuji, H.; Caricato, M.; Li, X.; Hratchian, H. P.; Izmaylov, A. F.; Bloino, J.; Zheng, G.; Sonnenberg, J. L.; Hada, M.; Ehara, M.; Toyota, K.; Fukuda, R.; Hasegawa, J.; Ishida, M.; Nakajima, T.; Honda, Y.; Kitao, O.; Nakai, H.; Vreven, T.; Montgomery, J. A., Jr.; Peralta, J. E.; Ogliaro, F.; Bearpark, M.; Heyd, J. J.; Brothers, E.; Kudin, K. N.; Staroverov, V. N.; Keith, T.; Kobayashi, R.; Normand, J.; Raghavachari, K.; Rendell, A.; Burant, J. C.; Iyengar, S. S.; Tomasi, J.; Cossi, M.; Rega, N.; Millam, J. M.; Klene, M.; Knox, J. E.; Cross, J. B.; Bakken, V.; Adamo, C.; Jaramillo, J.; Gomperts, R.; Stratmann, R. E.; Yazyev, O.; Austin, J. A.; Cammi, R.; Pomelli, C.; Ochterski, J. W.; Martin, R. L.; Morokuma, K.; Zakrzewski, V. G.; Voth, G. A.; Salvador, P.; Dannenberg, J. J.; Dapprich, S.; Daniels, A. D.; Farkas, O.; Foresman, J. V.; Ortiz, J. V.; Cioslowski, J.; Fox, D. J. *Gaussian 09*, Revision D.01; Gaussian, Inc.: Wallingford, CT, 2013.

(52) Gadre, S. R.; Kulkarni, S. A.; Suresh, C. H.; Shrivastava, I. H. Basis set dependence of the molecular electrostatic potential topography. A case study of substituted benzenes. *Chem. Phys. Lett.* **1995**, 239, 273.

(53) Gadre, S. R.; Shirsat, R. N. *Electrostatics of Atoms and Molecules*; Universities Press, 2000.

(54) Kumar, A.; Yeole, S. D.; Gadre, S. R.; López, R.; Rico, J. F.; Ramírez, G.; Ema, I.; Zorrilla, D. DAMQT 2.1. 0: a new version of the DAMQT package enabled with the topographical analysis of electron density and electrostatic potential in molecules. *J. Comput. Chem.* **2015**, 36, 2350.

(55) López, R.; Rico, J. F.; Ramírez, G.; Ema, I.; Zorrilla, D. DAMQT 2.0: A new version of the DAMQT package for the analysis of electron density in molecules. *Comput. Phys. Commun.* **2015**, 192, 289.

(56) Barton, J. W.; Rowe, D. J. Polycyclic biphenylenes: Part V. The pmr spectra of annelated biphenylenes. *Tetrahedron* **1985**, 41, 1323.

(57) Schleifenbaum, A.; Feeder, N.; Vollhardt, K. P. C. The X-ray crystal structure of linear [3] phenylene. *Tetrahedron Lett.* **2001**, 42, 7329.

(58) Berris, B. C.; Hovakeemian, G. H.; Lai, Y. H.; Mestdagh, H.; Vollhardt, K. P. C. A new approach to the construction of biphenylenes by the cobalt-catalyzed cocyclization of o-diethynylbenzenes with alkynes. Application to an iterative approach to [3] phenylene, the first member of a novel class of benzocyclobutadienoid hydrocarbons. *J. Am. Chem. Soc.* **1985**, 107, 5670.

(59) Barton, J. W.; Walker, R. B. Benzo[3,4]cyclobuta[1,2-a]biphenylene, a new biphenylene system. *Tetrahedron Lett.* **1978**, 19, 1005.

(60) Diercks, R.; Vollhardt, K. P. C. Novel Synthesis of the Angular [3] Phenylene (Terphenylene) by Cobalt-Catalyzed Cyclization of Bis (2-ethynylphenyl) ethyne: a Molecule with an Internal Cyclohexatriene Ring. *Angew. Chem., Int. Ed.* **1986**, 25, 266.

(61) Saito, M. Synthesis and Reactions of Dibenzo [a, e] pentalenes. *Symmetry* **2010**, 2, 950.

(62) Konishi, A.; Okada, Y.; Nakano, M.; Sugisaki, K.; Sato, K.; Takui, T.; Yasuda, M. Synthesis and Characterization of Dibenzo[a,f]-pentalene: Harmonization of the Antiaromatic and Singlet Biradical Character. *J. Am. Chem. Soc.* **2017**, 139, 15284.

(63) Konishi, A.; Okada, Y.; Kishi, R.; Nakano, M.; Yasuda, M. Enhancement of Antiaromatic Character via Additional Benzoannulation into Dibenzo[a,f]pentalene: Syntheses and Properties of Benzo-[a]naphtho[2,1-f]pentalene and Dinaphtho[2,1-a,f]pentalene. *J. Am. Chem. Soc.* **2019**, 141, 560.

(64) Baranac-Stojanović, M.; Stojanović, M. The effect of two types of dibenzoannulation of pentalene on molecular energies and magnetically induced currents. *Phys. Chem. Chem. Phys.* **2019**, 21, 3250.

(65) Baranac-Stojanović, M. A DFT Study of the Modulation of the Antiaromatic and Open-Shell Character of Dibenzo [a, f] pentalene by Employing Three Strategies: Additional Benzoannulation, BN/CC Isosterism, and Substitution. *Chemistry* **2019**, 25, 9747.

(66) Kawai, S.; Takahashi, K.; Ito, S.; Pawlak, R.; Meier, T.; Spijker, P.; Canova, F. F.; Tracey, J.; Nozaki, K.; Foster, A. S.; Meyer, E. Competing annulene and radialene structures in a single anti-aromatic molecule studied by high-resolution atomic force microscopy. *ACS Nano* **2017**, *11*, 8122.

(67) Fowler, P. W.; Cotton, S.; Jenkinson, D.; Myrvold, W.; Bird, W. H. Equiaromatic benzenoids: Arbitrarily large sets of isomers with equal ring currents. *Chem. Phys. Lett.* **2014**, *597*, 30.

(68) Han, S.; Bond, A. D.; Disch, R. L.; Holmes, D.; Schulman, J. M.; Teat, S. J.; Vollhardt, K. P. C.; Whitener, G. D. Total syntheses and structures of angular [6]-and [7]phenylene: the first helical phenylenes (heliphenes). *Angew. Chem., Int. Ed.* **2002**, *41*, 3223.

(69) Mohler, D. L.; Kumaraswamy, S.; Stanger, A.; Vollhardt, K. P. C. 1,2,3,4-tetraethynylbenzene as a template for cobalt-catalyzed alkyne cocyclizations: synthesis of 2,3,8,9-tetrakis(trimethylsilyl) angular [3]phenylene and bent [5]phenylene (benzo[1'',2'':3,4;3'',4'':3',4']-dicyclobuta[1,2-b:1',2'-b']bisbiphenylene). *Synlett* **2006**, 2981.

(70) Fan, Q.; Yan, L.; Tripp, M. W.; Krejčí, O.; Dimosthenous, S.; Kachel, S. R.; Chen, M.; Foster, A. S.; Koert, U.; Liljeroth, P.; Gottfried, J. M. Biphenylene network: A nonbenzenoid carbon allotrope. *Science* **2021**, *372*, 852.

(71) Glidewell, C.; Lloyd, D. MNDO study of bond orders in some conjugated bi-and tri-cyclic hydrocarbons. *Tetrahedron* **1984**, *40*, 4455.

(72) Pino-Rios, R.; Solà, M. The Relative Stability of Indole Isomers Is a Consequence of the Glidewell-Lloyd Rule. *J. Phys. Chem. A* **2021**, *125*, 230.

(73) El Bakouri, O.; Poater, J.; Feixas, F.; Solà, M. Exploring the validity of the Glidewell—Lloyd extension of Clar's π-sextet rule: assessment from polycyclic conjugated hydrocarbons. *Theor. Chem. Acc.* **2016**, *135*, 205.

Electrostatic Potential for Exploring Electron Delocalization in Infinitenes, Circulenes, and Nanobelts

Puthannur K. Anjalikrishna, Shridhar R. Gadre,* and Cherumuttathu H. Suresh*

Cite This: https://doi.org/10.1021/acs.joc.2c02507

Read Online

ACCESS | 📊 Metrics & More | 📄 Article Recommendations | 🆂🅸 Supporting Information

ABSTRACT: The π-conjugation, aromaticity, and stability of the newly synthesized 12-infinitene and of other infinitenes comprising 8-, 10-, 14-, and 16-arene rings are investigated using density functional theory. The π-electron delocalization and aromatic character rooted in infinitenes are quantified in terms of molecular electrostatic potential (MESP) topology. Structurally, the infinitene bears a close resemblance of its helically twisted structure to the infinity symbol. The MESP topology shows that infinitene possesses an infinity-shaped delocalization of the electron density that streams over the fused benzenoid rings. The parameter

Electrostatic potential distribution of

infinitene   circulene   nanobelt

$\sum_{i=1}^{3} \Delta \lambda_i$, derived from the eigenvalues (λ_i) corresponding to the MESP minima, is used for quantifying the aromatic character of arene rings of infinitene. The structure, stability, and MESP topology features of 8-, 10-, 12-, 14-, and 16-infinitenes are also compared with the corresponding isomeric circulenes and carbon nanobelts. Further, the strain in all such systems is evaluated by considering the respective isomeric planar benzenoid hydrocarbons as reference systems. The 12-infinitene turns out to be the most aromatic and the least strained among all the systems examined.
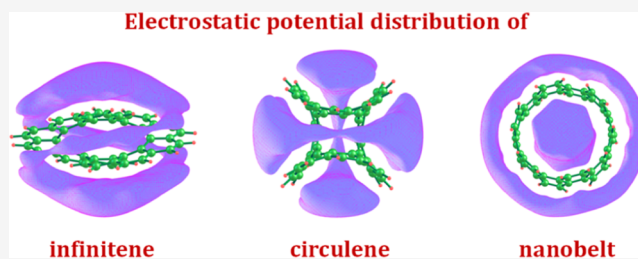
INTRODUCTION

The ability to form different allotropes makes the carbon atom versatile, leading to numerous new structures with unique physical, chemical, and biological properties.[1-4] In recent years, there have been significant advancements in the chemistry of nanocarbon structures, which have emerged as fascinating materials with potential applications in science and technology.[5] Among the various nanocarbon structures, cycloparaphenylene,[6,7] cycloarenes, carbon nanobelts (CNBs),[8-12] helical nanographene,[13,14] graphene nanoribbon,[15,16] and chiral π-conjugated macrocycle[17] have received significant attention. Furthermore, many attractive molecular carbon scaffolds[19,20] have been introduced and subjected to theoretical and experimental investigations.[18] The unique helical structure and inherent chirality of helicenes are utilized in asymmetric catalysis, molecular machines, molecular recognition, molecular self-assemblies, organic functional materials, and so forth.[19-22] Circulenes have also been explored in detail due to their potential optoelectronic properties. However, molecules combining circulenes and helicenes are not yet known.

Krzeszewski et al.[23] recently synthesized a simple and unique helically twisted figure-eight CNB, a condensed form of 12-benzene rings. The structure of this system can be viewed as a fusion of one homo-6-helicene unit with its chiral counterpart at their terminal rings and is regarded as "12-infinitene." Moreover, 12-infinitene belongs to the "$C_{48}H_{24}$" family and could be looked upon as a twisted helical isomer of 12-

circulene. It was named infinitene due to its close resemblance of its helically twisted structure to the infinity symbol. This could be regarded as a new class of molecules in the history of carbon nanostructures.[11,24-26] Christoph et al.[27] reported saddle-shaped 12-circulene created by the fusion of two 6-helicenes in a head-to-head and tail-to-tail fashion.

12-infinitene is the first example of a completely conjugated, helically twisted circulene, which has been successfully synthesized. Orozco-Ic et al.[28] brought out the aromaticity of 12-infinitene using magnetically induced current density and induced magnetic field analysis. Monaco et al.[29] studied the origin-independent current density induced by a perpendicular magnetic field in the infinitene molecule[30] that well-supports the findings by Orozco-Ic et al. Further, the properties of infinitene have been explored by various research groups.[29] Additionally, Fan et al.[31] synthesized chiral-twisted figure-eight CNBs that could be used for material applications.

The nonplanarity of 12-infinitene raises a question regarding the distribution of 48π-electrons over 70 C−C bonds for conserving its aromatic character. Also, there is a question on whether the nature of aromaticity exhibited by the system is

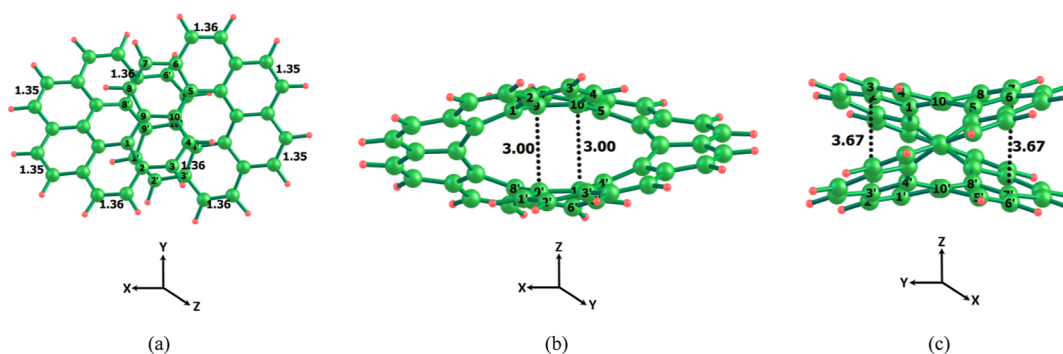**Figure 1.** Optimized geometry of 12-infinitene at the B3LYP/6-311G** level. The distances between the carbon centers are given in Å.

Hückel-type[32] or Möbius-type. Surprisingly, infinitene does not satisfy the Hückel or Möbius aromaticity criteria. Hence a detailed study is required for exploring its π-electron delocalization pathway and aromaticity.

An in-depth analysis of the electronic distribution in molecular systems helps to understand their chemical bonding, stability, reactivity, interactive behavior, aromatic character, and optoelectronic applications. The analysis based on molecular electrostatic potential (MESP)[33−35] is regarded as one of the most effective tools for understanding the localization/delocalization behavior of the electrons and predicting the chemical reactivity of the molecular systems. The MESP, $V(\mathbf{r})$, at any point in space, is a real physical quantity that shows the combined effect of nuclear and electronic charge distribution of molecular systems.[36,37] The most negative, three-dimensional potential minimum (V_m) in the MESP topology analysis indicates the electron-rich sites such as lone pairs and π-regions.[38] The present study uses the MESP topology analysis for the systematic investigation to interpret the intrinsic π-electron distribution and aromatic character in infinity-shaped molecules and their isomeric counterparts, viz., benzenoid circulenes and benzenoid nano-belts.

METHODOLOGY

All infinitene systems and other molecules explored in the study are optimized using density functional theory (DFT)-based B3LYP/6-311G** method[39,40] as implemented in the Gaussian 16 program package.[41] The optimized geometries are checked for their minimal nature by doing a frequency run and verifying that all harmonic frequencies are real. The Deformed Atoms in Molecules Quantum Theory package is used to perform the MESP topology computation.[42−45] The MESP, $V(\mathbf{r})$, at any point, $\mathbf{r}$, in the space is defined in eq 1, where $\rho(\mathbf{r})$ is the continuous electron density and Z_A is the charge on the nucleus of the atom A located at $\mathbf{R}_A$.[46−48]

$$V(\mathbf{r}) = \sum_A^N \frac{Z_A}{|\mathbf{r} - \mathbf{R}_A|} - \int \frac{\rho(\mathbf{r}')d^3r'}{|\mathbf{r} - \mathbf{r}'|} \quad (1)$$

The topological features $V(\mathbf{r})$ are derived using its first- and second-order partial derivatives and used for mapping its critical points (CPs). A CP is defined as a point where all first-order partial derivatives of $V(\mathbf{r})$ vanish. There are three eigenvalues (λ_1, λ_2, and λ_3) and corresponding eigenvectors associated with the Hessian matrix at each nondegenerate CP. The eigenvalues (λ) indicate the curvature of the function at the CP, and each eigenvector signifies the axis of the

curvature.[49] A nondegenerate CP is characterized by two numbers $(\mathbf{R}, \sigma)$, where "$\mathbf{R}$" and "σ," respectively, stand for the number of non-zero eigenvalues and the algebraic sum of the sign of eigenvalues. In the MESP topology, a $(3, +3)$ CP corresponds to a local minimum, a $(3, −3)$ CP corresponds to a local maximum, and $(3, −1)$ and $(3, +1)$ CPs are designated as saddle points.[50−52] Among the $(3, +3)$, $(3, +1)$, $(3, −1)$, and $(3, −3)$ CPs, the present investigation has focused on the characteristics of $(3, +3)$ CPs, which appear at the electron-dense regions.[53] We use the notation V_m to represent a $(3, +3)$ local minimum. Typically, V_m corresponds to the most negative-valued $V(\mathbf{r})$. The total deviation of λ values of a given system from those of benzene, viz., $\Delta\lambda_1$, $\Delta\lambda_2$, and $\Delta\lambda_3$ (eq 2), has been proposed for distinguishing the aromatic, nonaromatic, and antiaromatic C−C bonded π-regions in molecules.[55]

$$\sum_{i=1}^{3} \Delta\lambda_i = (\lambda_{1(\text{system})} - \lambda_{1(\text{benzene})}) + (\lambda_{2(\text{system})} - \lambda_{2(\text{benzene})})$$
$$+ (\lambda_{3(\text{system})} - \lambda_{3(\text{benzene})}) \quad (2)$$

The value of $\sum_{i=1}^{3} \Delta\lambda_i \leq 0.011$ au has recently been suggested for aromatic behavior, while a value between 0.011 and 0.035 au is recommended for identifying the nonaromatic character, and a value above 0.035 au is proposed for the antiaromatic nature.[54] To check the reliability of the B3LYP method, a benchmark study is also conducted with the DFT methods BP86, B3PW91, M06L, and wB97XD using the 6-311G** basis set in all cases. Though the absolute values of the SCF energy and MESP parameters differ to some extent, the relative order and the trend in values are almost identical in all cases (Figure S4). Hence, only the B3LYP/6-311G** values are discussed in the present work.

RESULTS AND DISCUSSION

12-Infinitene. The 12-infinitene system can be envisaged as a fused form of two 6-helicene units (6-helicene-a and 6-helicene-b) through ring fusions at the end portions. Figure 1 depicts its structure, wherein the two 6-helicene units are denoted using different color codes. In the top view of the structure (Figure 1a), a naphthalene unit (carbon centers C1−C10) of 6-helicene-a appears superimposed over another such unit from helicene-b (carbon centers C1′−C10′). The shortest distance of 3.00 Å is seen between C9 and C9′ and between C10 and C10′. The longest groove distance, 3.67 Å, is noticed for C2···C2′, C3···C3′, C6···C6′, and C7···C7′. The X-ray structure of this molecule showed C9···C9′ and groove
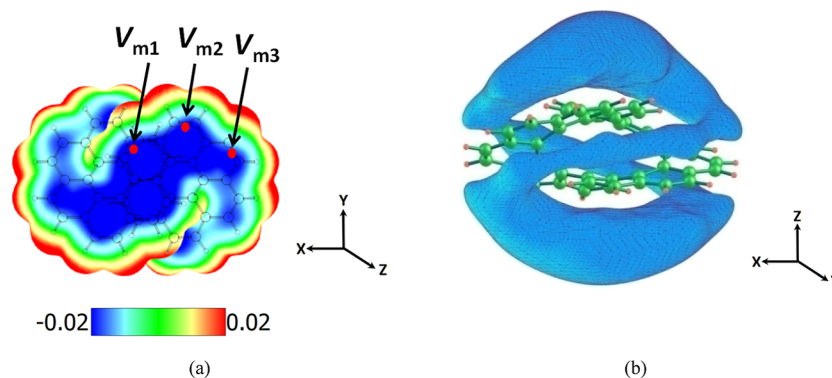
Figure 2. (a) MESP-textured electron density isosurface of value 0.001 au for 12-infinitene at the B3LYP/6-311G** level. Color coding from blue to red indicates MESP values in the range −0.02 to 0.02 au and (b) MESP is isosurface mapped at −0.01 au. The positions of MESP minima are denoted using red dots.
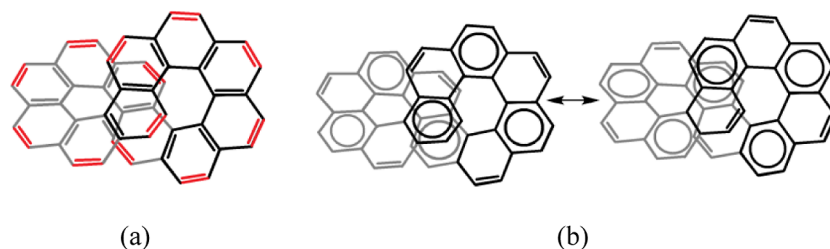

Figure 3. (a) MESP topology pattern and (b) resonance structures of 12-infinitene. The V_m positions associated with double bonds are shown in red.

distances of 2.92 and 3.64 Å, respectively. This is also borne out by the theoretical data (Table S1).[23]

The MESP textured on the 0.001 au (atomic unit) electron density isosurface in Figure 2a brings out the infinity shape of the electron distribution over the aromatic rings. The MESP topology features of 12-infinitene in Figure 2b show three distinct MESP minima, V_{m1}, V_{m2}, and V_{m3}, appearing above the symmetrically dissimilar C−C bonds. The convex-armchair edges (K-regions) characterized by the presence of V_m are more localized than others and are represented using double bonds with red color in Figure 3a (a total of 12 such bonds).[55] The armchair periphery in infinitene attributes more resonance stabilization for it.[56] The Clar's sextet-like electronic arrangement in armchair-edged systems reported by Rakhi and Suresh is well discernible here.[57]

This feature is also evident from their bond lengths (1.35 to 1.36 Å) and other bond lengths, which lie in the range of 1.42 to 1.48 Å (Figure 1a). The X-ray crystal structure data show a range of 1.33 to 1.36 Å for the shorter C−C bonds and 1.40 to 1.48 Å for the longer ones. For a representation of the molecule using alternate single and double bonds, the positions of the red-colored double bonds automatically fix the position of other double bonds. Thus, MESP topology suggests a chemical formula for 12-infinitene as given in Figure 3a.[23]

12-infinitene can also be represented as a resonance hybrid of two Clar's sextet structures (Figure 3b). Such a representation suggests that the π-electrons of the C−C bond at the 6−6 ring fusion are almost equally shared by both the rings. The three eigenvalues (λ_1, λ_2, and λ_3) for each V_m and the respective MESP values are given in Table 1. Among the three distinct V_m values of 12-infinitene, the V_{m1} corresponds to the most localized π-bond with a minimum value of −19.2 kcal/mol, which is more negative compared to the V_m of benzene, viz., −17.0 kcal/mol. However, V_{m2} and

Table 1. MESP Topology Features of Benzene and 12-Infinitene at the B3LYP/6-311G Level**[a]

		eigenvalues			
V_m type	MESP	λ_1	λ_2	λ_3	$\sum_{i=1}^{3} \Delta\lambda_i$
$V_{m\text{-benzene}}$	−17.0	0.0166	0.0027	0.0005	0.0000
V_{m1}	−19.2	0.0180	0.0065	0.0049	0.0095
V_{m2}	−16.2	0.0166	0.0056	0.0042	0.0066
V_{m3}	−14.5	0.0170	0.0061	0.0047	0.0079

[a](V_m values in kcal/mol and the eigenvalues in atomic units).

V_{m3} are less negative than those of benzene with minimum values of −16.2 and −14.5 kcal/mol, respectively. Similarly, the eigenvalues of V_{m1}, V_{m2}, and V_{m3} show a small variation vis-à-vis the V_m value of benzene. The total deviation in the eigenvalues, $\sum_{i=1}^{3} \Delta\lambda_i$, reflects the resemblance of the aromatic character of the system to that of benzene. The previous study stipulated that the eigenvalue deviation parameter $\sum_{i=1}^{3} \Delta\lambda_i$ is ≤0.011 au for all aromatic systems, lies between 0.011 and 0.035 au for all nonaromatic systems, and above 0.035 au for antiaromatic systems. In 12-infinitene, the $\sum_{i=1}^{3} \Delta\lambda_i$ values corresponding to each V_m are positive, and they fall in the range of 0.0066 to 0.0095 au. These data clearly indicate that the extent of π-electron delocalization ingrained in each ring of infinitene is only slightly lower than that of benzene. Typically, polycyclic benzenoid hydrocarbons show a diminished aromatic character than benzene.[58−60] Further, the criterion of $\sum_{i=1}^{3} \Delta\lambda_i$ also supports Clar's representation of the infinitene system (Figure 3b) wherein the ring with a numerically small deviation in the sum of eigenvalues
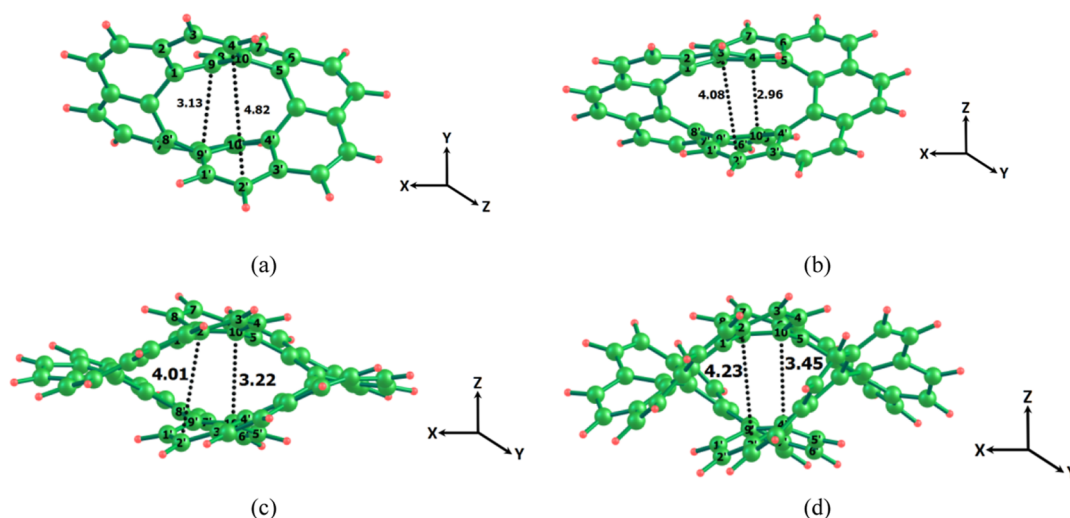
C

Figure 4. Optimized geometries of (a) 8- (b) 10-, (c) 14-, and (d) 16-infinitenes. The marked distances are in Å.

Table 2. MESP Topology Features of 8-, 10-, 14-, and 16-Infinitenes at the B3LYP/6-311G Level[a]**

| system | V_m type | MESP | eigenvalues | | | $\sum_{i=1}^{3} \Delta\lambda_i$ |
			λ_1	λ_2	λ_3	
8-infinitene	V_{m1}	−17.5	0.0234	0.0085	0.0075	0.0195
	V_{m2}	−15.4	0.0200	0.0081	0.0066	0.0148
	V_{m3}	−14.8	0.0170	0.0074	0.0057	0.0102
	V_{m4}	−12.9	0.0267	0.0090	0.0071	0.0229
10-infinitene	V_{m1}	−22.0	0.0167	0.0114	0.0053	0.0135
	V_{m2}	−16.0	0.0183	0.0067	0.0054	0.0105
	V_{m3}	−14.5	0.0197	0.0071	0.0061	0.0130
14-infinitene	V_{m1}	−20.3	0.0185	0.0067	0.0053	0.0106
	V_{m2}	−17.4	0.0178	0.0061	0.0049	0.0089
	V_{m3}	−14.6	0.0151	0.0048	0.0030	0.0030
	V_{m4}	−14.4	0.0170	0.0066	0.0046	0.0084
16-infinitene	V_{m1}	−23.3	0.0205	0.0067	0.0035	0.0108
	V_{m2}	−19.5	0.0195	0.0067	0.0057	0.0120
	V_{m3}	−16.0	0.0153	0.0048	0.0027	0.0029
	V_{m4}	−15.7	0.0154	0.0054	0.0033	0.0042

[a](V_m values in kcal/mol and eigenvalues in au).
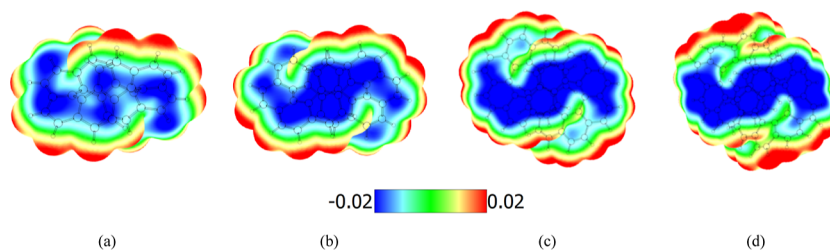
Figure 5. MESP textured on 0.001 au-valued electron density isosurface for (a) 8- (b) 10-, (c) 14-, and (d) 16-infinitenes at the B3LYP/6-311G** level. Color coding from blue to red indicates MESP in the range −0.02 to 0.02 au.

constitutes an aromatic sextet. The clockwise current density vector at the isosurface plotted at 0.025 au (Figure S10) using anisotropy-induced current density[61] shows the diatropic ring current induced by the external magnetic field which confirms the aromatic character of 12-infinitene.[62] The 12-infinitene and the planar circulene system kekulene are isomers wherein 12-infinitene is thermodynamically less stable than kekulene[24] by 60.1 kcal/mol, which is equivalent to ~1.0 kcal/mol

destabilization per C−C bond. Also, compared to the more strained isomeric [6,6]-CNB, 12-infinitene is more stable by 49.1 kcal/mol.

8-, 10-, 14-, and 16-Infinitenes: Structure and MESP Topology. The infinitene-shaped molecules comprising 8-, 10-, 14-, and 16-fused benzene rings are also analyzed for their structure, MESP topology features, π-electron distribution, and aromatic character. In 8-infinitene, the shortest nonbonded
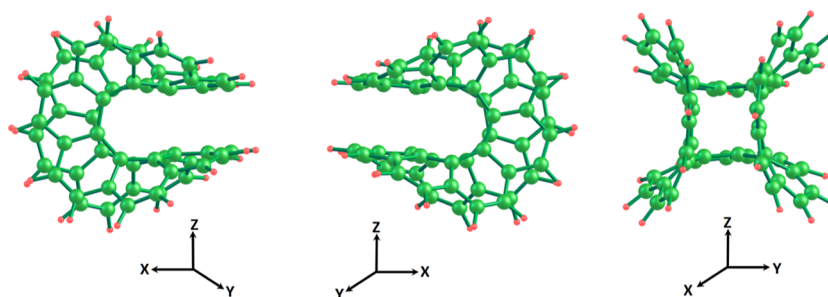
Figure 6. Saddle-shaped geometry of 14-circulene at the B3LYP/6-311G** level.
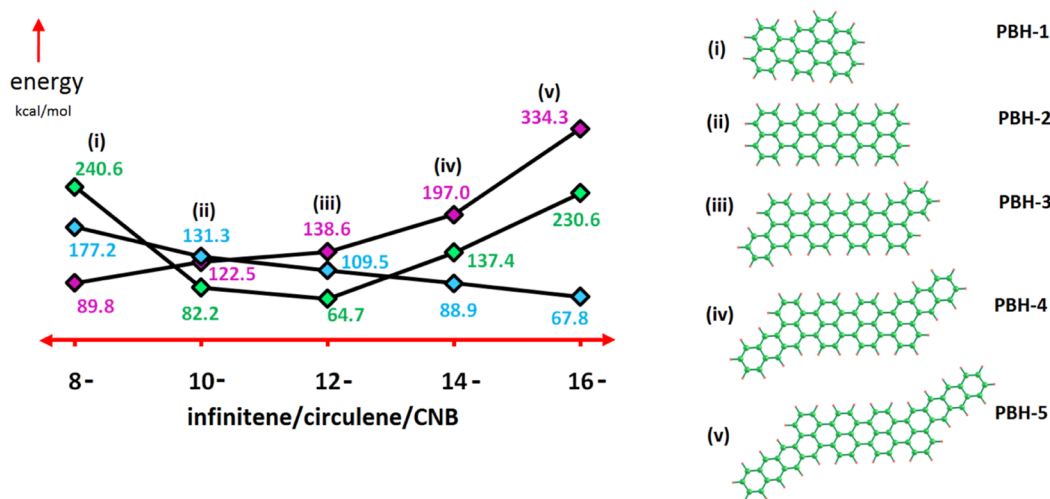

Figure 7. Energy of circulenes, belts, and infinitenes relative to their planar PBH counterparts at the B3LYP/6-311G** level. Magenta, blue, and green marks, respectively, indicate circulenes, belts, and infinitenes.

distance of 3.13 Å is seen for C9···C9′ and C10···C10′ for the superimposed "naphthalene-type" region as seen from the top. The longest groove distance of 4.82 Å is observed between C3···C1′ and C4···C2′ (Figure 4a). In 10-infinitene, the shortest CC distance (C9···C9′ and C10···C10′) and the longest groove distance (C3···C2′) are 2.96 and 4.08 Å, respectively. Similarly, the shortest CC distance (C9···C9′ and C10···C10′) and the longest groove distance (C2···C2′) in 14-infinitene are 3.22 and 4.01 Å, respectively. 16-infinitene appear as the most twisted with the shortest C···C distance of 3.45 Å and the longest groove distance of 4.23 Å. The MESP data and trends in eigenvalues are displayed in Table 2.

The MESP plotted on the 0.001 au-valued isodensity surface (Figure 5) clearly brings out the infinity shape of the electron distribution in 8-, 10-, 14-, and 16-infinitenes. The MESP analysis exhibits four MESP minima, viz., V_{m1}, V_{m2}, V_{m3}, and V_{m4}, indicating symmetrically nonequivalent π-localized regions of C−C bonds in 8-infinitene. The bonds with considerable double bond character are ~1.39 Å in length, while the other bonds appear in the range of 1.40−1.46 Å. The $\sum_{i=1}^{3} \Delta\lambda_i$ value corresponding to the V_m suggests a high nonaromatic character associated with the benzene rings. Similarly, in 10-infinitene, V_{m1}, V_{m2}, and V_{m3} correspond to relatively more localized π-regions in the molecule with C−C bond lengths lying between 1.37 and 1.38 Å. The $\sum_{i=1}^{3} \Delta\lambda_i$ value for both V_{m1} and V_{m3} is greater than the aromatic cutoff value 0.011 au while very close to that for V_{m2}. These data suggest the dominance of nonaromatic character over the aromatic one for all rings in 10-infinitene. Among the four

distinct MESP minima, viz., V_{m1}, V_{m2}, V_{m3}, and V_{m4} observed for 14-infinitene, the $\sum_{i=1}^{3} \Delta\lambda_i$ data indicate an aromatic character for rings labeled with V_{m2}, V_{m3}, and V_{m4} and nonaromatic for the other one. Similarly, in 16-infinitene, V_{m2} has the highest $\sum_{i=1}^{3} \Delta\lambda_i$ value which brings out the nonaromatic behavior associated with the corresponding ring, while rings embedded with V_{m1}, V_{m3}, and V_{m4} are expected to be aromatic. The nonaromatic V_m rings can be easily exposed for addition reactions and a few examples on transition-state models for HCl addition are given in the Supporting Information. Though all systems show infinity-shaped π-electron conjugation (Figure 5), the $\sum_{i=1}^{3} \Delta\lambda_i$ data clearly suggest nonaromatic character for many of the rings in them. The non-uniformity in the π-conjugation at C−C bonds in all infinitene systems is clearly reflected in the bond length alternation (BLA) as well[29,63] (Table S4). In general, BLA data support the aromatic character for all infinitenes.

Circulenes, Carbon Nanobelts, and Infinitenes: Relative Stability. Circulenes are macrocyclic arene systems for which the central n-sided ring is completely surrounded by benzenoids.[64] So far, the synthesis of different circulene systems consisting of 4-, 5-, 6-, 7-, and 8- fused benzene rings has been reported by various research groups wherein only 5-, 6-, and 7-circulenes have been synthesized without sub-stituents.[65] Among them, 4-circulene (quadrannulene)[66−68] and 5-circulene (corannulene)[69−71] appear bowl-shaped, while 6-circulene (coronene)[72] is endowed with a planar geometry. A saddle-shaped geometry is shown by 7-circulene (pleiadan-

Table 3. MESP Topology Features of 8-, 10-, 12-, 14-, and 16-Circulenes and CNBs at the B3LYP/6-311G Level[a]**

system	V_m type	MESP	$\sum_{i=1}^{3} \Delta\lambda_i$	system	V_m type	MESP	$\sum_{i=1}^{3} \Delta\lambda_i$
8-circulene	V_{m1}	−17.6	−0.0120	8-CNB	V_{m1}	−15.6	−0.0024
	V_{m2}	−17.3	0.0063		V_{m2}	−15.2	0.0160
	V_{m3}	−16.3	0.0087		V_{m3}	−13.7	−0.0087
10-circulene	V_{m1}	−20.5	−0.0089	10-CNB	V_{m1}	−15.1	−0.0037
	V_{m2}	−20.1	0.0049		V_{m2}	−15.0	0.0142
	V_{m3}	−19.0	0.0095		V_{m3}	−14.5	−0.0040
	V_{m4}	−18.3	0.0103		V_{m4}	−13.1	−0.0198
12-circulene	V_{m1}	−21.7	0.0009	12-CNB	V_{m1}	−15.0	−0.0046
	V_{m2}	−21.2	0.0232		V_{m2}	−14.8	−0.0023
	V_{m3}	−19.8	0.0084		V_{m3}	−14.6	0.0127
	V_{m4}	−18.9	0.0083		V_{m4}	−12.9	−0.0180
14-circulene	V_{m1}	−22.2	0.0079	14-CNB	V_{m1}	−15.0	−0.0052
	V_{m2}	−20.8	0.0036		V_{m2}	−14.6	−0.0010
	V_{m3}	−20.0	−0.0081		V_{m3}	−14.4	0.0117
	V_{m4}	−20.0	0.0068		V_{m4}	−12.7	−0.0166
16-circulene	V_{m1}	−22.8	0.0049	16-CNB	V_{m1}	−14.8	−0.0087
	V_{m2}	−21.7	−0.0056		V_{m2}	−14.4	0.0000
	V_{m3}	−21.2	0.0073		V_{m3}	−14.1	0.0109
	V_{m4}	−20.9	0.0081		V_{m4}	−12.5	−0.0156

[a]Most negative four V_m points are depicted, and full topology details are provided in the supporting information (V_m values in kcal/mol and eigenvalues in au).

nulene)[25,73,74] and 8-circulene.[75,76] The 8-circulene is the largest circulene synthesized so far, and the synthesis of several of its derivatives is reported by different groups.[65,75−81] Hopf and co-workers predicted the shape and strain energy of *n*-circulenes (where *n* = 3 to 20) based on a computational study.[68] According to them, the circulenes from *n* = 7 to 16 are saddle shaped and those from *n* = 17 to 20 are helics-shaped. The belt-shaped compounds, exclusively composed of fused benzene rings, are regarded as CNBs and have been used as a powerful gem for the synthesis of carbon nanotubes (CNTs). A belt segment of armchair [6,6]-CNT comprising of 12-arene rings (12-CNB) synthesized by Povie et al.[11] was the first member from the CNB family. Later, higher members of CNBs of various sizes and shapes were reported by various research groups.[10,14,82−86] There are CNBs containing non-benzenoid rings[87−90] and hetero-atoms,[91−93] wherein the incorporation of hetero-atoms radically alters the electronic properties of belts, leading to diverse applications in functional materials. Circulenes, CNBs, and infinitenes made up of n-benzenoid rings (represented with the molecular formula $C_{2n}H_n$) are isomers. They are expected to show π-electron distribution and aromaticity features characteristic to their unique structure. Circulenes show a saddle shape with a negative curvature, and Figure 6 depicts the geometry of a representative example, 14-circulene. From 8-circulene to 16-circulene, the depth of the curved region increases, which indicates increasing strain effect in higher circulenes.

A $C_{2n}H_n$ polycyclic benzenoid hydrocarbon (PBH) in the planar configuration is expected to be more stable than the isomeric circulene, CNB, and infinitene mainly due to the least strain effect in the planar state. In Figure 7, the energies of 8-, 10-, 12-, 14-, and 16-circulenes/infinitenes/nanobelts are compared relative to the energy of PBH systems, viz., PBH-1, PBH-2, PBH-3, PBH-4, and PBH-5 which correspond to the molecular formulae $C_{32}H_{16}$, $C_{40}H_{20}$, $C_{48}H_{24}$, $C_{56}H_{28}$, and $C_{64}H_{32}$, respectively. Figure 7 clearly shows that in the case of

nanobelts, as the radius of the belt increases, stability of the system increases due to the decrease in strain energy. A strong linear trend in energy change is observed for this series. An exactly opposite trend in stability is observed for the *n*-circulenes as the strain effect increases substantially with the increase in "*n*." In the case of infinitenes, 8-infinitene shows the highest energy difference compared to the isomer PBH-1, whereas 12-infinitene shows the least energy difference compared to the isomer PBH-3. The relative energy data in Figure 7 also show that 10- and 12-infinitenes are significantly more stable than the corresponding nanobelts and circulenes, whereas the stability order for others is 8-infinitene < 8-CNB < 8-circulene; 14-circulene < 14-infinitene < 14-CNB and 16-circulene < 16-infinitene < 16-CNB. Among all the nonplanar structures, 12-infinitene is the most stable one.

Circulenes and CNBs: MESP Topology. Table 3 shows the MESP topology parameters such as the V_m value and the eigenvalue parameter $\sum_{i=1}^{3} \Delta\lambda_i$ for circulenes and CNBs. The eigenvalues, viz., λ_1, λ_2, and λ_3 corresponding to each V_m are given in Supporting Information Table S2. The $\sum_{i=1}^{3} \Delta\lambda_i$ values indicate largely aromatic character for these systems akin to that of benzene for all benzenoid rings of circulenes. In 8-, 10-, and 12-circulenes, V_m points showing $\sum_{i=1}^{3} \Delta\lambda_i > 0.01$ au are noticed at the curved regions. Since MESP at the curved region is influenced by π-regions of rings from above and below, the high magnitude of $\sum_{i=1}^{3} \Delta\lambda_i$ need not necessarily indicate the nonaromatic character as the CC bonds observed at these regions are similar to those for the other regions. However, it can be attributed to the localization of electron density between the two benzene rings at the curved regions. The $\sum_{i=1}^{3} \Delta\lambda_i$ data of CNBs clearly suggest that all −HCCH− bonds of the CNB possess a strong olefin character as the $\sum_{i=1}^{3} \Delta\lambda_i$ value of V_m observed at this region (inner/outer regions) is always higher than 0.01 au. Analysis of V_m values
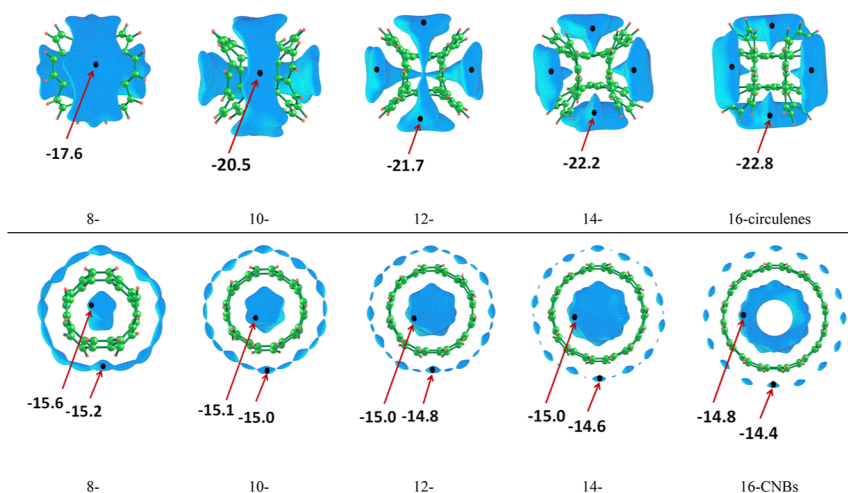
Figure 8. MESP isosurfaces (value −0.02 au) of circulenes and CNBs. The most negative V_{m1} for circulenes and V_{m1} and V_{m2} values at the B3LYP/6-311G** level are given in kcal/mol.

suggest that the MESP negative character gradually increases as the size of the circulene increases, whereas a slight decrease in the magnitude of MESP is observed with the increase in the size of the CNBs. Further illustration of this MESP feature is evident from the MESP isosurface plots given in Figure 8. In circulenes, the curved regions show accumulation of electron density, and the deeper the curvature of the circulene, the more localized and more negative is the MESP. In CNBs, the MESP distribution clearly distinguishes both the exterior and interior regions. The interior MESP is more localized than the exterior one, whereas the absolute magnitudes of MESP at both the regions do not show significant deviations.

Infinitenes, Circulenes, and CNBs: Distinction Based on Li+ Binding Affinity. The electron-rich characters of infinitene, circulene, and CNB can be assessed by evaluating their strength of interaction with a cation such as Li+ since the electron-rich sites are expected to show larger interaction than the other ones. The Li+ binding at the exterior (P1) and interior (P2) electron-rich regions in infinitene, circulene, and CNB are depicted in Figure 9 and the binding energy (BE) data are given in Table 4. The Li+ complexes show significantly higher stability with infinitene, circulene, and CNB systems compared to aromatic systems such as benzene, naphthalene, anthracene, chrysene, and pyrene. In all cases, the binding of cation at P2 is more stable wherein the cation−π-interaction is supported by π-centers from multiple rings, whereas at P1, the binding is mostly directed toward one π-center. In infinitenes, the binding efficiency gradually increases with the size of the system, whereas in circulenes, the binding strength increases up to 12-circulene and then decreases. In CNBs, the binding energy shows only a minor variation, and their binding strength is significantly lower than those of infinitenes and circulenes. Among all systems studied, the infinity-shaped systems appear more effective for inducing cation−π interaction than others.

CONCLUSIONS

The π-electron delocalization and aromatic character of the recently synthesized 12-infinitene molecule is quantified in terms of MESP topology features. The MESP topology describes the double bond distribution in the system and provides a unique definition of the chemical formula that also supports Clar's aromatic sextet structure for each benzenoid
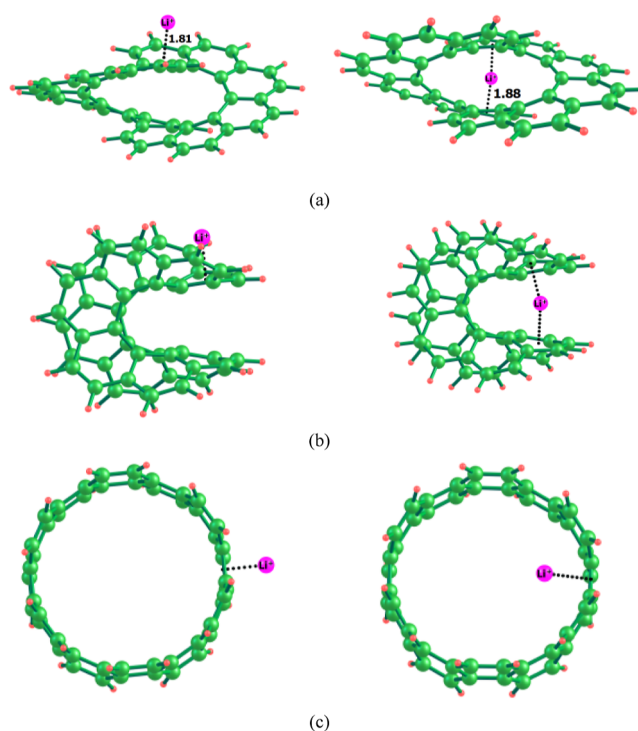

Figure 9. Binding of Li+ in the exterior and interior electron-rich regions in (a) infinitene, (b) circulene, and (c) CNB at the B3LYP/6-311G** level.

ring. The possibility of other infinitenes containing 8-, 10-, 14-, and 16-arene rings is also evaluated using DFT, and the trend in π-electron delocalization as well as aromatic character is analyzed on the basis of the three eigenvalues (λ_i) of the Hessian matrix at the (3, +3) V_m CPs. Such an MESP topology-guided analysis confirms most of the benzene rings of infinitenes as aromatic, while nonaromatic localization is observed in a few. For all cases, MESP distribution visualized in terms of isosurface plots clearly shows the infinity-shaped delocalization of the electron density that runs over all fused benzene rings.

The eigenvalue parameter $\sum_{i=1}^{3} \Delta\lambda_i$ suggests 12-infinitene to be highly aromatic, while a strong localization of certain CC π-

Table 4. Comparison of Li$^+$ Binding in Infinitene, Circulene, and CNB at the Exterior Position (P1) and the Interior Position (P2)[a]

			BE					
			infinitene		circulene		CNB	
system	BE	infinitene/circulene/CNB	P1	P2	P1	P2	P1	P2
benzene	−39.6	8	−52.2	−59.3	−53.8	−54.5	−49.6	−54.4
naphthalene	−42.3	10	−53.4	−63.9	−54.5	−67.5	−50.6	−51.8
anthracene	−44.7	12	−55.9	−66.0	−56.5	−69.3	−51.2	−50.9
chrysene	−45.9	14	−58.1	−69.3	−59.2	−70.2	−51.7	−52.3
pyrene	−45.8	16	−61.7	−72.5	−61.7	−64.0	−51.9	−52.4

[a]Values in kcal/mol.

bonds induces a slight nonaromatic character to other infinitenes. The stability of infinitenes is evaluated by comparing the energy of infinitenes relative to their isomeric planar PBH systems, circulenes, and CNBs. The relative energy data reveal that 12-infinitene is not only the stable infinitene but also the most stable system of all systems, including nanobelts and circulenes. However, the stability order for other systems can be expressed as 8-infinitene < 8-CNB < 8-circulene; 10-infinitene < 10-circulene < 10-CNB; 14-circulene < 14-infinitene < 14-CNB; and 16-circulene < 16-infinitene < 16-CNB. The MESP studies show that electron density is mostly accumulated at the curved-regions in circulenes and the exterior regions in CNBs. The $\sum_{i=1}^{3} \Delta\lambda_i$ shows a high aromatic character for all benzenoid rings of circulenes, while all—HCCH— bonds exhibit a strong olefin character in CNBs. Also, the V_m data indicate that the MESP negative character gradually increases as the size of the circulene increases, while only a slight decrease in the magnitude of MESP is observed with the increase in the size of the CNBs. Further, the electron-rich character of infinitene, circulene, and CNB is evaluated by the cation-binding strength, wherein the infinity-shaped molecules are observed to possess greater cation−π interactions compared to circulenes and nanobelts. This study has brought out an MESP topological viewpoint of infinitenes, circulenes, and nanobelts, shedding light on the extent of π-conjugation, aromatic features, and stability ingrained in infinitenes compared to circulenes and nanobelts.

ASSOCIATED CONTENT

Data Availability Statement

The data underlying this study are available in the published article and its Supporting Information.

⬛ Supporting Information

The Supporting Information is available free of charge at https://pubs.acs.org/doi/10.1021/acs.joc.2c02507.

Crystallographic data of 12-infinitene (CCDC 2113525), optimized geometries, detailed MESP topological features, Cartesian coordinates, SCF energy, and transition state models for all systems (PDF)

AUTHOR INFORMATION

Corresponding Authors

Shridhar R. Gadre − *Department of Scientific Computing, Modelling and Simulation, Savitribai Phule Pune University, Pune 411007, India;* ⦿ orcid.org/0000-0003-3234-3959; Email: gadre@unipune.ac.in

Cherumuttathu H. Suresh − *Chemical Sciences and Technology Division, CSIR-National Institute for Interdisciplinary Science and Technology, Thiruvananthapuram 695019 Kerala, India; Academy of Scientific and Innovative Research (AcSIR), Ghaziabad 201002, India;* ⦿ orcid.org/0000-0001-7237-6638; Phone: +91-471-2515472; Email: sureshch@gmail.com

Author

Puthannur K. Anjalikrishna − *Chemical Sciences and Technology Division, CSIR-National Institute for Interdisciplinary Science and Technology, Thiruvananthapuram 695019 Kerala, India; Academy of Scientific and Innovative Research (AcSIR), Ghaziabad 201002, India*

Complete contact information is available at:
https://pubs.acs.org/10.1021/acs.joc.2c02507

Notes

The authors declare no competing financial interest.

⬛ ACKNOWLEDGMENTS

⬛ REFERENCES

(1) Falcao, E. H.; Wudl, F. Carbon allotropes: beyond graphite and diamond. *J. Chem. Technol. Biotechnol.* 2007, *82*, 524−531.

(2) Hirsch, A. The era of carbon allotropes. *Nat. Mater.* 2010, *9*, 868−871.

(3) Slepičková Kasálková, N.; Slepička, P.; Švorčík, V. Carbon nanostructures, nanolayers, and their composites. *Nanomaterials* 2021, *11*, 2368.

(4) Rao, R.; Pint, C. L.; Islam, A. E.; Weatherup, R. S.; Hofmann, S.; Meshot, E. R.; Wu, F.; Zhou, C.; Dee, N.; Amama, P. B.; Carpena-Nuñez, J.; Shi, W.; Plata, D. L.; Penev, E. S.; Yakobson, B. I.; Balbuena, P. B.; Bichara, C.; Futaba, D. N.; Noda, S.; Shin, H.; Kim, K. S.; Simard, B.; Mirri, F.; Pasquali, M.; Fornasiero, F.; Kauppinen, E. I.; Arnold, M.; Cola, B. A.; Nikolaev, P.; Arepalli, S.; Cheng, H.-M.; Zakharov, D. N.; Stach, E. A.; Zhang, J.; Wei, F.; Terrones, M.; Geohegan, D. B.; Maruyama, B.; Maruyama, S.; Li, Y.; Adams, W. W.; Hart, A. J. Carbon Nanotubes and Related Nanomaterials: Critical Advances and Challenges for Synthesis toward Mainstream Commercial Applications. *ACS Nano* 2018, *12*, 11756−11784.

(5) Zhdanov, V. P. Catalytic Conversion of Hydrocarbons and Formation of Carbon Nanofilaments in Porous Pellets. *Catal. Lett.* 2022, 1.

(6) Jasti, R.; Bhattacharjee, J.; Neaton, J. B.; Bertozzi, C. R. Synthesis, Characterization, and Theory of [9]-, [12]-, and [18]-

Cycloparaphenylene: Carbon Nanohoop Structures. *J. Am. Chem. Soc.* **2008**, *130*, 17646−17647.

(7) Kayahara, E.; Patel, V. K.; Yamago, S. Synthesis and Characterization of [5]Cycloparaphenylene. *J. Am. Chem. Soc.* **2014**, *136*, 2284−2287.

(8) Eisenberg, D.; Shenhar, R.; Rabinovitz, M. Synthetic approaches to aromatic belts: building up strain in macrocyclic polyarenes. *Chem. Soc. Rev.* **2010**, *39*, 2879−2890.

(9) Segawa, Y.; Yagi, A.; Matsui, K.; Itami, K. Design and synthesis of carbon nanotube segments. *Angew. Chem., Int. Ed.* **2016**, *55*, 5136−5158.

(10) Cheung, K. Y.; Watanabe, K.; Segawa, Y.; Itami, K. Synthesis of a zigzag carbon nanobelt. *Nat. Chem.* **2021**, *13*, 255−259.

(11) Povie, G.; Segawa, Y.; Nishihara, T.; Miyauchi, Y.; Itami, K. Synthesis of a carbon nanobelt. *Science* **2017**, *356*, 172−175.

(12) Li, Y.; Kono, H.; Maekawa, T.; Segawa, Y.; Yagi, A.; Itami, K. Chemical Synthesis of Carbon Nanorings and Nanobelts. *Mater. Res.* **2021**, *2*, 681−691.

(13) Sakamoto, Y.; Suzuki, T. Tetrabenzo [8] circulene: aromatic saddles from negatively curved graphene. *J. Am. Chem. Soc.* **2013**, *135*, 14074−14077.

(14) Cheung, K. Y.; Chan, C. K.; Liu, Z.; Miao, Q. A Twisted Nanographene Consisting of 96 Carbon Atoms. *Angew. Chem., Int. Ed.* **2017**, *56*, 9003−9007.

(15) Gu, Y.; Qiu, Z.; Müllen, K. Nanographenes and Graphene Nanoribbons as Multitalents of Present and Future Materials Science. *J. Am. Chem. Soc.* **2022**, *144*, 11499.

(16) Saraswat, V.; Jacobberger, R. M.; Arnold, M. S. Materials science challenges to graphene nanoribbon electronics. *ACS Nano* **2021**, *15*, 3674−3708.

(17) Hasegawa, M.; Nojima, Y.; Mazaki, Y. Circularly Polarized Luminescence in Chiral π-Conjugated Macrocycles. *ChemPhotoChem* **2021**, *5*, 1042−1058.

(18) Zheng, W.; Ikai, T.; Oki, K.; Yashima, E. Consecutively fused single-, double-, and triple-expanded helicenes. *Nat. Sci.* **2022**, *2*, No. e20210047.

(19) Newman, M. S. A new synthesis of coronene. *J. Am. Chem. Soc.* **1940**, *62*, 1683−1687.

(20) Newman, M. S.; Wheatley, W. B. Optical Activity of the 4,5-Phenanthrene Type: 4-(1-Methylbenzo[c]phenanthryl)-acetic Acid and 1-Methylbenzo[c]phenanthrene1. *J. Am. Chem. Soc.* **1948**, *70*, 1913−1916.

(21) Shen, Y.; Chen, C.-F. Helicenes: Synthesis and Applications. *Chem. Rev.* **2012**, *112*, 1463−1535.

(22) Urbano, A. Recent Developments in the Synthesis of Helicene-Like Molecules. *Angew. Chem., Int. Ed. Engl.* **2003**, *42*, 3986−3989.

(23) Krzeszewski, M.; Ito, H.; Itami, K. Infinitene: A Helically Twisted Figure-Eight [12]Circulene Topoisomer. *J. Am. Chem. Soc.* **2022**, *144*, 862−871.

(24) Krieger, C.; Diederich, F.; Schweitzer, D.; Staab, H. A. Molecular structure and spectroscopic properties of kekulene. *Angew. Chem., Int. Ed. Engl.* **1979**, *18*, 699−701.

(25) Pun, S. H.; Wang, Y.; Chu, M.; Chan, C. K.; Li, Y.; Liu, Z.; Miao, Q. Synthesis, Structures, and Properties of Heptabenzo[7]-circulene and Octabenzo[8]circulene. *J. Am. Chem. Soc.* **2019**, *141*, 9680−9686.

(26) Guo, Q.-H.; Qiu, Y.; Wang, M.-X.; Fraser Stoddart, J. Aromatic hydrocarbon belts. *Nat. Chem.* **2021**, *13*, 402−419.

(27) Christoph, H.; Grunenberg, J.; Hopf, H.; Dix, I.; Jones, P. G.; Scholtissek, M.; Maier, G. MP2 and DFT Calculations on Circulenes and an Attempt to Prepare the Second Lowest Benzolog, [4]-Circulene. *Chem. Eur. J.* **2008**, *14*, 5604.

(28) Orozco-Ic, M.; Valiev, R. R.; Sundholm, D. Non-intersecting ring currents in [12] infinitene. *Phys. Chem. Chem. Phys.* **2022**, *24*, 6404−6409.

(29) Freixas, V. M.; Tretiak, S.; Fernandez-Alberti, S. Infinitene: Computational Insights from Nonadiabatic Excited State Dynamics. *J. Phys. Chem. Lett.* **2022**, *13*, 8495−8501.

(30) Monaco, G.; Zanasi, R.; Summa, F. F. Magnetic Characterization of the Infinitene Molecule. *J. Phys. Chem. A* **2022**, *126*, 3717−3723.

(31) Fan, W.; Matsuno, T.; Han, Y.; Wang, X.; Zhou, Q.; Isobe, H.; Wu, J. Synthesis and Chiral Resolution of Twisted Carbon Nanobelts. *J. Am. Chem. Soc.* **2021**, *143*, 15924.

(32) Schleyer, P. V. R. Introduction: aromaticity. *Chem. Rev.* **2001**, *101*, 1115−1118.

(33) Gadre, S. R.; Bapat, S. V.; Sundararajan, K.; Shrivastava, I. H. A general parallel algorithm for the generation of molecular electrostatic potential maps. *Chem. Phys. Lett.* **1990**, *175*, 307−312.

(34) Gadre, S. R.; Kulkarni, S. A.; Shrivastava, I. H. Molecular electrostatic potentials: A topographical study. *J. Chem. Phys.* **1992**, *96*, 5253−5260.

(35) Scrocco, E.; Tomasi, J. The electrostatic molecular potential as a tool for the interpretation of molecular properties. *New concepts II*; Springer, 1973; pp 95−170.

(36) Gadre, S. R.; Pathak, R. K. Nonexistence of local maxima in molecular electrostatic potential maps. *Proc.—Indian Acad. Sci., Chem. Sci.* **1990**, *102*, 189−192.

(37) Gadre, S. R.; Shrivastava, I. H. Shapes and sizes of molecular anions via topographical analysis of electrostatic potential. *J. Chem. Phys.* **1991**, *94*, 4384−4390.

(38) Shirsat, R. N.; Bapat, S. V.; Gadre, S. R. Molecular electrostatics. A comprehensive topographical approach. *Chem. Phys. Lett.* **1992**, *200*, 373−378.

(39) Becke, A. D. A new mixing of Hartree−Fock and local density-functional theories. *J. Chem. Phys.* **1993**, *98*, 1372−1377.

(40) Becke, A. D. Density-functional exchange-energy approximation with correct asymptotic behavior. *Phys. Rev. A* **1988**, *38*, 3098−3100.

(41) Frisch, M. J.; Trucks, G. W.; Schlegel, H. B.; Scuseria, G. E.; Robb, M. A.; Cheeseman, J. R.; Scalmani, G.; Barone, V.; Petersson, G. A.; Nakatsuji, H.; Li, X.; Caricato, M.; Marenich, A. V.; Bloino, J.; Janesko, B. G.; Gomperts, R.; Mennucci, B.; Hratchian, H. P.; Ortiz, J. V.; Izmaylov, A. F.; Sonnenberg, J. L.; Williams-Young, D.; Ding, F.; Lipparini, F.; Egidi, F.; Goings, J.; Peng, B.; Petrone, A.; Henderson, T.; Ranasinghe, D.; Zakrzewski, V. G.; Gao, J.; Rega, N.; Zheng, G.; Liang, W.; Hada, M.; Ehara, M.; Toyota, K.; Fukuda, R.; Hasegawa, J.; Ishida, M.; Nakajima, T.; Honda, Y.; Kitao, O.; Nakai, H.; Vreven, T.; Throssell, K.; Montgomery, J. A., Jr.; Peralta, J. E.; Ogliaro, F.; Bearpark, M. J.; Heyd, J. J.; Kudin, K. N.; Staroverov, V. N.; Keith, T. A.; Kobayashi, R.; Normand, J.; Raghavachari, K.; Rendell, A. P.; Burant, J. C.; Iyengar, S. S.; Tomasi, J.; Cossi, M.; Millam, J. M.; Klene, M.; Adamo, C.; Cammi, R.; Ochterski, J. W.; Martin, R. L.; Morokuma, K.; Farkas, O.; Foresman, J. B.; Fox, D. J. *Gaussian 16*, Rev. A.03: Wallingford, CT, 2016.

(42) Kumar, A.; Yeole, S. D.; Gadre, S. R.; López, R.; Rico, J. F.; Ramírez, G.; Ema, I.; Zorrilla, D. DAMQT 2.1. 0: a new version of the DAMQT package enabled with the topographical analysis of electron density and electrostatic potential in molecules. *J. Comput. Chem.* **2015**, *36*, 2350−2359.

(43) López, R.; Rico, J. F.; Ramírez, G.; Ema, I.; Zorrilla, D. DAMQT: A package for the analysis of electron density in molecules. *Comput. Phys. Commun.* **2009**, *180*, 1654−1660.

(44) López, R.; Rico, J. F.; Ramírez, G.; Ema, I.; Zorrilla, D. DAMQT 2.0: A new version of the DAMQT package for the analysis of electron density in molecules. *Comput. Phys. Commun.* **2015**, *192*, 289−294.

(45) López, R.; Rico, J. F.; Ramírez, G.; Ema, I.; Zorrilla, D.; Kumar, A.; Yeole, S. D.; Gadre, S. R. Topology of molecular electron density and electrostatic potential with DAMQT. *Comput. Phys. Commun.* **2017**, *214*, 207−215.

(46) Gadre, S. R.; Shirsat, R. N. *Electrostatics of Atoms and Molecules*; Universities Press, 2000.

(47) Bader, R. F.; Tal, Y.; Anderson, S. G.; Nguyen-Dang, T. T. Quantum topology: theory of molecular structure and its change. *Isr. J. Chem.* **1980**, *19*, 8−29.

l

(48) Gejji, S. P.; Suresh, C. H.; Babu, K.; Gadre, S. R. Ab Initio Structure and Vibrational Frequencies of $(CF_3SO_2)_2$N-Li$^+$ Ion Pairs. *J. Phys. Chem. A* **1999**, *103*, 7474–7480.

(49) Kumar, A.; Gadre, S. R.; Mohan, N.; Suresh, C. H. Lone Pairs: An Electrostatic Viewpoint. *J. Phys. Chem. A* **2014**, *118*, 526–532.

(50) Yeole, S. D.; Gadre, S. R. Topography of scalar fields: molecular clusters and π-conjugated systems. *J. Phys. Chem. A* **2011**, *115*, 12769–12779.

(51) Bijina, P. V.; Suresh, C. H.; Gadre, S. R. Electrostatics for probing lone pairs and their interactions. *J. Comput. Chem.* **2018**, *39*, 488–499.

(52) Phukan, A. K.; Kalagi, R. P.; Gadre, S. R.; Jemmis, E. D. Structure, reactivity and aromaticity of acenes and their BN analogues: A density functional and electrostatic investigation. *Inorg. Chem.* **2004**, *43*, 5824–5832.

(53) Gadre, S. R.; Bendale, R. D. On the similarity between molecular electron densities, electrostatic potentials and bare nuclear potentials. *Chem. Phys. Lett.* **1986**, *130*, 515–521.

(54) Anjalikrishna, P. K.; Suresh, C. H.; Gadre, S. R. Electrostatic Topographical Viewpoint of π-Conjugation and Aromaticity of Hydrocarbons. *J. Phys. Chem. A* **2019**, *123*, 10139–10151.

(55) Anjalikrishna, P. K.; Gadre, S. R.; Suresh, C. H. Antiaromaticity–Aromaticity Interplay in Fused Benzenoid Systems Using Molecular Electrostatic Potential Topology. *J. Phys. Chem. A* **2021**, *125*, 5999–6012.

(56) Rieger, R.; Müllen, K. Forever young: polycyclic aromatic hydrocarbons as model cases for structural and optical studies. *J. Phys. Org. Chem.* **2010**, *23*, 315–325.

(57) Rakhi, R.; Suresh, C. H. Optoelectronic Properties of Polycyclic Benzenoid Hydrocarbons of Various Sizes and Shapes for Donor-π-Acceptor Systems: A DFT Study. *ChemistrySelect* **2021**, *6*, 2760–2769.

(58) Solà, M. Forty years of Clar's aromatic π-sextet rule. *Front. Chem.* **2013**, *1*, 22.

(59) Suresh, C. H.; Gadre, S. R. Clar's Aromatic Sextet Theory Revisited via Molecular Electrostatic Potential Topology. *J. Org. Chem.* **1999**, *64*, 2505–2512.

(60) Vijayalakshmi, K. P.; Suresh, C. H. Pictorial representation and validation of Clar's aromatic sextet theory using molecular electrostatic potentials. *New J. Chem.* **2010**, *34*, 2132–2138.

(61) Herges, R.; Geuenich, D. Delocalization of Electrons in Molecules. *J. Phys. Chem. A* **2001**, *105*, 3214–3220.

(62) Lu, C.; Chen, P.; Sheng, H.; Li, C.; Wang, J. Physical mechanism on linear spectrum and nonlinear spectrum in double helical carbon nanomolecule–infinitene. *Spectrochim. Acta, Part A* **2022**, *282*, 121674.

(63) Garner, M. H.; Bro-Jørgensen, W.; Pedersen, P. D.; Solomon, G. C. Reverse Bond-Length Alternation in Cumulenes: Candidates for Increasing Electronic Transmission with Length. *J. Phys. Chem. C* **2018**, *122*, 26777–26789.

(64) Dopper, J. H.; Wynberg, H. Heterocirculenes a new class of polycyclic aromatic hydrocarbons. *Tetrahedron Lett.* **1972**, *13*, 763–766.

(65) Hensel, T.; Andersen, N. N.; Plesner, M.; Pittelkow, M. Synthesis of heterocyclic [8] circulenes and related structures. *Synlett* **2016**, *27*, 498–525.

(66) Kumar, B.; King, B. T. Synthesis of 1,8,9,16-Tetrakis-(trimethylsilyl)tetra-cata-tetrabenzoquadrannulene. *J. Org. Chem.* **2012**, *77*, 10617–10622.

(67) Bharat; Bhola, R.; Bally, T.; Valente, A.; Cyrański, M. K.; Dobrzycki, Ł.; Spain, S. M.; Rempała, P.; Chin, M. R.; King, B. T. Quadrannulene: A Nonclassical Fullerene Fragment. *Angew. Chem., Int. Ed.* **2010**, *49*, 399–402.

(68) Christoph, H.; Grunenberg, J.; Hopf, H.; Dix, I.; Jones, P. G.; Scholtissek, M.; Maier, G. MP2 and DFT Calculations on Circulenes and an Attempt to Prepare the Second Lowest Benzolog, [4]-Circulene. *Chem.—Eur. J.* **2008**, *14*, 5604–5616.

(69) Barth, W. E.; Lawton, R. G. Dibenzo[ghi,mno]fluoranthene. *J. Am. Chem. Soc.* **1966**, *88*, 380–381.

(70) Scott, L. T.; Hashemi, M. M.; Meyer, D. T.; Warren, H. B. Corannulene. A convenient new synthesis. *J. Am. Chem. Soc.* **1991**, *113*, 7082–7084.

(71) Wu, Y.-T.; Siegel, J. S. Aromatic Molecular-Bowl Hydrocarbons: Synthetic Derivatives, Their Structures, and Physical Properties. *Chem. Rev.* **2006**, *106*, 4843–4867.

(72) Shen, H.-C.; Tang, J.-M.; Chang, H.-K.; Yang, C.-W.; Liu, R.-S. Short and efficient synthesis of coronene derivatives via ruthenium-catalyzed benzannulation protocol. *J. Org. Chem.* **2005**, *70*, 10113–10116.

(73) Yamamoto, K.; Harada, T.; Nakazaki, M.; Naka, T.; Kai, Y.; Harada, S.; Kasai, N. Synthesis and characterization of [7]circulene. *J. Am. Chem. Soc.* **1983**, *105*, 7171–7172.

(74) Yamamoto, K.; Harada, T.; Okamoto, Y.; Chikamatsu, H.; Nakazaki, M.; Kai, Y.; Nakao, T.; Tanaka, M.; Harada, S.; Kasai, N. Synthesis and molecular structure of [7]circulene. *J. Am. Chem. Soc.* **1988**, *110*, 3578–3584.

(75) Feng, C.-N.; Hsu, W.-C.; Li, J.-Y.; Kuo, M.-Y.; Wu, Y.-T. Per-Substituted [8] Circulene and Its Non-Planar Fragments: Synthesis, Structural Analysis, and Properties. *Chem.—Eur. J.* **2016**, *22*, 9198–9208.

(76) Feng, C. N.; Kuo, M. Y.; Wu, Y. T. Synthesis, structural analysis, and properties of [8] circulenes. *Angew. Chem.* **2013**, *125*, 7945–7948.

(77) Sakamoto, Y.; Suzuki, T. Tetrabenzo[8]circulene: Aromatic Saddles from Negatively Curved Graphene. *J. Am. Chem. Soc.* **2013**, *135*, 14074–14077.

(78) Miller, R. W.; Duncan, A. K.; Schneebeli, S. T.; Gray, D. L.; Whalley, A. C. Synthesis and structural data of tetrabenzo [8] circulene. *Chem.—Eur. J.* **2014**, *20*, 3705–3711.

(79) Thulin, B.; Wennerstrom, O. Synthesis of (2.2)(3,6)-Phenanthrenophanediene. *Acta Chem. Scand.* **1976**, *7*, 369.

(80) Márquez, I. R.; Castro-Fernández, S.; Millán, A.; Campaña, A. G. Synthesis of distorted nanographenes containing seven- and eight-membered carbocycles. *Chem. Commun.* **2018**, *54*, 6705–6718.

(81) Dias, F. S.; Machado, W. S. Investigation of the thermal conductivity of tetrabenzo [8] circulene (TB8C) by molecular dynamics simulation. *Mol. Simul.* **2021**, *47*, 1002–1009.

(82) Povie, G.; Segawa, Y.; Nishihara, T.; Miyauchi, Y.; Itami, K. Synthesis and Size-Dependent Properties of [12], [16], and [24] Carbon Nanobelts. *J. Am. Chem. Soc.* **2018**, *140*, 10054–10059.

(83) Yagi, A.; Segawa, Y.; Itami, K. Armchair and Chiral Carbon Nanobelts: Scholl Reaction in Strained Nanorings. *Chem* **2019**, *5*, 746–748.

(84) Han, Y.; Dong, S.; Shao, J.; Fan, W.; Chi, C. Synthesis of a Sidewall Fragment of a (12,0) Carbon Nanotube. *Angew. Chem., Int. Ed.* **2021**, *60*, 2658–2662.

(85) Xia, Z.; Pun, S. H.; Chen, H.; Miao, Q. Synthesis of Zigzag Carbon Nanobelts through Scholl Reactions. *Angew. Chem., Int. Ed.* **2021**, *60*, 10311–10318.

(86) Bergman, H. M.; Kiel, G. R.; Handford, R. C.; Liu, Y.; Tilley, T. D. Scalable, Divergent Synthesis of a High Aspect Ratio Carbon Nanobelt. *J. Am. Chem. Soc.* **2021**, *143*, 8619–8624.

(87) Du, X.-S.; Zhang, D.-W.; Guo, Y.; Li, J.; Han, Y.; Chen, C.-F. Towards the Highly Efficient Synthesis and Selective Methylation of $C(sp^3)$-Bridged [6]Cycloparaphenylenes from Fluoren[3]arenes. *Angew. Chem., Int. Ed.* **2021**, *60*, 13021–13028.

(88) Li, Y.; Segawa, Y.; Yagi, A.; Itami, K. A Nonalternant Aromatic Belt: Methylene-Bridged [6]Cycloparaphenylene Synthesized from Pillar[6]arene. *J. Am. Chem. Soc.* **2020**, *142*, 12850–12856.

(89) Chen, H.; Gui, S.; Zhang, Y.; Liu, Z.; Miao, Q. Synthesis of a Hydrogenated Zigzag Carbon Nanobelt. *CCS Chem.* **2021**, *3*, 613–619.

(90) Zhang, Q.; Zhang, Y.-E.; Tong, S.; Wang, M.-X. Hydrocarbon Belts with Truncated Cone Structures. *J. Am. Chem. Soc.* **2020**, *142*, 1196–1199.

(91) Xie, J.; Li, X.; Wang, S.; Li, A.; Jiang, L.; Zhu, K. Heteroatom-bridged molecular belts as containers. *Nat. Commun.* **2020**, *11*, 3348.

(92) Tan, M.-L.; Guo, Q.-H.; Wang, X.-Y.; Shi, T.-H.; Zhang, Q.; Hou, S.-K.; Tong, S.; You, J.; Wang, M.-X. Oxygen- and Nitrogen-Embedded Zigzag Hydrocarbon Belts. *Angew. Chem., Int. Ed.* **2020**, *59*, 23649−23658.

(93) Wang, J.; Miao, Q. A Tetraazapentacene−Pyrene Belt: Toward Synthesis of N-Doped Zigzag Carbon Nanobelts. *Org. Lett.* **2019**, *21*, 10120−10124.

🕮 Recommended by ACS

PCCP

PAPER

Check for updates

Utilization of the through-space effect to design donor–acceptor systems of pyrrole, indole, isoindole, azulene and aniline†

Puthannur K. Anjalikrishna[ab] and Cherumuttathu H. Suresh ![ORCID]*[ab]

Molecular electrostatic potential (MESP) topology analysis reveals the underlying phenomenon of the through-space effect (TSE), which imparts electron donor–acceptor properties to a wide range of chemical systems, including derivatives of pyrrole, indole, isoindole, azulene, and aniline. The TSE is inherent in pyrrole owing to the strong polarization of electron density (PoED) from the formally positively charged N-center to the C_3C_4 bonding region. The $N \rightarrow C_3C_4$ directional nature of the TSE has been effectively employed to design molecules with high electronic polarization, such as bipyrroles, polypyrroles, phenyl pyrroles, multi-pyrrolyl systems and N-doped nanographenes. In core-expanded structures, the direction of electron flow from pyrrole units towards the core leads to highly electron-rich systems, while the opposite arrangement results in highly electron-deficient systems. Similarly, the MESP analysis reveals the presence of the TSE in azulene, indole, isoindole, and aniline. Oligomeric chains of these systems are designed in such a way that the direction of electron flow is consistent across each monomer, leading to substantial electronic polarization between the first and last monomer units. Notably, these designed systems exhibit strong donor–acceptor characteristics despite the absence of explicit donor and acceptor moieties, which is supported by FMO analysis, APT charge analysis, NMR data and λ_{max} data. Among the systems studied, the TSEs of many experimentally known systems (bipyrroles, phenyl pyrroles, hexapyrrolylbenzene, octapyrrolylnaphthalene, decapyrrolylcorannulene, polyindoles, polyazulenes, etc.) are unraveled for the first time, while numerous new systems (polypyrroles, polyisoindoles, and amino-substituted benzene polymers) are predicted to be promising materials for the creation of donor–acceptor systems. These findings demonstrate the potential of the TSE in molecular design and provide new avenues for creating functional materials.

Introduction

When a molecule interacts with another molecule, or when it is excited, the electron density is transferred from the electron-rich molecule/site (donor, D) to the electron-deficient molecule/site (acceptor, A).[1–5] Typically, donors are conjugated molecules with high HOMO energy levels, whereas acceptors are conjugated molecules with low LUMO energy levels. A conjugated donor–acceptor (D–A) system is formed by linking the D and A by a covalent bond or a spacer moiety.[6] D–A systems have found widespread application in organic photovoltaic devices.[7] Many studies have recently been undertaken to characterize the

mechanisms of D–A based charge-transfer processes in optoelectronic systems such as solar cells, light-emitting diodes (LEDs), organic photovoltaics (OPVs), field-effect transistors (FETs), conducting polymers, and so on.[8–10] Appropriate substituents are used to fine tune the donating effect of the D and the accepting effect of the A. Typical donors include +M/+I substituents such as –OH, –NH$_2$, –OR and –NR$_2$, or heterocyclic moieties such as thiophenes, whereas typical acceptors include functional groups with the −M/−I effect such as –NO$_2$, –CN, –CHO, –COOH, and their combinations.[11] N,N-dimethylamino- and nitro-/cyano- groups are the most effective D and A substituents, respectively.[12,13] Planarization enhances the D–A effect by permitting effective conjugation (through-bond effect) between the D and A units.

Pyrrole (**P**), a five-membered aromatic N-heterocycle, is found in nearly all heterocyclic structures.[10] Pyrrole derivatives have been widely used in the construction of organic semiconducting materials, conducting polymers, photovoltaics, fluorescent materials and FETs.[14–20] The six structural isomers of

^{a} *Chemical Sciences and Technology Division, CSIR-National Institute for Interdisciplinary Science and Technology, Thiruvananthapuram, Kerala, 695019, India. E-mail: sureshch@niist.res.in*

^{b} *Academy of Scientific and Innovative Research (AcSIR), Ghaziabad, 201002, India*
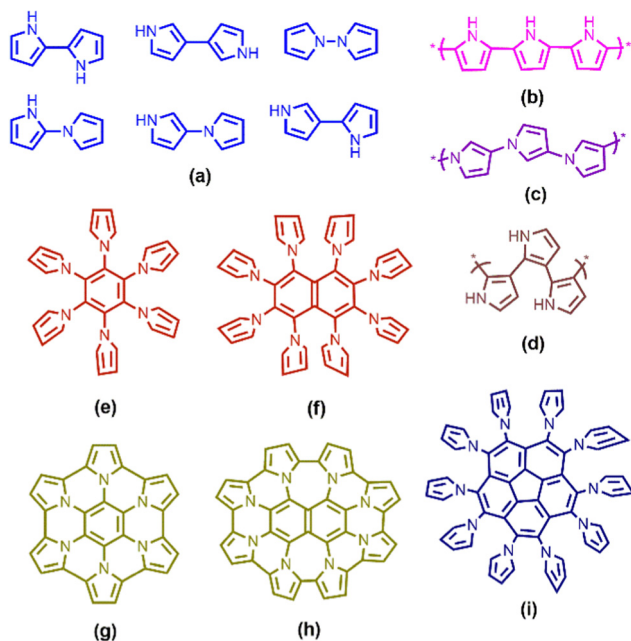
Fig. 1 Oligomers of pyrrole and its poly-condensed/open forms in aromatic hydrocarbons.

Fig. 2 Oligomers of azulene, indole, isoindole, aniline and star-like azulene systems.

bipyrroles (^2P) have been synthesized (Fig. 1(a)).[20–38] Polypyrroles with C_2–$C_{2'}$ linkages (Fig. 1(b)) are well-known biocompatible conducting polymers,[24,39] while polypyrroles constructed from C_3–$N_{1'}$ connections (Fig. 1(c)) and C_3–$C_{2'}$ connections (Fig. 1(d)) are yet to be reported. Due to their sterically bulky structures and exceptional optoelectronic properties,[17,40–46] a variety of multi-pyrrolyl aromatic systems, such as hexapyrrolylbenzene[47,48] (Fig. 1(e)) and octapyrrolylnaphthalene[48,49] (Fig. 1(f)), have been synthesized in the past and are considered as building blocks of bigger π-conjugated systems. Oki *et al.* recently reported a core-expanded, nonplanar, pyrrole-fused azacoronene with N-doped heptagonal rings (Fig. 1(g) and (h)) and presented a unique approach to synthesize N-doped nano-graphenes utilizing multi-pyrrolyl polycyclic aromatic hydrocarbons.[44,50] Xu *et al.* recently synthesized[51] decapyrrolylcorannulene (Fig. 1(i)) and demonstrated its application as a host for fullerenes.[52]

The synthesis of an azulene homopolymer with distinctive 2,6′-connectivity[53,54] paved the way for the development of novel azulene-based functional materials (Fig. 2(a)).[55–59] Star-like azulene derivatives (Fig. 2(b)) were used to create polyelectrochromic materials, multielectron redox catalysts and compounds capable of exhibiting multi-electron transfer behaviour.[60,61] Polyindoles with C_3–$N_{1'}$ (Fig. 2(d)) and C_3–$C_{2'}$ (Fig. 2(e)) linkages are conducting polymers that are suitable for fabrication of electro-rheological fluids, energy storage devices, and corrosion inhibitors.[62–69] To date, no polyisoindoles (Fig. 2(c)) have been synthesized. Polyaniline is widely recognized as a conducting polymer,[70,71] while the synthesis of amino-substituted benzene polymers remains an unexplored area of research, yet to be achieved (Fig. 2(f)).

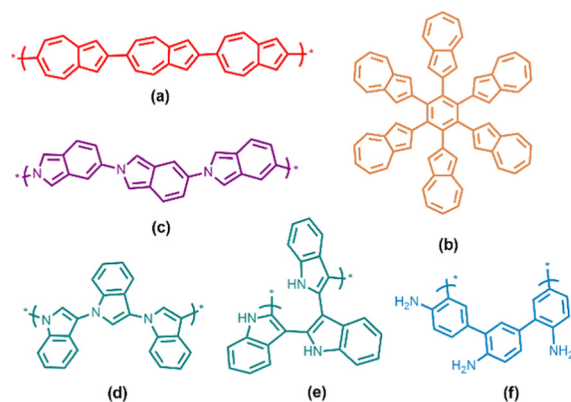The electronic effects that operate through the interconnected network of both σ- and π-bonds are collectively known

as the through-bond effect (TBE), which includes both resonance and inductive effects.[72] In contrast, the term through-space effect (TSE) pertains to electronic interactions between atoms or groups of atoms that are not directly bonded to each other, but exert influence on one another through three-dimensional space. More recent research studies[73–76] have demonstrated that the TSE predominates in many situations that were previously assumed to be produced primarily by the TBE. Many attempts have been made in the past to evaluate the TSE using a wide range of substituents.[77–84] These studies revealed that substituent effects in cation–π interactions are mostly caused by the TSE rather than the TBE.[85]

The chain-type and core-expanded chemical systems depicted in Fig. 1 and 2 are not like typical D–A systems, because they lack discrete D and A units. Using density functional theory (DFT), we investigate their structural characteristics, as well as those of several isomers.[86–89] Furthermore, molecular electrostatic potential (MESP) topology analysis has been performed to evaluate their electronic features. The MESP characteristics highlight the TSE phenomenon in these systems, which results in the substantial polarization of electron density (PoED) from one end to the other for chain-type structures and from the periphery to the interior or the interior to the periphery for core-expanded structures.

Methodology

The DFT method at the M06-2X/6-311G+(d,p)[90–92] level using the standard protocols as implemented in the Gaussian16 suite of programs[93] is used to optimize all the molecular structures considered for the study. The optimized structures were confirmed as energy minima by vibrational frequency analysis. The wave function constructed using the global hybrid functional with 54% HF exchange in conjunction with the 6-311G+(d,p) basis set is expected to give a sufficiently accurate description of the electron density, $\rho(\mathbf{r})$, and the corresponding MESP, $V(\mathbf{r})$. The MESP has been regarded as an efficient tool for exploring the structures and reactivities of molecules. The MESP maps are used for illustrating the delocalized and localized nature of

electrons and the most negative value of the MESP of the molecule is denoted as V_m. The MESP $V(\mathbf{r})$ at a point $\mathbf{r}$ is defined in eqn (1),

$$V(\mathbf{r}) = \sum_A^N \frac{Z_A}{|\mathbf{r} - \mathbf{R}_A|} - \int \frac{\rho(\mathbf{r}')\mathrm{d}^3\mathbf{r}'}{|\mathbf{r} - \mathbf{r}'|} \qquad (1)$$

where Z_A is the charge on nucleus A located at $\mathbf{R}_A$, and $\rho(\mathbf{r}')$ is the molecule's continuous electronic density and N is the total number of nuclei. In the above equation, the first and second terms on the right hand side represent the bare nuclear potential (BNP) and electronic contribution, respectively. The value of MESP could be negative, zero, or positive, compared to the electron density, which takes only non-negative values. The dominance of the second term over the first term represents the regions of high electron concentration and the MESP exhibits negatively valued minima and saddles at this point. The dominance of the nuclear contribution is represented by regions with a positive MESP. All the first-order derivatives of $V(\mathbf{r})$ vanish ($\nabla V(\mathbf{r}) = 0$) at the critical point (CP). In the topology analysis, the MESP minimum (V_m) would also be denoted as (3, +3) CP,[94,95] where eigenvalues of its Hessian matrix will show three positive values. By employing the cubegen utility within the Gaussian 16 program, both the V_m values and the distribution of the MESP on the isodensity surface are computed. The π-electron cloud of the molecule can be displayed by plotting a suitable negative-valued MESP isosurface. Furthermore, Bader's quantum theory of atoms in molecules (QTAIM) analysis, based on the electron density distribution, is carried out using the AIMAll program package.[96] To check the reliability of the M06-2X method, a benchmark study is also conducted using the DFT methods B3LYP, M06-L, and wB97XD and the 6-311G+(d,p) basis set in all the cases (Table S1, ESI†).

Results and discussion

MESP topology of pyrrole, furan and thiophene systems

The location and value of V_m of the pyrrole MESP structure vary greatly from those of furan and thiophene systems (Fig. 3). The pyrrole V_m (-27.9 kcal mol^{-1}) is positioned over the C_3C_4 bond, which has a greater single bond character (1.42 Å) than C_2C_3 and C_4C_5. Moreover, the N-center lacks a V_m, indicating that the N lone pair is used for cyclic π-electron conjugation. The V_m is found over C_2C_3 and C_4C_5 bonds in furan and thiophene systems. The V_m points are also observed in the oxygen lone pair region, but the sulphur lone pair has no identifiable localization in the MESP topology, which may be related to the diffuse nature of its outermost electrons. The MESP distribution on the isodensity surface (Fig. 3(d)) clearly demonstrates the high electronic polarization in pyrrole when compared to both furan and thiophene systems. Pyrrole has a large dipole moment, 1.91 D, in the direction from the N-center to the midway region of C_3C_4 (Fig. 3(g)), but furan and thiophene systems have a minor dipole moment in the direction from C_3C_4 to the heteroatom.[97] Consequently, the MESP
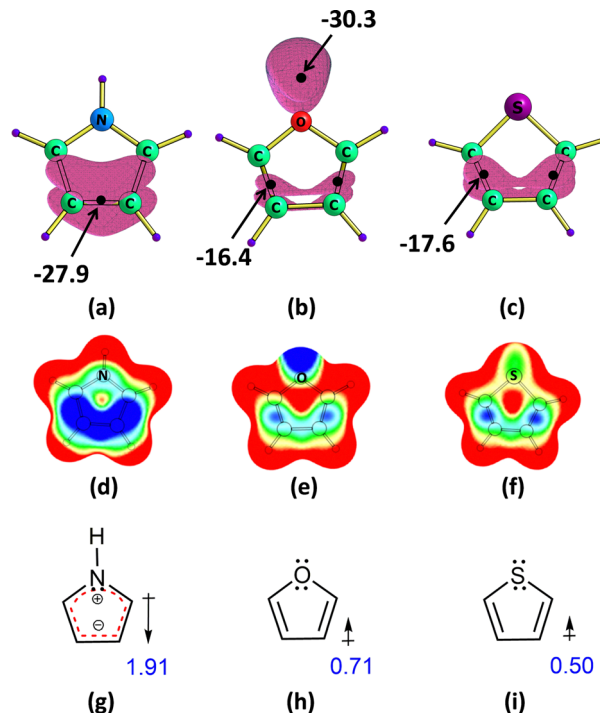

Fig. 3 The MESP isosurfaces of (a) pyrrole, (b) furan and (c) thiophene systems plotted at -0.040, -0.025 and -0.025 a.u. (atomic unit), respectively. Parts (d)–(f) show the MESP mapped on to the 0.01 a.u. electron density isosurface and (g)–(i) show the directions of dipole moments of pyrrole, furan and thiophene systems, respectively. Colour coding from blue to red indicates MESP values in the range -0.02 to 0.02 a.u. The V_m and dipole moment values are given in kcal mol^{-1} and Debye (D), respectively.

topology study validates the following intrinsic electronic features of pyrrole.

(1) The pyrrole N-center is electron deficient and positively charged.

(2) Strong PoED occurs in the direction from the N-center to the C_3C_4 bonding region.

Bipyrroles

Fig. 4 depicts the MESP distribution of six bipyrroles *viz.* $^2P_{C2C2'}$, $^2P_{C3C3'}$, $^2P_{N1N1'}$, $^2P_{C2N1'}$, $^2P_{C3N1'}$ and $^2P_{C3C2'}$, wherein the subscript refers to the bonded atoms between the two rings. The PoED occurs in each pyrrole unit, from N_1 to C_3C_4 (for ring 1) or from $N_{1'}$ to $C_{3'}C_{4'}$ (for ring 2), which is depicted in the schematic diagrams (Fig. 4). Compared to pyrrole, the bipyrroles show significant variation in the MESP distribution in each ring, which can be correlated with the ring-to-ring connectivity and the direction of the PoED. The MESP distribution in the bipyrroles can be easily assessed using the direction of the PoED in each pyrrole unit (represented using arrows in Fig. 4). When the arrows point inward ($\rightarrow\leftarrow$), as in $^2P_{C3C3'}$, the inner regions show more negative MESP values than outer areas, and when they point outward ($\leftarrow\rightarrow$), as in $^2P_{N1N1'}$ and $^2P_{C2N1'}$, depletion of the negative MESP from the interior is evident. The PoED effect is maximum when the arrows are oriented in the same direction ($\rightarrow\rightarrow$), as in $^2P_{C3N1'}$ and $^2P_{C3C2'}$. The parallel orientation of arrows ($\rightleftarrows$), as in $^2P_{C2C2'}$, has a
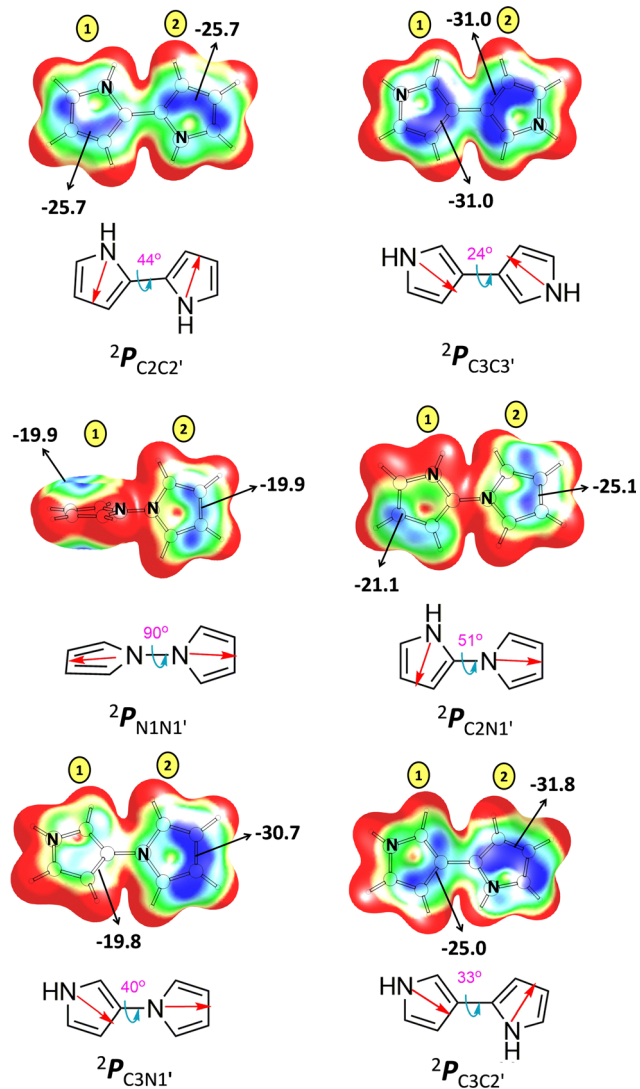
Fig. 4 The MESP mapped on to the 0.01 a.u. electron density isosurface of bipyrroles (^2P), where colour coding from blue to red indicates MESP values in the range -0.03 to 0.03 a.u. The MESP minimum (V_m) corresponding to each ring is given in kcal mol^{-1} and the direction of electron flow is denoted using red arrows.

negligible impact on MESP distribution. The MESP results clearly show that depending on the atom to which the second pyrrole unit is coupled, the pyrrole unit acts as an electron donating (D) or as an electron withdrawing unit (A).

For instance, the high negative V_m observed for $^2P_{C3C3'}$, compared to pyrrole, suggests the D character of pyrrole units, whereas the less negative V_m values for $^2P_{C2C2'}$ and $^2P_{C2N1'}$ indicate the A character of the pyrrole units. For $^2P_{C3N1'}$ and $^2P_{C3C2'}$, the substantial reduction in the magnitude of V_m for the first ring and the remarkable enhancement in the V_m value of the second ring compared to pyrrole suggest the D–A character of the systems. Despite the fact that the PoED in $^2P_{C3C2'}$ is not as powerful as that in $^2P_{C3N1'}$, the dipole moment of 2.86 D found for the former indicates that the C_3C_2' connection also leads to considerable PoED in a single direction. The

twist angle (θ) between the pyrrole units in bipyrroles is high. The two pyrrole rings are arranged orthogonally in $^2P_{N1N1'}$, while the θ values of other bipyrroles $^2P_{C2C2'}$, $^2P_{C3C3'}$, $^2P_{C2N1'}$, $^2P_{C3N1'}$ and $^2P_{C3C2'}$ are 44°, 24°, 51°, 40° and 33°, respectively. The electronic polarization in the system is enhanced when the monomer dipoles are aligned in a parallel orientation compared to a system with an acute angle. High θ values indicate minor levels of extended π-conjugation (TBE). Hence, we anticipate that the polarization between the two pyrrole units will be greatly influenced by the highly directional TSE as well.

Polypyrroles

The MESP analysis of bipyrroles, $^2P_{C3N1'}$ and $^2P_{C3C2'}$, shows the donor feature of one pyrrole unit and the acceptor feature of the other. The ring that donates electron density becomes less negative in the MESP (D), while the other becomes more negative (A) compared to pyrrole. The donor-to-acceptor electron flow can be extended through a chain of pyrrole units that are connected through either C_3–N_1' or C_3–C_2' connectivity. In polypyrroles, the extension of electron flow from one pyrrole unit to other is investigated further *viz.* $^nP_{C3N1'}$ and $^nP_{C3C2'}$, where n = 3–6. The unidirectional TSE from the first to the second and subsequent pyrrole rings is characterized in terms of the V_m value of each ring (Fig. S1, ESI†). The magnitude of V_m of the first pyrrole ring (ring 1) in each system is significantly reduced when compared to pyrrole, showing its high electron deficient character, but the magnitude of V_m of the last ring is significantly enhanced suggesting its electron rich character (Table 1).

This implies substantial polarization due to the TSE from the first to the last pyrrole unit through the C_3–N_1' or C_3–C_2' connection. Fig. 5 shows a clear illustration of this phenomenon utilizing the MESP mapped on to a 0.01 a.u. electron density surface. The depleted electron density in the first ring is evident as red regions, whereas the accumulated electron density on the last ring is apparent as an intense blue region. For instance, for $^6P_{C3N1'}$, the V_m is -11.4 kcal mol^{-1} for the first ring and -35.5 kcal mol^{-1} for the last ring. Similarly, in $^6P_{C3C2'}$, the first and sixth rings show V_m at -16.9 and -38.5 kcal mol^{-1}, respectively. In general, the magnitude of V_m progressively increases from the first to the last ring. The maximum negative character of the MESP in the last ring and the substantially decreased amount of negative MESP in all other rings suggest strong PoED in each pyrrole unit of polypyrroles

Table 1 The V_m values (in kcal mol^{-1}) of the first and last pyrrole units in $^nP_{C3N1'}$ and $^nP_{C3C2'}$ polypyrroles

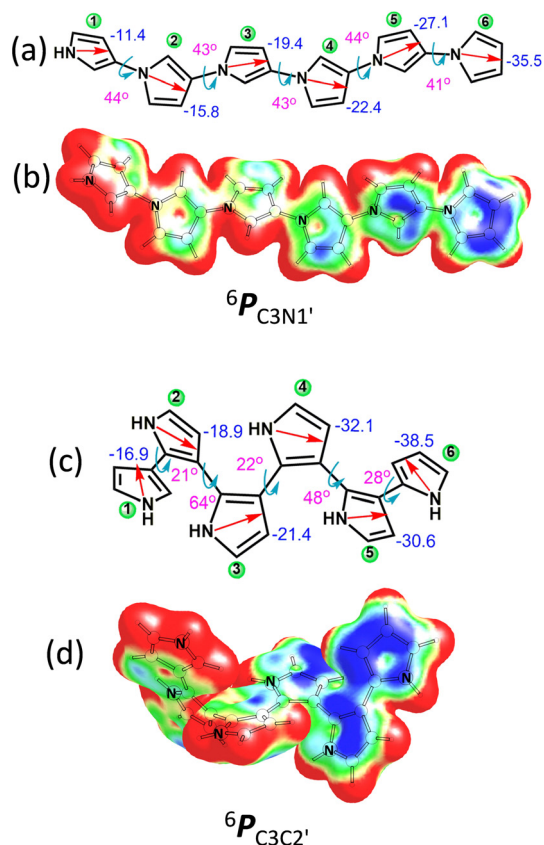| Polypyrrole	V_m of the first ring	V_m of the last ring
$^3P_{C3N1'}$	-15.9	-32.7
$^4P_{C3N1'}$	-13.6	-34.0
$^5P_{C3N1'}$	-12.2	-34.9
$^6P_{C3N1'}$	-11.4	-35.5
$^3P_{C3C2'}$	-19.5	-33.1
$^4P_{C3C2'}$	-20.1	-36.7
$^5P_{C3C2'}$	-17.4	-37.5
$^6P_{C3C2'}$	-16.9	-38.5

Fig. 5 The direction of the TSE and the variation in the V_m value of each pyrrole ring in (a) $^6P_{C3N1'}$ and (c) $^6P_{C3C2'}$ connected polypyrroles. The V_m values are given in kcal mol^{-1} (blue font) and pyrrole rings from left to right are numbered from 1 to 6, respectively. The dihedral angle at the C_3–$N_{1'}$ and C_3–$C_{2'}$ junctions between the adjacent rings are given in the pink font. The MESP mapped on to the 0.01 a.u. electron density isosurface of (b) $^6P_{C3N1'}$ and (d) $^6P_{C3C2'}$ polypyrroles, with colour coding from blue to red indicating MESP values in the range −0.03 to 0.03 a.u.

with the C_3–$N_{1'}$ and C_3–$C_{2'}$ connections (Fig. S1, ESI†), which is reflected in their dipole moments too. For instance, when compared to the dipole moment of pyrrole, which is 1.91 D, the chain structures $^3P_{C3N1'}$, $^4P_{C3N1'}$, $^5P_{C3N1'}$, and $^6P_{C3N1'}$ show higher values, viz. 6.02, 8.28, 10.57, and 13.21 D, respectively. Similarly, the dipole moments are 4.22, 5.39, 6.35 and 6.28 D, respectively, for $^3P_{C3C2'}$, $^4P_{C3C2'}$, $^5P_{C3C2'}$, and $^6P_{C3C2'}$, due to the molecular design strategy that keeps the monomeric dipoles more or less in the same direction.

The HOMOs of all $^nP_{C3N1'}$ and $^nP_{C3C2'}$ are found at the most electron-rich pyrrole unit, but the LUMO is always found as the antibonding orbital of the N–H bond at the first pyrrole unit (Fig. S2a, ESI†). In the case of an N-phenyl substituted polypyrrole (Ph-$^6P_{C3N1'}$ in Fig. S2b, ESI†), the HOMO is confined around the end pyrrole unit, while a π^* orbital localized on the phenyl ring is the LUMO. The molecular orbital distributions clearly support the phenomenon of the TSE as the HOMO and LUMO are distributed mainly over A and D units, respectively.

Fig. 5 also depicts the dihedral angle (θ) at the C_3–$N_{1'}$ and C_3–$C_{2'}$ junctions in $^nP_{C3N1'}$ and $^nP_{C3C2'}$ systems, respectively. The θ of $^nP_{C3N1'}$ polypyrroles ranges from 41° to 45°, whereas

that of $^nP_{C3C2'}$ polypyrroles ranges from 25° to 64°. The $^nP_{C3C2'}$ systems have more twisted and zigzaggedly arranged pyrrole units than $^nP_{C3N1'}$ systems (Fig. S1, ESI†). Since the monomeric units are significantly twisted in the oligomers, the TSE is considered more influential for the electronic polarization than the through bond resonance effect. A constrained optimization of $^5P_{C3N1'}$ at $\theta = 0°$ yields $^{5'}P_{C3N1'}$, a planar structure that is 4.4 kcal mol^{-1} less stable than $^5P_{C3N1'}$ (Fig. S3, ESI†). Although planarity improves the through bond resonance interaction, the electronic polarization is found to be significantly higher for the twisted structure than the planar structure, suggesting that the TSE is more dominating than the TBE in the twisted system. To further demonstrate the directionality of the TSE, a $(P_{C3N1'})_6$ cluster is constructed as shown in Fig. 6, wherein the orientation of each pyrrole unit is fixed as per the structure of $^6P_{C3N1'}$ with a distance of separation of $\cong$ 2.0 Å between the adjacent pyrroles. The MESP distribution of the $(P_{C3N1'})_6$ cluster shows steady enhancement in negative character from the first to the last pyrrole and this pattern, very similar to $^6P_{C3N1'}$, confirms the directional nature of electron flow. Similarly, $(P_{C3N1'})_n$ and $(P_{C3C2'})_n$ clusters showed MESP patterns very similar to $^nP_{C3N1'}$ and $^nP_{C3C2'}$ systems, respectively (Fig. S4 and S5, ESI†). Although the pyrrole units are not bonded through σ- or π-bonds, significant electronic polarization occurs from the first monomer to the last monomer. This observation strongly emphasizes the significant role of the TSE in driving the polarization phenomenon within the $^nP_{C3N1'}$ and $^nP_{C3C2'}$ systems. In all cases, the TSE imparts D character to the first pyrrole unit and A character to the last one, despite the absence of an unambiguous D or A moiety. Furthermore, the atomic polar tensor (APT)[98] charges offer compelling evidence for the donor characteristics of the first pyrrole unit and the acceptor characteristics of the last pyrrole unit in $^nP_{C3N1'}$ systems (Fig. S6, ESI†).

Phenyl pyrrole systems

The MESP distribution in 1-, 2-, and 3-phenyl pyrroles (1-**PhP**, 2-**PhP** and 3-**PhP**) is depicted in Fig. 7. The direct connection
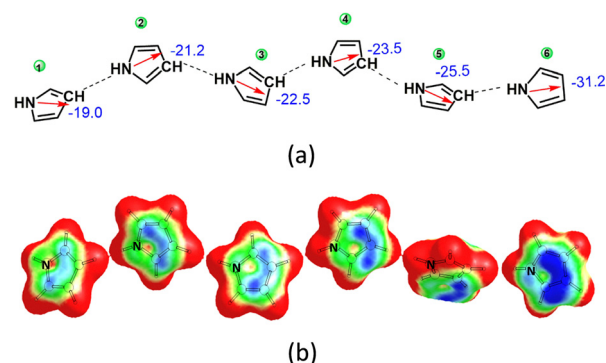

Fig. 6 (a) Illustration of the of TSE in the $(P_{C3N1'})_6$ cluster. Pyrroles are numbered from 1 to 6 and the V_m value of each ring is given in kcal mol^{-1}. (b) The MESP of $(P_{C3N1'})_6$ is mapped on to the 0.01 a.u. electron density isosurface, where colour coding from blue to red indicates MESP values in the range −0.03 to 0.03 a.u.
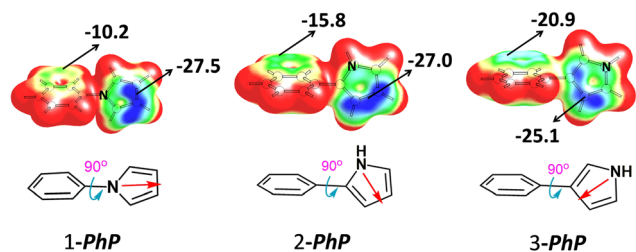
Fig. 7 The MESP mapped on to the 0.01 a.u. electron density isosurface for 1-, 2- and 3-phenyl pyrroles (**PhP**). Colour coding from blue to red indicates MESP values in the range −0.03 to 0.03 a.u. and the V_m values are given in kcal mol⁻¹.

between the N-center and the phenyl ring in 1-**PhP**[99–103] results in a significant reduction in the magnitude of V_m at the phenyl ring (−10.2 kcal mol⁻¹), whereas V_m at the pyrrole ring is essentially unaffected. The V_m values at the phenyl and pyrrole moieties in 2-**PhP**[104–106] are close to those of benzene (−17.8 kcal mol⁻¹) and pyrrole (−27.9 kcal mol⁻¹), respectively, demonstrating the null effect of phenyl-C_2 connection on electron distribution. The polarization direction in 3-**PhP** is from the pyrrole to the phenyl unit, which results in a considerable enhancement of the V_m of the phenyl ring to −20.9 kcal mol⁻¹. The study strongly emphasizes the significant role of the TSE in inducing polarization within **PhP** systems.

The highly directional nature of the TSE in phenyldipyrroles (**PhDP**s), *viz.* (1,1′-**PhDP**), (2,2′-**PhDP**), (3,3′-**PhDP**), and (1,3′-**PhDP**), is obvious from the MESP distribution (Fig. S7, ESI†). The outwardly pointed arrows (← →) in 1,1′-**PhDP** show a depletion in electron density on the phenyl ring, whereas the inwardly pointed arrows (→ ←) in 3,3′-**PhDP** indicate an enhancement of electron density. The parallel orientation of arrows (⇌) in 2,2′-**PhDP** suggests that pyrrole units have an essentially minimal TSE effect on the phenyl ring, but the arrows in the same direction (→ →) in 1,3′-**PhDP** indicate a push–pull effect of electron density from the C-connected pyrrole unit to the N-connected one.

The direction of electron flow in hexapyrrolylbenzene systems (**HPB**$_{N1}$, **HPB**$_{C2}$ and **HPB**$_{C3}$) is depicted in Fig. 8, where **HPB**$_{N1}$ and **HPB**$_{C3}$ are experimentally known and **HPB**$_{C2}$ is yet to be synthesized.[107] The six arrows pointing outward in **HPB**$_{N1}$ indicate the maximum electron withdrawal effect at the core benzene ring, whereas the six arrows pointing inward in **HPB**$_{C3}$ indicate the flow of electron density from each pyrrole unit to the core unit. Their MESP distribution validates this hypothesis, since **HPB**$_{N1}$ and **HPB**$_{C3}$ show highly positive and negative MESP values, respectively, over the central arene ring. The arrows in **HPB**$_{C2}$ indicate the PoED within the pyrrole rings and its impact on the central arene ring, where the TSE is expected to be the lowest. Moreover, the PoED effect exhibited by pyrrole units is well discernible in experimentally known octapyrrolylnaphthalene (**OPN**$_{N1}$) and decapyrrolylcorannulene (**DPC**$_{N1}$) systems, where the core units (naphthalene or corannulene) are devoid of the MESP minimum as eight/ten arrows are pointing outward (Fig. S8 and S9, ESI†). This implies a
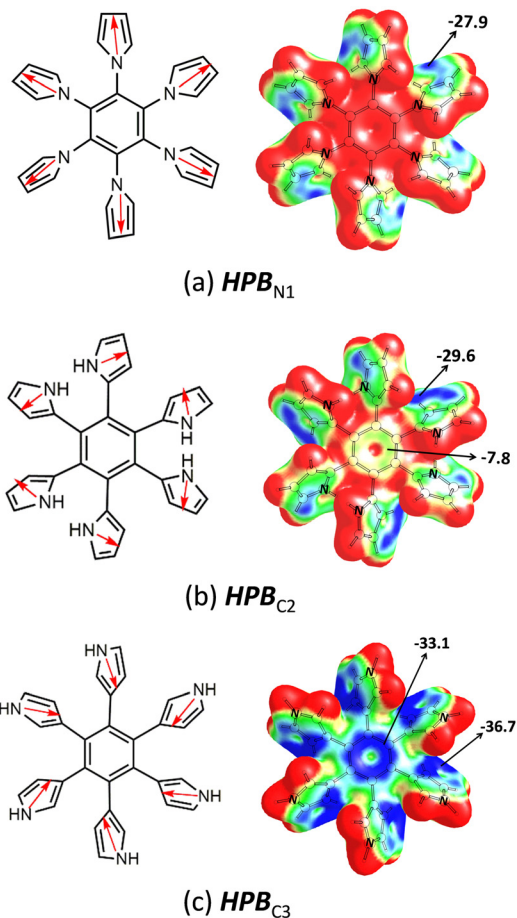

(a) HPB$_{N1}$

(b) HPB$_{C2}$

(c) HPB$_{C3}$

Fig. 8 The direction of electron flow in hexapyrrolylbenzene (**HPB**) compounds is denoted using red arrows. The MESP mapped on to the 0.01 a.u. electron density isosurface shows colour coding from blue to red, which indicates MESP values in the range −0.03 to 0.03 a.u., and the V_m values are given in kcal mol⁻¹.

substantial electron withdrawal effect on the core, and the core might be rendered electron rich by linking it to the C_3 center of pyrrole units. In **OPN**$_{C3}$ and **DPC**$_{C3}$ systems, the eight/ten arrows representing the PoED effect from pyrrole units to the core suggest the highly electron rich character of the core region. In general, the directionality of the TSE can be considered as the basis for the strong polarization in all phenyl pyrrole systems.

N-doped nanographene systems

The directionality of the TSE as seen from MESP patterns can be used to interpret the electronic distribution in intra-molecularly coupled polypyrrolyl systems, such as N-doped nanographenes (Fig. 9(a)–(e)). The arrow representations clearly indicate the electron density depletion at the core benzene/naphthalene ring in experimentally known **HPB**$_{N1}$6σ and **OPN**$_{N1}$8σ, and the accumulation of electron density at the benzene/naphthalene core unit in **HPB**$_{C3}$6σ and **OPN**$_{C3}$8σ. Moreover, as shown in Fig. 9(b), the TSE on C_2 connected **HPB**$_{C2}$6σ is negligible. In all systems, the MESP distribution perfectly corresponds to this prediction. Of the systems
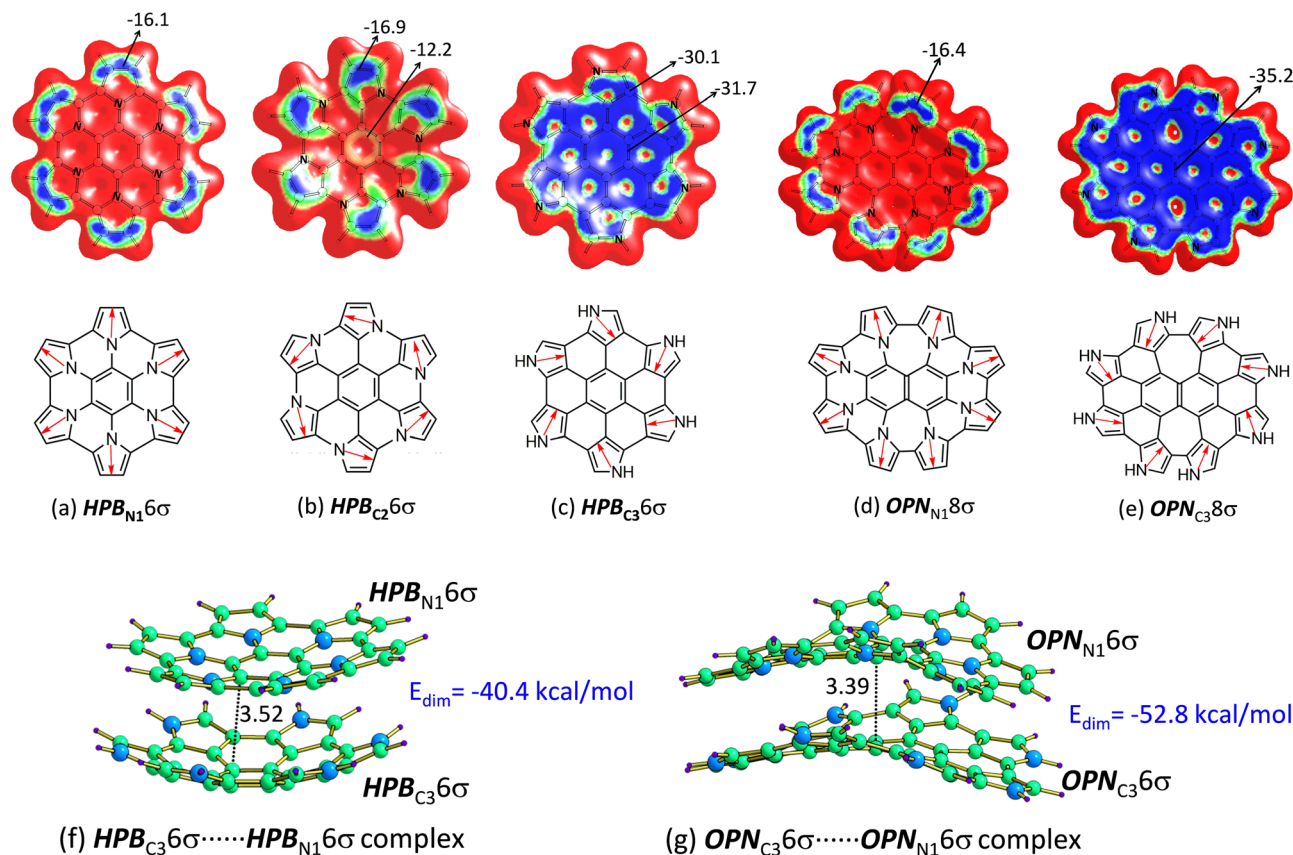
Fig. 9 (a)–(e) The direction of electron flow in intra-molecularly coupled hexapyrrolylbenzene (**HPB**6σ) and octapyrrolylnaphthalene (**OPN**8σ) compounds denoted using red arrows. For the MESP mapped on to the 0.01 a.u. electron density isosurface, colour coding from blue to red indicates MESP values in the range −0.01 to 0.01 a.u., respectively, and V_m values are given in kcal mol^{-1}. (f) and (g) are complementary complexes of **HPB**$_{C3}$6σ···**HPB**$_{N1}$6σ and **OPN**$_{C3}$6σ···**OPN**$_{N1}$6σ, respectively, wherein nearest non-covalent interatomic distances are given in Å.

investigated here, **HPB**$_{C2}$6σ, **HPB**$_{C3}$6σ and **OPN**$_{C3}$8σ are yet to be synthesized. Analysis of MESP topology leads to smart molecular design strategies for the construction of both electron-rich and electron-deficient core-expanded structures.

Complementary interactions in dimers

Electrostatic complementarity plays a pivotal role when D–A molecules assemble to form dimer (D–A)$_2$ complexes. In this context, the D unit of the first monomer interacts with the A unit of the second monomer, and *vice versa*. For instance, the pyrrole dimer shows a dimerization energy (E_{dim}) of −7.6 kcal mol^{-1}. Additionally, the E_{dim} values of polypyrroles exhibit consistent enhancement with an increase in the number of pyrrole units. As an example, when comparing ($^2P_{C3N1'}$)$_2$ with ($^6P_{C3N1'}$)$_2$, E_{dim} experiences a nearly two-fold increase, changing from −15.6 kcal mol^{-1} to −29.3 kcal mol^{-1} (Fig. S10, ESI†). This steady enhancement in E_{dim} can be attributed to the pronounced electronic polarization observed across multiple pyrrole units.

In the case of core expanded systems, **HPB**$_{C3}$6σ can be paired with **HPB**$_{N1}$6σ to obtain electrostatic complementarity.[108] Such a complex, **HPB**$_{C3}$6σ···**HPB**$_{N1}$6σ, shows an E_{dim} of −40.4 kcal mol^{-1} (Fig. 9(f)). Similarly, the pair of **OPN**$_{C3}$6σ and **OPN**$_{N1}$6σ (Fig. 9(g)) shows an E_{dim} of −52.8 kcal mol^{-1} due

to the high electrostatic complementarity. The electrostatic complementarity observed in these core-expanded systems holds significant potential for the construction of charge transfer complexes, offering promising applications.[109]

Indole, isoindole, azulene and aniline systems

The MESP topology analysis has been performed on indole (**I**), isoindole (**iI**), azulene (**Az**), and aniline (**An**) systems to gain better insight into the PoED and the phenomenon of the TSE. The **I** has two V_m points, −22.0 and −24.1 kcal mol^{-1}, which correspond to the five- and six-membered rings, respectively, whereas **iI** exhibits only one V_m, −25.8 kcal mol^{-1}, for the six-membered ring. The more negative V_m of **iI** compared to **I** can be attributed to the PoED, which is directed from the N-center to the six-membered ring. In **Az**, the five-membered ring is electron richer than the seven-membered ring. Consequently, the seven-membered ring behaves as a donor to the other ring, the acceptor. In **An**, the V_m of the arene ring (−23.1 kcal mol^{-1}) is observed near the *para*-carbon C$_4$, indicating the directionality of the TSE from the amino group to the *para*-site.

The directional nature of the TSE is utilized to design highly polarized oligomers of **I** ($^nI_{C3N1'}$, $^nI_{C3C2'}$ and $^nI_{C6N1'}$) (Fig. S13–S15, ESI†), **iI** ($^nil_{C5N1'}$) (Fig. S16, ESI†), **Az** ($^nAz_{C1C6'}$) (Fig. S17, ESI†), and **An** ($^nAn_{C4C2'}$) (Fig. S18, ESI†), where *n* = 2–6.
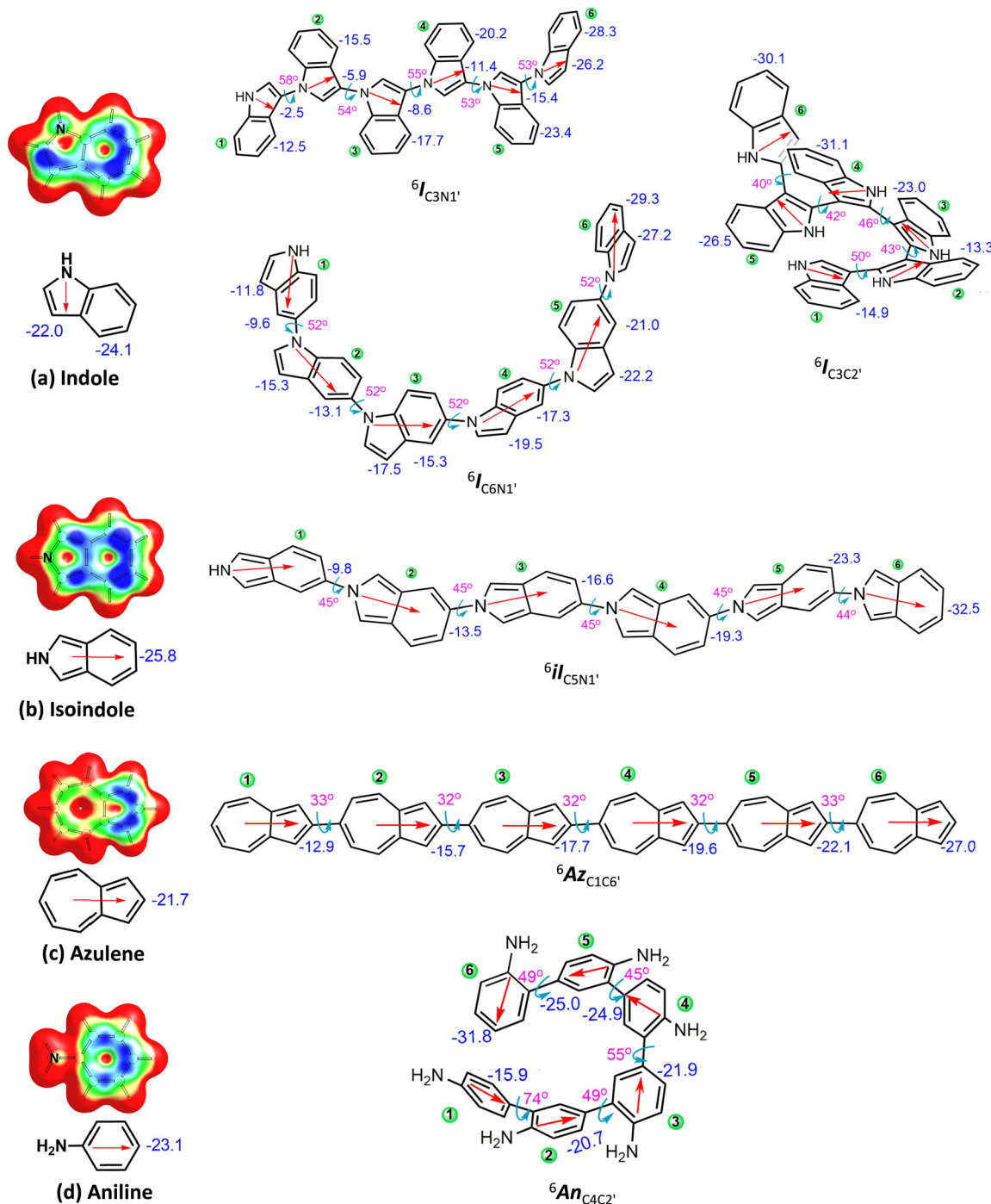
Fig. 10 The MESP mapped on to the 0.01 a.u. electron density isosurface of indole (*I*), isoindole (*iI*), azulene (*Az*) and aniline (*An*) systems, where colour coding from blue to red indicates MESP values in the range −0.02 to 0.02 a.u. The TSEs in terms of V_m values (in kcal mol^{-1}) for a representative set of systems, *viz.* $^6I_{C3N1'}$, $^6I_{C3C2'}$, $^6I_{C6N1'}$, $^6iI_{C5N1'}$, $^6Az_{C1C6'}$ and $^6An_{C4C2'}$, are also given. The red arrows represent the direction of electron flow.

The monomers are connected in a manner to get a unidirectional TSE for the oligomer. Fig. 10 depicts the TSE in terms of the V_m value for a representative set of systems, *viz.* $^6I_{C3N1'}$, $^6I_{C3C2'}$, $^6I_{C6N1'}$, $^6iI_{C5N1'}$, $^6Az_{C1C6'}$ and $^6An_{C4C2'}$. In all the cases, the last monomer unit exhibits a remarkable gain in the magnitude of V_m, while the first monomer exhibits a dramatic drop. The distribution of V_m clearly suggests the strong D–A

feature of the oligomers. In $^nP_{C3N1'}$, $^nP_{C3C2'}$, $^nI_{C3N1'}$, $^nI_{C3C2'}$, $^nI_{C6N1'}$, $^niI_{C5N1'}$, $^nAz_{C1C6'}$, and $^nAn_{C4C2'}$, the HOMO–LUMO gap decreases steadily with '*n*' moving from 1 to 6, in the range 1.1–2.0 eV (Table S2, ESI†).

Katagiri *et al.* reported the synthesis of $^3Az_{C1C6'}$ and other isomers, the terazulenes.[55] The excellent n-type behaviour exhibited by $^3Az_{C1C6'}$ as an organic field-effect transistor could
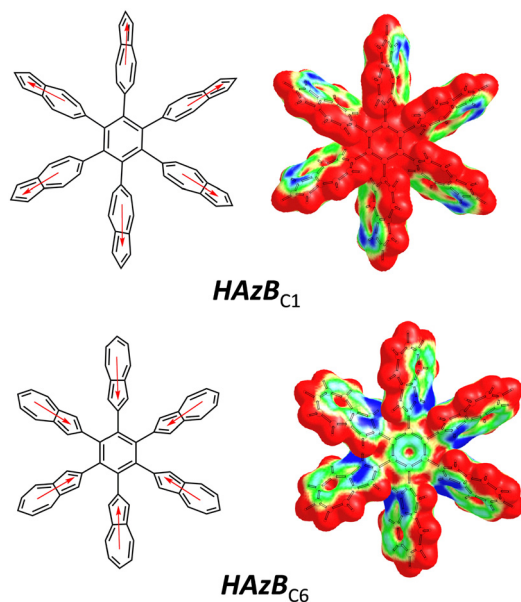
Fig. 11 The direction of electron flow in **HAzB** systems is denoted using red arrows. The MESP is mapped on to the 0.01 a.u. electron density isosurface, where colour coding from blue to red indicates MESP values in the range −0.02 to 0.02 a.u.

Fig. 12 Relationship between chemical shift, δ (in ppm), at the C_3 centers (represented using a red circle) and MESP V_m (in kcal mol^{-1}) at the first pyrrole ring (in yellow) and last pyrrole ring (in pink) in $^{n}P_{C3N1'}$ systems ($^{2}P_{C3N1'}$ to $^{6}P_{C3N1'}$).

be attributed to the TSE, which leads to the unidirectional flow of electron density. Also the electron-rich or deficient character of the central arene ring of the star-like azulene systems (**HAzB**) can be well described using the phenomenon of the TSE (Fig. 11). Connecting the five-membered ring of **Az** to the arene pushes more electron density towards the core, whereas the reverse effect occurs when the connection is made with the seven-membered ring. The D–A aspect originating from the directional nature of the electron polarization and the TSE is further confirmed by the MESP analysis of clusters of **I**, **iI**, **Az**, and **An** (Fig. S19, ESI†).

NMR data

The D–A feature of oligomeric systems is observed in the nuclear magnetic resonance (NMR) data also. The correlation between the chemical shift at the C_3 center (δ_C) and the V_m value of the first and last pyrrole rings in $^{n}P_{C3N1'}$ is illustrated in Fig. 12. In all cases, the first rings show a considerably higher δ_C than the last rings, indicating the deshielded and shielded environments of the first and last rings, respectively. Thus, the NMR data clearly support the donor nature of the first and acceptor nature of the last pyrrole units. Similarly, the δ_H data also agree with the D–A character of $^{n}P_{C3N1'}$ (Fig. S20, ESI†). Furthermore, NMR analysis is conducted on other oligomeric systems, *viz.*, $^{n}P_{C3C2'}$, $^{n}I_{C3N1'}$, $^{n}I_{C3C2'}$, $^{n}I_{C6N1'}$, $^{n}iI_{C5N1'}$, $^{n}Az_{C1C6'}$, and $^{n}An_{C4C2'}$. In each case, a strong correlation is observed between the chemical shift at the H, C, or N-center and the MESP. The first monomer unit consistently exhibited significant deshielding, indicating its strong D character. Conversely, the last monomer unit consistently demonstrated substantial shielding, indicating its strong A character.
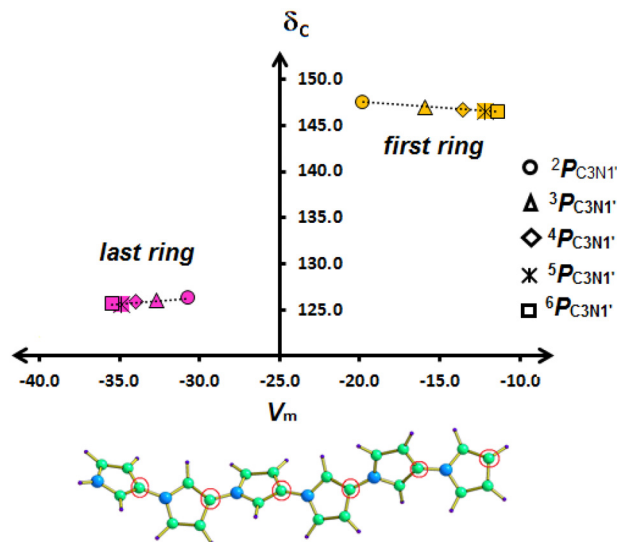
Absorption spectra

The theoretical λ_{max} of several known compounds is analysed in this study.[40,50,51,53,56,67,110,111] The TSE induced electronic polarization phenomenon exhibited by molecular systems can be correlated with the absorption spectra of these molecules. Fig. 13 illustrates the simulated absorption spectra of $^{n}P_{C3N1'}$, emphasizing the occurrence of a red shift from $^{2}P_{C3N1'}$ to $^{6}P_{C3N1'}$. This phenomenon can be attributed to the substantial increase in electron density in the last ring of $^{n}P_{C3N1'}$. A similar red shift in absorption spectra is observed for $^{n}P_{C3N1'}$, $^{n}P_{C3C2'}$, $^{n}I_{C3N1'}$, $^{n}I_{C3C2'}$, $^{n}I_{C6N1'}$, $^{n}iI_{C5N1'}$, $^{n}Az_{C1C6'}$, and $^{n}An_{C4C2'}$ systems, indicating the strong D–A character of these molecules (Fig. S21, ESI†).

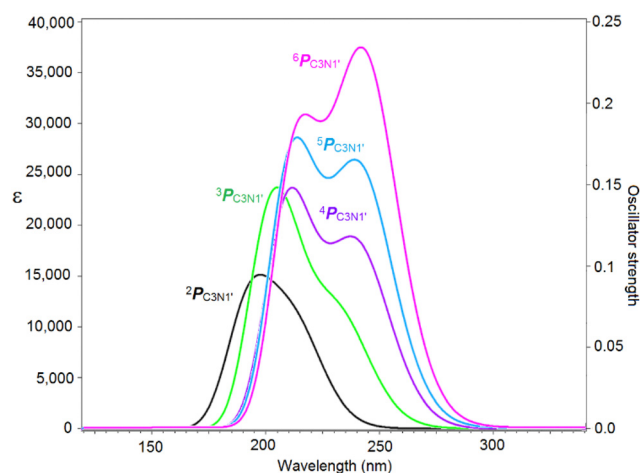Fig. 13 Simulated absorption spectra of $^{n}P_{C3N1'}$ systems (ε is given in L mol^{-1} cm^{-1}).

We have applied Ciofini *et al.*'s procedure to compute the difference in total electron density between the ground and excited states of representative examples 1-***PhP*** and ***HPB***$_{N1}$ (Fig. S22, ESI†) to verify the electronic polarization within these systems.[112,113] The density maps unequivocally indicate that areas of electron density depletion are primarily localized around the pyrrole unit, whereas a noticeable augmentation in electron density is observed within the central benzene unit. This analysis underscores the distinct electronic behaviours of these molecules, shedding light on their unique polarization patterns and electronic structures.

Conclusions

The fundamental phenomenon of the TSE is unravelled for a variety of molecular systems using MESP topology analysis, which confirmed that it is highly directional in nature. The pyrrole molecule inherently shows the electronic polarization characterized by an electron-deficient N-center and an electron-rich C_3C_4 region. By aligning the TSE of pyrrole units in the same direction, polypyrrole systems with high electronic polarization can be made. The TSE effect in polypyrroles is nearly unaffected by the twist angle between adjacent pyrrole units. Polypyrroles show strong D–A character from one end to the other due to the TSE, as these systems are devoid of specific D or A moieties. Furthermore, the TSE clearly explains the electron rich/deficient feature of experimentally known phenylpyrrole, hexapyrrolylbenzene, octapyrrolylnaphthalene, and decapyrrolylcorannulene systems as well as the newly designed core-expanded structures such as N-doped nanographenes. A highly directed TSE in azulene, indole, isoindole, and aniline systems is also disclosed here. This intrinsic D–A character of pyrrole and other molecules is utilized here to develop oligomeric systems with enhanced D–A character by connecting the negative pole of the monomer dipole with the positive pole of another monomer. The MESP-analysis of oligomers, core-expanded structures and noncovalent clusters proved the predominance of the TSE over the TBE, which creates a strong D–A feature in all such systems. The data such as APT charge, FMO, complementary interactions in dimers, NMR chemical shift and λ_{max} support the strong D–A character of the molecular systems. Tuning the directionality of the TSE opens up a new molecular design strategy to construct D–A systems without specific donors and acceptors.

Author contributions

The manuscript was written through contributions of all the authors. All authors have given approval to the final version of the manuscript.

Conflicts of interest

There are no conflicts to declare.

Acknowledgements

References

1 A. B. Parusel, *Phys. Chem. Chem. Phys.*, 2000, **2**, 5545–5552.

2 J. Jortner, *J. Chem. Phys.*, 1976, **64**, 4860–4867.

3 G. Zerza, M. C. Scharber, C. J. Brabec, N. S. Sariciftci, R. Gomez, J. L. Segura, N. Martín and V. I. Srdanov, *J. Phys. Chem. A*, 2000, **104**, 8315–8322.

4 W. U. Huynh, J. J. Dittmer, W. C. Libby, G. L. Whiting and A. P. Alivisatos, *Adv. Funct. Mater.*, 2003, **13**, 73–79.

5 J. J. Dittmer, E. A. Marseglia and R. H. Friend, *Adv. Mater.*, 2000, **12**, 1270–1274.

6 D. Zhang and M. Heeney, *Organic Donor–Acceptor Systems*, Wiley Online Library, 2020, vol. 9, p. 1251.

7 J. Singh, M. R. Nagar, C. P. Sharma, N. M. Gupta, A. Choudhury, K. S. Rawat, R. P. Vats, S. Gupta, J.-H. Jou and A. Goel, *ACS Appl. Opt. Mater.*, 2022, **1**, 229–243.

8 G. Pourtois, D. Beljonne, J. Cornil, M. A. Ratner and J. L. Brédas, *J. Am. Chem. Soc.*, 2002, **124**, 4436–4447.

9 M. Cyr, S. Brixi, A. Ganguly, B. H. Lessard and J. L. Brusso, *Dyes Pigm.*, 2023, **210**, 110964.

10 A. Gomez-Zavaglia and R. Fausto, *J. Phys. Chem. A*, 2004, **108**, 6953–6967.

11 B. Albinsson, M. P. Eng, K. Pettersson and M. U. Winters, *Phys. Chem. Chem. Phys.*, 2007, **9**, 5847–5864.

12 O. V. Kuznetsova, A. N. Egorochkin and O. V. Novikova, *Russ. J. Gen. Chem.*, 2006, **76**, 554–562.

13 F. Bureš, *RSC Adv.*, 2014, **4**, 58826–58851.

14 D. Ateh, H. Navsaria and P. Vadgama, *J. R. Soc., Interface*, 2006, **3**, 741–752.

15 C. Bulumulla, R. Gunawardhana, P. L. Gamage, J. T. Miller, R. N. Kularatne, M. C. Biewer and M. C. Stefan, *ACS Appl. Mater. Interfaces*, 2020, **12**, 32209–32232.

16 J. Du, C. Bulumulla, I. Mejia, G. T. McCandless, M. C. Biewer and M. C. Stefan, *Polym. Chem.*, 2017, **8**, 6181–6187.

17 M. Lazerges, K. I. Chane-Ching, S. Aeiyach, S. Chelli, B. Peppin-Donnat, M. Billon, C. Lombard, F. Maurel and M. Jouini, *J. Solid State Electrochem.*, 2009, **13**, 231–238.

18 X. Zou, S. Cui, J. Li, X. Wei and M. Zheng, *Front. Chem.*, 2021, **9**, 671294.

19 H. Wu, Y. Wang, X. Qiao, D. Wang, X. Yang and H. Li, *Chem. Mater.*, 2018, **30**, 6992–6997.

20 S. K. Dey and D. A. Lightner, *J. Org. Chem.*, 2007, **72**, 9395–9397.

21 Y. Tan and K. Ghandi, *Synth. Met.*, 2013, **175**, 183–191.

22 H. Rapoport and N. Castagnoli, *J. Am. Chem. Soc.*, 1962, **84**, 2178–2181.

23 W. Flitsch and F.-J. Lüttig, *Liebigs Ann. Chem.*, 1987, **1987**, 893–894.

24 T. Jarosz and P. Ledwon, *Mater. Sci. Eng., C*, 2021, **14**, 281.

25 S. Maity, A. Dubey and S. Chakraborty, *J. Ind. Text.*, 2021, **51**, 152–173.

26 S. Ahmad, *Polym. Eng. Sci.*, 2009, **49**, 916–921.

27 R. Gleiter and J. Ritter, *Tetrahedron*, 1996, **52**, 10383–10388.

28 M. Wang, *Polymers*, 2016, **8**, 373.

29 J. G. Andino, S. Mazumder, K. Pal and K. G. Caulton, *Angew. Chem., Int. Ed.*, 2013, **52**, 4726–4732.

30 F. Heidarizadeh and S. Asadipour, *Iran. Chem. Commun.*, 2015, **3**, 187–198.

31 E. Orti, F. Tomas and J. Sanchez-Marin, *J. Mol. Struct.*, 1983, **104**, 197–206.

32 A. Cihaner, O. Mert and A. S. Demir, *Electrochim. Acta*, 2009, **54**, 1333–1338.

33 M. Farnier, S. Soth and P. Fournari, *Can. J. Chem.*, 1976, **54**, 1083–1086.

34 C. C. Hughes, A. Prieto-Davo, P. R. Jensen and W. Fenical, *Org. Lett.*, 2008, **10**, 629–631.

35 L. Fu and G. W. Gribble, *Tetrahedron Lett.*, 2008, **49**, 3545–3548.

36 F. Heidarizadeh and S. Asadipour, *Iran. Chem. Commun.*, 2015, **3**, 187–198.

37 A. A. Kanakis and V. Sarli, *Org. Lett.*, 2010, **12**, 4872–4875.

38 L. Goldenberg, R. Lyubovskaya, I. Nazarova and O. Roschupkina, *Synth. Met.*, 1991, **40**, 393–396.

39 K. Maksymiuk, *Electroanalysis*, 2006, **18**, 1537–1551.

40 H. Biemans, C. Zhang, P. Smith, H. Kooijman, W. Smeets, A. Spek and E. Meijer, *J. Org. Chem.*, 1996, **61**, 9012–9015.

41 M. Lazerges, M. Jouini, P. Hapiot, P. Guiriec and P.-C. Lacaze, *J. Phys. Chem. A*, 2003, **107**, 5042–5048.

42 M. Jouini, M. Lazerges, S. Chelly, M. Billon, C. Lombard, B. Pepin-Donat and C. Pernelle, *Synth. Met.*, 2008, **158**, 681–683.

43 K. Hrnčariková, Á. Szöllősy and D. Végh, *ARKIVOC*, 2006, **2**, 124–129.

44 K. Oki, M. Takase, N. Kobayashi and H. Uno, *J. Org. Chem.*, 2021, **86**, 5102–5109.

45 Y. Sasaki, M. Takase, N. Kobayashi, S. Mori, K. Ohara, T. Okujima and H. Uno, *J. Org. Chem.*, 2021, **86**, 4290–4295.

46 F. Wu, K. Oki, J. Xue, S. Mori, M. Takase, Z. Shen and H. Uno, *Org. Lett.*, 2022, **24**, 80–84.

47 M. Navakouski, H. Zhylitskaya, P. J. Chmielewski, M. Żyła-Karwowska and M. Stępień, *J. Org. Chem.*, 2020, **85**, 187–194.

48 X. Qiao, M. A. Padula, D. M. Ho, N. J. Vogelaar, C. E. Schutt and R. A. Pascal, *J. Am. Chem. Soc.*, 1996, **118**, 741–745.

49 X. Zhou, Z. Li, H. Wang, M. Kitamura, K.-I. Kanno, K. Nakajima and T. Takahashi, *J. Org. Chem.*, 2004, **69**, 4559–4562.

50 K. Oki, M. Takase, S. Mori, A. Shiotari, Y. Sugimoto, K. Ohara, T. Okujima and H. Uno, *J. Am. Chem. Soc.*, 2018, **140**, 10430–10434.

51 Y.-Y. Xu, H.-R. Tian, S.-H. Li, Z.-C. Chen, Y.-R. Yao, S.-S. Wang, X. Zhang, Z.-Z. Zhu, S.-L. Deng and Q. Zhang, *Nat. Commun.*, 2019, **10**, 1–9.

52 Y. Zhang, R. Guan, M. Chen, Y. Shen, Q. Pan, Y. Lian and S. Yang, *Inorg. Chem.*, 2021, **60**, 1462–1471.

53 T. Morita and K. Takase, *Bull. Chem. Soc. Jpn.*, 1982, **55**, 1144–1152.

54 Q. Sun, I. C.-Y. Hou, K. Eimre, C. A. Pignedoli, P. Ruffieux, A. Narita and R. Fasel, *Chem. Commun.*, 2019, **55**, 13466–13469.

55 Y. Yamaguchi, M. Takubo, K. Ogawa, K.-I. Nakayama, T. Koganezawa and H. Katagiri, *J. Am. Chem. Soc.*, 2016, **138**, 11335–11343.

56 J. Huang, S. Huang, Y. Zhao, B. Feng, K. Jiang, S. Sun, C. Ke, E. Kymakis and X. Zhuang, *Small Methods*, 2020, **4**, 2000628.

57 Q. Fan, D. Martin-Jimenez, D. Ebeling, C. K. Krug, L. Brechmann, C. Kohlmeyer, G. Hilt, W. Hieringer, A. Schirmeisen and J. M. Gottfried, *J. Am. Chem. Soc.*, 2019, **141**, 17713–17720.

58 J. R. Dias, *J. Phys. Org. Chem.*, 2007, **20**, 395–409.

59 J. Xiang, W. L. Tan, J. Zhang, Y. Wang, C. Duan, C. R. McNeill, X. Yang, C. Ge and X. Gao, *Macromolecules*, 2022, **55**, 8074–8083.

60 S. Ito, M. Ando, A. Nomura, N. Morita, C. Kabuto, H. Mukai, K. Ohta, J. Kawakami, A. Yoshizawa and A. Tajiri, *J. Org. Chem.*, 2005, **70**, 3939–3949.

61 K. Nakagawa, T. Yokoyama, K. Toyota, N. Morita, S. Ito, S. Tahata, M. Ueda, J. Kawakami, M. Yokoyama and Y. Kanai, *Tetrahedron*, 2010, **66**, 8304–8312.

62 A. Thadathil, J. Kavil, G. R. Kovummal, C. P. Jijil and P. Periyat, *ACS Omega*, 2022, **7**, 11473–11490.

63 A. K. Singh and R. Prakash, *2nd National Workshop on Advanced Optoelectronic Materials and Devices*, 2008.

64 B. Sari, N. Yavas, M. Makulogullari, O. Erol and H. I. Unal, *React. Funct. Polym.*, 2009, **69**, 808–815.

65 T. Plachý, J. Žitka, M. Mrlík, P. Bažant, M. Kadlečková, M. Trchová and J. Stejskal, *Polymer*, 2021, **217**, 123448.

66 B. Purty, R. B. Choudhary, A. Biswas and G. Udayabhanu, *Polym. Bull.*, 2019, **76**, 1619–1640.

67 C. J. Verma, A. S. Keshari, P. Dubey and R. Prakash, *Vacuum*, 2020, **177**, 109363.

68 M. B. Gómez Costa, J. M. Juárez, M. L. Martínez, J. Cussa and O. A. Anunziata, *Microporous Mesoporous Mater.*, 2012, **153**, 191–197.

69 T. Tüken, B. Yazıcı and M. Erbil, *Surf. Coat. Technol.*, 2006, **200**, 4802–4809.

70 A. H. Majeed, L. A. Mohammed, O. G. Hammoodi, S. Sehgal, M. A. Alheety, K. K. Saxena, S. A. Dadoosh, I. K. Mohammed, M. M. Jasim and N. U. Salmaan, *Int. J. Polym. Sci.*, 2022, **2022**, 9047554.

71 V. Babel and B. L. Hiran, *Polym. Compos.*, 2021, **42**, 3142–3157.

72 E. Brodskaya, G. V. f Ratovskii and M. G. Voronkov, *Russ. Chem. Rev.*, 1993, **62**, 919.

73 F. Cozzi, R. Annunziata, M. Benaglia, M. Cinquini, L. Raimondi, K. K. Baldridge and J. S. Siegel, *Org. Biomol. Chem.*, 2003, **1**, 157–162.

74 S. E. Galembeck, R. P. Orenha, R. M. Madeira, L. B. Peixoto and R. L. Parreira, *J. Braz. Chem. Soc.*, 2021, **32**, 1447–1455.

75 S. Puhl, T. Steenbock, C. Herrmann and J. Heck, *Angew. Chem., Int. Ed.*, 2020, **59**, 2407–2413.

76 M. Saraswat and S. Venkataramani, *Phys. Chem. Chem. Phys.*, 2018, **20**, 4386–4395.

77 Q. Zhang, H. Lei, H. Guo, Y. Wang, Y. Gao, W. Zhang and R. Cao, *ChemSusChem*, 2022, **15**, e202200086.

78 E. M. Nolan and R. Linck, *J. Am. Chem. Soc.*, 2000, **122**, 11497–11506.

79 I. Azcarate, C. Costentin, M. Robert and J.-M. Savéant, *J. Am. Chem. Soc.*, 2016, **138**, 16639–16644.

80 K. Bowden and E. J. Grubbs, *Chem. Soc. Rev.*, 1996, **25**, 171–177.

81 W. Adcock and N. A. Trout, *Chem. Rev.*, 1999, **99**, 1415–1436.

82 R. J. Burns, I. K. Mati, K. B. Muchowska, C. Adam and S. L. Cockroft, *Angew. Chem., Int. Ed.*, 2020, **132**, 16860–16867.

83 J. Simó Padial, J. Poater, D. T. Nguyen, P. Tinnemans, F. M. Bickelhaupt and J. Mecinović, *J. Org. Chem.*, 2017, **82**, 9418–9424.

84 S. E. Wheeler and K. N. Houk, *J. Chem. Theory Comput.*, 2009, **5**, 2301–2312.

85 S. E. Wheeler and K. N. Houk, *J. Am. Chem. Soc.*, 2009, **131**, 3126–3127.

86 A. Becke, *J. Chem. Phys.*, 1993, **98**, 5648–5652.

87 R. Parr and W. Yang, *Density-Functional Theory of Atoms and Molecules*, Oxford University Press, New York, 1989.

88 C. Lee, W. Yang and R. G. Parr, *Phys. Rev. B: Condens. Matter Mater. Phys.*, 1988, **37**, 785.

89 R. G. Parr, *Density Functional Theory of Atoms and Molecules*, Springer, Dordrecht, 1980.

90 Y. Zhao and D. G. Truhlar, *Theor. Chem. Acc.*, 2008, **120**, 215–241.

91 E. G. Hohenstein, S. T. Chill and C. D. Sherrill, *J. Chem. Theory Comput.*, 2008, **4**, 1996–2000.

92 R. Ditchfield, W. J. Hehre and J. A. Pople, *J. Chem. Phys.*, 1971, **54**, 724–728.

93 M. J. Frisch, G. W. Trucks, H. B. Schlegel, G. E. Scuseria, M. A. Robb, J. R. Cheeseman, G. Scalmani, V. Barone, G. A. Petersson, H. Nakatsuji, X. Li, M. Caricato, A. V. Marenich, J. Bloino, B. G. Janesko, R. Gomperts, B. Mennucci, H. P. Hratchian, J. V. Ortiz, A. F. Izmaylov, J. L. Sonnenberg, D. Williams-Young, F. Ding, F. Lipparini, F. Egidi, J. Goings, B. Peng, A. Petrone, T. Henderson, D. Ranasinghe, V. G. Zakrzewski, J. Gao, N. Rega, G. Zheng, W. Liang, M. Hada, M. Ehara, K. Toyota, R. Fukuda, J. Hasegawa, M. Ishida, T. Nakajima, Y. Honda, O. Kitao, H. Nakai, T. Vreven, K. Throssell, J. A. M. Jr., J. E. Peralta, F. Ogliaro, M. J. Bearpark, J. J. Heyd, E. N. Brothers, K. N. Kudin, V. N. Staroverov, T. A. Keith, R. Kobayashi, J. Normand, K. Raghavachari, A. P. Rendell, J. C. Burant, S. S. Iyengar, J. Tomasi, M. Cossi, J. M. Millam, M. Klene, C. Adamo, R. Cammi, J. W. Ochterski, R. L. Martin, K. Morokuma, O. Farkas, J. B. Foresman and D. J. Fox, *Gaussian 16 Rev. A. 03*, Wallingford, CT, 2016.

94 S. R. Gadre and R. N. Shirsat, *Electrostatics of atoms and molecules*, Universities Press, 2000.

95 S. R. Gadre, S. A. Kulkarni and I. H. Shrivastava, *J. Chem. Phys.*, 1992, **96**, 5253–5260.

96 P. S. V. Kumar, V. Raghavendra and V. Subramanian, *J. Chem. Sci.*, 2016, **128**, 1527–1536.

97 G. Marino, *J. Heterocycl. Chem.*, 1972, **9**, 817–819.

98 J. Cioslowski, *J. Am. Chem. Soc.*, 1989, **111**, 8333–8336.

99 K. Meindl, J. Henn, N. Kocher, D. Leusser, K. A. Zachariasse, G. M. Sheldrick, T. Koritsanszky and D. Stalke, *J. Phys. Chem. A*, 2009, **113**, 9684–9691.

100 H.-C. Ma and X.-Z. Jiang, *J. Org. Chem.*, 2007, **72**, 8943–8946.

101 A. F. L. O. M. Santos and M. A. V. Ribeiro, da Silva, *J. Chem. Thermodyn.*, 2010, **42**, 734–741.

102 S. Murali and W. Rettig, *J. Phys. Chem. A*, 2006, **110**, 28–37.

103 T. Yoshihara, V. A. Galievsky, S. I. Druzhinin, S. Saha and K. A. Zachariasse, *Photochem. Photobiol. Sci.*, 2003, **2**, 342–353.

104 C. A. Figueira and P. T. Gomes, *Catal. Lett.*, 2015, **145**, 762–768.

105 J. Wen, R.-Y. Zhang, S.-Y. Chen, J. Zhang and X.-Q. Yu, *J. Org. Chem.*, 2012, **77**, 766–771.

106 R. D. Rieth, N. P. Mankad, E. Calimano and J. P. Sadighi, *Org. Lett.*, 2004, **6**, 3981–3983.

107 F. Ammon, S. T. Sauer, R. Lippert, D. Lungerich, D. Reger, F. Hampel and N. Jux, *Org. Chem. Front.*, 2017, **4**, 861–870.

108 C. H. Suresh and S. Anila, *Acc. Chem. Res.*, 2023, **56**, 1884–1895.

109 A. Sosorev, D. Dominskiy, I. Chernyshov and R. Efremov, *Int. J. Mol. Sci.*, 2020, **21**, 5654.

110 J. W. ApSimon, D. G. Durham and A. H. Rees, *J. Chem. Soc., Perkin Trans. 1*, 1978, 1588–1594.

111 K. Kaeriyama and H. Masuda, *Synth. Met.*, 1991, **41**, 389–392.

112 T. Le Bahers, C. Adamo and I. Ciofini, *J. Chem. Theory Comput.*, 2011, **7**, 2498–2506.

113 R. L. Birke and J. R. Lombardi, *Nanomaterials*, 2021, **11**, 1491.

ROYAL SOCIETY
OF CHEMISTRY

Check for updates

Topology of electrostatic potential and electron density reveals a covalent to non-covalent carbon–carbon bond continuum†

Puthannur K. Anjalikrishna,[ab] Shridhar R. Gadre*[c] and Cherumuttathu H. Suresh ![ORCID]*[ab]

The covalent and non-covalent nature of carbon–carbon (CC) interactions in a wide range of molecular systems can be characterized using various methods, including the analysis of molecular electrostatic potential (MESP), represented as $V(\mathbf{r})$, and the molecular electron density (MED), represented as $\rho(\mathbf{r})$. These techniques provide valuable insights into the bonding between carbon atoms in different molecular environments. By uncovering a fundamental exponential relationship between the distance of the CC bond and the highest eigenvalue (λ_{v1}) of $V(\mathbf{r})$ at the bond critical point (BCP), this study establishes the continuum model for all types of CC interactions, including transition states. The continuum model is further delineated into three distinct regions, namely covalent, borderline cases, and non-covalent, based on the gradient, λ'_{v1}, with the bond distance of the CC interaction. For covalent interactions, this parameter exhibits a more negative value than -5.0 a.u. Å^{-1}, while for non-covalent interactions, it is less negative than -1.0 a.u. Å^{-1}. Borderline cases, which encompass transition state structures, fall within the range of -1.0 to -5.0 a.u. Å^{-1}. Furthermore, this study expands upon Popelier's analysis of the Laplacian of the MED, denoted as $\nabla^2\rho$, to encompass the entire spectrum of covalent, non-covalent, and borderline cases of CC interactions. Therefore, the present study presents compelling evidence supporting the concept of a continuum model for CC bonds in chemistry. Additionally, this continuum model is further explored within the context of C–N, C–O, C–S, N–N, O–O, and S–S interactions, albeit with a limited dataset.

Introduction

With regard to the possibility of creating large networks of covalent connections with itself and other elements, the carbon atom stands out amid all the chemical elements. The supremacy of the carbon–carbon (CC) bond among all the other linkages observed in organic molecules is well-known.[1] Since the carbon atom is neither highly electropositive nor electronegative, electrons are more likely to be shared between two carbon atoms to yield a covalent bond. The single bond between the carbon atoms, known as a σ-bond, is commonly described to be formed by the interactions of sp^3-hybridized orbitals. Carbon atoms can also form a π-bond under a sp^2-

hybridized state or two π-bonds in a sp-hybridized state. Some CC linkages are also regarded as aromatic or antiaromatic ones, depending on the nature of the π-conjugation. The carbon–carbon non-covalent bonding scenario describes weak attractive interactions between carbon centers saturated by either σ-bonds or by both σ- and π-bonds. The typical single bond (C_{sp^3}–C_{sp^3}) to triple bond ($C_{sp}\equiv C_{sp}$) distance lies in the range 1.54 to 1.20 Å, while the non-covalent C···C distance is around 3.0 Å. Hounshell *et al.* reported[2] that one of the C–C bonds in hexaphenylethane is significantly longer compared to the normal C–C one, due to the steric repulsion between the six phenyl groups present in it. To learn more about the atypical covalent bonds (long bonds, strained bonds, or short bonds), many attempts have been made in the past[3–16] which led to the discovery of many bulky systems with substantially elongated C–C bonds. The CC bond formation reactions are one of the most actively explored topics in organic chemistry. The discovery of new methodologies for effective CC bond formation has gained prominence, as evidenced by the recent Nobel awards in chemistry.[17] The CC bond formation is the prime step in most of the organic synthesis reactions for the

a Chemical Sciences and Technology Division, CSIR-National Institute for Interdisciplinary Science and Technology, Thiruvananthapuram, Kerala, 695019, India. E-mail: sureshch@niist.res.in

b Academy of Scientific and Innovative Research (AcSIR), Ghaziabad, 201002, India

c Departments of Chemistry and Scientific Computing, Modelling & Simulation, Savitribai Phule Pune University, Pune 411007, India

development of the carbon framework of organic compounds.[18] Carbonaceous clusters are important in many fields of study, including astrochemistry, materials science, structural chemistry, *etc.*[19] Special structural and electrical properties of multiple bonds reveal intriguing chemical characteristics of the system under study. The strong CC bonds create a huge variety of molecular structures, many of which are crucial components of the basic life framework.[20]

Bonds and related entities, such as bond length, bond strength, bond order, *etc.*, have been the most frequently used for the interpretation of many chemical phenomena.[21] To comprehend the chemical reactivity and the properties of a molecular system, one must have a quantitative understanding of the electronic influence on an atom in that system.[22] Each atom in a molecular system is strongly influenced by the electrons as well as nuclei of the neighbouring atoms. For exploring the basic features of the molecular structure and reactivity,[23] a detailed understanding of molecular scalar fields is found to be useful. The molecular electrostatic potential (MESP) has been widely used for exploring the electronic structure, chemical bonding in covalent and non-covalent contexts, and the interaction between atomic and molecular systems.[24–29] By employing a trustworthy *ab initio* or density functional theory (DFT) method to solve the Schrödinger equation, it is possible to calculate the molecular electron density (MED),[30,31] as well as MESP of the system under study with high accuracy. Politzer and co-workers pioneered the systematic application of MESP to forecast the molecular regions susceptible to electrophilic and nucleophilic attack.[32–35] Later, Gadre, Suresh, and others made fundamental contributions to the understanding of the topological characteristics of MESP and also developed the algorithms and software for the MESP topology analysis.[23,25,36–38]

The MESP and MED topology analyses are considered to be powerful tools to analyze the electronic distribution in σ-, π-, non-covalently bonded and non-bonded regions in molecules. Recently developed DAMQT (deformed atoms in molecules quantum theory) software[39,40] also offers the MESP topology computation.[41–44] DAMQT is a package for the analysis and visualization of MESP and MED in atoms and molecules, and related properties such as deformation density, as well as the critical points of MESP and MED.[45] The topology of the MESP and MED provide a comprehensive overview of bonding.

In the present study, topology analysis using MESP and MED is carried out on a wide variety of molecular systems containing different types of CC bonds (such as C–C, C=C, C≡C). We also examine strained, sterically crowded, aromatic systems as well as those incorporating non-covalent interactions. The topology of the MESP and MED reveals a CC bond continuum and suggests a MESP-based relationship that connects the CC distance and eigenvalue of the highest magnitude (λ_{v1}). The continuum may be divided into three regions using MESP topology analysis, *viz.* covalent, non-covalent, and borderline cases. By defining borderline cases between covalent and non-covalent bonds, we attempt to give a new dimension to the analysis based on the Laplacian, $\nabla^2\rho$ reported by Popelier.[46,47]

Methodology

The topology analysis of MESP and MED has been carried out on a large variety of molecular systems consisting of σ-, π-, and non-covalently bonded CC regions to characterize the nature of BCPs and to introduce an ideal covalent to non-covalent regime. All molecular systems explored in the present study were optimized using the M06-2X/6-311G(d,p) level of theory[48] implemented in the Gaussian 16 program package,[49] with a check on the minimal nature by doing a vibrational frequency run and verifying that all the frequencies are real for all systems, except for the transition state structures. The MESP topology computations on molecular geometries have been carried out using the DAMQT package[42–44,50] and Bader's quantum theory of atoms in molecules (QTAIM) analysis is carried out using the AIMAII package.[51–53] The MESP $V(\mathbf{r})$, at a given point $\mathbf{r}$ is defined as the work carried out in bringing a test positive charge from infinity to the reference point $\mathbf{r}$ which is given by eqn (1), where Z_A is the charge on nucleus A, located at $\mathbf{R}_A$.

$$V(\mathbf{r}) = \sum_{A}^{N} \frac{Z_A}{|\mathbf{r} - \mathbf{R}_A|} - \int \frac{\rho(\mathbf{r}')\mathrm{d}^3 r'}{|\mathbf{r} - \mathbf{r}'|} \tag{1}$$

The first term on the right hand side of eqn (1) is the bare nuclear potential (V_{bnp}) and the second term represents the electronic contribution (V_ρ). Therefore, eqn (1) can also be represented as shown in eqn (2), *viz.*

$$V(\mathbf{r}) = V_{\text{bnp}} - V_\rho \tag{2}$$

The MED, $\rho(\mathbf{r})$, describes the probability distribution of electrons in the system and can be extracted from the corresponding wave function by a suitable integration followed by the substitution $\mathbf{r} = \mathbf{r}_1$, in eqn (3);

$$\rho(\mathbf{r}) = N \sum_{\sigma} |\Psi(\mathbf{x}_1, \mathbf{x}_2, \ldots \mathbf{x}_N)|^2 \mathrm{d}^3 \mathbf{r}_2 \ldots \mathrm{d}^3 \mathbf{r}_N \big|_{\mathbf{x}_1 = \mathbf{x}} \tag{3}$$

where $\Psi(\mathbf{x}_1, \mathbf{x}_2 \ldots \mathbf{x}_N)$ represents the multidimensional wave function, $\mathbf{x}_i$ denotes the combined spatial ($\mathbf{r}$) and spin (σ) coordinate of the electron i, and N is the number of electrons.[25,30,31,54,55]

The topology mapping leads to the identification of critical points (CPs) where all the first order partial derivatives of the function are zero. There are three eigenvalues, (λ_{v1}, λ_{v2}, and λ_{v3}) and the corresponding eigenvectors associated with the Hessian matrix at each non-degenerate CP wherein eigenvalues indicate the curvature of the function at the CP and the respective eigenvector signifies the axis of the curvature independent of the choice of molecular coordinate system.[56] A non-degenerate CP is characterized by two numbers (R, σ); where 'R' and 'σ' respectively stand for the number of non-zero eigenvalues and the algebraic sum of the sign of the λ_i. Among the four types of non-degenerate CPs in MESP topology, *viz.* (3, +3), (3, +1), (3, −1), and (3, −3), the (3, +3) CP corresponds to a local minimum, a (3, −3) CP corresponds to a local maximum and (3, −1) and (3, +1) are designated as saddle points.[57–59] Among them, the present investigation is focused mainly on the characteristics of (3, −1) CPs observed between a pair of

bonded atoms of a molecule, which are also called the bond critical points (BCP).

Similar to MESP topology, MED topology[30,31,60] exhibits (3, +3), (3, +1), (3, −1), and (3, −3) CPs. Here, (3, +3) CP appears in caged structures while a (3, +1) CP typically appears for a ring structure. The (3, −1) CP is the BCP and (3, −3) CP generally corresponds to the nuclear positions or non-nuclear maxima in MED.[46] The BCP is located along the bond path where the $\rho(\mathbf{r})$ is at its lowest value.[61] The three eigenvalues of the Hessian matrix corresponding to electrostatic potential are designated as λ_{v1}, λ_{v2}, and λ_{v3} while that of electron density are represented as $\lambda_{\rho1}$, $\lambda_{\rho2}$, and $\lambda_{\rho3}$. In MESP, the direction of the eigenvector corresponding to the largest eigenvalue λ_{v1} (red arrow) is always perpendicular to the CC bond, while the eigenvectors associated with λ_{v2} (blue arrow) and λ_{v3} (green arrow) are oriented parallel to the CC bond plane (Fig. S1, ESI†).

Results and discussion

MESP topology analysis

Covalent CC bonds in hydrocarbons and carbon clusters. The MESP topology showing the (3, −1) CPs observed for a representative set of C–C single bonded systems such as typical alkanes, strained cycloalkanes, caged structures, and sterically crowded structures are depicted in Fig. 1 while the topological features of all other saturated structures are shown in Fig. S2 and S3 (ESI†). In general, the $V(\mathbf{r})$ value at the CP decreases with an increase in the length of the C–C bond. For the alkane series, the $V(\mathbf{r})$ is observed in a narrow range 0.623 to 0.631 a.u. The elongation in C–C bond length in strained cycloalkane and caged structures is clearly reflected in the $V(\mathbf{r})$ value. Significantly long C–C bond distances, d_{CC} (1.65 to 1.82 Å) in sterically bulky structures is evident from the smaller $V(\mathbf{r})$ ranging from 0.381 to 0.503 a.u. (Fig. S4, ESI†) compared to other saturated systems. Fig. 2 depicts the distribution of (3, −1) CPs in a representative set of systems containing C=C and aromatic bonds. The BCP in ethylene is located at the midpoint of the C=C bond with a high $V(\mathbf{r})$ of 1.021 a.u. (Fig. 2a). Generally, BCP values corresponding to formal CC double ($C_{sp^2}=C_{sp^2}$) and formal CC single ($C_{sp^2}–C_{sp^2}$) bonds in alkenes appear in the

vicinity of 1.10 and 0.70 a.u., respectively (Fig. 2b). The terminal double bond always shows a high $V(\mathbf{r})$ compared with the interior ones (Fig. S5, ESI†). Due to the symmetry, benzene has only one type of BCP, 0.886 a.u. located at the midpoint of each CC bond (Fig. 2c), whereas as per the symmetry, naphthalene shows four types of non-equivalent BCPs (Fig. 2d). Among the four BCPs of naphthalene, the largest and smallest BCP values stand for the shortest and longest CC bonds, respectively. In general, due to the inherent conjugation effect, the CC bond length of polycyclic benzenoid hydrocarbons (PBHs) appears in the range between 1.36 to 1.51 Å, which are characterized by $V(\mathbf{r})$ ranging from 0.722 to 0.950 a.u. (Fig. S6, ESI†). The BCP distribution also detects the alternate single and double bond feature of olefinic systems in terms of the low and high values of $V(\mathbf{r})$, respectively. Typically, the difference between the $V(\mathbf{r})$ of the formal CC single and CC double bond in olefins ($\Delta V(\mathbf{r})$) is 0.225 a.u. In antiaromatic cyclobutadiene, the $\Delta V(\mathbf{r}) = 0.410$ a.u. is significantly larger than the olefins. The $\Delta V(\mathbf{r})$ of annulene is 0.219 a.u. and that of fullerene is 0.122 a.u., suggesting more delocalized CC bond distribution in the latter than the former. Three non-equivalent $V(\mathbf{r})$ of the seven membered ring in azulene 0.910, 0.902 and 0.899 a.u. are very close to that of benzene indicating that it has a stronger aromatic character than the five membered ring, which is characterized by two non-equivalent $V(\mathbf{r})$ 0.858 and 0.860 a.u. In cyclophanes, the $V(\mathbf{r})$ between 0.895 and 0.886 a.u., very close to that of benzene indicates more aromatic character for the CC bonds in rings, while the bridged $C_{sp^3}–C_{sp^3}$ bonds are characterized by smaller $V(\mathbf{r})$. The $V(\mathbf{r})$ data given in Table 1 clearly reveal the presence of C–C and $C_{aromatic}–C_{aromatic}$ bonds in carbon nanotubes and C–C, C=C and $C_{aromatic}–C_{aromatic}$ bonds in graphene sheets.

The distribution of (3, −1) CPs in a representative set of systems containing C≡C bonds is illustrated in Fig. 3. Alkynes (or polyynes[62]) always exhibit very high $V(\mathbf{r})$ values compared to alkanes and alkenes. The $C_{sp}≡C_{sp}$ bond in acetylene is characterized by the $V(\mathbf{r})$ value of 1.402 a.u. For formal CC single and formal CC triple bonds in alkynes, the $V(\mathbf{r})$ values appear in the vicinity of 1.00 and 1.42 a.u., respectively and they show large $\Delta V(\mathbf{r})$, 0.412 a.u. between the $V(\mathbf{r})$ of $C_{sp}≡C_{sp}$ and $C_{sp}–C_{sp}$ (Fig S8, ESI†). The large $V(\mathbf{r})$ value of 1.241 a.u. observed for the
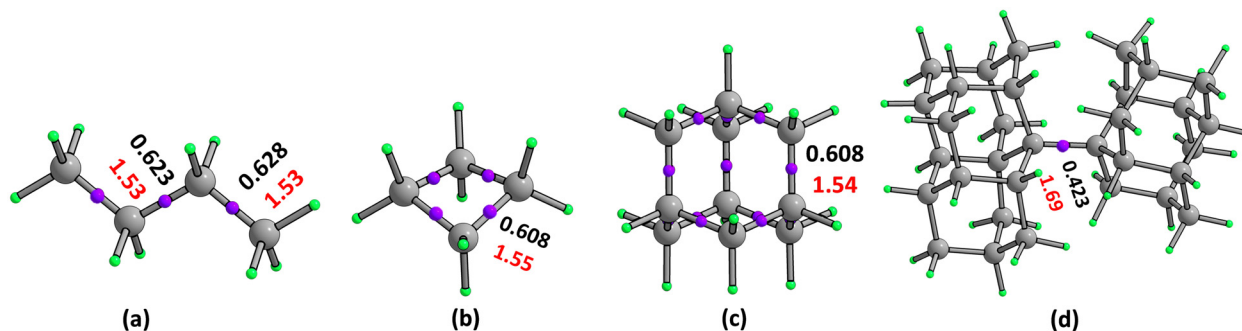

Fig. 1 The MESP (3, −1) CP distribution in a selected set of systems bearing C–C bonds. The MESP value at the BCP (in a.u.) and bond length (in Å) are represented in black and red fonts, respectively.
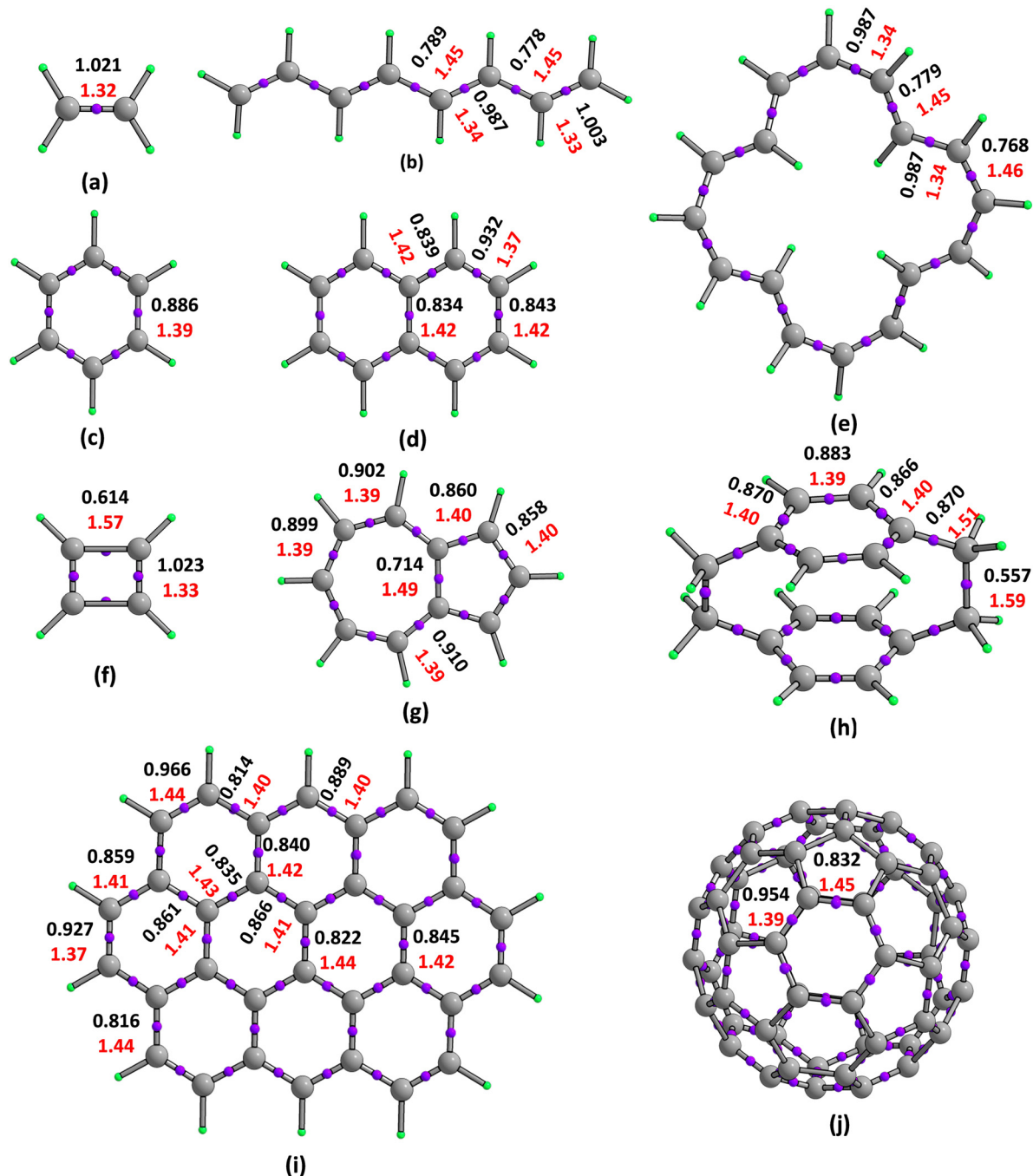
Fig. 2 The MESP (3, −1) CP distribution in a selected set of systems containing C=C bonds. The MESP value at the CP (in a.u.) and bond length (in Å) are represented in black and red fonts, respectively.

C2 molecule signifies its triple bond character. Furthermore, the (3, −1) CP distribution in the selected set of carbon rings is illustrated in Fig. S9 (ESI†) *viz.* C6, C8, C10, C12, *etc.*[63] The uniform $V(\mathbf{r})$ shows a cumulenic character anticipated for the structure of a carbon ring (Cn) with bond angle alternation if $n = 4N + 2$, while two types of BCP with $\Delta V(\mathbf{r})$, 0.367 a.u. supports the acetylenic character with bond length alternation if $n = 4N$ (Fig. S9, ESI†). In heterocyclic systems containing N, O and S, the $V(\mathbf{r})$ ranging between 0.923 and 0.882 a.u., 1.086 and

0.596 a.u. and 1.062 and 0.910 a.u. represent $C_{aromatic}$–$C_{aromatic}$, C–C and C=C bonds, respectively. The $V(\mathbf{r})$ observed for such systems are given in Table 1. The $V(\mathbf{r})$ values clearly suggest the double bond character exhibited by most of the carbon subsulfides[12] and carbon subchalcogenides.[19,64–68] Furthermore, the MESP topology study is conducted on anionic, cationic, radical systems and some neutral molecules (Fig. 4) containing multiple type of bonds such as C–C, C=C, C≡C, aromatic bonds, *etc.*

Table 1 The general trend in the MESP value of (3, −1) BCP for different types of systems

Type of system	Bond type	d_{CC} in Å	$V(\mathbf{r})$ in a.u.
Alkane	C–C	1.53	0.623–0.631
Cycloalkane	C–C	1.50–1.55	0.743–0.609
Cage	C–C	1.54–1.56	0.608–0.593
Sterically crowded	C–C	1.56–1.82	0.503–0.381
Olefin	C–C	1.32–1.34	1.025–0.987
Olefin	C=C	1.45–1.46	0.789–0.762
PBH	$C_{aromatic}$–$C_{aromatic}$	1.39	0.886–0.888
PBH	C–C	1.42–1.51	0.722–0.844
PBH	C=C	1.36–1.38	0.950–0.904
Antiaromatic (cyclobutadiene)	C–C	1.57	0.614
Antiaromatic (cyclobutadiene)	C=C	1.33	1.023
Azulene	$C_{aromatic}$–$C_{aromatic}$	1.39–1.40	0.910–0.858
Azulene	C–C	1.49	0.714
Cyclophane	$C_{aromatic}$–$C_{aromatic}$	1.39–1.40	0.895–0.886
Cyclophane	C–C	1.50–1.59	0.682–0.557
Annulene	C–C	1.44–1.46	0.799–0.768
Annulene	C=C	1.34–1.36	0.987–0.960
Fullerene	C–C	1.45	0.832
Fullerene	C=C	1.39	0.954
Carbon nanotube	C–C	1.45	0.805
Carbon nanotube	$C_{aromatic}$–$C_{aromatic}$	1.41	0.878–0.877
Graphene	$C_{aromatic}$–$C_{aromatic}$	1.40–1.41	0.889–0.866
Graphene	C–C	1.41–1.44	0.861–0.814
Graphene	C=C	1.36–1.37	0.966–0.927
Heterocyclic	$C_{aromatic}$–$C_{aromatic}$	1.39–1.40	0.923–0.882
Heterocyclic	C–C	1.39–1.55	1.086–0.596
Heterocyclic	C=C	1.33–1.40	1.062–0.910
Carbon rings	C–C	1.36–1.39	1.031–1.071
Carbon rings	C=C	1.28–1.32	1.167–1.229
Carbon rings	C≡C	1.22–1.30	1.398–1.241
Carbon subsulfides/subchalcogenides	C=C	1.26–1.29	1.308–1.202
Carbon subsulfides/subchalcogenides	C–C	1.38	1.043
Alkynes	C–C	1.35–1.38	1.078–1.004
Alkynes	C≡C	1.20–1.22	1.416–1.395
Mixed	$C_{aromatic}$–$C_{aromatic}$	1.38–1.39	0.900–0.854
Mixed	C–C	1.43–1.54	0.864–0.613
Mixed	C=C	1.33–1.34	1.022–0.975
Mixed	C≡C	1.20–1.21	1.397–1.370

The distribution of (3, −1) CPs in a representative set of organometallic[69] and hypervalent carbon compounds[70] containing different CC bonds is shown in Fig. 5. For CC bonds ranging from 1.38 to 1.53 Å containing Li, Si, Ge, Cr, Fe, *etc.* the $V(\mathbf{r})$ value falls between 1.073 to 0.613 a.u.

Transition state structures as borderline cases

A transition state (TS) in a chemical reaction is essentially a configuration attained by reactants during complex formation where a local maximum value of the potential energy is obtained. Michael addition,[71–74] cycloaddition[75–77] and rearrangement[78–80] (Claisen,[81] Cope,[82] Wittig[78,83] *etc.*) reactions usually exhibit TS that involve significant interaction between carbon atoms of reactants. Cycloaddition is a pericyclic chemical reaction in which two or more independent π-systems combine with cyclic electron movement, culminating in the formation of a ring with a net decrease in bond multiplicity. The reaction facilitates the strongest carbon–carbon bond formation in a single step without using specific nucleophile or electrophile moieties. If the carbon skeleton of a molecule is rearranged to produce a structural isomer of the original molecule or a substituent frequently moves from one atom to another within the same molecule it is termed a rearrangement reaction. The majority of rearrangement processes involve the breaking and/or formation of C–C, C–O, or C–N bonds (Fig. 6). The addition of a nucleophile (or a carbanion) to an α, β-unsaturated carbonyl compound that contains a functional group which is electron-withdrawing in nature, is known as the Michael Addition. It belongs to a class of reactions that are extremely useful for facilitating the formation of new carbon–carbon bonds (Fig. 7).

The highest d_{CC} in the chemical systems so far investigated in the present study is 1.82 Å, while longer CC bonds are seen in TS structures. The d_{CC} values observed in TS structures prompt the question of whether the CC interaction is covalent or noncovalent? Therefore, a detailed investigation is required for exploring the bond character and the trend in eigenvalues. A selected set of such TS structures involving formation, rearrangement, cleavage[84] or activation[85] of CC bonds from various organic reactions are considered for the study and the nature of CC interaction is quantified using MESP. The $V(\mathbf{r})$ value −0.099 to 0.428 a.u. in TS structures indicates weak interactions between CC centers at a distance ranging between 2.45 to 1.92 Å. The d_{CC} and $V(\mathbf{r})$ data show that CC interactions observed in TS structures are regarded as borderline cases. The detailed MESP topology of various TS corresponding to different reactions is given in Table S13 (ESI†).
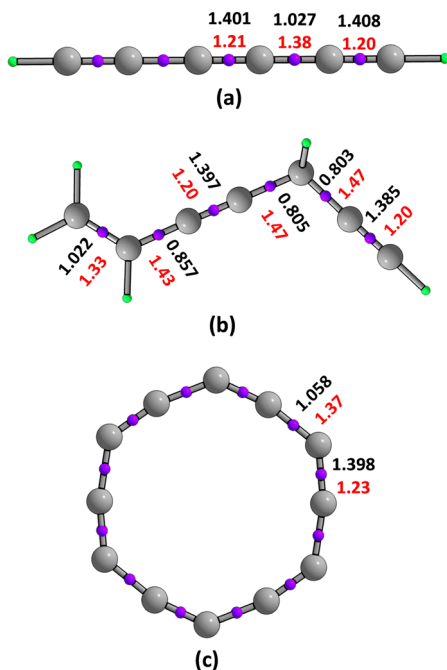
Fig. 3 The MESP (3, −1) CP distribution in a selected set of systems containing C≡C bonds. The MESP value at the CP (in a.u.) and bond length (in Å) are represented in black and red fonts, respectively.
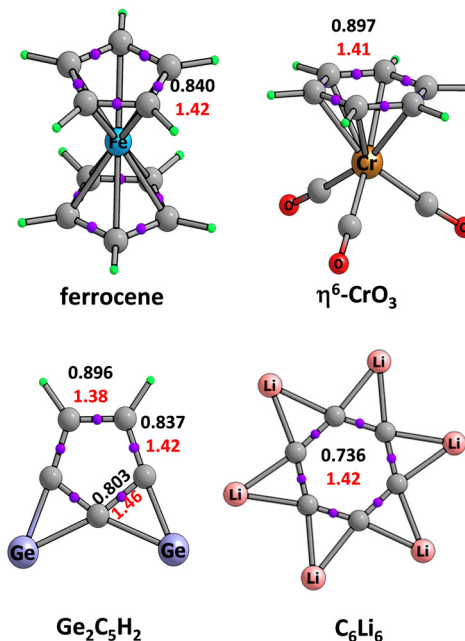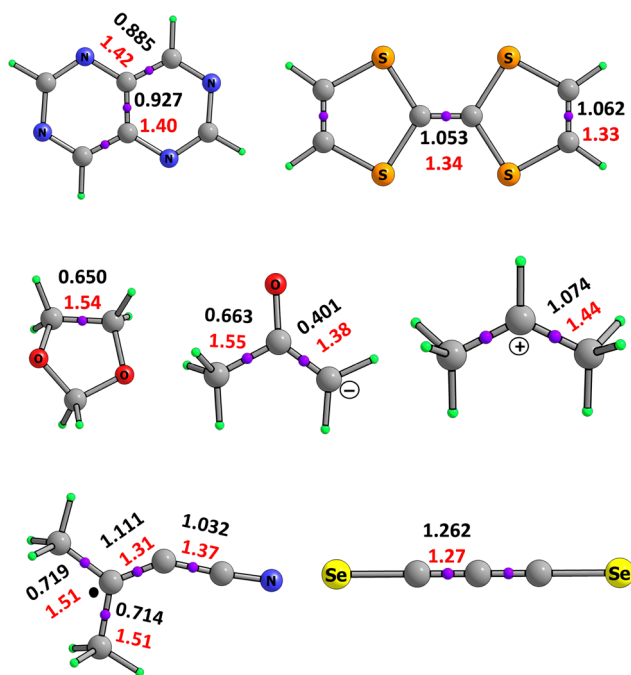

Fig. 4 The MESP (3, −1) CP distribution in different types of CC bonds of heterocyclic, anionic, cationic and radical systems. The MESP value at the CP (in a.u.) and bond length (in Å) are represented in black and red fonts, respectively.

Non-covalent C···C interactions

Temporary fluctuations in electronic distribution occur within molecules when they come close to each other. These fluctuations

Fig. 5 The MESP (3, −1) CP distribution in a representative set of organometallic and hypervalent systems. The MESP value at the CP (in a.u.) and bond length (in Å) are represented in black and red fonts, respectively.

give rise to attractive interactions known as van der Waals forces, which are generally weaker compared to ionic or covalent bonds. In this study, we focused on examining van der Waals C···C interactions in various dimeric molecules using the MESP topology. The C···C interactions were observed at distances ranging from 3.06 to 3.51 Å, as shown in Fig. 8. The associated $V(\mathbf{r})$, varied between 0.842 to −0.028 a.u., as depicted in Fig. S14 (ESI†). Furthermore, we investigated the non-covalent C···C interactions within an encapsulated system by optimizing the endohedral complex $C_2@C_{60}$, where the C_2 unit possesses a triplet character (Table S15, ESI†). In this system, C_2 is stabilized by 24.8 kcal/mol and displays six BCPs. The C···C distances corresponding to these BCPs fall within the range 2.95–3.11 Å, and the corresponding $V(\mathbf{r})$ values are within the range 0.072–0.066 a.u.

Analysis of MESP topology parameters

The data of $V(\mathbf{r})$, V_{bnp} and V_ρ at the BCP, plotted against the d_{CC} for all the CC interactions considered in the study is depicted in Fig. 9a. Both V_{bnp} and V_ρ show a random distribution while $V(\mathbf{r})$ shows mostly a decreasing exponential trend with the d_{CC} as shown in Fig. 9b. Thus, the relationship between $V(\mathbf{r})$ and d_{CC} suggests a CC bond continuum, irrespective of the nature of the CC bond whether it is covalent, non-covalent or borderline. In Fig. 9b, some points deviate from the general exponential trend which represent electron deficient systems such as cations and electron rich systems such as anions or π-systems with CC triple bonds. A negative $V(\mathbf{r})$ value is observed for highly electron rich systems such as diyne dimer. At the equilibrium CC bonding distance, the V_{bnp} balances with the V_ρ for the lowest $V(\mathbf{r})$.

The eigenvalues λ_{v1}, λ_{v2} and λ_{v3} plotted against d_{CC} are shown in Fig. 10. For all the systems, the magnitude of the
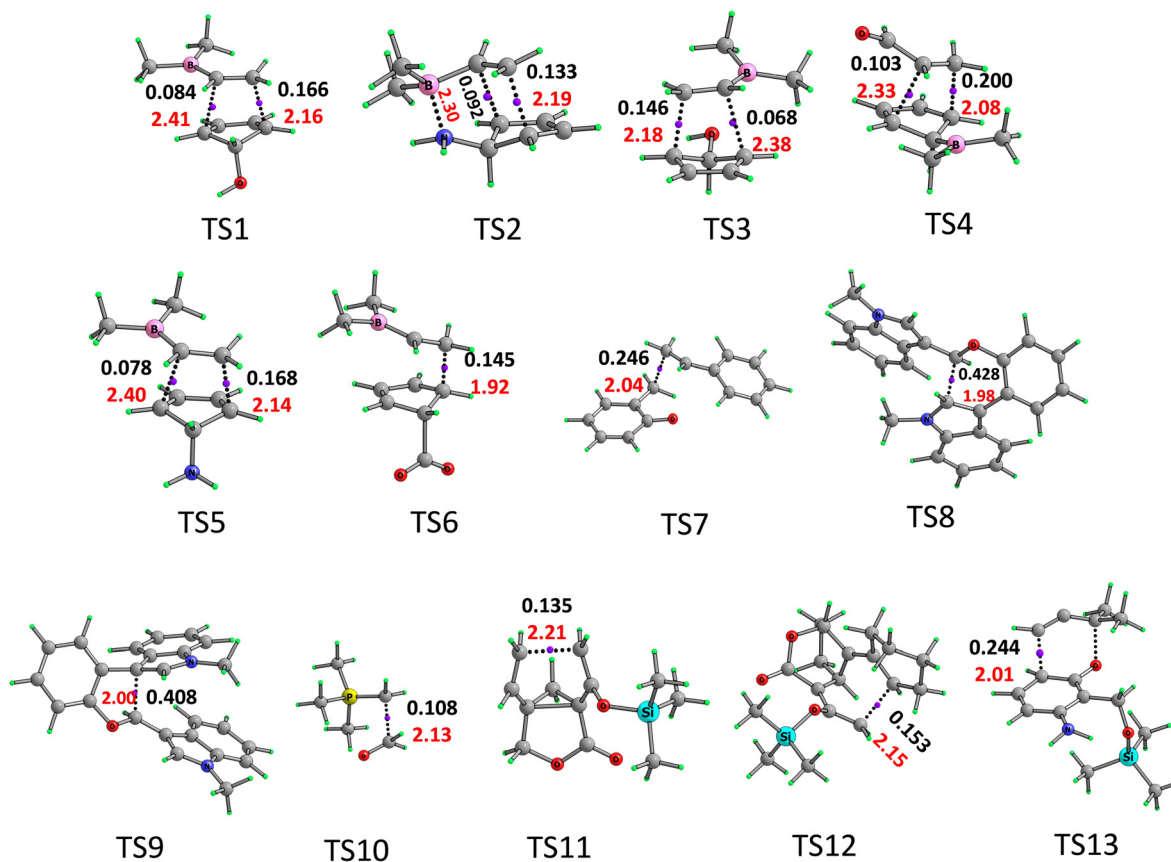
Fig. 6 The MESP (3, −1) CP distribution at the longest/weak CC interaction in a transition state model from cycloaddition (TS1–TS7, ESI†), ring closure (TS8–TS9), Wittig (TS10), Cope (TS11–TS12) and Claisen (TS13) rearrangement reactions. The MESP value at the CP (in a.u.) and bond length (in Å) are represented in black and red fonts, respectively.
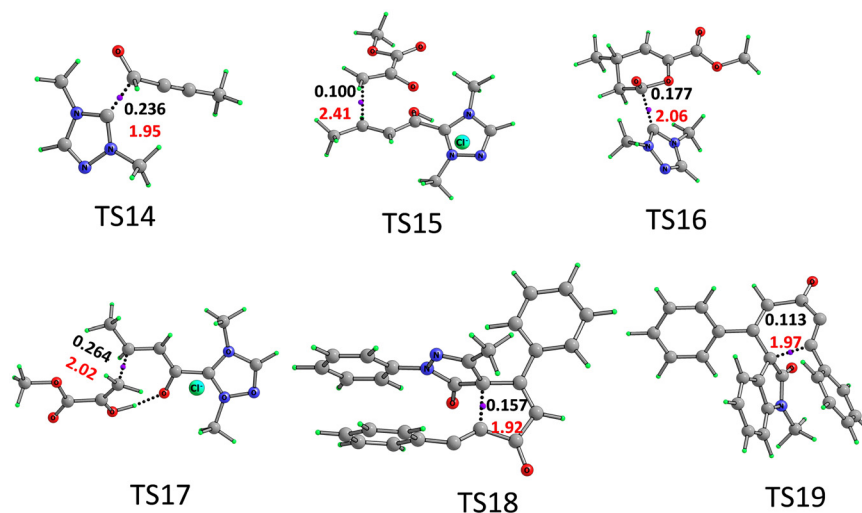

Fig. 7 The MESP (3, −1) CP distribution at the longest/weak CC interaction in a transition state model from Michael addition reactions. The MESP value at the CP (in a.u.) and bond length (in Å) are represented in black and red fonts, respectively.

positive eigenvalue λ_{v1} appears very large compared to the magnitude of both the negative eigenvalues, *viz.* λ_{v2} and λ_{v3}. Also values of λ_{v2} and λ_{v3} are very close to each other. Hence, λ_{v1}

is considered as the most sensitive eigenvalue parameter to define the CC bond character. The plots in Fig. 10 display the variations in the three eigenvalues with respect to the d_{CC}. An
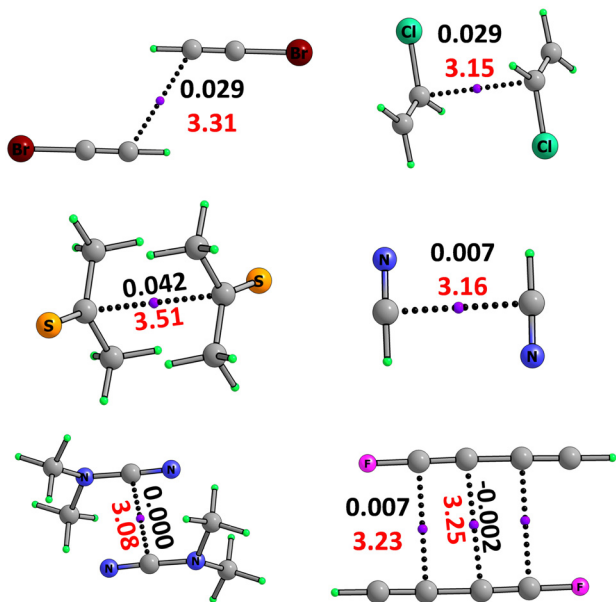
Fig. 8 The MESP (3, −1) CP distribution corresponding to non-covalent CC interactions in dimers. The MESP value at the CP (in a.u.) and bond length (in Å) are represented in black and red fonts, respectively.

exponential function fits almost perfectly ($R^2 = 0.9917$) to define a correlation between the d_{CC} and λ_{v1}. The correlation predicts that CC bond interaction is a continuum, irrespective of the nature of the CC bond, whether it is covalent, non-covalent or borderline case.

The CC bond continuum observed at the M06-2X/6-311G(d,p) level of theory gives the following fit.

$$\lambda_{v1} = 170.82e^{(-2.271d_{CC})} \qquad (4)$$

where d_{CC} is the CC bond distance in Å. Therefore,

$$d_{CC} = \frac{\ln(170.82/\lambda_{v1})}{2.271} \qquad (5)$$

The prediction of d_{CC} using eqn (5) is near perfect. The slope of eqn (5), $\lambda'_{v1} = (d(\lambda_{v1})/d(d_{CC}))$ is in the range −25.88 to −0.13 a.u. Å^{-1} for the d_{CC} range 1.20 to 3.51 Å. For d_{CC} around 3.0 Å, the λ_{v1} value is close to zero while λ'_{v1} is less negative than −1.0 a.u. Å^{-1}. Here, we propose d_{CC} in the range 2.95 to 3.51 Å in the non-covalent category wherein λ'_{v1} is less negative than −1.0 a.u. Å^{-1}.

In all TSs, the d_{CC} corresponding to bond formation shows λ'_{v1} in the range −1.52 to −4.97 a.u. Å^{-1}. As a generalization, we propose λ'_{v1} in the range −1.0 to −5.0 a.u. Å^{-1} as borderline cases between non-covalent and covalent interactions and this corresponds to d_{CC} in the range 1.92 to 2.63 Å. All d_{CC} corresponding to λ'_{v1} more negative than −5.0 a.u. Å^{-1} are selected in the covalent category. For instance, the longest covalent CC bond in the data set is 1.82 Å having $\lambda'_{v1} = -6.26$ a.u. Å^{-1} while the shortest one is 1.20 Å having $\lambda'_{v1} = -25.88$ a.u. Å^{-1} (Tables S1–S14, ESI†). Fig. 10 also depicts the covalent, non-covalent and borderline cases. Moreover,
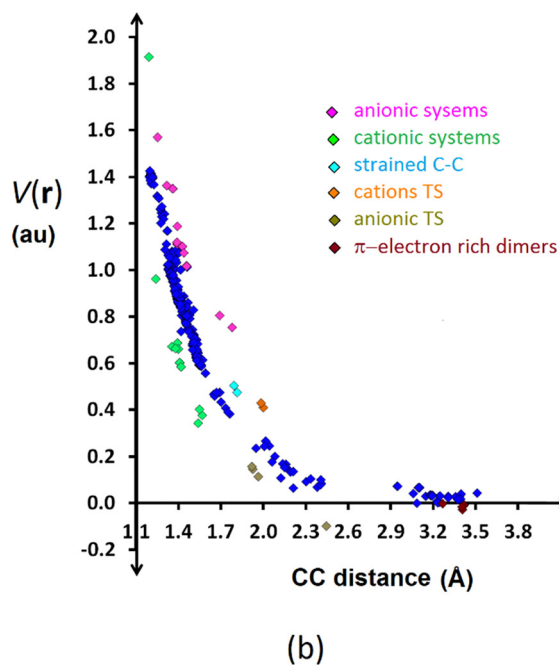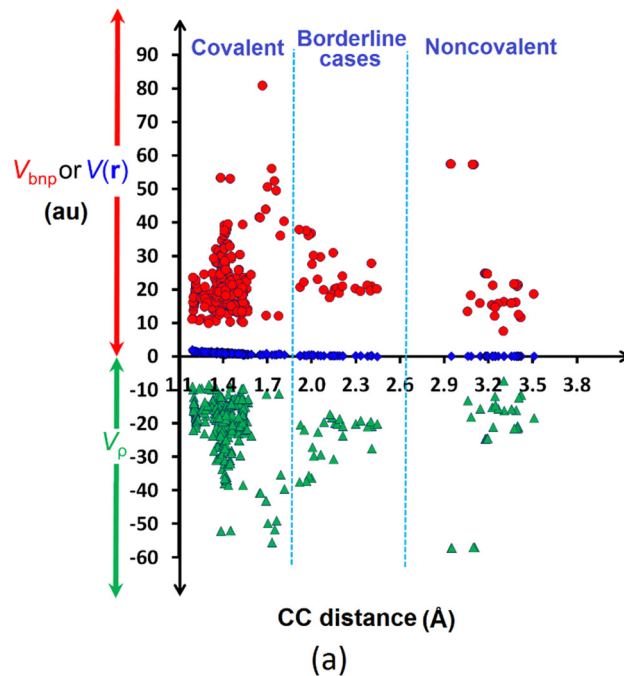

Fig. 9 Distribution of nuclear (V_{bnp}), electronic (V_{ρ}) and total MESP ($V(\mathbf{r})$) at bond CP, with respect to CC bond distance. The red, blue and green marks indicate V_{bnp}, $V(\mathbf{r})$ and V_{ρ}, respectively.

the eigenvector corresponding to the highest λ_{v1} is always in the direction of CC bonds in all the molecules studied here.

A benchmark analysis is also performed with the DFT techniques M06-L, wB97XD and B3LYP for a large variety of representative systems to assess the reliability of the M06-2X approach. Fig. 11 depicts the correlation between the largest positive eigenvalue and the CC bond distance. In all cases, a near perfect exponential relationship is obtained. The correlation at M06-
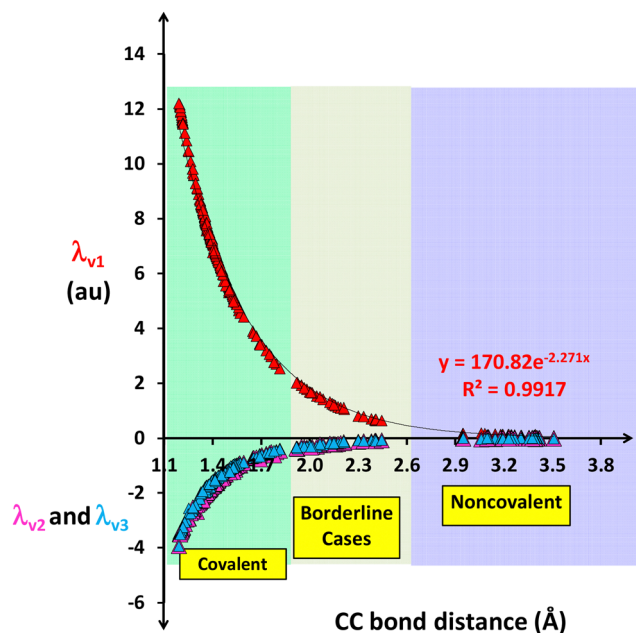
Fig. 10 The exponential variation of λ_{v1}, λ_{v2} and λ_{v3} with CC bond distance.

L is nearly identical to the M06-2X level in terms of the coefficient and exponent in the equation. Compared to these two levels, the

wB97XD level results show a slightly smaller magnitude for both coefficient and exponent. The correlation at the B3LYP level is notable for the significantly smaller magnitude of coefficient. The results from the first three methods are considered as superior considering the in-built dispersion effect in such methods.

QTAIM analysis

The concept of "Atoms in Molecules" (AIM) has evolved as a consequence of the fact that molecules may be partitioned into atoms whose energies can be precisely computed using quantum mechanics.[86] The quantum theory of AIM (QTAIM) has developed over the past few decades into a tool to connect the *ab initio* wave functions with chemical understanding.[87] The key parameters used in QTAIM theory are the MED, $\rho(\mathbf{r})$ at the BCP and the Laplacian of $\rho(\mathbf{r})$, *viz.* $\nabla^2\rho(\mathbf{r})$, at that point. The $\nabla^2\rho(\mathbf{r})$ distinguishes between two major categories of bonds.[47] If $\nabla^2\rho(\mathbf{r}) > 0$, the bond is referred to as a closed-shell interaction, which includes ionic bonds, hydrogen bonds, van der Waals interactions, *etc.* If $\nabla^2\rho(\mathbf{r}) < 0$, the bond is a shared interaction, such as covalent and polar bonds. The $\nabla^2\rho(\mathbf{r})$ can be negative only if the first two eigenvalues $\lambda_{\rho1}$ and $\lambda_{\rho2}$ dominate over the third eigenvalue $\lambda_{\rho3}$, indicating that ρ is concentrated toward the BCP. If $\lambda_{\rho3}$ dominates over $\lambda_{\rho1}$ and $\lambda_{\rho2}$, the $\nabla^2\rho = \lambda_{\rho1} + \lambda_{\rho2} + \lambda_{\rho3}$ (or $\lambda_{\rho\text{total}}$) becomes positive, where $\rho(\mathbf{r})$ increases rapidly away from the BCP.[46,88] To validate the non-covalent interactions among atoms in molecules, Popelier's
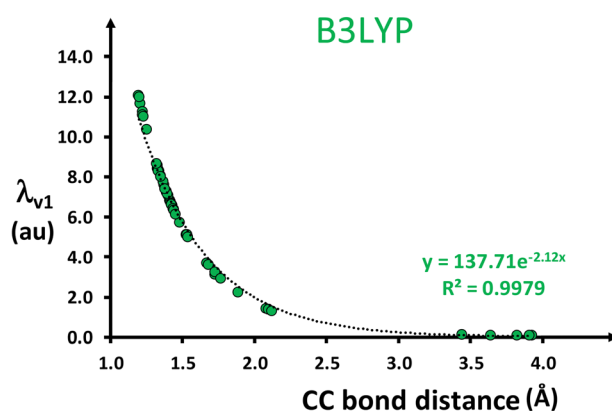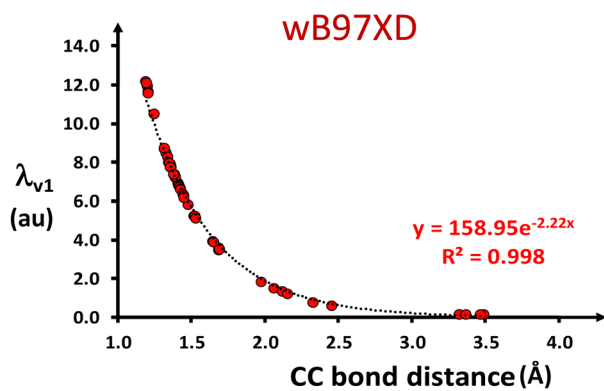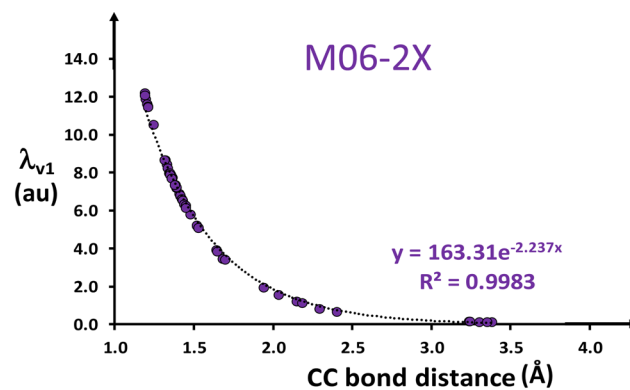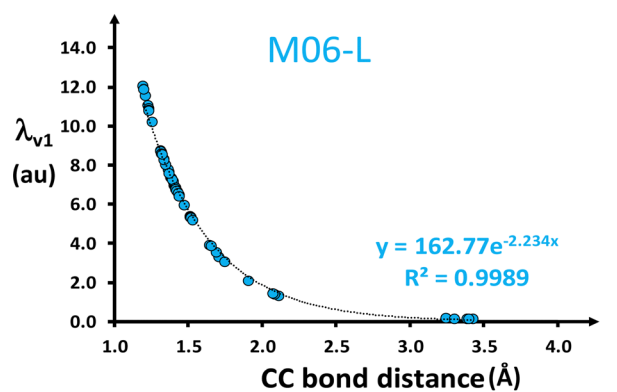

Fig. 11 The exponential variation of λ_{v1} with CC bond distance using different levels of theory.

$\nabla^2\rho$ theory has been utilized in several studies.[46,88–93] A QTAIM study focusing only on a particular bonding interaction, including both covalent and non-covalent interactions of a large variety of systems is yet to be reported. Here, we conduct this kind of study on CC bonding interactions based on Popelier's $\nabla^2\rho$ theory. Furthermore, QTAIM analysis is carried out to reveal the covalent to non-covalent CC bond continuum in terms of the electron density.

The covalent CC bonds from a wide variety of molecular systems such as alkanes, strained systems, alkenes, alkynes, carbon clusters, heterocyclic systems, PBHs *etc.* show $\rho(\mathbf{r})$ values ranging from 0.133 to 0.410 a.u. with corresponding $\nabla^2\rho$ ranges between -1.228 and -0.009 a.u. The $\rho(\mathbf{r})$ value for non-covalent CC bonds ranges from 0.004 to 0.009 a.u. while their $\nabla^2\rho$ is between 0.032 and 0.013 a.u. The $\rho(\mathbf{r})$ at the weakest CC bond of TS structures from diverse organic reactions is seen to lie between 0.0271 to 0.1023 a.u. with $\nabla^2\rho$ between -0.025 to 0.054 a.u. A representative set of examples is shown in Fig. 12.

Fig. 13a depicts the plot of $\rho(\mathbf{r})$ against the d_{CC} of all the molecules (the full QTAIM data is given in Tables S15–S27, ESI†). Irrespective of the nature of the CC interactions, the $\rho(\mathbf{r})$ shows an exponential decay with an increase in d_{CC}. This data again confirms the CC bond continuum in chemistry. The variation of $\lambda_{\rho i}$ at BCP with d_{CC} shows that the negative eigenvalues, $\lambda_{\rho 1}$ and $\lambda_{\rho 2}$ show very similar values for all the systems (Fig. 13b). In the case of the positive eigenvalue $\lambda_{\rho 3}$, from very short CC to the typical CC single bond distance, the value rises sharply and thereafter, decreases exponentially. The shape of d_{CC} *versus* $\lambda_{\rho 3}$ curve suggests that the $\lambda_{\rho 3}$ can attain same value for a short as well as long CC distance. For instance, in tetraacetylene, $\lambda_{\rho 3}$ corresponding to a C≡C with distance

1.21 Å is 0.113 a.u. whereas the TS structure with d_{CC} 2.41 Å also shows a similar value for $\lambda_{\rho 3}$, 0.116 a.u. Hence, it is difficult to differentiate the nature of the CC bond based only on the eigenvalues.

Fig. 14 illustrates the Popelier's $\nabla^2\rho$ theory. Here, $\nabla^2\rho$ is plotted against d_{CC} and as per Popelier's criterion, the negative $\nabla^2\rho$ values correspond to a covalent bond and the remaining ones indicate non-covalent bonds. As shown in Fig. 14, all the negative $\nabla^2\rho$ can be fitted on a straight line with $R^2 = 0.9458$. This suggests that the highest negative $\nabla^2\rho$ corresponds to the shortest CC bond while a negative value close to zero points to one of the weakest covalent CC bonds. Here, the d_{CC} value 1.94 Å observed in a TS is regarded as the weakest covalent CC bond on the basis of the lowest negative $\nabla^2\rho$ value, -0.013. The majority of the d_{CC} in TSs showed positive $\nabla^2\rho$ very close to zero. Though the magnitude of the three eigenvalues are significantly greater than zero for all the TSs, the close to 'zero' behaviour of $\nabla^2\rho$ is observed for them due to $\lambda_{\rho 3} \cong -(\lambda_{\rho 1} + \lambda_{\rho 2})$. In the case of systems showing d_{CC} around 3.0 Å or higher, the $\nabla^2\rho$ is positive and close to zero because all the three eigenvalues are close to zero. These cases clearly fall under the category of non-covalent CC interactions. It may be noted that the borderline cases of TS cannot be clearly distinguished from the non-covalent cases using only the $\nabla^2\rho$ criterion. For borderline cases, $\nabla^2\rho$ is close to zero with the condition that the magnitudes of all three eigenvalues are significantly higher than zero.

Beyond CC interactions

Among all types of covalent and non-covalent atom–atom bonding interactions, the CC interaction is the most unique
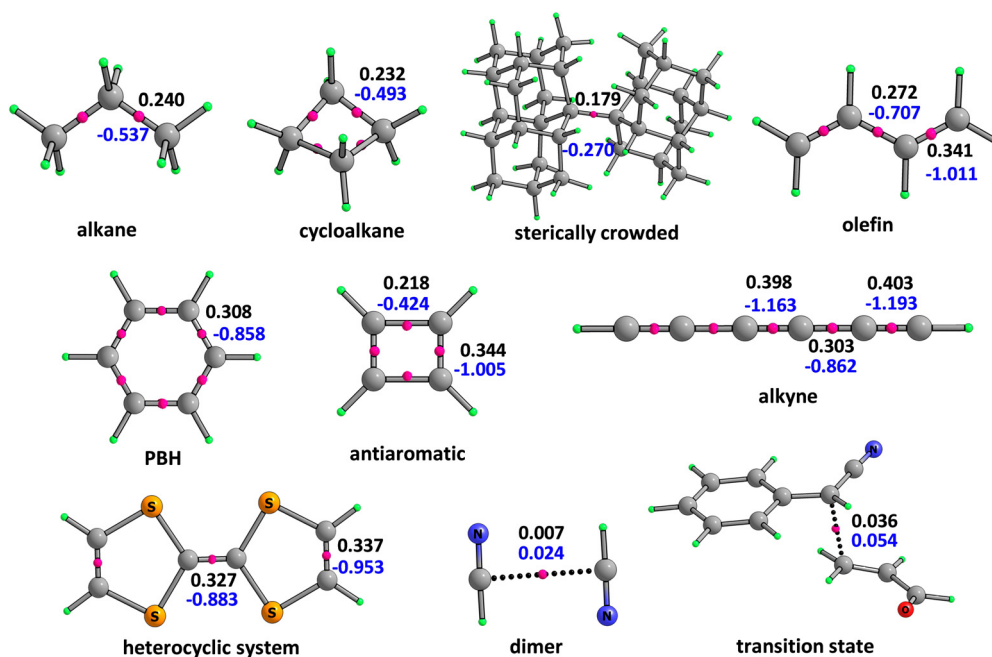

Fig. 12 The MED (3, −1) CP distribution in a selected set of systems. The $\rho(\mathbf{r})$ value at the BCP and $\nabla^2\rho$ (in a.u.) are represented in black and blue fonts, respectively.
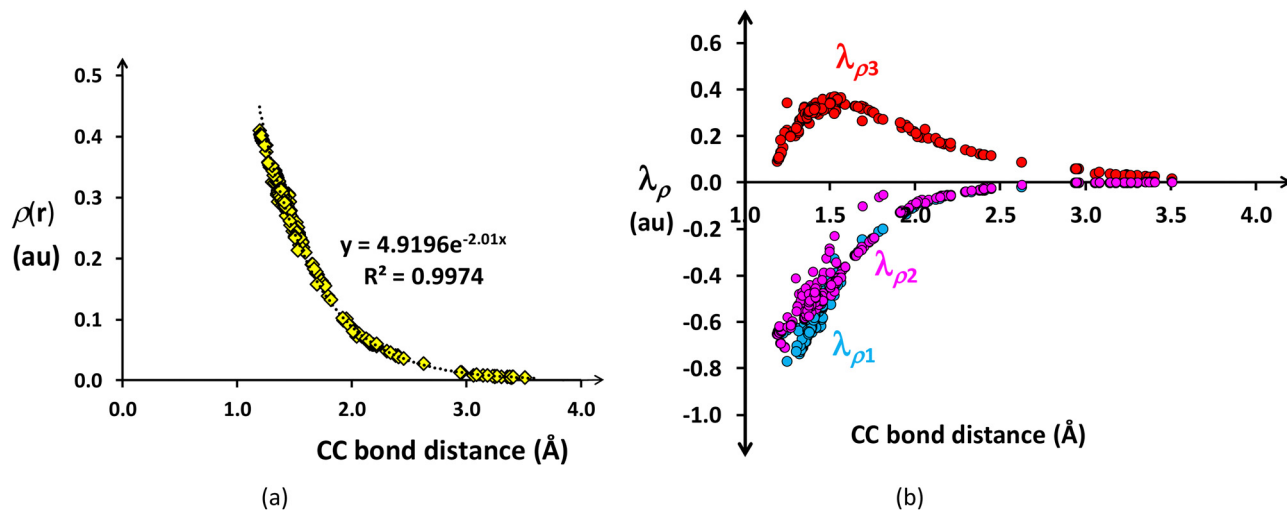
Fig. 13   (a) Relationship between electron density, $\rho(\mathbf{r})$ and CC bond distance. (b) Variation of eigenvalues with CC bond distance.
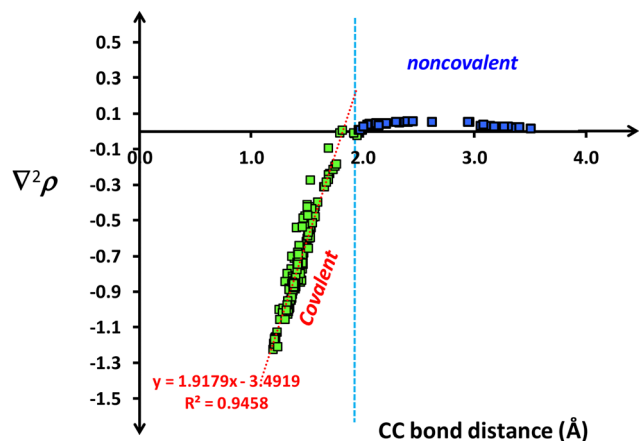

Fig. 14   Correlation between the $\nabla^2\rho$ value at the BCP and the CC bond distance.

as it shows the largest variation in the nature and strength, across millions of carbon compounds. The exponential relationship in eqn (4) describes the entire world of CC interaction in chemistry and it emerges as a fundamental relationship in chemical bonding theory. The exponent -2.271 and coefficient 170.82 of eqn (4) is unique to the level of DFT used, M06-2X/6-311G(d,p). Similar exponential relationships may exist for bonding between other atoms. However, screening of all types of atom–atom interactions is a herculean task. Moreover, unlike CC interactions, a large variety of bonding type may not be available for all other atoms for a trustworthy derivation of the equation.

For a limited set of data, an exploratory MESP topology analysis is conducted for atom–atom interactions such as C–N, C–O, C–S, N–N, O–O, and S–S, in molecules from diverse experimental and theoretical investigations.[94–100] The study takes into account the covalent, non-covalent, and borderline cases. In all cases, the magnitude of the positive eigenvalue λ_{v1} showed relatively large values compared to the magnitude of

both λ_{v2} and λ_{v3}, wherein $\lambda_{v2} \cong \lambda_{v3}$. The plot of bond distance *versus* the positive eigenvalue showed strong exponential relationships in all cases (Fig. S14–S19, ESI†). Thus, the elaborate study of CC interactions and the limited study of other interactions clearly support that the chemical bonding scenario fits into a continuum model across covalent, non-covalent and borderline cases.

Conclusions

MESP topology analysis has been carried out on a large variety of molecular systems containing various types of CC interactions using the M06-2X/6-311G(d,p) level of theory as well as using a benchmark set of DFT methods. The $V(\mathbf{r})$ value is observed in different ranges for different types of CC bond interactions *viz.* single, double, triple, aromatic, π-conjugated, organometallics, strained, sterically crowded, transition states, non-covalent, *etc.* The relationship between the MESP $V(\mathbf{r})$ at BCP and CC distance suggests a CC bond continuum in chemistry which encompasses all kinds of covalent, non-covalent and borderline cases such as transition states. At the equilibrium CC bonding distance, the V_{bnp} balances with the V_{ρ} for the lowest $V(\mathbf{r})$. An exponential function fits almost perfectly to define a fundamental correlation between the CC distance and the highest eigenvalue λ_{v1} of the MESP BCP. This relationship confirms the continuum nature of CC bonds in chemistry. The slope of the exponential function, λ'_{v1} suggests the demarcation of the continuum in three regions *viz.* covalent, non-covalent and borderline cases. The λ'_{v1} more negative than -5.0 a.u. Å^{-1} for covalent and less negative than -1.0 a.u. Å^{-1} for non-covalent CC bonds, while λ'_{v1} between -1.0 and -5.0 a.u. Å^{-1} defines the borderline cases between non-covalent as well as covalent CC interactions. The CC bond continuum is further supported by the MED value at the BCP. For the first time, Popelier's $\nabla^2\rho$ analysis on chemical bonding is tested exclusively for a single variety of bonding

interaction – the CC interaction. The $\nabla^2\rho$ theory applies to all covalent interactions and non-covalent interactions whereas borderline cases such as transition states can be addressed by invoking the nature of all three eigenvalues of the BCP. For the borderline cases, the magnitude of all three eigenvalues is significantly larger than zero whereas their sum, the $\nabla^2\rho$ is close to zero. We extend our analysis to explore the validity of these concepts in the context of other atom–atom interactions, specifically focusing on C–N, C–O, C–S, N–N, O–O, and S–S bonds, although with a limited dataset. By conducting a comprehensive examination of CC interactions and an initial exploration of other interactions, our findings unequivocally demonstrate the existence of a bond continuum within the realm of chemistry.

Author contributions

The manuscript was written through contributions of all the authors. All authors have given approval to the final version of the manuscript.

Conflicts of interest

There are no conflicts to declare.

Acknowledgements

References

1 A. S. Goldman, *Nature*, 2010, **463**, 435–436.

2 W. D. Hounshell, D. A. Dougherty, J. P. Hummel and K. Mislow, *J. Am. Chem. Soc.*, 1977, **99**, 1916–1924.

3 Y. Ishigaki, T. Shimajiri, T. Takeda, R. Katoono and T. Suzuki, *Chem*, 2018, **4**, 795–806.

4 T. Takeda, H. Kawai, R. Herges, E. Mucke, Y. Sawai, K. Murakoshi, K. Fujiwara and T. Suzuki, *Tetrahedron Lett.*, 2009, **50**, 3693–3697.

5 S. Kammermeier, R. Herges and P. G. Jones, *Angew. Chem., Int. Ed. Engl.*, 1997, **36**, 1757–1760.

6 P. R. Schreiner, L. V. Chernish, P. A. Gunchenko, E. Y. Tikhonchuk, H. Hausmann, M. Serafin, S. Schlecht, J. E. Dahl, R. M. Carlson and A. A. Fokin, *Nature*, 2011, **477**, 308–311.

7 K. Tanaka, N. Takamoto, Y. Tezuka, M. Kato and F. Toda, *Tetrahedron*, 2001, **57**, 3761–3767.

8 B. Kahr, D. Van Engen and K. Mislow, *J. Am. Chem. Soc.*, 1986, **108**, 8305–8307.

9 A. A. Fokin, L. V. Chernish, P. A. Gunchenko, E. Y. Tikhonchuk, H. Hausmann, M. Serafin, J. E. Dahl, R. M. Carlson and P. R. Schreiner, *J. Am. Chem. Soc.*, 2012, **134**, 13641–13650.

10 A. A. A. Delgado, A. Humason, R. Kalescky, M. Freindorf and E. Kraka, *Molecules*, 2021, **26**, 950.

11 E. J. J. Korpela, J. R. Carvalho, H. Lischka and M. Kertesz, *J. Phys. Chem. A*, 2023, **127**, 4440–4454.

12 T. Kubo, Y. Suga, D. Hashizume, H. Suzuki, T. Miyamoto, H. Okamoto, R. Kishi and M. Nakano, *J. Am. Chem. Soc.*, 2021, **143**, 14360–14366.

13 H. Kawai, T. Takeda, K. Fujiwara, T. Inabe and T. Suzuki, *Cryst. Growth Des.*, 2005, **5**, 2256–2260.

14 J. Li, R. Pang, Z. Li, G. Lai, X.-Q. Xiao and T. Müller, *Angew. Chem., Int. Ed.*, 2019, **58**, 1397–1401.

15 F. Toda, K. Tanaka, Z. Stein and I. Goldberg, *Acta Crystallogr., Sect. C: Cryst. Struct. Commun.*, 1996, **52**, 177–180.

16 S. Grimme and P. R. Schreiner, *Angew. Chem., Int. Ed.*, 2011, **50**, 12639–12642.

17 M. Rueping and I. Atodiresei, in *Comprehensive Chirality*, ed. E. M. Carreira and H. Yamamoto, Elsevier, Amsterdam, 2012, pp. 345–373.

18 N. G. Schmidt, E. Eger and W. Kroutil, *ACS Catal.*, 2016, **6**, 4286–4311.

19 M. Agúndez, J. Cernicharo and M. Guélin, *Astron. Astrophys.*, 2014, **570**, A45.

20 L. Di Costanzo and S. Geremia, *Molecules*, 2020, **25**, 3555.

21 S. Shahbazian, *Chem. – Eur. J.*, 2018, **24**, 5401–5405.

22 C. H. Suresh and N. Koga, *J. Am. Chem. Soc.*, 2002, **124**, 1790–1797.

23 S. R. Gadre, S. A. Kulkarni and I. H. Shrivastava, *J. Chem. Phys.*, 1992, **96**, 5253–5260.

24 C. H. Suresh, G. S. Remya and P. K. Anjalikrishna, *Wiley Interdiscip. Rev.: Comput. Mol. Sci.*, 2022, **12**, e1601.

25 S. R. Gadre, C. H. Suresh and N. Mohan, *Molecules*, 2021, **26**, 3289.

26 R. Bonaccorsi, E. Scrocco and J. Tomasi, *J. Chem. Phys.*, 1970, **52**, 5270–5284.

27 E. Scrocco and J. Tomasi, *New concepts II*, Springer, 1973, pp. 95–170.

28 E. Scrocco and J. Tomasi, *Advances in quantum chemistry*, Elsevier, 1978, vol. 11, pp. 115–193.

29 A. Pullman and B. Pullman, *Q. Rev. Biophys.*, 1981, **14**, 289–380.

30 R. F. W. Bader, *Acc. Chem. Res.*, 1985, **18**, 9–15.

31 R. Bader, Clarendon, *A Quantum Theory*, Oxford, UK, 1990.

32 P. Politzer and D. G. Truhlar, *Chemical applications of atomic and molecular electrostatic potentials: reactivity, structure, scattering, and energetics of organic, inorganic, and biological systems*, Springer Science & Business Media, 2013.

33 P. Politzer, K. C. Daiker and R. A. Donnelly, *Cancer Lett.*, 1976, **2**, 17–23.

34 P. Politzer, R. A. Donnelly and K. C. Daiker, *J. Chem. Soc., Chem. Commun.*, 1973, 617–618.

35 J. S. Murray and P. Politzer, *Wiley Interdiscip. Rev.: Comput. Mol. Sci.*, 2011, **1**, 153–163.

36 R. K. Pathak and S. R. Gadre, *J. Chem. Phys.*, 1990, **93**, 1770–1773.

37 S. R. Gadre and R. K. Pathak, *Proc. - Indian Acad. Sci., Chem. Sci.*, 1990, **102**, 189–192.

38 S. R. Gadre and R. N. Shirsat, *Electrostatics of atoms and molecules*, Universities Press, 2000.

39 A. Kumar, R. López, F. Martínez, G. Ramírez, I. Ema, D. Zorrilla, S. D. Yeole and S. R. Gadre, *Comput. Phys. Commun.*, 2022, **279**, 108460.

40 R. López, I. Ema, G. Ramírez, D. Zorrilla, S. R. Gadre, A. Kumar and S. D. Yeole, *DAMQT*, 3(2), 2020.

41 A. Kumar, S. D. Yeole, S. R. Gadre, R. López, J. F. Rico, G. Ramírez, I. Ema and D. Zorrilla, *J. Comput. Chem.*, 2015, **36**, 2350–2359.

42 R. López, J. F. Rico, G. Ramírez, I. Ema and D. Zorrilla, *Comput. Phys. Commun.*, 2015, **192**, 289–294.

43 R. López, J. F. Rico, G. Ramírez, I. Ema, D. Zorrilla, A. Kumar, S. D. Yeole and S. R. Gadre, *Comput. Phys. Commun.*, 2017, **214**, 207–215.

44 R. López, J. F. Rico, G. Ramírez, I. Ema and D. Zorrilla, *Comput. Phys. Commun.*, 2009, **180**, 1654–1660.

45 J. F. Rico, R. Lopez, I. Ema and G. Ramirez, *THEOCHEM*, 2005, **727**, 115–121.

46 P. L. A. Popelier, *J. Phys. Chem. A*, 1999, **103**, 2883–2890.

47 P. L. Popelier, *J. Mol. Model.*, 2022, **28**, 276.

48 Y. Zhao and D. G. Truhlar, *Theor. Chem. Acc.*, 2008, **120**, 215–241.

49 M. J. Frisch, G. W. Trucks, H. B. Schlegel, G. E. Scuseria, M. A. Robb, J. R. Cheeseman, G. Scalmani, V. Barone, G. A. Petersson, H. Nakatsuji, X. Li, M. Caricato, A. V. Marenich, J. Bloino, B. G. Janesko, R. Gomperts, B. Mennucci, H. P. Hratchian, J. V. Ortiz, A. F. Izmaylov, J. L. Sonnenberg, D. Williams-Young, F. Ding, F. Lipparini, F. Egidi, J. Goings, B. Peng, A. Petrone, T. Henderson, D. Ranasinghe, V. G. Zakrzewski, J. Gao, N. Rega, G. Zheng, W. Liang, M. Hada, M. Ehara, K. Toyota, R. Fukuda, J. Hasegawa, M. Ishida, T. Nakajima, Y. Honda, O. Kitao, H. Nakai, T. Vreven, K. Throssell, J. A. Montgomery, J. E. Peralta, F. Ogliaro, M. J. Bearpark, J. J. Heyd, E. N. Brothers, K. N. Kudin, V. N. Staroverov, T. A. Keith, R. Kobayashi, J. Normand, K. Raghavachari, A. P. Rendell, J. C. Burant, S. S. Iyengar, J. Tomasi, M. Cossi, J. M. Millam, M. Klene, C. Adamo, R. Cammi, J. W. Ochterski, R. L. Martin, K. Morokuma, O. Farkas, J. B. Foresman and D. J. Fox, *Gaussian 16, Rev. A.03*, Wallingford, CT, 2016.

50 A. Kumar, S. D. Yeole, S. R. Gadre, R. López, J. F. Rico, G. Ramírez, I. Ema and D. Zorrilla, *J. Comput. Chem.*, 2015, **36**, 2350–2359.

51 Á. M. Pendás and C. Gatti, *Complementary Bonding Analysis*, 2021, p. 43.

52 C. Gatti, *Computational Materials Discovery*, 2018, p. 117.

53 F. Jensen, *Wiley Interdiscip. Rev.: Comput. Mol. Sci.*, 2013, **3**, 273–295.

54 R. F. Bader, *Chem. Rev.*, 1991, **91**, 893–928.

55 P. S. V. Kumar, V. Raghavendra and V. Subramanian, *J. Chem. Sci.*, 2016, **128**, 1527–1536.

56 A. Kumar, S. R. Gadre, N. Mohan and C. H. Suresh, *J. Phys. Chem. A*, 2014, **118**, 526–532.

57 S. D. Yeole and S. R. Gadre, *J. Phys. Chem. A*, 2011, **115**, 12769–12779.

58 P. V. Bijina, C. H. Suresh and S. R. Gadre, *J. Comput. Chem.*, 2018, **39**, 488–499.

59 A. K. Phukan, R. P. Kalagi, S. R. Gadre and E. D. Jemmis, *Inorg. Chem.*, 2004, **43**, 5824–5832.

60 J. Pilmé, E. Renault, F. Bassal, M. Amaouch, G. Montavon and N. Galland, *J. Chem. Theory Comput.*, 2014, **10**, 4830–4841.

61 A. Malloum and J. Conradie, *Data Brief*, 2022, **40**, 107766.

62 K. Remya and C. H. Suresh, *Phys. Chem. Chem. Phys.*, 2015, **17**, 27035–27044.

63 K. Remya and C. H. Suresh, *RSC Adv.*, 2016, **6**, 44261–44271.

64 T. Salomon, J. B. Dudek, Y. Chernyak, J. Gauss and S. Thorwirth, *J. Mol. Spectrosc.*, 2021, **378**, 111456.

65 S. Thorwirth, T. Salomon, S. Fanghänel, J. Kozubal and J. Dudek, *Chem. Phys. Lett.*, 2017, **684**, 262–266.

66 B. A. McGuire, M.-A. Martin-Drumel, K. L. K. Lee, J. F. Stanton, C. A. Gottlieb and M. C. McCarthy, *Phys. Chem. Chem. Phys.*, 2018, **20**, 13870–13889.

67 M. C. McCarthy, J. H. Baraban, P. B. Changala, J. F. Stanton, M.-A. Martin-Drumel, S. Thorwirth, C. A. Gottlieb and N. J. Reilly, *J. Phys. Chem. Lett.*, 2015, **6**, 2107–2111.

68 J. B. Dudek, T. Salomon, S. Fanghänel and S. Thorwirth, *Int. J. Quantum Chem.*, 2017, **117**, e25414.

69 P. R. Remya and C. H. Suresh, *Dalton Trans.*, 2015, **44**, 17660–17672.

70 P. Das and P. K. Chattaraj, *Chemistry*, 2022, **4**, 1723–1756.

71 L. R. Domingo, J. A. Sáez and M. Arnó, *Org. Biomol. Chem.*, 2014, **12**, 895–904.

72 M. J. Sarma, S. Jindani, B. Ganguly, S. Pabbaraja and G. Mehta, *J. Org. Chem.*, 2022, **87**, 884–891.

73 J. A. Izzo, Y. Myshchuk, J. S. Hirschi and M. J. Vetticatt, *Org. Biomol. Chem.*, 2019, **17**, 3934–3939.

74 S. Thiyagarajan, R. V. Sankar, P. K. Anjalikrishna, C. H. Suresh and C. Gunanathan, *ACS Catal.*, 2022, **12**, 2191–2204.

75 H. Wang, Y. Wang, K.-L. Han and X.-J. Peng, *J. Org. Chem.*, 2005, **70**, 4910–4917.

76 D. Taherinia and A. Fattahi, *Sci. Rep.*, 2022, **12**, 22225.

77 D. Svatunek, R. P. Pemberton, J. L. Mackey, P. Liu and K. N. Houk, *J. Org. Chem.*, 2020, **85**, 3858–3864.

78 S. R. Nath and K. A. Joshi, *Phys. Chem. Chem. Phys.*, 2018, **20**, 21457–21473.

79 V. Cachatra, A. Almeida, J. Sardinha, S. D. Lucas, A. Gomes, P. D. Vaz, M. H. Florêncio, R. Nunes, D. Vila-Viçosa, M. J. Calhorda and A. P. Rauter, *Org. Lett.*, 2015, **17**, 5622–5625.

80 M. J. Sarma, S. Jindani, B. Ganguly, S. Pabbaraja and G. Mehta, *J. Org. Chem.*, 2021, **87**, 884–891.

81 M. Ramirez, V. Vece, S. Hanessian and K. N. Houk, *J. Org. Chem.*, 2021, **86**, 17955–17964.

82 C. W. Lee, B. L. H. Taylor, G. P. Petrova, A. Patel, K. Morokuma, K. N. Houk and B. M. Stoltz, *J. Am. Chem. Soc.*, 2019, **141**, 6995–7004.

83 R. Robiette, J. Richardson, V. K. Aggarwal and J. N. Harvey, *J. Am. Chem. Soc.*, 2006, **128**, 2394–2409.

84 A. Asha, J. Ravindran, S. Suma, C. H. Suresh and R. S. Lankalapalli, *ChemistrySelect*, 2020, **5**, 2545–2550.

85 C. Challa, S. Varughese, C. H. Suresh and R. S. Lankalapalli, *Org. Lett.*, 2017, **19**, 4219–4222.

86 R. F. Bader and P. Beddall, *J. Chem. Phys.*, 1972, **56**, 3320–3329.

87 P. L. A. Popelier, F. Aicken and S. O'Brien, *Atoms in molecules*, Prentice Hall, Manchester, 2000.

88 P. L. A. Popelier, *The Chemical Bond*, 2014, pp. 271–308.

89 T. J. Mooibroek, *Molecules*, 2019, **24**, 3370.

90 A. Bauzá, T. J. Mooibroek and A. Frontera, *Chem. – Eur. J.*, 2014, **20**, 10245–10248.

91 V. Georgakilas, M. Otyepka, A. B. Bourlinos, V. Chandra, N. Kim, K. C. Kemp, P. Hobza, R. Zboril and K. S. Kim, *Chem. Rev.*, 2012, **112**, 6156–6214.

92 S. J. Grabowski, W. A. Sokalski, E. Dyguda and J. Leszczyński, *J. Phys. Chem. B*, 2006, **110**, 6444–6446.

93 J. Dutta, D. K. Sahoo, S. Jena, K. D. Tulsiyan and H. S. Biswal, *Phys. Chem. Chem. Phys.*, 2020, **22**, 8988–8997.

94 L. Maestre, R. Dorel, Ó. Pablo, I. Escofet, W. M. C. Sameera, E. Álvarez, F. Maseras, M. M. Díaz-Requejo, A. M. Echavarren and P. J. Pérez, *J. Am. Chem. Soc.*, 2017, **139**, 2216–2223.

95 Y.-Y. Jiang, T.-T. Liu, X. Sun, Z.-Y. Xu, X. Fan, L. Zhu and S. Bi, *Org. Biomol. Chem.*, 2018, **16**, 5808–5815.

96 A. Frontera, *C*, 2020, **6**, 60.

97 V. R. Mundlapati, D. K. Sahoo, S. Bhaumik, S. Jena, A. Chandrakar and H. S. Biswal, *Angew. Chem., Int. Ed.*, 2018, **57**, 16496–16500.

98 J. Baltrusaitis, E. V. Patterson and C. Hatch, *J. Phys. Chem. A*, 2012, **116**, 9331–9339.

99 K. Arai, M. Noguchi, B. G. Singh, K. I. Priyadarsini, K. Fujio, Y. Kubo, K. Takayama, S. Ando and M. Iwaoka, *FEBS Open Bio*, 2013, **3**, 55–64.

100 O. Dmitrenko, C. Thorpe and R. D. Bach, *J. Org. Chem.*, 2007, **72**, 8298–8307.